



# **Dégradation de l'acier inoxydable soumis à la contrainte : L'influence des contraintes sur la cinétique de passivation, et la cristallographie de la fissuration dans des milieux acides**

Hazem Mubarak

## **► To cite this version:**

Hazem Mubarak. Dégradation de l'acier inoxydable soumis à la contrainte : L'influence des contraintes sur la cinétique de passivation, et la cristallographie de la fissuration dans des milieux acides. Matériaux. École Nationale Supérieure des Arts et Métiers, 2016. Français. ⟨NNT : 2016ENAM0069⟩. ⟨tel-01562914⟩

**HAL Id: tel-01562914**

**<https://pastel.hal.science/tel-01562914v1>**

Submitted on 17 Jul 2017

**HAL** is a multi-disciplinary open access archive for the deposit and dissemination of scientific research documents, whether they are published or not. The documents may come from teaching and research institutions in France or abroad, or from public or private research centers.

L'archive ouverte pluridisciplinaire **HAL**, est destinée au dépôt et à la diffusion de documents scientifiques de niveau recherche, publiés ou non, émanant des établissements d'enseignement et de recherche français ou étrangers, des laboratoires publics ou privés.



HAL Authorization

École doctorale n° 432 : Science des Métiers de l'ingénieur

**Doctorat ParisTech**

**T H È S E**

pour obtenir le grade de docteur délivré par

**l'École Nationale Supérieure d'Arts et Métiers**

**Spécialité “ Science et Mécanique des Matériaux ”**

*présentée et soutenue publiquement par*

**Hazem MUBARAK**

09 décembre 2016

**Dégradation de l'acier inoxydable 304L en milieux acides  
Influence des contraintes sur la cinétique de passivation  
et les mécanismes de fissuration à l'échelle cristalline**

Directeur de thèse :

**Laurent BARRALLIER**, Professeur, Arts et Métiers ParisTech

**Kevin OGLE**, Professeur, Chimie ParisTech

Co-encadrement de la thèse :

**Polina VOLOVITCH**, Maître de conférences (HDR), Chimie ParisTech

**Sébastien JEGOU**, Maître de conférences, Arts et Métiers ParisTech

**Jury**

**M. Vincent JI**, Professeur, Université de Paris Sud

**Mme. Halina KRAWIEC**, Professeur, Université de Sciences et Technologies, Cracovie

**M. Vincent VIGNAL**, Professeur, Université de Bourgogne

**M. Laurent BARRALLIER**, Professeur, Arts et Métiers ParisTech

**M. Kevin OGLE**, Professeur, Chimie ParisTech

**Mme. Polina VOLOVITCH**, Maître de Conférences (HDR), Chimie ParisTech

**M. Sébastien JEGOU**, Maître de Conférences, Arts et Métiers ParisTech

Président  
Rapporteur  
Rapporteur  
Examineur  
Examineur  
Examineur  
Examineur





<b>Résumé Global</b>	<b>1</b>
<b>Dissertation Abstract</b>	<b>15</b>
<b>I. Problem Statement and Proposed Strategy</b>	<b>23</b>
<b>1 State of Art: Stress Corrosion Cracking of Stainless Steel</b>	<b>23</b>
1.1 Corrosion and Degradation of Stainless Steel . . . . .	23
1.1.1 Introduction about corrosion . . . . .	23
1.2 Stainless Steel . . . . .	25
1.2.1 Stainless steel families . . . . .	25
1.2.2 Ferritic stainless steel . . . . .	25
1.2.3 Austenitic stainless steel . . . . .	25
1.3 Corrosion Electrochemistry in Aqueous Solutions . . . . .	26
1.3.1 Basics of aqueous corrosion . . . . .	26
1.3.2 Effect of solution composition on the polarization curve parameters . . . .	27
1.4 Passive Films on Stainless Steel . . . . .	27
1.4.1 Overview . . . . .	27
1.4.2 Passive film composition . . . . .	28
1.4.3 Electrical aspects of passive film . . . . .	28
1.4.4 Non-uniformity in passive film . . . . .	28
1.5 Mechanism of Corrosion Resistance for Stainless Steel . . . . .	28
1.5.1 Effect of elemental composition of the material . . . . .	28
1.5.2 Effect of microstructure and texture . . . . .	30
1.5.3 Effect of mechanical deformation . . . . .	30
1.5.4 Effect of stress on corrosion/passivation . . . . .	30
1.6 Passivation Kinetics of Stainless Steel . . . . .	33
1.6.1 In alkaline and neutral electrolytes . . . . .	33
1.6.2 In acidic electrolytes . . . . .	36
1.6.3 Comments on the $\log(i)$ vs $q^{-1}$ passivation cureves . . . . .	38
1.6.4 Quantification of passivation kinetics . . . . .	41
1.7 Stress Corrosion Cracking (SCC) . . . . .	45
1.7.1 Definition . . . . .	45
1.7.2 Phenomenological description . . . . .	46
1.7.3 Crack initiation . . . . .	46
1.7.4 Pit to crack transition . . . . .	46
1.8 Crack Propagation Mechanisms in SCC . . . . .	46

1.8.1	Dissolution models . . . . .	47
1.8.2	Adsorption based mechanisms: AIDE . . . . .	49
1.8.3	Hydrogen based mechanisms . . . . .	49
1.8.4	Mechanical fracture models . . . . .	51
1.9	Fracture Mechanics of Stainless Steel . . . . .	53
1.9.1	Stress concentration factor . . . . .	54
1.9.2	Fracture modes I, II, and III . . . . .	56
1.9.3	Fracture by SCC . . . . .	57
1.9.4	SCC propagation rate . . . . .	57
1.9.5	Modeling of SCC . . . . .	58
1.9.6	Determination of $K_{ISCC}$ . . . . .	59
1.10	Crystallographic Aspects of SCC . . . . .	60
1.11	Bibliographical Conclusions . . . . .	61
1.11.1	The phenomenological description of SCC . . . . .	61
1.11.2	Quantified modeling of SCC . . . . .	61
1.11.3	Influence of stress on stainless steel passivation . . . . .	62
1.11.4	Influence of the micro-structure crystallography . . . . .	62
1.12	Research Strategy and Specification . . . . .	62
1.12.1	Scope and objectives . . . . .	62
1.12.2	Experimental strategy . . . . .	63
1.12.3	Realization . . . . .	64
1.12.4	Originality . . . . .	64
<b>2</b>	<b>Experimental Techniques</b>	<b>67</b>
2.1	Material Used for Experiments . . . . .	67
2.2	Chemical Composition of the Base Material . . . . .	68
2.2.1	SpectromaXx . . . . .	68
2.2.2	Carbon and sulfur elemental analysis . . . . .	68
2.2.3	Mechanical properties . . . . .	69
2.2.4	Sample shape and dimensions . . . . .	69
2.3	Polarization Corrosion Test . . . . .	70
2.3.1	Linear polarization corrosion test . . . . .	70
2.3.2	Polarization curve of passive materials . . . . .	72
2.4	Experimental Setup . . . . .	73
2.4.1	Conventional electrochemistry . . . . .	73
2.4.2	ICP, AESEC . . . . .	74
2.4.3	Experimental conditions . . . . .	76
2.4.4	Methodology of treating the data . . . . .	78
2.5	SEM, EBSD, and EDS . . . . .	80
2.6	XRD . . . . .	80
2.7	Surface preparation for observation/EBSD . . . . .	80
<b>3</b>	<b>Characterization of the Base Material</b>	<b>81</b>
3.1	Chemical Composition . . . . .	81
3.2	Optical Analysis . . . . .	82
3.3	SEM . . . . .	83
3.3.1	Upper surface and cross-section . . . . .	83
3.3.2	Transverse direction . . . . .	83
3.4	EBSD . . . . .	87
3.5	XRD . . . . .	87
3.6	Tensile Tests . . . . .	91
3.7	Conclusions . . . . .	92

<b>II. Electrochemical Work</b>	<b>93</b>
<b>4 Electrochemical and Corrosion Analysis</b>	<b>93</b>
4.1 Polarization Curves Analysis . . . . .	93
4.1.1 Conventional: stressed/non-stressed . . . . .	93
4.1.2 Summary, results and conclusions . . . . .	115
4.2 Potentio-static Pulse Testing . . . . .	116
4.2.1 Experimental conditions . . . . .	117
4.2.2 Experimental set I: stressed/unstressed samples . . . . .	117
4.2.3 Results: . . . . .	117
<b>5 Passivation Analysis</b>	<b>137</b>
5.1 Potentiostatic Pulse Testing . . . . .	137
5.2 Passivation Rate . . . . .	138
5.3 Passive Film Formation kinetics . . . . .	139
5.4 Passive Film Formation in Acidic Mediums . . . . .	140
5.4.1 Fraction of charge due to Fe dissolution( $f_{Fe}$ ) based on the metallic mass fractions: . . . . .	141
5.4.2 Fraction of charge due to the rest of metallic elements . . . . .	144
5.4.3 Calculating the metallic dissolution fractions based on polarization curve . . . . .	146
5.4.4 Reproducing the current profile during passivation . . . . .	147
5.5 Quantification of Passive Film Quality . . . . .	150
5.6 Influence of Stress on Passivation Kinetics and Film Properties . . . . .	153
5.7 Influence of Stress on Film Thickness and Protection Ability . . . . .	155
5.7.1 Based on charge concept (conventional techniques) . . . . .	155
5.7.2 Based on concentration measurement (AESEC) . . . . .	157
5.8 Conclusions . . . . .	159
<b>III. Mechanics of SCC</b>	<b>161</b>
<b>6 Corrosion Morphology and Cracking Crystallography</b>	<b>161</b>
6.1 Calculation of the Applied Stress . . . . .	161
6.2 Experimental Procedure: . . . . .	163
6.2.1 Immersion tests . . . . .	163
6.2.2 Flow electrochemical cell tests . . . . .	163
6.3 Results and Discussion . . . . .	163
6.3.1 Classical immersion tests . . . . .	163
6.3.2 Flow cell OCP SCC tests . . . . .	168
6.3.3 Chemical composition analysis near the crack tip . . . . .	178
6.3.4 Effect of surface state: polished/non-polished . . . . .	180
6.3.5 SCC under residual stress . . . . .	180
6.3.6 EBSD maps for selected cracks . . . . .	182
6.4 Conclusions . . . . .	183
<b>7 Simulation and Modeling of Cracking</b>	<b>187</b>
7.1 Introduction . . . . .	187
7.2 Do existing Models Cover the Considered Conditions? . . . . .	187
7.3 Semi-Elliptical Cracking Aspects . . . . .	188
7.3.1 Cracking kinetics along ( $b$ ) and ( $c$ ) direction . . . . .	189
7.3.2 Propagation rate along ( $b$ ) vs ( $c$ ) direction . . . . .	189
7.4 Estimation and simulation of cracking statistics . . . . .	191
7.4.1 The upper crack length ( $2c$ ) . . . . .	192
7.4.2 The crack depth ( $b$ ) . . . . .	193

7.5	XRD Analysis of Experimental Strain Fields . . . . .	197
7.5.1	Effect of SCC on applied and residual stress . . . . .	197
7.5.2	Effect of stress relaxation on cracking . . . . .	198
7.6	Conclusions . . . . .	200
<b>IV.</b>	<b>Conclusions and Perspectives</b>	<b>203</b>
<b>8</b>	<b>Conclusions and Perspectives</b>	<b>203</b>
8.1	Conclusions . . . . .	203
8.1.1	Electrochemical statistics . . . . .	203
8.1.2	Statistics of potentiostatic pulse testing . . . . .	204
8.1.3	Passivation kinetics . . . . .	204
8.1.4	SCC fractography and crystallography . . . . .	205
8.1.5	SCC modeling . . . . .	205
8.2	Perspectives . . . . .	206
8.2.1	Electrochemistry . . . . .	206
8.2.2	Passivation kinetics . . . . .	206
8.2.3	SCC kinetics and fracture mechanics . . . . .	207
	<b>Appendices</b>	<b>209</b>
<b>A</b>	<b>Chemical Composition of the Base Material</b>	<b>209</b>
<b>B</b>	<b>Chemical Composition of a Selected Surface Defect</b>	<b>211</b>
<b>C</b>	<b>Simulation of the Experimental Applied Strain</b>	<b>213</b>
<b>D</b>	<b>Granular Statistics by EBSD Analysis</b>	<b>217</b>
<b>E</b>	<b>Electrolyte Preparation</b>	<b>221</b>
<b>F</b>	<b>Derivation of the Dissolution Current Formula</b>	<b>223</b>
<b>G</b>	<b>Multi-Element Corrosion System</b>	<b>225</b>
<b>H</b>	<b>Selection of Potential Zones on the Polarization Curve</b>	<b>227</b>
<b>I</b>	<b>Graphs Related to Passivation Analysis</b>	<b>229</b>
<b>J</b>	<b>Early Surface State During SCC of a Mirror-polished Sample</b>	<b>231</b>

Arts et Métiers ParisTech/Chimie ParisTech  
Ecole doctorale n° 432 : Science des Métiers de l'ingénieur  
Doctorat ParisTech

THESE  
pour obtenir le grade de docteur délivré par  
l'Ecole Nationale Supérieure d'Arts et Métiers  
Spécialité:  
"Science et Mécanique des Matériaux"

2016

*Dégradation de l'acier inoxydable 304L en milieux acides :  
Influence des contraintes sur la cinétique de passivation et les mécanismes de  
fissuration à l'échelle cristalline*

Ce document présente le résumé d'un travail de quatre ans de recherche sur la corrosion sous contraintes (stress corrosion cracking **SCC**) d'acier inoxydable. Cette thèse est un prérequis du diplôme de doctorat dans le domaine des Sciences et Mécanique des Matériaux, accréditée par l'école doctorale de **SMI** (des Sciences des Métiers de l'Ingénieur) de Paris. Le travail expérimental a été tenu dans les laboratoires suivants : « Mechanics, Surfaces, and Materials Processing » (**MSMP**) à l'Ecole Nationale Supérieure d'Arts et Métiers (**ENSAM**) et le laboratoire de Physico-chimie de Surfaces à l'Ecole Nationale Supérieure de Chimie de Paris (**ENSCP**).

## Introduction

La corrosion sous contraintes (**SCC**) est l'un des faits les plus communs de fissuration assisté par l'environnement. C'est un phénomène complexe décrivant la fissuration sous-critique des matériaux, résultant de l'interaction synergétique de facteurs mécaniques, électrochimiques et métallurgiques [79]. Ainsi, le phénomène de SCC est difficile à prévoir, puisqu'il nécessite la co-existence de trois facteurs : contrainte mécanique (appliquée ou résiduelle), matériau susceptible et un environnement corrosif.

L'élimination de l'un de ces facteurs peut empêcher ou baisser le seuil de SCC. Ces trois

éléments devraient être bien définis dans le but d'avoir de sécurité à la conception. Les principaux paramètres liés à l'environnement corrosif sont le potentiel électrochimique, le pH, la présence des ions agressifs (chlorure, etc.) dans l'électrolyte et la température. En ce qui concerne les paramètres mécaniques, ils se résument aux deux points suivants : le type et l'intensité de contrainte. Finalement, les facteurs métallurgiques importants sont d'une part la composition chimique aussi que la forme chimique et la distribution spatiale des éléments d'alliage et des impuretés, qui définira en particulier, la possibilité de l'épuisement des éléments nécessaires à la formation de la couche passive tels que chrome [11].

## Corrosion sous contrainte : état d'art

### Description phénoménologique

L'apparence de SCC a été décrite selon deux catégories de modèles phénoménologiques. La première catégorie concerne des modèles dans lesquels la force motrice de propagation de fissures est la dissolution métallique à la pointe de la fissure. Ces modèles décrivent le processus de propagation de la fissure par des étapes successives de rupture de la couche passive, la dissolution du métal, et la reconstruction en pointe de fissure [162, 183]. En outre, la dissolution qui s'effectue sur la surface successivement exposée après chaque étape de glissements, est intensifiée par la modification de la composition chimique de l'électrolyte au fond de la fissure et cela jusqu'à la nouvelle passivation. La deuxième catégorie des modèles de SCC est celle dans laquelle la propagation de fissure reste une rupture mécanique. Le développement de la fissure peut être divisé en des processus de propagation fragiles et des processus ductiles. Les modèles mécaniques de fissuration ductile abritent la formation d'un tunnel de corrosion et la plasticité localisée activée par la corrosion tandis que les modèles de fissuration fragile englobent la rupture et le clivage-induit par la couche passive [11, 72, 99, 100, 101, 127]. La combinaison des différents mécanismes proposés est possible, particulièrement pendant les différentes étapes de la SCC : de la nucléation de la fissure, à sa propagation et le clivage. L'étude expérimentale des mécanismes de SCC à l'échelle microscopique est compliquée de par : 1) l'existence de plusieurs axes d'interactions multi-échelles entre le matériau et l'électrolyte et 2) des difficultés techniques de l'observation directe de la pointe de la fissure en temps réel. Généralement, les surfaces de rupture de la fissure sont observées ex-situ après la SCC, causant ainsi la perte des détails nécessaires pour étudier la mécanique de la SCC.

### Les modèles quantitatifs de la SCC

Ils existent des modèles qui essaient de quantifier la propagation des fissures et de prédire la possibilité de la SCC. Les modèles existant prennent en compte l'effet synergétique d'oxydation localisé à la pointe de la fissure, et de la mécanique accélérée par l'effet de la contrainte locale [8, 58, 126, 142, 146, 164]. Dans ces modèles, la perte progressive de matière est calculée pendant chaque cycle de rupture du film passif et la repassivation suivante du matériau (reformation du film passif). La fréquence de ces cycles est contrôlée par le taux de la déformation locale près de la pointe de la fissure et le seuil de contraintes mécaniques pour la rupture de la couche passive. En utilisant ce type de modélisation, Shoji a effectué une prédiction cohérente de la cinétique SCC comparée aux tests dans des conditions d'opération en réacteur à eau légère [164]. Ce modèle a été amélioré par D. Macdonald et al. pour prendre en compte la forme approximative semi-elliptique de la fissure produite par la SCC [159]. Ce modèle permet de prévoir que l'orientation de l'axe mineur de la fissure est perpendiculaire à la surface exposée à la corrosion. Cependant, il ne fournit aucune information statistique concernant le ratio des axes de l'ellipse pour des fissures analysées; aucune méthodologie d'évaluation statistique de ces données n'est proposée à ce jour.

Des modèles présentés traitent les aspects mécaniques et la dissolution séparément, aucun

d'eux n'a considéré l'effet direct de la contrainte sur la dissolution métallique active, passivation ou la cinétique de croissance du film passif et les propriétés de la couche passive. En outre, aucun d'entre eux n'a présenté la prédiction de la SCC dans des milieux acides. Pour expliquer, par exemple, le clivage préférentiel le long des plans cristallographiques de bas indices de Miller, ils ne proposent aucune considération pour la microstructure locale du matériau, l'orientation des joints de grain, et l'orientation cristallographique près de la pointe de la fissure, comme cela a été décrit dans les modèles d'émission des dislocations induites par adsorption (adsorption-induced dislocation emission **AIDE**) et de la plasticité localisée améliorée par corrosion (corrosion enhanced localized plasticity **CELP**) (section 1.8).

### **L'influence des contraintes sur la passivation**

Les processus mécaniques et le traitement thermique jouent un rôle important dans le comportement en corrosion, à cause du changement de la microstructure [89] et de la composition locale. Un exemple est celui de la sensibilisation où le chrome est « piégé » sous forme de précipités au joints de grain et devient non-accessible pour la formation du film passif [79]. L'écrouissage d'acier inoxydable a été montré comme un autre facteur qui peut ralentir la passivation [43]. Dans un autre travail il a été montré qu'une grande densité des dislocations produits par l'écrouissage avant le traitement thermique peut bloquer la mobilité du chrome vers les joints de grains et donc réduire l'effet de sensibilisation du matériau à la corrosion sous contrainte [35]. Quelques travaux ont démontré que les contraintes peuvent modifier la structure et l'épaisseur de la couche passive, la résistance de transfert de charge à travers la couche passive, et l'activité électrochimique de la surface [122, 188]. Cependant, ces effets ont été rarement corrélés avec le type et la valeur des contraintes dans le matériau. Nous n'avons pas trouvé d'article présentant des données quantitatives sur la cinétique de passivation de matériaux soumis à des contraintes. Ainsi, aucune donnée n'existe sur l'effet qu'ont les contraintes sur les propriétés de la couche passive.

### **L'influence de la structure cristallographique sur la passivation**

Concernant la cristallographie du SCC des alliages cubiques face centrés (FCC), il est largement accepté que la SCC s'initialise selon des plans  $\{111\}$  de glissement qui ont l'énergie de surface la plus basse et présente donc, de point de vue thermodynamique, la dissolution la moins défavorable dans ces directions. En ce qui concerne les aciers austénitiques, une rupture préférentielle est observée dans la famille de plans  $\{111\}$ . Alors que pour les matériaux ayant faible quantité de nickel la tendance de la rupture concerne plutôt les plans  $\{110\}$ . Ces caractéristiques cristallographiques communs indiquent que la mécanique de la corrosion sous contrainte et l'orientation des fissures sont influencées par la microstructure locale et la cristallographie au voisinage de la pointe de la fissure [116, 117]. Cependant, dans tous les travaux examinés, aucune relation n'a été faite entre la rupture par SCC et la forme de la fissure (élancement de l'ellipse), qui ont des valeurs différentes de  $K_I$ . En outre, aucune considération n'a été faite par rapport à l'influence de la valeur de contrainte sur la cristallographie de fissuration, et aucune donnée statistique n'a été fournie.

## **Objectifs et stratégie du travail de recherche**

### **Objectifs**

L'objectif de ce travail de recherche est de combler les lacunes résumées dans la partie précédente. D'une manière générale, tous les modèles de SCC décrivant les mécanismes de propagation des fissures ont un terme inévitable qui décrit la dissolution chimique et un autre terme mécanique pour expliquer la propagation préférentielle à la pointe de la fissure. Différents modèles ont



tenté de justifier la propagation des fissures dans la SCC et se sont basés sur les quatre raisons suivantes [102] :

1. Les matériaux sous contraintes appliquées ou résiduelles ont une activité chimique plus élevée que ceux soumis à aucune contrainte. Cela implique une plus grande dissolution au voisinage de la pointe de la fissure, et donc, la propagation de la fissure peut être partiellement expliquée par cette dissolution préférentielle. Comme il a été indiqué précédemment, cette hypothèse n'a jamais été vérifiée. En plus, quelques données montrent que les fissures sont développées dans les plans cristallographiques les moins réactifs. Cependant aucune statistique sur des plans cristallographiques par lesquels les fissures se développent n'a encore été présentée.
2. Les contraintes et les déformations sont élevées au voisinage de la pointe de la fissure. Cela conduit à une activation locale des systèmes de glissement au voisinage de la pointe de la fissure provoquant la décomposition de la couche passive, et l'exposition du matériau à une corrosion excessive. De plus, des valeurs élevées de contraintes locales pourraient déstabiliser la couche passive reconstruite sur la pointe de la fissure. Cela entraînerait la formation d'une couche passive sur la pointe de la fissure plus défectueuse que celle se situant sur les zones non soumises aux contraintes. Ces zones sont représentées par les surfaces de rupture. De même, la vérification de cette hypothèse nécessite de trouver un lien entre le type et l'intensité des contraintes et la qualité du film passif ce qui n'a pas été fait.
3. Sur les surfaces de la fissure, la dissolution est limitée en raison de la ségrégation d'éléments plus nobles. Cela se traduit par une diminution de l'activité anodique sur les facettes, et par la formation d'une couche composée avec les éléments de la structure noble présente en surface.
4. Les conditions chimiques locales à proximité de la pointe de la fissure sont plus agressives que celles au voisinage de la fissure. Cela peut être dû à une plus grande concentration d'hydrogène due à un transfert limité ou à une dissolution initiale locale plus intense. Une vérification directe de cette hypothèse nécessite une comparaison de l'activité à proximité de pointe et sur les surfaces ce qui est difficilement réalisable.

## Stratégie expérimentale

A partir des problématiques exposées dans l'approche bibliographique et des objectifs fixés précédemment, des procédures expérimentales alternatives ont été proposées afin de vérifier, chaque hypothèse séparément :

**L'impact de la contrainte sur l'activité électrochimique :** Si le matériau présente une activité plus élevée en raison des contraintes appliquées, cette activité supplémentaire pourrait être détectée par le courant extérieur enregistré lors des essais de polarisation effectués sur des échantillons soumis ou non à des contraintes dans des électrolytes acides (0.5-5 M  $\text{H}_2\text{SO}_4$ ) avec et sans chlorure.

**L'impact des contraintes sur la passivité :** Pour étudier la construction de la couche passive et sa dissolution, il est nécessaire d'effectuer une analyse minutieuse des transitoires de courant de passivation, obtenus lors de la polarisation par une tension de passivation dans des essais potentiostatiques pulsées classiques. Cela devrait être réalisé par un ICP, afin d'obtenir des concentrations quantitatives de la dissolution métalliques. A partir des informations qui seront obtenues sur la cinétique de la construction passive de la couche, son épaisseur, et sa composition chimique.

**La qualité de la couche passive :** Dans certaines conditions de passivation, une couche des éléments nobles peut s'accumuler à la surface et agir comme une barrière de protection tel

que dans certains cas l'accumulation de cuivre métallique sur la surface de l'acier 304 [131, 132]. L'enrichissement de la surface peut être vérifié par l'analyse de données obtenues par AESEC.

**Les conditions d'agressivité locales :** Si l'intensité de la dissolution par rapport aux matériaux sous contrainte est prouvée, les conditions d'agressivité locales (tel qu'une haute concentration d'hydrogène) peuvent être confirmées. Cela implique d'avoir une dissolution plus intensive, une perte locale au niveau du matériau, et une intensité plus élevée de la production d'hydrogène et donc son absorption / adsorption conduisant à la fragilisation localisée. Cela peut expliquer l'abaissement local de  $K_I$  à la pointe de la fissure, ce qui conduit à la rupture. Ceci peut être vérifié à la fois à l'aide des transitoires de courant et des taux de dissolution obtenus à partir des expériences conventionnelles d'électrochimie et d'une approche avec l'ICP avec des échantillons soumis ou non à une contrainte appliquée.

**Les aspects de la fissuration :** L'analyse statistique des fissures après des expériences de SCC permet de cibler le rôle de la grandeur de la contrainte, du pH de l'électrolyte, du contenu en chlorure, et du potentiel appliqué sur la propagation de la fissure et de définir le facteur mécanique ou chimique responsable de la nature de dégradation. Cette approche nécessite une procédure expérimentale et post-expérimentale, par laquelle des données statistiquement valides peuvent être produites. Ces dernières donneront des réponses fiables à propos de la cinétique de fissuration, de la ramification et du changement d'orientation.

Un autre facteur d'intérêt est de corrélérer la morphologie de la fissuration, la charge mécanique appliquée et la microstructure au voisinage de la fissure. Le procédé doit comprendre l'estimation statistique et la validation des mesures effectuées, telles que la longueur de la fissure et la morphologie (ratio des axes de l'ellipse) des fissures elliptiques produites par la SCC, mais également l'orientation cristallographique des plans de la fissure.

**L'interaction mécano-chimique :** La méthodologie développée doit être en mesure de prendre en considération l'influence des variables mécaniques et chimiques sur les différents aspects étudiés de la SCC. Ceci signifie une recherche des corrélations entre la fissuration/corrosion et les variables correspondantes. Ces variables concernent par exemple : l'état de contrainte appliqué avec différentes intensités, l'acidité (pH) de la solution, le contenu en chlorure et l'hydrodynamique de l'électrolyte à la surface du matériau. Des données sur la modification ou non du mode de rupture ou de l'orientation cristallographique, qui se développe selon la grandeur de la contrainte subie par le matériau appuiera les hypothèses sur l'interaction des facteurs mécaniques et chimiques.

**Pour conclure :** L'objectif de ce travail est centré autour de quatre axes à savoir : 1) déterminer si les contraintes résiduelles ou appliquées peuvent être reliées quantitativement à la cinétique de repassivation, 2) vérifier si la dissolution métallique (activité électrochimique) peut être modifiée par la présence des contraintes résiduelles ou appliquées, 3) accumuler une statistique sur les orientations cristallographiques les plus susceptibles d'apparaître lors de la SCC, ainsi que connaître la morphologie et la cristallographie de propagation des fissures dans l'acier 304 L pour différentes valeurs de contraintes de traction et 4) proposer un modèle permettant de lier la distribution des contraintes locales et la morphologie de fissuration.

## La réalisation

L'acier 304 L a été choisi pour cette étude. Des tests de corrosion sur des échantillons sous contraintes et non soumis à des contraintes ont été réalisés. L'étude a été menée en quatre étapes :

1. Adaptation de la cellule électrochimique. Nous avons choisi de mesurer la réactivité des échantillons non seulement en mesurant la réponse électrochimique mais également en essayant de confirmer la construction ou la dissolution du film passif par une mesure directe de la composition de solution à tous les moments de l'expérience. Pour cela nous avons utilisé le couplage d'une cellule électrochimique à circulation avec l'analyse simultanée de la composition chimique de solution par la spectroscopie d'émission atomique par ICP

(AESEC, atomique emission spectroelectrochemistry) (section : 2.4.2). La cellule existante de AESEC a été utilisée pour des échantillons avec et sans contraintes de traction uniaxiale contrôlée par le rayon de courbure de support. Pour réaliser ces expériences il a fallu :

- Résoudre les problèmes relatifs à : la conception, au confinement de la solution, à l'écoulement du liquide, au contrôle de la nature et à la grandeur des contraintes appliquées.
  - Valider les résultats obtenus avec cette cellule par des essais effectués avec des systèmes sans circulation de l'électrolyte (cellule stagnante).
2. Caractérisation de matériaux de base. La microstructure et la composition chimique du matériau a été caractérisées en utilisant la microscopie optique et la microscopie électronique à balayage (MEB) couplées avec la spectroscopie d'énergie dispersés (EDS). La cristallographie locale a été obtenue grâce à l'analyse par diffraction des électrons rétrodiffusés (EBSD) et la diffraction de rayons X (XRD) qui a été employée pour l'analyse de la contrainte « moyenne ». En plus d'une analyse spatiale statistique des concentrations élémentaires sur la surface, la composition chimique du matériau a également été vérifiée. Les propriétés mécaniques ont été analysées en utilisant l'essai de traction classique le long du sens du laminage, transversale et directions longitudinales.
  3. Tests des matériaux sous contraintes et sans contrainte en conditions corrosives avec l'aide de deux types d'expériences :
    - Des expériences sur la SCC où la fissuration de l'échantillon est produite afin d'effectuer une étude sur la morphologie post mortem de la surface de la fissure, les aspects cristallographiques de la fissuration et la cinétique/mécanique de la rupture. Cela implique une analyse SEM, EBSD, EDS des fissures produites. Le champ des contraintes appliquées et relaxées par la SCC ont été analysés à l'aide des méthodes XRD diffractométriques.
    - Des mesures électrochimiques afin de détecter s'il y a un effet des contraintes sur les vitesses de dissolution élémentaires et sur le courant total de la corrosion en utilisant des méthodes conventionnelles et l'approche AESEC. Les résultats ont été exploités pour comprendre la formation et la déstabilisation de la couche passive d'oxyde.
  4. L'analyse des résultats. L'application des résultats obtenus pour répondre aux questions spécifiées requises pour modéliser la SCC. Cela comprend l'analyse des champs de contraintes avant et après la fissuration, la fissuration cristallographie, la cinétique de propagation, et la ramification des fissures. En plus de la cinétique d'oxydation en surface, et de l'influence des contraintes sur les processus chimiques de surface, tout en abordant également des aspects de la rupture.

## Originalité

L'originalité de ce travail de recherche est le couplage pluridisciplinaire des aspects mécaniques et chimiques de la corrosion sous contrainte. En plus, l'introduction des analyses statistiques sur la cristallographie de la fissuration et le lien entre la distribution de contraintes locales et le développement des fissures.

Les essais de corrosion avec et sans contraintes ont été effectuées, en utilisant les différents états de contraintes, avec une mesure (in-situ), simultanée du courant de corrosion et de la composition chimique de l'électrolyte. Ainsi, l'interaction synergétique entre les aspects mécaniques et chimiques est recherchée expérimentalement. Ce fut le cas pour la cinétique d'oxydation et les propriétés des couches passives d'une part et la cristallographie, ainsi que les aspects de propagation de la fissure d'autre part.

Finalement, l'analyse XRD diffractométrique des contraintes / résiduelles ou appliquées ont été réalisées pour définir l'état mécanique du matériau initial, après la déformation de l'échantillon, et éventuellement après le test de corrosion sous contrainte afin de démontrer la relaxation des contraintes au cours de l'essai.

## Structure et résumé de la thèse

La structure de cette thèse peut être divisée en quatre principales parties :

### Partie I : Problématique et stratégie proposée

Cette partie contient trois chapitres. Tout d'abord, un **résumé global** du travail réalisé. Ensuite, le problème est énoncé et pour finir, une présentation rapide de la méthodologie et des objectifs est proposée.

Le **chapitre 1** représente un état d'art de la problématique de corrosion sous contrainte. Il commence par une introduction sur la corrosion, puis une présentation des matériaux peu sensibles à la corrosion : les aciers inoxydables. Les bases de l'électrochimie sont abordées dans cette partie, avec la définition des principaux termes et méthodes tels que les courbes de polarisation mais également un rappel des paramètres qui les affectent.

En outre, le phénomène de passivation de l'acier inoxydable est développé en abordant la composition du film passif ainsi que les propriétés de ce film. En raison de leur importance par rapport à ce travail, les facteurs qui influencent la formation et les propriétés de la couche passive sont détaillés : composition chimique du matériau, composition et microstructure locale, facteurs mécaniques, y compris : l'écrouissage, traitement thermique, et contraintes appliquées.

De même, les modèles existants sur la cinétique de passivation dans des milieux alcalins et acides sont expliqués, ainsi que les paramètres de la quantification. Par la suite, la SCC est définie et une brève bibliographie spécifique aux mécanismes apparaissant lors de ses différentes étapes : l'amorçage, la transition de l'amorçage à la fissure, et éventuellement les modèles de propagation de la fissure ont été discutés.

Une partie importante de ce chapitre est consacrée à la rupture mécanique, où le concept de facteur d'intensité,  $K_I$ , est considéré, mais également le facteur d'intensité de contrainte sous SCC,  $K_{ISCC}$ . Dans ce contexte, les modèles quantitatifs de SCC, qui tiennent compte de la dissolution et des facteurs mécaniques, sont discutés. Le chapitre se termine par un résumé des données sur la cristallographie de la SCC. Enfin, les objectifs du projet de recherche sont présentés et la stratégie est proposée mais également l'originalité ainsi que la méthodologie expérimentale.

Le **chapitre 2** est consacré aux techniques expérimentales, avec un rappel de leurs principes scientifiques, et leur utilisation dans nos recherches. Les schémas du dispositif expérimental sont également donnés avec la description opérationnelle utilisée. La production expérimentale des essais de la polarisation est expliquée, avec un rappel des termes électrochimiques qui concernent ce sujet.

La technique de l'AESEC [131], avec le couplage entre la cellule d'écoulement électrochimique et l'ICP, est présentée. La méthodologie proposée pour traiter le signal de sortie [130], permettant d'obtenir les taux de dissolution élémentaires, a été clarifié. Les procédures expérimentales fréquemment utilisées, telles que la polarisation et les programmes de potentiomètres dynamiques cycliques, sont aussi largement documentées. Les essais de base de caractérisation mécanique et la composition chimique sont expliqués, ainsi que leur procédure expérimentale, et le traitement des données effectuées. Le chapitre fournit également un rappel sur les techniques de caractérisation microstructurale du matériau : SEM, EBSD, EDS et XRD.

Le **troisième chapitre** présente les résultats de la caractérisation du matériau de base. La présence de précipités contenant du soufre et du manganèse est détectée sur la surface, ces précipités étant distribués aléatoirement. Ils représentent des sites préférentiels pour la corrosion

car ils empêchent la formation d'un film passif homogène, ceci est très certainement à l'origine des problèmes de dispersions statistique des résultats obtenus lors des essais électrochimiques.

## Partie II : L'analyse électrochimique

Cette partie traite des essais potentiodynamiques de polarisation linéaire et de polarisation cyclique; les analyses et leurs résultats sont présentées dans deux chapitres. Dans le **chapitre 4**, la différence statistique est recherchée entre la réponse électrochimique des échantillons sous contrainte ( $\sigma = 280$  MPa) et d'autres sans contrainte. Le comportement est testé avec plusieurs électrolytes et avec différents états de surface.

**Résultats :** Bien que l'influence du polissage miroir de la surface est détectée par la technique de mesure, l'effet des contraintes sur l'activité de surface n'est pas détecté pour la majorité des cas traités. Cependant, les contraintes dans le matériau expliquent une différence mesurable de la charge de passivation.

La charge de passivation est définie par la quantité d'échange de charge lors de la polarisation par une tension de passivation jusqu'à arriver à un état passif prédéfini. L'état passif ( $j_p$ ) était défini à  $j = j_p = 1 \text{ mA.cm}^{-2}$  comme montré dans la figure 1 où la densité de courant totale est  $j_p$ .

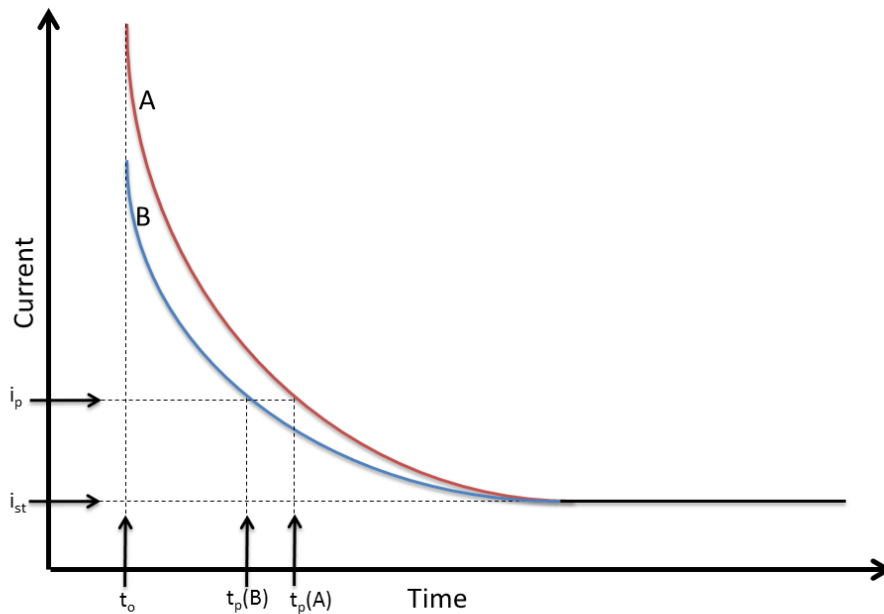


Figure 1: Le critère de repassivation défini à  $i_p$ . Le test A nécessite plus de temps pour atteindre l'état passif ( $i_p$ ) que le test B [90]

Puisque  $q_p$  est l'intégral du courant total  $j_p$ , cette quantité reflète la charge nette consommée par les réactions chimiques de surface au cours de la transition de l'état actif à l'état passif. Ainsi, plus cette charge est importante, plus la matière doit être oxydée pour former la couche de passivation avec la qualité de protection identique. La charge est plus grande pour les échantillons sous contraintes, la reconstruction de la couche passive s'avérant plus compliquée pour des matériaux sous contraintes.

Le **chapitre 5** est consacré à l'analyse de la phase de repassivation dans des expériences présentées dans le chapitre 4. Dans les solutions acides, la majeure partie du courant anodique mesuré pendant la passivation est due à la dissolution du matériau, et seulement une petite partie à des réactions d'oxydation formant la couche passive [109, 132].

Des mesures in-situ sont effectuées pour des transitoires de corrosion et des vitesses de

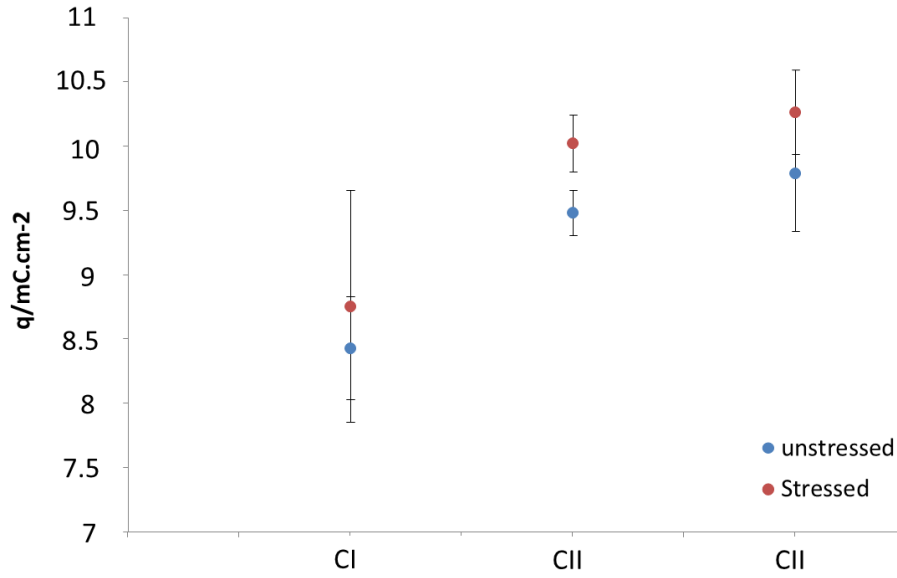


Figure 2: Illustration du moyen de la charge de passivation pour les trois cycles de passivation des échantillons sous contrainte et non-soumis à la contrainte.

dissolution élémentaires utilisant un couplage de la cellule électrochimique avec l'analyse de la solution par spectroscopie d'émission atomique (AESEC) [132].

L'AESEC est également utilisé pour mesurer les courants élémentaires des éléments métalliques et soustraire ce courant de dissolution du courant total externe mesuré. A travers ce calcul, nous avons séparé la partie de courant dans laquelle seule l'oxydation de la couche passive a eu lieu.

En utilisant les données sur des fractions des différents ions présents dans la couche passive calculés ainsi, le modèle de conduction ionique sous tension élevée (HFIC) est mis à jour afin de calculer l'épaisseur de la couche passive, en utilisant la charge correspondante au courant consommé lors des réactions d'oxydation. La pente des courbes représentée sur la figure 3 (entre  $j = (-3 \text{ et } -5) \text{ mA.cm}^{-2}$ ) donne une mesure directe du taux de passivation et la conductivité ionique de la couche passive, qui est inversement proportionnelle à la qualité de cette couche [90, 33].

**Résultats :** En utilisant le HFIC modèle, l'analyse quantitative de l'évolution de la densité du courant en fonction du temps a révélé l'exact zone d'application du HFIC modèle, (zone II sur la figure 4). En plus, l'analyse a précisé le zones de nucléation (zone I) et décomposition (zone III) de la couche passive comme les montre la figure 4. Ceci a été mobilisé pour calculer la vitesse de passivation en utilisant la pente  $cBV$  dans zone II, où le HFIC modèle est applicable.

Il a été conclu par la valeur  $cBV$  (figure 5) que la contrainte a causé une réduction mesurable de la vitesse de passivation, qui se traduit par l'augmentation de la dissolution métallique avant l'obtention de la passivation. Cela veut dire que l'effet de la contrainte est de produire une couche moins protectrice mais également plus épaisse ( $1,640 \pm 0,031 \text{ nm}$ ) par rapport à ( $1,580 \pm 0,028 \text{ nm}$ ) dans le cas d'un échantillon non soumis à la contrainte.

### Part III : Mechanics of SCC

Dans cette partie, la corrosion sous contrainte est produite pour différentes concentrations de solutions d'acide sulfurique, contenant des chlorure. Les fissures obtenues ont été analysées à l'aide de la microscopie électronique à balayage (MEB), et la diffraction d'électrons rétrodiffusés (EBSD).

L'objectif du **chapitre 6** est d'examiner la morphologie et la cristallographie des fissures

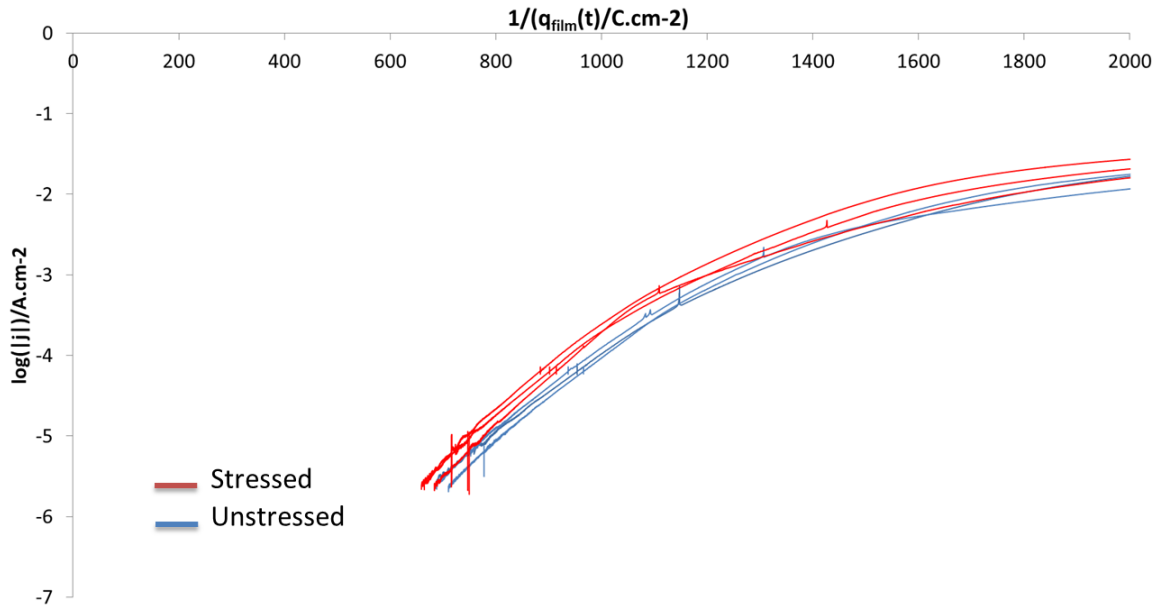


Figure 3: Courbes du deuxième cycle de passivation anodique pour les tests (sous contrainte et non soumis à la contrainte) dans 2 M  $\text{H}_2\text{SO}_4$ .

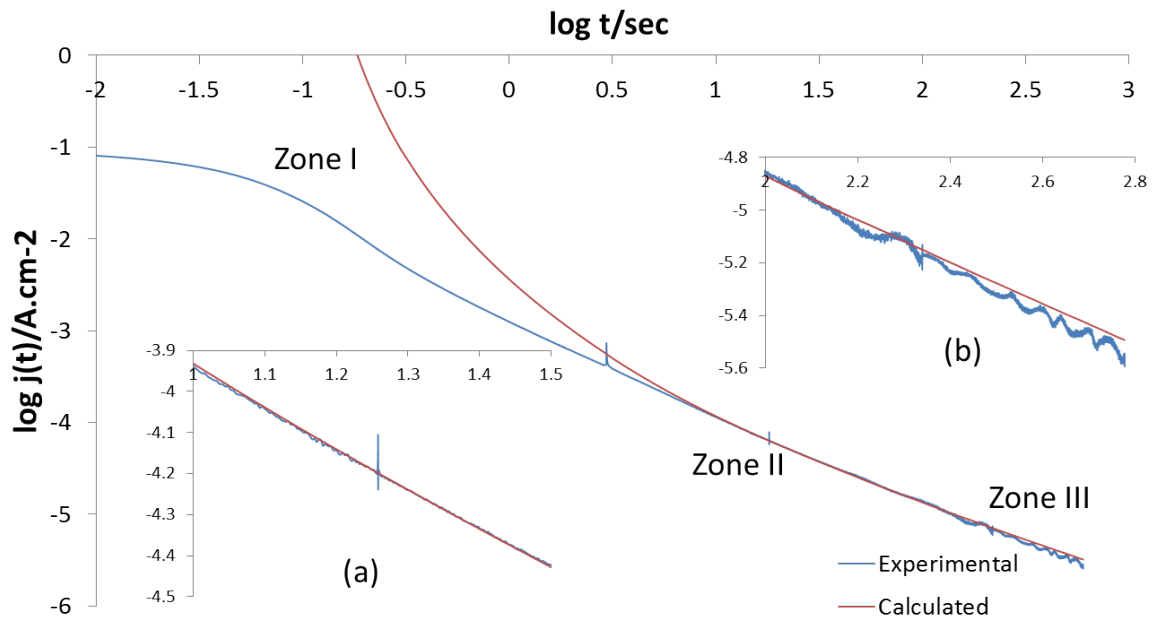


Figure 4: Densité de courant de passivation,  $j$ , calculé à partir de l'épaisseur de la couche passive, par rapport aux données expérimentales pour le cycle de passivation CII, pour l'acier inoxydable 304L, dans 2 M  $\text{H}_2\text{SO}_4$ .

obtenues, et la cinétique de l'évolution de la SCC. Une méthode est proposée pour accéder à la cristallographie de la fissuration est basée sur la technique EBSD, en utilisant les trois angles d'Euler et l'orientation de la fissure sur la surface, comme les montre la figure 6. Des preuves de l'influence des microstructures caractéristiques sur la direction de la rupture ont été prises en considération.

**Résultats :** L'observation des fissures au MEB a révélé des plans de glissement successifs et les dissolutions qui en découlent sur les facettes des fissures obtenues.

Il a été démontré que, pour les tests de SCC sous  $\sigma = 250$  MPa à 2 M  $\text{H}_2\text{SO}_4$  + 2 M de NaCl, la fissuration a eu lieu préférentiellement sur les plans  $\{111\}$  pour 37% des cas, et 48% des cas sur  $\{110\}$  plans.

Pour le système cubique à face centrée, les plans  $\{111\}$  sont ceux sur lesquels le glissement se produit. Cependant, les plans de rupture pourraient être de la famille  $\{110\}$  en raison de l'accumulation égale de dislocation sur les plans  $\{111\}$  primaires et conjugués [105]. Cependant, en réduisant les contraintes appliquées et en utilisant des conditions de corrosion moins sévères que ci-dessus, des résultats différents sont obtenus, comme indiqué dans les tableaux 1 et 2. Les origines cristallines des fissurations dans différents cas ont été discutées.

Table 1: Statistiques de la coupe transversale sur les plans de rupture préférentiels, avec  $\sigma = 210$  MPa, dans 2 M  $\text{H}_2\text{SO}_4$  + 0.5 M NaCl.

Famille des plans	$\{111\}$	$\{211\}$	$\{102\}$	$\{110\}$	$\{100\}$	$\{221\}$
Nombre	11/43	7/43	12/43	8/43	3/43	2/43

Table 2: Statistiques de la surface supérieure sur les plans de rupture préférentiels, avec  $\sigma = 210$  MPa, dans 2 M  $\text{H}_2\text{SO}_4$  + 0.5 M NaCl.

Famille des plans	$\{111\}$	$\{211\}$	$\{102\}$	$\{110\}$	$\{100\}$	$\{221\}$
Nombre	10/78	23/78	22/78	12/78	3/78	8/78

Les observations faites au MEB ont montré que la vitesse de la fissuration a une relation non linéaire avec le temps d'exposition. Des piqures surfacique apparaissant entre 2 et 8 heures, les longueurs des fissures moyennes étaient (21, 27, 93, 245, 360)  $\mu\text{m}$  pour des temps d'exposition de (16, 21, 42, 88, 125) heures respectivement. Par la suite, nous avons accéléré la cinétique initiale de SCC grâce à l'application d'une impulsion de potentiel cathodique constant optimisé. En effet les expériences sur des échantillons soumis seulement à leur contrainte résiduelle initiale ont donné lieu au SCC avec une cinétique très lente. Une autre observation a été faite lors de ces tests. L'apparition des premières piqures surfaciques corrélées avec la stabilisation du potentiel électrochimique mesuré, et ensuite aucune modification du potentiel n'a été observée lors de l'apparition des premières fissures (entre 16 et 21 heures). Cela montre l'impossibilité de détecter le phénomène du SCC par la mesure de potentiel.

Le **chapitre 7** présente une introduction à la simulation de la SCC et la modélisation des paramètres du ce modèle. En industrie, l'estimation de la vitesse de propagation de la fissure est basée sur les dimensions de la fissure, son facteur d'intensité de contrainte  $K_I$ , ainsi que les charges appliquées.

Abaqus est utilisé pour proposer une modélisation multi-échelle de la fissuration sur l'ensemble de l'échantillon/support courbé. Pour les fissures elliptiques étudiées dans notre cas, la modélisation nécessite une valeur précise de leur rapport d'élongation ( $b/c$ ). Ainsi, une méthodologie est proposée pour estimer la validité des mesures effectuées de  $b$  et  $c$ . Les champs de contraintes résiduelles/appliquées sont déterminés pour un échantillon à son état initial non déformé, après la déformation et après l'essai de SCC d'une durée de 125 heures.



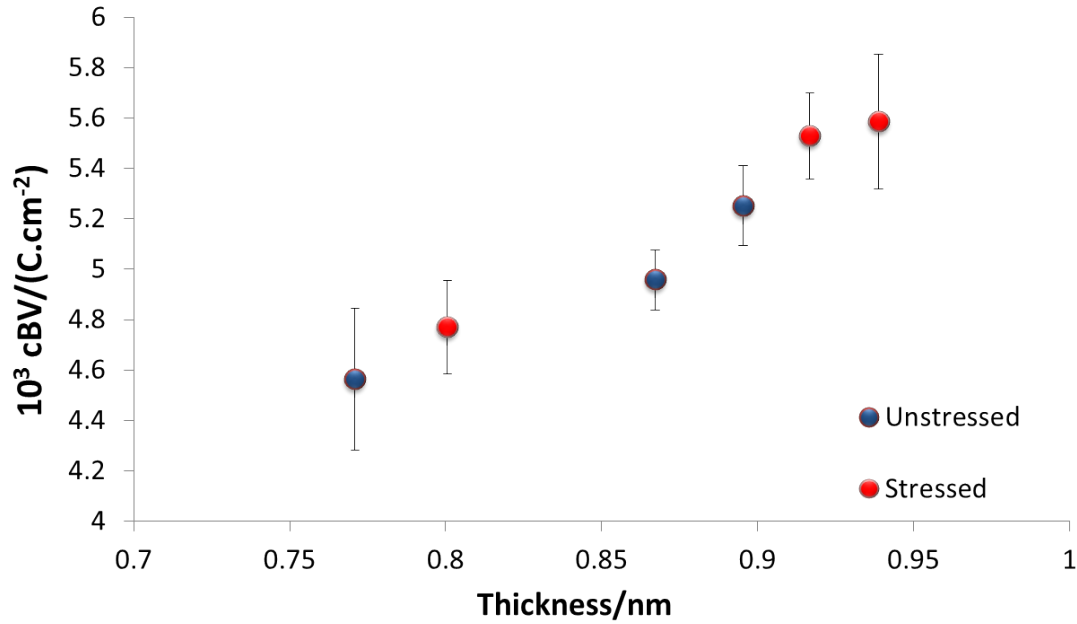


Figure 5: Epaisseur de la couche passive (à  $j = 1 \text{ mA.cm}^{-2}$ ) (d'échantillons sous contraintes et non soumis aux contraintes) dans  $2 \text{ M H}_2\text{SO}_4$ .

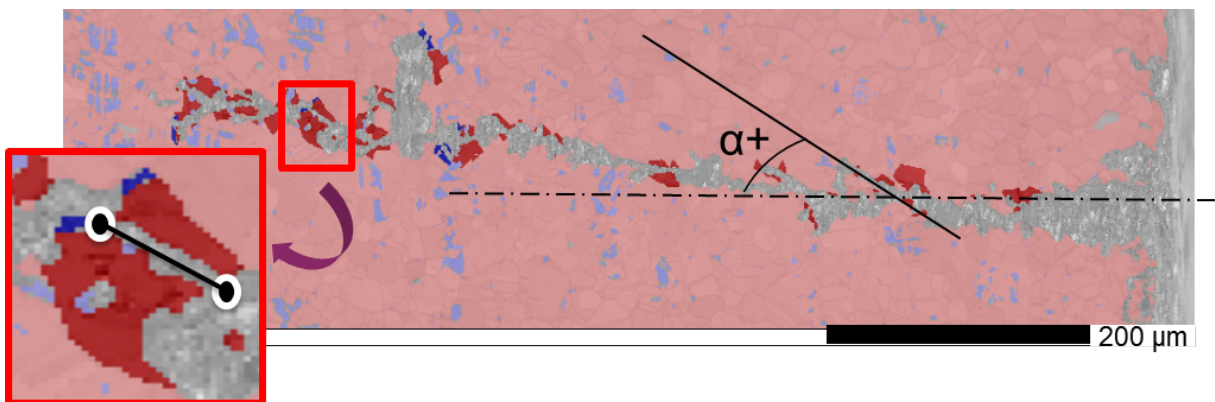


Figure 6: Isolation des grains subis TGSCC de la carte de l'EBSD.

**Résultats :** La simulation macroscopique d'une contrainte de traction sur l'échantillon a confirmé les valeurs calculées précédemment. L'estimation de la longueur mesurée et la profondeur des fissures a révélé des statistiques valables en dimension  $c$ , cependant peu de données statistiques étaient disponibles pour l'analyse de la profondeur de la fissure ( $b$ ). Les statistiques de  $b$  ont été améliorées par une simulation MATLAB. La simulation commence par la génération d'une fissure représentative ayant les dimensions expérimentales  $b_{avg}$  et  $c_{avg}$ . Cette fissure représentative est ensuite coupée aléatoirement sur sa longueur  $2c$ . Pour chaque coupe, la profondeur correspondante ( $L$ ) est calculée. La production d'un nombre suffisamment élevé de sections aléatoires donne une distribution statistique plus représentative à la profondeur de la fissure, comme le montre la figure 7.

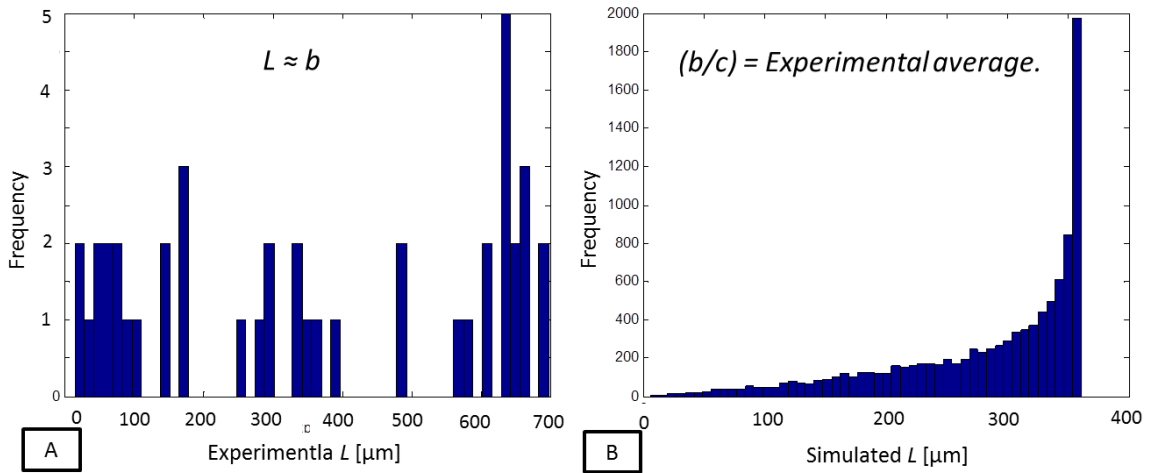


Figure 7: Résultats de simulation de la profondeur de la fissure ( $L$ ). (A): Les données expérimentales, en supposant  $b = L$  du test considéré. (B): La distribution statistique améliorée par la simulation de la profondeur des fissures.

L'analyse des contraintes par XRD (figure 8), avant et après SCC, permet d'expliquer certains aspects de fissuration, tels que l'arrêt de fissures et son orientation macroscopique.

#### Part IV: Conclusions et perspectives

Cette partie est développée dans le **chapitre 8**, qui traite l'ensemble des contributions fournies par cette recherche. On y trouve également des perspectives pertinentes de l'étude.

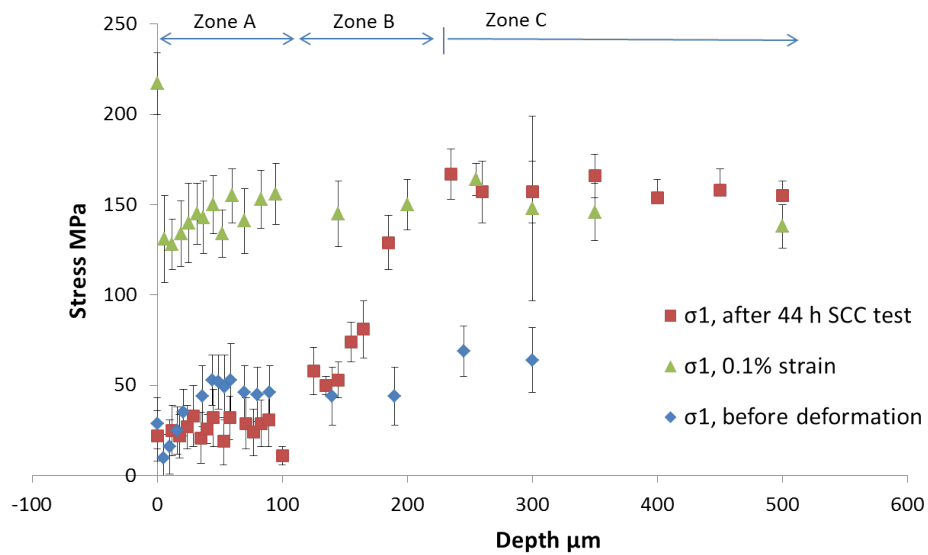


Figure 8: Analyse des contraintes (résiduelles/appliquées) en fonction de la profondeur : (a) Contraintes résiduelles initiales de l'échantillon avant déformation (b) Contraintes après la déformation sur le support. (c) Contraintes après essai de SCC durant 125 heures.

Arts et Métiers ParisTech/Chimie ParisTech  
Ecole doctorale N° 432: Science des Métiers de l'ingénieur  
Doctorat ParisTech

A dissertation submitted in partial fulfillment  
of the requirements for the degree of:  
Doctor of Philosophy  
in  
Materials Science and Mechanics

Arts et Métiers ParisTech  
2016

*Degradation of 304L stainless steel in acidic solutions :  
Influence of stress on passivation kinetics, and cracking mechanisms at  
crystallographic scale*

This document represents a summary of the work done through four years of research on the stress corrosion cracking of stainless steel. This dissertation is done as a partial fulfillment of the doctorate of philosophy degree in the domain of Materials and Solid Mechanics accredited within the doctoral school of **SMI** (Sciences des Métiers de l'Ingénieur) of Paris. The experimental work was held in the labs of Mechanics, Surfaces, and Materials processing (**MSMP**), Ecole Nationale Supérieure d'Arts et Métiers (**ENSAM**), and the laboratory of Physico-Chemistry of surfaces, Ecole Nationale Supérieure de Chimie de Paris (**ENSCP**).

## Originality

The originality in the present research is the possibility to multi-axially study SCC mechanical and chemical aspects. The mechanical and electrochemical aspects of interest are analyzed by statistical basis. By performing corrosion and SCC tests with different stress states, in-situ measurement of corrosion current and elementary concentration of leaching solution for stressed or relaxed samples. Thus, the synergistic interaction between the mechanical and chemical aspects is experimentally sought. This was the case equally for what refers to oxidation kinetics and passive film properties from one side, and the cracking crystallographic and propagation kinetics from the other side.

SEM pre and post-experimental observations were performed to understand the corrosion morphology and fractography of samples having different surface preparations and stress states, tested in different electrolytes. This was combined with the crystallographic and chemical maps analyzing selected zones of interest using EBSD and EDS respectively.

Last but not least, XRD analysis of the applied/residual stresses was conducted for the initial material state, after straining the sample, and eventually after the SCC test.

## Dissertation Structure and Summary

The structure of this dissertation can be divided into four main parts as given in the following sections.

### Part I: Problem statement and proposed strategy

In this part, the four chapters are included. **The first chapter** represents an overall summary of the research work, a summary of the problem in consideration, and a quick presentation of the proposed methodology and objectives.

**Chapter 1** is the literature review of SCC. It starts with an introduction about corrosion, then a presentation of the stainless steel. The basics of electrochemistry are then discussed, with the definition of the main parameters such as the polarization curves, and the factors affecting it. Furthermore, the passivation of stainless steel is discussed for its composition, electrical aspects. Due to their relative importance to the present work, the factors affecting passive film formation and properties were reviewed such as the bulk composition of the material, its microstructure, and mechanical factors, including: cold working, heat treatment, and applied stress. Likewise, the existing models of passivation kinetics in alkaline and acidic mediums were explained, along with the quantification parameters. Right after, SCC was defined and a review was made about its different stages: initiation, pit-to-crack transition, and eventually the crack propagation models. An essential part of this chapter was dedicated to fracture mechanics, where the concept of stress intensity factor,  $K_I$ , was considered, and how SCC stress intensity factor,  $K_{ISCC}$ , relates to this. In this context, the quantified models of SCC which consider the dissolution and mechanical factors were discussed. The chapter ends with a review of the crystallography of SCC and the bibliographical conclusions. Last but not least, the strategy and objectives of the present research project are presented, and the originality along with the proposed experimental methodology.

**Chapter 2** is devoted to the experimental techniques, where a reminder is given to their scientific principle and their use in our research. Moreover, the schematic diagrams of the experimental setup are given along with the detailed operational description. Experimental production of the polarization tests was explained, along with a reminder about the related electrochemical terms. A review was made about the technical description of AESEC [131], with the experimental set-up coupling the electrochemical flow cell to ICP. The methodology proposed to treat the output signal [130] to obtain the elemental dissolution rates was clarified. The chapter provides a reminder about the involved material characterization techniques: SEM, EBSD, EDS, and XRD. The frequently used experimental procedures such as the polarization and the cyclic potentiodynamic programs were documented as well. Basic tests of mechanical and chemical material characterization were explained along with their experimental procedure, and data treatment. **The third chapter**, and last in this part, gives the results of the basic material characterization.

### Part II: Electrochemical work

This part treats the electrochemical linear and pulse potentiostatic corrosion tests, where the analysis are presented in two chapters. In **chapter 4**, statistical difference is sought between

stressed samples ( $\sigma = 280$  MPa) and others in their relaxed states. Different electrolytes and surface states have been used in this study.

**Results:** Though the influence of mirror-polishing the surface was detected by the measuring technique, the effect of the applied stress on surface activity was not detected for the treated cases, except for the passivation charge  $q_p$ . This quantity of charge exchange,  $q_p$ , the surface undergoes starting from the application of the passivation pulse until getting to a predefined passive state  $j_p$ , as shown in Fig. 9. In this study,  $j_p$  is set to  $1 \text{ mA.cm}^{-2}$ , where  $j$  is the total current density. The result is illustrated in Fig. 10.

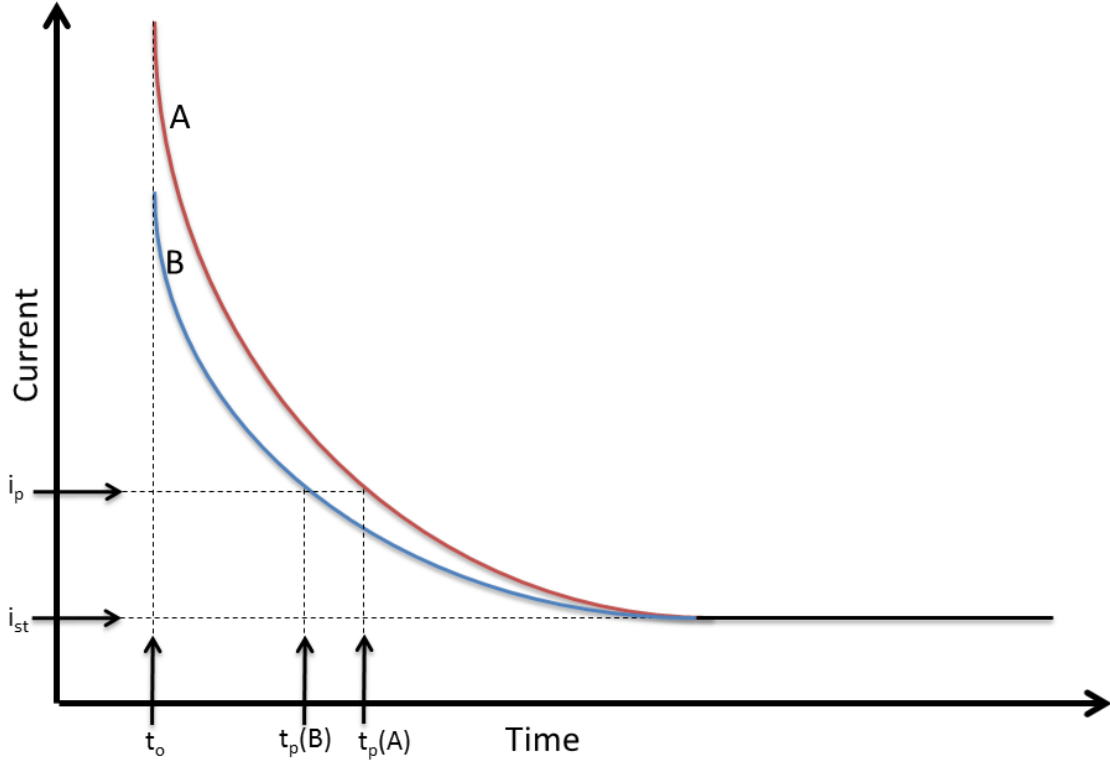


Figure 9: The passivation criterion defined at  $i = i_p$ . Test A requires less time to get to the passive state defined by  $(i_p)$  than the case for test B [90]

Since  $q_p$  is the integration of the total current  $j_p$ , this quantity reflects the net of the surface reactions during the transition from an active to a passive state. Thus, the higher this charge is the more intense surface reactions, which was the case for stressed samples.

**Chapter 5** was devoted to studying the passivation period of the experiments presented in chapter 4. In acidic solutions, the major part of anodic current measured during passivation is due to metallic dissolution, and only partially to oxidation reaction forming the passive film [109, 132]. In-situ measurements were performed for the corrosion transients and elemental dissolution rates using Atomic Emission Spectroelectrochemistry (AESEC) [132]. This was used to calculate the current portion due to metallic dissolution. Having this calculated made it possible to separate the current portion spent on passive film formation from the total external current measured by conventional electrochemical techniques. By this result, high field ion conduction model (HFIC) was updated to calculate the passive film thickness using the charge corresponding to the current consumed in the oxidation reaction. The slope of the curves shown in Fig. 11 gives a direct measure of the passivation rate and thus film ionic conductivity, which is inversely proportional to the protection quality of the passive film [90, 33].

**Results:** Quantitative analysis revealed the zone of application of the HFIC, besides the

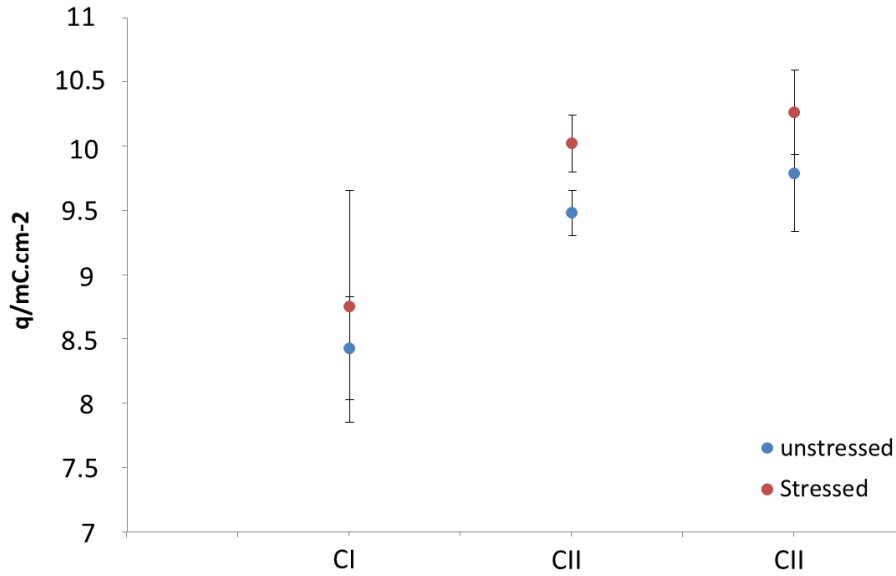


Figure 10: Illustration of the average passivation charge for the three passivation cycles of stressed and unstressed samples.

zone of passive film nucleation, and break up as shown in Fig. 12. This was used to calculate the corresponding passivation rate using the slope  $cBV$  representing the passivation rate. It was concluded that stress caused a measurable reduction of the passivation rate, as indicated by the  $cBV$  value, producing a thicker, yet less protective, a passive film of  $(1.64 \pm 0.031)$  nm compared to  $(1.58 \pm 0.028)$  nm in the case of relaxed samples (Fig. 13).

### Part III: Mechanics of SCC

In this part of the research, SCC was produced in different concentrations of chloride containing sulfuric acid solutions. The obtained cracks were analyzed using both Scanning Electron Microscope (SEM) and Electron Backscatter Diffraction (EBSD). **Chapter 6** was concerned in the morphology and the crystallography of the obtained cracks from one side, and the kinetics of SCC evolution from another side. A method was proposed to access the cracking crystallography based on EBSD technique, using the three Euler angle and the orientation of the crack on the scanned surface, as shown in Fig. 14. Evidences of the influence of micro-structural features on the the cracking direction were taken into consideration.

**Results:** Crack observation using SEM revealed clear traces of successive slipping planes and consequent dissolutions on the facets of the obtained cracks. It was shown that, for SCC tests under  $\sigma = 250$  MPa in 2 M  $H_2SO_4 + 2$  M NaCl, cracking preferentially took place over  $\{111\}$  for  $(3/4)$  of cases and  $\{110\}$  for the rest. These results are in agreement with recent SCC models, such as CELP. For face-centered cubic crystals, 111 planes are those over which slipping occurs. However, rupture planes could be of 110 family due to equal dislocation-pile-up on the primary and conjugate 111 planes [105]. However, different results were obtained for lower applied stress and less severe corrosion conditions, as given by Tables 3 and 4.

Table 3: Cross-section statistics about the preferential rupture planes, where  $\sigma = 210$  MPa in 2 M  $H_2SO_4 + 0.5$  M NaCl.

Plane family	$\{111\}$	$\{211\}$	$\{102\}$	$\{110\}$	$\{100\}$	$\{221\}$
Counts	11/43	7/43	12/43	8/43	3/43	2/43

Table 4: Upper surface statistics about the preferential rupture planes, where  $\sigma = 210$  MPa in 2 M  $\text{H}_2\text{SO}_4 + 0.5$  M NaCl.

Plane family	$\{111\}$	$\{211\}$	$\{102\}$	$\{110\}$	$\{100\}$	$\{221\}$
Counts	10/78	23/78	22/78	12/78	3/78	8/78

SEM observation shows that crack propagation has a non-linear relation with exposure time. Starting from surface pits appearing between 2-8 hours to (21, 27, 93, 245, 360)  $\mu\text{m}$  crack lengths for an exposure time of (16, 21, 42, 88, 125) hours respectively. Acceleration of SCC kinetics was possible by the application of an optimized constant cathodic potential pulse. Experiments of samples subjected only to their initial residual stress resulted in SCC with very slow kinetics.

Registering the open circuit potential (OCP) during the SCC tests revealed that the OCP gets stable by the first crack initiation at (16-20) hour. Hence, the OCP value is invariant during the crack propagation, which adds another difficulty in characterizing the electrochemistry of SCC.

**Chapter 7** represents an introduction to the simulation and modeling of selected parameters related to SCC. In service, the estimation of the crack propagation rate is based on the present crack dimensions, its corresponding stress intensity factor  $K_I$ , as well as the applied loads. As an initiation to multi-scale finite element modeling of the cracking from a mechanical point of view, the sample/curved support assembly was built in Abaqus environment. For the elliptical cracks in our case, modeling requires the right value of their aspect ratio ( $b/c$ ). Thus, a methodology was proposed to estimate the validity of the conducted measures of  $b$  and  $c$  dimensions. In addition to this, the residual/applied stress fields were produced for the sample at its initial undeformed state, after the stress application, and after SCC test of 125 hours.

**Results** The macroscopic simulation of the tensile stress on the sample confirmed those calculated earlier. Estimation of the measured length and depth revealed valid statistics for the dimension  $c$ , but no enough statistics were available for the crack depth ( $b$ ). To improve the statistics of the measured crack depth  $b$ , a Matlab simulation is introduced. The simulation starts by generating a representative crack having the average experimental dimensions  $b$  and  $c$ . This representative crack is then sectioned at random locations over its length  $2c$ . For each random section, the corresponding depth ( $L$ ) is calculated. Producing high enough number of random sections gives the appropriate statistical distribution to the crack depth as shown in Fig. 15.

Measurement of stress profiles by XRD technique (Fig. 16) explained some cracking aspects, such as the crack arrest, and its macroscopic orientation.

## Part IV: Conclusions and perspectives

This part is given in **chapter 8**, which discusses the overall contributions provided by this research, the conclusions, and the future perspectives.



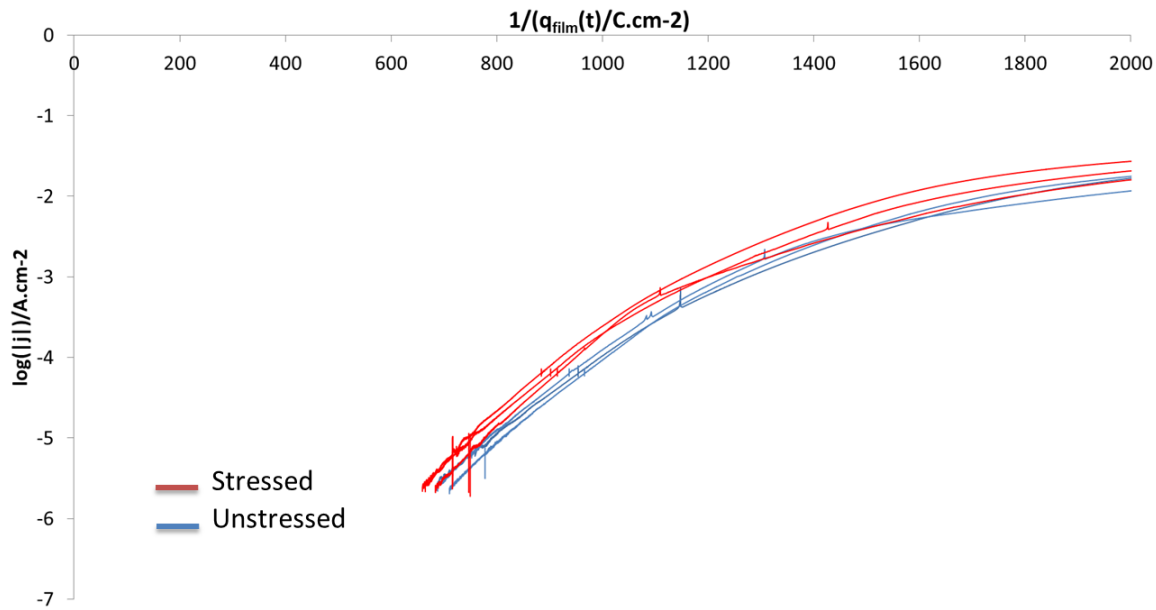


Figure 11: The second cycle passivation anodic curves for stressed and unstressed tests in 2 M  $\text{H}_2\text{SO}_4$  plotted on  $\log j(t)$  vs  $1/q(t)$  axis.

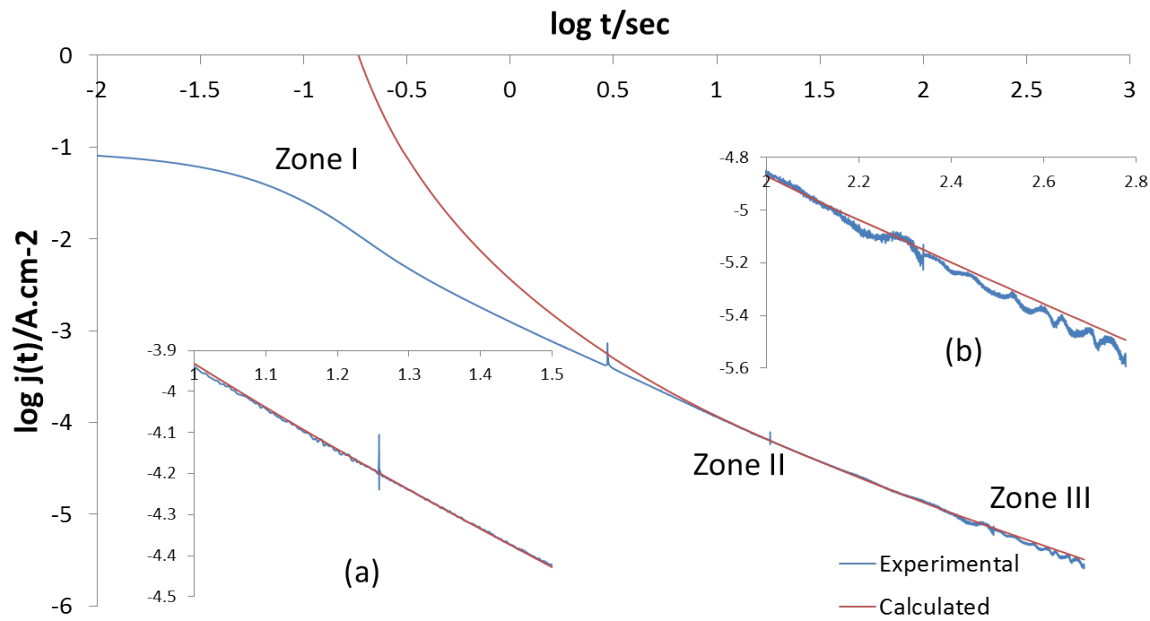


Figure 12: The passivation current density,  $j$ , as calculated based on the passive film thickness, compared to that recorded experimentally for CII passivation cycle on an unstressed 304L stainless steel in 2 M  $\text{H}_2\text{SO}_4$ .

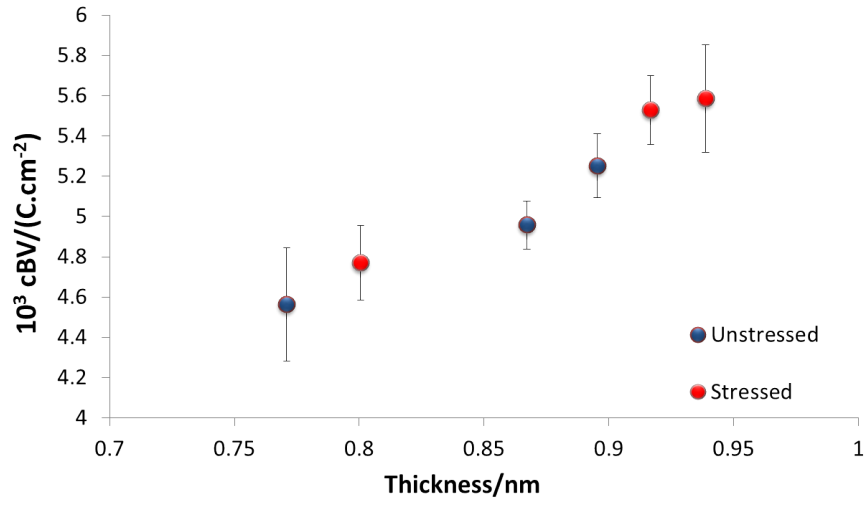


Figure 13: Passivation thickness vs  $cBV$  of stressed and unstressed samples during the three passivation cycles in 2 M  $\text{H}_2\text{SO}_4$  electrolyte.

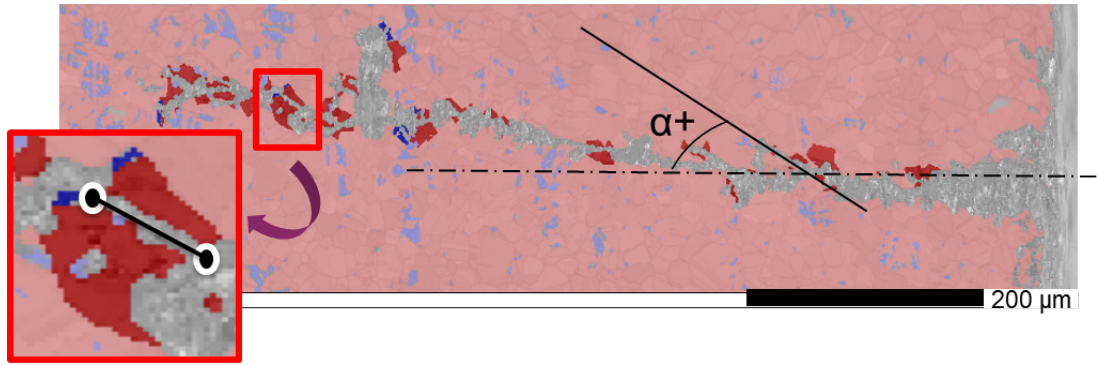


Figure 14: Isolation of TGSCC grains in EBSD map.

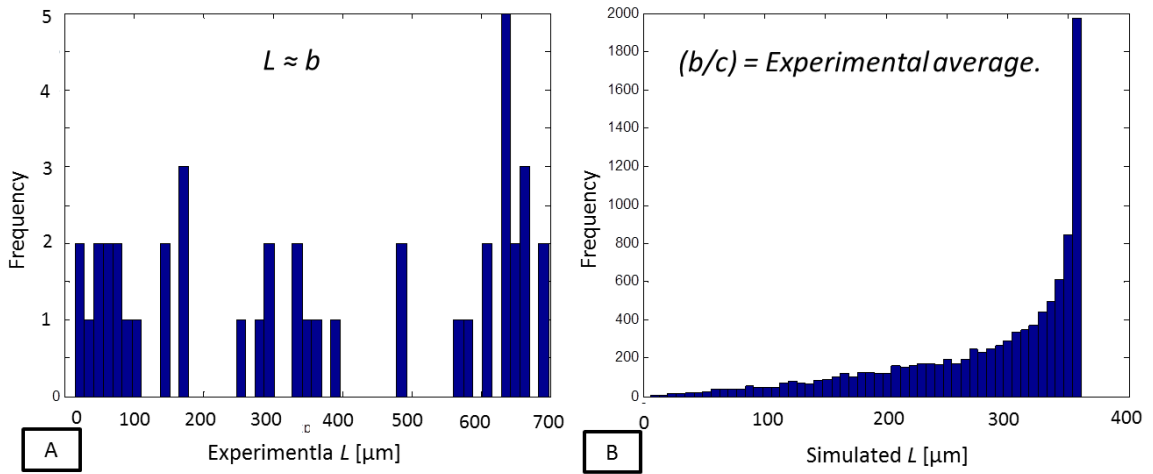


Figure 15: Results of  $(L)$  simulations. (A): The experimental data, assuming  $b = L$  of the considered test. (B): The improved statistical distribution of crack depth produced by randomly sectioning a crack having  $(b, c) = (L_{\text{avg}}, c_{\text{avg}})$ .

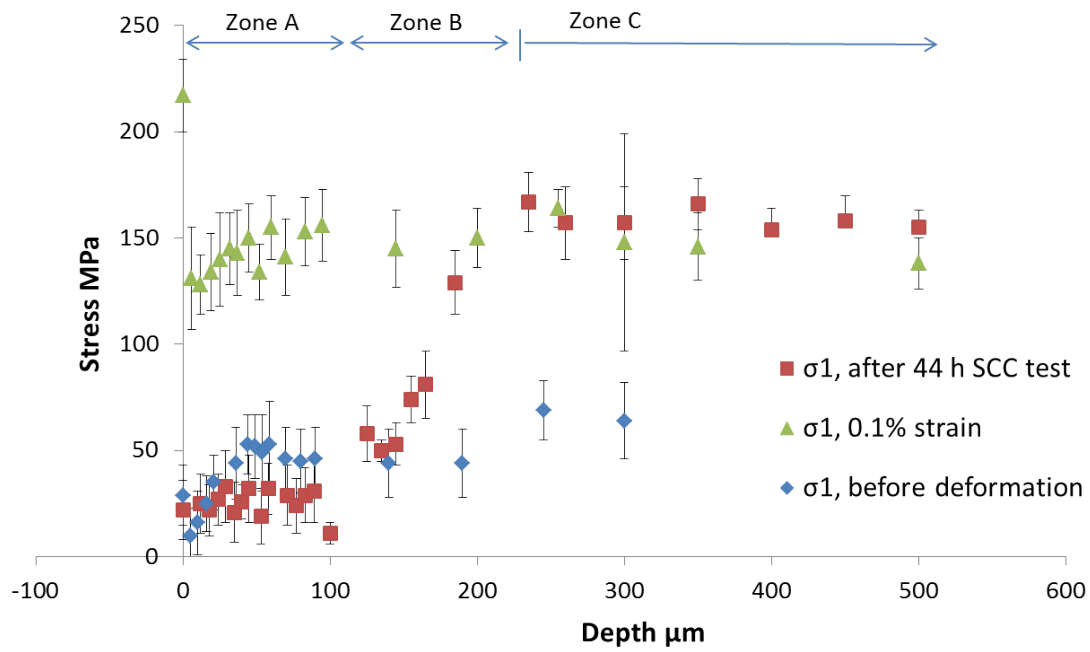


Figure 16: Stress field calculated by XRD measurement of: (a) The residual stress of the initial sample before straining. (b) The applied stress after deformation on the curved support. (c) The stress field after SCC 125 h test.

---

## State of Art: Stress Corrosion Cracking of Stainless Steel

---

### 1.1 Corrosion and Degradation of Stainless Steel

This chapter aims to give a reminder about basics of metallic corrosion, specifically; stainless steel. It starts with the basics behind the electrochemical nature of corrosion, the parameters controlling it, and how electrochemistry is used to better understand and predict metallic corrosion. Then, a summary of the most remarkable SCC models providing a phenomenological description of the main mechanisms of stainless steel corrosion. To understand cracking in corrosive environments, it was essential to go through fundamental concepts of fracture mechanics, and the engineering parameters controlling them. The chapter ends with a bibliographic conclusion in addition to the proposed research strategy.

#### 1.1.1 Introduction about corrosion

Corrosion is best defined as the deterioration of materials due to reactions with their environments [11, 63, 154, 168, 191]. Materials sensitive to corrosion include metals, polymers, and ceramics. In practice, these materials are the essence of all parts used for the construction of machines, process equipment, and many other manufacturing products. Corrosive environments are usually liquids, even though certain solid-solid reactions might be considered as corrosion under special conditions. The concept of corrosion can be better understood by stating some examples like [144]:

- The material degradation observed as steel and cast iron rusting in water or humid air. A famous example of this the corrosion of domestic and industrial water tanks and supplying pipes, and all other exposed steel structures.
- In automotive cooling systems, where the cooling systems made of copper, aluminum, and cast iron corrode.
- Turbine blades corrosion in gas turbines as they interact with hot combustion gasses.

Metallic corrosion can be classified into three major groups [11]:

1. Aqueous (Wet) corrosion: in this kind of corrosion, the corrosive environment is water with dissolved species.
2. Corrosion in fluids other than water; such as molten metals and fused salts.

### 3. Dry (chemical) Corrosion, where corrosion takes place in a dry gas environment.

In our current study, corrosion of metals is of the main interest, austenitic stainless steel specifically.

Different corrosion types are encountered in all materials application depending on the surrounding environment, as illustrated in Fig. 1.1 [11].

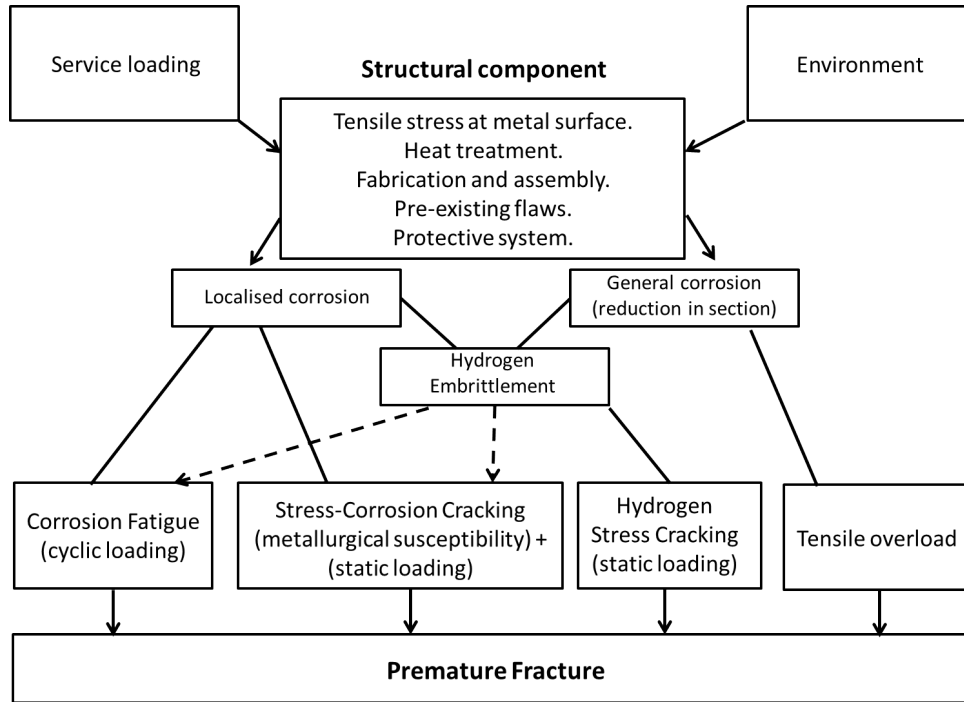


Figure 1.1: Environmentally induced corrosion leading to component failure. From Donald O. in [11].

Following the definition of corrosion stated before, mechanisms of material degradation due to the interaction with its environment are varied. In general, corrosion happens at the atomic, molecular, or ionic transport process taking place at the material interface. These transport processes usually consist of more than one defined step. The slowest step of those is the one of interest, as it mainly determines the rate of overall corrosion, and this rate, of course, should be as low as possible. The transport processes cannot be observed directly on their atomic scale, so it is necessary to find other measurements, which indirectly indicate these mechanisms. Examples of corrosion measurement are the following [11, 18]

1. Rate of weight or dimension change.
2. Rate of corrosive product buildup in the environment.
3. Changes in the surface as observed by optical or electron microscopy.
4. Changes of mechanical or physical properties of the material.
5. For electrochemical corrosion, measurement of potential and current can give a direct indication about the corrosion.

Due to its importance in our study, the following section will explain in detail the electrochemistry of corrosion of stainless steel.

## 1.2 Stainless Steel

Stainless steels are defined as iron-based alloys with at least 10.5 % Cr content [11]. Having this high chromium percentage with the presence of other alloying elements, stainless steels provide a remarkable corrosion resistance [86]. This made stainless steel an attractive material used in all industrial applications, for either mild or severe conditions are expected [128].

### 1.2.1 Stainless steel families

Following the different crystal structure and strengthening properties, stainless steels are classified into five families. Each family has its own mechanical properties and corrosion resistance. These five families are ferritic, austenitic, martensitic, duplex, and precipitation hardening stainless steel.

In the following sections, the ferritic and austenitic stainless steel families are defined for their main properties, and a with a particular emphasis on 304L stainless steel which is the material used throughout this research.

### 1.2.2 Ferritic stainless steel

Ferrite has a body-centered cubic structure and it is classified as magnetic. This family of materials is known for its high yield strength but low ductility and work hardenability. It passes through the transition from ductile to brittle behavior over a narrow temperature range. This transition can happen at ambient temperature with high carbon and nitrogen content. Its solubility for interstitial elements is yet extremely low. This family of stainless steel is very resistant against chloride stress corrosion cracking, making it a very suitable material for thermal transfer applications.

### 1.2.3 Austenitic stainless steel

Face-centered cubic is the crystal structure of austenitic stainless steel. This change in the crystal structure can be accomplished by the aid of austenite stabilizers, such as nickel, manganese, and or nitrogen. It is nonmagnetic and shows relatively low yield strength. It has high ductility, rapid work-hardening rates, and high toughness.

Austenitic stainless steel, especially grade 304, is a commonly used material due to its favorable mechanical properties and its easy production. Chromium content in this stainless steel is limited due to processing difficulties. Adding molybdenum thus comes as an alternative to improve its corrosion resistance. Nitrogen addition improves the stability of austenite phase. Thanks to this addition, it's possible to produce austenitic stainless steel with 6 % Mo for extra corrosion resistance in chloride environments.

Welding and longer-term thermal exposure can sensitize the steel and make it susceptible to intergranular corrosion. This is due to chromium carbide precipitation at grain boundaries during the thermal exposure, leaving the adjacent areas with depleted chromium content. Sensitization can be limited by lowering the carbon content to less than 0.03 %, or using stabilized grades with additions of carbide-stabilizing elements such as titanium and niobium.

The problem of chloride SCC shows up in the common austenitic grades such as 304 and 316. All austenitic grades have a certain degree of susceptibility, but most grades with high-nickel and high molybdenum grades are sufficiently resistant to stress corrosion cracking for a wide range of engineering applications.

In the present work, the metal chosen for the experimental work is austenitic stainless steel of grade 304L as named by the American Iron and Steel Institute (AISI), or S30400 following the designation of the Unified Numbering System (UNS). The prefix "L" in 304L refers to the low

carbon content in this grade compared to that of 304 stainless steel. This reduction of carbon gives this grade higher resistance to SCC as will be explained later in section 1.5.1.

According to AISI standards [35, 17], the elemental composition of 304L stainless steel is given Table 1.1.

Table 1.1: Elemental composition of 304L stainless steel according to AISI standards

Element	Cr	Mn	Ni	C	Si	P	S
Weight %	18-20	2	8-12	0,03	1	0,045	0,03

## 1.3 Corrosion Electrochemistry in Aqueous Solutions

### 1.3.1 Basics of aqueous corrosion

In aqueous corrosion, the simplest mechanism is that the metallic atoms at the corrosion environment enter the solution as metal ions. Electrons liberated from the metal are conducted through the metal to sites where they get consumed by species in contact with the metal. In more complicated cases, compounds such as hydroxides, oxides, or sulfides precipitate as a result of the metal ion combination with other species in the solution, or those ions can move through the solution by forming complex ions [11].

Corrosion process therefore consists of an anodic and a cathodic reaction, as shown in the Fig. 1.2 [18]:

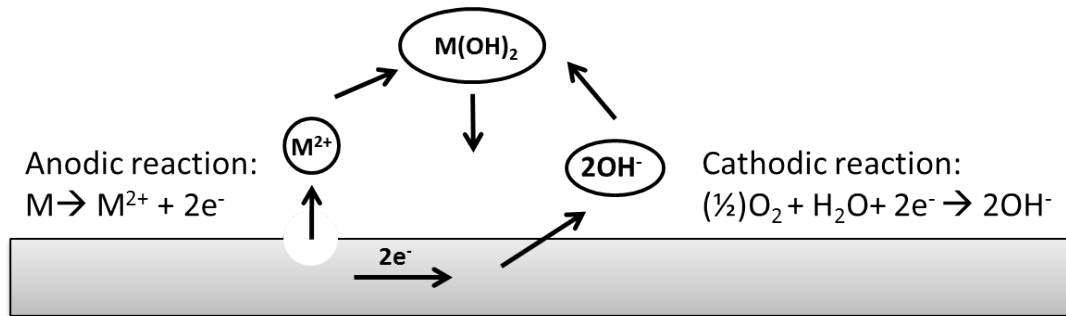


Figure 1.2: Metallic aqueous corrosion in an electrolyte containing oxygen. From [18].

In the oxidation (anodic) reaction, the metal is dissolved as  $M^{2+}$  ions and transfers to the electrolyte. The (cathodic) reaction in this example is the reduction of oxygen. The dissolution of the metal in the anodic reaction releases electrons, which are conducted through the metal to cathodic reaction areas where they are consumed.

Fig. 1.2 represents the corrosion electrochemical cell. The force that drives the corrosion reaction in this cell is the cell voltage, which is represented as the potential difference between the cathode and anode.

There are certain conditions to be satisfied in order for this corrosion circuit to operate. The first to mention is the conductivity of the electrolyte, which represents the liquid corrosive environment. The transfer of ions through the material closes the electrical circuit, and thus the second condition of the conductivity of the material in contact with the corrosive environment. Under these conditions, the metal dissolves by wet corrosion, and the mechanism of this corrosion is electrochemical.

Normally, in neutral environments, the dominating cathodic reaction is oxygen reduction. Other electrolyte conditions can make hydrogen reduction an important cathodic reaction, or the reduction of carbonic acid  $H_2CO_3$  as is the case in oil and gas production.

### 1.3.2 Effect of solution composition on the polarization curve parameters

A polarization curve is like a fingerprint that is a characteristic of the combination of the metal and environment at which it was produced. The polarization curve shape is a function of the nature of the anodic and cathodic reactions taking place at different applied potential values. These reactions differ in their types and rates according to factors like the applied potential, the acidity level, and the presence or not of certain species in the corrosive environment. An example of 304 stainless steel polarization curves produced with different concentrations of  $\text{H}_2\text{SO}_4$ , and the potential sweep rates as shown in Fig. 1.3 (A) and (B) [4].:

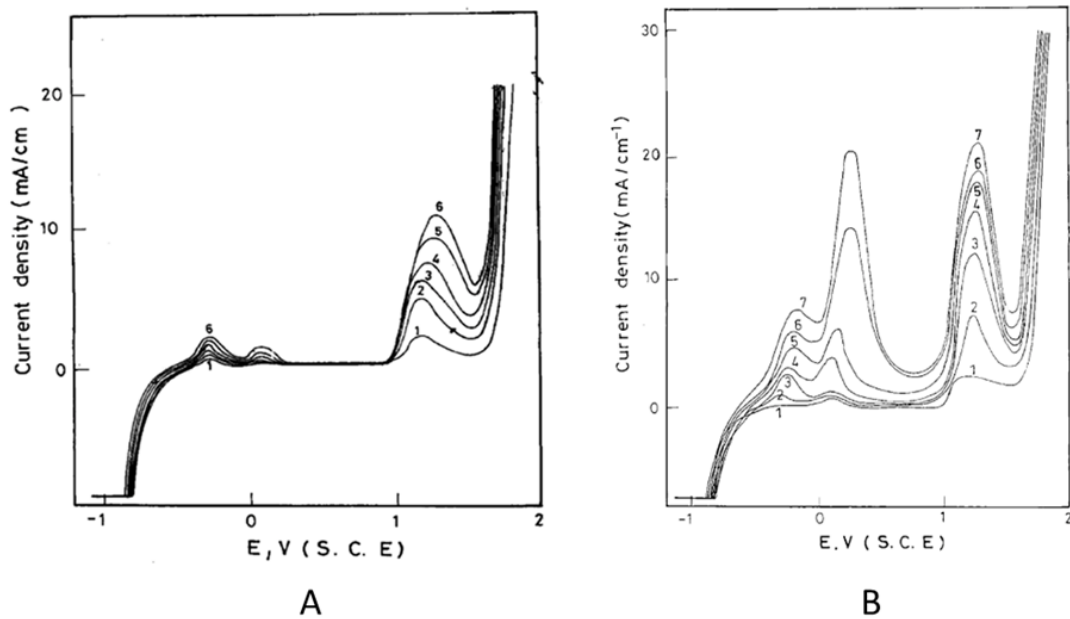


Figure 1.3: Polarization curves of 304 stainless steel produced at  $25^\circ\text{C}$  (A): using a sweep rate of  $50 \text{ mV.s}^{-1}$  to check the effect of  $\text{H}_2\text{SO}_4$  concentrations on the polarization curve. (1): 0.1 M, (2): 0.3 M, (3): 0.5 M, (4): 0.7 M, (5): 0.9 M, (6): 1 M. (B): using a 0.5 M  $\text{H}_2\text{SO}_4$  solution to check the effect of different scan rates on the polarization curve. (1):  $10 \text{ mV.s}^{-1}$ , (2):  $50 \text{ mV.s}^{-1}$ , (3):  $100 \text{ mV.s}^{-1}$ , (4):  $250 \text{ mV.s}^{-1}$ , (5):  $500 \text{ mV.s}^{-1}$ , (6):  $750 \text{ mV.s}^{-1}$ , (7):  $1 \text{ mV.s}^{-1}$ . From [4].

## 1.4 Passive Films on Stainless Steel

### 1.4.1 Overview

Iron-chromium alloys are of considerable technical interest because of their corrosion resistance which is attributed to their ability to form a protective passive layer at sufficiently high chromium content. Though the passive oxide film less than 5 nm thick, it is very adherent to the surface and exhibits a remarkable chemical stability. Though, with sufficiently aggressive environments, this film starts to break-up locally which allows material degradation at those locations.

Research has shown that for alloys of high chromium percentages such as 15%, chromium shows a dominating effect in the overall properties of the alloy [135, 163]. For such alloys, a passive film forms over the surface granting better corrosion resistance and acting as a barrier between the alloy and the corrosive environment, which protects the alloy against further material degradation.



### 1.4.2 Passive film composition

It is well accepted now that in the passive and pre-passive potential range, iron is preferentially dissolved from the alloy's surface. Consequently, chromium oxide accumulates on the surface in the form of Cr(III) through this affected layer of dissolution, which defines the passive layer [19, 87, 88, 68, 75, 113].

The passive film was proved to form by simultaneous oxidation of the iron and chromium along with a selective dissolution of the iron [84, 85, 46, 87].

The passive film has a bi-layer structure. The inner layer consists of mixture of iron and chromium oxides  $\text{Cr}_2\text{O}_3$ , while the outer layer is a hydroxide film of  $\text{CrOOH}$  or  $\text{Cr}(\text{OH})_3$  [6, 113, 134, 196]. The thickness of the passive film measured by XPS, or AES is in the range of 1.2 to 3 nm [87]. Nevertheless, the measured thickness depends on many factors such as the applied potential during the passivation, anodizing time, and the used electrolyte. In addition to this, a local variation of the environment around the passive film is possible during measurements made by XPS and AES for example, which might modify the film thickness [33]. For a certain chromium percentage in the alloy, the passive film shows different corrosion resistance depending on the film formation process, and the structure of the film. These parameters can be altered by small additions of other alloying elements. Enrichment of the passive film with these additional elements is not sufficient to explain the improved corrosion resistance [74, 73]. Recent studies have shown that the crystallization and chromium enrichment and nickel content can affect the crystallization rate of the passive film [114].

From another point of view, external factors can influence greatly the film thickness, composition, and chromium content. First to mention is the passivation potential [62, 75, 77, 137], the nature of the electrolyte in contact with the alloy's surface [113, 136, 62, 77], and also the surface annealing treatment [6].

### 1.4.3 Electrical aspects of passive film

From an electrical point of view, passive films forming on stainless steels are well accepted to have semiconducting properties. This feature acts as a key mechanism of protection. The inner layer of the passive film is formed of p-type, while the outer is of n-type. Semi-conductivity is attributed to having  $\text{Cr}_2\text{O}_3$  [65] in the inner layer in addition to chromium vacancies and oxygen excess [189]. On the other side of the outer layer  $\text{Fe}^{2+}$  ions in interstitial sites [66, 29, 30], some oxygen vacancies [103, 104, 166], and could be due to hydrogen atoms captured by the film [148].

### 1.4.4 Non-uniformity in passive film

Chemical and electronic structures of the passive film are often non-uniform along the surface of the alloy. Therefore, it's expected to have some local special properties on this film. A recent work has revealed sub-micrometer surface heterogeneities, acting as a precursor location for intergranular corrosion on stainless steels of grade 304L and 316L. These heterogeneities were attributed to having sub-micrometer sulfide inclusion in the passive film [43]. Another evidence of the formation of oxide/hydroxide heterogeneities was observed during anodic scan within the passive region of the polarization curve [111, 112].

## 1.5 Mechanism of Corrosion Resistance for Stainless Steel

### 1.5.1 Effect of elemental composition of the material

The effect of the main alloying elements on the corrosion resistance and other properties of stainless steel will be discussed. The focus will be for austenitic stainless steel as it's the subject of this work [11]

### ***Chromium***

This is the principal element in forming the passive film. Though other elements can change the efficiency of chromium in forming the passive film, but it's the presence of chromium which defines the alloy of stainless steel. The minimum content of chromium at which the passive film is observed to form is 10.5 %, but at this level, the passive film is only sufficient to resist mild corrosive environments. Increasing its content to 17-20 % highly improves the quality and stability of the passive film as the case for austenitic stainless steels. On the other hand, a very high content of chromium has an adverse effect to the mechanical properties, fabricability, weldability, and the use of the alloy in thermal applications. Therefore, other elemental content must be altered to further improve the corrosion resistance of stainless steel.

### ***Nickel***

This element stabilize the austenitic structure, granting better mechanical properties and easier fabrication. This element enhances repassivation, especially in reducing environments, and gives better corrosion resistance in mineral acids. At percentages of 8–10 %, the material is susceptible to SCC, but raising nickel content to 30% can improve this character on the contrary. It improves a lot of mechanical properties such as yield strength, toughness, and resistance to reducing acids. For ferritic stainless steel, it has the effect of increase the susceptibility to SCC in concentrated solutions of magnesium chloride.

### ***Manganese***

In association with nickel, manganese has a similar effect as nickel. Resistance to galling wear is one of the special features gained by high manganese content. But care should be taken not to replace all nickel with manganese. At such condition with interaction with sulfur, it produces manganese sulfide, affecting directly pitting corrosion resistance.

### ***Molybdenum***

It plays an important role with chromium in the stability of the passive film in the presence of chlorides. It grants an effect of increased resistance to the initiation of pitting and crevice corrosion. No definitive mechanism has yet been provided on the way molybdenum plays this protection role [109]. Slightly additional percentage of Mo can improve the corrosion and healing properties. Such is the difference between 304L and 316L stainless steel. Though the fact that both Auger electron spectroscopy (AES) and X-ray photo-electron spectroscopy (XPS) showed the presence of molybdenum in the resulting passive film, was depleted at the film-electrolyte interface [109]. As was proposed by [62], the presence of molybdenum raises the electric field through the film. This causes the dissolution to accelerate in the earlier passivation process, which brings up the onset of passivation earlier, and eventually render the material more resistant to chloride induced pitting for example.

Extra notes on the role of Mo in corrosion protection of stainless steel in acidic media are provided at the end of section 1.6.2.

### ***Carbon***

It allows hardenability by heat treatment, which is they key function in martensitic stainless steel. Otherwise, carbon has the effect of reducing corrosion resistance of stainless steel as it reacts with chromium. It's also very bad for the toughness in ferritic stainless steel.

### ***Nitrogen***

In austenitic stainless steel, it improves the resistance against pitting corrosion. It strengthens the steel due to retarding the formation of  $\sigma$  phase of chromium-molybdenum. By minimizing chromium and molybdenum segregation, it proves to be very important for the duplex steels, in addition to increasing its austenitic content. It reduces the mechanical properties of ferritic stainless steels.

### 1.5.2 Effect of microstructure and texture

Due to incorrect heat treatment, stainless steel microstructure can undergo changes affecting its mechanical and corrosion properties. Two essential related aspects are to be discussed here, namely: sensitization and intermetallic phases.

**Sensitization:** Sensitization is considered the most serious problem due to the process of carbide precipitation at grain boundaries. A process affecting austenitic stainless steel as it's subjected to thermal processing, or even used in an application with thermal exposure in the range of 425 – 870 °C for 304 stainless steel. The time of sensitization will be the parameter determining the carbide precipitation at grain boundaries. Due to this process, the area beside the grain boundaries becomes depleted in chromium, which makes this depleted area susceptible to corrosion. This leads to having very low resistance to intergranular corrosion, due to the dissolution of the chromium depleted layer surrounding the grain. Sensitization can further lower the resistance to other forms of corrosion such as pitting, crevice, and SCC. Sensitized stainless steel can be healed by an annealing process, where the chromium diffuses back to the alloy matrix solution.

**Intermetallic phases:** Precipitations of sigma phase or other intermetallic phases have the effect of increasing the susceptibility to corrosion. In high-chromium and high-molybdenum stainless steels, sigma phase can show up which is a chromium-molybdenum-rich phase resulting in susceptibility to intergranular corrosion, pitting and crevice corrosion. This problem can be healed using solution annealing of the affected metal.

### 1.5.3 Effect of mechanical deformation

Influence of mechanical working on material corrosion has been investigated by many reporters. As an example; studies of the effect of cold work on 304 stainless steel has shown that passivity was more difficult to obtain in the case of highly deformed specimens [43]. Decreased dry corrosion resistance is observed for 304 stainless steel subjected to deformation [91]. In other work, deformation of stainless steel at room temperature followed by heat treatment proved to improve the corrosion resistance, as the case for steels deformed at room temperature [35]. For example, it was found that cold working the steel before sensitization gave complete absence of sensitization after several hours of heat treatment [145, 91]. Cold working also lowered the susceptibility of this material to SCC [110].

### 1.5.4 Effect of stress on corrosion/passivation

In the context of stress corrosion cracking, it's vital to discuss the effect that mechanical stress might have on corrosion rate for a given material/environment combination. Such an effect, if proved, has a potential to partially explain the reason why dissolution is favored at crack tips, where stress has its maximum value.

One explanation of this result is that lattice relaxation and reconstructions take place mainly due to surface atoms having fewer neighbors than those in the bulk of the material. This forces the electron charge to be redistributed. A conclusion can be made that atomic adsorption on the surface from the surrounding environment involves charge transfer, resulting in surface-lattice perturbations. These arguments describe the material in the absence of stress. Theoretically, stress should affect adsorption and surface relaxation and reconstructions, however, available experimental data on this is limited [14].

Chemical composition and the electrochemical properties of the protective passive film are affected by the stress state of the stainless steel. Studies of the passive film formed on metal

with different stress cases were done by [122] for 302 stainless steel. This study revealed a lot of interesting results concerning the effect of the stress case in terms of its value; elastic or plastic, and nature; compression or tension on the corresponding properties of the passive film which forms over the alloy's surface.

The study considered a U-bent stressed specimen, having both tensile and compressive stress on the different faces of the specimen. The passive film was thicker on the surface having the tensile stress compared to those having compressive stress or unstressed samples. The morphology of the surface of this passive film was also rough in the case of tensile stress indicating a strong attack. On the contrary, for the compressive and non-stressed surface it was fine with clear marks of slip steps for the case of the compressed surface. Fig. 1.4 shows the difference between the surfaces indicated.

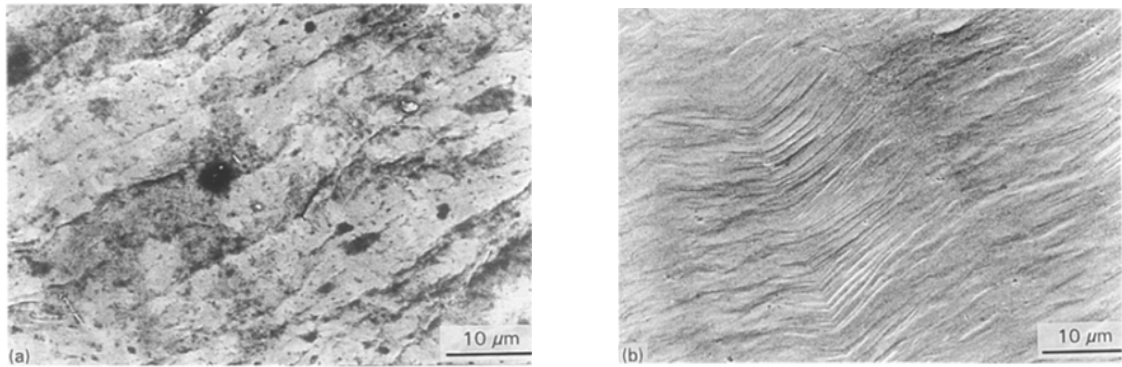


Figure 1.4: Scanning electron micrographs showing the effect of passivation of 302 stainless steel surfaces under (a): tensile strain (b): compressive strain. From [122]

In terms of formation rapidity, the passive film was built faster on the surface of the unstressed samples than for stressed ones. However, it was found that the oxide film formed on a compressively stressed surface was more compact than that for the case of tensile stressed surface.

The electrochemical behavior was accordingly different depending on the subjected stress values. It was found that the anodic current density was higher for the strained specimen than the unstrained one, which reflects the quality of protection provided by the passive film.

Strained samples were immersed in a sulphuric acid solution under a voltage of + 450 mV/SCE (in the passive domain) and the anodic current density was studied as a function of immersion time. The decrease in the anodic current densities was quicker for an elastically strained sample than that for a plastically strained one.

Regardless of the state of the stress if it's elastic or plastic, the thickness of the chromium rich area is enhanced by the effect of the tensile stress, where the opposite happened under compressive straining.

These results were confirmed for 316 stainless steel [123, 188]. It was noticed for 316 however, that the Mo diffusion through the passive film was reduced as an effect of having the stress field, regardless of the nature of applied stress. Local electrochemical measurement techniques helped to better characterization of passivation phenomenon. Scanning vibrating micro-electrode (**SVME**) and local electrochemical impedance spectroscopy (**LEIS**) were used to locally characterize the electrical current densities resulting from corrosion reactions corresponding to different cases of studies. A research aiming to characterize the local effect of stress concentration near the crack tip of a pre-cracked sample of x-70 pipeline steel was conducted [181].

The results of LEIS experiment showed a noticeable drop in the impedance near and ahead of the crack tip, and it increases with distance from the crack tip. The current density map

obtained by SVME made it very clear that the current density near the crack tip had the highest value, compared to the other regions of the specimen. These two maps showing the impedance and the local current density are shown in Fig. 1.5:

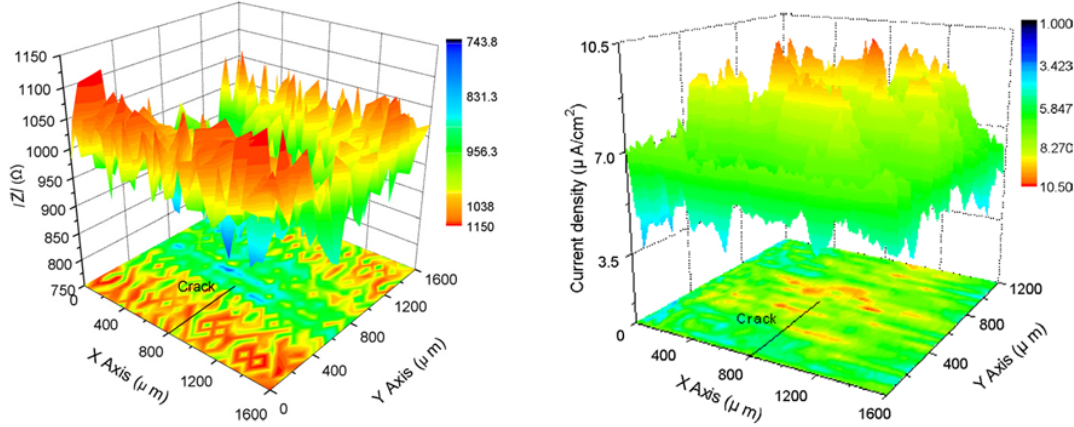


Figure 1.5: A: LEIS mapping on the area around the crack tip specimen under tensile stress. B: SVM map showing the local current densities. Ref. [181]

In their study [181], different applied tensile force was used, and the results exhibited that the charge transfer resistance of the passive film decreased with the increased applied stress. Having less resistance means more corrosion current passing through the film which means eventually having more anodic dissolution rate. However, in the material's elastic domain, very slight difference in the charge transfer resistance was noticed. A significant difference was only pronounced in cases where the applied stress had values of more than 80 % of the yield strength. This is believed to be the threshold required to activate significant slip systems, which leads to having more dislocations resulting from having permanent slip bands on the steel, which will eventually enhance the activity of the steel.

It was noticed in this study that the local current density near the crack tip, and thus the local dissolution is accelerated along the test time. This was thought to be a result of having the crack propagated, which results in having higher values of stress concentrations near the crack tip, which again will increase the local dissolution there. This interaction between dissolution and stress explains the phenomenon of stress corrosion cracking of steel.

The influence of applying the stress before and after the formation of the passive film over the surface of the metal has also been investigated [188]. It was found that the properties of the inner oxide layer are not changed as a function of the applied stress when the stress was applied after aging the passive film. However, the doping of the outer hydroxide layer showed a proportional effect on the applied stress, where the density of the donors is increased, which shifts the potential barrier slightly toward cathodic potential. This could enhance the adsorption of chloride ions.

In this study, more significant results were obtained as the stress was applied before the formation of the passive film. Using different stress values in this condition results shown that three recognized behaviors as given below:

1. When the stress value is below 20 % of the yield strength, no changes were observed on the passive film compared to its properties on the non-stressed specimens.
2. For stress values between 20 % and 70 % of yield strength, a higher density of both donors and acceptors is found.

3. For more than 70 %, microplasticity is observed, and the passive film is highly doped, causing the differential capacitance to increase noticeably. However, the potential barrier between the passive film and the electrolyte is unchanged.

Charge transfer is enhanced above applied 30 % yield stress, but the kinetics of charge transfer at the barrier didn't show any change. This leads to increased pitting corrosion susceptibility, and the time for pitting under a static loading condition.

## 1.6 Passivation Kinetics of Stainless Steel

As seen in the previous section, the main advantage of stainless steel is its ability to nucleate and grow passive films. This is how stainless steel is protected against corrosion, and thus called stainless steel. When it comes to understanding the basic mechanisms of corrosion phenomena such as stress corrosion cracking or corrosion fatigue, it's essential to characterize the passivation kinetics of the concerned material/environment. In the literature, two principal laws have been documented describing the growth of passive films as explained below [62]:

1. Inverse logarithmic law: The passive film growth is controlled by ion conduction under high voltage conditions.
2. Direct logarithmic law: The film growth is controlled by a place exchange mechanism.

In the following two subsections, the passivation kinetics of stainless steel will be studied according to the corrosive environment.

### 1.6.1 In alkaline and neutral electrolytes

It was shown [175] that for 18Cr-8Ni, passive film growth in unbuffered solutions follows a logarithmic growth law. The main contribution provided by this work was showing that  $\log(i)$  is proportional to  $\log(t)$ , where  $i$  is the current density during passivation, and  $t$  is the time duration starting from the passivation onset. In conditions where the electric field across the film is high, the gradient of  $\log(i)/\log(t)$  is close to  $-1$ . However, this kinetics described were very difficult to identify from an inverse logarithmic rate equation [26]. Cabrera and Mott [28] were the first to argue the mechanism of high field ion conduction, which can be approximated as the inverse logarithmic rate equations.

For stainless steel, different researchers [25, 27, 109] showed that passive film construction is controlled by ion conduction in high field. In their experiments to study passivation, 304L stainless steel was studied. For this material, a fresh surface was obtained by mechanical removal of the metal surface. To perform this, they used the potentiostatically controlled scratching electrode technique in 1.0 M KOH solution at a potential of - 605 mV vs standard hydrogen electrode; anodic domain as seen from the polarization curve in Fig. 1.6 and 1.7. It is clear from the polarization curves that for the steady state surface (as received: having an initial oxide film), the current is much lower than that of the bare surface. This is due to the existence of an initial oxide layer over the metal which limits the polarization current. This film is removed mechanically using the scratching electrode for the case of the bare metal. Though the current densities show clearly a huge difference between the two surface states, however, the cathodic and anodic domains remained the same. These domains of potential depend on the metallic composition of the material for a given environment.

The information registered during these experiments reflect the characteristics of the bare surface reaction and the passive film nucleation and build up. Their results confirmed empirically the linear relation between  $\log(i)$  and  $\log(t)$  during the passivation process. This result was confirmed by [90, 93, 62, 33, 22], where [90], for example, studied the effect of applied potential on these curves, as given in Fig. 1.8 a and b, which shows the polarization curve as well as

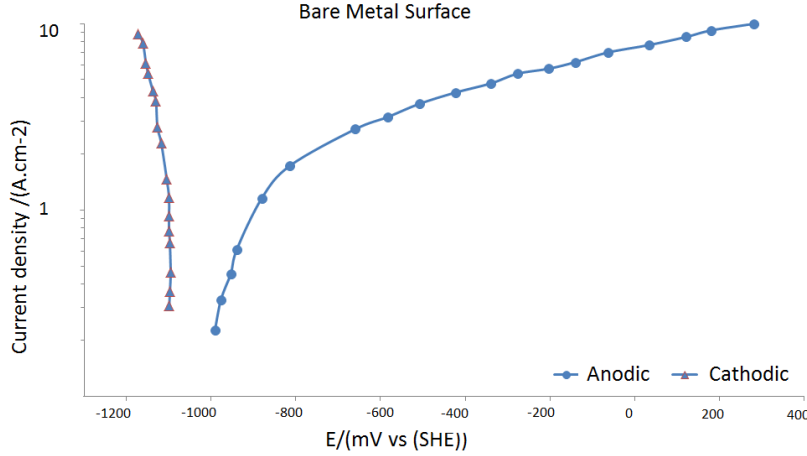


Figure 1.6: Polarization curve of bare surface of 304L stainless steel in 1.0 M KOH electrolyte. Adapted from [26]

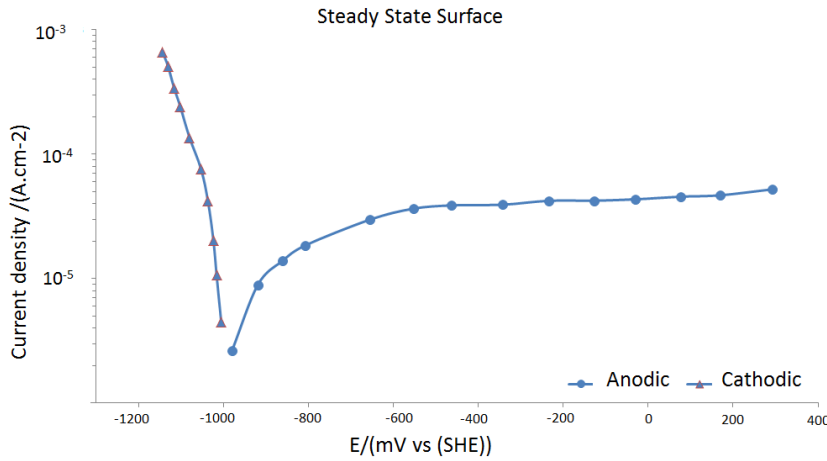


Figure 1.7: Polarization curve of steady state surface of 304L stainless steel in 1.0 M KOH electrolyte. Adapted from [26]

the passivation current transients. It's noticed that though the curves tend to shift up as the potential increases, the slope of the curves represented by  $\alpha$  remains very close to -1 as indicated in Fig. 1.8 b.

Similar experiments [26] revealed a slope,  $\alpha$ , ranging between  $-0.9$  to  $-1.3$  depending on the applied potential, with an average of  $-1.0 \pm 0.11$ . The linearity shown by the current transients was sustained over more than two decades of current density and time.

Based on these observation, Burstein et al [26] discussed the kinetics of ion conduction through a growing passive film as given by the following equation:

$$i(t) = 2A \sinh\left(\frac{BV}{h(t)}\right) \quad (1.1)$$

In this equation,  $i(t)$  is the current conducted through the film at the considered instant of time  $t$ .  $A$  and  $B$  are parameters linked to the activation energy for mobile ion migration.  $V$  is the potential drop across the film of  $h(t)$  thickness. In conditions where electric drop across the film  $V/h(t)$  is high, Eq.1.1 can be reduced to:

$$i(t) = A \exp\left(\frac{BV}{h(t)}\right) \quad (1.2)$$

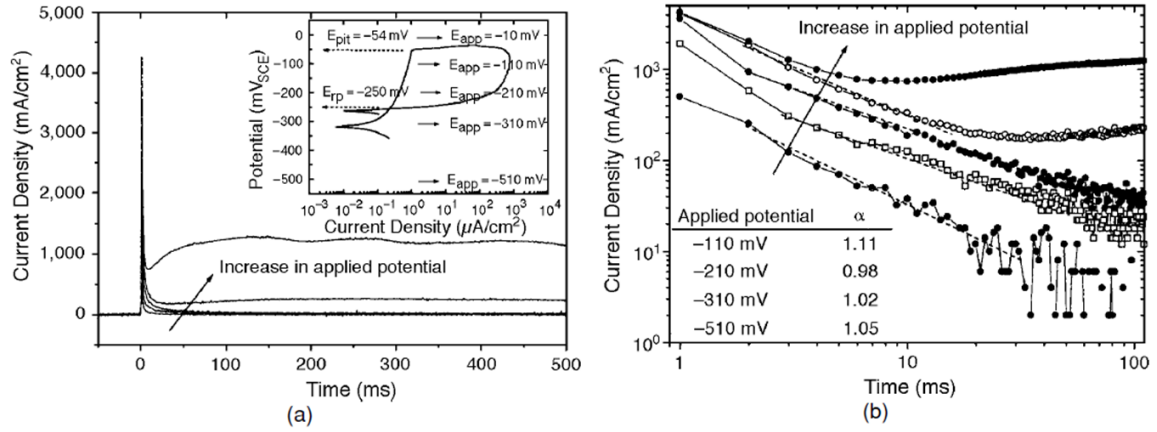


Figure 1.8: Passivation current transients obtained for 304 stainless steel in deaerated 4 M NaCl. The curves are given in (a) normal axis, and (b) logarithmic axis. The polarization curve of this material/environment is provided as well. [90]

Faraday's law can be used to correlate the passive film thickness with the charge spent to construct this passive film by the equation:

$$q_{\text{film}}(t) = \frac{zF\rho}{M} h(t) \quad (1.3)$$

Where  $z$  is the number of transferred electrons per ion, which can be assumed as 3 for stainless steel.  $F$  is Faraday's constant. The film density  $\rho$  was based on a film composed of  $\text{Fe}_2\text{O}_3$  and  $\text{Cr}_2\text{O}_3$ , and the same about the molecular mass of the film  $M$ . The instant of time defining  $t = 0.0$  is the moment indicating the beginning of anodic reaction over the scratched surface. According to this,  $q_{\text{film}}(t)$  is the charge exchange due to oxidation reaction forming the passive film until the moment  $t$ . This amount of current can then be used, by rearranging Eq.1.3, to calculate the passive film thickness at moment  $t$  as given in Eq.1.4:

$$h(t) = \frac{Mq_{\text{film}}(t)}{zF\rho} \quad (1.4)$$

By substituting  $h(t)$  given by Eq.1.4 into Eq.1.2, and taking the logarithm of both sides of the equation, we get:

$$\log i(t) = \log A + \frac{BVzF\rho}{2.3Mq_{\text{film}}(t)} \quad (1.5)$$

Setting  $c$  to be equal to  $\frac{zF\rho}{2.3M}$ , Eq.1.5 becomes:

$$\log i(t) = \log A + \frac{cBV}{q_{\text{film}}(t)} \quad (1.6)$$

This equation shows the relation between  $\log i(t)$  and the inverse of  $q_{\text{film}}(t)$  as a linear relation. For the curves illustrated in Fig. 1.8, they can be represented as suggested by Eq.1.6, as shown in Fig. 1.9. The high initial current density as shown in Fig. 1.8 is due to the alloy being dissolved before the beginning of passive film nucleation and construction processes [62]. The scatter of data points at longer passivation times is due to film thickening and the corresponding variation of ion conduction rate [62].

As observed from Fig. 1.9, the slopes of the curves depend on the applied potential. Remarks of this will be given later in section 1.6.4 concerned with the quantification of passivation quality and kinetics.



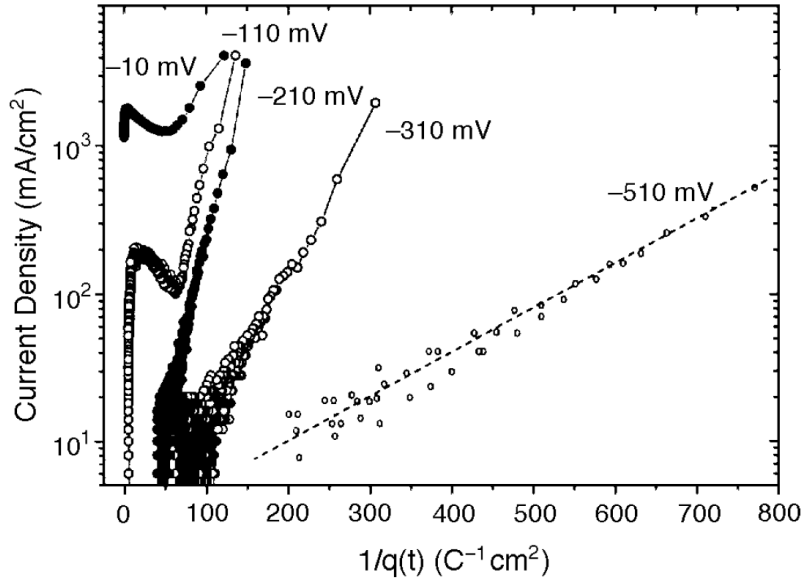


Figure 1.9: Passivation current transients obtained for 304 stainless steel in deaerated 4 M NaCl with different applied potential [90].

The anodic current measured during repassivation is assumed to be consumed for two anodic processes; namely: the metallic dissolution reactions, and oxidation reaction forming the passive film.

It was demonstrated [26] for stainless steel in alkaline and neutral electrolytes, such as chloride solution, that the anodic current measured during the passivation is consumed mostly to form a passive film on the scratched surface. This means that the anodic current due to metal dissolution is negligibly small for such conditions. This assumption is valid as long as the experiment doesn't lead to a pitting or a general corrosion. In such cases  $q_{\text{film}}(t)$  can be assumed to be approximately equal to  $q_{\text{total}}(t)$  due to the external anodic current registered during passivation. According to this, the passivation kinetics can be described by Eq.1.6 with  $q_{\text{film}}(t)$  being replaced directly by  $q_{\text{total}}(t)$  to give:

$$\log i(t) = \log A + \frac{cBV}{q_{\text{total}}(t)} \quad (1.7)$$

The effect of having high metallic dissolution such as in acidic electrolytes violates the use of Eq. 1.7. Therefore, the application of the high field ion conduction model for stainless steel passivation in acidic solutions requires a careful consideration. This will be the subject of the following subsection.

### 1.6.2 In acidic electrolytes

It was shown in the previous analysis that for stainless steels in alkaline and neutral electrolytes, the passive film thickness can be calculated using Faraday's law using the charge consumed to construct the passive film. This charge was assumed to be equal to the total charge exchange, as registered by the external total current during the passivation process.

In acidic solutions, however, this is no longer the case; as the major part of anodic current measured during passivation is due to metallic dissolution, while oxidation reaction forming the passive film is only a minor portion of this current [109, 132]. In these conditions, HFIC model can be used to describe stainless steel passivation [109, 160].

The excessive metallic dissolution on the surface results in a Fe-free film which acts as a passive protecting layer against corrosion [109, 132]. According to HFIC model, the rate of growth of this Fe-free film controls the passivation kinetics for such conditions. Thus, according

to their analysis, Eq.1.5 can still be used to describe the passivation kinetics if  $q_{\text{film}}(t)$  is corrected to:

$$q_{\text{film}}(t) = q_{\text{total}}(t)(1 - f) \quad (1.8)$$

The factor  $f$  in Eq. 1.8 is the fraction of current due to metallic dissolution from the metal surface, where Fe dissolution has the major contribution. Rewriting Eq.1.2 with this correction made to adapt to acidic media gives:

$$i(t) = A \exp \left( \frac{BzF\rho V}{Mq_{\text{total}}(t)(1 - f)} \right) \quad (1.9)$$

Substituting Eq.1.8 into Eq.1.9 and taking the log of both sides gives:

$$\log i(t) = \log A + \frac{cBV}{q_{\text{film}}(t)} \quad (1.10)$$

where  $c$  is equal to  $\frac{zF\rho}{2.3M}$  as defined earlier. It is astonishing that the passivation kinetics, having such huge and fast dissolution components, still follows the high field ion conduction model and Eq.1.2. Fig. 1.10

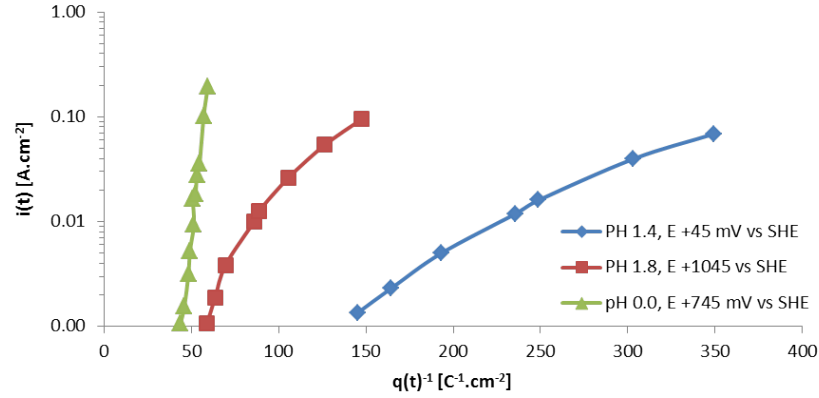


Figure 1.10: Passivation current transients obtained for 316L stainless steel in acidic electrolyte. From [109]

It is clear from Fig. 1.10 the linearity described by Eq.5.3 is valid, but the slope is modified by the factor  $(1 - f)^{-1}$  corresponding to the correction due to the dissolution component, causing the curve to be much steeper than those obtained in alkaline and neutral media.

In order to estimate the  $f$  fraction, Burstein and Marshall [109] assumed that the major contribution to metallic dissolution in acidic electrolytes is due to Fe [132], and thus calculated the factor  $f_{\text{Fe}}$  associated Fe dissolution only. To estimate the fraction of the total anodic charge density linked to Fe oxidation, the oxidation number of each of the metal ions existing in the film were assumed. The numbers they took [109] for the oxidation charge were: Fe(II), Cr(III), Ni(II), and Mo(III). These are typical values for the metallic oxidation numbers in an acidic medium. For these conditions, a fraction of  $f_{\text{Fe}} = 0.64$  was estimated as the total anodic charge density exchanged is accompanied with Fe oxidation. Care should be taken to the fact that if the iron charge Fe(III) was considered instead of Fe(II), the fraction  $f_{\text{Fe}}$  can be even greater. It's obvious that if all charge numbers on all oxidized metal atoms were equal, the  $f_{\text{Fe}}$  fraction would be equal to the ion fraction of iron in the alloy.

By conducting several passivation tests over stainless steel in pH=0.0 and varying the passivation potential, Marshall et al. [109] assumed that it was acceptable with the charge numbers they used, the fraction of film dissolved into the electrolyte represents approximately the iron component. On the other hand, other metallic dissolution such as Cr, Cu, Mo, or Mn were not taken into consideration in their calculations and model.

According to the experimental results of Burstein et al [27], the surface gets to its passive state after it was totally depassivated mechanically as presented in Fig. 1.11. It is noticed that for the acidic electrolytes with 0.0 pH, the passivation becomes more difficult at longer times, resulting in higher charge exchange than that required barely to construct the film. This might be resulting from local film dissolution and repassivation process. This explains the deviation from the initial slope of the linear current decay for the experiment with 0.0 pH.

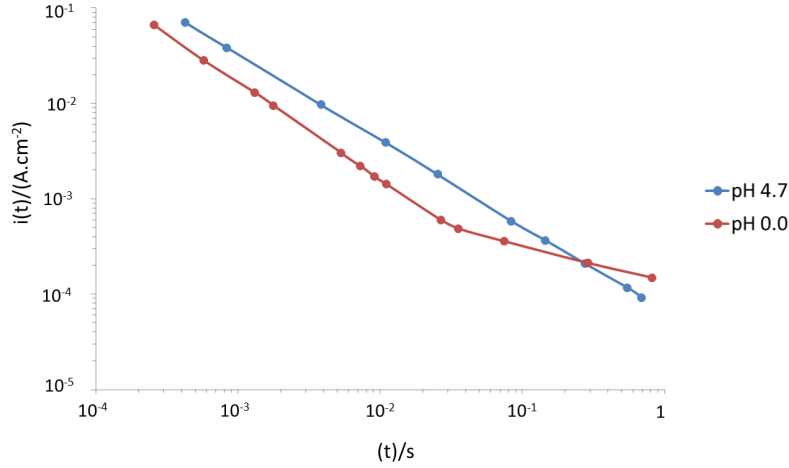


Figure 1.11: Current decay during passivation of stainless steel in acidic medium under passive applied potential. From [27].

In particular, by the conclusions of [27, 109] about the passive film and the mechanism by which it is constructed in such severe environments, the loss of iron by excessive dissolution from the growing oxide film acts as a constructive dissolution. Constructive, due to the fact that the remaining components of the film rearrange in a way such that passivation is obtained. This is to be distinguished from the metallic dissolution causing a rapid corrosion of the material.

In 304L stainless steel, the diffusion rate of iron ions in the film to the film/electrolyte interface controls the dissolution rate of the material. As was explained in the high field ion conduction model in 1.6.1, the voltage across the film is responsible for ionic transfer through the film. The presence of Mo in the alloy's matrix allows the Fe dissolution to start at a quite earlier stage in the growth of the film. This early stage of preferential Fe dissolution is accompanied by an equally early stage of Cr enrichment, and as a result, the metal obtains quicker its passivity due to the chromium oxide accumulation in the passive film [109].

By the same mechanisms, pitting and SCC resistance can be explained in the presence of chloride ion,  $\text{Cl}^-$ . It's well known that the attack of the material by  $\text{Cl}^-$  causes a local acidification of the electrolyte in the pit, or the crack tip. The synergistic effect of Mo with Cr to improve the passivity and pitting resistance is explained as the  $\text{Cl}^-$  attacks initially the Fe ions very quickly, causing a quicker enrichment with Cr and thus chromium oxide, which causes the pit or the crack tip to passivate quicker [109].

### 1.6.3 Comments on the $\log(i)$ vs $q^{-1}$ passivation curves

The linearity described by the high field ion conduction model in Eq.1.6 between  $\log(i)$  vs  $q^{-1}$  can be seen in Fig. 1.9. Still, it's noticed that, in certain passivating conditions, there are zones where the curves deviate from this linearity, and the data points scatter in a way that requires careful understanding. The purpose of this section is to explain these features of the  $\log(i)$  vs  $q^{-1}$  passivation curve, and how they are influenced by the different parameters such as solution composition and the applied potential.

**Effect of  $\text{Cl}^-$  concentration:** To start, the linearity mentioned earlier is better detected in Fig. 1.12 as indicated by a region (I) of the given passivation curves. These scratch-passivation experiments [62] are conducted on 444 alloy under the same experimental conditions as explained in the figure's description. It's noticed that the effect of increasing the  $\text{Cl}^-$  concentration is to shift the curve up, which means more dissolution and more charge exchange. Another observed effect of increasing the  $\text{Cl}^-$  concentration is reducing the scatter of data points, as illustrated in Fig. 1.12. Graham reported considerable general and pitting corrosion by SEM observation of passivating surfaces in the presence of  $\text{Cl}^-$ , which was not the case in pure  $\text{H}_2\text{SO}_4$ . The scatter of data in region (II) is due to the growth and thickening of the passive film which alters the ionic transfer.

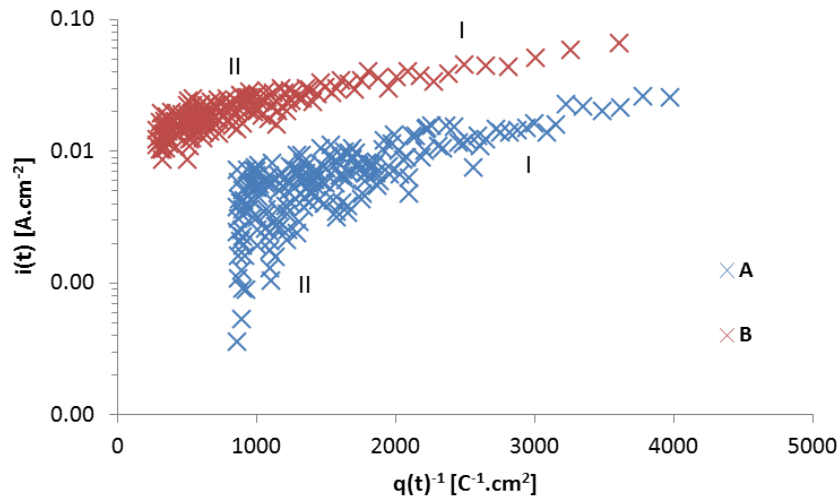


Figure 1.12: Repassivation of 444 alloy under an applied potential of -870 mV vs SHE (active region) in (A): 0.1 M  $\text{H}_2\text{SO}_4$ , (B): 0.1 M  $\text{H}_2\text{SO}_4$  + 0.1 M  $\text{Cl}^-$ . From [62].

**Effect of acidity level (pH):** Effect of acidity level is shown by the three experimental curves given in Fig. 1.10. The more the electrolyte is acidic, the more metallic dissolution, and thus increasing the slope of the curves by the dissolution correction factor  $(1 - f)$  as was explained earlier in 1.6.2. Shortly, more acidity means higher iron dissolution, and yet quicker. This results in quicker passive film enrichment in chromium and eventually reaching quicker passivation in a process described as the constructive dissolution.

**Effect of applied potential during passivation:** Graham [62] has performed the passivation experiments shown in Fig. 1.13. For these curves, the applied potential is in the passive domain for (A) and (B), and transpassive in the case of (C) and (D). Comparing experiment (C) with and (A) and (B), we notice that the tendency was the same for the three of them, which reflects a similarity in the passive film construction mechanism, with more ion exchange in the case of transpassive experiment (C). This causes the curve to shift towards the left hand side. However, adding  $\text{Cl}^-$  in the transpassive conditions has produced a new region over the curve as indicated in region (III). This can be explained by the passive film being broken since the solution/applied potential conditions were not good enough to maintain the passivity. This irreparable film break-up causes an increase in the dissolution current density with time as region (III) suggests. This was confirmed by post-experimental SEM observation of the concerned surface.

The description given above will be complete if we consider the curves mentioned earlier in Fig. 1.12. Passivation transients obtained using passive applied potential or active applied potential have similar trend, with one only difference for the slopes. The gradients of curves corresponding to passive conditions are higher, indicating quicker passivation kinetics.

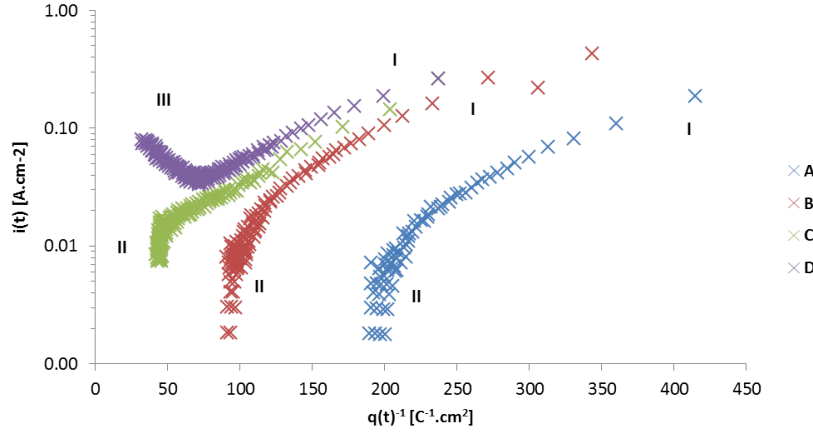


Figure 1.13: Repassivation of 444 alloy in different applied potential and electrolyte composition. 0 mV vs SHE (passive region) in (A): 0.1  $\text{H}_2\text{SO}_4$ , (B): 0.1 M  $\text{H}_2\text{SO}_4$  + 0.1 M  $\text{Cl}^-$ . 870 mV vs SHE (transpassive region) in (C): 0.1  $\text{H}_2\text{SO}_4$ , (D): 0.1 M  $\text{H}_2\text{SO}_4$  + 0.1 M  $\text{Cl}^-$ . From [62].

**Zone I, II, and III:** To make a brief summary, Fig. 1.14 gives the effect of varying the applied potential for fixed solution composition, and the effect of chloride ion concentration for a given applied potential. These zones are a function of the alloy's composition,  $\text{Cl}^-$  concentration, and the applied potential during the passivation process. In order to clarify this, a description of the different regions will be given as follows [62]:

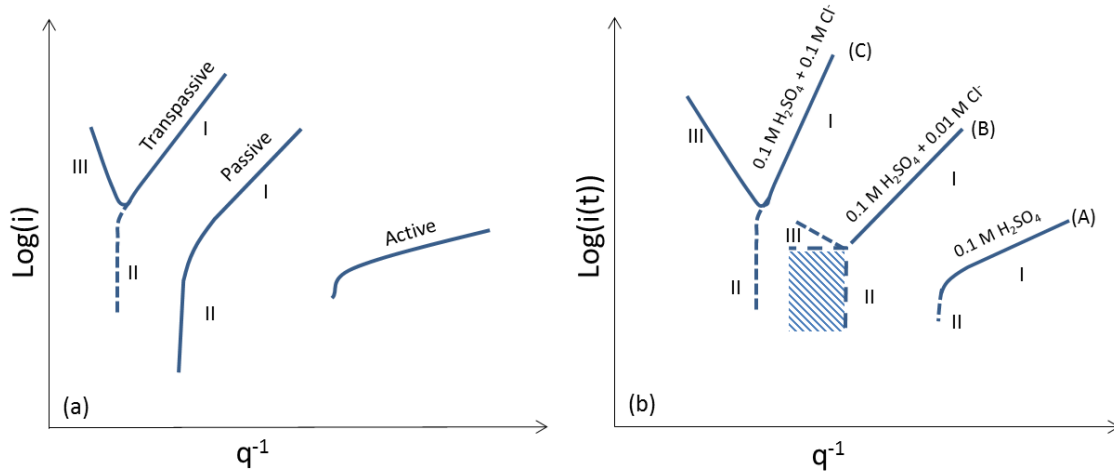


Figure 1.14: Representation of the different regions on the passivation transients. (a): the influence of the applied potential for a specific solution composition. (b): the effect of the solution composition with a specific applied potential. From [62].

- **Zone (I):** This zone corresponds to the initial film nucleation and build up, with a thickness in the order of one or two mono-layers. The more corrosion resistant the material, the more is this zone characterized by linearity. Where for less resistant materials, a deviation from linearity point appears at high charge values. As seen in Fig. 1.14(b), the slope gets steeper in this zone as the  $\text{Cl}^-$  concentration is increased. This is due to the depassivating effect granted by  $\text{Cl}^-$  ions, which makes the passivation kinetics get slower. The same tendency is observed in Fig. 1.14 (a) as the applied potential during the scarce passivation is altered between active, passive, or transpassive.

- Zone (II): This zone indicates favorable passivation conditions in terms of the applied potential and  $\text{Cl}^-$  concentration. The effective passivation obtained assures steady state current density [164]. The dimensions of this hatched zone have a significant importance to characterize the passivation, which is explained in the following paragraph (Hatched zone).
- Hatched zone:  
Generally, the width (horizontal) indicates the stability of the passive film and the time duration for recording the passivation transients. Likewise, for the height is an indication about local film break-up and repair processes. The scatter of data this zone is due to the growth and thickening of the passive film which alters the ionic transfer. This is due to the dissolution of the passive film as the  $\frac{V}{h_{\text{film}}}$  ratio gets lower due to film thickening.
- Zone (III):  
This zone is an indication of pitting corrosion initiation and propagation. Bad passivation conditions in terms of the applied potential and or the  $\text{Cl}^-$  concentration are behind the development of this zone. This zone is highly favored by the presence of chloride ions, especially in transpassive applied potential conditions.

### 1.6.4 Quantification of passivation kinetics

In the previous sections, the transient currents obtained during passivation were explained for their different aspects and the significance of the different zones on these curves.

Undoubtedly, the intrinsic nature of passivation and its kinetics depend on numerous factors, starting from the alloy composition and microstructure [117], to solution properties such as its pH, chloride concentration, and ending by the applied electrical potential during the passivation process [90].

Understanding passivation kinetics help to better predict the materials' behavior in a given environment, and how susceptible it can be to local failure modes such as pitting corrosion and stress corrosion cracking. This is where it becomes necessary to develop a quantified measure of the passivation kinetics, and the passivation quality.

In the work done by Kwon et al, [90], the passivation of 304 stainless steel in chloride solution was studied using an ampero-chronometric method, as was given earlier in Fig. 1.8 (a) and (b). In this experimental set, the passivation was tested for the same material/solution conditions, with different applied potentials. From the experimental curves shown in Fig. 1.8 (a), a peak in the anodic current was detected in the beginning of the passivation process, indicating the oxidation reactions of the bare metal surface at that instant. Starting from that, the anodic current starts decreasing in what looks like an exponential way until it reaches a steady state current value, which is limited due to the formation of a protecting passive film over the surface. The peak current seemed to get higher with the increase of the applied potential, reflecting more intense oxidation reaction.

**The slope ( $\alpha$ ) of  $\log i(t)$  vs  $\log t$  curves:** These transients were plotted on logarithmic scale in Fig. 1.8 (b), as described by the empirical formula [90] given in Eq.1.11.

$$i(t) = a t^{-\alpha} \text{ or } \log i(t) = -\alpha \log(t) + k \quad (1.11)$$

Where  $\alpha$  is the decay gradient, which is believed to be a constant for a given electrolyte/material, and the constants  $a$  and  $k$  are linked to the oxidation rate of the initial bare surface. It's noticed that the curves in Fig. 1.8 (b) are clearly separated indicating higher current density as the applied potential is increased, which again reflects more intense oxidation reaction. However, the passivation process is detected by those curves, thanks to their slopes  $\alpha$ , which indicate a progressive decrease in the anodic current with time.

Consequently, this made the decay gradient,  $\alpha$ , a potential candidate to characterize the passivation kinetics, and to compare the different material/environment combinations.

It turns out that for the given curves in Fig. 1.8 (a) and (b), the calculated values of  $\alpha$  (shown on Fig. 1.8 (b)) were tightly close to each other, with a value of  $\alpha \simeq 1$ , making the detection of the clear difference in the passivation rate and kinetics non-detectable by this measure.

This forces a redefinition of the quantification of passivation kinetics, such that passivation experiments given in Fig. 1.8 (and others) can be distinguished easily for their true passivation ability and passivation rate. Particularly, if this newly defined criterion is to be used to quantify local failure phenomenon such as SCC, the charge transfer during passivation should be taken into account as well [90], according to what was suggested by Scully in the constant charge criterion for SCC propagation [161].

To get into the definition of the new criterion, an illustrated example explaining the problem faced earlier is given in Fig. 1.15, where curve (A) and (B) represent two different passivation experiments with clearly different passivation kinetics.

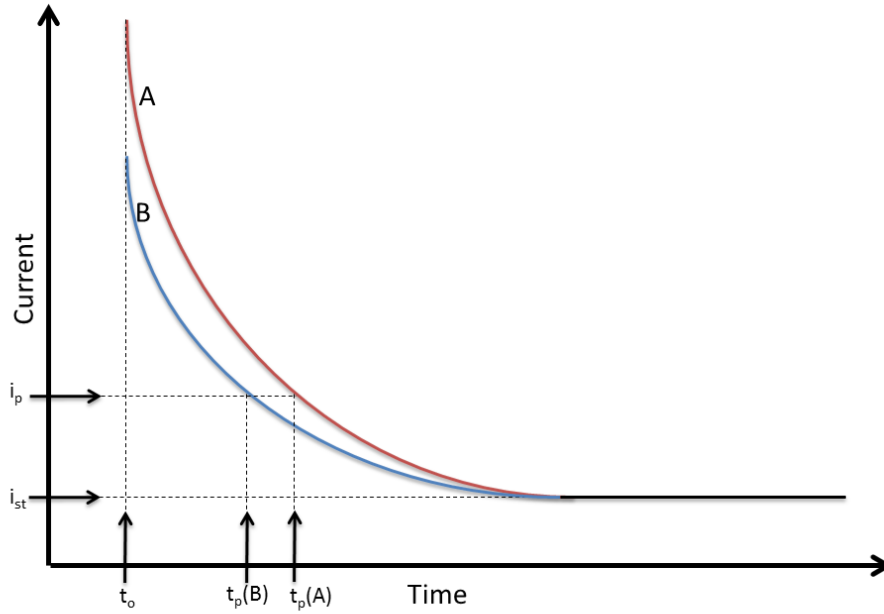


Figure 1.15: Repassivation criterion redefined using the repassivation time. From [90]

In this figure, the normal axes are used to represent the current registered during the passivation process, starting from the application of the passivation pulse at moment  $t_0$  until a long enough time where the anodic current seems to get stable with a value of  $i_{st}$ .

To quantify the passivation of these two experiments, a given degree of passivation should be determined such as the passivation (or repassivation) current indicated by  $i_p$  in Fig. 1.15. The time at which the anodic current reduces to reach  $i_p$  is thus defined as the repassivation time, as indicated by  $t_p(A)$  and  $t_p(B)$  for curves A and B respectively.

The passivation would be surely faster when the repassivation time is shorter. If we consider the two experiments A and B in Fig. 1.15, the repassivation time for experiment A was longer than that of B to reach the same degree of passivation defined by  $i_p$  [90]. It's important to notice here that the chosen degree of passivation should not be equal to that of the steady state current,  $i_{st}$ , reached as the passive film is completely constructed. Doing so might falsify the estimated time of passivation  $i_p$ , as can be easily observed from Fig. 1.15. This means that the degree of passivation should be higher than the steady state current obtained after the stable construction of the passive film so that the kinetics of passivation reactions are measured while they are taking place.

If this criterion is taken into account to quantify the passivation of the experiments given in Fig. 1.8, the passivation rate is shown to decrease as the applied potential is increased [90].

Distinguishing the passivation rates was possible indirectly, the charge exchange for the different experiments was included in this criterion as the area under the current-time curve starting from  $t_o$  until the repassivation time  $t_p$  of the considered experiment, as shown in Fig. 1.15.

In the following, a better criterion will take the entire history of the charge exchange during the passivation process as a quantification criterion of passivation rate and passivation quality.

**The slope ( $cBV$ ) of  $\log(i)$  vs  $\log(1/q)$  curve:** The passivation transients shown in Fig. 1.8 (a) and (b) can alternatively be represented as suggested by the high field ion conduction model (**HFIC**) which was described earlier in Eq.1.6, and is given here in Eq.1.12 as a reminder. The resulting curves are given in Fig. 1.9.

$$\log i(t) = \log A + \frac{cBV}{q_{\text{film}}(t)} \quad (1.12)$$

The high field ion conduction model [28] describes the activation energy barrier for ionic transfer through the passive film under an applied potential to be proportional to the field strength ( $V/h(t)$ ) and  $B$ , where  $V$  is the potential difference across the film,  $h(t)$  is the passive film thickness calculated by Eq.1.4 ( $h(t) = Mq_{\text{film}}(t)/zF\rho$ ), and  $B$  is a parameter linked to the activation energy for mobile ion migration, as was presented earlier [25, 90, 109, 26].

With this presentation of passivation on  $\log(i)$  vs  $\log(1/q)$  axis, the difference in the passivation rate is now detected clearly for the experiments conducted with different passivation potential, as shown by the slope of the curves given in Fig. 1.9.

Consequently, the slope of the linear zone described by Eq.1.12 on  $\log(i)$  vs  $1/q(t)$  curve (zone II in Fig. 1.14) is a very effective measure of the repassivation rate [33, 90].

According to HFIC model, the lower the activation energy barrier for ionic transfer through the film makes it easier for charge exchange and thus will have a higher ( $cBV$ ) value [90] which can be a direct indication of the passive film quality. Since the protectiveness of a passive film is characterized by its ability to limit the ionic conduction, then, the higher the ( $cBV$ ) value is expected to indicate more defective film with faster ionic conduction rate [90].

In Fig. 1.9, the slope of these curves,  $cBV$ , increased with the applied potential until reaching a certain limit where an inflection point showed up. Starting from this inflection point, the linearity described by Eq.1.12 was no longer valid.

An explanation can be given to the passivation behavior vs the applied potential based on the quality of the passive film. According to Kwon [90], as the applied potential increased, the  $cBV$  value increased indicating a decreased passive film quality. Whereas, at the potential where the inflection point appeared, the resistance of the passive film to ionic transfer decreased to a value below which the metallic dissolution took place by fast ion movement, resulting in pitting corrosion as was confirmed by SEM images [90]. However, results of 304 stainless steel passivation experiments made by Ogle is contradictory to this explanation [132].

From the curves of Fig. 1.9, the slope ( $cBV$ ) has increased with the applied potential. If this is compared to what was found earlier (the degree of repassivation vs the repassivation time) for the same experiments, the slope  $cBV$  decreased with an increase in passivation rate.

**The slope  $cBV$  vs the passive film thickness** An important trait of the passive film in addition to its protectiveness is its thickness, which when both are considered together reflect the compactness of this film.

As discussed earlier, the passive film thickness at a given moment can be calculated using the portion of charge spent to construct that film by Faraday's law, as was given by Eq.1.4 ( $h(t) = Mq_{\text{film}}(t)/zF\rho$ ). If the two curves (A) and (B) given in the example shown in Fig. 1.15 are considered, their corresponding passive film thickness at moment  $t_p$  can be calculated



similarly. Obviously, from the area under the current density curve representing the total charge exchange during passivation until moment  $t_p$ , the charge  $q(t_p)$  for (A) is more significant than that of (B), which indicates a thicker film formed on (A) than that on (B). This implies that for alloy (B), the passivation was satisfied faster than that of (A), and thinner film in the same time. The passivation rate of (A) as indicated by the slope ( $cBV$ ) has a lower value than that of (B). Therefore, a conclusion can be made here that for a given electrochemical conditions, a lower ( $cBV$ ) value indicates a faster passivation with a thinner and more protective film. This conclusion is confirmed by [5] who concluded from his results on Fe-25Cr-20Ni single crystal passivation experiments in boiling  $MgCl_2$  that a thicker passive film formed on stainless steel is more porous and defective.

In addition to the sensitivity of ( $cBV$ ) value to the applied potential as was shown in Fig. 1.9, it was also sensitive to  $Cl^-$  concentration, solution temperature, and the percentage of the alloying elements such as Cr, Mo, and Ni [33]. For example, Fe-18, 20, 25, and 29 Cr were tested for their passivation [33] in the same electrochemical conditions, which gave lower current density as the Cr concentration increased as shown in Fig. 1.16 (a), (b), and (c).

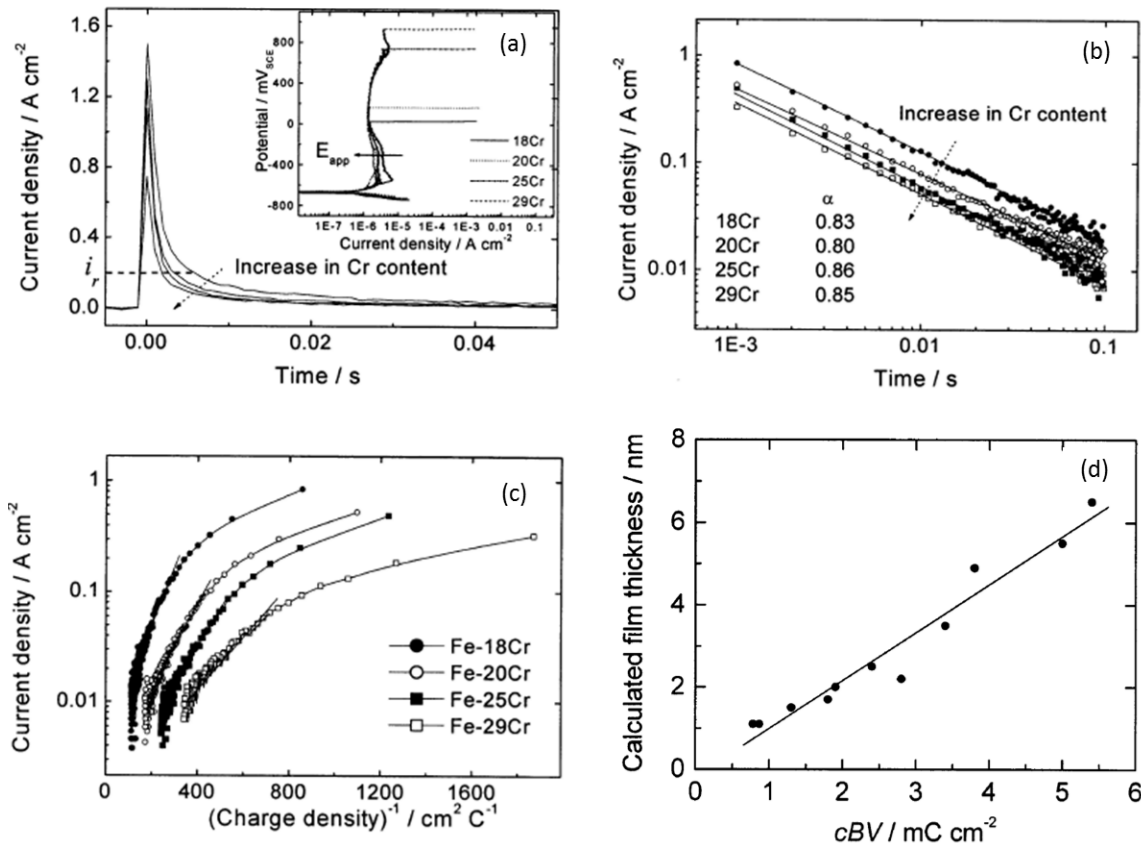


Figure 1.16: (a), (b), and (c): the repassivation of Fe-Cr stainless steel with different Cr content [33], (d): The ( $cBV$ ) vs passive film thickness for the different passivation tests done by [33].

On the other hand, ( $cBV$ ) value decreased as the Cr concentration increased in the alloy's matrix as shown in Fig. 1.16 (c), indicating faster passivation and a better passivation quality. This method was used to study the repassivation of duplex stainless steel in chloride solution [22], where the passivation kinetics and how it varies with the different parameters showed to be similar to those of austenitic stainless steel.

Figure 1.16 (d) gives an interesting summary of the different passivation experiments performed by [33], where the ( $cBV$ ) value was plotted vs the passive film thickness (calculated at steady state after passivation). The graph shows that the passive film thickness is linearly

proportional to ( $cBV$ ) value regardless of the alloy's composition.

From here, a conclusion can be stated that the lower the ( $cBV$ ) value for a given alloy/environment, the faster the reapssivation rate for that alloy, with a thinner (explained below) and more protective passive film.

## 1.7 Stress Corrosion Cracking (SCC)

### 1.7.1 Definition

Stress corrosion cracking (**SCC**) is one of the most common environmental assisted cracking phenomena. SCC is a complex phenomenon describing sub-critical cracking of materials driven by the synergistic interaction of mechanical, electrochemical and metallurgical factors [79].

Material exposure to hydrogen-containing environments such as gaseous hydrogen or hydrogen sulfide can cause hydrogen to get internally adsorbed into the material leading eventually to cracking due to what's known as hydrogen embrittlement (**HE**) [97]. For its importance, HE is discussed with more details in section 1.8.3.

Liquid metal embrittlement (**LME**) is a totally different phenomenon causing materials to undergo sub-critical cracking when they are in contact with liquid metals [82]. However, SCC is often associated with hydrogen generation at crack tips, which often leads to it being confused with HE.

There are common phenomenal similarities between HE, LME, and SCC. Among the three environment assisted cracking phenomena mentioned earlier, SCC is the most complex.

What makes SCC a seriously difficult to understand and predict is the necessary co-existence of three factors: mechanical stress (tensile or residual), susceptible material, and a corrosive environment.

In principle, the elimination of any of these factors can prevent or lower the threshold cracking of SCC. These three factors should be well defined and known in order to have a safe design and operation. Electrochemical parameters of importance are oxidizing potential, pH, impurity concentration, and temperature. On the other hand, mechanical parameters are stress, stress intensity, and strain rate. At last but not least, metallurgical factors of interest can be the bulk composition, yield strength, deformation character, and localized micro-chemistry; such as passive-film-forming elements depletion, or enrichment of corroding elements [11].

SCC has two possible morphologies, which are:

1. Transgranular SCC (**TGSCC**): where the crack propagates through the grains of the alloy.
2. Intergranular SCC (**IGSCC**) : where the cracks propagate along the grain boundaries.

The morphology could be also a mixture of the two, or can even switch from one to another in the same alloy. IGSCC or TGSCC takes place as a function of the conditions of the corrosive environment, the microstructure, or the stress/strain state. IGSCC is the common mode in aluminum alloys, alpha brass, and low-alloy steels. However, for chromium-based and austenitic stainless steel, the popular mode is TGSCC [95]. Sensitization and cold work are two main factors that favor IGSCC of austenitic alloys like stainless steel and nickel-based alloys [79]. SCC usually propagates in a perpendicular direction to the principal stress. Furthermore, cracks can have different branching degrees depending on the crystallographic aspects and the crack's surrounding conditions.

Crack branching and sudden changes in cracking direction at grain boundaries can be explained. As the crack propagates and faces any nonmetallic inclusion, lattice discontinuity or unfavorably oriented grain boundary, the stress concentration at the crack tip reduces to a level that is lower from that required for the crack to proceed [83].

Since cracks propagate with little or even no macroscopic plastic deformation, this fact gives SCC a brittle like appearance. Most alloys can undergo SCC in at least one environment/loading condition. Conditions for the occurrence of SCC differ from one alloy to another.

SCC phenomenon can be divided into two different stages: crack initiation, and crack propagation. The initiation time can vary from a short period time or many years. The crack propagation can be split into two stages: the slow propagation phase, and the fast propagation phase.

### 1.7.2 Phenomenological description

#### 1.7.3 Crack initiation

Various causes can be mentioned when talking about crack initiation. Some of those are intrinsic material defects such as porosity [37], or pre-existing crack-like defects resulting from machining or assembly [156].

Initiation sites can be developed due to pitting corrosion of stainless steels. The way this operates is by pit initiation, pit growth and finally pit to crack transition [186]. Pitting initiates preferentially on random surface defects sites such as oxide inclusions [16], carbide precipitates [193], sulphide inclusions [158, 179, 190, 192]. Corrosion pits can develop at grain boundaries due to preferential dissolution resulting from a less protective oxide film, or chromium depletion due to sensitization [24]. However, this is how intergranular corrosion takes place as well, which is equally a very promising SCC initiation site.

Other localized corrosions that can trigger stress corrosion cracking are crevice corrosion and de-alloying [98]. In systems subjected to dynamic cyclic loading, fatigue cracks can be very good initiation sites for stress corrosion cracking [139].

In stainless steel, the slipping of bands along the  $\{111\}$  planes can cause local oxide film rupture if the slipping occurs close to the surface, which acts as an initiation site for SCC [170].

In a corrosive environment, tensile applied/residual stress is required to make the transition from these initiation sites to SCC. It was reported that stainless steel was susceptible to SCC due to the presence residual stresses attributed to plastic deformation of the surface during machining [61]. In the same study, stress corrosion cracks didn't propagate in the domain where compressive residual stress dominated [61]. In other tests, [21] samples having compressive surface residual stress, no cracking was observed after immersion in  $\text{MgCl}_2$  electrolyte.

Fig. 1.17 illustrates some of the possible initiation sites for SCC [102].

#### 1.7.4 Pit to crack transition

As seen in section 1.7.3, the pit initiation site can be described as a deterministic process. Consequently, deterministic pit growth models have been developed based on anodic dissolution kinetics [20]. The pit-crack transition takes place once the pit grows to a critical size. It was proposed [44, 184] that at this stage of pit growth, its depth exceeds the threshold depth required to initiate a crack. Accordingly, the resulting crack will propagate with a higher rate than that of the pit. A possible factor to determine the pit-crack transition to SCC is if the stress around pits exceeds the yield strength [185].

In the next section, crack growth, and the proposed models describing this process are discussed.

## 1.8 Crack Propagation Mechanisms in SCC

Many attempts were made in the literature to give a universal model of SCC [80, 107]. At the present, however, no single mechanism has been proposed that can describe all aspects of SCC. The developed models can briefly be applied to particular systems, but not to the others, meaning that no universal models of SCC exist.

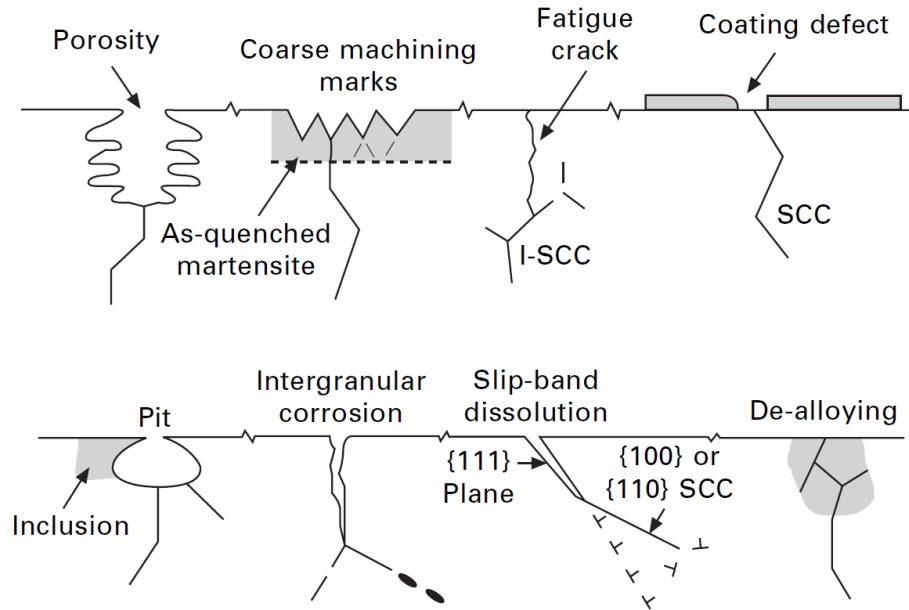


Figure 1.17: Possible initiation sites of SCC. [102].

Crack growth can be basically attributed to one of four atomistic processes. These can be listed as follows [191]:

1. Atomic dissolution at the crack tip into the environment.
2. Movement of atoms at the crack tip due to shear as a result of dislocation emission.
3. Decohesion, represented by atoms being separated at the crack tip due to a tensile force.
4. Diffusion of atoms from the surface of the crack tip to behind the crack tip.

A number of mechanisms of SCC have been suggested based on these four fundamental phenomena. These mechanisms can be listed under two main classifications based on their principle of explanation; the dissolution based models, and models involving mechanical fracture in the crack, as shown in Fig. 1.18. These models will be described in details in the following sections although it should be kept in mind that these models are still controversial.

### 1.8.1 Dissolution models

This dissolution mechanism describes corrosion crack propagation by the assumption that preferential dissolution occurs at the crack tip, leading to crack growth with time. According to these models, crack-tip dissolution is attributed either chemical active path or mechanical activity. The chemical active path model suggests that the crack follows locations favoring atomic dissolution simply due to the chemical composition of this path which is less corrosion-resistant than that of the bulk of the material. This could be due to anodic precipitates or chromium depletion along grain boundaries for example resulting from thermal treatment. On the other hand, the mechanical active path assumes that cracking follows stress concentration at the crack tip, which might favorably activate dissolution, or activate slipping mechanisms [162, 183].

In these mechanisms, limited dissolution takes place behind the crack-tip. This is explained by the build-up of protective films of variable quality on the fracture facets. This protection is due to one or a combination of three main justifications [102]:

1. The total dissolution of present anodic micro-chemical features.

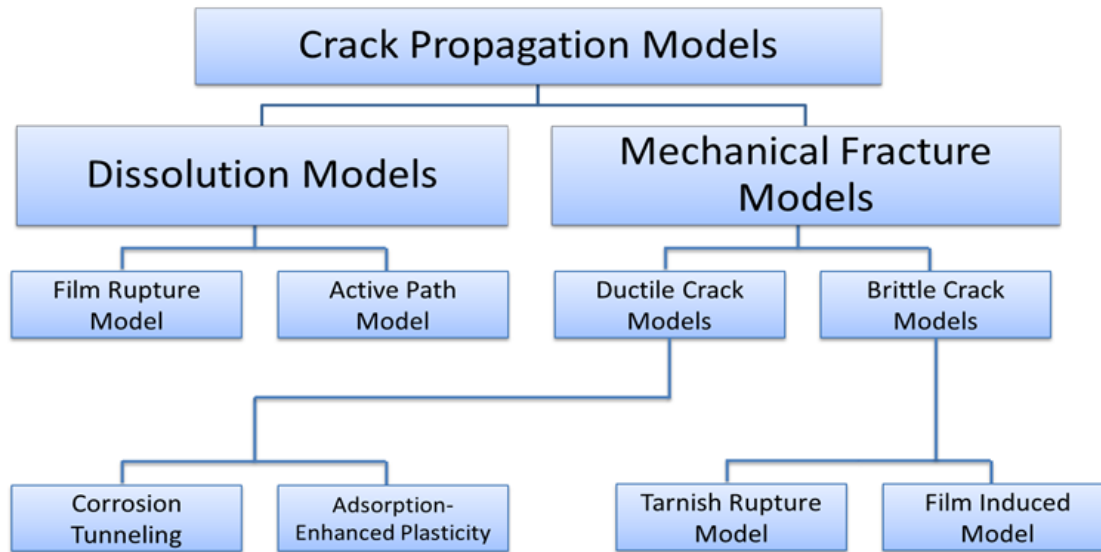


Figure 1.18: A diagramme representing Crack propagation Models. [181]

2. Stress relaxation after the crack opening.
3. Less aggressive environment than that at the crack-tip.

Particularly, among many suggested models, research has excluded all but two models of interest; namely: film rupture anodic dissolution model and active path model [11]. The first of those is described in the following section.

### Film rupture anodic dissolution model

This model, also called the “slip-dissolution model”, assumes that extremely localized anodic dissolution at the crack tip causes the crack to grow. The passive oxide film protecting the sides of the crack is fractured as a result of plastic strain in the metal at the crack tip, which causes a localized corrosion at that point [95, 57].

A cyclic process of film rupture by slipping steps due to stress, dissolution, and film repair causes the crack to keep propagating [69, 71, 45, 161], as illustrated in Fig. 1.19. Other investigators assumed that the rate of film rupture at the crack tip is greater than repassivation rate, so the crack tip will be always in the active state after the passive film rupture, this later model is called Active Path Model [187, 172, 173].

Figure 1.19 represents SCC as described by the film rupture model. Passive film rupture is induced by the slipping system due to stress, and the electrochemical process (between state 3 and 4) represents the rapid dissolution of the freshly revealed surface by the corrosive environment, and the passive film builds-up again at state 4.

The dissolution at the crack tip is attributed to either an active path generated at the crack tip as a result of stress/strain, or to a chemically active path due to anodic precipitates or segregants near grain boundaries [102]. Electrochemically, the process can be illustrated using a hypothetical polarization curve as given in Fig. 1.20. In this figure, the metallic surface is supposed to be initially in the passive state (state 1).

The mechanical slipping due to stress exposes the fresh surface in the active state (2) due to the rupture of the passive protecting film by the slipping mechanism. Finally, the freshly exposed surface repassivates but only after the dissolution of a significant amount of the metal.

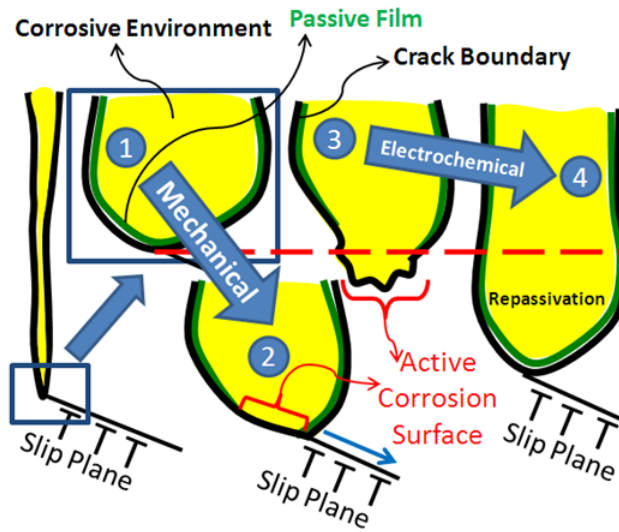


Figure 1.19: Representation of SCC as film rupture model describes it.

Morphological observations of cracking surfaces indicate discontinuous cracking and crack arrest characteristics, which supports this model. On the other hand, surfaces of TGSCC are flat, and match precisely on both sides of the crack, proving very little dissolution during crack propagation. From here, film rupture model is accepted mainly for IGSCC of ferritic steels in passivating environments [140, 143], and to sensitized stainless steels [57, 55, 124, 56, 7], but not for TGSCC [147].

### 1.8.2 Adsorption based mechanisms: AIDE

Adsorption-induced dislocation-emission **AIDE** mechanism has been applied to SCC, hydrogen embrittlement, and liquid metal embrittlement. The model is based on the proposition that adsorption-active media has the potential to decrease the surface energy, which affects directly the deformation/fracture of solids, making it easier to crack a material in liquid contact; which is known as the wetting effect [152]. This model argues that adsorption weakens inter-atomic bonds, thus promotes dislocation nucleation near crack tip [99, 100, 101], consequently, cleavage-like brittle fractures are produced, as illustrated in Fig. 1.21.

Voids forming ahead of the crack tip cause crack propagation as they merge due to dislocation emission from the crack tip. Fig. 1.22 illustrates the crack propagation direction. As seen in Fig. 1.22, slipping takes place equally along both sides of the crack, in an alternative way. These slipping planes and directions correspond to the crystallographic planes having the lowest energy; low index  $\{111\}$  planes for FCC materials. Thus, cracking takes place alternatively along them, giving a macroscopic rupture plane bisecting the angle between them, giving  $\{100\}$   $\langle 111 \rangle$  or  $\{110\} \langle 100 \rangle$  for FCC materials [102].

### 1.8.3 Hydrogen based mechanisms

As an adsorbed element, hydrogen can cause a direct effect on material deformation and fracture, as discussed in 1.8.2. The presence of hydrogen weakens the inter-atomic bonds associated with dislocation emission and decohesion at the crack tip. The adsorption of hydrogen and other elements differ in that hydrogen diffusion occurs near the crack tip and a few atomic layers ahead. This makes it easy for it to access the microvoids generated in the plastic zone near the crack tip, which improve the chances of cleavage or decohesion as illustrated in Fig. 1.21

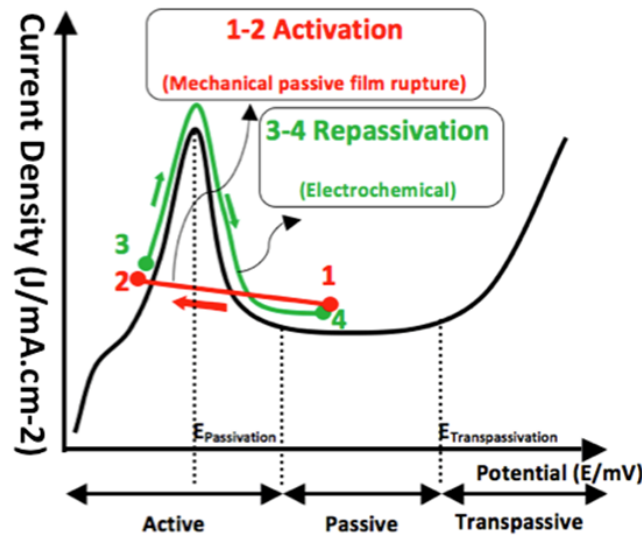


Figure 1.20: Polarization curve showing a passivation, activation cycle.

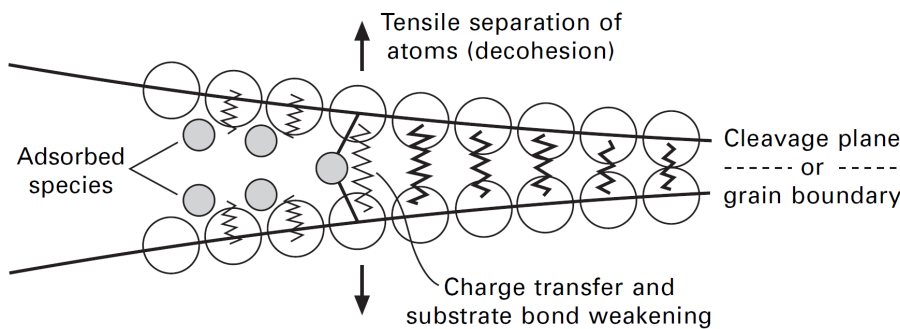


Figure 1.21: Adsorption effect on weakening inter-atomic bonds [102].

and 1.23. Mechanisms based on this fact cover SCC in high strength steels, nickel alloys, and titanium alloys. However, some researchers questioned the applicability of these models on FCC systems such as austenitic stainless steels [151, 11, 76].

Embrittlement is favored by acidification of local environment at the crack-tip by cation hydrolysis of water [31] and having a material with inclusions segregated in grain boundaries such as sulfur, phosphorus, antimony [11]. Cleavage, intergranular separation or highly localized plastic fractures are direct consequences of hydrogen absorption in the metal [127].

SCC fracture surfaces have common features with that caused by hydrogen embrittlement. So, all mechanisms SCC based on hydrogen associate crack propagation with adsorbed hydrogen (on the surface and within a few atomic layers), absorbed hydrogen (as for adsorbed but further ahead of the crack tip), and eventually hydride formation at crack tips. A model was suggested explaining the mechanism of hydrogen embrittlement, according to which grain-boundary impurities enhance the absorption of cathodic hydrogen [92]. This model shows how impurity segregation improves hydrogen absorption, rather than explaining a new cracking technique. A schematic diagram is shown in Fig. 1.23, showing the hydrogen absorption and the development of IGSCC in the case of applied stress.

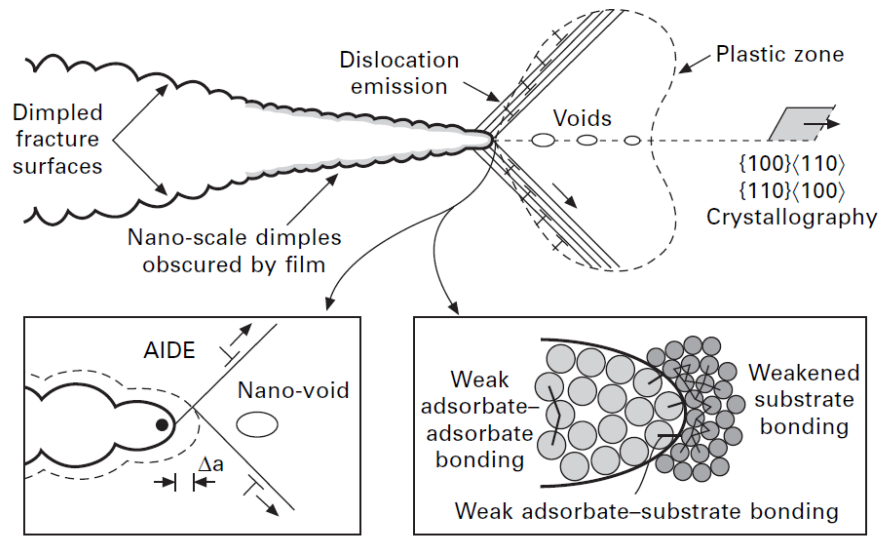


Figure 1.22: AIDE model describing SCC. Voids nucleated in the plastic zone merge along the low index crystallographic planes causing the crack propagation in that direction [102].

#### 1.8.4 Mechanical fracture models

These models also assume that the crack propagates by dissolution, but the main contributor to cracking is a mechanical fracture at the remaining bands due to stress concentration at the crack front, where corrosion occurs [72]. In the mechanical fracture models, cracking can be divided into brittle and ductile crack propagation. Ductile mechanical models cover corrosion tunneling and adsorption enhanced plasticity models. While brittle cracking models cover tarnish rupture and film-induced cleavage SCC mechanisms [11].

##### The corrosion tunnel model

This model [180] assumes that an array of tiny tunnels is formed by corrosion at the slip steps. As a result of the growth of these tunnels, in both diameter and length, the remaining bands between them can not hold the applied stress, causing a mechanical ductile fracture. According to the observed cracking fractography, it was assumed that the effect of applied tensile stress on a material is to change the morphology of those tunnels from round cross-sectioned to thin flat shots as illustrated in Fig. 1.24 [167].

TGSCC can be explained by the mechanical fracture of these slots between the corrosion tunnels. It was found that in austenitic stainless steel in the presence of tensile load, the dimension of these corrosion tunnels can be atomic, which is in accordance with the fractography observed in TGSCC [167].

##### Film-induced cleavage model

This model is based on the proposition that dealloying or vacancy injection could induce brittle fracture. An example of this is the brittle fracture triggered in  $\alpha$ -brass in ammonia solution as a result of surface dezincification [59]. Based on this, a more recent model was established assuming that a brittle crack in the thin protecting layer crosses the film/matrix interface with little loss in velocity will cause the ductile matrix to undergo a brittle cracking. This crack propagates and eventually stops as a result of plastic deformation on the crack tip, which gives it a blunt shape. The crack grows by multiple repetitions of this process [165]. This mechanism is illustrated in Fig. 1.25 [147].



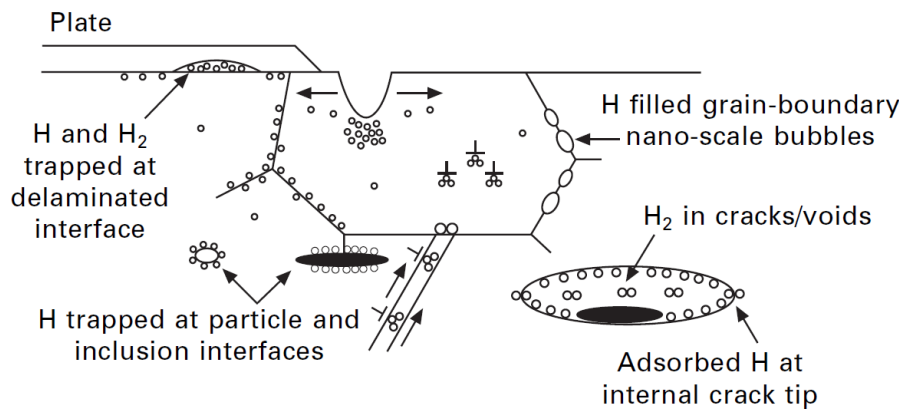


Figure 1.23: Illustration potential locations for embrittlement leading to SCC initiation and growth.

It was believed that the material was embrittled by short range order between the slip bands where the crack propagates. The feature of crack-jumping was proven by the same investigators using optical microscopy [43], and later by scanning electron microscopy [147].

According to the film induced cleavage model, crack jumping is not a feature of face-centered cubic crystals like those in austenitic stainless steels. This means that the entire role is played by the film itself; such that it has to launch a crack with high enough velocity, hundreds of meters per second, within this nanometric thin film [125, 31]. For the passive film being brittle, dense, and strongly bonded to the surface, it's very effective to serve this function.

This is the only model explaining the crack arrest features, the cleavage-like morphology, and the discontinuous nature of crack propagation [81].

### Corrosion enhanced localized plasticity (CELP)

This model explains transgranular SCC for ductile FCC materials where metallic dissolution, adsorbed and absorbed hydrogen are associated. According to this model [105, 106], the crack propagation process takes place over several distinct steps as explained below [102, 105, 106] and illustrated in Fig. 1.26:

1. **Depassivation-Slip step formation:** Local oxide film rupture or depassivation occurs at the crack tip, introducing localized anodic dissolution on  $\{111\}$  slip planes near the crack tip. This results in the formation of a slip step.
2. **Dissolution-Crack blunting:** Local critical shear stress for dislocation activity can be lowered due to dissolution and hydrogen absorption/adsorption. Having high stress concentration in addition to possible vacancy production due to dissolution induces mobile dislocations injection. These factors, in addition to enhanced localized plasticity at  $\{111\}$  slip planes stimulates localized shearing on  $\{111\}$  planes. as the shearing takes place, the crack blunting is reduced.
3. **Local stress build-up:** The enhanced local plasticity continues to boost the dislocation emission which gets blocked by material obstacles. Such obstacles can be simple like grain boundaries, while others can be complicated such as bundles and Lomer-Cottrell locks generated by earlier stress application. These blocks act as a hardened zone of the material facing the zone of enhanced plasticity where dislocations are active. Having these two zones produces dislocation pile-ups which increases the value of local stress.

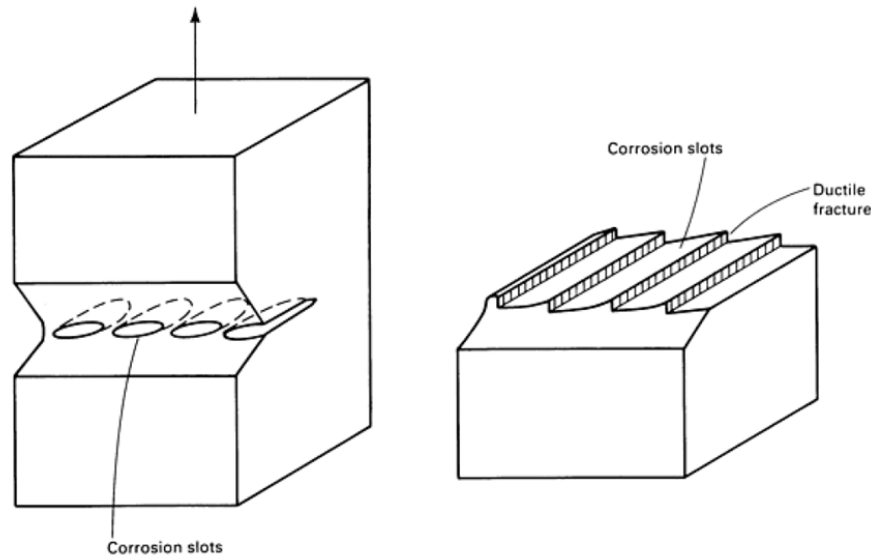


Figure 1.24: Schematic diagram of the tunnel mechanism of SCC and flat slot formation.

4. **Reaching  $K_{Ic}$ :** Hydrogen adsorption/absorption can affect the local  $K_{Ic}$  value. Since pile-ups accumulate until this local  $K_{Ic}$  reduced value is reached, thus initiates crack tip decohesion or cracking by Stroh-like mechanism near these pile-ups.
5. **Decohesion-crack shielding:** Adsorbed/absorbed hydrogen reduces the decohesion energy of the  $\{111\}$  planes. Hence, normal stress on  $\{111\}$  planes can be high enough to open the crack along the  $\{111\}$  microfacets. Once this is done, new dislocations are emitted on a symmetrical plane relative to the general crack plane, causing the new crack tip to become shielded.

According to this model [105], cracking takes place on  $\{111\}$ ,  $\{100\}$ , and  $\{110\}$  depending on the crystallographic orientation. The cracking cycle mentioned might lead to regular zigzag changes on cracking planes on  $\{111\}$  and or  $\{100\}$  facets.

From this, the role of the corrosion/dissolution in cracking is crucial in an indirect way. It provides the hydrogen at the crack tip which will be absorbed and adsorbed locally causing an enhanced local plasticity at the crack tip.

The model proposes that the crack tip [105], based on the loading mode (I, II, or mixed) and the grain orientation, dislocations are nucleated on a preferential slip plane. These dislocations pile up against the obstacles later. Similar cleavage resulting from pile-ups induced by Frank-Read sources has been studied and quantified earlier by [47, 176].

## 1.9 Fracture Mechanics of Stainless Steel

For high strength materials such as stainless steel, the stress field is highly affected near local defects such as cracks. Thus, a design based on elastic analysis might be insufficient in such cases. Furthermore, when a crack reaches a critical length, a catastrophic propagation rate takes over, even in conditions where the macroscopically applied stress is much lower than that causing yield or failure in a classical tensile test [155].

The case gets even more complicated when it comes to SCC, which can take place at very low tensile stress for susceptible materials in corrosive environments. Stresses as low as 5 % of the yield stress can be sufficient to trigger cracking [102, 191].

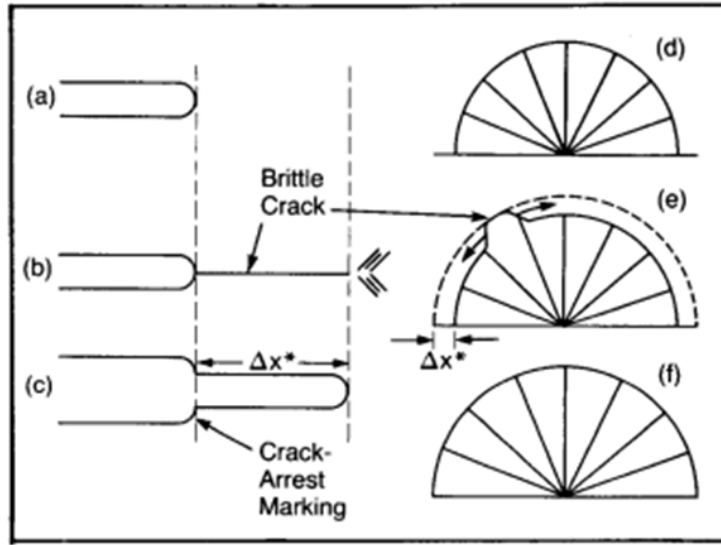


Figure 1.25: An illustration of TGSCC. (a-c): sections at the crack tip. (d-f): plan view of a semicircular crack  $\Delta x^*$  represents crack propagation length per event.

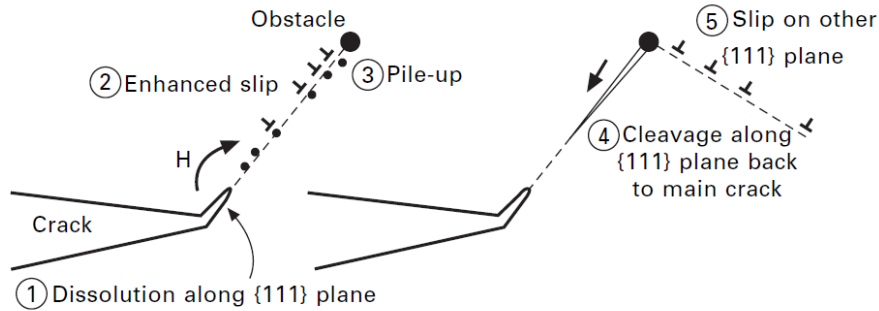


Figure 1.26: An illustration of CELP model showing the crack propagation steps [102].

### 1.9.1 Stress concentration factor

Alan Griffith was among the first to set quantitative relations for the stability of cracks based on energy criteria [39]. This marked the beginning of the branch of science called “fracture mechanics”, which gained a serious attention during the 20<sup>th</sup> century [39]. The main contribution of this science is setting relations between crack length, the material’s inherent resistance to crack growth, and the stress threshold causing high-speed propagation leading to failure [155].

**Griffith Criterion for Crack propagation:** For a body subjected to elastic stress, the strain energy can be calculated as the area under the stress-strain curve as given by Eq.1.13:

$$U = \frac{\sigma_{\infty}^2}{2E} \quad (1.13)$$

Where (U) is the strain energy per unit volume, ( $\sigma_{\infty}$  is the macroscopically applied stress, and ( $E$ ) is Young’s modulus. If we consider the case of a crack in such a body as shown in Fig. 1.27, there is an area around the crack that can’t sustain the load, which reduces the total stored strain energy.

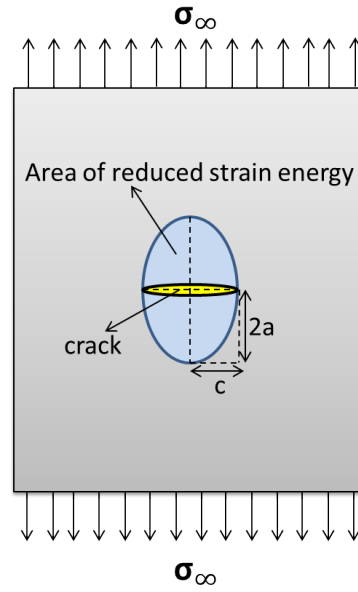


Figure 1.27: An infinite stressed body including a central crack. From [155, 39]

If this area is assumed to be elliptical with the dimensions shown in Fig. 1.27. Accordingly, this reduction of energy can be calculated as given by Eq.1.14:

$$U = \pi(2a)(c)B \frac{\sigma_{\infty}^2}{2E} \quad (1.14)$$

Where the volume of the ellipse is given by  $(\pi(2a)(c)B)$ , with  $(B)$  being a unit depth.

For an ideal brittle material, cracking causes an energy release which is absorbed in the form of surface energy ( $W$ ) that can be expressed by Eq.1.15:

$$W = (2cB)(2\gamma_s) = 4cB\gamma_s \quad (1.15)$$

Where  $(2cB)$  is the projected surface area of the crack,  $\gamma_s$  is the surface energy per unit area, and the factor 2 referring to the two crack facets.

By an energy balance criterion, Griffith states that for an increment of crack propagation, the crack will grow if the released energy is greater than the absorbed energy, as expressed by Eq.1.16:

$$\frac{dU}{dc} \geq \frac{dW}{dc} \quad (1.16)$$

After the derivation, Eq.1.17 is obtained:

$$\sigma_{\infty} \sqrt{\pi c} = \sqrt{2E\gamma_s} \quad (1.17)$$

According to this fracture theory, for the crack to grow, a critical strain energy release rate ( $G_c$ ) is required which equals twice the effective surface energy,  $\gamma_{\text{eff}}$ , as given by Eq.1.18, where  $G = (1/2B)(dU/dc)$ .

$$G_c = 2\gamma_s \quad (1.18)$$

The energy method was later replaced by stress concepts after the definition of stress field near cracks by numerical techniques. By this,  $(\gamma_s)$  and  $(\gamma_{\text{eff}})$  were replaced by the stress intensity factor ( $K$ ) and a critical value ( $K_c$ ), such that  $K = \sqrt{EG}$ , as given by Eq.1.19:

$$K_c = \sqrt{EG_c} = \sigma_{\infty} \sqrt{\pi c} \quad (1.19)$$

This equation represents the crack growth criterion, by which ( $K_c$ ) is the critical value of  $K$  above which the crack grows. The stress intensity factor as seen by Eq.1.19 increases by either the loading conditions, ( $\sigma_\infty$ ), or the crack length, ( $2c$ ). If the crack is of three-dimensional geometry,  $K$  increases as the crack depth ( $b$ ) increases, as will be explained in section: 1.9.6.

### 1.9.2 Fracture modes I, II, and III

By a linear elastic model, cracking can be decomposed into three modes as shown in Fig. 1.28 based on the crack facets' displacement direction [39, 155]:

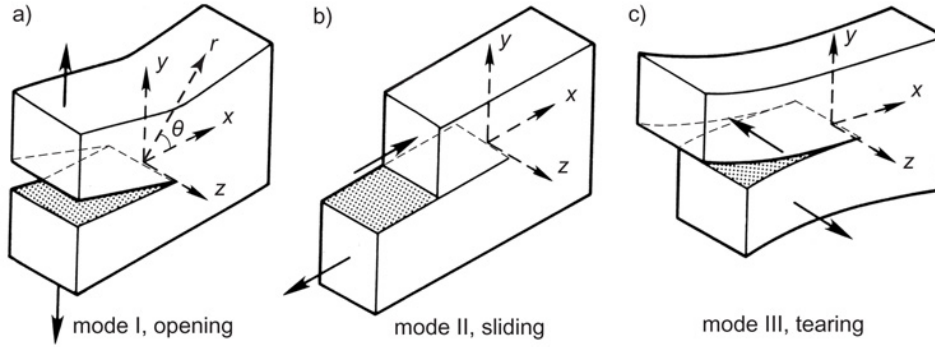


Figure 1.28: The three decomposed fracture modes. From [3].

- Mode I: the opening displacement in the  $y$  direction as shown in Fig. 1.28 (a). This mode is similar to the climb of an edge dislocation.
- Mode II: the sliding displacement along the  $x$  direction as shown by Fig. 1.28(b). This mode is similar to the glide of an edge dislocation.
- Mode III: the tearing displacement along the  $z$  direction as shown in Fig. 1.28(c). This mode is similar to a screw dislocation.
- Mode I and II are considered as plane strain case for a thick body, while a plane stress case for a thin plate [39].

If the crack is assumed to have a flat front and a zero radius of curvature at its tip, by linear elastic mechanics, for a specific point near the crack tip, ( $r, \theta$ ) in Fig. 1.28, the local stress can be derived for each of these modes. For mode I, the stress components are given by Eq.1.20-1.22 [39, 155]:

$$\sigma_x = \frac{K_I}{\sqrt{2\pi r}} \cos \frac{\theta}{2} \left( 1 - \sin \frac{\theta}{2} \sin \frac{3\theta}{2} \right) + \dots \quad (1.20)$$

$$\sigma_y = \frac{K_I}{\sqrt{2\pi r}} \cos \frac{\theta}{2} \left( 1 + \sin \frac{\theta}{2} \sin \frac{3\theta}{2} \right) + \dots \quad (1.21)$$

$$\tau_{xy} = \frac{K_I}{\sqrt{2\pi r}} \cos \frac{\theta}{2} \cos \frac{3\theta}{2} \sin \frac{\theta}{2} + \dots \quad (1.22)$$

As explained earlier,  $K_I$  in the previous equations represents the stress intensity factor, which holds information about stress intensity at the crack tip. According to Eq.1.19, which gives  $K_I$  to a central crack of length  $2c$ ,  $K_I$  depends on the applied stress ( $\sigma_\infty$ ), the crack length ( $c$ ), and the sample's geometry (depth).

The subscript I refers to fracture mode I. In an analogical way, the equations can be derived for mode II and III as well. The second term represented by the dots in these equations may be

neglected for distances ( $r \leq 0.1c$ ) [155]. For other cracks, geometries, and loading conditions,  $K_I$  is well tabulated in references such as [51].

### 1.9.3 Fracture by SCC

For plane-strain conditions, this critical value is known as the plane-strain fracture toughness ( $K_{Ic}$ ). If this value is exceeded, the crack will have an unstable growth as shown in Fig. 1.29(a).

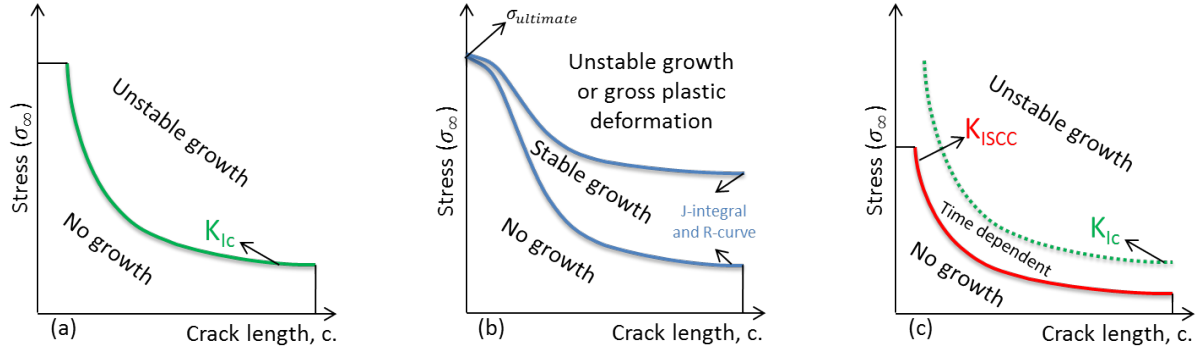


Figure 1.29: The cracking behavior as a function of the crack length and the stress intensity factor. From [12].

For elasto-plastic conditions, stable crack growth might happen, with excessive plastic deformation as shown in Fig. 1.29(b). In such conditions, non-linear J-integral and R-curve concepts are used to define the shown limits.

In specific cracking conditions such as fatigue or SCC, sub-critical crack growth takes place at ( $\Delta K_{th}$ ) or ( $K_{ISCC}$ ). The threshold intensity factor, ( $K_{th}$ ), can be as low as 5% of the stress intensity factor for fast fracture ( $K_{Ic}$ ), as illustrated by Fig. 1.29 (c) [102].

The reasons for the propagation of SCC at sub-critical values of  $K$  were discussed in the literature. The first to mention is the local fracture toughness reduction as an effect locally enhanced plasticity and possible hydrogen embrittlement near the crack tip as explained by CELP model (section 1.8.4) [105]. Other reasons were given by Staehle [171] such as: brittle film due to dealloying, oxygen diffusion in the grain boundary, and the influence of hydrogen to facilitate dislocation movement.

### 1.9.4 SCC propagation rate

According to experimental observation, the crack propagation rate, (**CPR**), shows two distinguished regimes when the stress intensity factor is varied, as illustrated in Fig. 1.30 [102].

The first zone is right after exceeding SCC threshold ( $K_{ISCC}$ ), where the CPR increases greatly as  $K$  increases. In the second zone, the CPR remains almost constant, regardless of the present  $K$  value. Some materials show a third zone where the CPR is proportional to  $K$ , just before reaching ( $K_{Ic}$ ) [102].

By the least modification of the material/environment system of SCC, the CPR can be extremely altered. Experimental work [36] showing the effect of  $Cl^-$  and  $O_2$  concentration on accelerating SCC propagation rate of 316 SS. Reported rates ranged between  $(2 - 120)10^{-8} \text{ mm.s}^{-1}$ , where even a  $Cl^-$  concentration in the order of 1 ppm can influence the CPR.

Examples of experimental SCC propagation rates related to pressurized water reactor operational conditions are conducted by [41, 40]. The CPR in 2000  $\mu\text{g/kg}$  oxygenated high purity water is about  $6.7 \cdot 10^{-7} \text{ mm.s}^{-1}$ , while in hydrogenated water conditions (HWC) it was  $3.41 \cdot 10^{-8} \text{ mm.s}^{-1}$ , making a conclusion that the crack growth acceleration by  $[Cl^-]$  in HWC conditions are much lower than that in oxygenated water.

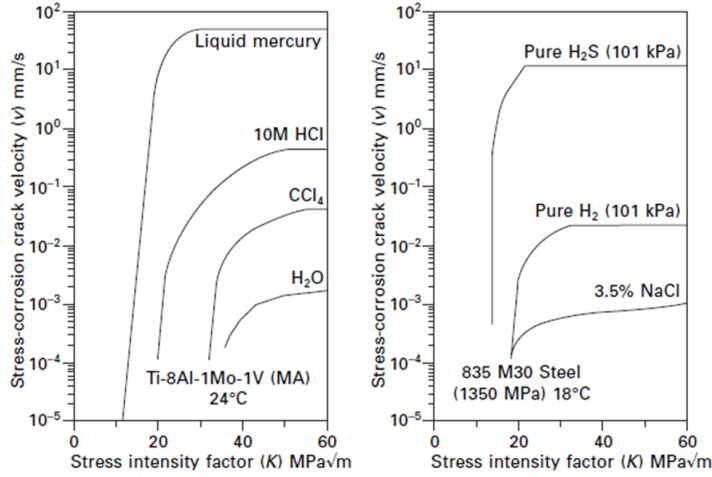


Figure 1.30: SCC propagation rate as a function of stress intensity factor. (a): Ti alloy in the indicated environments, From [48], and Ti alloy in mercury [102]. (b): High strength steel in NaCl, From [115], HE steel in H<sub>2</sub>S [102]

Concerning the electrochemical potential, three critical zones (A, B, and C) are identified on the polarization curve where SCC is accelerated [39], as shown in Fig. 2.5. Zone (A) represents the cathodic zone, where hydrogen embrittlement is favored. While in zone (C) SCC is possible after pit initiation and severe corrosion processes. And the last is zone (B), where the passive film is in a meta-stable state, favoring SCC. To overcome the anodic dissolution due to bad potential values, cathodic protection method is often applied to the concerned component.

### 1.9.5 Modeling of SCC

According to Staehle [171], the following seven variables must be considered in any attempt to produce a quantified mechanistic model of SCC: 1) Electrochemical potential, 2) pH level, 3) Identification and concentration of dissolved species, 4) Alloy composition, 5) Alloy structure, 6) Stress nature and state, 7) Temperature. If one of these variables is not considered in modeling, the resulting model will suffer shortcomings.

Most of the current crack propagation models include steps of passivity break-up, and the consequent dissolution until repassivation again. According to this, a SCC can be seen as localized oxidation at the crack tip, in addition to the enhanced mechanics by the local stress and strain [146, 164]. If the crack propagation is ascribed to the dissolution rate at the crack tip, the crack propagation rate can be found by relating the quantity of matter loss at each passivity break-up/recovery, and the local strain rate which defines the frequency of such process [58, 142, 8, 126]. This can be expressed as given by Eq.1.23:

$$\frac{dc}{dt} = \left( \frac{M}{\rho z F} \right) \left( \frac{Q_d}{t_d} \right) \quad (1.23)$$

where:  $t_d = \varepsilon_d / \dot{\varepsilon}_{ct}$ , with  $t_d = \varepsilon_d$  being threshold strain for degradation of the protective film, and  $\dot{\varepsilon}_{ct}$  being plastic strain rate at the crack tip. For the quantity  $Q_d$ , it represents the charge transfer during the dissolution/repassivation cycle. Using such equation requires fundamental data for oxidation kinetics and crack tip mechanics.

In his work, Shoji made an interesting review is about recent evidence for and against this model. Furthermore, his work focused on using several asymptotic fields of strain rates along with general oxidation kinetic laws to determine the crack propagation rate as given by Eq.1.23 for different material/environment combinations. Particularly, simulated light water reactor conditions were used for their solid state oxidation kinetic laws for the calculation of crack

propagation rate. Using asymptotic strain fields such as those proposed by [67, 78, 153], the calculated results showed to be consistent with experimental crack propagation rates.

This model was later included in the coupled environment fracture model (CEFM) [159]. The dependency of CPR on  $K$  was accurately predicted by CEFM. Concerning the semi-elliptical cracks, the model predicts that the orientation of the minor axis of the ellipse should be perpendicular to the surface, as observed experimentally. This is in agreement with the location of maximum  $K$  for an elliptical crack as calculated by Eq.1.24.

### 1.9.6 Determination of $K_{ISCC}$

The threshold stress intensity factor for SCC can be determined experimentally using different methods as explained [38]. As an example, either smooth or notched samples are used in slow-strain testing. Slow-raising load tests can be used as well, which give lower  $K_{ISCC}$  values than constant-load strain tests, making them more adapted to conservative applications [102].

In service, when a crack is detected, an estimation of the crack propagation rate should be conducted, which is based on the crack's present stress intensity factor ( $K_I$ ). For this, safety regulation codes provide tabulated data of  $K_I$  as a function of their geometry, and dimensions, which are based on stress calculations as given by Eq.1.20 to 1.21.

It's often the case in boiling water reactor secondary circuit that cracking in pressurized stainless steel vessels initiates by having an irregular crack front, but rapidly switches to a semi-elliptical shape [197, 159].

SCC has been reported in nickel alloy welds in nuclear power plants, where cracks were identified as two dimensional semi-elliptical cracks [120, 9]. A particularity about some of these cracks is that the aspect ratio, defined as the depth over half of the length, is greater than 1 [120].

Current power plant operation codes provide a variety of solutions for the stress intensity factor, but not for cracks having an aspect ratio greater than 1 [120]. Empirical solutions are available for an aspect ratio up to 2.5, such as that given by Newman et al [124]. Others used finite element methods ranging from 2 to 8 [120], based on a method they proposed called the influence function.

An interesting solution for an aspect ratio up to 2 was given by Fett [49, 50]. His solution is based on the well-known limit case considerations of the arbitrary stress field, where he separated it into a constant and a linear stress contributions. For these components, the solutions for the stress intensity factor are known. In a later work [52], the weighting functions were used to find a solution for stress intensity factor was obtained as well for an oblique crack in a semi-infinite plate.

**Elliptical cracks:** Fig. 1.31 shows the general case of an infinite body having an ellipsoidal crack with semi-axis  $c$  and  $b$  uniaxially loaded in mode I. For a semi-elliptical central crack, the outer surface of the body is in  $(y - z)$  surface. For such a crack, the stress intensity factor will vary along the tip profile [39], which can be calculated by Eq.1.24:

$$K_I(\phi) = \frac{\sigma_\infty \sqrt{\pi c}}{E(\beta)} (\sin^2 \phi + \frac{c^2}{b^2} \cos^2 \phi)^{1/4} \quad (1.24)$$

In this equation, the elliptical integral,  $E(\beta)$ , is given by Eq.1.25:

$$E(\beta) = \int_0^{\pi/2} (1 - \beta^2 \cos^2 \phi)^{1/2} d\phi \quad (1.25)$$

Where  $\beta^2 = 1 - (c/b)^2$ , and  $\phi$  is the angle parameter of the ellipse, as shown in Fig. 1.31. According to Eq.1.24,  $K_I$  takes the maximum at the minor axis of the ellipse, and it increases as the difference between  $b$  and  $c$  gets higher [39].



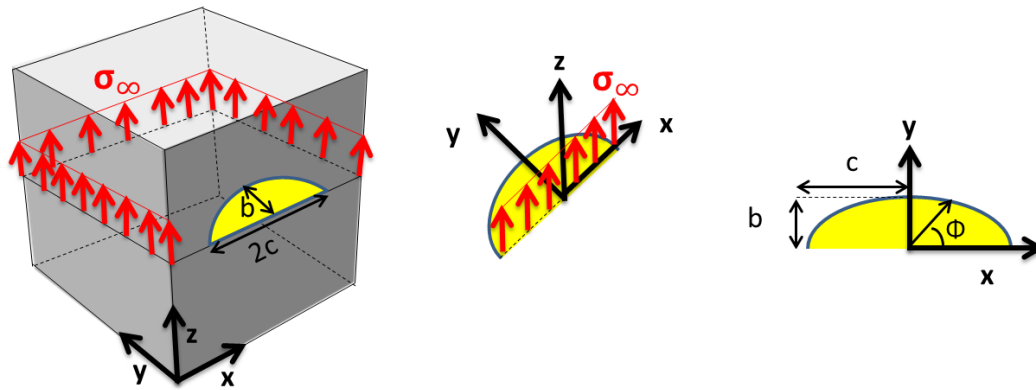


Figure 1.31: An elliptical crack having  $b$  and  $c$  semi-axis, and loaded by a homogeneous load  $\sigma_{\infty}$ .

## 1.10 Crystallographic Aspects of SCC

It's well known that SCC can be either inter-granular, transgranular, or a mixture of both [64, 194, 154, 119]. Cracking mode and possible transition depend on several factors, such as: material composition, stacking fault energy, grain size, applied/residual stress, strain rate, and the solution composition [42, 117].

Texture effect on the corrosion behavior of stainless steel showed to alter the pitting corrosion potential of 304L stainless steel in sulfuric acid solution [89]. For a study conducted on mild steel, closed-packed crystal planes showed better passivation properties and corrosion resistance [34]. However, such reason on their own cannot justify SCC features such as cleavage and shear steps. This led to other models including mechanical factors to explain TGSCC such as film induced model [39].

TGSCC has been often reported to have crystallographic features [94, 198, 5, 53, 105]. Meletis provided a review of SCC crystallography, covering materials of different lattice structure and different environments [117], from which some of the following results are reported.

Cracking crystallography depends on the lattice structure of the fractured material [117, 10], thus, only FCC materials will be of our interest here. Hines and Hugill noticed cracks to change direction as they encounter grain or twin boundary, as an evidence of crystallographic aspects [117].

Characterization of SCC was performed conventionally either by two-surface trace analysis, X-ray diffraction, and etch-pit development [117].

SCC tests were performed by Scully [69] on 304 stainless steel in  $5 \text{ M H}_2\text{SO}_4 + 0.5 \text{ M NaCl}$  at room temperature, using U-bent samples. SEM analysis of the obtained cracks showed that the crack propagation occurred along  $\{111\}$  planes. Cracking was explained as a result of the interaction of dislocation pile-ups, causing transgranular corrosion acceleration. In another work [70], Scully also used boiling  $\text{MgCl}_2$  solutions to perform SCC tests on 304 stainless steel. Results revealed cracking to take places on  $\{110\}$  plane, with extensive slipping on  $\{111\}$  planes resulting in a fracture facet including a mixture of these planes.

Loathan [96] studied 304 and 304L SS SCC tests in either boiling 42%  $\text{MgCl}_2$  conditions, or 100 ppm  $[\text{Cl}^-]$  solutions. Linear arrays of preferential pitting formed along  $\{111\}$  planes and cracks preferentially occurred at stacking faults and dislocation arrays. All the observed cracks were of  $\{111\}$  family. Other preferential orientations were found by Liu et al. [117] for 304 and 310 steel, where fracture facets were of  $\{100\}$  planes for 310 steel, while  $\{211\}$  and  $\{110\}$  family of planes were for 304 steels. An indication of  $\{310\}$  and  $\{210\}$  fracture planes was made by Silcock [117] in single crystal 316 SS SCC, which is in agreement of another work done by Marek [108].

Direct observation of SCC of thin 304 SS sheets in 42% boiling  $\text{MgCl}_2$  reported the internal wall of etch pits to be composed of  $\{111\}$  planes [195]. On the other hand, cracks showed to propagate along  $\{111\}$  planes at the grain level, while fracture planes composing this orientation were more of  $\{100\}$  or  $\{110\}$  rather than  $\{111\}$  planes.

SEM was used by Tromans [182] to characterize SCC fractography of single phase copper based alloys and austenitic steel. Results show that TGSCC initiated along the  $\{111\}$  planes, which were correlated to alloys having a planar arrangement of dislocations. Furthermore, preferential dissolution take place on dislocations, forming the main crack nucleation sites. This preferential tendency was ascribed to the raising tensile stress from dislocations. This description corresponds to a model suggested by Robertson and Tetelman [10], where preferential chemical dissolution takes place at Cottrell-Lomer sessile dislocations, which initiates a cracking site. The number of dislocation pile-ups on the primary and conjugate 111 slipping system determines the cracking direction. The model predicts  $\{110\}$  or  $\{100\}$  fracture plane if the number of dislocation pile-ups is equal on each of the two  $\{111\}$  planes. However, if the dislocations pile up on one  $\{111\}$  plane, a maximum normal tensile stress resulting from such dislocations across a plain tilted at  $70.5^\circ$  to the slip containing the group [10]. This angle in FCC system corresponds to the another  $\{111\}$  plane [177, 117].

Recent SCC models included these common crystallographic aspects, such as CELP (section 1.8.4), and AIDE model (section 1.8.2) [99, 100, 102, 101].

## 1.11 Bibliographical Conclusions

### 1.11.1 The phenomenological description of SCC

Phenomenologically, SCC was described by two categories of models. The first is the dissolution-based models, describing the crack propagation process as a result of successive steps of passive film break-up, dissolution, and healing at the crack tip [162, 183]. Furthermore, the severe dissolution of the freshly exposed surface after each slipping step is intensified by the specific chemical conditions near the crack tip until it passivates again. SCC in the mechanical fracture models can be divided into brittle and ductile crack propagation processes. Ductile mechanical models cover corrosion tunneling and absorption enhanced plasticity models. While brittle cracking models cover tarnish rupture and film-induced cleavage models [11]. According to mechanical fracture models, SCC could be ductile as given by corrosion tunneling and absorption enhanced plasticity models. Nevertheless, SCC can also be brittle as seen by models covering tarnish rupture, and film-induced cleavage models [11]. Models based on environmentally assisted mechanical fracture argue the reduced mechanical properties near the crack tip as a result of local absorption and adsorption of chemical species, such as hydrogen [72, 99, 100, 101, 127].

The wide range of proposed mechanisms in the literature led to no eventual agreement on which specific mechanism operates for a given material/environment system. However, a combination of the different proposed mechanisms is possible, especially during the different stages of SCC; nucleation, propagation, and cleavage. The reason behind this complexity is the multi-axial and multi-scale material/electrolyte interactions. Another reason is that present techniques are incapable of making direct crack tip observation. Generally, characterization methods rely on crack facet observation which is usually corroded after the SCC, causing loss of the fine details required to correctly study the cracking mechanics.

### 1.11.2 Quantified modeling of SCC

A lot of progress has been made on the quantification of SCC propagation and prediction. These models took into account the synergistic effect of localized oxidation at the crack tip, in addition to the enhanced mechanics by the local stress and strain [142, 8, 126, 146, 164, 58]. These models calculated the step-wise loss of matter through each passivity break-up/heal cycle,

which is controlled by the rate of the local strain near the crack tip, and the threshold strain for passive film break-up. Using such models Shoji reported a successful prediction of SCC kinetics compared to SCC tests in light water reactor conditions [164]. This model was upgraded by D. Macdonald and coworkers to take into account the semi-elliptical approximate shape of SCC cracks [159], which predicted correctly the orientation of the minor axis of the crack to be perpendicular to the corrosion-exposed surface. No statistics have been made about the elliptical aspect ratio of the analyzed cracks, neither a statistical estimation methodology of these data.

Though these models were well developed, none of them considered the direct effect of stress on active metal dissolution, passivation and film growth kinetics, and passive film properties. Furthermore, none of them presented a prediction of SCC in acidic mediums. In addition to this, no consideration was made for the local micro-structure of the material, the orientation of grain boundaries, or the crystallographic orientation near the crack-tip, as was described in AIDE and CELP models (section 1.8).

### 1.11.3 Influence of stress on stainless steel passivation

Mechanical processes and heat treatment play an important role in corrosion behavior, as an effect of altering its micro-structure [89], and the local composition such as the case in sensitization, and surface mechanical properties [79]. Mechanical deformation of stainless steel by cold working was reported to increase the difficulty to get to passivation state [43]. On another work, it was reported that cold working the material before heat treatment caused a total absence of sensitization, which reduces the susceptibility of this material to SCC [35].

Evidences of the influence of stress on surface activity, the charge transfer resistance through the passive film, and its structure/thickness have been reported in the literature [122, 188]. However, very little was made to quantitatively correlate those effects and the stress state. Nevertheless, none of the investigated literature gave quantified measures for the kinetics of passivation taking place over stressed materials, and consequently, no data are found on the effect it takes on the passive film properties.

### 1.11.4 Influence of the micro-structure crystallography

According to the literature review, no global agreement concerning the crystallography of SCC of FCC alloys has been reached. But as a conclusion, SCC is accepted to initiate along  $\{111\}$  slip planes as a result of dissolution. For austenitic SS, the plane family  $\{100\}$  is a preferential cracking plane, while it tends to be of  $\{110\}$  in low nickel based materials. These common crystallographic features indicate that SCC operating mechanics and the crack orientation are influenced by the local micro-structure and crystallography near the crack tip [116, 117]. However, in all the previously reviewed work, no distinction has been made to fracture by SCC at the minor or the major axis of the semi-elliptical cracks, where the variation of  $K_I$  values along the crack's profile might lead to better understanding of the fractographic aspects.

## 1.12 Research Strategy and Specification

### 1.12.1 Scope and objectives

The objective of this research is to fill for the shortcomings summarized in bibliographical conclusions. This involves electrochemical and SCC fractographic experimentation and analysis.

As seen in section 1.8, all SCC models describing crack propagation mechanisms had inevitable dissolution and mechanical terms to explain the preferential propagation at the crack tip. Different models tried to justify crack propagation in SCC based on four possible reasons [102]:

1. Materials under applied/residual stress have higher chemical activity than that of it in the relaxed state. This implies more dissolution near the crack tip, and thus, the crack propagation might be partially explained by this preferential dissolution.
2. Higher stress and strain value near the crack tip. This leads to local slipping systems activation near the crack tip which causes the film to break down, exposing the material to excessive corrosion. In addition to that, high local stress values might cause the passive film constructed on the crack tip to be more defective than that constructed over the relaxed areas represented by the crack facets.
3. On the crack facets, the dissolution is limited due to the depletion of the anodic microstructural features which produces a protective layer with the noble elements left on the surface.
4. Local chemical conditions near the crack tip resulting in more aggressive conditions than that at the crack facet. This might be due to more hydrogen concentration for its transfer being limited, or due to an initial more intense local dissolution.

### 1.12.2 Experimental strategy

From these possible explanations, experimental procedures might be held to check for each of them separately as listed below.

**Effect of stress on activity:** If the material has higher activity due to the applied stress, this additional activity might be detected by the external current registered during polarization tests performed on stressed and non-stressed samples in a selected environment.

**Effect of stress on the Passivity:** To study passive film construction and its dissolution, it requires careful analysis of the passivation current transients obtained during the application of a passivation pulse in conventional cycling experiments. This should be done hand in hand with ICP, to give the quantitative metallic dissolution concentrations. From these combined, information will be obtained on the kinetics of passive film construction, its thickness, and chemical composition.

**Passive film quality:** In certain passivation conditions, after all the anodic features have been dissolved from the material's surface, a layer of the left noble elements act as a protection barrier between the corrosive environment and the bulk of the material [131, 132]. This is to be verified again, in addition to checking whether the applied stress has an influence on this layer or not. This can be answered after the careful analysis of the ICP experiments.

**Local aggressive conditions:** If the intensity of dissolution over stressed materials is proved, this point can be confirmed. This implies having more intensive dissolution and higher local material loss, higher intensity of hydrogen production and thus its absorption/adsorption leading to local embrittlement. This can explain the lowering the local  $K_I$  at the crack tip, leading to fracture at the SCC intensity factor  $K_{Ic}$ . This can be checked out using both the current transients and the dissolution rates obtained from conventional and ICP experiments.

**Cracking aspects:** This involves exploiting SCC experiments to answer questions about the cracking nature such as the influence of stress magnitude, electrolyte acidity, chloride content, or the applied potential on crack propagation. Another objective is to establish an experimental and post-experimental procedure by which statistically valid data can be produced to give reliable answers about cracking kinetics, branching, and changing orientation. Other factors of interest are the macroscopic and microscopic relation of cracking with the applied load and the microstructure near the crack tip. The process should include statistical estimation and validation of the performed measures, such as the crack length and the aspect ratio of the SCC elliptical cracks, in addition to the crystallographic orientation of the fracture planes.

**Mechano-chemical interaction:** The developed methodology should be able to take into consideration the influence of mechanical and chemical variables on the different studied aspects of SCC. This stands for the scope of this research and beyond, where correlations are sought

between the considered trait of cracking/corrosion and the corresponding variables. Examples of these variables are: the applied stress state, the solution acidity, and the chloride content, and the hydrodynamics of the electrolyte over the material's surface.

### 1.12.3 Realization

in order to perform these corrosion experiments over stressed and non-stressed samples, the research will take place in four distinct stages:

1. The existing cell used in AESEC (section: 2.4.2) can be used to study samples with residual stresses. This cell has to be adapted such that it fits samples with a controlled uniaxial stress state. This assembly is to be coupled to the ICP in order to study the corrosion of the material under the effect of selected states of applied stress. This stage includes:
  - Solving the problems of the hermetic design, liquid flow, and stress control.
  - Validation of this new cell by the tests performed with previously existing systems, such as the stagnant cell.
2. Detailed microstructure characterization of the base material is to be performed using optical and electronic microscopy (SEM, EBSD, EDS) as well as diffraction methods (residual stress analysis). Recognizing the chemical composition of the bulk of the material is a vital step in this characterization, in addition to a statistical spatial analysis of the elemental concentrations over the surface. The mechanical properties are to be analyzed using the conventional tensile test along the rolling, transverse, and longitudinal directions.
3. Selected case studies of stressed materials will be subjected to SCC tests. This involves two main experimental branches:
  - SCC experiments where cracking is produced in order to perform a post mortem morphological study of the fracture surface, cracking crystallographic aspects, and the cracking kinetics/mechanics. This involves SEM, EBSD, EDS analysis of the produced cracks. The applied stress and how it is affected by SCC is to be analyzed using XRD methods.
  - Measurement of the corrosion leaching concentration curves, along with the polarization curves, will be performed using conventional and AESEC methods. This is exploited to understand the formation of the oxide passive layer.
4. Applying the obtained results to reply the specified questions required to model SCC. This includes the stress analysis before and after cracking, cracking crystallography, propagation kinetics, and branching aspects. In addition to surface oxidation kinetics, and the influence of stress on surface chemical processes and cracking aspects.

### 1.12.4 Originality

The originality in the present research is the possibility to multi-axially study SCC mechanical and chemical aspects. By performing corrosion and SCC tests with different stress states, in-situ measurement of corrosion current and elementary concentration of leaching solution for stressed or relaxed samples. Thus, the synergistic interaction between the mechanical and chemical aspects is experimentally sought. This was the case equally for what refers to oxidation kinetics and passive film properties from one side, and the cracking crystallographic and propagation aspects from the other side.

SEM pre and post experimental observation was performed to understand the corrosion morphology and fractography of samples having different surface preparations and stress states, tested in different electrolytes. This was combined with the crystallographic and chemical maps analyzing selected zones of interest using EBSD and EDS respectively.

Last but not least, XRD analysis of the applied/residual stresses was conducted for the initial material state, after straining the sample, and eventually after the SCC test.



## Experimental Techniques

Different experimental techniques/tools were used throughout this research. Table 2.1 gives a summary of them and the main purpose for which they were used.

Table 2.1: The experimental tools used throughout the present research and their main purpose.

Experimetal tool	Purpose/Main function
SpectroMaXx	Surface elemental composition analysis of the considered alloy.
Leco CS-300	Carbon and sulfur content percentage analysis for the alloy in hand.
Tensile test	Characterizing the mechanical properties of the alloy.
Conventional Electro-chemistry	Performing corrosion tests while controlling/measuring the current and potential.
ICP-OES	Elemental analysis of the flow cell downstream solutions.
SEM	Observation of surface topography or morphology.
EDS	Chemical analysis of the surface elemental composition.
EBSD	Obtaining information about crystallographic orientations, and other related statistical data.
XRD	Applied/residual stress analysis, in addition to phase and texture.
Matlab	Simulation of random crack sectioning, in addition to classical calculations.
Catia	Computer aided design for sample and support drafting.
Abaqus	Finite element simulation and modeling of sample straining.
LateX	Documentation of the conducted scientific work.

The following sections explain the experimental methods one by one.

### 2.1 Material Used for Experiments

Stainless Steel (SS) of 304L grade was selected to be used in these experiments. The material was industrially in the form of a metal sheet of  $\approx 1.65$  mm thickness. This is a widely used grade in commercial applications, and it has an equal importance in nuclear industry [23, 15, 116, 168, 170, 174, 191].



## 2.2 Chemical Composition of the Base Material

### 2.2.1 SpectromaXx

To analyze the chemical composition of the material in hand, the

**Principle:** SpectromaXx allows the evaporation of the material's sample by a disruptive discharge over the surface. The liberated atoms and ions are thus excited emitting light with wavelengths representing the considered elements. This radiation is directed towards the optical and measuring system using the CDD\* camera.

The acquired data are then compared to a calibration database, which is already stocked in the machine. This allows the calculation of the corresponding concentrations which are then provided as an output of the analysis [169].

\*CDD: Charge-coupled device, or in other words, photo-sensitive detecting device.

**Procedure:** Two samples were cut, having the dimensions of  $3 \times 4$  cm. The surface was conditioned by mechanical rough polishing, for the purpose of getting rid of the industrial surface finishing aspects. The two samples were studied for their chemical composition on the back and the face of the sample (the surface which is usually protected by the plastic film when received from the industry). On each face, 6 points were taken for the analysis as shown in Fig. 2.1. Results are given in section: 3.1.

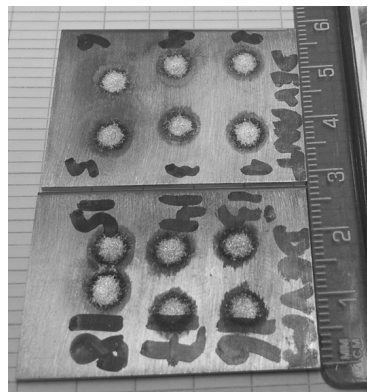


Figure 2.1: Sample after the chemical analysis performed by SpectromaXx.

### 2.2.2 Carbon and sulfur elemental analysis

For elementary dosing of the metal in hand, carbon and sulfur content can be measured by carbon and sulfur analyzer; namely: Leco cs-300.

In order to perform this experiment, the alloy should be formed into chip-shape specimens (metal shavings) so that they are easy to get molten during the experiment.

This analysis technique provides a high accuracy for the elementary composition of carbon and sulfur of the alloy in hand.

**Principle:** The sample shaving is melted by the aid of a stream of purified oxygen. As a result,  $\text{CO}_2$  and  $\text{SO}_2$  gasses are produced from the carbon and sulfur contained in the alloy. Quantification of these gasses is then conducted by infrared detection. The detection limit of this equipment is up to 0.005% by weight of the sample [1].

**Sample preparation:** To prepare 9 g of metal chips (shavings).

**Procedure:** Calibrating the machine with standards of previously known percentages of carbon and sulfur content. Standard to be used for the calibration should correspond more or less to the expected carbon and sulfur content [1]. According to AISI for standard grades of stainless steel, the percentage of carbon and sulfur are 0.08% and 0.03% respectively [11]. Therefore, two standards were suggested to be used for calibration, which are shown for their carbon and sulfur content in Table 2.2:

Table 2.2: Concentration of the standards used for signal calibration.

Standard	Carbon % by wt.	Sulfur % by wt.
1st	0.047% $\pm$ 0.002	0.0267% $\pm$ 0.0011
2nd	0.055 $\pm$ 0.001	0.0092 $\pm$ 0.0006

In order to get statistically accepted results, three samples of the alloy in hand are tested for their carbon and sulfur content, with each of the standards used. Their average is eventually taken as the final result indicating the percentage of each. Results are given in section: 3.1.

### 2.2.3 Mechanical properties

Three tensile tests were performed at each of the following directions: the rolling (RD), transverse (TD) and 45/ direction (45/D). The dimensions of the tensile samples are illustrated in Fig. 2.2. Experimental results are given in section: 3.6.

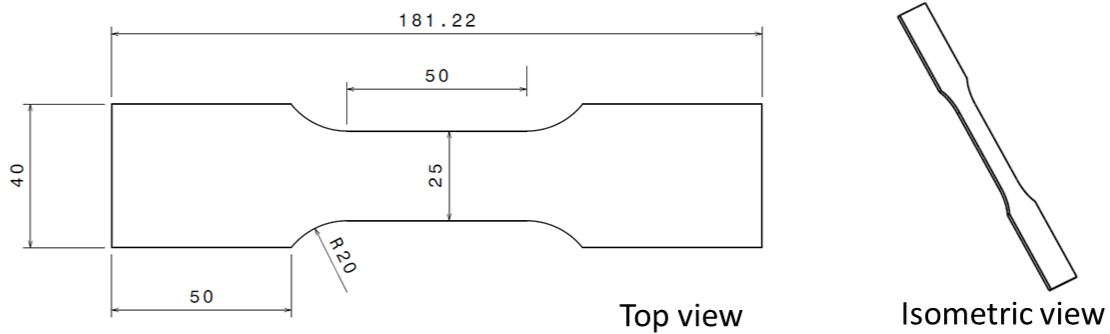


Figure 2.2: The dimensions (mm) of the tensile samples of 304L stainless steel.

### 2.2.4 Sample shape and dimensions

The material is industrially provided in sheets of 1.67 mm thickness, with one face protected by a self-adherent plastic film.

Thus, samples were prepared to fit the electrochemical cell and the mechanical supports which are designed to apply predetermined strain values as will be explained right after this section.

The dimensions and the sample are shown in Fig. 2.3. Samples were cut by water jet, to avoid possible residual or thermal effects attributed to conventional cutting techniques.

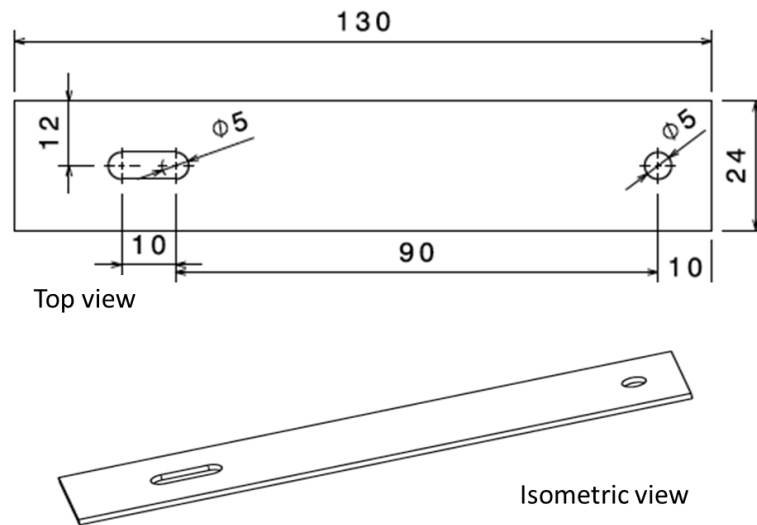


Figure 2.3: The dimensions (mm) and the shape of the corrosion test samples of 304L stainless steel.

## 2.3 Polarization Corrosion Test

### 2.3.1 Linear polarization corrosion test

Classically, due to their simplicity and the low experimental costs, weight loss techniques were used to determine the corrosion rate of a given metal of interest. However, these techniques have the disadvantage of requiring long experimental time, thus more rapid methods have been sought.

Since the electrochemical nature of corrosion was discovered, electrochemical methods for corrosion testing have been developed and used. These methods have been employed to develop knowledge about material corrosion and understand corrosion mechanisms.

#### Polarisation definition

According to ASTM [13], "polarization" is defined as the change from the open circuit electrode potential as a result of the passage of current. Polarization testing methods are those tests where the potential of the metallic piece is changed while registering the corresponding produced current as a function of the applied potential. The variation of potential could be step-wise (potentiostatic) or continuous (potentiodynamic).

#### Mixed Potential Theory

Electrochemical polarization and testing methods have proven to be very useful tool since their birth in 1922 [2]. This was the reason for the development of the mixed potential theory, which helped explain the experimental results obtained by the polarization experiments.

Mixed potential theory takes into account the hypothesis that during an electrochemical reaction, other than double layer charging, there is no charge accumulation. A second main consideration in this theory is that any electrochemical reaction can be divided into two or more partial independent anodic or cathodic reaction [60]. Here, an important assumption is that the anodic and cathodic areas of the metal surface have the same potential, which is the corrosion potential. This assumption means that the anodic and cathodic reactions are not separated in areas. Local separation of anodic/cathodic reaction will lead to potential variation from one site

to another, which violates the assumption of having the same potential. So, both anodic and cathodic reactions occur exactly on the same location over the entire corroding metal surface [130].

To have a quick representation of what has been explained, a simple case where a metal surface reacts with one anodic reaction producing an anodic current density, ( $j_a$ ), and a cathodic reaction producing a cathodic current density, ( $j_c$ ). If linear polarization is performed around the open circuit potential of this metal, the total current density,  $j_{total}$ , can be recorded as a function of voltage and plotted as shown in Fig. 2.4 (a) and (b) [121, 119, 168].

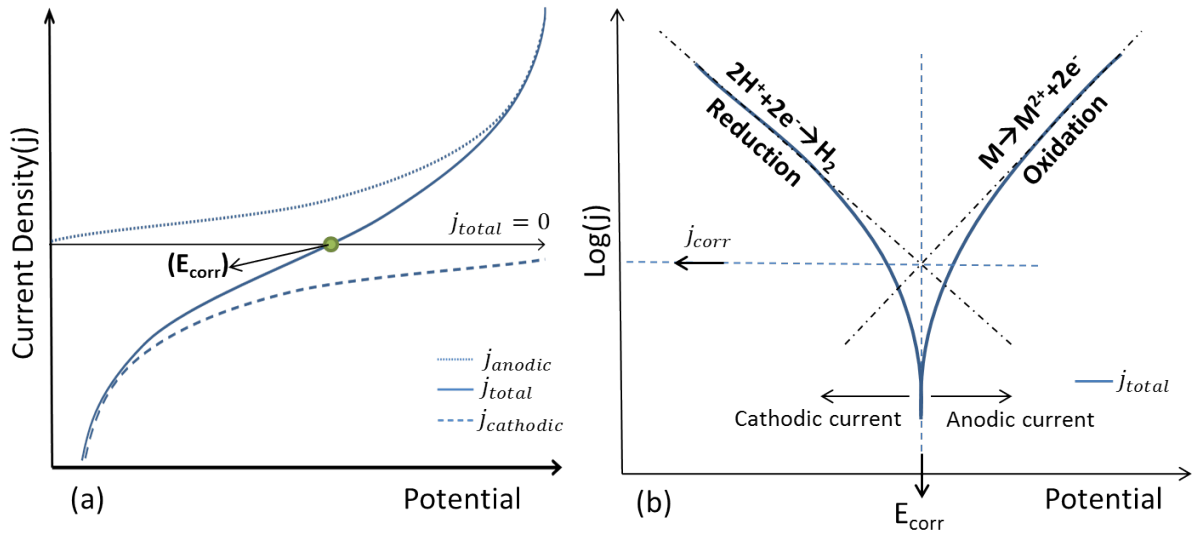


Figure 2.4: Polarization curve showing the cathodic and anodic current density curves, and the total (measured) current density.

The total (or equally external) current, ( $i_{total}$ ), is the current detected during polarization by the testing equipment, which is the summation of the anodic current,  $i_c$ , and the cathodic current,  $i_a$ , at a given applied voltage as expressed by Eq.2.1.

$$i_{total} = i_c + i_a \quad (2.1)$$

The current density,  $j/(\text{mA} \cdot \text{cm}^{-2})$ , is obtained by dividing the considered current,  $i/\text{mA}$ , over the area of the working electrode that is exposed to the electrolyte,  $A/\text{cm}^2$ , as given by Eq.2.2.

$$j = \frac{i}{A} \quad (2.2)$$

In the diagram shown in Fig. 2.4 (a), the total current density is plotted versus the applied potential which gives what is called a polarization curve. When plotted to a semi-log axis as shown in Fig. 2.4 (b), the corrosion potential,  $E_{corr}$ , can be determined. At  $E_{corr}$ , the magnitudes of the anodic and the cathodic currents are equal as shown by Eq.2.3. This magnitude of current is named the corrosion current  $i_{corr}$  as illustrated in Fig. 2.4 (b) [130, 168].

$$(i_{corr} = i_a = -i_c) \text{ at } E_{corr} \quad (2.3)$$

When the material is left to the open circuit potential,  $E_{corr}$ , for conditions where  $A_a$  and  $A_c$  are assumed equal, the corrosion rate of that metal can be expressed by  $i_{corr}$ , where  $A_a$  and  $A_c$  are the anodic and cathodic areas of the working electrode respectively. At such conditions, zero total current is measured as the anodic and cathode reactions are equal in absolute value, as given by Eq.2.4:

$$i_{\text{total}} = 0; i_a = -i_c \quad (2.4)$$

Note: An example of corrosion current and the relation between the anodic, cathodic and total measured current for a multi-element corrosion system is given in Appendix G.

### 2.3.2 Polarization curve of passive materials

A polarization curve has a couple of common features that will be explained below. Normally, this description applies to a pure metal, where there is only one cathodic and anodic process taking place. For an alloy such as stainless steel which is composed of a huge matrix of elements, there are multiple anodic and cathodic processes occurring in parallel during the polarization test. For this case, the summation of all cathodic processes at one side,  $\Sigma i_c(m)$ , and that of the anodic processes on the other side,  $\Sigma i_a(m)$  compete together resulting in the total current measured during the experiment as given by Eq.2.5, where (m) refers to any given metal from the alloy's matrix.

$$i_{\text{total}} = \Sigma i_a(m) + \Sigma i_c(m) \quad (2.5)$$

Thus, for the case of stainless steel polarization in an acid medium such as de-aerated sulphuric acid, a polarization curve with well-defined features is obtained. Features of main concern in the present work are [18, 54]:

- Corrosion potential ( $E_{\text{corr}}$ ): This was discussed previously in section 2.3.1.
- Critical current density ( $i_{\text{cr}}$ ): This current represents the maximum corrosion current density, followed by a strong decrease in the current density, due to passive film formation over the metal surface.
- Passivation Potential ( $E_{\text{pass}}$ ): This is the potential value corresponding to  $i_{\text{cr}}$  on the polarization curve.

A representative polarization curve showing these points is shown in Fig. 2.5

As shown in Fig. 2.5, the current curve is divided into three main domains, which can be listed as [54, 130]:

1. Active domain: In this domain, the material behaves as was described earlier in Fig. 2.4 (a), where anodic and cathodic reactions are significant. A slight increase in the oxidation power (by the applied potential) results in an increase in the corrosion rate. This domain should be avoided in order to protect the material from severe corrosion.
2. Passive domain: The beginning of this region is detected when an increase in the oxidation power results in a sudden decrease in the corrosion rate. This is due to reaching the critical current, ( $E_{\text{passivation}}, j_{\text{critical}}$ ) which is enough to construct the passive film, protecting the metal surface from interaction with the surrounding corrosive environment. Starting from  $E_a$ , an increase in the oxidation power result in very negligible variation in the corrosion rate, since the material's surface is well protected by the passive film. Between the states  $E_{\text{passivation}}$  and  $E_a$ , the material's state is meta-stable. All material applications should be operated to sustain itself within this domain for a safe utilization of the material.
3. Transpassive domain: In this domain, due to the high voltage difference, the passive film starts to collapse, resulting in severe and pitting corrosion.

The description given above of the polarization curve is simplified to cover the scope of this research. For stainless steel in oxidizing acids such as  $\text{H}_2\text{SO}_4$ , other advanced features might be expected such as cathodic loops after the passivation peak. Readers are invited to consult more developed references for extra information on this topic, such as [104] which covers wide aspects of linear potential sweep and cyclic voltammetry.

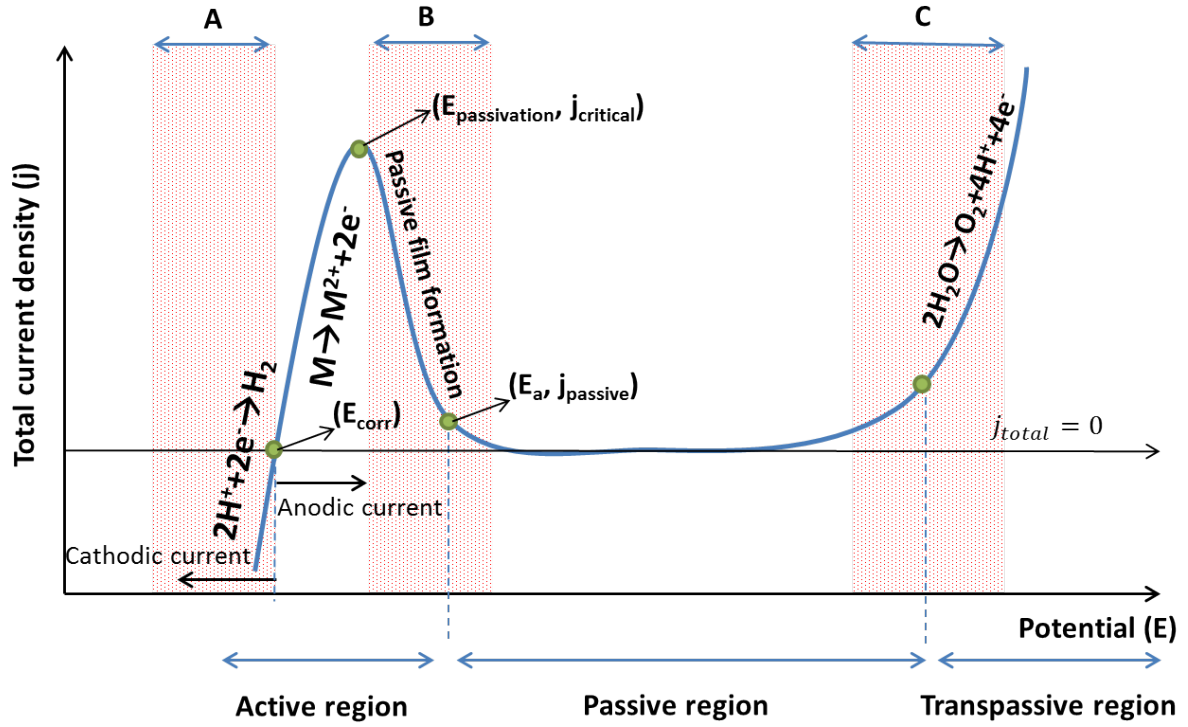


Figure 2.5: Polarization curve showing features of interest. Zone A, B, and C are the critical potential zones for SCC.

## 2.4 Experimental Setup

### 2.4.1 Conventional electrochemistry

As seen in previous sections 2.3.1 and 2.3.2, polarization is a very useful tool to access information related to metal corrosion. Experimental electrochemistry involves measurements of potential, current, and polarization measurement using an externally applied potential or current [63]. Here, the supplied current should match a certain value of the potential difference, which represents the polarization  $\Delta E$ . This potential difference is between the applied potential  $E_{ap}$  and the open circuit potential  $E_{OC}$  [130].

$$\Delta E = E_{ap} - E_{OC}$$

A device called a potentiostat/galvanostat performs the variation of potential in order to apply certain current. A potentiostat is a device that can measure current at certain value of potential, where a galvanostat is a device recording potential at certain current value.

Three-electrode electrochemical cell is usually required to perform the polarization curves. The name comes from the three electrodes of this cell are:

1. The working electrode: which is the metal/alloy being tested.
2. A reference electrode: which should be at a constant equilibrium potential, which is taken as a reference value for other measurements.
3. A counter electrode: to balances the current observed at the working electrode, usually it's made of platinum.

In this thesis, two electrochemical cells were used: stagnant cell, and a flow cell, both of which are three-electrode cells.

**Conventional cell specifications:** An illustration of the stagnant cell is shown in Fig. 2.6. In this cell, Ag/AgCl reference electrode was used, while a platinum electrode was used as the counter electrode. The potentiostat used was multi-channel BioLogic VMP3 providing 61 fA and 61  $\mu$ V for the current and voltage resolutions. The working electrode was exposed to the electrolyte through a viton gasket of 6 mm diameter sealing the sample-cell connection. The cell has a circular cross-section of 5 cm, with a capacity of 25 mL of electrolyte.

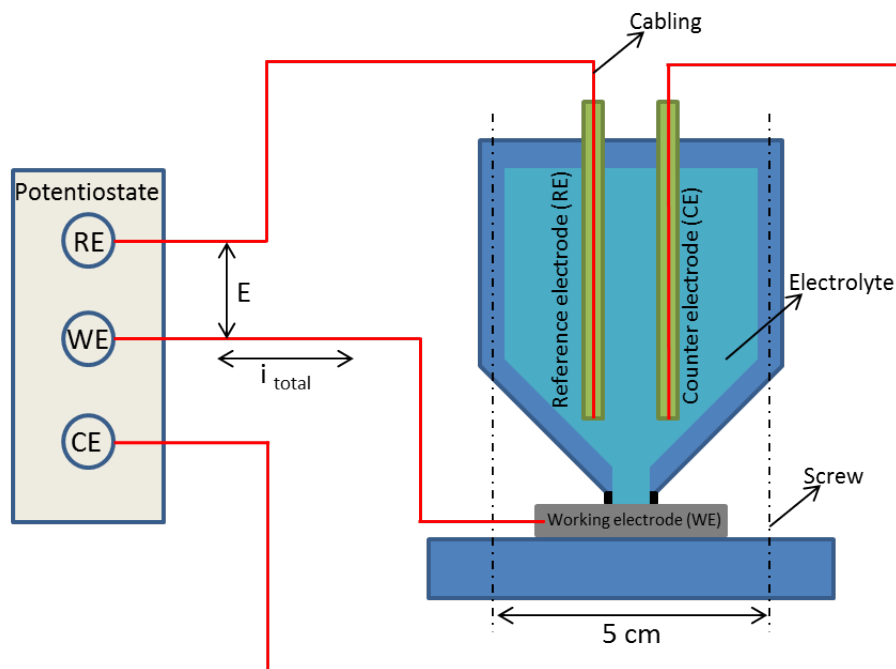


Figure 2.6: Three-electrode electrochemical cell. RE: Reference Electrode. CE: Counter Electrode. WE: Working Electrode.

Advantages of this cell are the low electrolyte quantity required during the experiment (8 mL), the visibility of the exposed surface to the electrolyte, and the rapidity in its assembly and preparation. Disadvantages are the variation of electrolyte acidity and composition due to possible elemental dissolution towards the electrolyte, gas bubbles nucleated on the surface might remain stagnant which partially blocks the surface beneath from the reaction taking place leading to local variations over the surface which might lead to false interpretation of the results and lower the reproduction accuracy of the experiments.

### 2.4.2 ICP, AESEC

In conventional electrochemistry, only the net electrical current passing through the system can be accessed. Accordingly, no information can be obtained about the details of the partial oxidation and reduction processes [129]. In this work, detailed quantified information about atomic dissolution rates was required, representing a major portion of the anodic current. To have an access to this, inductively coupled plasma optical emission spectrometer (ICP-OES) [133, 131, 129] was coupled with a flow electrochemical cell in what is called atomic emission spectroelectrochemistry method (AESEC). Electrolyte flow rate was fixed to 0.3 mL.min<sup>-1</sup>. The electrodes used were: Ag/AgCl for the reference electrode, a platinum wire was used as the counter electrode, and the tested material (304L stainless steel) acts as the working electrode, as illustrated in Fig. 2.8.

**AESEC:** This technique is illustrated in Fig. 2.7, which divides the system into three main parts:

- The reaction system (A): where the electrochemical flow cell allows a solid flat surface of the working electrode under testing to be exposed to a flowing electrolyte. A peristaltic pump was used to maintain a continuous flow of the electrolyte through the cell, and delivering it to the nebulizer and the cyclonic spray chamber before entering the plasma.
- ICP-OES spectrometer (B): which is placed downstream of the cell, allowing the analysis of the leaching solution leaving the flow cell for its elemental composition.
- Fast electronics (C): an electronic system performing the real-time monitoring and acquisition of the emission intensities and the electrochemical data as a function of time.

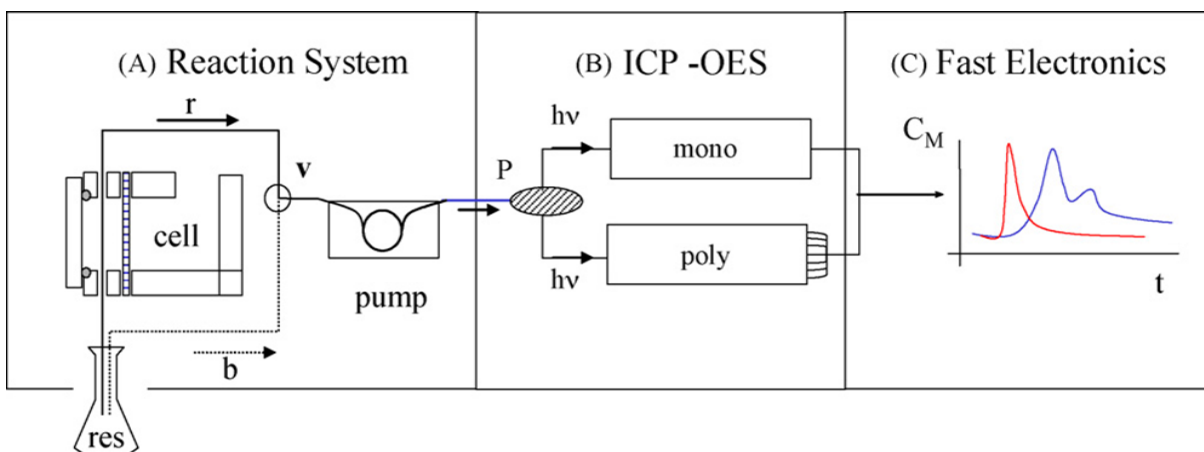


Figure 2.7: The three main stages of AESEC technique, with arrows indicating the direction of electrolyte flow during the experiment. (res): electrolyte reservoir. (b): background experiment. (r): cell bypass. (v): a switch between a background and reaction measurement. (P): the plasma torch. ( $h\nu$ ): photo emission. (mono): monochromator. (poly): polychromator. ( $C_M$ ): Concentration of the considered elements calculated based on their emission intensity (not shown). Adapted from [131]

**The flow cell:** The flow electrochemical cell is schematically shown in Fig. 2.8. The structure of the cell is divided into two main compartments, in the first of which the electrolyte flows over the exposed area of the working electrode. The flow rate is  $3 \text{ mL} \cdot \text{min}^{-1}$ , having a bath against the direction of gravity as indicated by the dashed line in Fig. 2.8, which stimulates the removal of possible generated gas bubbles from the surface during the experiment. A porous membrane performs the separation from the second compartment containing a stagnant electrolyte, the counter and reference electrodes. This membrane allows the ionic exchange between the working electrode and the other electrodes, without mixing the electrolytes in the two compartments.

**ICP-OES:** HORIBA Joben Yvon, SAS. (Ultima 2C<sup>TM</sup>) commercial ICP atomic emission spectrometer was coupled to the downstream of the flow cell. The principle of atomic detection in this technique is illustrated in the diagram given in Fig. 2.9.

The leaching solution downstream the electrochemical cell is aspirated into the energy source represented by the plasma, where the atoms get ionized or excited. The relaxation of these excited atoms leads to radiation emission at different wavelengths ( $I\lambda$ ) depending on each element. These radiations can be detected in the polychromator or the monochromator phototubes, for which Table:2.3 gives the technical details.

**Fast electronics:** Signals received from the phototubes were monitored in real time using Quantum<sup>TM</sup> software and data acquisition package provided by HORIBA. The intensity measurements of 250 k data points per second were averaged over periods set to 1 second for data



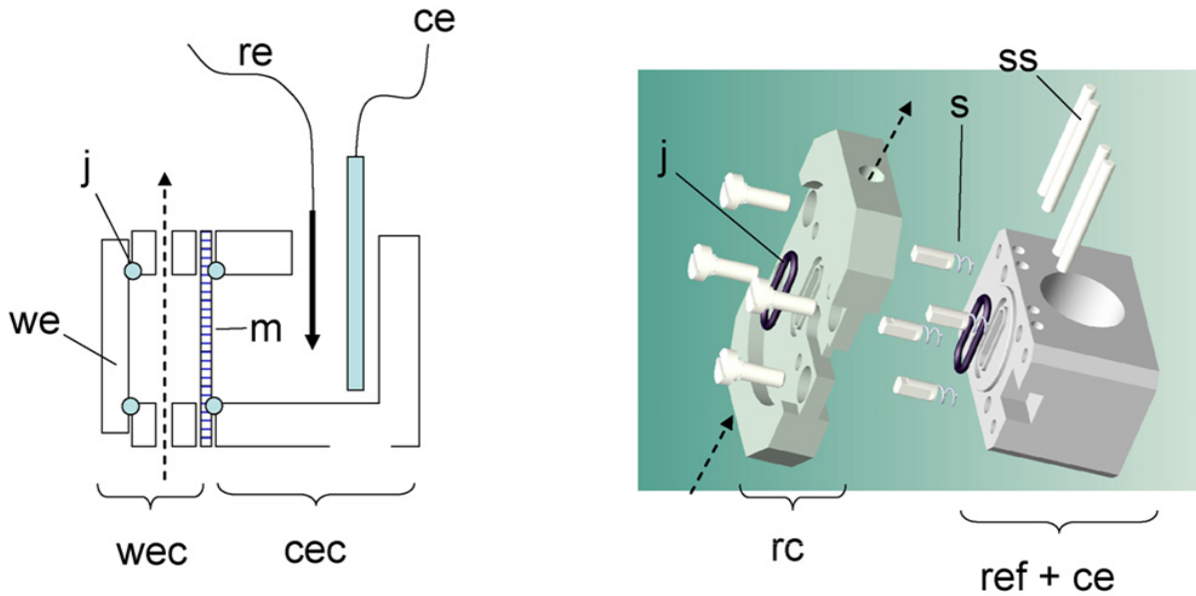


Figure 2.8: The composition of the flow cell. (wec): the working electrode compartment. (cec): counter electrode compartment. (j): the gasket. (m): the membrane. (we): the working electrode. (ce): the counter electrode. (ref): the reference electrode. (s) springs. (ss) spring supports. Adapted from [131]

Table 2.3: The technical description of the monochromator and polychromator.

	Polychromator	Range/nm	Monochromator	Range/nm
Configuration	Paschen-Runge	-	Czerny-Turner	-
Focal plane/M	0.5	-	1.0	-
Holographic grating		-		-
groove/mm	3600	-	2400	-
Resolution/nm	1st order: 0.025	165-408	Practical: 0.005	120-320
	2nd order: 0.015	165-408	0.010	320-800

monitoring and registration. To fit AESEC experiments, the electronic system was modified to include the current and potential data channels delivered by the potentiostat. In order to be consistent with the spectroscopic emission signals, these channels were amplified and offset. Stability of potential signals was verified to approximately 0.05 mV. Thanks to this modification, the spectrometer and electrochemical data were collected with the same time base, simplifying the correlation of the transitory signals.

### 2.4.3 Experimental conditions

All corrosion tests were performed at room temperature, which was fixed by the air conditioning system to a set temperature equals to 24°C. Solutions used were water based, with NaCl (up to 2 M) and H<sub>2</sub>SO<sub>4</sub> (up to 5 M) additives according to the experimental objectives. Chemical products were of reagent grade, while the water used was prepared by 18.2 MΩ Millipore<sup>TM</sup> purification system. The conventional electrochemical cell is made of epoxy glass, while the flow cell is made of teflon. The capillary tubes used and the sealing gaskets were of viton, which is required for the high acidic concentrations used.

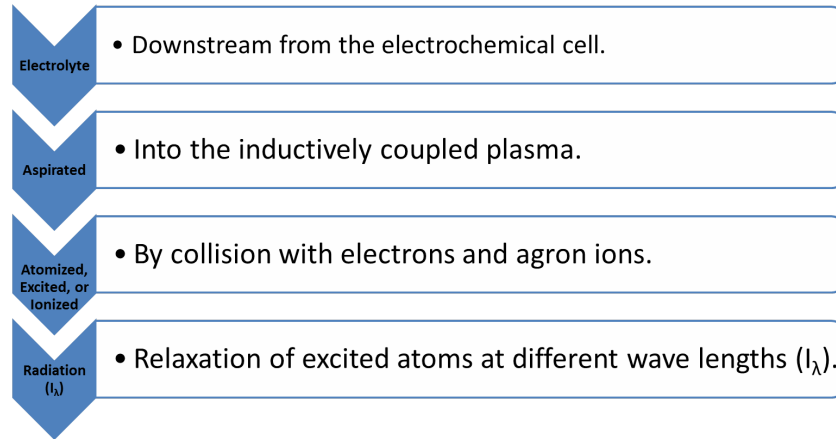


Figure 2.9: A flow diagram showing the main steps in the detection of atomic composition of the leaching solution by AESEC technique.

### Polarization experiments

The potentiodynamic program used to produced the polarization curves throughout this research is given in Table: 2.4.

Table 2.4: The program used for the production of the polarization curves.

Process	OCP	Anodic Activation	Sweep Rate	OCP
Duration Details	5 min.	5 min. @-0.9 V	0.5 mV.s <sup>-1</sup> [ -0.9V to 1 V]	5 min.

### Passivation experiments

For the passivation experiments (conventional and AESEC), 2 M H<sub>2</sub>SO<sub>4</sub> at room temperature was the electrolyte used to test the two stress cases:

1. The reference material without any applied stress. Though this sample might have residual stresses due to fabrication processes, but it will be called the "unstressed" sample through this research.
2. The stressed case with  $\sigma = 280$  MPa. This is the highest stress value that was possible to be applied, which is in the plastic domain of the material. This maximum stress was used to find the maximum possible electrochemical effect that it might have.

### SCC tests

For the SCC test, two solutions were used:

1. 2 M H<sub>2</sub>SO<sub>4</sub> + 2 M NaCl: this was used to perform the first SCC tests. The purpose was to check if these severe electrolyte conditions can crack the stressed sample or not without heating. The tested cases were  $\sigma = (280, 250)$  MPa.
2. 2 M H<sub>2</sub>SO<sub>4</sub> + 0.5 M NaCl: this was the second solution used with samples of  $\sigma = 210$  MPa. The purpose was to have less aggressive electrolyte and applied stress such that the cracks are not severely attacked.

**Potentiodynamic program:** For the potentiodynamic cycling experiments, the applied potentials and corresponding duration are optimized to simulate the film breakup-repassivation process taking place in SCC. Table 2.5 gives the details of the potentio-dynamic program used for these cycling experiments (conventional and AESEC).

Table 2.5: Optimized potentio-dynamic program used for cycling experiments:

Process	(OCP)	Cathodic activation	(OCP)	Anodic passivation	(OCP)
Duration\s	300	70	300	600	300
Potential\ (V vs Ag/AgCl)	OCP	-0.7	OCP	+0.5	OCP

### Surface condition

The surface condition was in many experiments the as-received surface, after being ultrasonically cleaned in an ethanol bath for about 15 min. However, in other cases, the surface was mirror-polished. Details about surface conditions will be given case by case during the research.

#### 2.4.4 Methodology of treating the data

The ICP gives back a data sheet having information about the emission intensity of each element in the streaming solution in addition to the current and potential, all as a function of time. As was proposed by Ogle et al [131, 132], the elemental concentrations in the downstream solution can be calculated out of their corresponding intensities by calibration to concentration standards of the elements of interest, as given by Eq.2.6.

$$C_m = \frac{(I_\lambda - I_\lambda^o)}{k_\lambda} \quad (2.6)$$

where:

- $C_m$ : the instantaneous concentration of element  $m$  in the leaching solution  $/(\mu\text{g/mL})$ .
- $I_\lambda$ : intensity of the wavelength corresponding to element  $m$  in the solution  $/(V)$ .
- $I_\lambda^o$ : background intensity of the wavelength corresponding to element  $m$  in the solution  $/(V)$ .
- $k_\lambda$ : background sensitivity factor for the wavelength corresponding to element  $m$  in the solution.

Consequently, the elementary dissolution rate can be calculated as given by Eq.2.7:

$$\nu_m = \frac{f C_m}{A} \quad (2.7)$$

Where:

- $\nu_m$ : the dissolution rate of element  $m$   $/(\mu\text{g.s}^{-1}.\text{cm}^{-2})$ .
- $f$ : solution flow rate into the ICP  $/(mL.min^{-1})$ .
- $A$ : area of the corrosion exposed working electrode to the electrolyte  $/(cm^2)$ .

It's always interesting to calculate the equivalent electrical current,  $i_m$ , corresponding to this elemental dissolution. This process can be done using Faraday's law as given by eq.2.8:

$$i_m = zF\nu_m = \frac{zFfC_m}{M} \quad (2.8)$$

Where:

- $z$ : the number of valance electrons for the element in consideration.
- $F$ : Faraday's constant  $/(C.mol^{-1})$ .
- $M$ : the atomic mass of element  $m$   $/(g.mol^{-1})$ .

The selective dissolution rate of a certain element can be calculated as well. This is possible by taking the dissolution reference as the perfect simultaneous dissolution rate based on the measured iron dissolution and comparing this to the measured actual dissolution of the element of interest. This is shown symbolically as given by Eq.2.9:

$$\nu'_m = \nu_m - \alpha\nu_{Fe} \quad (2.9)$$

Where:

- $\alpha$ : the ratio of mass fraction of element  $m$  in the alloy's matrix to that of the iron;  $X_m/X_{Fe}$ .
- $\nu'_m$ : The selective dissolution of element  $m$   $/(μg.s^{-1}.cm^{-2})$ .
- $\nu_m$ : The measured dissolution rate of element  $m$   $/(μg.s^{-1}.cm^{-2})$ .
- $\nu_{Fe}$ : The measured dissolution rate of element Fe  $/(μg.s^{-1}.cm^{-2})$ .

According to the reaction conditions for a given element, the selective dissolution for that element,  $\nu'_m$ , can result in three options which can interpreted as follows:

1. Positive: surface depletion of element  $m$ ; excessive selective dissolution.
2. Zero: perfect simultaneous dissolution of element  $m$ .
3. Negative: Surface enrichment with element  $m$ .

Having the selective dissolution quantified allows the quantification of the enrichment or depletion of element  $m$ ,  $Q'_m$   $/(μg.cm^{-2})$ , over a given period of time ( $t_1$ ,  $t_2$ ), as given by Eq.2.10:

$$Q'_m = \int_{t_1}^{t_2} \nu'_m(t) dt \quad (2.10)$$

The last step is the calculation of the thickness,  $\theta$   $/(10^{-6}.cm)$ , built or dissolved from the surface of the material corresponding to certain value of  $Q'_m$ , this can be found by Eq.2.11:

$$\theta = \frac{Q'_m}{\rho} \quad (2.11)$$

Where  $\rho$  is the density of element  $m$   $/(g.cm^{-3})$ . Using Eq.2.11, the passive film thickness can be calculated assuming the excess Cr, in the form of  $Cr_2O_3$ , with a density of  $5.21 g.cm^{-3}$ .

## 2.5 SEM, EBSD, and EDS

**SEM:** JSM-7100F scanning electron microscope (SEM) was used to perform the electronic imaging. This microscope is of field emission gun type (FEG). The hardware provides the control over five degrees of freedom. The first to mention are the three coordinates controlling the sample position inside the SEM chamber (x,y,z). For the rotation: it's possible to control the orientation about the z axis defined by the angle ( $R$ ), in addition to the possibility to incline the sample from the horizontal position if required. Low vacuum mode allows the operation at low pressure values in the range of (10-50) Pa, which allows the sample charging. Imaging can be done by secondary electrons SEi, or backscatter electrons (BSE) allowing image production in topographical (Topo) or composition (Compo) basis. The machine is operated by the software called: PC-SEM. For imaging, the parameters used were often: 15 kV acceleration voltage, and 20 mm working distance.

**EDS:** As a result of the primary beam interaction with sample's atoms, shell transitions take place in the sample being tested causing X-ray emission. This emission is a characteristic parameter of the parent atoms. Thus, measuring the intensity of this radiation allows elemental recognition in what's called Energy Dispersive X-ray Spectroscopy (EDS). Having a sampling depth of 1-2  $\mu\text{m}$ , EDS can provide qualitative elemental composition analysis over the sample surface, or if standards are used, can even be quantitative.

The hardware part consists of the processor and the analyzer. The device is of Oxford instruments X-max 20 mm<sup>2</sup>, having Si (Li) detector. The software used to operate it is Inca 4.15.

**EBSD:** HKL Oxford instruments (Nordlys)EBSD detector is used in addition to a phosphor screen CCD camera. The data acquisition and treatment is performed by the aid of CHANNEL 5 suite of programs, allowing the manipulation, analysis, and display of EBSD data. The suite consists of several tools allowing the user to control EBSD acquisition, produce pole figures and inverse pole figures, in addition to the generation of EBSD maps out of the crystallographic orientation data.

Settings used for EBSD analysis was the same as those for SEM, with the difference in the inclination sample's surface by 70° of the beam.

## 2.6 XRD

Siemens D500 X-ray Power Diffraction (XRD) system was used to perform the residual-applied stress analysis using  $\sin^2\psi$  method [32]. Mn tube and Cr filter were used to fit with stainless steel experimental conditions. The tube was operated at 600 W (20 mA/30 mV). Analysis were based on the diffraction of {311} planes of austenite, using 13 equally spaced  $\psi$  angles between  $-42.6^\circ$  and  $45^\circ$ . To calculate the stress from the measured strain, the used X-ray elastic constants were  $\frac{1}{2}S_{2hkl} = 6.98 \text{ MPa}^{-1}$  and  $S_{1hkl} = -1.87 \text{ MPa}^{-1}$ .

## 2.7 Surface preparation for observation/EBSD

The chemical surface attack was sometimes required to reveal grain boundaries, or as a surface preparation for EBSD experiments. The attack typical time is 120 seconds at 15 V, though sometimes a longer duration was necessary. The oxalic acid of 10% (by volume) was to apply this chemical attack after mirror-polishing the surface to 1  $\mu\text{m}$  grit.

---

Characterization of the Base Material

---

### 3.1 Chemical Composition

SpectroMaXx was used to analyze the elemental composition of the alloy in hand. Leco CS-300 combustion analyzer was used to measure the sulfur and carbon dose in the alloy. Detailed description of these experiments are provided in section 2.2.1, and 2.2.2.

**Results:** The average for the analysis given on the face of the samples is given in the Table3.1:

Table 3.1: Face elemental concentrations measured by SpectroMaXx.

Element	Fe	Cr	Ni	Si	Cu	Mo	Co	N
% by wt	71.564	17.390	7.972	0.341	0.314	0.242	0.153	0.081
Element	V	Mn	P	C	Sn	Nb	S	As
% by wt	0.078	0.040	0.033	0.025	0.019	0.017	0.006	0.005

It's noticed that the carbon content in our material is less than that of 304 SS. This will be checked in the next analysis with a Leco cs-300 technique, which is more sensitive to such low concentrations.

For the purpose of statistical analysis, and to check the local variation of the elemental concentration from one spot to another on the material's surface. This will give a verification for the noise level expected when performing electrochemical testing on the surface. Comparison is held as well with the back of the surface. The result of this study is provided in Appendix: A.

**Conclusions of composition spatial analysis:** From Fig. A.1, it's noticed that Fe concentration is higher on the face of the sample. It's noticed from Fe and Cr concentration distributions given in Fig. A.1 and Fig. A.2 over all selected points that these two concentrations are somehow complementary to each other. In other words, when the Fe concentration is above the average, the Cr concentration has the tendency to fall below the average, forming inverse patterns one to the other. to in a pattern.

Thus, from Fig. A.2, the face has a lower concentration of Cr than that on the back of the sample. In the majority of cases, seen the spatial statistical concentration distribution, the deviation from the average remained under controlled limits of less than one standard deviation. Thus, it can be accepted to be stated that the elemental concentration is homogeneous over

a given surface, other than elsewhere observed by other techniques (SEM, EDS...). For this purpose, the surface over which all electrochemical and corrosion tests will be always the face of the samples, which is industrially protected by a removable self-adherent plastic film.

**Results of sulfur and carbon analysis:** The averages and the standard deviations for the six measures are given in Table 3.2:

Table 3.2: Analysis results for carbon and sulfur content in the alloy in hand.

Standard Used	Carbon % by wt.	Sulfur % by wt.
1st	<b>0.03444 % <math>\pm</math> 0.00168</b>	0.00825 % $\pm$ 0.00050
2nd	0.03571 % $\pm$ 0.00175	<b>0.00603 % <math>\pm</math> 0.00036</b>
AISI (304)	<b>0.08%</b>	<b>0.03%</b>

Accordingly, the measures with the lower standard deviation (marked in bold) will be taken, and we can conclude that the percentage of carbon is 0.03444 % and the percentage of the sulfur is 0.00603 %. By this analysis, the material is confirmed to be 304L stainless steel rather than 304, due to the low level of carbon content as compared to that of AISI standards.

**Summary of the chemical composition:** Table 3.3 is a summary of the results of both analysis made here for carbon and sulfur content performed by Leco cs300, and that for the rest of the metals performed by SpectromaxX.

Table 3.3: Analysis of the chemical composition of the base material 304L SS, based on Leco CS-300 and Spectromax analysis.

Element	Fe	Cr	Ni	Si	Cu	Mo	Co	N
% by wt	71.564	17.390	7.972	0.341	0.314	0.242	0.153	0.081
Element	V	Mn	P	C	Sn	Nb	S	As
% by wt	0.078	0.040	0.033	0.034	0.019	0.017	0.006	0.005

The chemical composition is compared to AISI standards for 304 and 304 L SS, as given by Table 3.4:

Table 3.4: AISI standards for 304 and 304L ss composition vs our material.

	AISI	AISI	Measured
%	304 SS	304L SS	Our Material
Cr	18-20	18-20	17.390 ± 0.058
Mn	2	2	1.687 ± 0.007
Ni	8-10.5	8-12	7.972 ± 0.034
C	0.08	0.03	0.025 ± 0.0017
Si	1	1	0.341 ± 0.008
P	0.045	0.045	0.033 ± 0.001
S	0.03	0.03	0.006 ± 0.0004

## 3.2 Optical Analysis

After mirror polishing the surface, it was necessary to have an image representing the reference surface. Fig. 3.1 shows the sample state before (a), and after (b) polishing.

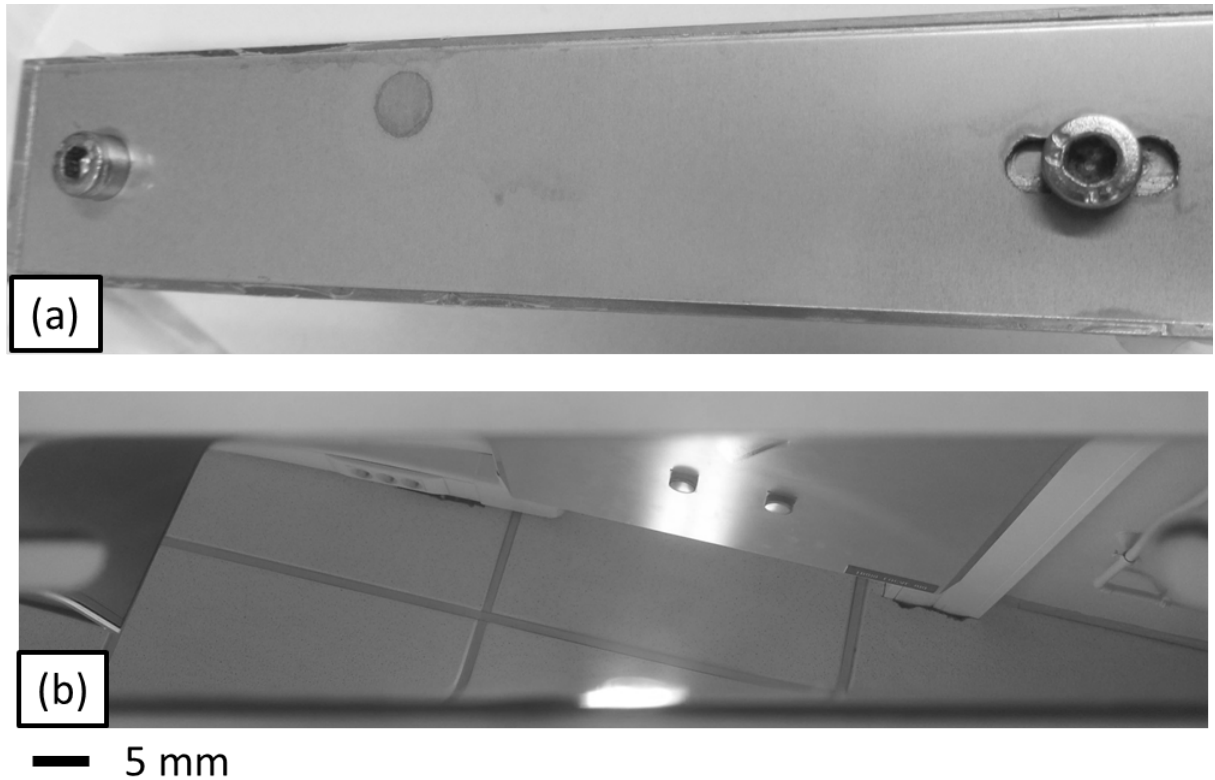


Figure 3.1: Initial surface state of the used samples. (a): non-polished sample. (b): mirror polished sample.

An optical microscope was used to check the surface for possible defects. Some features could be detected on the shiny surface, which might be inclusions or voids such as those shown in Fig. 3.2 (a). Applying oxalic acid chemical attack to this polished surface revealed the grain boundaries. However, by only using optical observation, the detection and identification of defects were not easy tasks.

### 3.3 SEM

In this analysis, the three surfaces of the sample illustrated in Fig. 3.3 were characterized.

The samples were mirror polished, followed by an oxalic acid chemical attack to reveal the grains and the grain boundaries.

#### 3.3.1 Upper surface and cross-section

The two surfaces that will be dealt mainly within this research are the upper surface and the cross section of the samples. Figure 3.4 gives the typical SEM images of both of them. In these two directions, material defects and flaws were detected, which had more or less similar aspects. Examples of representative defects are shown in Fig. 3.5. Chemical composition analysis of the detected defects was performed by EDS. The resulting elemental concentration maps are given in Fig. 3.6. Based on this analysis, the defects are believed to be due to sulfur oxide inclusions.

#### 3.3.2 Transverse direction

The transverse direction is analyzed by SEM imaging. Typical surface morphology and defects are given in Fig. 3.7 (a) and (b) respectively. The defects in this direction tended to be extended laterally, in parallel to the horizon as shown by the red arrow in Fig. 3.7 (a). The defect included



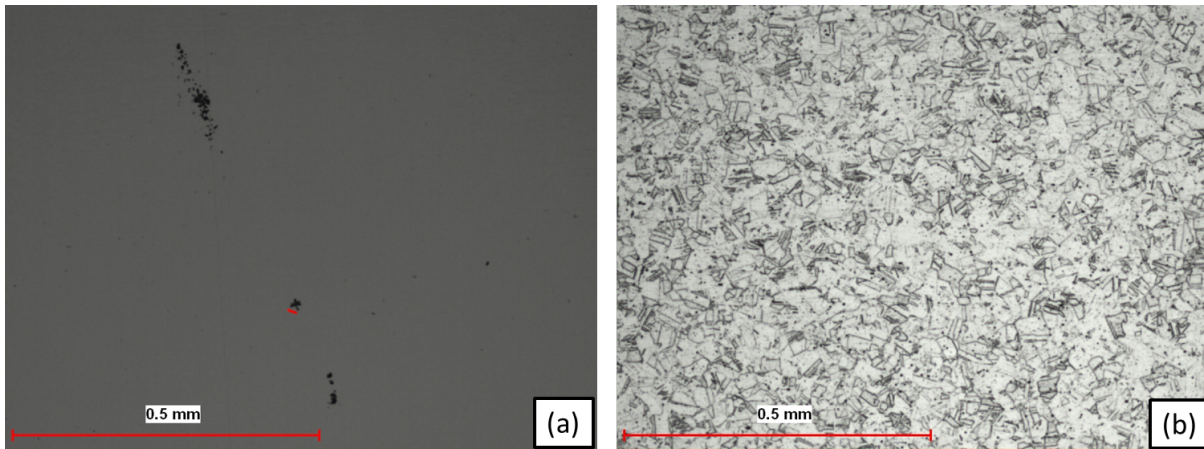


Figure 3.2: Optical observation of the polished sample. (a): Mirror polished samples with surface defects. (b): Mirror finished surface, followed by oxalic chemical attack.

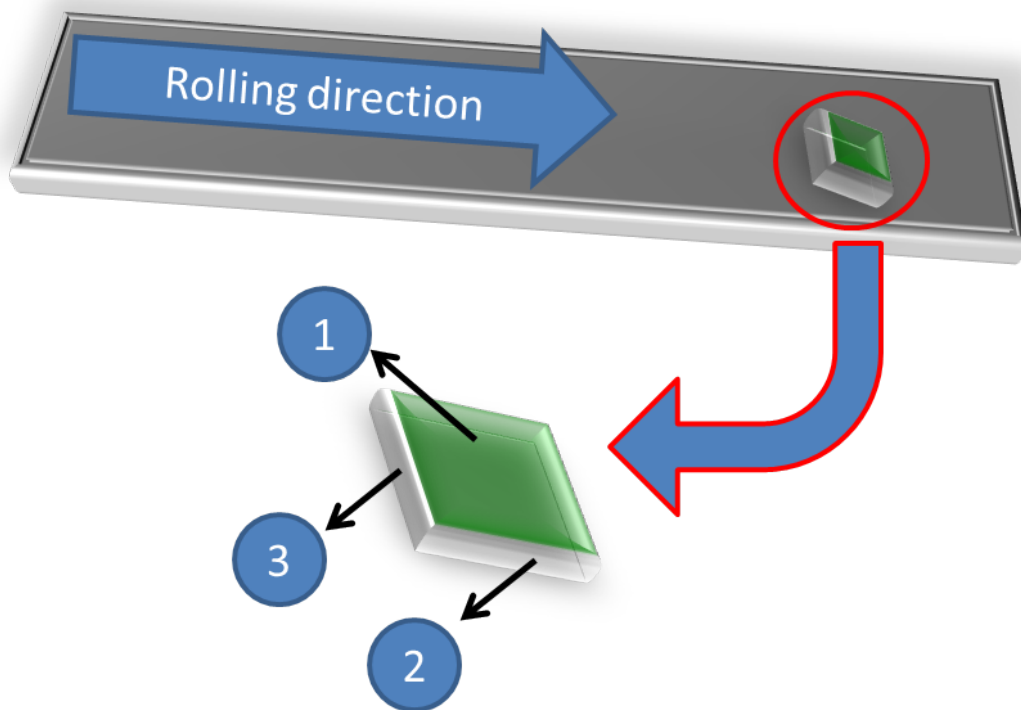


Figure 3.3: The three sample surfaces. (1): upper surface (top view). (2): longitudinal direction (cross-section). (3): Transverse direction.

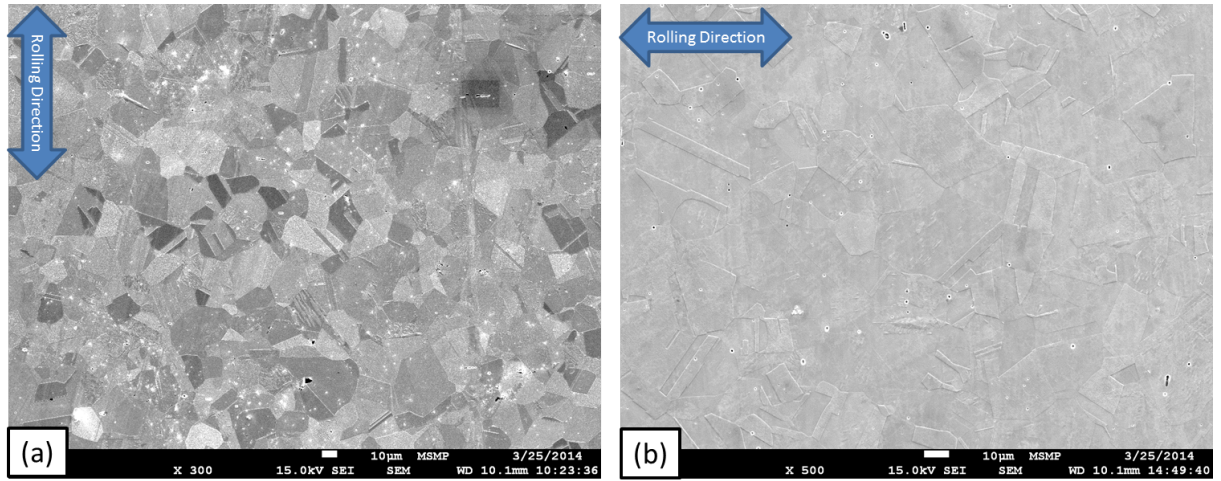


Figure 3.4: SEM characterization of the base material. (a): upper surface (top view). (b): longitudinal direction (cross-section).

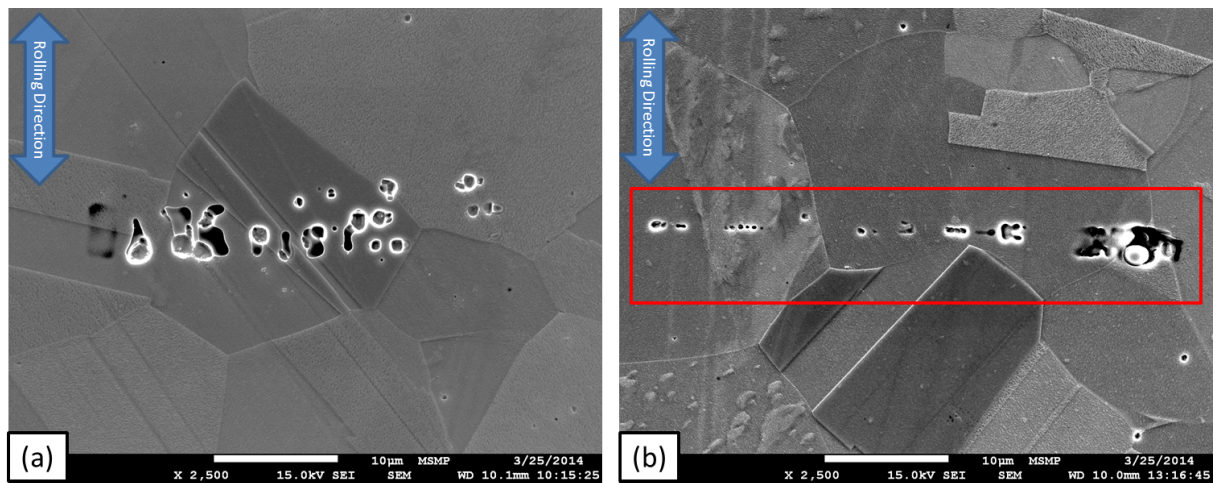


Figure 3.5: Examples of upper surface defects. (a): continuous voids perpendicular to rolling direction. (b): selected defect for EDS analysis given in Fig. 3.6.

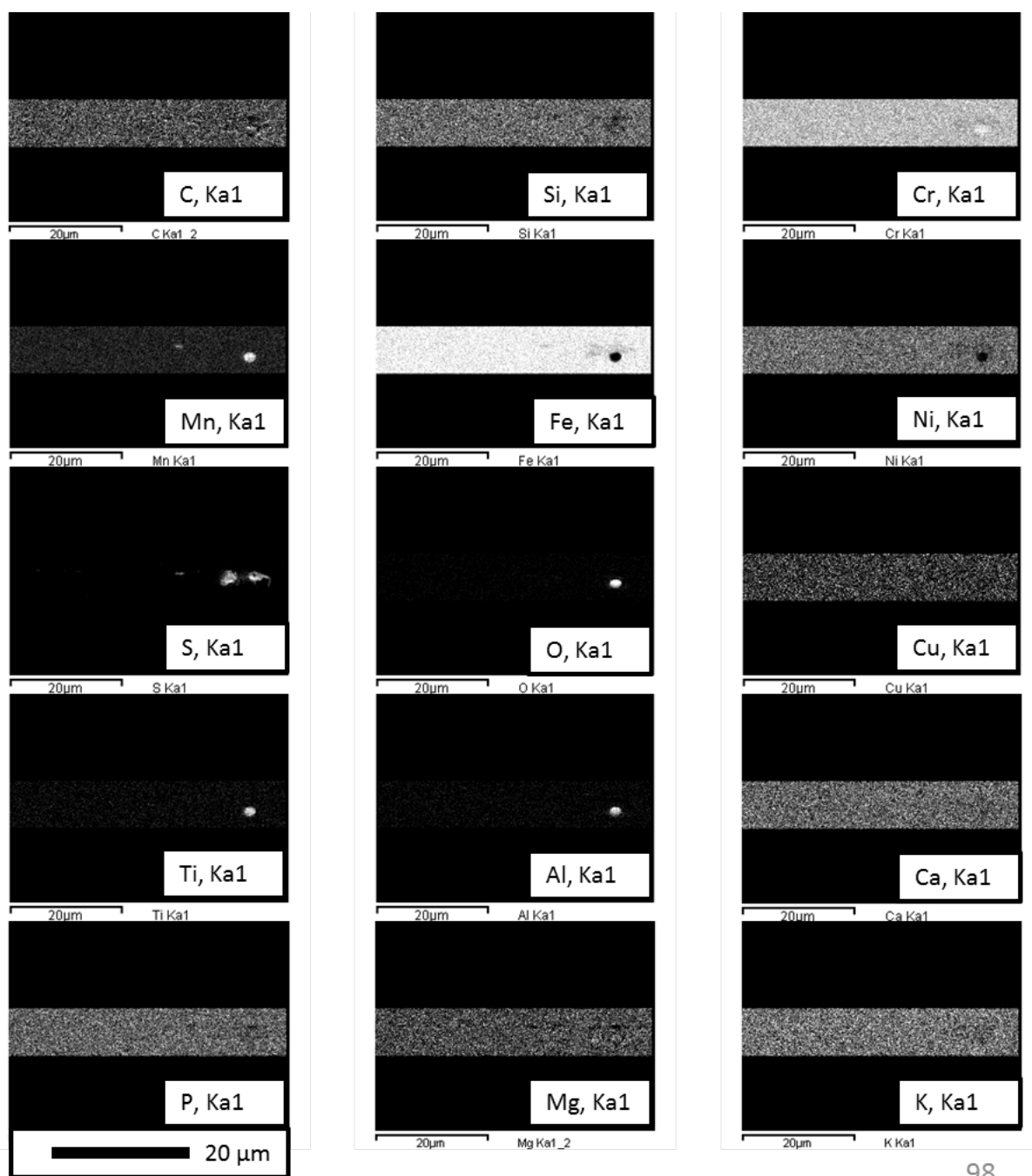


Figure 3.6: EDS analysis of a selected upper surface defect shown in Fig. 3.5 (b).

in the red triangle in Fig. 3.8 (b) is selected for an EDS analysis, whose results are given in Fig. 3.8. Again, results reveal high sulfur concentration inside the defect, implying this defect is a sulfur inclusion.

However, other selected defects (on the three directions equally), gave high concentrations in Mn. An example is provided in appendix: B.

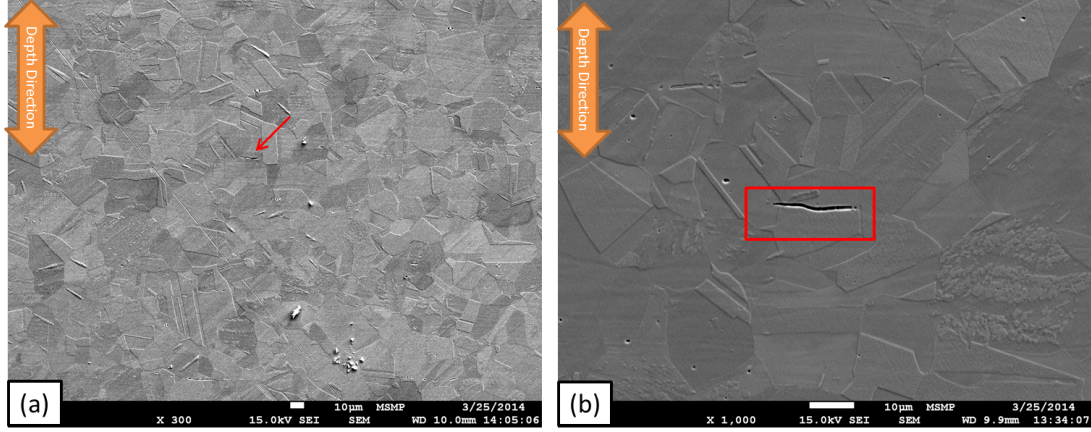


Figure 3.7: SEM characterization of the base material in the transverse direction. (a): Typical surface morphology. (b): a selected defect for EDS analysis, given in Fig. 3.8.

### 3.4 EBSD

The EBSD analysis was conducted over the material's three directions indicated in Fig. 3.3. The purpose was to get statistical information about the grains, the possible phases, and the crystallographic orientations.

As an example, Fig. 3.9 (a) and (b) present the All Euler and the phase map respectively.

The analysis reveals two phases in the present material, FCC and BCC stainless steel. The grain orientation can be represented using Pole figures, as given in Fig. 3.10 for the FCC, and BCC grains. It's noticed that the BCC grains are more textured than the FCC grains.

Statistical graphs for the distribution of grain area, the equivalent diameter, the grains' aspect ratio, and the number of neighbor grains are provided in Appendix: D for this map. If the grains of area less than 4 pixels are neglected, a summary about the significant features as follows:

- Average granular area =  $117 \mu\text{m}^2$ .
- The average equivalent diameter =  $10.7 \mu\text{m}$ .
- The average aspect ratio = 2.1.
- The percentage of BCC grains was about 3 %, compared to 97 % for FCC phase.

Where the aspect ratio is the major over the minor lengths of an ellipse having an equivalent area of the considered grain.

Such information is vital for material modeling when it comes to the selection of a representative volume element. Similar analysis was conducted to the two other directions, which gave more or less close results to the one presented in this section.

### 3.5 XRD

The initial residual stress of the material has been measured along the rolling direction ( $\phi = 0^\circ$ ), and in the transverse direction ( $\phi = 90^\circ$ ).

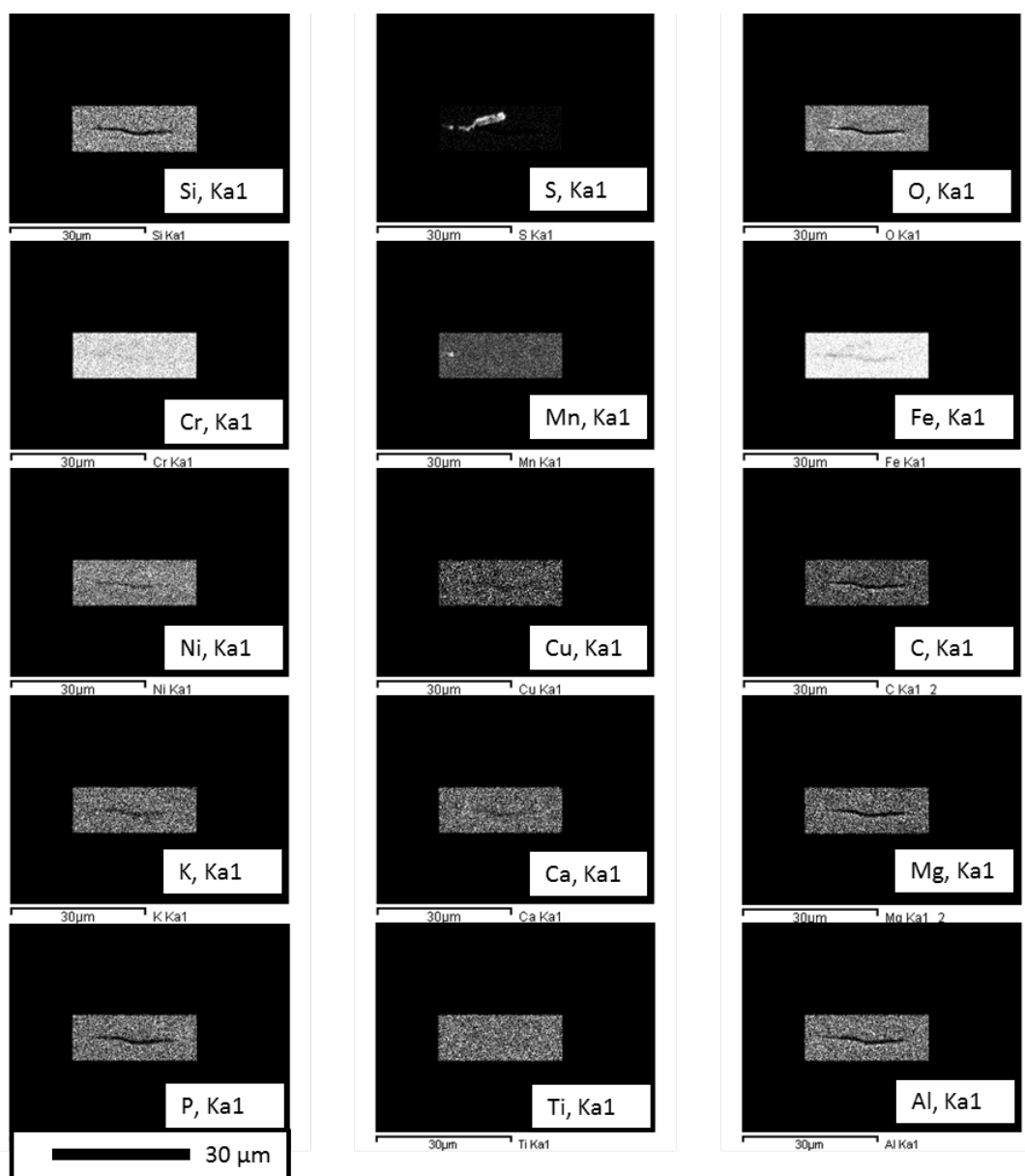


Figure 3.8: EDS analysis of a selected upper surface defect shown in Fig. 3.5 (b).



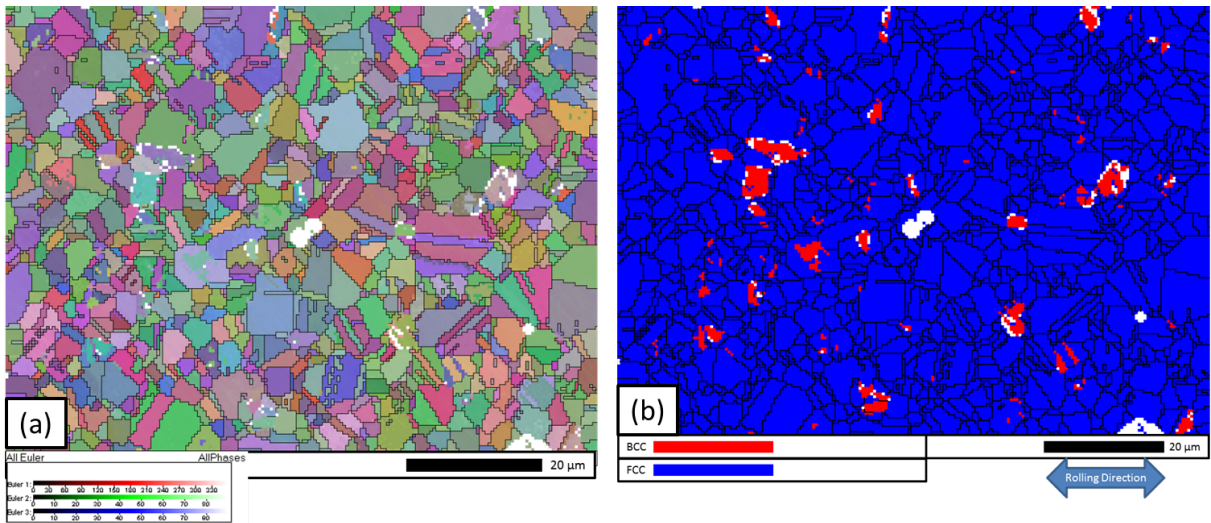


Figure 3.9: EBSD analysis of the cross section. (a) All Euler orientation map. (b): Phase map.

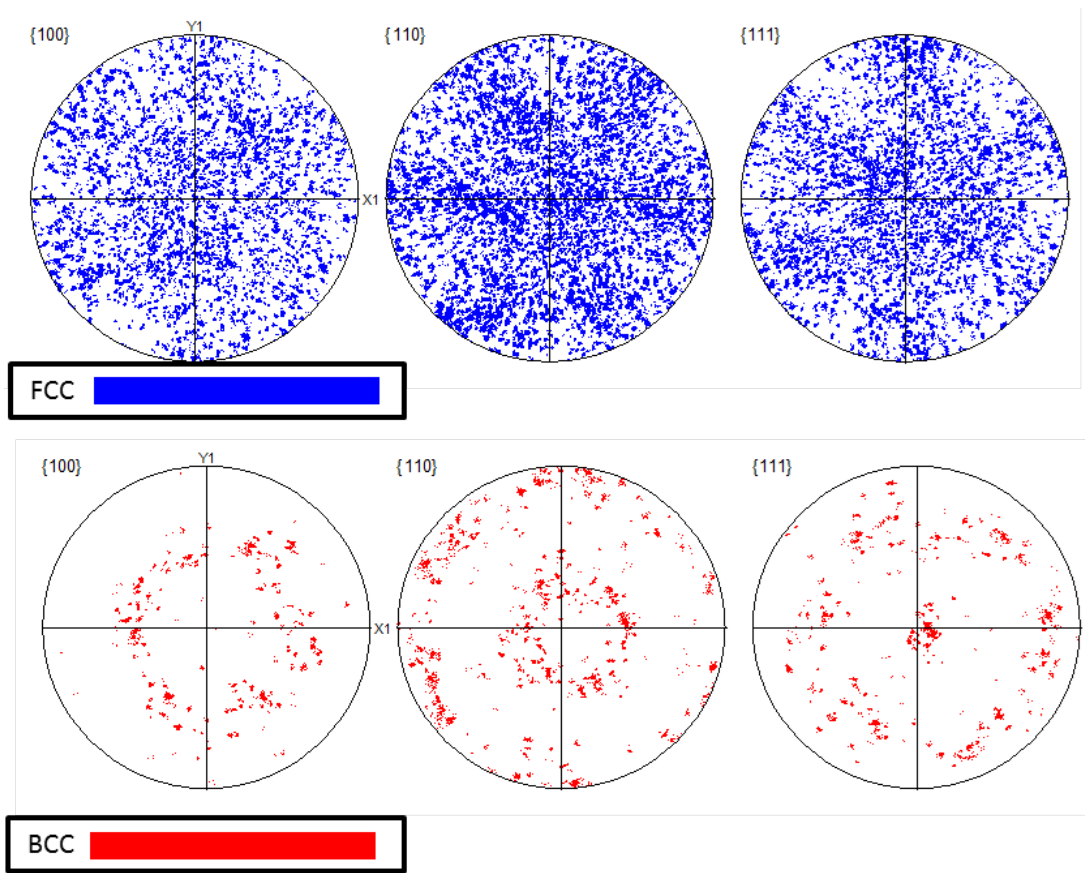


Figure 3.10: Pole figures of FCC and BCC grains in the base material.

$\phi = 0$ : Figure 3.11 gives the normal and shear stress along the rolling direction. The normal stress is the stress component along the rolling direction ( $\sigma_1$  in Fig. 6.1), while the shear stress is the stress component on the perpendicular surface to the normal stress ( $\tau_{23}$  in Fig. 6.1). Thus, for  $\phi = 0$ , the sample has a normal tensile stress having a gradient in the first 40  $\mu\text{m}$  between 30-50 MPa, and gets almost a constant afterward in the bulk of the material, with fluctuating values around 50 MPa. The shear stress is negligible, having values in the range of (-10 , zero) MPa.

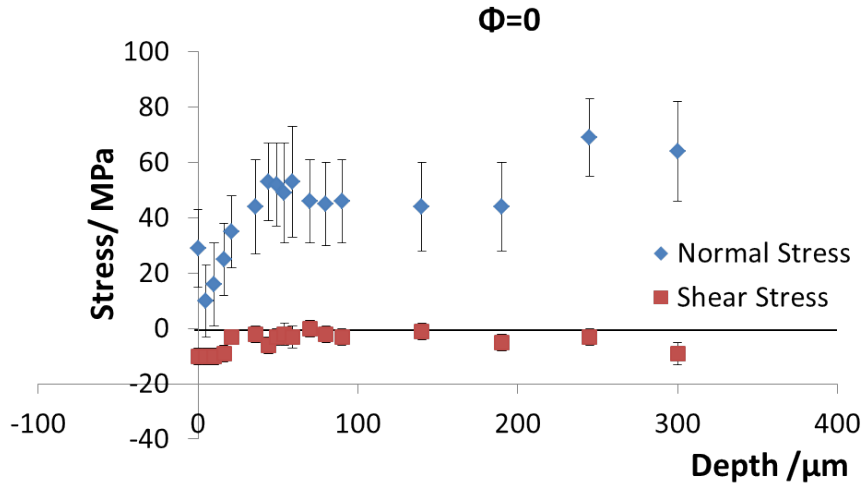


Figure 3.11: The initial residual stress in the sample along the rolling direction ( $\phi = 0$ ).

$\phi = 90^\circ$ : For this direction, Fig. 3.12 presents the values of the normal and shear stress through the depth of the sample. In this direction, the normal component is compressive stress, having the lowest values near the surface with a steep gradient within the first 30  $\mu\text{m}$ , and then it tends to be constant in the bulk of the material, having a value of  $\sigma_2 = -10$  MPa. On the other hand, the shear stress is more or less constant through the material's profile, having a value of about 15 MPa.

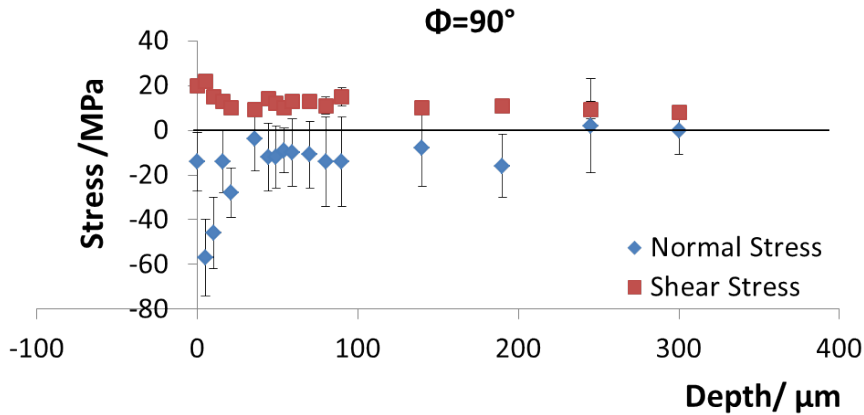


Figure 3.12: The initial residual stress in the sample along the transverse direction ( $\phi = 90^\circ$ ).

These initial residual stresses are probably resulting from the mechanical industrial processes that the material has undergone during the fabrication processes, such as the rolling, and surface strain hardening.

### 3.6 Tensile Tests

The mechanical behavior of the material as characterized by the tensile tests which were described in section:2.2.3 are given in Fig. 3.13. These curves refer to the tests in the rolling direction, which had the same characteristics to the tests in the two other directions.

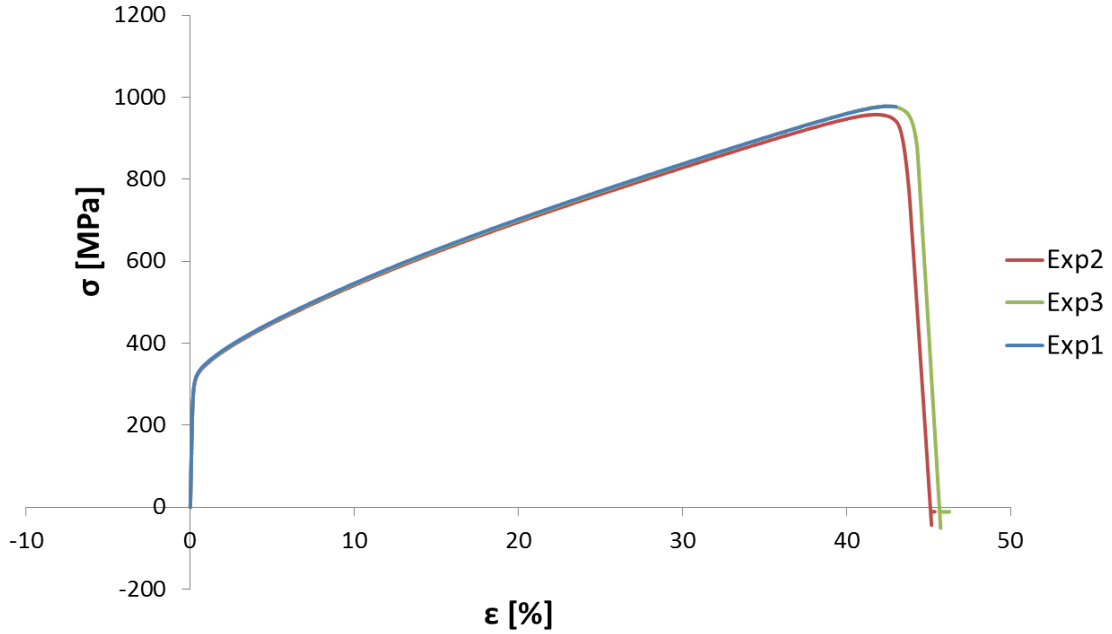


Figure 3.13: The true curve of the tensile test along the rolling direction.

The numerical values concerning the three directions (engineering and true) are summarized in Table: 3.5:

Table 3.5: Mechanical properties by true tensile test.

avg	RD	TD	45°D
E/[GPa]	210	211	200
stdv	9	4	2
$\sigma_{0,02\%}$ /[MPa]	251	266	253
stdv	51	6	5
$\sigma_R$ /[MPa]	1000	989	972
stdv	7	9	12

Considering the rolling direction, the modulus of elasticity is given as  $E = 210$  GPa, while  $\sigma_{0.2} = 250$  MPa is the elastic limit corresponding to 0.2 % $\epsilon$ , and eventually, the fracture limit is  $\sigma_R = 1000$  MPa.

Due to the smooth elastic-plastic transition that this material shows as presented in Fig. 3.13, Ramberg-Osgood equation can be used to describe the mechanical behavior of this material [150]. Accordingly, the strain is given by Eq.3.1:

$$\epsilon = \frac{\sigma}{E} + K\left(\frac{\sigma}{E}\right)^n \quad (3.1)$$

The term  $\sigma/E$  represents the elastic part of the strain, while  $K(\frac{\sigma}{E})^n$  represents the plastic part. The constants  $n$  and  $K$  are material properties describing the strain hardening. Taking only the elastic part of the equation and taking the logarithm of both sides gives Eq.6.3:



$$\ln(\varepsilon_P) = \ln(K) + n \ln\left(\frac{\sigma}{E}\right) \quad (3.2)$$

This relationship represents a linear relationship between the plastic strain,  $\varepsilon_P$ , and  $\sigma/E$  in logarithmic basis. The slope of this line is equal to the constant  $n$ , while  $k$  is the exponential of its y-intercept. In the domain of interest of our current experiments, where  $\varepsilon < 5\%$ ,  $n$  and  $k$  are 8.23, and  $5.4 \cdot 10^{20}$  respectively.

### 3.7 Conclusions

The following conclusions can be drawn about the initial material characterization:

- The chemical composition analysis of the used material in this work is 304L SS with the chemical composition fitting to AISI standards.
- Surface spatial chemical analysis revealed a slight variation in chemical composition, but in general, it is accepted that the surface has a homogeneous composition when compared to the corrosion exposed area.
- Surface flows were detected using SEM observation. The EDS chemical analysis of typical flows showed high sulfur and manganese content of these flows.
- EBSD statistical analysis about the grain size gave: average grain area =  $117 \mu\text{m}^2$ , and an average equivalent diameter =  $10 \mu\text{m}$ .
- The material has tensile residual stresses, starting from 30 MPa at the surface, having a steep gradient in the first 100  $\mu\text{m}$ , reaching about 65 MPa at depth = 175  $\mu\text{m}$ .
- The mechanical properties measured by the tensile test in the three directions of the material are comparable. As a summary, they can be given as: the modulus of elasticity  $E = 210 \text{ MPa}$ , the elastic limit  $\sigma_{0.02\%} = 250 \text{ MPa}$ , and the fracture stress  $\sigma_R = 1000 \text{ MPa}$ .

---

Electrochemical and Corrosion Analysis

---

Through all the experiments performed in this chapter and chapter 5, the magnitude of the applied stress was fixed to  $\sigma = 280$  MPa, which is higher than the elastic limit ( $\sigma_{\text{elastic}} = 250$  MPa). This value was the highest possible among several other choices, such that the effect of applied stress on corrosion is measured and characterized.

## 4.1 Polarization Curves Analysis

### 4.1.1 Conventional: stressed/non-stressed

In this section, polarization tests were performed to check if stressed stainless steel ( $\sigma = 280$  MPa) grant a different corrosion behavior than non-stressed metal. These tests are relatively quick and are very convenient for comparison purposes.

**Scope:** An exploratory set of experiments was held in order to check which solution conditions can render the curves with least noise and the maximum reproducibility. SCC can take place at room temperature in sulphuric acid solution, where submersion experiments are done with relatively long time durations, which are no less than five days [70]. This process is highly accelerated if chloride ion is added to the electrolyte, even at low concentrations [161].

At this stage of the research, SCC was not sought during the polarization experiments, where specimens are subjected to corroding environments for much shorter time than that required to develop any crack initiation. The purpose instead is in the first place to check for different solution composition/concentrations, the stability, and reproducibility of the electrochemical transients. Then, to check in terms of these transients if the current density reflects any effect due to the applied stress over the material.

Thus, solutions of different concentrations of sulfuric acid with sodium chloride were used as an electrolyte for this set of experiments. This was also an effective way to check the sensitivity of the experimental technique to certain factors such as solution acidity (pH) and chloride ion concentration  $[\text{Cl}^-]$ . Another purpose of this set of experiment is to select one of these conditions to further make a bigger statistical experiment set comparing stressed and unstressed samples.

### Electrolyte selection

The stagnant electrochemical cell which was explained in section: (2.4.1) is used for these exploratory experiments. The potentiostatic program used to make the polarization curves is given in Table: 2.4.

Sulfuric acid  $\text{H}_2\text{SO}_4$  was used as an electrolyte to perform these experiments due to its anion ability to give a great stabilizing effect over the repassivation process and subsequently the constructed passive film [62]. Accordingly, the following solutions were nominated for producing the exploratory curves for stressed and unstressed samples:

Table 4.1: Concentrations of the proposed electrolytes.

Solution	A	B	C	D	E
$\text{H}_2\text{SO}_4$ [M]	–	5	5	2	2
NaCl [M]	0.05	–	0.5	–	0.05

For each of these solutions, three polarization experiments were performed on unstressed samples, and an additional one or more experiment with the stressed state. The later mentioned aims to give a quick estimation if the effect of stress in these different solutions can be detected, and how this effect is pronounced according to each electrolyte. The resulting polarization curves are shown in Fig. 4.1 - 4.5. In addition to this, the optical observation was made for the post-experimental surfaces, as illustrated in Fig. 4.6.

### Discussion, analysis, and conclusions

The purpose of this analysis is to select the electrolyte giving the best reproducible polarization curves. To compare these curves statistically, two current points of interest, illustrated in Fig. 4.7, were considered:

- $j_{\text{critical}}$ : which was defined earlier as the maximum external current density registered before the passivation starts. This is expected to give a glance about the corrosion reaction intensity of the concerned surface.
- $j_{\text{minimum}}$ : which is the minimum external current density registered during the passivation potential domain. This is measure reflects the charge exchange isolation quality furnished by the constructed passive film on the metal surface.

For each set of experiments conducted in one of the proposed electrolytes, the average values of  $j_{\text{critical}}$  and  $j_{\text{minimum}}$  were calculated. Table: 4.2 shows the numerical results.

Table 4.2: The solutions used for polarization curves along with their concentrations. The figures in brackets (\*) represent the electrolyte composition and concentration in units of Mol as:  $([\text{NaCl}]/[\text{H}_2\text{SO}_4])$ .

Measure/ Electrolyte	A(0/0.05)*	B(5/0)	C(5/0.5)	D(2/0)	E(2/0.05)
$j_{\text{critical}}[\text{mA.cm}^{-2}]$	0.025	2.957	45.047	0.468	1.141
<b>RDS</b> ( $j_{\text{critical}}$ )	82.11	6.380	0.920	26.90	10.92
$j_{\text{minimum}}[\text{mA.cm}^{-2}]$	0.411	0.005	0.025	0.002	0.004
<b>RDS</b> ( $j_{\text{minimum}}$ )	20.61	6.18	17.95	14.18	9.494

The optical observation in Fig. 4.6 of the post-experimental surfaces after the polarization test reveals clearly the effect of increasing the  $\text{H}_2\text{SO}_4$  concentration. Traces near the borders of the corroded spot in Fig. 4.6 refers to locations where hydrogen was blocked near the joint, which causes local variation in the ionic transfer, and thus, the local intensity of the chemical reaction. Furthermore, in conditions of pure NaCl, even at this low concentration of 0.05 M, a violent pitting corrosion were generated at the boundaries near the joint, which is somehow similar to crevice corrosion. However, the effect of  $\text{Cl}^-$  ion was less present as it was combined with the sulfuric acid. This could be ascribed to the augmented intensity of hydrogen generation

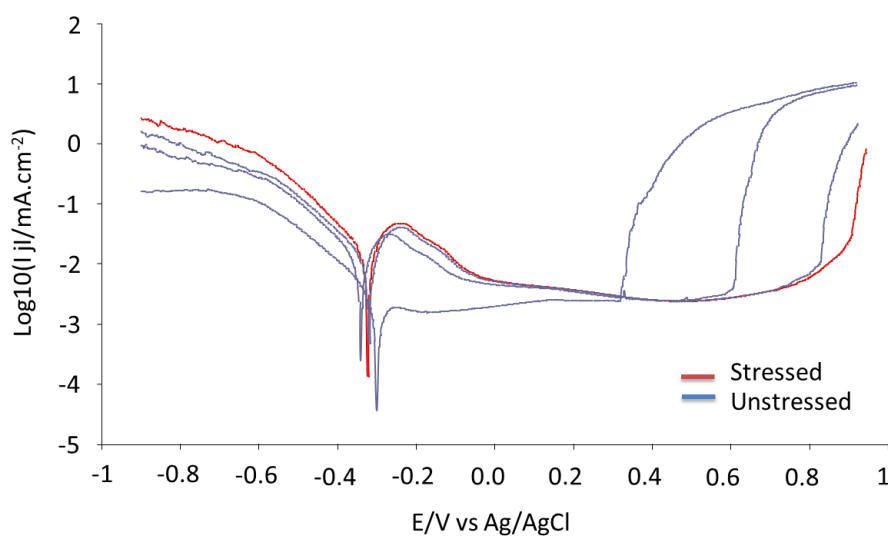


Figure 4.1: Polarization curve in 0.05 M NaCl produced by the stagnant cell. Blue: unstressed samples. Red: stressed sample.

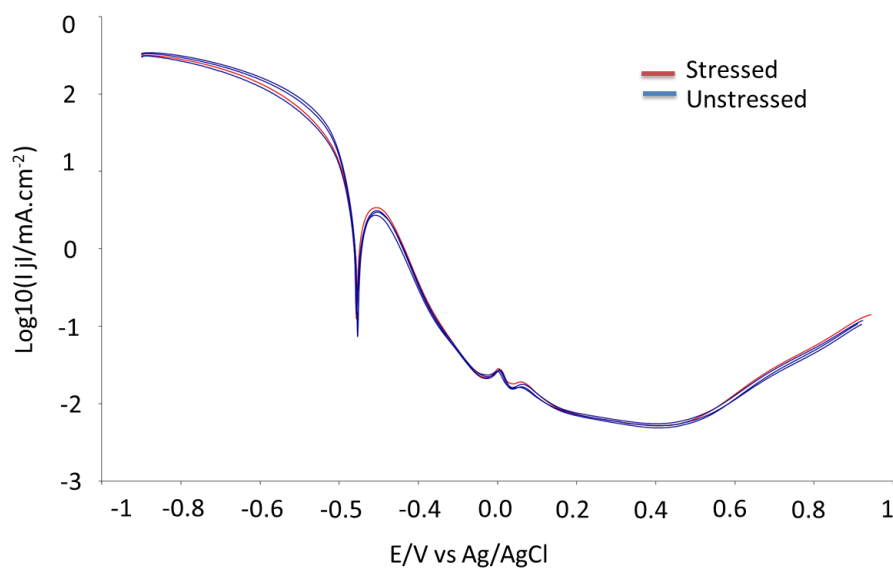


Figure 4.2: Polarization curves in 5 M  $\text{H}_2\text{SO}_4$  produced by the stagnant cell.

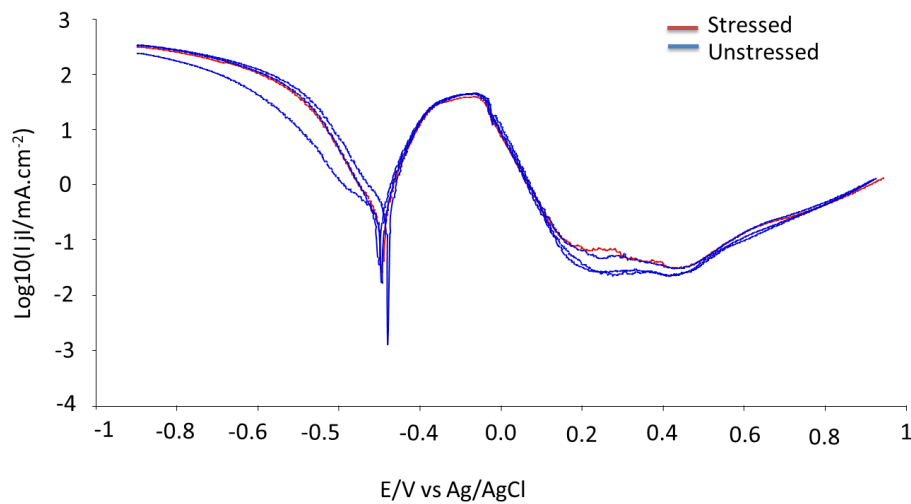


Figure 4.3: Polarization curves in 5 M  $\text{H}_2\text{SO}_4$  + 0.5 M NaCl produced by the stagnant cell. Blue: unstressed samples.

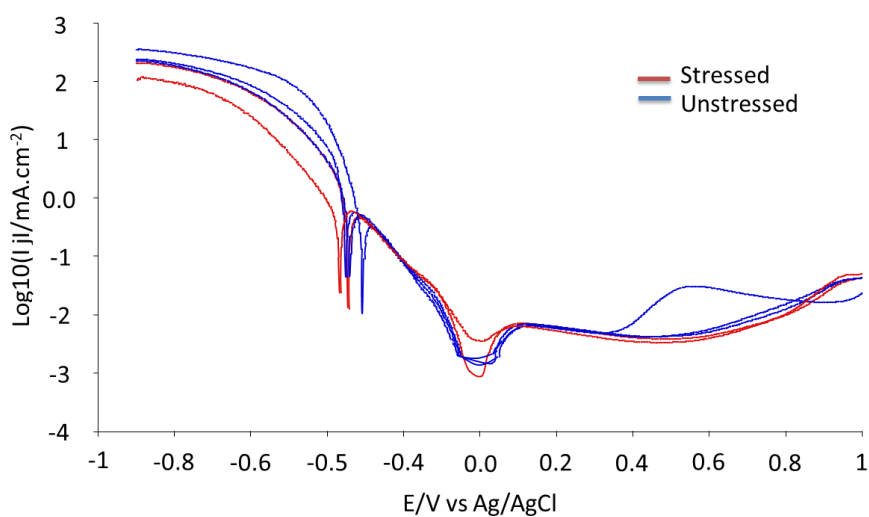


Figure 4.4: Polarization curves in 2 M  $\text{H}_2\text{SO}_4$  produced by the stagnant cell.

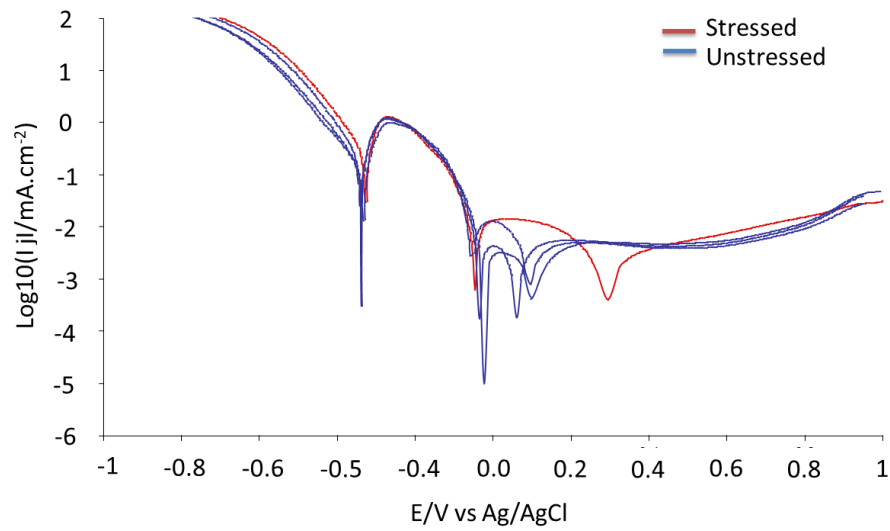


Figure 4.5: Polarization curves in 2 M  $\text{H}_2\text{SO}_4$  + 0.05 M NaCl produced by the stagnant cell. Blue: unstressed samples. Red: stressed sample.

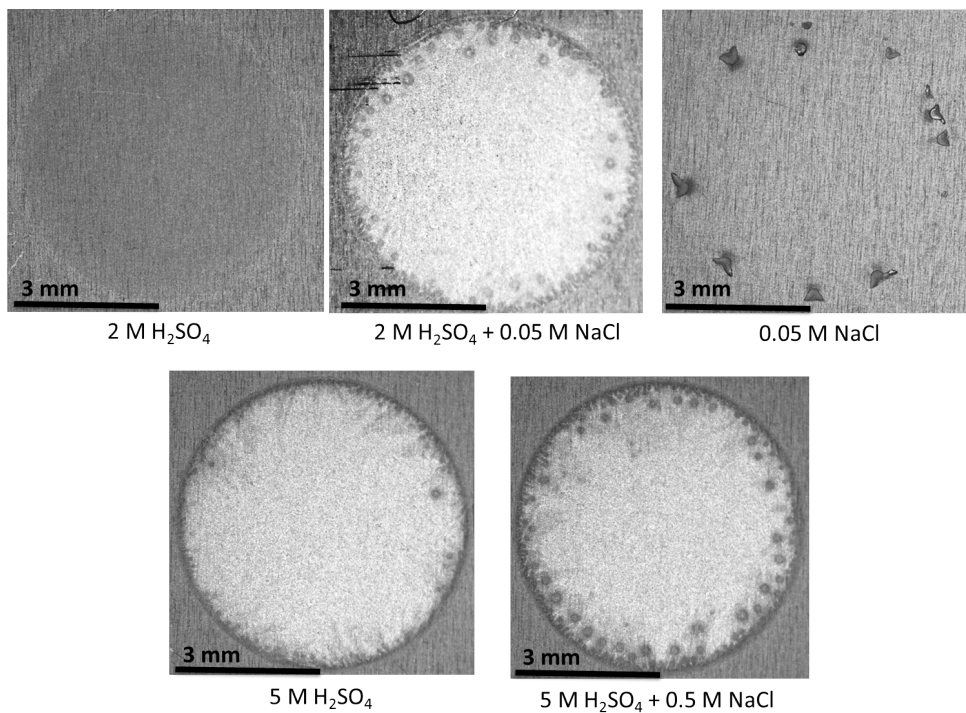


Figure 4.6: Post experimental surfaces of unstressed 304L stainless steel after the polarization experiments in the proposed electrolytes.

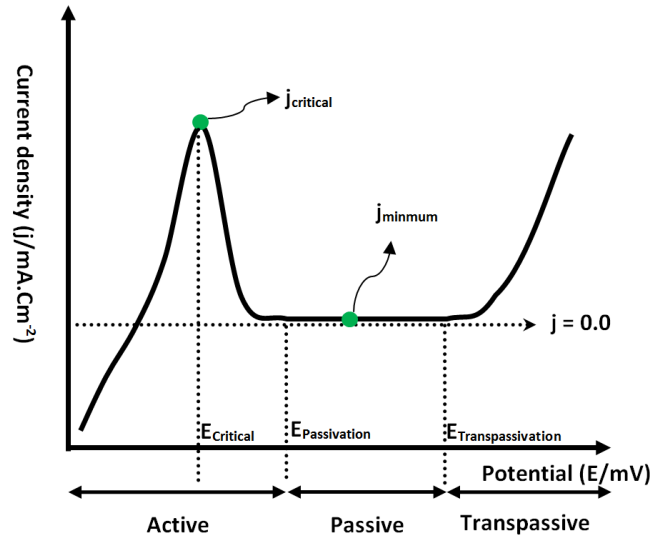


Figure 4.7: The points selected for the statistical analysis on the polarization curve.

in cases where acid was added, which prevents the blockage of the hydrogen bubbles near the joint.

Generally, as seen from the obtained curves in Fig. 4.1 - 4.5, the effect of increasing the chloride ion tends to increase the randomness in the system. This is expected due to the fact that  $\text{Cl}^-$  causes passive film local break-ups, and resulting localized dissolutions and possibility to pit initiation. So, for better reproducibility, the chloride concentration, if required, is best to be kept very low.

Seen that the values of  $j_{\text{critical}}$  and  $j_{\text{minimum}}$  separately are not of the same order according to the used electrolyte, the relative standard deviation (RSD) of these values was used to characterize the experimental dispersion of the considered values in the different electrolytes. To have a visual presentation of the RSD values, Fig. 4.8 shows them for the five proposed electrolytes.

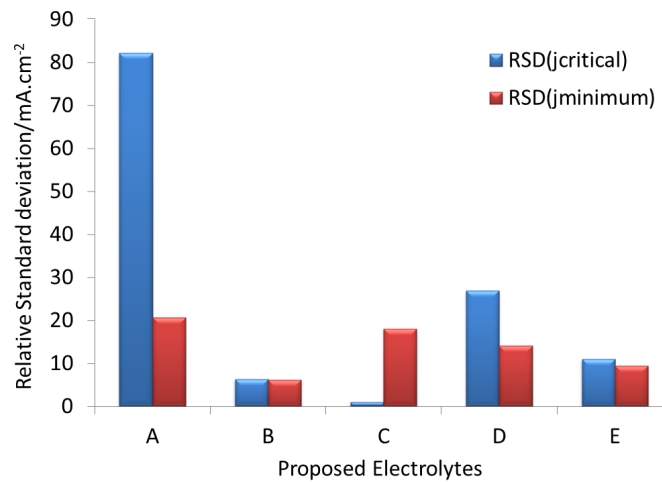


Figure 4.8: Relative standard deviation for  $j_{\text{critical}}$  and  $j_{\text{minimum}}$  of the proposed experimental electrolytes.

### Conclusions:

- Considering the RSD values for  $j_{\text{critical}}$  and  $j_{\text{minimum}}$  for the five proposed electrolytes, it turns out solution B: 5 M  $\text{H}_2\text{SO}_4$  is the one having the least RSD values. This suggests that B electrolyte is promising to give statistically valid results due to having the best experimental reproducibility, as illustrated clearly from 4.8.
- Testing a stressed sample in each of the previous experimental sets couldn't be so conclusive. No general trend was observed for the stressed polarization curve compared to those in relaxed conditions. In addition to this, seen the huge data scatter standard deviation for  $j_{\text{critical}}$  and  $j_{\text{minimum}}$  the one experiment is statistically not enough to give such. In addition to that, optical observation of post-experimental surfaces of stressed and unstressed samples showed no remarkable features due to the presence of stress. An example is given in Fig. 4.9 in the case of stressed and unstressed experiments in 2 M  $\text{H}_2\text{SO}_4$ .
- More experiments should be conducted using 5 M  $\text{H}_2\text{SO}_4$  for the purpose of having better statistics to check if the applied stress has an effect on the intensity of the corrosion reaction.

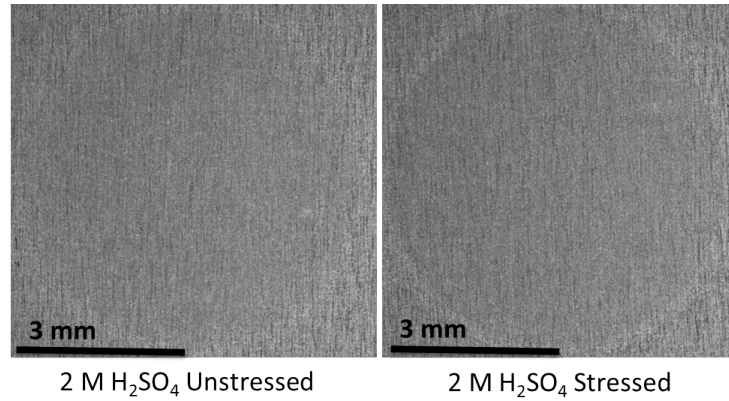


Figure 4.9: Effect of stress on post-experimental surface of 304L after polarization experiments in 2 M  $\text{H}_2\text{SO}_4$ .

### More statistical experiments

Now that 5 M  $\text{H}_2\text{SO}_4$  was selected as the suitable electrolyte, experiments are resumed to check for the effect of stress on the intensity of the corrosion reaction. Another objective of this part is to check the sensitivity of the experimental technique to mechanical surface treatment such as polishing and the related possible modification of the surface residual stress value.

For all the following experiments, the same potentiodynamic program explained earlier in Table: 2.4 is applied.

**Stressed vs non-stressed samples:** The first experimental set was dedicated to increasing the number of tests performed on stressed samples ( $\sigma = 280$  MPa). Three polarization curves were produced for each case of stressed and non-stressed samples, using the stagnant electrochemical cell. The obtained polarization curves are shown in Fig. 4.10:

The activity of the corrosion reaction was measured using  $j_{\text{critical}}$  and  $j_{\text{minimum}}$  values as shown in Table 4.3, while the values are illustrated in Fig. 4.11 with their corresponding experimental error.

So, from Fig. 4.11, there is no significant difference in terms of the current densities. The experimental domain of error covers the detected difference.



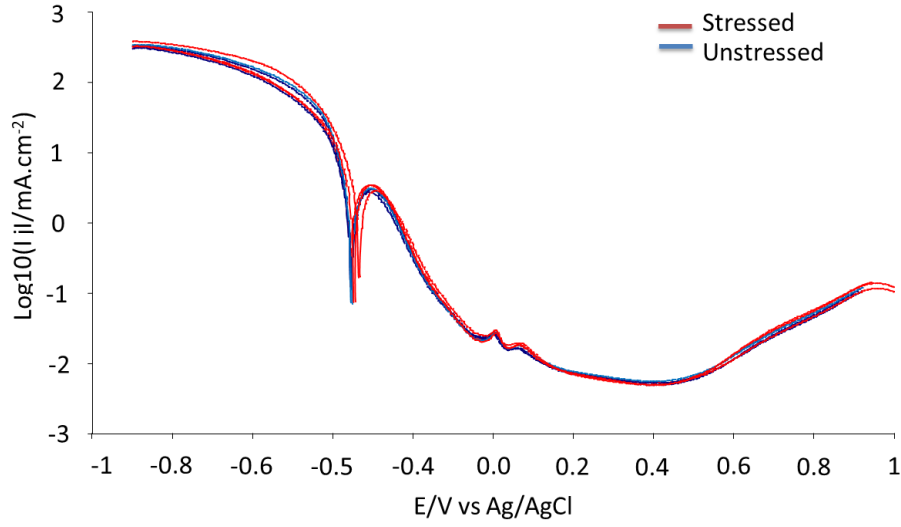


Figure 4.10: Polarization curves of stressed and unstressed 304L SS unpolished samples in 5 M  $\text{H}_2\text{SO}_4$  (stagnant cell).

Table 4.3:  $j_{\text{critical}}$  and  $j_{\text{minimum}}$  values for stressed and non-stressed samples during polarization in 5 M  $\text{H}_2\text{SO}_4$  (stagnant cell).

	$j_{\text{critical}}$	$[\text{mA.cm}^{-2}]$	$j_{\text{minimum}}$	$[\text{mA.cm}^{-2}]$
	average	standad deviation	average	standad deviation
Unstressed	2.95	0.15	0.0052	0.0002
$\sigma = 280 \text{ MPa}$	3.23	0.25	0.0050	0.0001

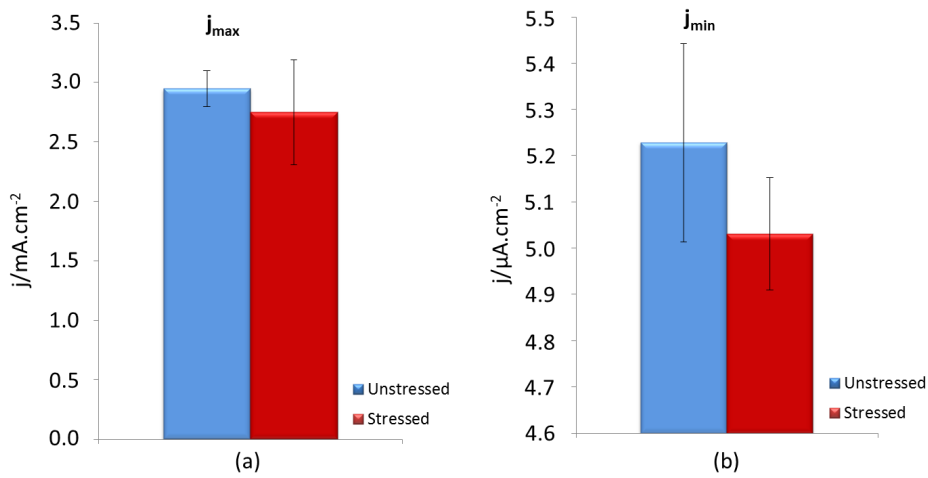


Figure 4.11: Illustration of (a):  $j_{\text{critical}}$  and (b):  $j_{\text{minimum}}$  values for stressed and non-stressed samples during polarization in 5 M  $\text{H}_2\text{SO}_4$  (stagnant cell).

Another way to check for the surface status are the values of the open circuit potential (OCP) of the surface before and after the polarization test. The OCP curves related to these experiments are given in Fig. 4.12.

As seen from these curve, for OCP before the polarization, the slope is negative, indicating surface state being changed towards the active state. The sudden fall in OCP values around 200 s. from about 0.0 V to -300 mV (vs Ag/AgCl) is due to passivity breakdown, which took place only in two cases for these experiments, while the others continued to be degraded in a stable way.

The curves representing OCP values before the polarization, Fig. 4.12 (a) are quite scattered due to different possible surface initial passivity, or due to the presence of more local anodic/cathodic features within the specific area exposed to corrosion. On the other hand, this was not the case for OCP values after the polarization, Fig. 4.12 (b). More compact curves indicate reproducible surface state, seen that the possible anodic/cathodic surface features were dissolved during the polarization sweep.

To make this more representative, the history OCP values was analyzed for the different experiments at three selected states as indicated below:

1.  $OCP_i$ : the initial value of OCP as the solution come into contact with the sample, calculated as the average of data points registered during the first 10 seconds.
2.  $OCP_{pre}$ : the OCP value of the sample just before the polarization takes place. This value was calculated as the average of data points registered during the last 10 seconds of the OCP period preceding the polarization test.
3.  $OCP_f$ : the final OCP value of the surface after the polarization test was conducted. This was calculated as the average OCP value over the last 10 seconds of the OCP period following the polarization test.

The purpose of these points is to try to statistically check for the evolution of the surface state from the beginning of the experiment until the end. For the OCP curves presented in Fig. 4.12, the  $OCP_i$ ,  $OCP_{pre}$ , and  $OCP_f$  are given in Table 4.4, and illustrated with their experimental error in Fig. 4.17.

Table 4.4:  $OCP_i$ ,  $OCP_{pre}$ , and  $OCP_f$  values for stressed and non-stressed samples in 5 M  $H_2SO_4$  (stagnant cell). \* avg: Average, stdv: Standard Deviation.

(OCP/V vs Ag/AgCL)	$OCP_i$		$OCP_{pre}$		$OCP_f$	
	avg.*	stdv.*	avg.	stdv.	avg.	stdv.
Unstressed	0,41	0,08	0,09	0,30	0,42	0,01
Stressed	0,46	0,06	0,08	0,28	0,43	0,01

Though the  $OCP_i$  values were different, by the end of the first OCP period, the surfaces degraded to get to more or less the same OCP state as indicated by their  $OCP_{pre}$  values. So, the initial industrial surface was passive, and this film might break up by barely being in contact with the concentrated sulfuric acid. More interesting is the surface states after the polarization tests indicated by  $OCP_f$ , showing very close OCP values representing reproducible surface state by the end of the polarization, which is passive according to the obtained  $OCP_f$  values. The fine error bars related to  $OCP_f$  indicate high experimental accuracy, and the huge variation of the  $OCP_i$  and  $OCP_{pre}$  is physical and related to real surface features causing this variation.

⇒ This experimental set gave no conclusion about any pronounced effect of stress on corrosion, neither on the current density reflecting the corrosion reaction intensity nor on the OCP values representing the surface states.

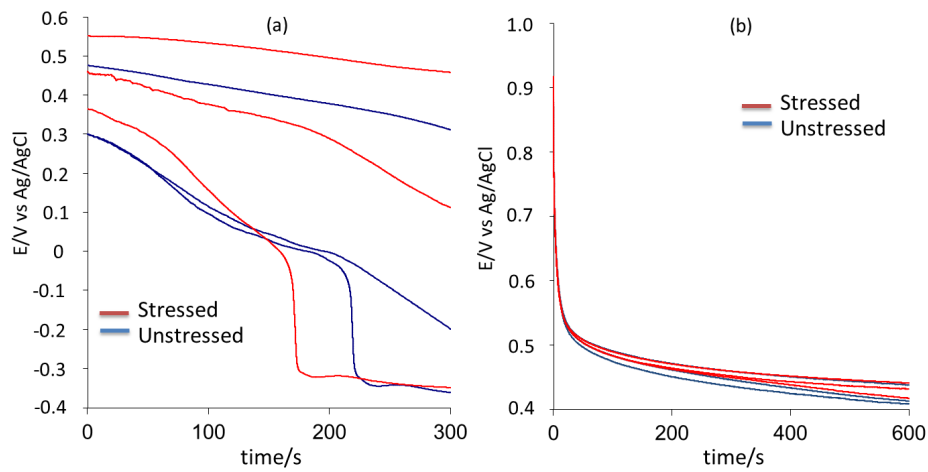


Figure 4.12: OCP curves for stressed and non-stressed samples in 5 M H<sub>2</sub>SO<sub>4</sub> (stagnant cell). (a): before the polarization test. (b): after the polarization test.

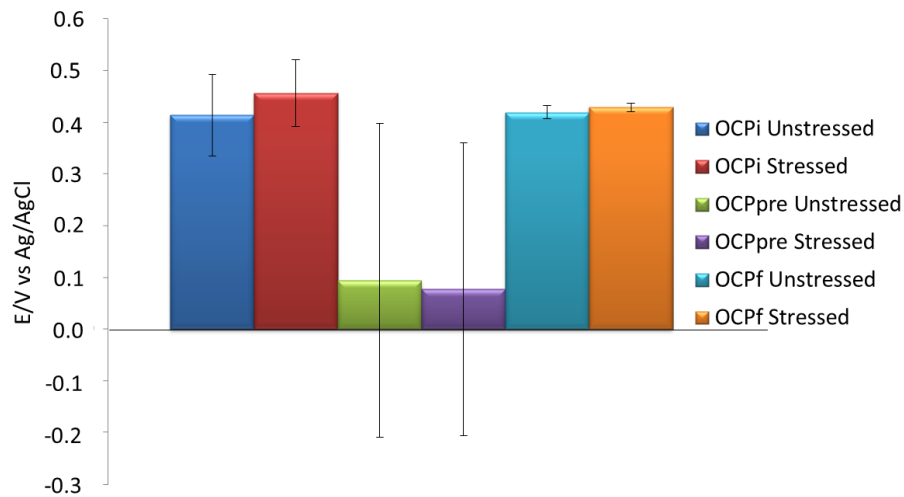


Figure 4.13: OCP<sub>i</sub>, OCP<sub>pre</sub>, and OCP<sub>f</sub> values for stressed and non-stressed samples in 5 M H<sub>2</sub>SO<sub>4</sub> (stagnant cell).

### Unstressed (Polished vs non-polished) samples

After the results obtained in the previous experimental set, it was believed that the effect of stressed was not detected. This was thought to be due to thermo-chemical or mechanical finishing of the material's surface. Thus, mirror polishing the samples was suggested in order to obtain a more controlled initial surface state.

Samples were polished to 1200-grit, passing by 240, and 500-grit disks. Polishing was followed by ultrasonic cleaning in ethanol for 15 min. to make sure that the polishing particles are removed from the surface. The same potentiodynamic program mentioned earlier in Table 2.4 was used again for these polarization tests.

In the beginning, the effect of simply polishing the samples was verified. Thus, unstressed polished and non-polished samples were tested. The resulting polarization curves are given in Fig. 4.14.

The curves referring to polished surfaces were more separated from each other than those representing the non-polished samples, as shown in Fig. 4.14. To study these curves,  $j_{\text{critical}}$  (or equally  $j_{\text{max}}$ ) and  $j_{\text{minimum}}$  were determined for the different experiments as given in Table 4.5, and illustrated in Fig. 4.19.

Table 4.5:  $j_{\text{critical}}$  and  $j_{\text{minimum}}$  values for polished and non-polished samples during polarization in 5 M  $\text{H}_2\text{SO}_4$  (stagnant cell).

	$j_{\text{critical}}/\text{mA.cm}^{-2}$		$j_{\text{minimum}}/\text{mA.cm}^{-2}$	
	average	standard deviation	average	standard deviation
Unpolished	2.95	0.15	0.0052	0.0002
Polished	2.75	0.44	0.0037	0.0003

It's clear from Fig. 4.14 and Fig. 4.19 that there was no significant difference concerning  $j_{\text{critical}}$  values of both cases, due to the high experimental error indicated by the error bars. On the other hand,  $j_{\text{minimum}}$  was remarkably lower in the case of the polished surface. This can be attributed to the construction of more isolating passive film for the case of polished samples. Another check on this can be made by the OCP evolution before and after the polarization, which is given in Fig. 4.16.

The first remark on the OCP evolution before the polarization is that, in general, polished samples had active surface since the beginning of the contact with the acid having  $\text{OCP}_i$  equals to -0.31 V (vs Ag/AgCl) as indicated by Table 4.6. However, on the non-polished samples, the protective passive film kept the OCP of the surface to be 0.41 V (vs Ag/AgCl) within the passive domain. This suggests the total removal of the protective passive layer as the surface was mechanically polished. In some of the polished samples, a quick transfer of OCP values took place within the first few seconds of contact with the solution. For these cases, between the moment the sample was polished until the experiment time, the surface was oxidized to produce a fine fragile passive film which couldn't resist as much as the initial industrial passive film in the case of non-polished samples.

Table 4.6: OCP statistics before the polarization tests.

OCP/ V (vs Ag/AgCl)	$\text{OCP}_i$		$\text{OCP}_{\text{pre}}$		$\text{OCP}_f$	
	avg.	stdv.	avg.	stdv.	avg.	stdv.
Unpolished	0.41	0.08	0.09	0.30	0.419	0.0121
Polished	-0.31	0.10	-0.31	0.10	0.421	0.0118

To get a better understanding of the statistical analysis of the different OCP values, they are illustrated in Fig. 4.17.

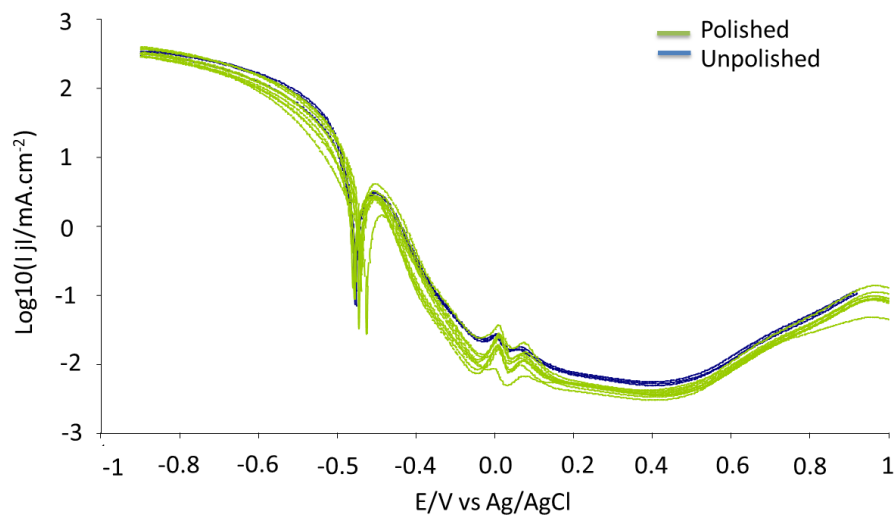


Figure 4.14: Effect of polishing on polarization curves of stressed and unstressed 304L SS samples in 5 M  $\text{H}_2\text{SO}_4$  (stagnant cell).

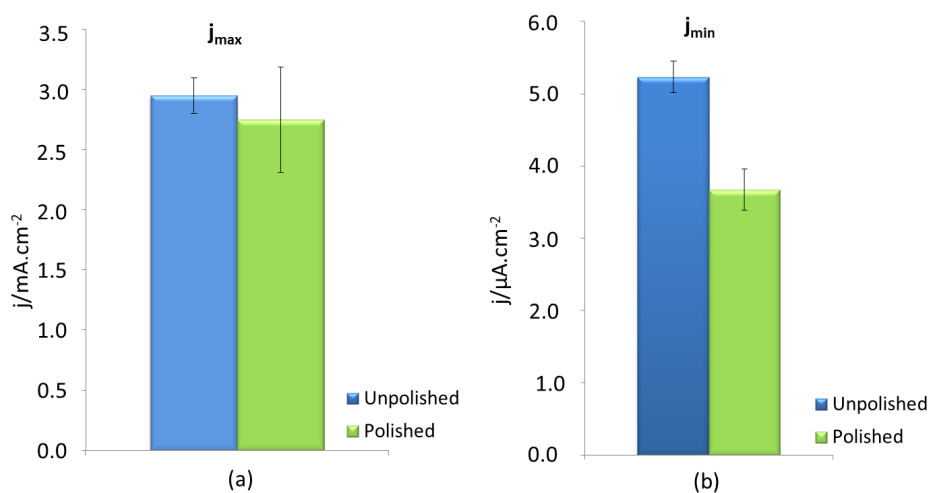


Figure 4.15: Illustration of (a):  $j_{\text{critical}}$  and (b):  $j_{\text{minimum}}$  values for polished and non-polished samples during polarization in 5 M  $\text{H}_2\text{SO}_4$  (stagnant cell).

## OCP curves

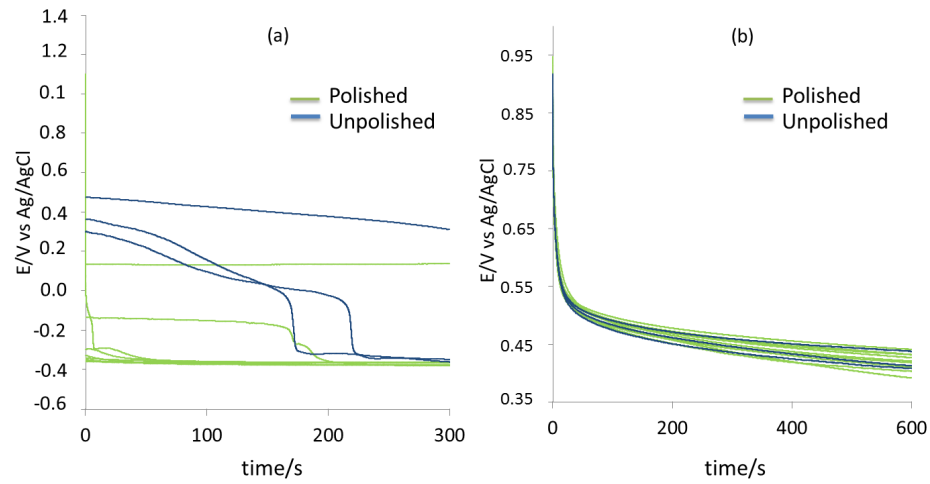


Figure 4.16: OCP curves for polished and non-polished unstressed samples in 5 M H<sub>2</sub>SO<sub>4</sub> (stagnant cell). (a): before the polarization test. (b): after the polarization test.

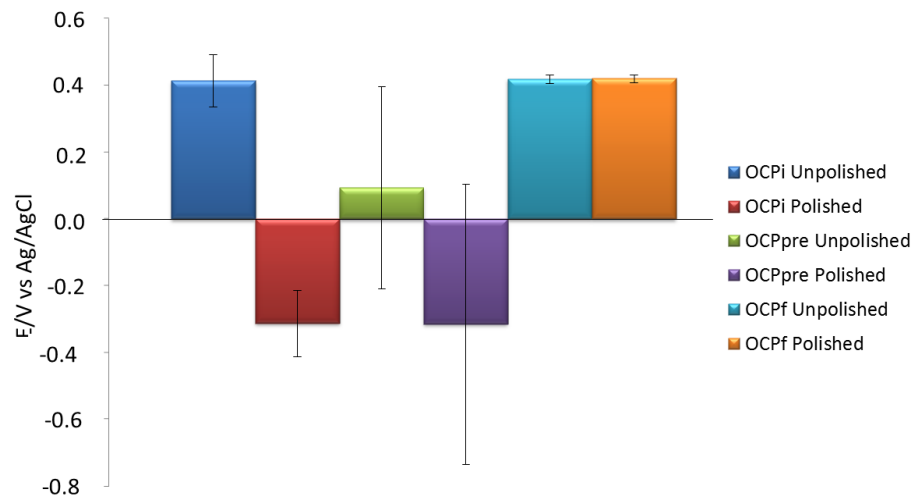


Figure 4.17: OCP<sub>i</sub>, OCP<sub>pre</sub>, and OCP<sub>f</sub> values for stressed and non-stressed samples in 5 M H<sub>2</sub>SO<sub>4</sub> (stagnant cell).

Amazingly, though the surfaces started by totally different  $OCP_i$  values, both cases obtained the same  $OCP_f$  values. This reflects the effectiveness of the passivation process conducted during the polarization test, rendering both surfaces (initially polished and non-polished) the same final stable passive state with  $OCP_f$  equals to 0.42 V (vs Ag/AgCl).

⇒ Polishing did remove the initial industrial passive film, causing the initial OCP state of the surface to be active. Nevertheless, the surface state after the polarization test was identical for both of surfaces in terms of  $OCP_f$  values.

⇒ Passivation was easier to obtain in the case of polished samples, as indicated by less  $j_{critical}$  required. And this was confirmed by the better passivation obtained eventually, allowing less current exchange  $j_{minimum}$  as the passive film was totally developed after the polarization test.

### Polished (Stressed vs non-stressed) samples

Since polishing the surface was tested to give a controlled initial surface state and a better passivation as measured by  $j_{minimum}$  value, it was used in all the following experiments as an initial surface preparation. Hence, polished stressed and unstressed samples were subjected to polarization tests using the potentiodynamic program given earlier in Table 2.4.

The surface was mechanically polished starting from 240-grit disks, then 500-grit, and eventually 1200-grit. Fifteen-minute ultrasonic cleaning in ethanol was made afterward to remove all polishing residuals. The used solution kept to be 5 M  $H_2SO_4$ , and the experiments were conducted in the stagnant cell.

The obtained polarization curves are shown in Fig. 4.18. Having a quick look on these polarization curves, the curves related to stressed samples were remarkably compact in the cathodic part compared to the unstressed ones. However, this effect was less present in the other regions of the curve.

The  $j_{critical}$  and  $j_{minimum}$  values are calculated for these tests, and given in Table 4.7, and illustrated in Fig. 4.19 along with the error bars.

Table 4.7:  $j_{critical}$  and  $j_{minimum}$  values for polished stressed and unstressed samples during polarization in 5 M  $H_2SO_4$  (stagnant cell).

	$j_{critical}/mA.cm^{-2}$		$j_{minimum}/mA.cm^{-2}$	
	avg	stdv	avg	stdv
Unstressed	2.75	0.44	0.0037	0.0003
Stressed	3.29	0.14	0.0036	0.0002

From Fig. 4.19, the  $j_{critical}$  value for stressed samples seems to be higher in the case of stressed samples, though the error bars are to the limits to make this difference equal to the experimental error. For the  $j_{critical}$  value, it was more or less the same for both cases.

A check on the OCP evolution before and after the polarization might give some indications. For this, the OCP curves are presented in Fig. 4.16. It is noticed that the surface in some cases had an initiation of a passive film, which was very quickly dissolved as it came into contact with the acidic electrolyte. Apart from those, the  $OCP_i$  values indicate an active surface from the beginning. No clear difference was detected between stressed or unstressed tests.

The statistics about the  $OCP_i$ ,  $OCP_{pre}$ , and  $OCP_f$  points on these curves are given in Table 4.8, and illustrated graphically in Fig. 4.21.

The statistics about OCP values are presented graphically in Fig. 4.21. As all OCP values concerned were physically equal for both tests conducted in stressed and unstressed conditions. The surface converted from being in the active domain to being the passive domain after the polarization test was conducted. This means that during the polarization sweep, all cathodic features on the surface were dissolved, giving an anodic final reproducible surface.

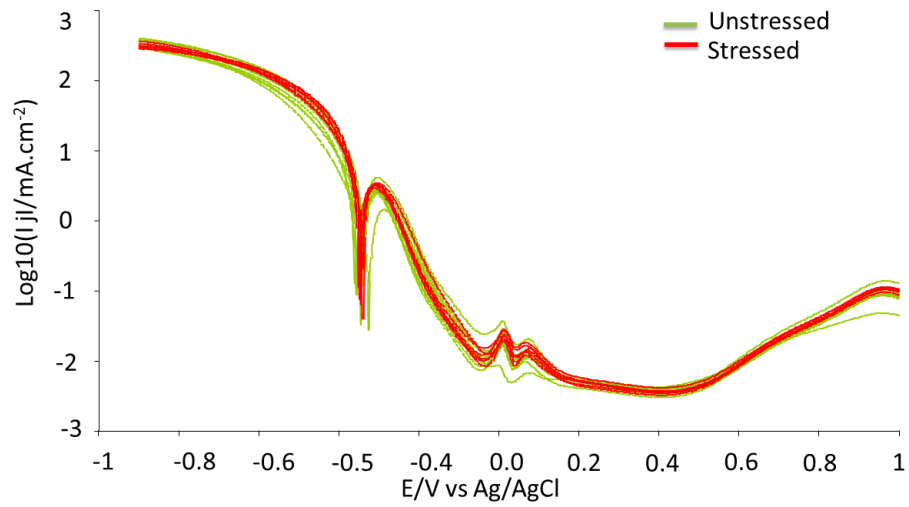


Figure 4.18: Effect of applied stress on polarization curves of polished 304L SS samples in 5 M  $\text{H}_2\text{SO}_4$  (stagnant cell).

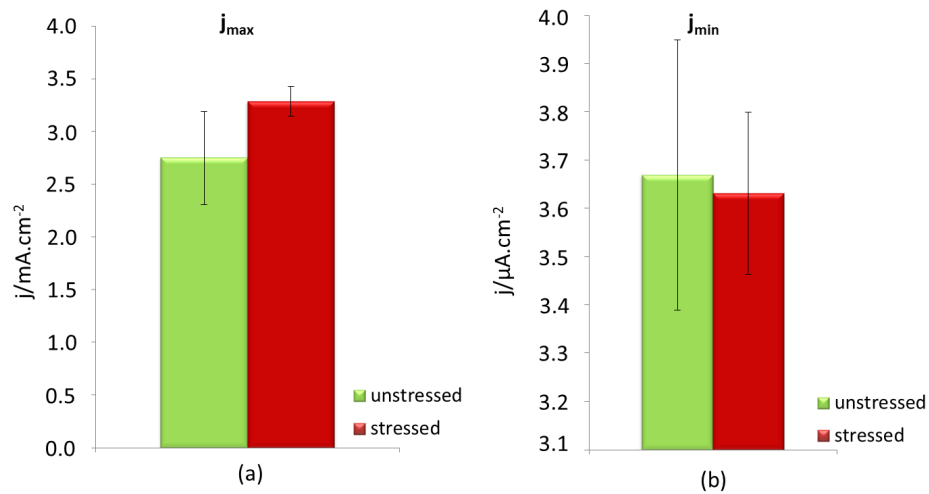


Figure 4.19: Illustration of (a):  $j_{critical}$  and (b):  $j_{minimum}$  values for polished stressed and unstressed samples during polarization in 5 M  $\text{H}_2\text{SO}_4$  (stagnant cell).

Table 4.8:  $\text{OCP}_i$ ,  $\text{OCP}_{pre}$ , and  $\text{OCP}_f$  values related to polished stressed and unstressed polarization tests.

OCP/ V (vs Ag/AgCl)	$\text{OCP}_i$		$\text{OCP}_{pre}$		$\text{OCP}_f$	
	avg	stdv	avg	stdv	avg	stdv
Unstressed	-0.31	0.10	-0.31	0.10	0.42	0.01
Stressed	-0.25	0.11	-0.32	0.09	0.43	0.01



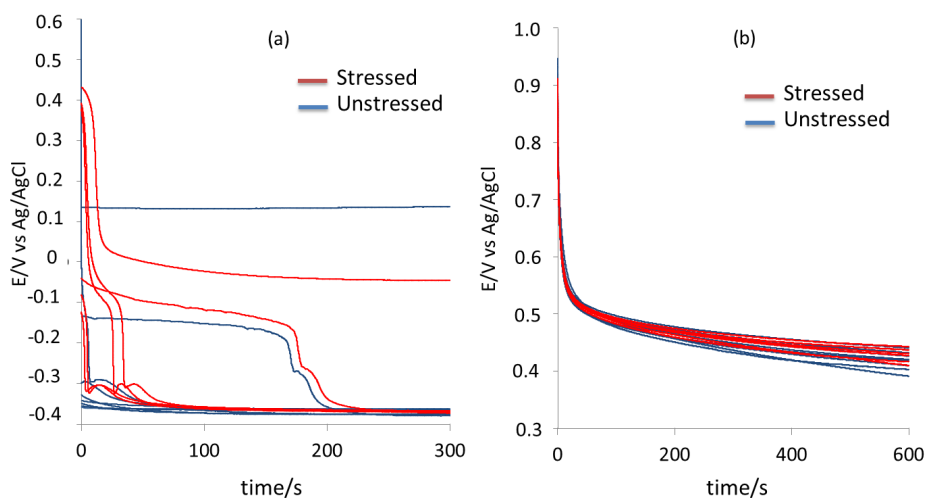


Figure 4.20: OCP curves for polished stressed and unstressed samples in 5 M  $\text{H}_2\text{SO}_4$  (stagnant cell). (a): before the polarization test. (b): after the polarization test.

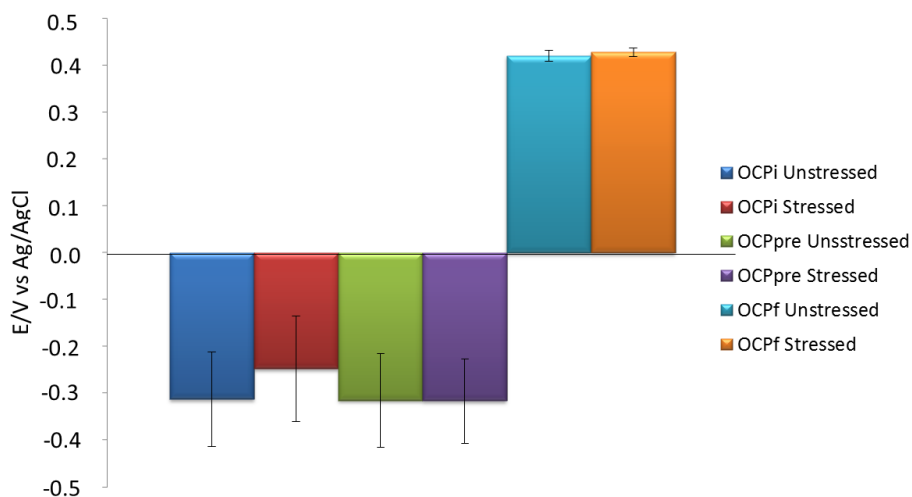


Figure 4.21:  $\text{OCP}_i$ ,  $\text{OCP}_{\text{pre}}$ , and  $\text{OCP}_f$  values for stressed and non-stressed samples in 5 M  $\text{H}_2\text{SO}_4$  (stagnant cell).

At this point, it might be of interest to show all the previously obtained polarization curves overlapping in the same figure, this is presented in Fig. 4.22. Just as a reminder, all these polarization curves were for the same material

### Introducing the flow cell

All previous experiments were conducted using the stagnant cell, where the same quantity of solution remains static over the surface, except for the agitation caused by the gas generation. This has the risk of changing the electrolyte conditions due to metallic dissolution towards the electrolyte. Furthermore, since the corrosion produces hydrogen excessively during polarization, this gas might partially isolate the surface from the electrolyte and thus the ionic exchange over short or long periods of time. Traces of hydrogen bubbles over the surface were detected after optical observation of the polarized spots, as indicated in Fig. 4.6 for experiments with 5 M  $\text{H}_2\text{SO}_4$  + 0.5 M NaCl for instance.

To fix these problems, the flow cell was used in the next experiments, where the electrolyte is renewed instantaneously and the generated gas is expected to be removed with the outlet flow, as was described earlier in section: 2.4.2.

At first, for comparison purposes with previously made experiments, three unstressed polished samples were subjected to the polarization program given earlier in Table 2.4. These were compared to the curves related to the unstressed polished samples produced previously in section Experiments III of this section. The resulting polarization curves are given in Fig. 4.23.

The effect of having a flowing electrolyte on the polarization curve was obvious, especially in the cathodic part of the curve. The cathodic current was expected to be higher in the flowing cell since it allows the generated hydrogen gas to be immediately removed, which assures a better electrolyte/surface interaction, and eventually more intense reaction.

Unexpectedly, the cathodic current was 5-6 times higher in the case of the stagnant cell compared to that in the flow cell. Even though the circulating solution should immediately remove the forming gas way, but since the gas formation rate is very intense, the confined volume of the cell blocks the gas partially inside, making the reaction eventually slower. Considering this, and looking to the curves for 5 M  $\text{H}_2\text{SO}_4$ , using the stagnant cell is much better in terms of reproducibility.

Another possible reason for the difference between the cathodic currents obtained by the stagnant/flow cells is that the experimental procedure during the five-minute open circuit potential (OCP) period before the polarization scan starts. For the stagnant cell, the solution was all the time 5 M  $\text{H}_2\text{SO}_4$ , and the experiment can be started instantaneously at the moment where the electrolyte is filled in the cell. This can not practically be done in the case of the flow cell since the electrolyte flow rate has to be fixed before, and electrolyte leakage has to be limited. To do this, the flowing fluid used is water, to make sure that the surface has the least possible oxidation. For this, the experimental procedure was as explained in Table:4.9.

Table 4.9: Electrolyte exposure before the polarization program is applied.

	$\text{H}_2\text{O}$	5 M $\text{H}_2\text{SO}_4$
<b>Stagnant cell</b>	—	5 min.
<b>Flow cell</b>	1 min.	4 min.

Since the polished surface is usually active, being exposed to water could start the passivation process, and as a result, the cathodic current to be lower than expected, due to the presence of some protective passive film.

As of what concerns the  $j_{\text{critical}}$  and  $j_{\text{minimum}}$  values, the statistics of the performed experiments is given in Table:4.10, and illustrated in Fig. 4.24. No significant difference was detected, though  $j_{\text{minimum}}$  was slightly lower in the case of stagnant cell.

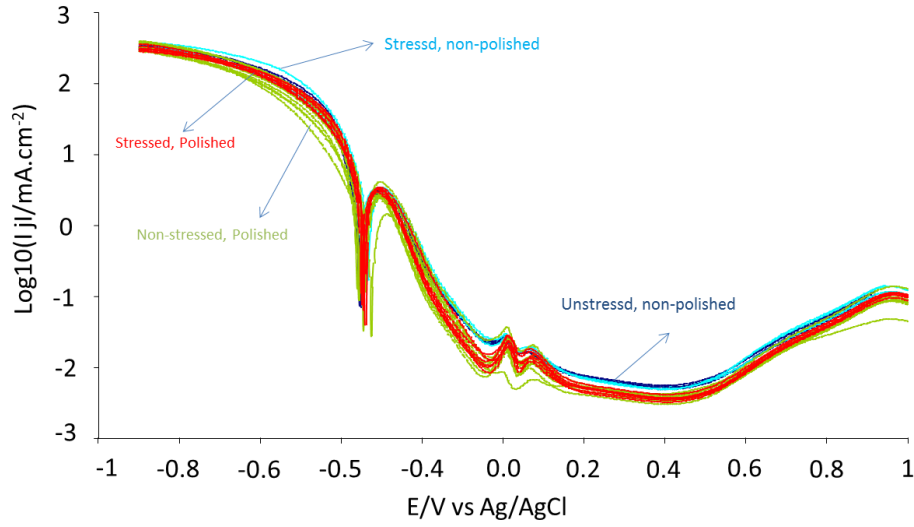


Figure 4.22: All polarization curves of 304L stainless steel in 5 M  $\text{H}_2\text{SO}_4$  (stagnant cell).

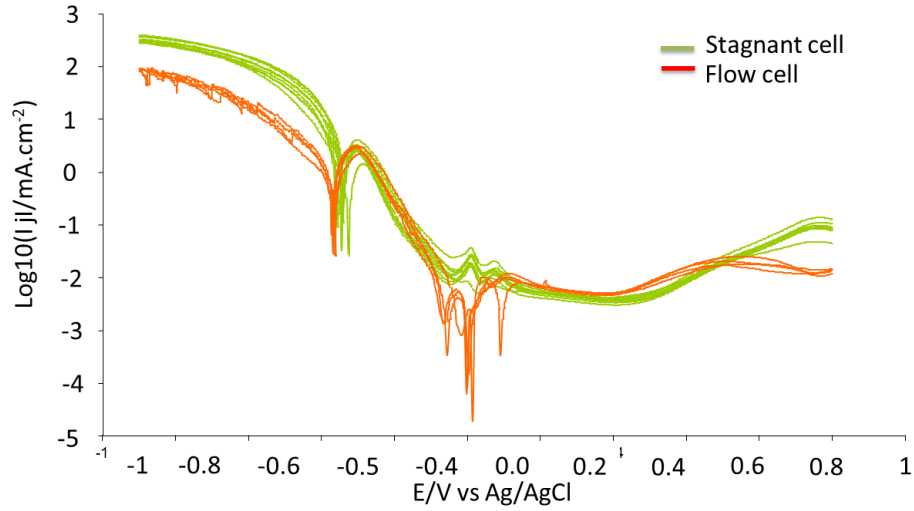


Figure 4.23: Flow vs stagnant cell on polarization curves produced in 5 M  $\text{H}_2\text{SO}_4$  (unstressed samples).

Table 4.10:  $j_{\text{minimum}}$  and  $j_{\text{critical}}$  values for the experiments of flow vs stagnant cell.

	$j_{\text{critical}}/\text{mA.cm}^{-2}$		$j_{\text{minimum}}/\text{mA.cm}^{-2}$	
	avg	stdv	avg	stdv
Stagnant	2.75	0.44	0.0037	0.0003
Flow	2.88	0.30	0.0045	0.0005

From Fig. 4.25, the effect of renewing the electrolyte by the flow cell can be clearly noticed on the OCP evolution especially on the post-polarization OCP curves. Statistical data concerning the OCP points of interest is given in the Table:4.11.

Table 4.11:  $OCP_i$ ,  $OCP_{pre}$ , and  $OCP_f$  values related to polished polarization tests performed in stagnant vs flow cell.

	$OCP_i/V$		$OCP_{pre}/V$		$OCP_f/V$	
	avg	stdv	avg	stdv	avg	stdv
Stagnant	-0.31	0.10	-0.31	0.10	0.42	0.01
Flow	0.09	0.18	0.02	0.21	0.56	0.10

Fig. 4.26 gives visual representation of these values along with their error bars. For the flow cell, the  $OCP_f$  value was higher than that of the stagnant cell. If these values are located on the polarization curve given in Fig. 4.22, it is noticed that  $OCP_f = 0.56$  V for the flow cell is more shifted toward the transpassive domain than the stagnant cell with  $OCP_f = 0.42$  V which is in the passive domain. This suggests lower surface passivation quality in the case of flow cell than that produced by the stagnant cell. This lower passivation quality is confirmed by  $j_{minimum}$  value for both cells, where it was again slightly higher for the flow cell ( $4.5$  vs  $3.7$ )  $\pm 0.3$   $\mu A.cm^{-2}$  indicating less ionic transfer resistance.

### Adding NaCl to check the effect of stress

Now that the parameters of the flow cell are mastered, it was suggested to check the effect of adding NaCl to the electrolyte. Thus, three stressed and three unstressed samples were tested in 5 M  $H_2SO_4$  + 5 M NaCl electrolyte in the flow cell. The resulting polarization curves are given in Fig. 4.27.

The effect of adding  $Cl^{-1}$  on the polarization curve is so clear, yet, the curves corresponding to stressed and unstressed curves are spread indistinguishably. Table 4.12 show the values corresponding to the stressed unstressed tests.

Table 4.12:  $j_{critical}$  and  $j_{minimum}$  values for polished stressed and unstressed samples during polarization in 5 M  $H_2SO_4$  + 0.05 M NaCl (flow cell).

	$j_{critical}/mA.cm^{-2}$		$j_{minimum}/mA.cm^{-2}$	
	avg	stdv	avg	stdv
Unstressed	14.71	1.15	0.054	0.046
Stressed	16.46	2.54	0.058	0.027

The  $j_{critical}$  and  $j_{minimum}$  values indicated in Table 4.12 are illustrated along with their error bars in Fig. 4.28.

The stress state of the sample was unrelated to the obtained  $j_{critical}$  and  $j_{minimum}$  values. However, the effect of the added chloride ion was very remarkable. With this slight added concentration of 0.5 M NaCl, the  $j_{critical}$  became about five times its value in the corresponding electrolyte without NaCl. On the other hand,  $j_{minimum}$  was ten times bigger for the case of added NaCl, indicating lower passivation quality, as expected.

The last to check is the OCP evolution before and after the polarization test, for which the curves are given in Fig. 4.29.

As seen, the breakdown of the initial fine passive film as the fluid is switched from water to acid at 120 second time, though in some cases it resisted but with gradual degradation towards the active domain. No clear separation between the curves is observed based on the stress state.

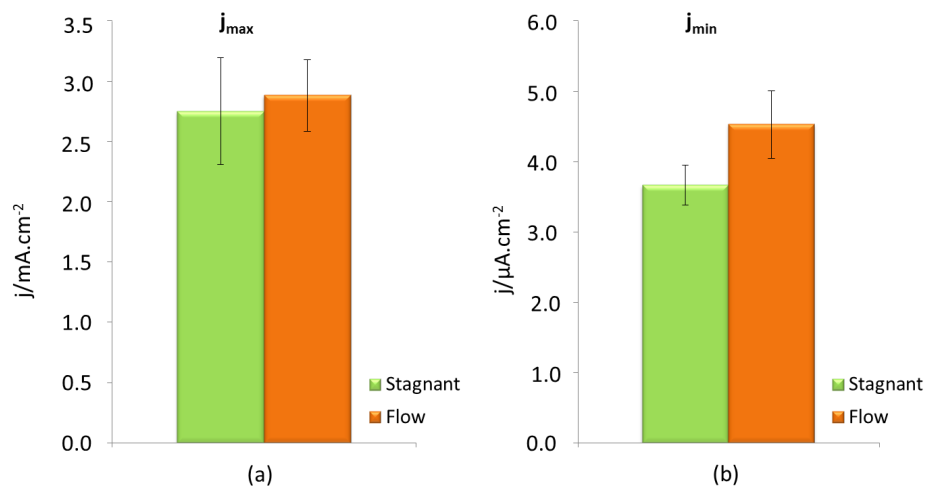


Figure 4.24: Illustration of (a):  $j_{\text{critical}}$  (or equally  $j_{\max}$ ) and (b):  $j_{\text{minimum}}$  values for 304L polished samples during polarization in 5 M H<sub>2</sub>SO<sub>4</sub> stagnant vs flow cell.

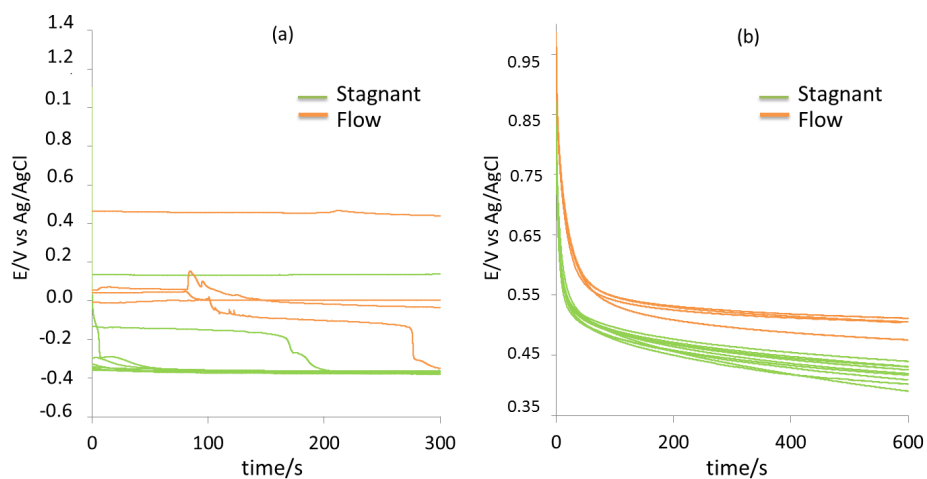


Figure 4.25: OCP curves for polished samples in 5 M H<sub>2</sub>SO<sub>4</sub> stagnant vs flow cell. (a): before the polarization test. (b): after the polarization test.

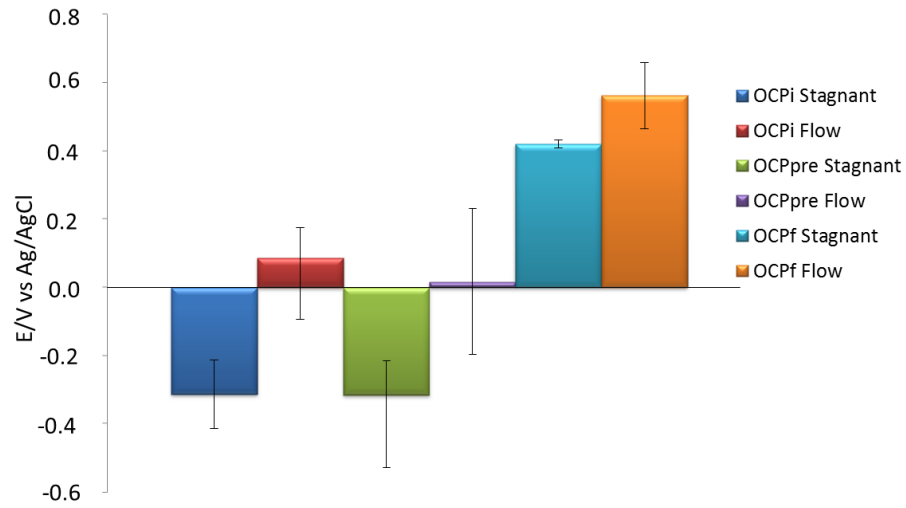


Figure 4.26: Illustration of OCP<sub>i</sub>, OCP<sub>pre</sub>, and OCP<sub>f</sub> values for polished samples in 5 M H<sub>2</sub>SO<sub>4</sub> stagnant vs flow cell.

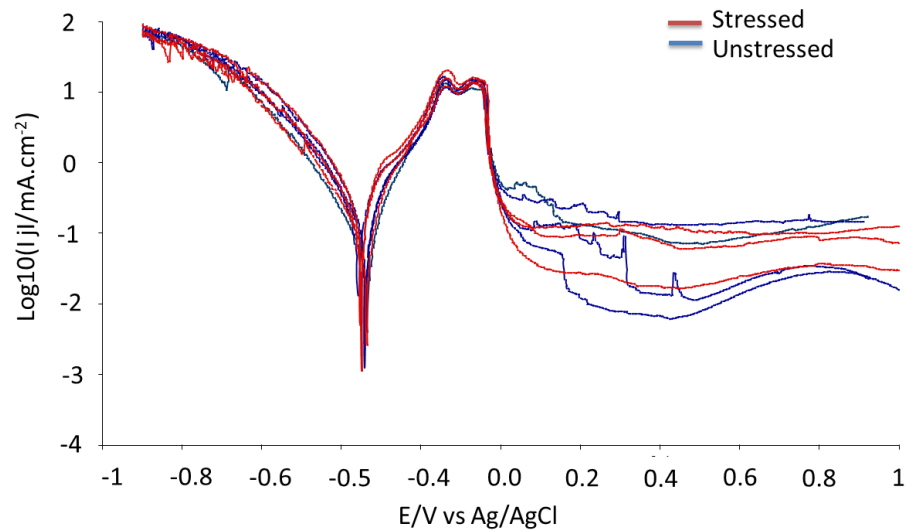


Figure 4.27: Stress effect on polarization curves of 304L polished samples produced in 5 M H<sub>2</sub>SO<sub>4</sub> + 0.05 M NaCl (Flow cell).

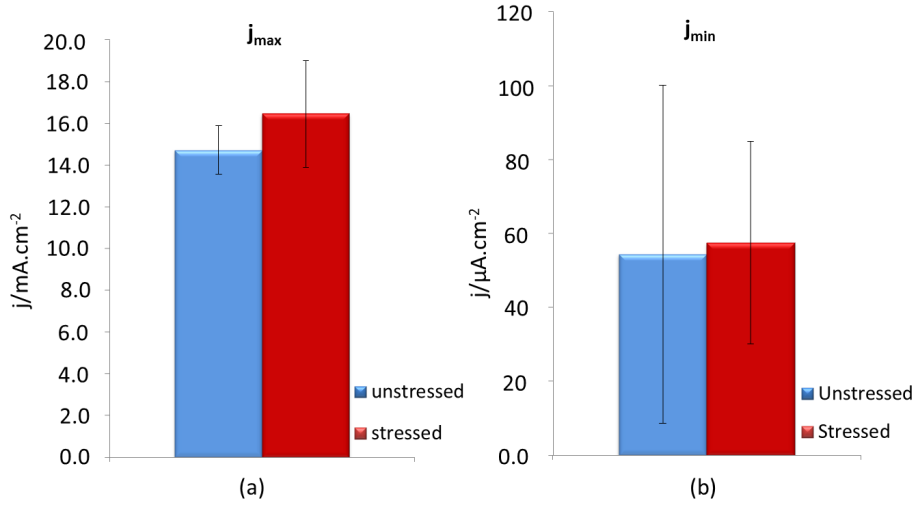


Figure 4.28: Illustration of (a):  $j_{\text{critical}}$  (or equally  $j_{\max}$ ) and (b):  $j_{\text{minimum}}$  values for polished stressed and unstressed samples during polarization in 5 M H<sub>2</sub>SO<sub>4</sub> + 0.05 M NaCl (flow cell).

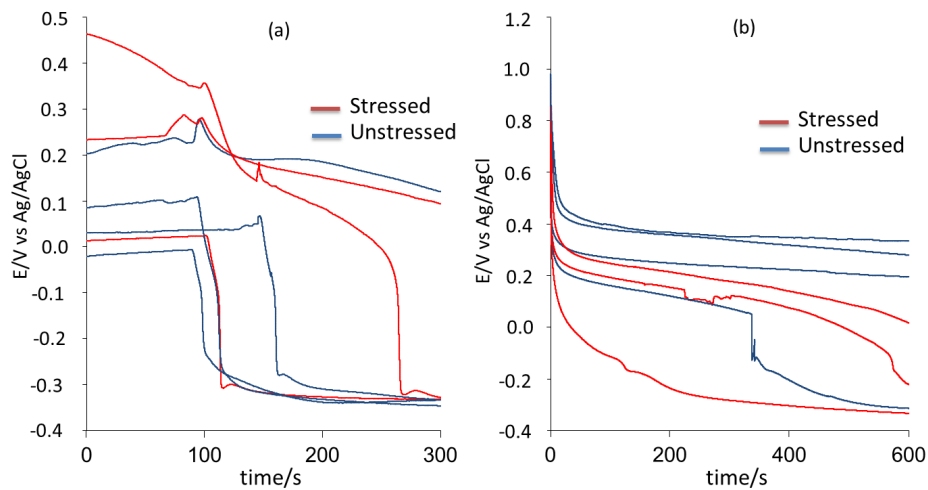


Figure 4.29: OCP curves for polished stressed and unstressed samples in 5 M H<sub>2</sub>SO<sub>4</sub> + 0.05 M NaCl (stagnant cell). (a): before the polarization test. (b): after the polarization test.

Statistically, Table 4.13 give the numerical values for points  $OCP_i$ ,  $OCP_{pre}$ , and  $OCP_f$ , which are illustrated in Fig. 4.30 as well for clarity.

Table 4.13:  $OCP_i$ ,  $OCP_{pre}$ , and  $OCP_f$  values related to polished stressed and unstressed polarization tests in 5 M  $H_2SO_4$  + 0.05 M NaCl (flow cell).

OCP/ V (vs Ag/AgCL)	$OCP_i$		$OCP_{pre}$		$OCP_f$	
	avg	stdv	avg	stdv	avg	stdv
Unstressed	0.076	0.070	-0.222	0.173	0.124	0.219
Stressed	0.237	0.150	-0.186	0.190	-0.176	0.131

All selected OCP points for the statistical analysis indicated no significant effect of the applied stress state. Even for  $OCP_f$  values as indicated in Fig. 4.30, the experimental error covers the indicated difference.

Post-experimental optical surface characterization was performed to check for any possible special features obtained on the stressed samples such as crack initiation, or pitting corrosion. Fig. 4.31 gives the surfaces obtained for three unstressed samples (upper line), and two stressed samples(lower line).

The optical observation, Fig. 4.31, gave no special surface corrosion features attributed to the applied stress. However, traces of air bubbles being trapped partially on the surface during the experimental time were detected, as seen by the black circular traces. This has the effect of producing a surface with local variation in the state (passive/active) which will increase the experimental error in of the registered current density or the OCP values.

#### 4.1.2 Summary, results and conclusions

##### Summary:

- Among five suggested solutions with different  $H_2SO_4$  and NaCl concentrations, 5 M  $H_2SO_4$  showed to be the solution giving the most reproducible polarization curves.
- More experiments were performed for a statistical purpose, aiming to check for any possible influence of the applied stress on the corrosion reaction intensity or any other corrosion related aspect.
- Selected current density points on the polarization curve ( $j_{critical}$  and  $j_{minimum}$ ) were used to check the corrosion reaction intensity.
- The OCP surface status was also analyzed statistically using three selected points of interest ( $OCP_i$ ,  $OCP_{pre}$ , and  $OCP_f$ ) covering the initial surface state, in addition to that before, and after the polarization test.
- Mirror polishing the samples was introduced to get a more controlled initial surface state.
- Two different electrochemical cells were tested: the stagnant cell, where the electrolyte remains static during the test, and the flow cell, where the electrolyte is renewed instantaneously during the experiment.

##### Results:

- Through experimental sets I to VI given in section (4.1.1), the electrochemical measuring method was checked for its validity in detecting experimental condition variations such as the electrolyte composition, the initial surface state, or the electrochemical cell used.



- Testing the as-received material surface, with/without applied stress gave no conclusions about any pronounced effect of the applied stress on the corrosion related parameters (current densities and OCP states).
- Polishing influenced the initial surface state making it initially active, which is expected due to the accompanied removal of the passive film with the mechanical polishing.
- Polished samples tended to generate a passive film of higher quality as measured by less  $j_{\text{minimum}}$  value compared to samples without surface polishing. In all cases, the effect of applied stress was negligible compared to the effect of surface polishing or increasing  $\text{Cl}^-$  ion concentration for example. This tells that the measuring technique is sensitive enough to detect reaction intensity variation resulting from changing surface state, but not to the applied stress.
- Post-Experimental surface observation revealed no special features due to the effect of applied stress. However, gas bubbles were trapped over the surface, causing temporary surface isolation from the reaction, which eventually leads to increase the experimental error in the measured quantities: the current density and the OCP value.

### Conclusions:

- Polarization tests gave no evidence on the effect of applied stress was detected on the corrosion intensity, neither on the passivation quality.
- The effect of stress might have been masked by the high acidic concentration of the electrolyte which is reflected on the high current density obtained at relaxed conditions, making it difficult to detect small variations such as those due to the applied stress.
- Using the flow cell will be considered for the purpose of elementary dissolution rate analysis by AESEC technique (Ch.5).
- Cycling experiments aiming at testing the transient behavior of the stainless steel as it moves from active to passive states could give some interesting information on the kinetics of passivation such as repassivation time, and the stability of the passive film.
- Less concentrated acidic solution might be more favorable to use, due to less accompanied reaction intensity. This will cause less gas generation and thus less experimental error. In addition to this, micro-effects such as the corrosion reaction intensity increase due to stress might be not masked as the case was in 5 M  $\text{H}_2\text{SO}_4$ .

## 4.2 Potentio-static Pulse Testing

Mechanisms of passivation and passive film nucleation, formation, and growth have a vital importance when it comes to understanding local material degradation phenomena, such as SCC, pitting, or cavitation.

Hence, in this section, the material is subjected to dynamic potential experiments. In these “dynamic experiments” the applied potential over the surface is altered between active and passive states in a predefined potentiodynamic program (applied voltage and time duration).

**Purpose:** This stands to study the alloy’s inherent response as it’s passing from active to a passive state, and the other way around.

The obtained current/potential transients corresponding to active/passive state changes will eventually be analyzed. This analysis is promising to reveal elements reflecting the degree of passivation, its kinetics and quality, and consequently the material’s resistance to corrosion and SCC.

### 4.2.1 Experimental conditions

**Electrolyte:** The experiments were conducted at a controlled room temperature (air conditioning set temperature = 24 °C).

Sulfuric acid  $\text{H}_2\text{SO}_4$  was used as an electrolyte to perform these experiments due to its anion ability to give a great stabilizing effect over the repassivation process and subsequently the constructed passive film [62].

**Electrochemical cell** The flow cell was used for these experiments, which is explained in Fig. 2.8 at section: 2.4.2.

### 4.2.2 Experimental set I: stressed/unstressed samples

This is the first cyclic experimental set performed. The purpose was to check if by altering the surface state between active and passive conditions, any possible effect on the corrosion parameters can be detected as an effect of the applied stress.

**Samples and surface preparation:** Three samples of each stressed and unstressed state were used in these experiments to have statistically valid results. Samples were used as received (non-polished) after surface cleaning by water followed by a 10-minute ultrasonic ethanol bath.

**Electrolyte:** Based on the results of the previous section, 5 M  $\text{H}_2\text{SO}_4$  was believed to be a severe electrolyte that might mask secondary corrosion-related phenomenon such as the effect of an applied stress. For that, in the following set of experiments, the sulfuric acid concentration was reduced to 2 M  $\text{H}_2\text{SO}_4$ , hoping to reduce the intensity of the general corrosion reaction, allowing more possibility to detect some effect on the corrosion parameters due to the applied stress.

**Procedure:** For each experiment, three cycles of activation, OCP, passivation, ending by OCP were applied following The potentiodynamic program indicated in Table 2.5.

### 4.2.3 Results:

#### Initial OCP:

The first to mention is the initial OCP value for the samples, which is shown by Fig. 4.32.(a).

The jump in the curve at  $t = 120\text{--}150$  s corresponds to the electrolyte transition from water to sulfuric acid. Earlier in this work,  $\text{OCP}_{\text{pre}}$  was defined as the average OCP value over the last ten seconds of the indicated OCP period in Fig. 4.32(a). The  $\text{OCP}_{\text{pre}}$  values for stressed and unstressed are  $(475 \pm 16)$  vs  $(498 \pm 21)$  mV vs Ag/AgCl for stressed and unstressed samples respectively. In the present case,  $\text{OCP}_{\text{pre}}$  indicates that the surface is originally passive in its as-received state (unpolished), and this initial passivity was maintained even after the application of mechanical tensile stress. However, the difference between the  $\text{OCP}_{\text{pre}}$  values for stressed/unstressed was insignificant as indicated by the error bars shown in Fig. 4.32 (b), thus the surface state can be said to be initially identical.

#### Cathodic activation

The purpose of this step is to dissolve the passive layer existing on the surface of the material. As indicated in Table 2.5, the cathodic activation of the surface was performed by -700 mV applied potential pulse over a period of 70 seconds. These activation parameters were optimized to make sure an active surface is produced afterward, as will be verified by the OCP values after activation in the next cycling step. The activation step is supposed to simulate the fresh surface production

step after slip-system activation as explained in the SCC propagation models. In contrast, due to the material surface history and local inhomogeneities or defects, the dissolution of the passive film might not be uniformly accomplished over the entire surface. Though this might be considered as a potential source of experimental error, but since it exists in all the experiments equally, the effect is less serious where it comes to the comparison of stressed/unstressed tests' results.

The three activation cycles were recorded with a high acquisition resolution where necessary, reaching up to 5000 data point per second. The obtained curves are given in Fig. 4.33 to 4.35. In the three cycles, all samples behaved in more or less the same way, passing from a passive to active state within less than 10 s. One test was quite different, in the case of unstressed samples during cycle 2 and 3, where the cathodic current got gradually lower with time. This is believed to be due to the surface being partially blocked by some gas bubble, which limited the ionic exchange for this specific experiment. Thus, the depassivation analysis will be limited to the first 10 seconds, where this difference is less present.

The cathodic current show continual gradual increase until about  $t = 9.5$  s, where the current density reaches roughly about  $j = 24 \text{ mA.cm}^{-2}$ . This is where the surface starts an excessive dissolution until the end of the activation pulse, where intense hydrogen generation is observed. During the active dissolution, the current fluctuates about the value of  $j = 24 \text{ mA.cm}^{-2}$  reaching up to  $25.6 \text{ mA.cm}^{-2}$  at some instances ( $t = 21$  s), and getting as low as  $22.6 \text{ mA.cm}^{-2}$  in other instances ( $t = 60$  s).

In general, as the current reaches the steady dissolution phase, the fluctuation it shows had a wavy from. This is believed to be due to the process of hydrogen-bubble nucleation, growth, and departure, which reduces the ionic exchange smoothly during the nucleation-growth process, then the ionic exchange gets higher again at the onset of bubble departure from the surface.

Due to the very fast dissolution kinetics, the current transients are better understood on the logarithmic scale, where the first few fractions of second during the activation process is better observed. For instance, Fig. 4.36 gives the three activation cathodic current transients for one experiment performed on unstressed samples.

As illustrated by the curves in Fig. 4.36, four distinguished zones can be identified as listed below:

- Zone I: The charge exchange is limited to its lowest value due to the presence of the passive film surface and momentarily resisting the activation conditions.
- Zone II: The passive film starts steadily to dissolve, causing a gradual increase in surface activity as reflected by the given cathodic current, until it gets totally dissolved.
- Zone III: Steady state general corrosion due to the bulk metal dissolution.
- Zone IV: Decrease in dissolution current due to surface depletion of cathodic features and noble elements left behind.

In general, as seen in Fig. 4.36, the three activation cycles showed the four mentioned regimes of ionic exchange during the activation. For the second and third cycles, having a controlled surface history (by previous steps of the cycling experiments) the curves were highly reproducible and shared common aspects. In contrast, it's noticed that the curve corresponding to the first cycle (CI) had a quite different behavior compared to CII and CIII. Similarly, among the three cycles, the fourth regime was the most present in CI. These variations detected in CI are expected and are attributed to the surface industrial mechano-chemical processing such as acidic etching, or surface strain hardening.

Now, the moment comes to ask if the stressed samples behave differently and whether this difference can be detected or not. To have a vision on the general behavior of both cases during the different cycles, the three activation cycles were superimposed as given through Fig. 4.38 to Fig. 4.39.

Through the three cycles, a clear separation of the curves is detected during zone I, then the curves cross each other partially during zone II (in CII and CII), and some slight difference is detected in zone III. To analyze this statistically, the three points A, B, and C were selected as illustrated on Fig. 4.38. The interest of these points is explained as follows:

- Point A at  $t = 0.001$  s : being in zone I, this point represents the existing passive film resistance to ionic exchange on the surface/electrolyte interface.
- Point B at  $t = 0.1$  s : this point is representative of zone II, reflecting the current during the passive film dissolution process.
- Point C at  $t = 10$  s : the last point represent zone III, to check the general dissolution rate after the passive film has been dissolved.

For each of these selected points at a given cycle, the average cathodic current was calculated for the three experiments representing either stressed or unstressed states. The numerical values of the statistical study are given in Table 4.14 and 4.15, and are illustrated in Fig. 4.40 (a) and (b), and Fig. 4.41 (a).

Table 4.14: Cathodic current values for the selected points: A, B, and C during the three activation cycles for unstressed samples.

	CI		CII		CIII	
Point	avg	stdv	avg	stdv	avg	stdv
A	-5.29	0.16	-8.55	0.53	-8.99	0.33
B	-14.52	0.73	-16.41	0.82	-16.77	0.99
C	-21.20	0.63	-23.80	1.51	-24.06	1.19

Table 4.15: Cathodic current values for the selected points: A, B, and C during the three activation cycles for stressed samples.

	CI		CII		CIII	
Point	avg	stdv	avg	stdv	avg	stdv
A	-4.29	0.38	-9.65	0.12	-9.63	0.41
B	-14.39	0.34	-18.02	0.40	-17.42	0.15
C	-21.60	0.29	-25.12	0.07	-25.06	0.30

Concerning the cathodic current at point A in CI, it's noticed that for unstressed samples, the cathodic current was about  $(1 \pm 0.38)$  mA.cm<sup>-2</sup> higher than that for stressed case. Though the physical reason behind this difference was different from guessing, but The case was totally changed concerning this point in the consequent cycles, where the stressed samples showed higher cathodic current, which was the most significant in CII, with a difference of about  $(1.1 \pm 0.53)$  mA.cm<sup>-2</sup>. As seen from the values, the experimental error range makes it different to make real conclusions about the detected differences. From the general trend for the evolution of current values at point A through the three cycles, a remarkable increase in the cathodic dissolution was detected for CII and CIII compared to that for CI. This is believed to be due to the fresh bulk of the alloy exposure to the chemical dissolution in CII and CIII, while that was not the case for CI where possible residual stresses and previous chemical oxidation was conducted over the surface.

For points B and C, for the evolution of the cathodic current through the three cycles at these points, the trend was similar to that mentioned about point A. On the other hand, even though

the relative experimental error was extremely small, no significant difference can be mentioned between the stressed and unstressed cases.

One more parameter has the potential to hold information about the passive film properties is the slope of the curve given in zone II given in fig. 4.36 for the different performed experiments. This slope represents the kinetics of the gradual passive film dissolution, thus, a higher slope indicates a higher dissolution rate, and thus less resistant material to corrosion. The average of slopes for each of the three cycles was calculated, and is given for their numerical values in Table 4.16, and illustrated in Fig. 4.41 (b).

Table 4.16: Slopes of Zone II of the activation cycles for stressed and unstressed samples.

	CI		CII		CIII	
	avg	stdv	avg	stdv	avg.	stdv
Unstressed	0.367	0.008	0.244	0.011	0.241	0.015
Stressed	0.389	0.015	0.227	0.011	0.228	0.012

Regardless of the stress state of the sample, if CI is compared to CII and CIII, the initial industrial passive film in CI had the lower cathodic current value represented by point A, indicating less dissolution during zone I. On the other hand, the slope of zone II is remarkably higher for this initial passive film compared to those in CII and CIII ( $0.38$  vs  $0.24$ )  $\pm 0.015$ . This suggests that the experimentally constructed passive films which were dissolved in CII and CIII were more compact and resistant to dissolution, though their ionic conductivity were higher than the passive film dissolved in CI.

Nevertheless, the stress state didn't seem to influence rate as indicated by the slope of the curve in zone II, where the difference in the slope between stressed and non-stressed was comparable to the experimental error range through all the cycles.

#### Conclusions:

- The experimental curves were reproducible, where the cathodic current was registered during the activation steps through the cycles.
- Four distinguished zones were detected representing different current conduction/metallic dissolution phases.
- Thanks to the electrochemical curves obtained, the difference between the initial passivity existing industrially on the material's surface from the experimentally built film over the metal's surface was quantified. This difference was detected in terms of the dissolution cathodic current values at the three selected points of interest over the curve, in addition to the slope of zone II on the logarithmic scale, representing the passive film dissolution rate.
- Though the relative experimental error was quite low in both the cathodic current and the slopes of the curves, no significant influence could be detected due to the effect of the applied stress on the dissolution parameters.

#### OCP after activation

As a verification to the surface state after the passivation step, the surface OCP values were registered over a five-minute period to make sure of the stability of the surface and to have a measure about its state before the application of the passivation pulse.

The OCP evolution for both stressed and unstressed samples over the three cycles is given in Fig. 4.42 (a), (b), and in Fig. 4.43 (a). For all the curves, the OCP gets stable after about 60 seconds, with a slight gradient toward less cathodic potential. The curves representing CII and

CIII share common features since both of them had more or less similar surface history, while for CI it was different as an effect of the industrial surface preparation.

A study was performed over the  $OCP_{pre}$  values of these curves. Numerical data are presented by Table: 4.17, and illustrated in Fig. 4.43. From these, the first observation is that the surface tends to get less cathodic as the sample passes through CI, CII, to CIII. This can be explained due to the surface being subjected to the activation pulses where the cathodic features are dissolved, thus reducing their presence on the surface from a cycle to the next. As to the effect of the applied stress on the  $OCP_{pre}$ , it's noticed that in all the cycles, the detected difference is less than the experimental error domain, and consequently, the conclusion is that no difference was detected as an effect of the applied stress on OCP values in this step.

Table 4.17:  $OCP_{pre}$  values of the OCP periods in the three cycles after the activation pulse.

	CI		CII		CIII	
E/mV vs Ag/AgCl	avg	stdv	avg	stdv	avg	stdv
Unstressed	-397.8	0.8	-394.5	1.0	-389.5	1.4
Stressed	-395.7	2.2	-393.1	1.7	-389.1	1.7

The  $OCP_{pre}$  (average of OCP over the last 10 seconds of the OCP period) was calculated as given in Table 4.17, and illustrated in Fig. 4.43 (b).

In the three cycles,  $OCP_{pre}$  indicates an active surface potential domain, which means that the passive film was successfully dissolved. It's noticed that  $OCP_{pre}$  values get less cathodic as the experiment proceeds through CI to CIII. This indicates that the surface properties are not the same in the different cycles, and care should be taken if the comparison between cycles is performed. An explanation to this can be made as the metallic dissolution performed during the activation step was preferential to certain cathodic elements, leaving the surface with more noble elements, an effect which gets intensified as the experiment proceeds through the cycles.

### Anodic passivation

After the activation of the surface, and passing it to an OCP period, the anodic passivation step was applied. In this, a 10-minute potential pulse of +0.5 V (vs Ag/AgCl) was applied to the tested surface. Under this potential condition, the anodic reaction is favored, which causes the passive film build up. The current transients obtained tell the history during these minutes as given in Fig. 4.44 to Fig. 4.46.

Regardless of the stress state, it's noticed that through CI to CIII, the curves represent the current being reduced in a reproducible way from initial values as high as  $90 \text{ mA.cm}^{-2}$  to very low values of about  $2 \text{ }\mu\text{A.cm}^{-2}$ . Furthermore, for the three cycles equally, three significant current zones (I, II, and III) can be identified as shown in Fig. 4.45. These zones are explained as given below:

- Zone I: The bare metal surface is being exposed to the corrosive electrolyte under anodic potential conditions. This causes the surface to undergo high oxidation reaction for the first few fractions of second, as indicated by the flat curve in zone I.
- Zone II: This is the linear zone is where the curve shows a gradual decrease in the external current with almost a constant slope. During this period, the passive film is established over the surface, and continues the thickening process which increases its isolation, and thus lowering the charge exchange between the metal surface and the electrolyte. The transition between zone I and II indicates the period of passive film nucleation and starting its formation.
- Zone III: This zone has more or less the same slope as zone II, where the film formation process continues. The difference which can be seen by the zigzag behavior indicates

passive film local breakup and prepare processes. The horizontal width of this zone reflects the length of the experimental registration time, where the (vertical) height of the zone indicates the instability of the passive film in the given electrochemical conditions.

Table 4.18: Passive current value at point A for the three passivation cycles for stressed and unstressed samples.

	CI		CII		CIII	
j/mA.cm <sup>-2</sup>	avg	stdv	avg	stdv	avg	stdv
Unstressed	80	11	87	6	83	7
Stressed	82	8	90	4	95	4

In order to quantitatively analyze the passivization curves, two points were selected at  $\log(t/s) = -3$  and 1 as indicated by point A and B in Fig. 4.45. These two points are representative of the charge transfer regimes taking place in zone I for point A, and zone II to point B. For CIII in Fig. 4.46, the curves were zoomed to show the different experimental curves where points A and B were selected. The current values for the three cycles at point A and B are given as indicated by Table: 4.18 and 4.19 and illustrated in Fig. 4.47.

Table 4.19: Passive current value at point B for the three passivation cycles for stressed and unstressed samples.

	CI		CII		CIII	
j/tA.cm <sup>-2</sup>	avg	stdv	avg	stdv	avg	stdv
Unstressed	110	7	110	7	111	4
Stressed	111	12	116	7	106	3

It shows from the investigated points that the current doesn't evolve during the different cycles, an effect which is more present at point B than at point A. This indicates that the passivation is well controlled and established experimentally, and the process is reproducible at each of the cycles. For what concerns the effect of the applied stress on these current values, all the differences were insignificant when compared to the experimental error domain. However, the influence of the applied stress at CIII for point A was quite significant, as expected from the curve shown in Fig. 4.46, but still, the difference from the current values for the equivalent unstressed samples was very small to give real conclusions.

### Passivation charge

Another criterion that was investigated is the passivation time ( $t_p$ ), which is defined in the current work as the time it takes until the external current gets to certain predetermined value ( $j_p$ ), starting from the moment of the application of the passivation pulse  $t_0$ . In the present work, this value was set to  $j = 1 \text{ mA/cm}^{-2}$  as indicated by ( $t_p$ ) in Fig. 4.46. Accordingly, the longer the passivation time, the longer the intense oxidation reaction takes place over the surface before the passivation, and thus more metallic dissolution, and more susceptible the material to corrosion and SCC. This is analogous to what was done by Kwon et al. [90] in their analysis of stainless steel passivation. This duration was verified for the different performed tests and cycles, and the results are given in Table: 4.20.

The statistical data concerning the passivation time  $t_p$  don't show any trend favoring the stressed samples due to the high accompanied experimental error. Nevertheless, this parameter might be useful when it comes to comparing other experimental measures for the different experiments, such as the charge exchange. According to this, the passivation charge ( $q_p$ ) was

Table 4.20: Average passivation time for the three cycles of stressed and unstressed samples.

	CI		CII		CIII	
$t_p/s$	avg	stdv	avg	stdv	avg	stdv
Unstressed	1.25	0.17	1.28	0.09	1.35	0.05
Stressed	1.34	0.03	1.34	0.14	1.24	0.04

defined as the transferred charge starting from the beginning of the anodic pulse until passivation time  $t_p$ . The passivation charge is represented by the area under the passivation current curve until the passivation time, as given by equation 4.1.

$$q_p = \int_a^b j(t) dt \quad (4.1)$$

This criterion might be the most promising to detect any effect due to the applied stress on the passivation process. What makes it more interesting than all the other parameters investigated earlier is that it holds within it the entire history of the passivation process until that moment, instead of just focusing at one instant.

The passivation charge was calculated numerically as suggested by equation 4.1 for the concerned experiments as given in table: 4.21.

Table 4.21: The passivation charge calculated for the three cycles in stressed and unstressed experiments

	CI		CII		CIII	
$q_p/mC.cm^{-2}$	avg	stdv	avg	stdv	avg	stdv
Unstressed	8.43	0.40	9.48	0.18	9.79	0.45
Stressed	8.75	0.90	10.02	0.22	10.26	0.33

The significance of  $q_t$  quantity is important when it comes to local corrosion phenomenon such as SCC. This quantity gives an indication about the oxidation reaction intensity and the metallic dissolution of the surface in case of passivity breakup until obtaining the passivity again. As seen in Fig. 4.48, for CI and CIII, this quantity was the same for both samples, where the detected difference is lower than the experimental error. On the other hand, in CII, the two data points are totally separated. Though the difference is eventually too small ( $0.54 \pm 22$ )  $10^{-3}$  C.cm<sup>-2</sup>, but according to this experimental result, it turns out the stressed samples undergo higher charge exchange before obtaining the same degree of passivation as that compared to unstressed samples. Accordingly, during each cycle of activation-passivation, the higher metallic dissolution rate is expected to be detected in the stressed samples, which means more metallic loss, and can reveal significant information about the passive film formation kinetics and properties. This will be analyzed later in Chapter 5.

### OCP after passivation

The OCP evolution was registered over a 10-minute period at the end of each cycle. The purpose of this step is to check the stability of the surface after the passive film has been constructed, as well as knowing its galvanic value. Fig. 4.49 (a), (b), and Fig. 4.50 (a) represent the curves of the OCP periods of the three cycles for stressed and unstressed experiments.

The initial OCP value was + 500 mV vs Ag/AgCl, which corresponds to the applied potential value in the preceding step of anodic passivation. A quick fall in OCP value is witnessed within the first few seconds, reaching to about + 400 mV, where the evolution starts to decrease less steeply until the end of the end of the OCP step. Comparing the OCP curves obtained for three



Table 4.22:  $OCP_{pre}$  values for the three cycles after passivation step.

	CI		CII		CIII	
E/mV vs Ag/AgCl	avg	stdv	avg	stdv	avg	stdv
Unstressed	161	22	147	14	163	27
Stressed	129	10	143	26	121	4

cycles after activation to those we got here, it's noticed that the curves looked much alike for CI, CII, and CIII after the passivation, while CI looked quite differently after activation. This is due to the surface preparation until this step, which caused the constructed passive film in CI, CII, and CIII to be quite similar.

The higher the gradient in these curves (e.g: Fig. 4.49) the less stable is the surface, where this slope indicates the material transition toward less passive states. If we look back to the curves registered in the initial OCP acquisition at the beginning of the experiment fig4.32, there is a remarkable difference in the evolution of the curve with time, where the slope of the OCP curve was much smaller, keeping an OCP value of about  $(485 \pm 20)$  mV vs Ag/AgCl. This tells that just by the simple contact with the concentrated acid, the initial industrial surface is more stable than the experimentally built passive film. On the contrary, this was not the case where a cathodic potential is applied to the concerned surfaces.

To have a quantitative measure about the experimental values corresponding to stresses and unstressed samples, the  $OCP_{pre}$  was calculated for the different cycles in both cases, as given in Table: 4.22, and illustrated in Fig. 4.50 (b).

Apart from CIII, where a difference of  $(42 \pm 27)$  mV was detected, the other cycles didn't show a significant difference between the stressed and unstressed states. Regardless of the cycle number,  $OCP_{pre}$  values fluctuated equally around 140 mV, which is in the passive domain. This indicates that even though the OCP reduced during the 10 minutes of this OCP exposition, the passivity persisted to protect the surface from the external acidic electrolyte.

### Conclusions:

- In this experimental set, an electrolyte of 2 M  $H_2SO_4$  was used to perform potentiodynamic experiments on stressed and unstressed samples. Samples were subjected to an optimized potentiodynamic program where the material's surface passes through active to passive states in three repetitive cycles. The recorded electrochemical registered transients were analyzed to check for any possible influence for the applied tensile stress can be detected over the corrosion behavior as compared to samples in their relaxed state.
- The very initial OCP values before the cycles were applied indicated identical passive states of stressed and unstressed samples, with an OCP about  $(485 \pm 20)$  mV vs Ag/AgCl.
- During the activation step, the dissolution of the passive film was successfully achieved, reaching an intensive cathodic dissolution of 25 mA within less than 10 s.
- Four significant charge transfer zones were detected during the activation step: during the existence of the passive film, during the passive film dissolution, and as it thickens and gets to repeated passive film breakup-repair processes.
- The difference between the initial industrial passive film and the one experimentally build was successfully detected, indicating that the method holds for such analysis. However, no such difference was detected due to the influence of the applied mechanical stress over the surface.
- The OCP curves after the activation step confirmed stable active states of both surfaces, with an OCP value equals to  $(-390 \pm 2)$  mV vs Ag/AgCl.

- The passivation step showed that the passivation has very quick kinetics within the given conditions. Three significant charge transfer regimes were identified during the passivation process: before the passive film nucleation, during passive film build up, and as it starts thickening eventually.
- Regardless of the stress state and the number of the considered cycle, the passivation current had all the time the same value of  $(110 \pm 10) \mu\text{A}.\text{cm}^{-2}$  as the passive film was established over the surface (point B in Fig. 4.45). This indicates that the passivity was well established in a reproducible way in all the experiments through all the cycles.
- At point A in the third cycle of passivation, the oxidation intensity showed to be a little higher in the case of stressed samples than that of the relaxed samples, with a difference of  $(12 \pm 7) \text{mA}.\text{cm}^{-2}$ . This reflects more corrosion susceptibility before the passive film build up. However, the effect is of a minor importance due to the short effective time duration over which it takes place.
- The passivation charge showed to be higher for stressed samples, indicating more oxidation history during the passivation process. This can hold important interpretation concerning the passive film quality, properties, and its formation kinetics.
- The OCP curves after the passivation confirmed the stability of the passive film, with an OCP value equals to  $(150 \pm 20) \text{mV}$  vs Ag/AgCl.
- Apart from the passivation charge, the other studied electrochemical parameters concerning this experimental set gave statistically equivalent results for stressed and unstressed samples.
- The scatter in the experimental data might be due to the presence of sulfur and manganese precipitations, which were distributed in a random way on the surface as was seen during base material characterization. These precipitations prevent the formation of a homogeneous and stable passive film, and hence, can nucleate a cracking site, or cause the experimental non-reproducibility.
- The electrolyte might be highly acidic, forcing an intense reaction where minor phenomenon like the influence of stress on the surface activity and activation/passivation kinetics was masked.



Figure 4.30: Illustration of  $OCP_i$ ,  $OCP_{pre}$ , and  $OCP_f$  values for polished stressed and unstressed samples in 5 M  $H_2SO_4$  + 0.05 M NaCl (flow cell).

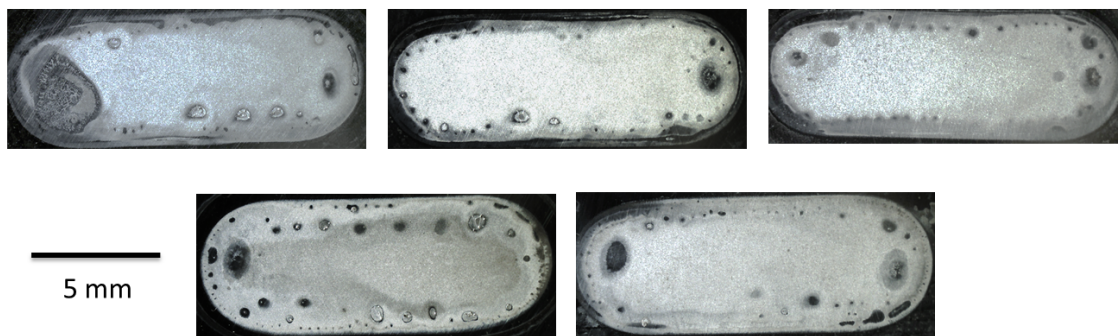


Figure 4.31: Effect of stress on post-experimental surface of 304L after polarization experiments in 5 M  $H_2SO_4$  + 0.05 M NaCl (flow cell). Upper line: Unstressed samples. Lower line: Stressed samples

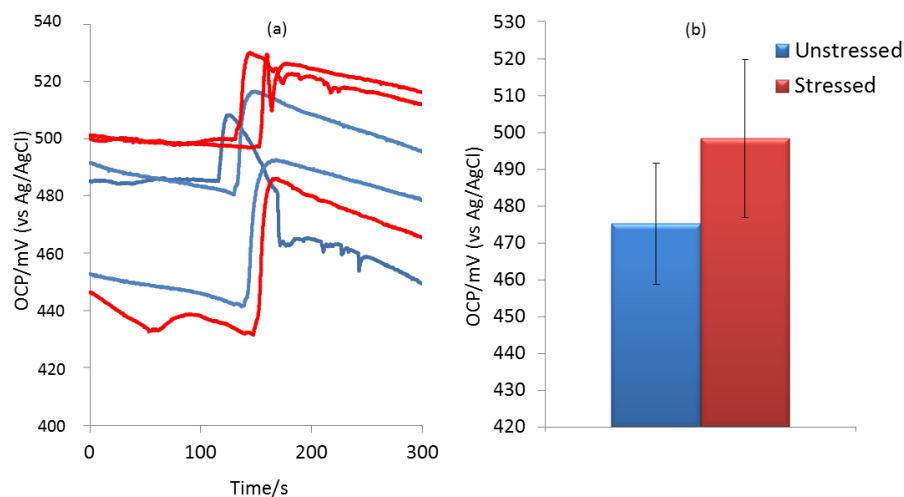


Figure 4.32: (a): Initial OCP evolution, before the cycling program is applied, showing the water/ 2 M H<sub>2</sub>SO<sub>4</sub> electrolyte switch. (b): the OCP<sub>pre</sub> values for stressed/ unstressed samples.

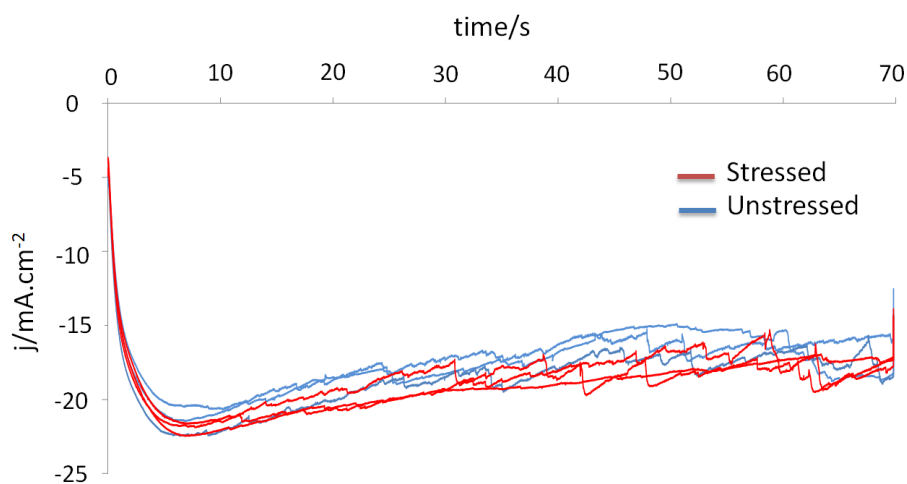


Figure 4.33: The second cycle 70-s activation step @ -700 mV (vs Ag/AgCl) performed on stressed and unstressed 304L SS samples in 2 M H<sub>2</sub>SO<sub>4</sub> (flow cell).

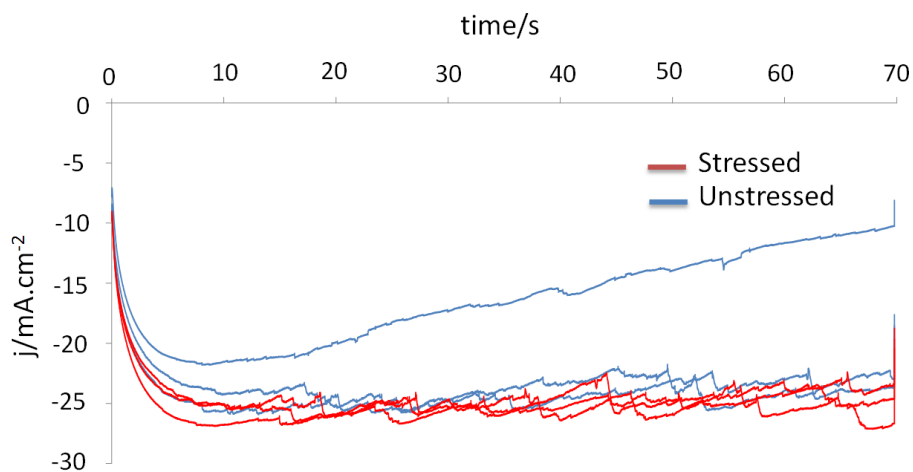


Figure 4.34: The second cycle 70-s activation step @ -700 mV (vs Ag/AgCl) performed on stressed and unstressed 304L SS samples in 2 M  $\text{H}_2\text{SO}_4$  (flow cell).

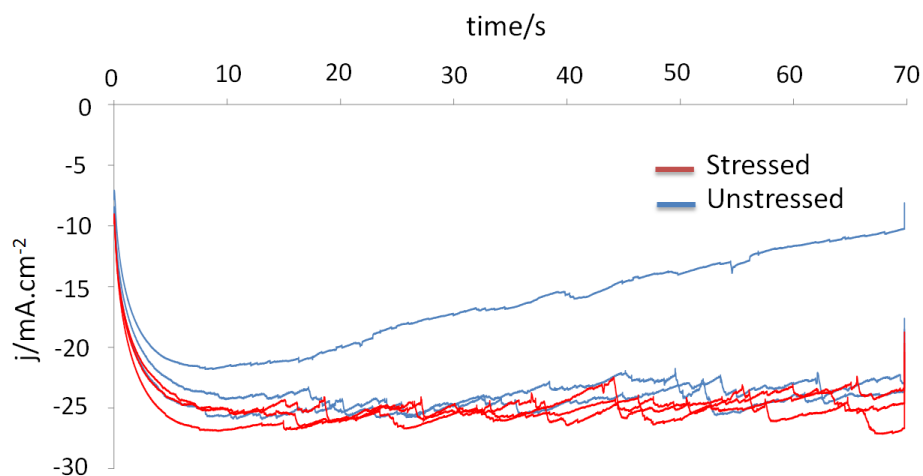


Figure 4.35: The 3rd cycle 70-s activation step @ -700 mV (vs Ag/AgCl) performed on stressed and unstressed 304L SS samples in 2 M  $\text{H}_2\text{SO}_4$  (flow cell).

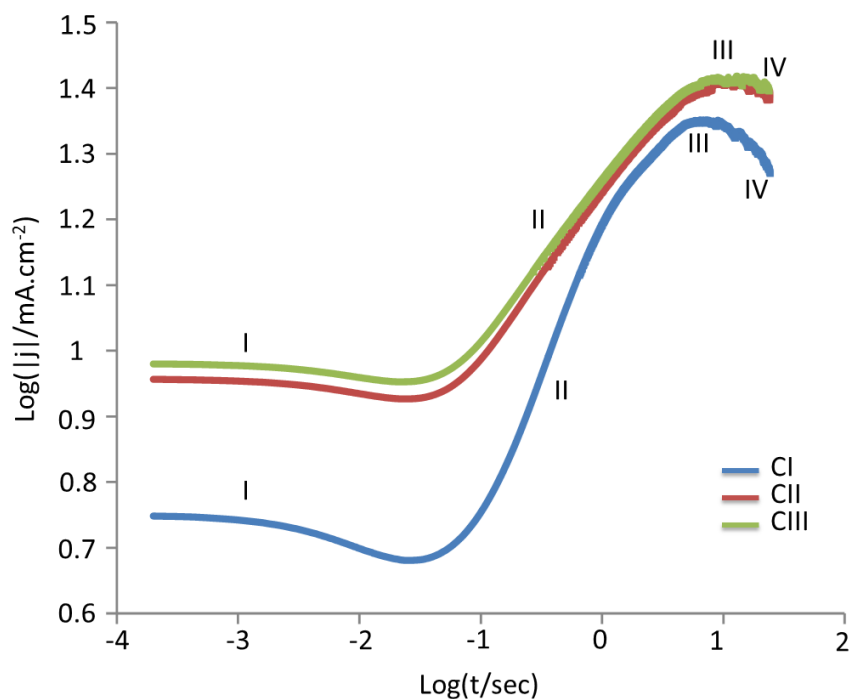


Figure 4.36: The three 70-s activation step @ -700 mV (vs Ag/AgCl) performed on unstressed 304L SS samples in 2 M  $\text{H}_2\text{SO}_4$  (flow cell).

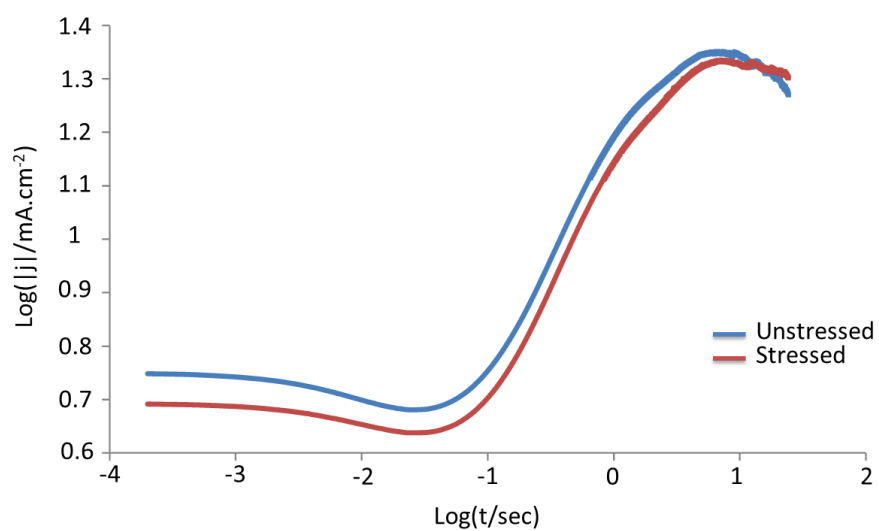


Figure 4.37: Stressed vs non-stressed activation during the first cycle in 2 M  $\text{H}_2\text{SO}_4$  (flow cell).

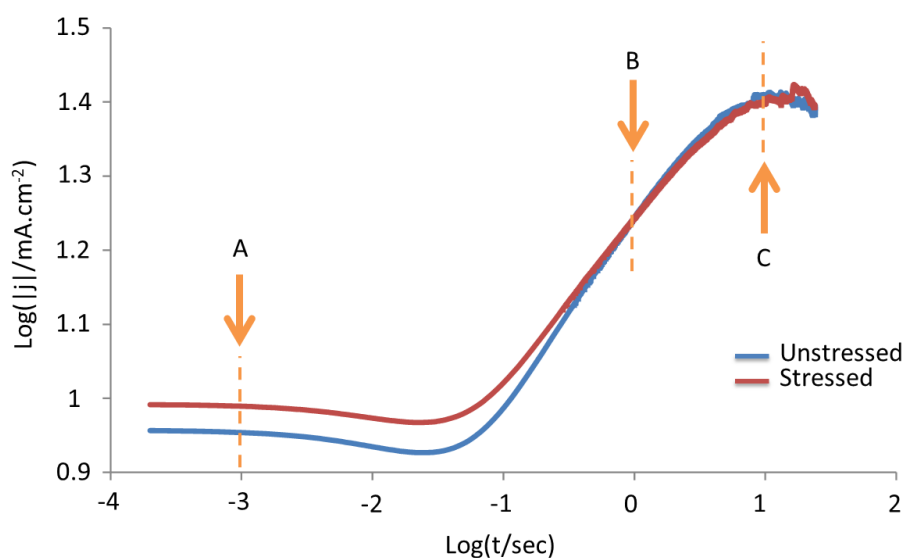


Figure 4.38: Stressed vs non-stressed activation during the second cycle in 2 M  $\text{H}_2\text{SO}_4$  (flow cell).

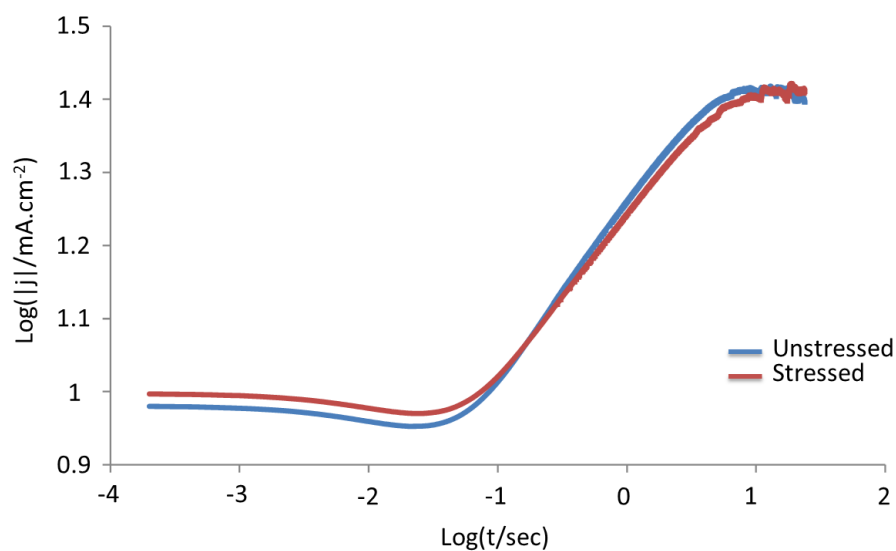


Figure 4.39: Stressed vs non-stressed activation during the second cycle in 2 M  $\text{H}_2\text{SO}_4$  (flow cell)

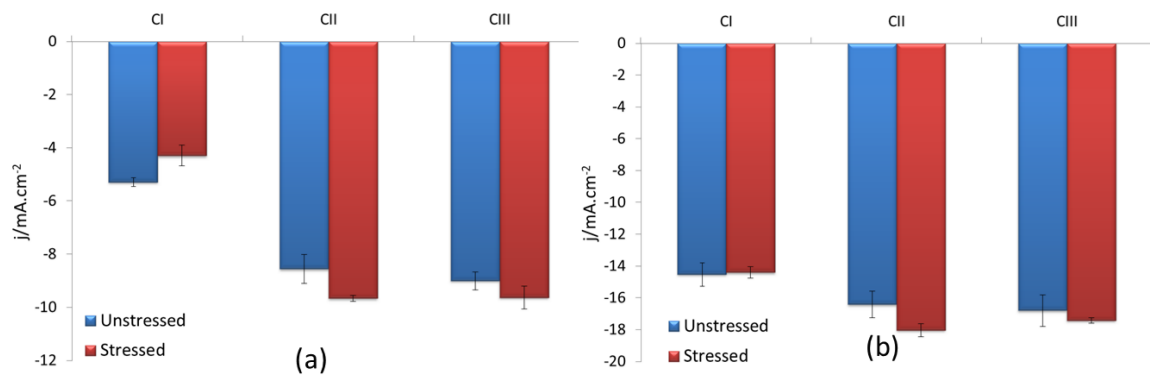


Figure 4.40: The 3rd cycle 70-s activation step @ -700 mV (vs Ag/AgCl) performed on stressed and unstressed 304L SS samples in 2 M  $\text{H}_2\text{SO}_4$  (flow cell).

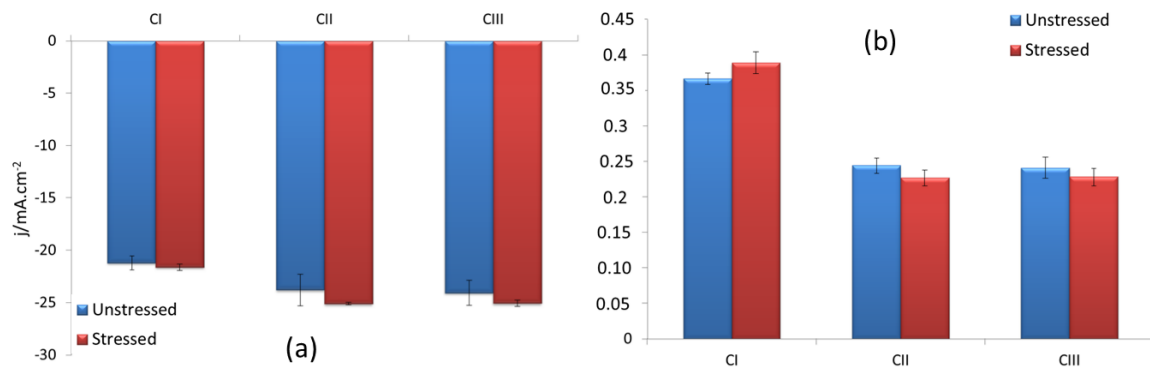


Figure 4.41: Illustration of the statistics of cathodic activation steps. (a): the cathodic current value for point C, (b): the slope of the curve in zone II.

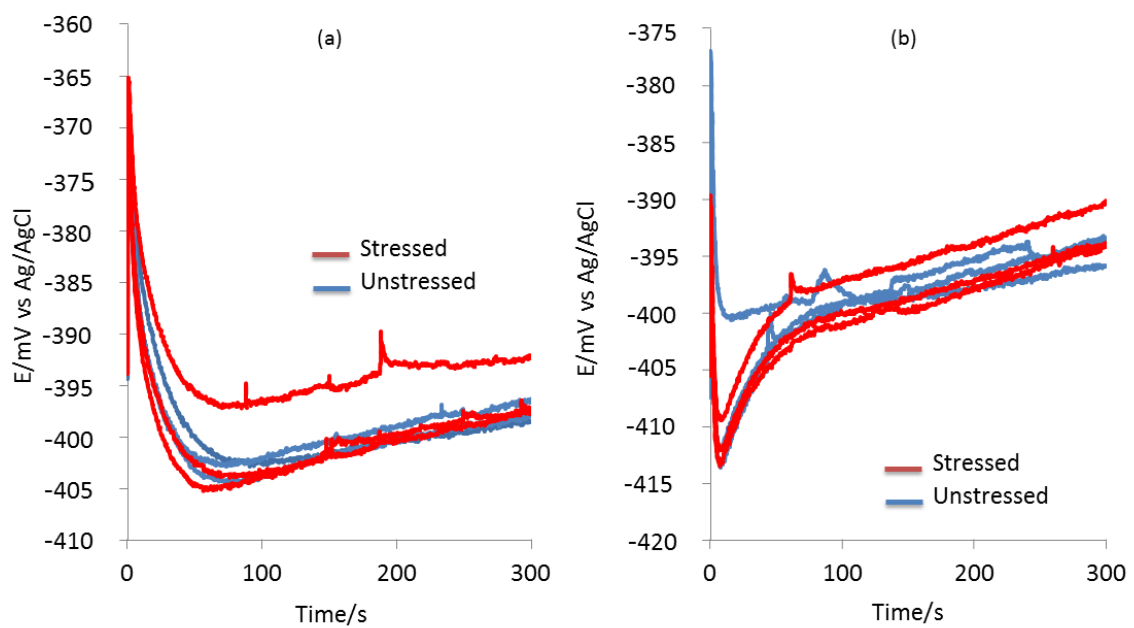


Figure 4.42: OCP evolution after activation step. (a): First cycle. (b): Second cycle.



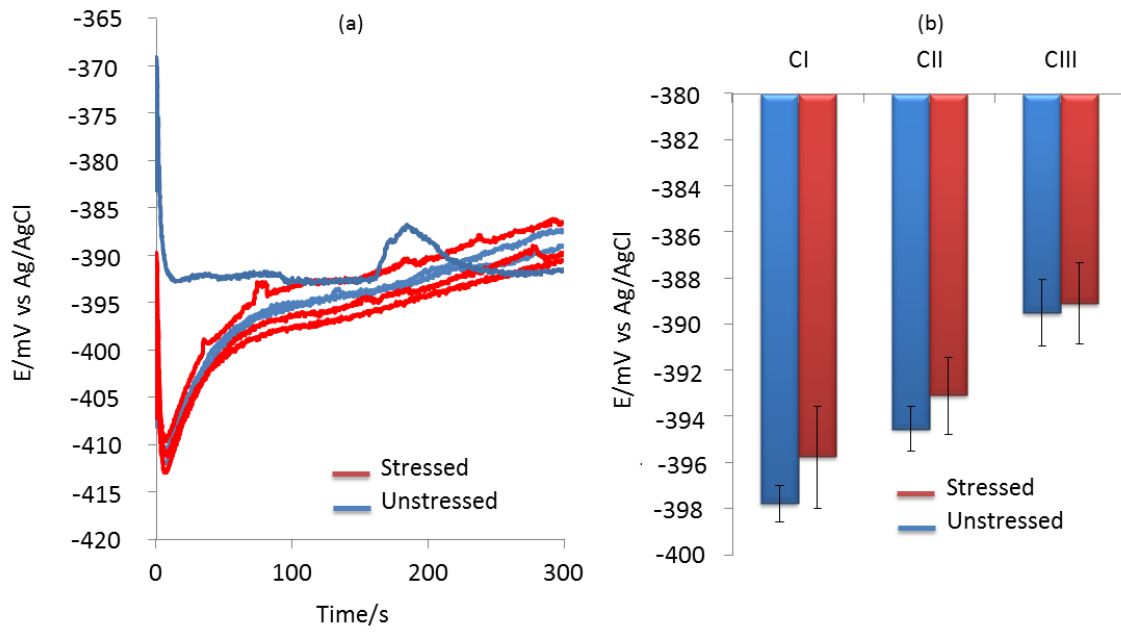


Figure 4.43: (a):OCP evolution after activation step in third cycle. (b): OCP<sub>pre</sub> value statistics for the three cycles.

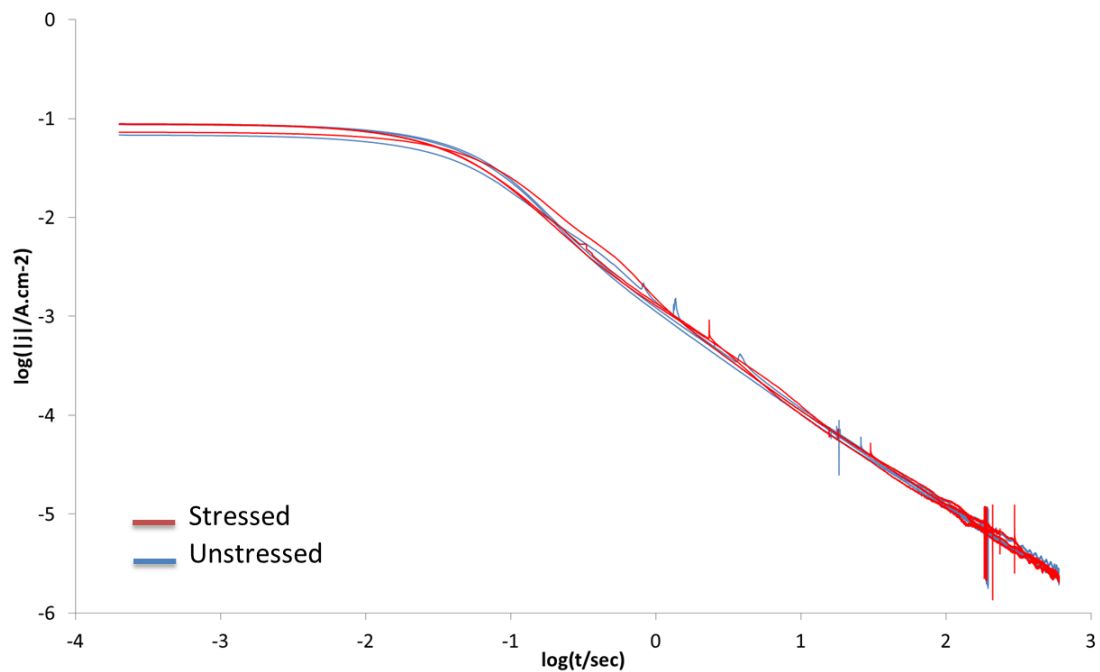


Figure 4.44: Current transients during the first cycle activation for the stressed and unstressed samples.

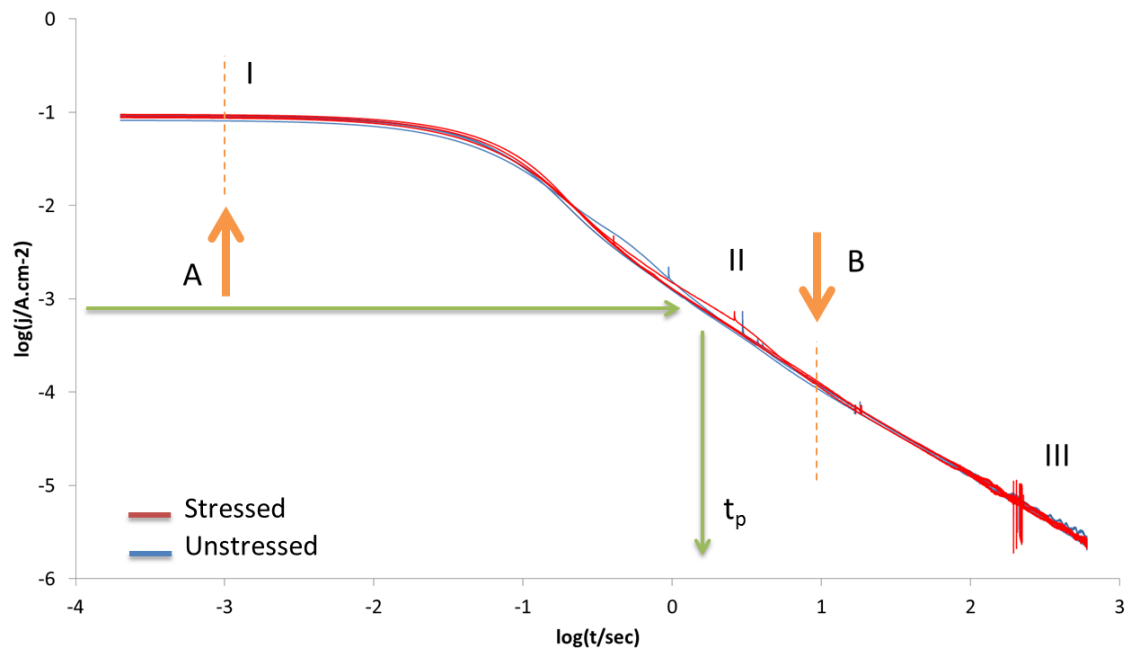


Figure 4.45: Current transients during the first cycle activation for the stressed and unstressed samples.

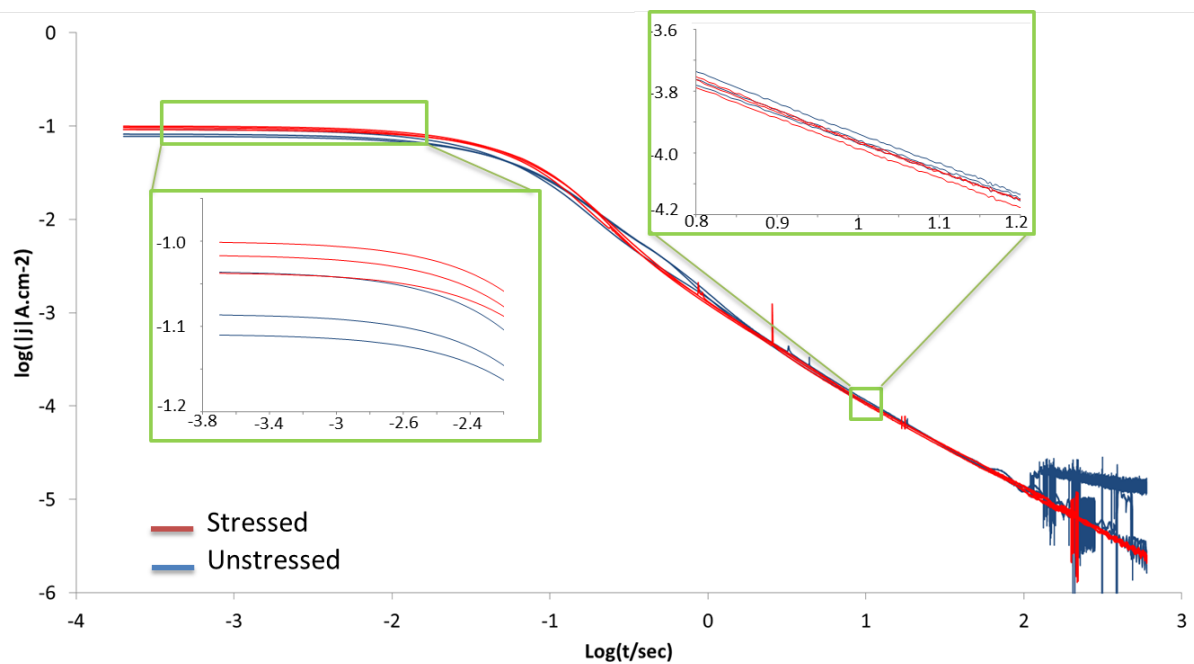


Figure 4.46: Current transients during the first cycle activation for the stressed and unstressed samples.

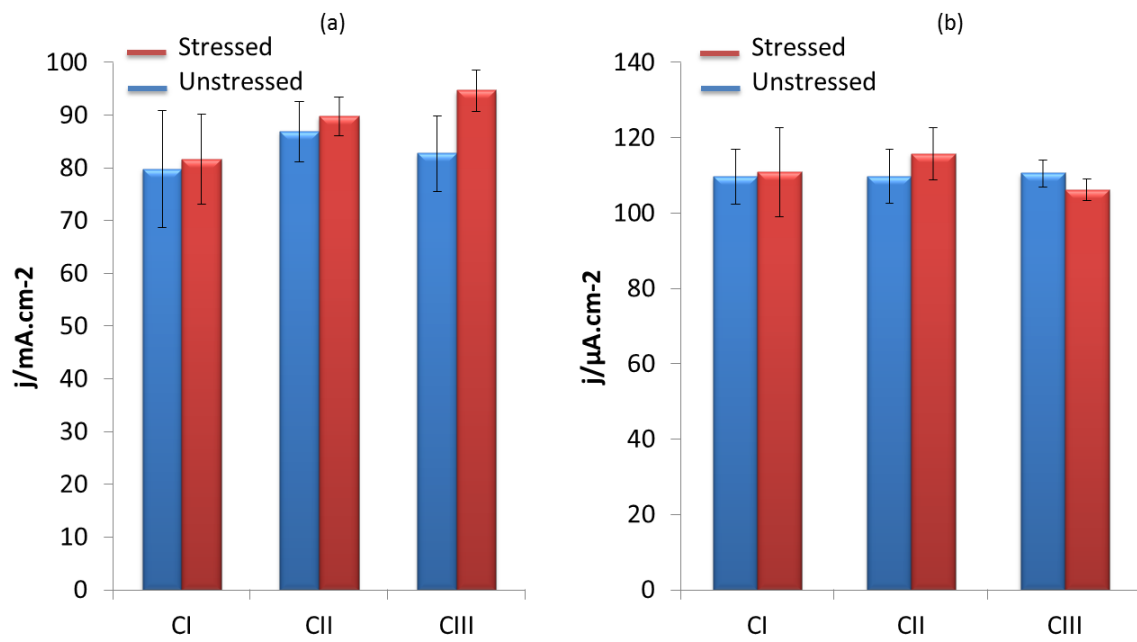


Figure 4.47: Illustration of the average passivation current values during the three passivation cycles. (a): Point A. (b): Point B.

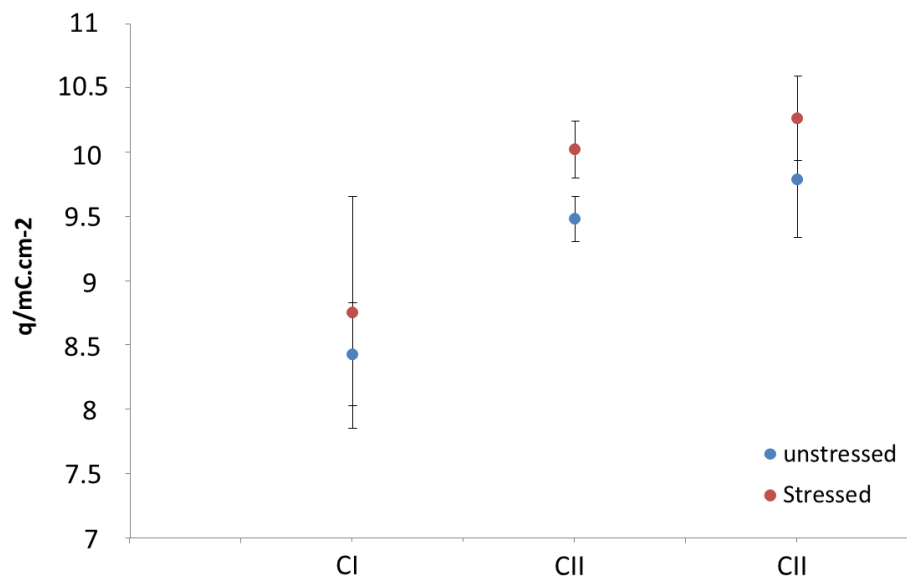


Figure 4.48: Illustration of the average passivation charge for the three passivation cycles of stressed and unstressed samples.

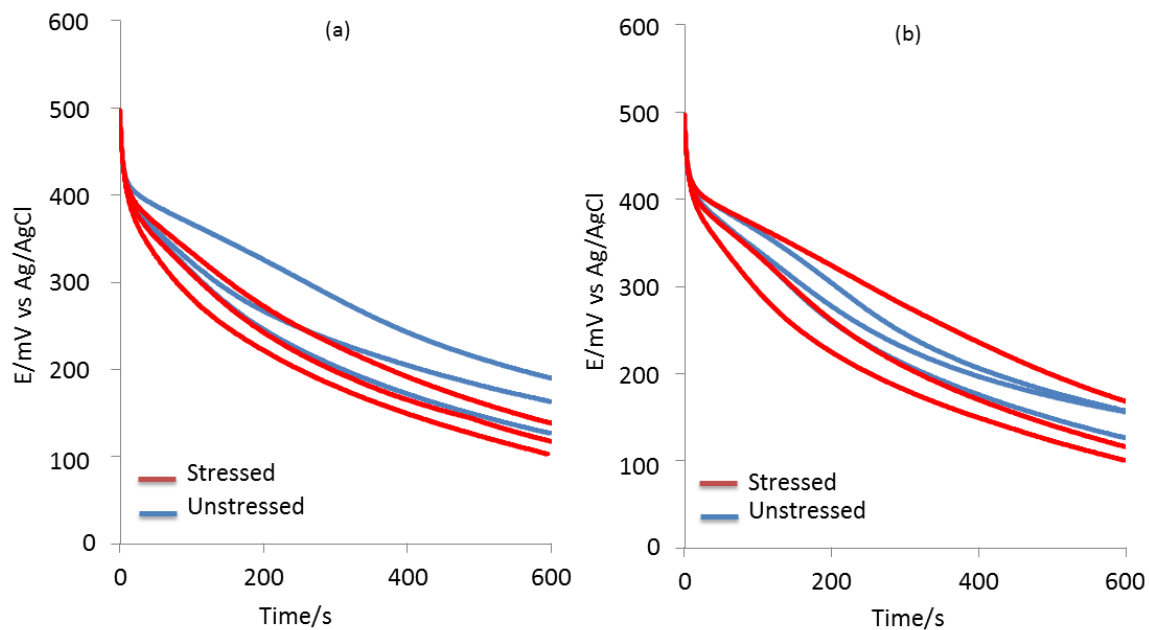


Figure 4.49: OCP evolution after passivation step. (a): First cycle. (b): Second cycle.

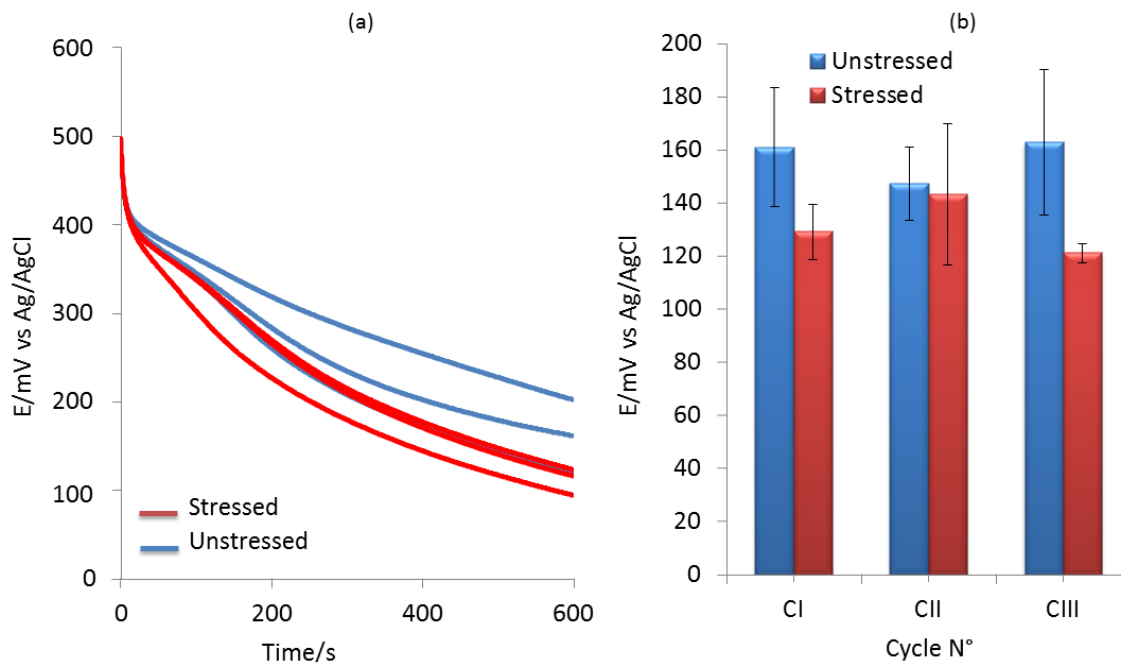


Figure 4.50: (a): OCP evolution after activation step in third cycle. (b):  $OCP_{pre}$  value statistics for the three cycles.



The purpose of this chapter is to study the passivation kinetics of stainless steel and to develop a model adapted to the acidic passivation experimental environment. By this, the different passivation parameters can be quantified, which allow the comparison between different passivation conditions. This model can be applied to check the influence of the variables controlling the passivation process; such as the applied stress or solution concentration, or any other parameter of interest.

## 5.1 Potentiostatic Pulse Testing

In chapter 4, the potentiostatic pulse testing was introduced and analyzed to characterize different corrosion related parameters and how they evolve during the different cycles such as the OCP values, the activation kinetics, and the passivation current. Concerning the passivation process, which was applied after electrochemically dissolving the passive film existing on the surface, interesting information could be accessed by the analysis of the current transients. Though the employed electrochemical method showed to be sensitive enough to detect variations in passive film properties depending on the way it was built (as received state vs experimentally built passive film), no significant difference was detected due to the presence of tensile applied stress. The only parameter where stress seemed to have a slight influence of possible significance was the passivation charge as was explained in chapter 4. Knowing that the charge transfer is an important indication of the passive film properties and its formation kinetics, the analysis is extended to try to quantify such parameters.

As a model is to be developed concerning the construction of the passive film and its formation kinetics, the analyzed passive films are desired to be stable, and their formation should be without interruptions. For this reason, the same experimental conditions used earlier with 2 M  $\text{H}_2\text{SO}_4$  electrolyte were chosen for the present analysis, as was explained in section: 2.4.3. The potentiodynamic program used is given in section: 2.4.3.

For the first few fractions of the second of passivation, the metal shows high current values, which indicates the strong oxidation reaction, as given in Fig. 4.44 to Fig. 4.46. This is expected as the metal bare surface is in contact with the corrosive medium. The very quick current reduction indicates the rapid passivation ability of this stainless steel in sulfuric acid under the applied passivation potential. Theoretically, for the passive film to build up, the anodic current have to overpass a critical passivation limit, and this clearly took place during the first few fraction of second of the applied anodic pulse.

## 5.2 Passivation Rate

After a debate on passive film growth kinetics, it was shown by [175] that the  $\log(j)$  is proportional to  $\log(t)$ , with  $j$  being the current density and  $t$  is the time during the passivation process. High field ion conduction mechanism was proposed later by [28] for the passivation, which was an approximation of the inverse logarithmic rate equations.

Later, Passive film construction on stainless steel was described by [27, 25, 109] to be controlled by ion conduction in high field. By using a scratching electrode, Burstein and Marshall [27, 25, 109] mechanically removed the as-received passive film while applying passivation potential in alkaline media and recorded the resulting passivation current. Thus, the bare surface passivation current confirmed empirically that the linear relation between  $\log(i)$  and  $\log(t)$  is valid, with a slope being in the range of -0.9 to -1.3 as a function of the applied potential. These results are in accordance with results obtained by Kwon et al [90].

Concerning our cycling experiments, regardless of the stress state, this linearity was a clear trait of all the passivation experimental curves through all the cycles. Example on this is the second passivation cycle given earlier in Fig. 4.45 showing the linear zone indicated by zone II. The slope ( $\alpha$ ) of this linear zone is calculated at each cycle and illustrated in Fig. 5.1.

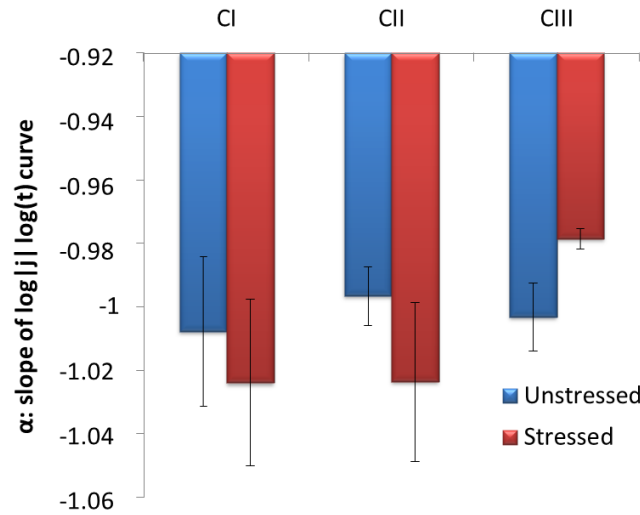


Figure 5.1: The slopes ( $\alpha$ ) of  $\log(j)$  vs  $\log(t)$  curves of the three passivation cycles in 2 M  $\text{H}_2\text{SO}_4$  (flow cell).

It's noticed that our experimental data gave slopes which were more or less tied to values of  $\alpha = (-1 \pm 0.006)$  in CI and CII, regardless of the stress state. For unstressed samples, this slope remained the same in CIII as well, while for the stressed sample, the passivation rate was lower than that of the unstressed ones as measured by the slopes  $\alpha = (-1.003 \text{ vs } -0.979) \pm 0.010$ , for unstressed and stressed samples respectively. Though the difference is quite small, but this lower slope of the stressed sample can be interpreted as a slight more difficulty to obtain passivation in the case of the stressed surface as compared to unstressed samples. This might be due to having a higher depletion of chromium in the case of the stressed samples than that in the unstressed ones, which might be linked to possible variation in the atomic diffusion in the alloy's matrix as an effect of the applied stress.

However, the passivation rate of tested samples seemed to fit to the previous work made by [27, 25, 109, 90] as measured from the slope of  $\log|j|$  vs  $\log(t)$  curves.

### 5.3 Passive Film Formation kinetics

The experimental observation given in the previous section indicate effective passivation of the material's surface after being totally activated. High passivation rates observed were in accordance with those found in the literature [27, 25, 109, 90, 93, 62, 33, 22].

As the linearity described by Burstein et al [26] for the kinetics of ion conduction through a growing passive was observed for our present experiments, high field ion conduction can be adapted to the passive film formation in the present experiments. The kinetic equation is given in Eq.1.1, where  $j(t) = (i(t)/\text{surface area of the working electrode})$  is the current density conducted through the film at the considered instant of time  $t$ . Since the voltage drop through the passive film is relatively high, Eq.1.2 applies to the present conditions.

To correlate the charge spent to construct the passive film to the corresponding thickness, Faraday's law, given by Eq.1.3, can be applied. In this equation,  $z$  is the number of transferred electrons per ion, which can be assumed as 3 for stainless steel.  $F$  is Faraday's constant, equals to  $9.64853399(24) \cdot 10^4 \text{ C.mol}^{-1}$ . The film density  $\rho$  taken as  $5.24 \text{ g.cm}^{-2}$  ( $\rho(\text{Fe}_2\text{O}_3) = 5.27 \text{ g.cm}^{-3}$ ,  $\rho(\text{Cr}_2\text{O}_3) = 5.21 \text{ g.cm}^{-3}$ ) M: the molecular mass of the film =  $165 \text{ g.mol}^{-1}$  ( $M(\text{Fe}_2\text{O}_3) = 160 \text{ g.mol}^{-1}$ ,  $M(\text{Cr}_2\text{O}_3) = 152 \text{ g.mol}^{-1}$ ).

The instant of time defining the moment ( $t = 0.0$ ) is the moment indicating the beginning of the application of the anodic pulse, where the surface is initially active. The amount of charge  $q_{\text{film}}(t)$  is the charge exchange (density) due to oxidation reaction forming the passive film until the moment  $t$ . By rearranging Eq.1.3,  $q_{\text{film}}(t)$  can be used to calculate the passive film thickness at moment  $t$  as presented by Eq.1.4.

The same derivation procedure presented in section 1.6.1 applies here leading eventually to Eq.1.6 which gives the relation between  $\log i(t)$  and  $(1/q_{\text{film}}(t))$  as a linear relation.

For the obtained passivation curves such as those presented in Fig. 4.44, they can be represented as suggested by Eq.1.6, in Fig. 5.2.

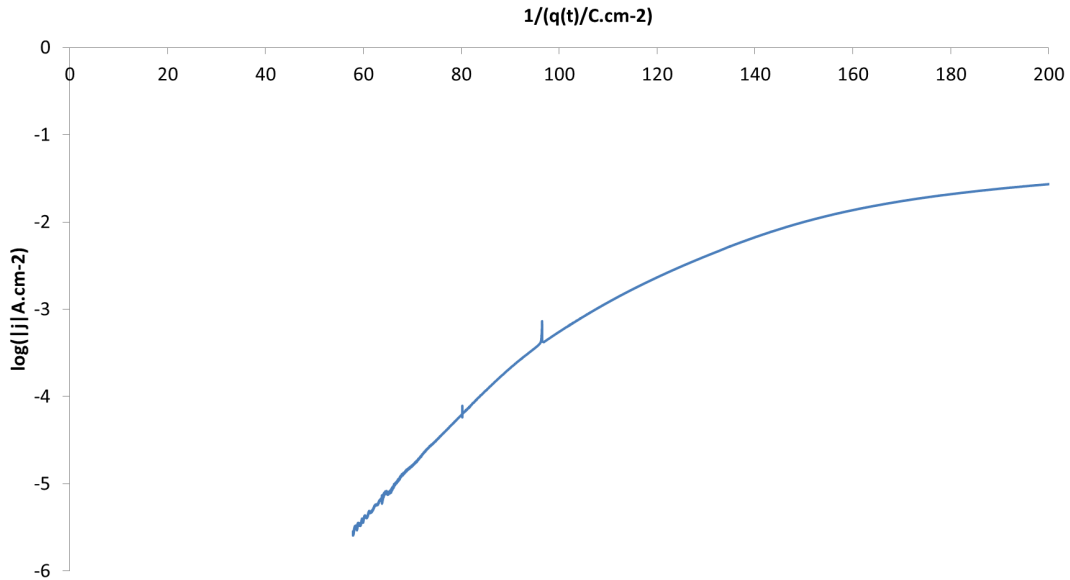


Figure 5.2: The second cycle passivation curves given as an example to check the validity of the linearity described by Eq.1.6.

So, as the curve demonstrates that the linearity described by the high field ion conduction model is valid for our experimental conditions. This is in agreement with previously obtained results on passivation by [90, 109, 27, 25].



In general, the anodic current  $j_{\text{total}}$  measured during passivation is composed of three main components as given by Eq.5.1. The component  $j_{\text{cathodic}}$  is due to the possible cathodic reactions during the passivation process, while  $j_{\text{dissolution}}$  is the current density resulting from metallic dissolution of the surface, and last but not least,  $j_{\text{film}}$  is the current portion due to oxidation reactions responsible for passive film formation.

$$j(t)_{\text{total}} = j_{\text{dissolution}} + j_{\text{film}} + j_{\text{cathodic}} \quad (5.1)$$

In alkaline and neutral solutions such as chloride solutions where  $j_{\text{cathodic}}$  is negligible [132], it was demonstrated that [26]  $j_{\text{total}}$  measured during passivation is consumed mainly to build the passive film. This means that the anodic current due to metallic dissolution is negligibly small in such conditions. This remains valid as long as no pitting corrosion is produced. In conditions where this is applicable,  $q_{\text{film}}$  can be assumed to be approximately equal to  $q_{\text{total}}$ . By making this substitution in Eq.1.6, Eq.1.7 is obtained, where  $q(t)$  is calculated by Eq.5.2:

$$q(t) = \int_0^t j(u) du \quad (5.2)$$

According to this equation, the passive film thickness can be calculated using Faraday's law as given in Eq.1.4 by the charge  $q_{\text{film}} \approx q_{\text{total}}$ . If this is applied to our present experiments using the passivation anodic current transients such as this given in Fig. 5.2, the thickness can be calculated for any given instant of time during the passivation process and results in the passive film profile given in Fig. 5.3.

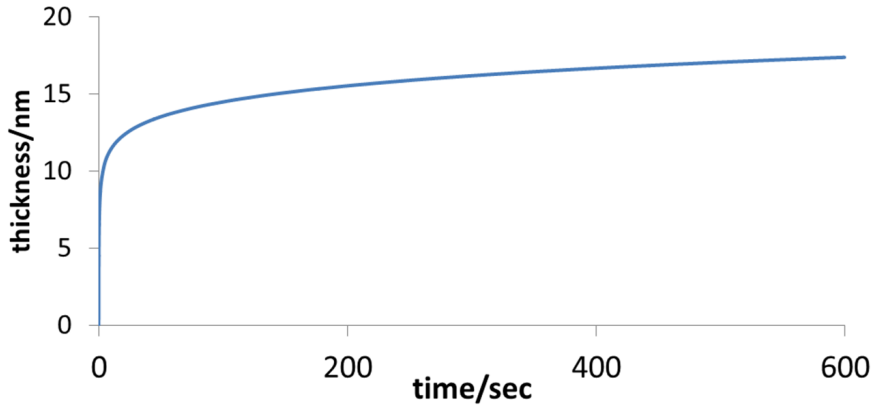


Figure 5.3: The evolution of the passive film thickness in 2 M  $\text{H}_2\text{SO}_4$  during the application of the anodic pulse as calculated by  $j_{\text{total}}$ .

For Eq.1.7 to hold, the corresponding resulting thickness is in the order of 16 nm as seen by Fig. 5.3. Clearly, this order of magnitude as a passive film thickness is not possible, since it's well-known in the literature that the passive film thickness is in the order of 1 nm. Therefore, this odd result can be explained as the electrolyte used in the experiments was acidic wherein the contribution of the metallic dissolution component  $j_{\text{dissolution}}$  to the total registered current  $j_{\text{total}}$  is considerably huge. This was not taken into account for the calculation of passive film thickness until this stage. To correct for this dissolution term, section 5.4 will take into consideration what was suggested in the literature to deal with this dissolution term, and will be applied to our present experiments.

## 5.4 Passive Film Formation in Acidic Mediums

As was explained in section: 1.6.2, the appropriate calculation of thickness requires taking into consideration this huge dissolution component, and by this, the HFIC can still be applied

[160, 109]. If the dissolution component is separated from the total registered current, the charge portion responsible for passive film formation can be calculated and used to calculate the correct thickness over which the high ion field conduction works as suggested by Eq.1.8.

The factor  $f$  in Eq.1.8 is the fraction of of total current due to metallic dissolution, where Fe dissolution forms the major contribution [109], which is confirmed by AESEC analysis of stainless steel polarization and passivation in 2 M  $\text{H}_2\text{SO}_4$  [131, 132], which was reproduced equally for our present material/environment as shown in Fig. 5.4 and Fig. 5.6.

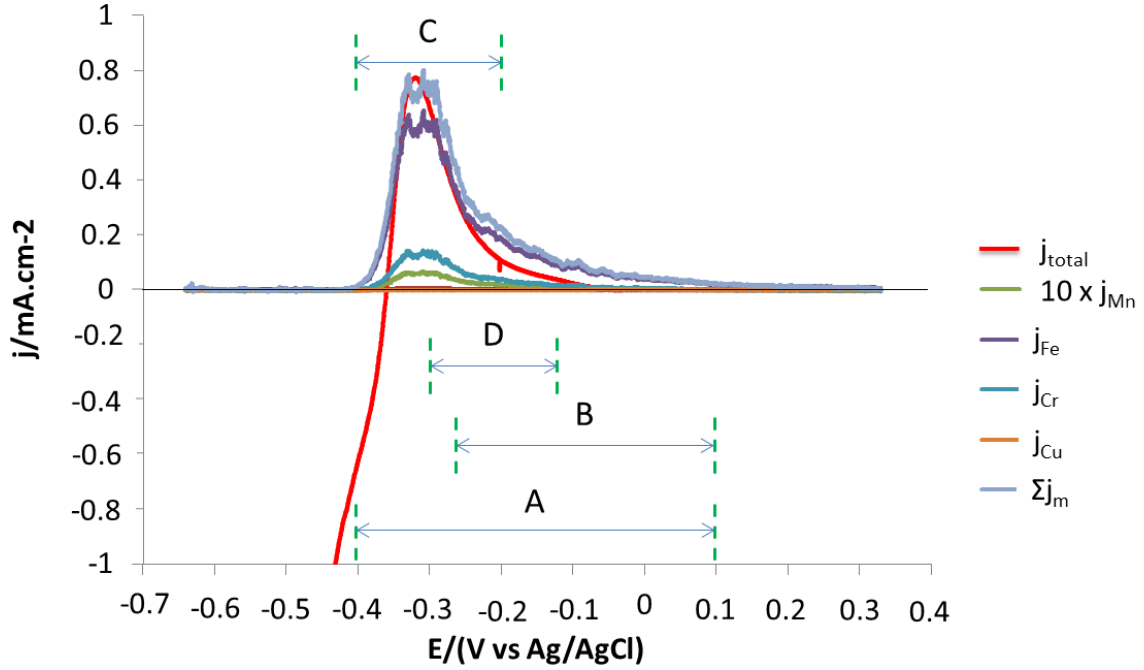


Figure 5.4: The polarization curve of 304L stainless steel showing the selected zones to calculate  $j_m/j_{\text{Fe}}$  ratio.

By substituting Eq.1.8 in Eq.1.4, then the modified version of Eq.1.1 which fits the acidic mediums can be given by Eq. 1.9. By taking the logarithm of both sides of Eq.1.9 with  $c = (zF\rho)/(2.3M)$ , we obtain:

$$\log i(t) = \log A + \frac{cBV}{q_{\text{total}}(t)(1-f)} \quad (5.3)$$

In the following analysis, the factor  $f$  will be calculated to count appropriately for the dissolution parameter.

#### 5.4.1 Fraction of charge due to Fe dissolution( $f_{\text{Fe}}$ ) based on the metallic mass fractions:

As was explained earlier and confirmed by ICP analysis of the leaching corrosion solutions during passivation experiments in 2 M  $\text{H}_2\text{SO}_4$ , the majority of the total registered current is due to the metallic dissolution, where five main metals are the most dominant; namely: Fe, Cr, Cu, Mn, Ni and Mo [132].

In order to formulate this for conditions where the cathodic current can be neglected, the total registered current can be expressed as given by Eq.5.4:

$$j(t)_{\text{total}} = j(t)_{\text{dissolution}} + j(t)_{\text{film}} \quad (5.4)$$

where  $j(t)_{\text{dissolution}}$  is defined as:

$$j(t)_{\text{dissolution}} = j_{\text{Fe}} + j_{\text{Cr}} + j_{\text{Cu}} + j_{\text{Mn}} + j_{\text{Ni}} \quad (5.5)$$

In order to quantify  $j(t)_{\text{film}}$  such that it's used in  $q_{\text{film}}$  as explained by the high field ion conduction model, the current due to metallic dissolution has to be separated from the total registered current. This can be obtained by rearranging Eq.5.4 as:

$$j(t)_{\text{film}} = j(t)_{\text{total}} - j(t)_{\text{dissolution}} \quad (5.6)$$

In an analysis of the corrosion leaching solution during passivation using AESEC, Ogle [132] calculated in-situe the dissolution current  $j(t)_{\text{dissolution}}$  corresponding to each metal.

Another way to quantify  $j(t)_{\text{film}}$  is by factoring the dissolution current out of the total current as:

$$j(t)_{\text{film}} = j(t)_{\text{total}}(1 - f) \quad (5.7)$$

where  $f$  is a factor representing the ratio of the dissolution current to the total registered current defined as:

$$f = \frac{j(t)_{\text{dissolution}}}{j(t)_{\text{total}}} \quad (5.8)$$

In their analysis, Burstein and Marshall [109] assumed that the major part of the metallic dissolution in acidic mediums is due to iron dissolution, which doesn't correspond to passive film construction, and consequently has to be taken out if the high field ion conduction model is to be applied appropriately for their acidic conditions. Based on this, the correction factor  $f$  was calculated taking into consideration only the iron dissolution, thus giving  $f_{\text{Fe}}$  factor. To calculate this fraction of anodic charge density related to Fe dissolution, they did an estimation of the oxidation numbers of the metals existing in the alloy matrix, in addition to the well-known mass fractions of the alloy's metallic composition.

The purpose of the present section is to calculate the  $f$  factor for our experiments in an analogical way to that was done by Marshall and Burstein. In a following step, this factor is to be enhanced such that it doesn't only take into account the iron dissolution, but all other metallic dissolution that could be detected during the passivation experiments as indicated in Fig. 5.4 and Fig. 5.6, and expressed by Eq.5.5 and Eq.5.8.

In our present work 2 M  $\text{H}_2\text{SO}_4$  was used, which is an equivalent acidic environment to that used by Marshall and Burstein in their experiments[109]. Thus, the same oxidation numbers they estimated are used for the analysis of our experiments, as indicated in Table: 5.1.

Table 5.1: Metallic oxidation numbers and their mass fraction in the alloy's matrix.

Element	Fe	Cr	Cu	Mn	Ni	Mo
Mass fraction %	71.56	17.39	0.31	1.69	7.97	0.24
Oxidation N°	II or III	III	II	II	II	III
Molar Mass ( $\text{g.mol}^{-1}$ )	55.85	52.00	63.55	54.94	58.69	95.96

In the total registered current, each metal of those mentioned in Table: 5.1 has its own share in the total metallic dissolution as was expressed by Eq.5.4. The current density resulting from that dissolution can be expressed by Eq.5.9, which is derived from Faraday's law (details of derivation and dimensions are given in Appendix F) :

$$j(t) = \frac{\nu(t) \cdot F \cdot Z}{M} \quad (5.9)$$

To calculate the fraction of current density due to Fe dissolution  $f_{Fe}$ , we proceed as shown next:

$$f_{Fe} = \frac{j_{Fe}}{j_{total}} \quad (5.10)$$

As  $j_{film} \ll j_{dissolution}$ , only to serve the step of calculation given in Eq.5.10, an approximation is made locally such that  $j_{total} \simeq j_{dissolution}$ . With this accepted for pragmatic reasons, Eq.5.10 can be rewritten as:

$$f_{Fe} = \frac{j_{Fe}}{j_{dissolution}} = \frac{j_{Fe}}{j_{Fe} + j_{Cr} + j_{Cu} + j_{Mn} + j_{Ni}} \quad (5.11)$$

For each metallic dissolution current, Eq.5.9 can be used to calculate  $j_m$ ,  $m$  refers to the concerned metal. Setting the constants  $b_m$  and  $\gamma_m$  as  $b_m = Z_m/M_m$ , and  $\gamma_m = \nu_m/\nu_m$  and substituting the variables corresponding to each current, Eq.5.11 becomes:

$$\frac{j_{Fe}}{j_{dissolution}} = \frac{1}{1 + \gamma_{Cr} \frac{b_{Cr}}{b_{Fe}} + \gamma_{Cu} \frac{b_{Cu}}{b_{Fe}} + \gamma_{Mn} \frac{b_{Mn}}{b_{Fe}} + \gamma_{Ni} \frac{b_{Ni}}{b_{Fe}}} \quad (5.12)$$

It was shown that for a specific element  $m$ ,  $\gamma_m$  is equal to the mass fraction of that element in the alloy's matrix [132] which is in agreement with the ratio of the dissolution rates in the experimental conditions used; 2 M  $H_2SO_4$ . Substituting the numerical values,  $f_{Fe}$  is found to be equal to 0.74. Clearly, this factor changes as a function of the oxidation number given for Fe. In reality, both oxides Fe(II) and Fe(III) form [27] in such experimental conditions. However, for the material used in our experiment; 304L stainless steel, Fe dissolution factor equals to 0.65 and 0.74 according to Fe(II) or Fe(III) respectively. Knowing this, the actual fraction due to Fe dissolution is expected to be between these two values. On the other hand, the  $f_{Fe}$  current fraction will vary following to the elements considered in  $j_{dissolution}$  current, as seen in Eq.5.11. To have a better idea about the range of possible values for this factor, Table: 5.2 gives a summary of the conducted analysis for this purpose.

Table 5.2:  $f_{Fe}$  factor calculated with oxidation number (II) and (III) with variable elements considered to share in  $j_{dissolution}$

	$Z_{Fe} = 2$	$Z_{Fe} = 3$
Elements Considered in $j_{dissolution}$	% ( $j_{Fe} / j_{dissolution}$ )	% ( $j_{Fe} / j_{dissolution}$ )
Fe, Cr, Cu, Mn, Ni, Mo	0.654	0.740
Fe, Cr, Cu, Mn, Ni	0.656	0.741
Fe, Cr, Cu, Mn	0.705	0.782
Fe, Cr, Cu	0.717	0.791
Fe, Cr	0.719	0.793

In our analysis, the factor corresponding to Fe(III) is taken as a first estimation, with the Fe, Cr, Cu, Mn, Ni, and Mo considered to share in  $j_{dissolution}$ , giving a value of  $f_{Fe} = 0.74$ . The approximations taken for this calculation can be checked for its validity, and it can be refined later if necessary.

If the factor  $f_{Fe}$  is used to correct for the calculation of the passive film thickness based on the current transients obtained during the passivation, the obtained evolution of the passive film thickness will be as presented in Fig. 5.5.

If this is compared to what was produced earlier in Fig. 5.3 before the introduction of  $f_{Fe}$ , the passive film thickness was reduced from of (16.2 to 4.2) nm at  $t = 300$  s. It's easily noticed that the newly obtained thickness is much closer to reality where it's believed to be about 1 nm. The calculations performed until this stage were a manifestation of what Marshall and Burstein proposed concerning the Fe dissolution in case of stainless steel passivation in acidic mediums

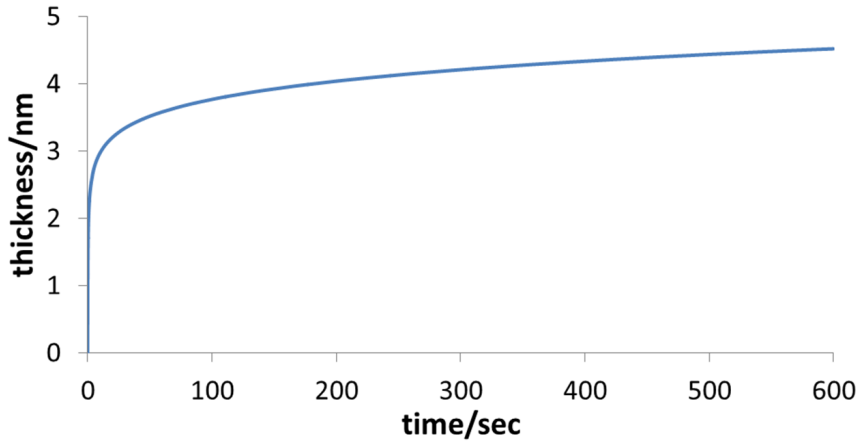


Figure 5.5: The evolution of the passive film thickness during the passivation period after the introduced correction of  $f_{\text{Fe}}$ .

[109]. In the following analysis, the metallic dissolution correction factor  $f$  will be improved to include the other metallic dissolution terms.

#### 5.4.2 Fraction of charge due to the rest of metallic elements

According to the analysis presented in the previous section concerning  $f_{\text{Fe}}$ , it's concluded that about  $3/4$  of the dissolution current is resulting only from the iron dissolution. Having this calculated raises the question if such a factor can be calculated for the other involved metallic dissolutions which form about  $1/4$  of  $j_{\text{dissolution}}$ , and eventually of  $j_{\text{total}}$ .

These metals can be recognized by the analysis of the elemental dissolution rates of the downstream corrosion solution by inductively coupled plasma atomic emission spectroscopy (AESEC) technique [132], according to which the elements Cr, Cu, Mn, Ni, and Mo were the most influencing in the metallic dissolution part.

Similarly, in our present work, in-situe analysis of the elemental concentration of the leaching corrosion solution was performed for an experiment of four cycles of activation/passivation on a non-stressed sample in the 2 M  $\text{H}_2\text{SO}_4$  at room temperature. The potentiodynamica program is the same as that mentioned in the experimental Chapter (2.4.3). The curves corresponding to the second cycle are given in Fig. 5.6.

In an analogy to what was done earlier about  $f_{\text{Fe}}$ , the other metallic correction factor can be defined as given by Eq.5.13, where  $m$  refers to the metal in consideration, and  $j_m$  is the anodic current due to the dissolution of an element  $m$  as calculated by Eq.5.9.

$$f_m = \frac{j_m}{j_{\text{total}}} \quad (5.13)$$

From the definition of  $f_{\text{Fe}}$  in Eq.5.10, it can be rearranged to give  $j_{\text{total}} = j_{\text{Fe}}/f_{\text{Fe}}$ . Substituting this in Eq.5.13, it gives:

$$f_m = \frac{j_m}{j_{\text{Fe}}} f_{\text{Fe}} \quad (5.14)$$

Now, the ratio  $j_m/j_{\text{Fe}}$  can be calculated thanks to the analysis made by AESEC technique mentioned earlier for the same experimental conditions where the elemental concentrations of the leaching solution were measured, and based on that the elemental dissolution current was calculated using Eq.5.9, which eventually gives the curve representing the dissolution current for each element,  $j_m$  as illustrated in Fig. 5.6 for one activation/passivation cycle.

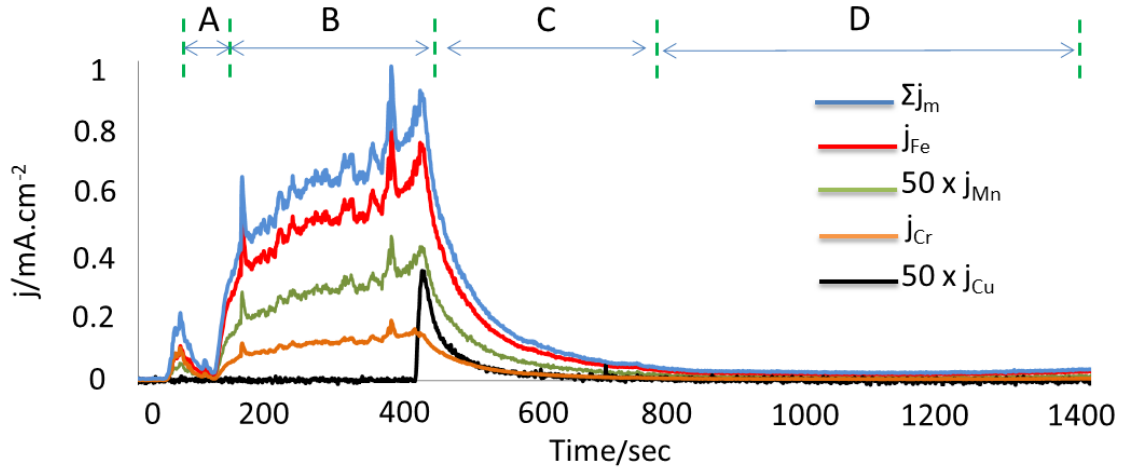


Figure 5.6: Elemental dissolution currents as measured by AESEC technique from the corrosion leaching solution concentrations during the second potentiostatic pulse tests. (A): Cathodic activation pulse(70 s at -700 mV vs Ag/AgCl). (B): OCP (300 s). (C): Passivation (300 s). (D): OCP (600 s).

In order to fit to the context of calculations which is concerned in passivation kinetics, the period over which the ratio  $j_m/j_{Fe}$  was calculated is chosen to be that during the application of the passivation pulse, which is indicated by region C in Fig. 5.6. The temporal resolution for the concentration measurement, and thus the data points for  $j_m$  is 1 data point per second. Thus, the ratio was calculated as the average of all registered data points over the entire passivation period as given in Eq.5.15:

$$\frac{j_m}{j_{Fe}} = \left( \sum_{p=1}^N \frac{j_m(p)}{j_{Fe}(p)} \right) / N \quad (5.15)$$

Where  $p$  represents the index of the considered data point, and  $N$  is the total number of registered data points during the passivation pulse.

The physical significance of this average calculated by Eq.5.15 is equivalent to  $\frac{j_m}{j_{Fe}}$  calculated out of the elemental concentrations of the solution accumulated during the application of the passivation pulse.

To have a measure whether the ratio  $j_m/j_{Fe}$  is stable over the different cycles of the experiment, this fraction was studied for  $j_{Cr}/j_{Fe}$  which has the second major importance in metallic dissolution after Fe. As given in Table:5.3, the ratio  $j_{Cr}/j_{Fe}$  seems to be stable over the four cycles, which makes it acceptable to use a constant for this ratio over the different cycles of the experiment. Same was assumed for the rest of elements in consideration, for which Table: 5.4 gives a summary of their average and standard deviation.

Table 5.3: Evolution of  $j_{Cr}/j_{Fe}$  over the four cycles of the experiment

	1 <sup>st</sup> Cycle	2 <sup>nd</sup> Cycle	3 <sup>rd</sup> Cycle	4 <sup>th</sup> Cycle	Avg	Stdv
$j_{Cr}/j_{Fe}$	0.221	0.214	0.218	0.218	0.218	0.002

If the ratio  $j_m/j_{Fe}$  is used in Eq.5.14, the corresponding dissolution correction factor  $f_m$  can be obtained for each considered element, as given in Table:5.5.

As indicated in Table:5.5, about 92 % of the total registered current during passivation is attributed to metallic dissolution. Consequently, the rest of the total current of about 8

% is assumed to be resulting from passive film oxidation reaction responsible for passive film formation.

The last correction of the passive film calculation thickness now can be introduced by employing the calculated correction factor  $\Sigma f_m$  which takes into account the five main metals dissolution component. The passive film thickness is calculated for all the measured data points over the passivation period (5000 data point / s) to give the profile shown in Fig. 5.7.

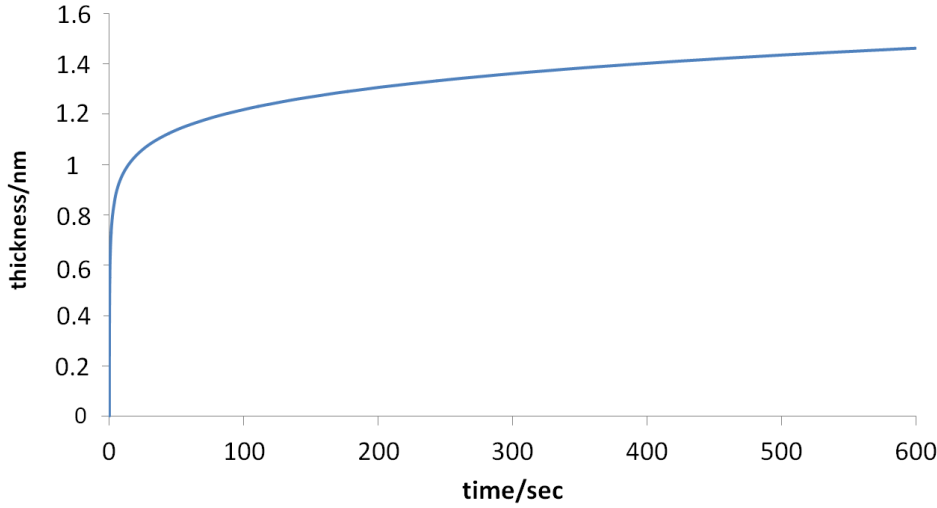


Figure 5.7: The evolution of the passive film thickness during the passivation period after the introduced correction of  $\Sigma f_m$ .

Using Eq.1.4, the calculated passive film thickness at  $t = 300$  s of the passivation pulse, the enhancement introduced by the correction factor taking into considerations the iron dissolution and the other metallic components is given in Table:5.6.

It's noticed from the obtained value for the last term where the dissolution of the five metals was taken into account for the calculation that the passive film thickness is now close to what's documented in the literature of about 1 nm [132]. By this, we can say that the passivation of stainless steel in the given acidic medium of 2 M  $\text{H}_2\text{SO}_4$  follows the high field ion conduction model as was suggested by Marshall and Burstein [109].

The originality added in the present work is being able to precisely quantify the amount of charge exchange spent on the different chemical processes, such that quantitative comparisons can be conducted on the different passivation parameters as will be seen in the following analysis.

Now that all the metallic dissolution fractions are calculated, the high field ion conduction model can be used with this correction factor to describe the passivation kinetics of our experiment of stainless steel in acidic medium appropriately as described by Eq.5.3, with  $f$  equals to  $\Sigma f$  calculated in Table:5.5.

### 5.4.3 Calculating the metallic dissolution fractions based on polarization curve

It is more standard and practical to use the polarization curve as a measure to characterize the electrochemical behavior of a given material. For this, the polarization test performed by AESEC technique for our stainless steel in 2 M  $\text{H}_2\text{SO}_4$  was used to check if, by this general curve, an estimation can be obtained directly for the dissolution correction factors  $j_m/j_{\text{Fe}}$  calculated in the previous section, without having to perform the exact same passivation experiment by AESEC each time. For this, four selected zones (A, B, C, and D) were analyzed for the  $j_m/j_{\text{Fe}}$  ratio as illustrated in Fig. 5.4. The numerical values are given in Table:5.7.

By comparing the corresponding values in Table:5.4 and Table:5.7, we notice that the correction factors can be estimated by calculating them from zone C or D as indicated in Fig. 5.4

with a good accuracy compared to the data obtained from the real passivation experiment. On the contrast, the correction factor of Cu was not fitting to the expected dissolution rates, but as it has the smallest influence over the totality of metallic dissolution current ( $f_{Cu} = 0.005$  vs  $\Sigma f_m = 0.916$ ), the approximation of using the polarization curve can still be accepted in cases where the exact passivation experiment is not available. Obviously, in the present work, the values calculated during the passivation experiment as given in Table:5.4 will be counted whenever required.

#### 5.4.4 Reproducing the current profile during passivation

So far, the passive film thickness was calculated over the entire period of the passivation pulse as was shown in Fig. 5.7. According to the high field ion conduction model (HFIC), the anodic current is controlled by an inverse logarithmic law as given by Eq.1.1, which can be reduced to Eq.1.2 for conditions where the potential drop across the film is high.

According to the HFIC model, as described by Eq.1.2, the ionic transfer through a passive film of thickness  $h(t)$  during the application of a potential  $V$ , passivation current  $j(t)$  can be theoretically calculated if the constants  $A$ , and  $B$  are known. These coefficients are a property of the passive film, defining the activation energy barrier for mobile ion migration through the film.

Sections (5.5 and 5.6) explain how to obtain these constant for a passive film produced in a given material/electrolyte combination. Shortly, as  $A$  and  $B$  are parameters describing the ionic transfer through the passive film, they are calculated by zone (II) of  $\log j(t)$  vs  $1/q(t)$  curve, as shown in Fig. 5.13, where the slope of this linear zone is equal to  $cBV$ , and its intercept is equal to  $\log(A)$ . The constants  $A$  and  $B$  were calculated for the second cycle (unstressed), giving  $1.41 \cdot 10^{-9} \text{ A.cm}^{-2}$ , and  $2.44 \cdot 10^{-6} \text{ cm.V}^{-1}$ .

Having the mobile ion migration constants,  $A$  and  $B$ , of the passive film calculated, in addition to the calculated passive film thickness at a given instant  $h(t)$  as was shown in section 5.4.2 (Fig. 5.7), the anodic current at a given instant  $t$  can be calculated using Eq.1.2. The calculated current,  $j_{calc}$ , is compared to the experimentally registered total current,  $j_{exp}$ , as shown in Fig. 5.8.

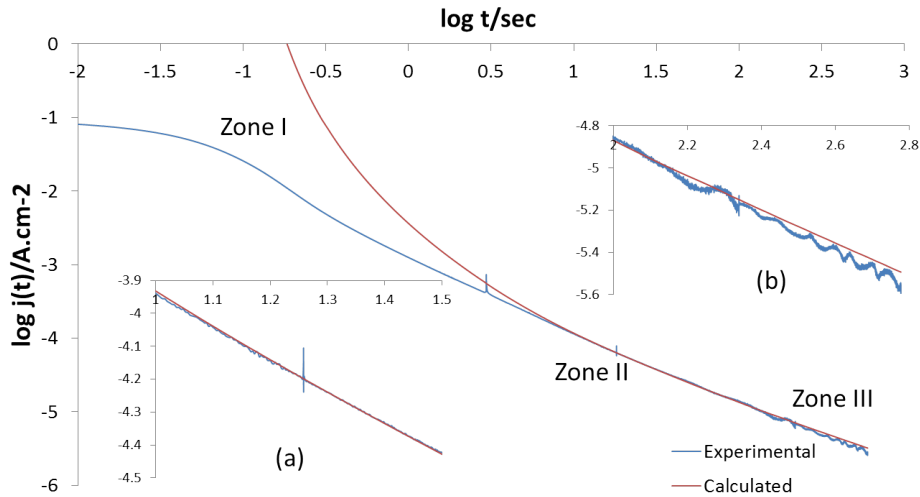


Figure 5.8: The passivation current density,  $j$ , as calculated by Eq.1.2 compared to that recorded experimentally for CII passivation cycle on an unstressed 304L stainless steel in 2 M  $\text{H}_2\text{SO}_4$ .

**Analysis of the three zones of the current transfer:** As seen from Fig. 5.8, the calculated current density,  $j_{calc}$ , was extremely high for the beginning of the passivation pulse (zone I),



and starts to decay and get closer to  $j_{\text{exp}}$  as the passive film thickens with time (zone II), then starts to deviate slightly from  $j_{\text{exp}}$  at (zone III).

Clearly, the two curves referring to  $j_{\text{calc}}$  and  $j_{\text{exp}}$  fit to a good degree in zone II. Indeed, this is the actual zone described by the HFIC model, where the passive film is fully constructed over the surface. One important fact to mention here is the difference between the actual topography and of the passive film, and  $h(t)$  used here as an input in HFIC Eq.1.2 to reproduce the passivation current  $i(t)$ . This can be understood better by the illustration given in Fig. 5.9, where (a) shows the real topography and the local variations in thickness, and (b) shows the equivalent thickness calculated by Faraday's law (Eq.1.4) using  $q_{\text{film}}$ .

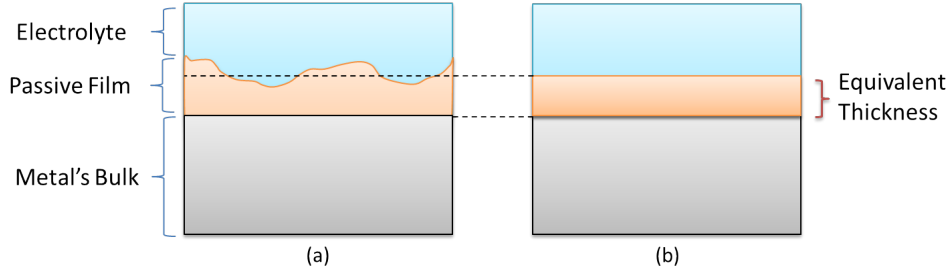


Figure 5.9: The passive film thickness where the HFIC applies. (a): The actual non-uniform topography and thickness of the passive film. (b): The equivalent thickness  $h(t)$  calculated by Faraday's law using  $q_{\text{film}}$ .

The reason for the local variation in thickness as shown in Fig. 5.9 (a) might be ascribed to local variation in chemical composition, surface history, or local chemistry. However, in this zone (II), the film topography is assumed flat, as the equivalent thickness is averaged over the surface when calculated by Eq.1.4. For this zone, the real and the averaged thickness seem to be reasonably related, as proved by the resulting  $j_{\text{calc}}$  when compared to  $j_{\text{exp}}$  being close enough.

On the other hand, the reason for which the calculated current was extremely high at the beginning of the passivation pulse as shown in zone (I) of Fig. 5.8 is that the HFIC does not simply apply in this domain. This can be better understood by considering Fig. 5.10.

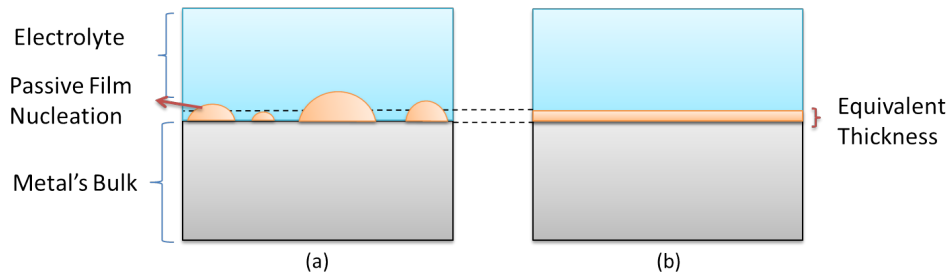


Figure 5.10: The passive film formation during zone I of the passivation period. (a): The initial discrete nucleation of the passive film over the bare surface. (b): The equivalent thickness  $h(t)$  calculated by Faraday's law using  $q_{\text{film}}$ .

Obviously, as illustrated by Fig. 5.10 (a), the metal surface is totally bare initially without any passive film over it, which starts to change gradually as local oxidation reactions start to nucleate the passive film with partial coverage of the metal surface (zone I in Fig. 5.13).

During this period, the charge transfer is not controlled by HFIC model, as no complete passive film is yet constructed. In reality, the oxidation reactions, and thus the anodic current, is limited in zone (I) as seen by  $j_{\text{exp}}$  in Fig. 5.8. This limitation could be resulting from one of the reaction rate-limiting steps such as [130]:

- Mass transport of reactive species in solution.

- Coupled chemical reactions.
- Ionic conduction in the electrolyte.

However, according to  $h(t)$  calculated by Eq.1.4 using  $q_{\text{film}}$ , the nucleation of the passive film is averaged to an equivalent very fine layer as shown in Fig. 5.10 (b). If this thickness is used in eq.1.2, the resulting  $j(t)$  will approach infinity as the layer thickness is very negligible and non-real. This starts to change gradually until the moment where the surface is totally covered by the passive film (transition between zone I to II), where the HFIC starts to apply.

Generally, when a thick enough passive film covers the metal's surface, the reaction limiting steps mentioned above are still valid, while being very negligible compared to the limitation imposed on the ionic conduction across the oxide film, which starts to apply at the beginning of zone II.

**Determining the HFIC domain (zone II):** The transition between current transfer regimes described by zone I (high current regime) to II (low current regime) is, however, not easy to define as seen in Fig. 5.13. Using the reproduced anodic current ( $j_{\text{calc}}$ ) by Eq.1.2 as described by HFIC might solve this problem of separating these two domains by a quantified measure. This can be done if the relative difference between  $j_{\text{calc}}$  and  $j_{\text{exp}}$  is studied over the duration of the passivation pulse as given by Eq.5.16:

$$\Delta j(t)\% = \frac{j(t)_{\text{calc}} - j(t)_{\text{exp}}}{j(t)_{\text{exp}}} 100\% \quad (5.16)$$

This relative difference,  $\Delta j(t)\%$ , was calculated for the present values over the passivation period. Fig. 5.11 below gives  $\log(\Delta j(t)\%)$  vs  $\log(t)$  over the passivation period.

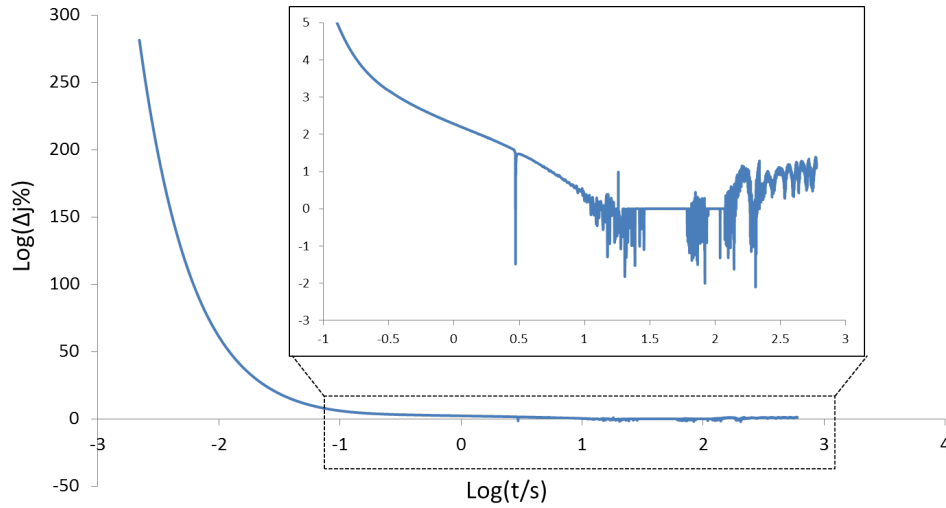


Figure 5.11: The relative difference between the current density  $j_{\text{calc}}$  and  $j_{\text{exp}}$ , as calculated by Eq.5.16 for CII passivation cycle on an unstressed 304L stainless steel in 2 M  $\text{H}_2\text{SO}_4$ .

To highlight a few points of interest, Table: 5.8 gives some selected instants during the passivation process along with the  $\Delta j(t)\%$  at that time.

As seen from Table: 5.8 and Fig. 5.11, the percentage error  $\Delta j(t)\%$  reduces with time until it reaches eventually a very small value at  $t = 20$  s. Starting from this instant ( $t = 20$  s), the two curves representing  $j_{\text{calc}}$  and  $j_{\text{exp}}$  get extremely close to each other and inseparable as shown in Fig. 5.8 (a). This gives a confirmation for the different calculated parameters;  $A$ ,  $B$ , and  $h(t)$  correspond to each other and fit to the actual experiment, and as a conclusion, the HFIC model applies for this material/electrolyte combination.

This remains the case over two decades of anodic current density, after which the relative error starts to fluctuate reaching about 20% due to passive film local break-up/repair process which defines zone III as shown in Fig. 5.8 (b), where the anodic current deviates (starting from  $t = 210$  s) from the linearity described by HFIC. The deviation in this zone can be justified by the dissolution of the passive film, as the electrical field strength,  $V/h_{\text{film}}$  gets lower due to film thickening [62]. This dissolution causes successive local film break-up/dissolution and repair processes as shown in Fig. 5.12(a).

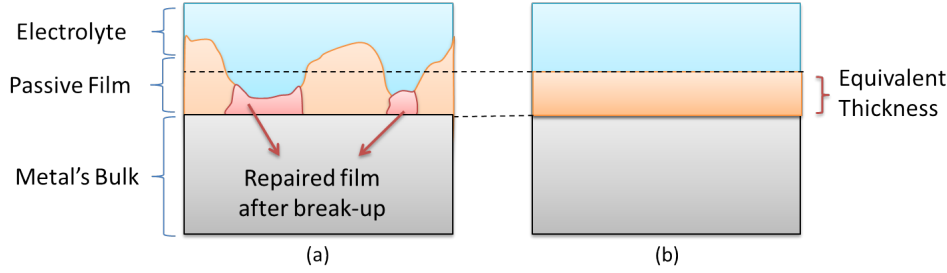


Figure 5.12: The passive film in zone III, where  $j(t)$  deviates from the HFIC. (a): The dissolution of film leading to local passivity break-up/repair processes. (b): The equivalent thickness  $h(t)$  calculated by Faraday's law using  $q_{\text{film}}$ .

An interesting remark about the  $j_{\text{calc}}$  is that it does not show the zig-zag shape that  $j_{\text{exp}}$  showed in zone III as illustrated in Fig. 5.8 (b). This is due to the way the thickness was calculated, which takes into account the accumulated charge ( $q_{\text{film}}$ ) until the concerned moment  $t$ , which will be increasing in a linear way on the  $\log(|j|)$  vs  $1/q_{\text{film}}$  curve, regardless of the possible film break-up/repair process. According to the thickness calculated, the hypothetical passive film at zone III is non-defective and continuously growing with time, as shown in Fig. 5.12 (b), and this explains the deviation of  $j_{\text{calc}}$  from  $j_{\text{exp}}$  in zone III.

As a summary, by this analysis, it was possible by a quantified measure to determine the domain over which the HFIC model applies. If it's accepted that the HFIC applies where  $\Delta j(t)\%$  is  $\leq 3\%$ , then the domain corresponds to that starting from  $t = 9.3$  s until  $t = 210$  s.

From  $t = 210$  s, the relative error and the deviation from linearity starts to increase gradually until  $t = 575$  s, where the relative error fluctuates around 10% in this period. This goes up to 25% between  $t = 575$  s and  $t = 600$  s due to accelerated film break-up and repair processes.

In the following sections, all the calculations to find the slope  $cBV$  over  $\log(|j|)$  vs  $1/q_{\text{film}}$  passivation curves were performed within the linear zone II described by HFIC as was determined precisely here, with an additional conservative domain  $\log(j) = -4$  to  $-5$  mA.cm<sup>-2</sup>.

## 5.5 Quantification of Passive Film Quality

Now that all the metallic dissolution fractions are quantified, the high field ion conduction model can be used to appropriately describe the passivation kinetics of our experiments of stainless steel passivation in acidic medium. For this, Eq.5.3 can be used with  $f$  equals to  $\Sigma f$  calculated in Table: 5.5.

If the passivation transient presented earlier in Fig. 5.2 is corrected for the charge portion responsible for passive film formation  $q_{\text{film}}$  instead of  $q_{\text{total}}$  which was used earlier, the resulting curve will be as presented in Fig. 5.13. As was described in section 1.6.3, on the obtained  $\log(|j|)$  vs  $1/q_{\text{film}}$  passivation curve, the two zones (I) and (II) were detected as illustrated on Fig. 5.13, where zone (I) indicates the stage where the passive film was in the nucleation process before the passive film total coverage of the material surface, and thickening process which is indicated by zone (II) [62].

The curves presented in Fig. 5.2 and Fig. 5.13 are zoomed towards zone (II) such that the passivation kinetics during this phase can be analyzed. It's noticed that the new curve in Fig.

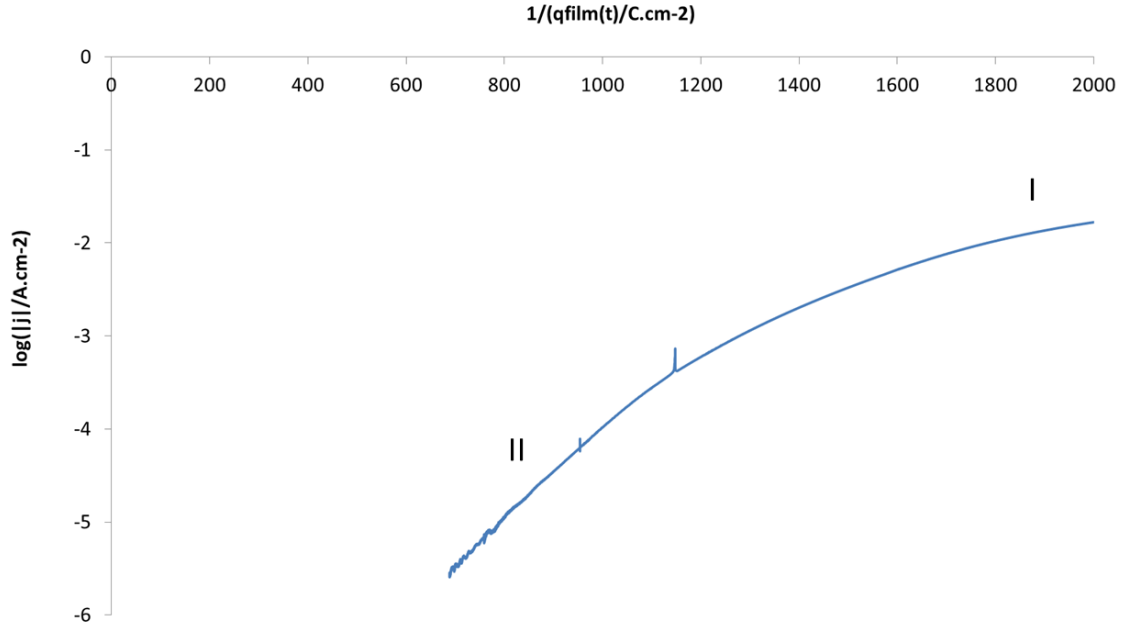


Figure 5.13: The second cycle passivation curve corrected to  $q_{\text{film}}$  as described by the high field ion conduction in Eq.1.6.

5.13 has the same form as the one before the correction by the dissolution component except for the abscissa, which is corrected obviously by a factor of  $1/(1-\Sigma f_m)$ . This effect alters the slope of the linear zone II on the curve by the same factor changing it from  $(5.7 \cdot 10^{-2}$  to  $4.8 \cdot 10^{-3}$ )  $\text{A.C.cm}^{-4}$ , where the current  $j(t)$  density is in  $\text{A.cm}^{-2}$  and the charge density  $q(t)$  is in  $\text{C.cm}^{-2}$ .

The reason why the precision in calculating this slope was highly demanded in our current research is its significance in characterizing the passivation process. Particularly, according to the high field ion conduction model [28], the slope of  $\log j(t)$  vs  $1/q(t)$  curve in zone (II), indicated by  $cBV$  in Eq.5.3, is a direct indication of the activation energy barrier for ionic transfer through the passive film by the effect of the applied potential [90]. Looking to Eq.5.3, this activation energy is proportional to the product of  $B$  and the field strength  $(V/h)$ , where  $h$  is the passive film thickness as was given by Eq.1.4 ( $h(t) = Mq_{\text{film}}(t)/zF\rho$ ). Accordingly, the higher value of the slope  $cBV$  indicates a lower activation energy barrier for the ionic transfer through the passive film. As the ionic conduction rate through a passive film is an indicator of its protection ability, an alloy with higher  $cBV$  value is expected to have a defective passive film allowing faster ionic transfer and so has lower protection ability [90].

**Stress corrosion cracking vs  $cBV$ :** As was introduced earlier, many models explained stress corrosion cracking by a sequence of micro-processes involving passive film break-up, dissolution, and repassivation [105, 107, 140]. The intrinsic repassivation rate of a given material is a function of the temperature, pH, chloride concentration, the applied potential during the passivation process, and the chemical composition of the alloy. On the other hand, the microstructure of the alloy and the loading configuration determines the rate of film rupture. Therefore, for a given alloy/environment where the loading condition is constant or having a constant strain rate, the intrinsic passivation rate of the alloy measured without the application of stress is an indicator of SCC susceptibility [90].

In addition to this, according to film induced cleavage model, the passive film must be brittle and firmly fused to the substrate for transgranular SCC to happen, which is necessary to initiate a crack with a tremendous velocity that enables this crack to keep propagating through the bulk of the material. According to this, film mechanical properties and its thickness and

compactness might have a great influence on SCC. If the porosity of the passive film as a result of de-alloying, for example, is sufficiently fine, this can be very effective to bolster the cleavage up in the substrate [102].

Here where it comes the interest of  $cBV$  value which is an effective measure to quantify the repassivation rate and the protection quality of the constructed passive film over a bare metal surface [33], and accordingly can be an indicator of SCC susceptibility. This measure was used in different studies on repassivation and SCC of stainless steels and iron based alloys [22, 33, 90]. In these works, the value of  $cBV$  was very sensitive to the variation of the passivation parameters such as the applied potential, alloy's composition, the  $Cl^-$  concentration, or the solution acidity and temperature.

The slope  $cBV$  of the  $\log j(t)$  vs  $1/q(t)$  curve is affected by  $q_{film}$  as was seen in this analysis, which is directly associated with the passive film thickness. It was shown that for passivation experiments using iron-based alloys with different compositions, the passive film thickness was linearly proportional to  $cBV$  value regardless of the alloy's composition [33]. This implies that a lower  $cBV$  value is associated with a thinner and more protective passive film with a higher repassivation rate [33].

Based on all of this, Kwon et al. [90] showed that with increased applied potential, solution temperature, or  $Cl^-$  concentration, the value of  $cBV$  increased in a gradual way, until a limiting value where an inflection point appeared on the  $\log j(t)$  vs  $1/q(t)$  curve, as illustrated in Fig. 5.14.

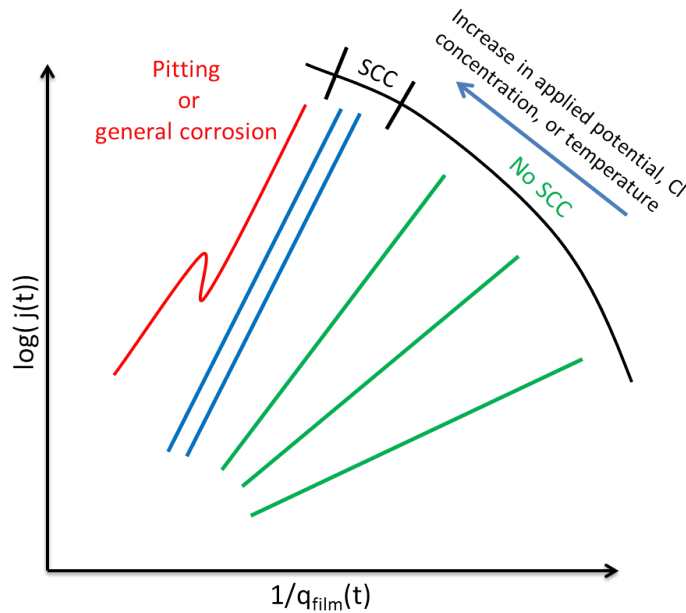


Figure 5.14: The indication of the slope  $cBV$  and how it varies according to the different passivation parameters.

According to the description of Fig. 5.14, which is based on experimental work on SCC [33, 90], the corrosion of the material was classified according to the  $cBV$  value. In the first domain, where  $cBV$  is low, general corrosion occurred, with no SCC detected due to favorable passive film properties. As the  $cBV$  reached the limiting value, SCC took place where the passivation rate was reduced to promote cracking and dissolution steps. Whereas at the last stage after the inflection point, severe and pitting corrosion was dominant where the passive film was unable to hold under the extreme applied conditions, namely: temperature,  $Cl^-$ , or the applied potential.

In the present work, the influence of the applied stress on the passivation kinetics is sought to be verified. Compared to the failure of slope  $\alpha$  of  $\log(j)$  vs  $\log(t)$  curves to detect any effect as

was shown in Chapter 4,  $cBV$  seems to be a promising measure to reveal a quantified measure of the effect that stress can have, if any, on the passivation kinetics and passive film properties as will be discussed in the following analysis in section 5.6.

## 5.6 Influence of Stress on Passivation Kinetics and Film Properties

In Ch.4, a set of potentio-cyclic experiments presented where 2 M  $H_2SO_4$  was used as a solution to test the stainless steel passivation/activation kinetics. These tests involved stressed and unstressed samples for the purpose of evaluating the possibility to detect and quantify the influence of the applied tensile stress on the corrosion of 304L stainless steel.

Among many criteria used to test the influence of stress, slope  $\alpha$  of  $\log(j)$  vs  $\log(t)$  curves was used to quantify the passivation rate. Yet, the  $\alpha$  value was more or less equal for both stressed ( $\sigma = 280$  MPa) and unstressed samples.

The case was more or less obtaining variations in the order of experimental error each time, which made it difficult to interpret them to physical phenomena. However, the most remarkable effect of stress was detected on the charge transfer during the passivation process, starting from the application of the passivation pulse until a predefined state of current density, identified as the passivation current  $j_p$  which was set to  $1 \text{ mA.cm}^{-2}$ .

Having an influence of the stress on the passivation charge urged the need to quantify the passivation rate by a criterion which takes into account the charge exchange. This measure was the  $cBV$  value which was introduced in the previous section.

The passivation anodic current transients obtained during the passivation experiments are plotted on the  $\log j(t)$  vs  $1/q(t)$  axis, giving Fig. I.1, Fig. 5.15, and Fig. I.2 which refer to passivation during cycle CI, CII, and CIII respectively.

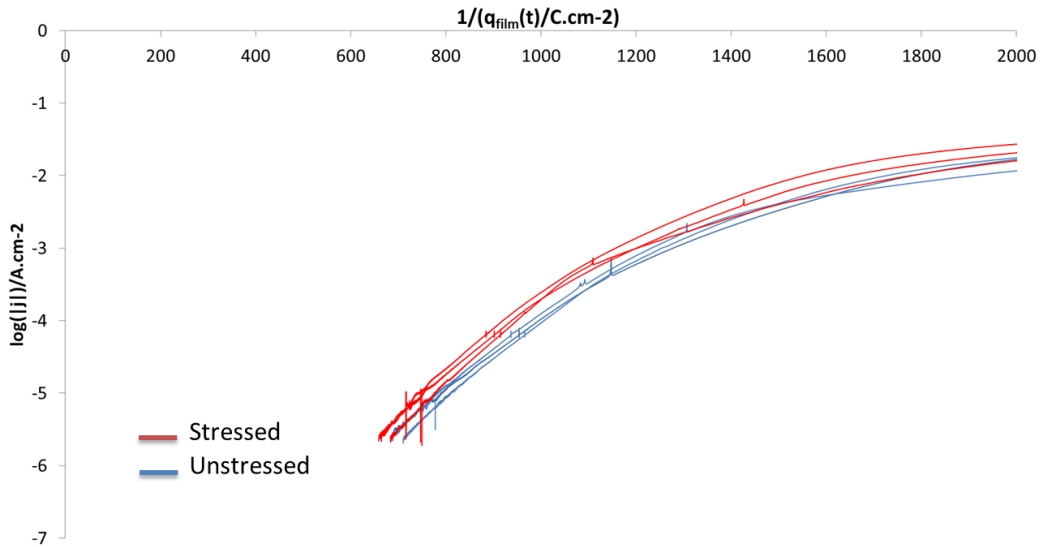


Figure 5.15: The second cycle passivation anodic curves for stressed and unstressed tests in 2 M  $H_2SO_4$  plotted on  $\log j(t)$  vs  $1/q(t)$  axis.

The curves in CI and CII were all reproducible showing the two linear domains; zone I indicating the high ion conduction regime during passive film nucleation, in addition to zone II indicating the low ion conduction regime during the passive film construction and thickening over the metal's surface. This is in accordance with the resulting curves of stainless steel passivation in acidic mediums as was obtained by Marshal and Burstein [27, 25, 109].

An exception for this was obtained for the unstressed samples in CIII for two experiments, where surface showed unrecoverable break-ups, probably due to local defects in the material, as indicated at the later portion of their curves in Fig. I.2. However, since these odd behaviors were detected in the last cycle at a late stage of the application of the passivation pulse, the data points in the zone of passivity break-up (starting from  $1/q_{\text{film}} \approx 800 \text{ C.cm}^{-2}$ ) were excluded from the calculations.

With these curves, the slope  $cBV$  was calculated in the low current transfer domain ( $\log(j) \in [-4,5] \text{ mA.cm}^{-2}$ , where the film is supposed to be thick enough for the high field ion conduction model to apply (zone II), as was quantified and determined earlier in section 5.4.4. The resulting values are illustrated in Fig. 5.16.

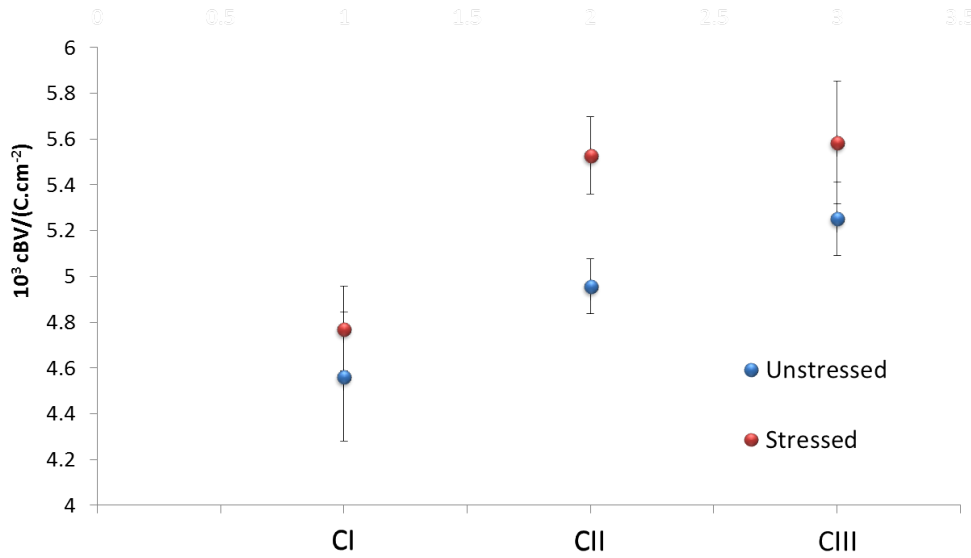


Figure 5.16: The passivation rate as measured by the slope  $cBV$  of zone II of the  $\log j(t)$  vs  $1/q(t)$  anodic passivation transients.

The observation on these curves is the evolution of the  $cBV$  value, regardless of the stress state, where the  $cBV$  value increases with each new passivation cycle. This implies reduced passivation rate with each new cycle. This might be due to the depletion of Cr from the surface during the cathodic activation step that preceded the passivation or could be due to and the dissolution during the previous cycles. Obviously, the difference between CI from one side and CII, CIII from the other side is bigger than the difference of  $cBV$  between CII and CIII. This is expected as the initial surface preparation is totally different from the surface state after the first cycle, where the surface has passed through a cycle of electrochemical polishing during the cathodic activation, which removed initial surface finishing effects such as residual stresses resulting from manufacturing processes. The initial industrial surface shows the lowest  $cBV$  value, which indicates a high passivation rate.

The second observation is the variation of the  $cBV$  value between the stressed and unstressed samples. For the first cycle, the two surfaces had more or less common history due to the industrial surface preparations. Before the second passivation pulse, the two samples passed the first cycle (including an activation + passivation step), and the cathodic activation of the second cycle. This probably has made a slight variation in the surface state in terms of the concentration of metallic composition on the surface due to diffusion effect in metallic dissolution as an effect of the applied stress. As a result, this made the stressed samples get a higher  $cBV$  value, which indicates a lower passivation rate of the stressed samples. This means that the stressed samples have the tendency to require more time to reach passivation as a result of having a lower passivation rate, which implies more metallic dissolution during an activation/passivation cycle



than that of a non-stressed sample. On the other hand, this was not a very clear conclusion to make about the third cycle, probably due to an excessive loss in Cr in both cases, which led to having more or less closer passivation kinetics in CIII.

The value of  $B$  can be calculated out of the slope, where  $V$  is the potential difference across the passive film  $\simeq 0.5V$ , and  $c$  is the constant introduced earlier  $9192.4 \text{ C.cm}^{-3}$ . In general, the calculated  $B$  values in our case were 1/8 to those obtained by Burstein et al. [27], for passivation experiments of 304L stainless steel in acidic mediums.

The other parameter sharing in the activation energy of the mobile ion transfer through the passive film is the constant  $A$ . For these experiments,  $\log(A)$  was calculated as the intercept of the section of the curve where  $cBV$  was calculated. The obtained results are given in Table: 5.9, and illustrated in Fig. 5.17.

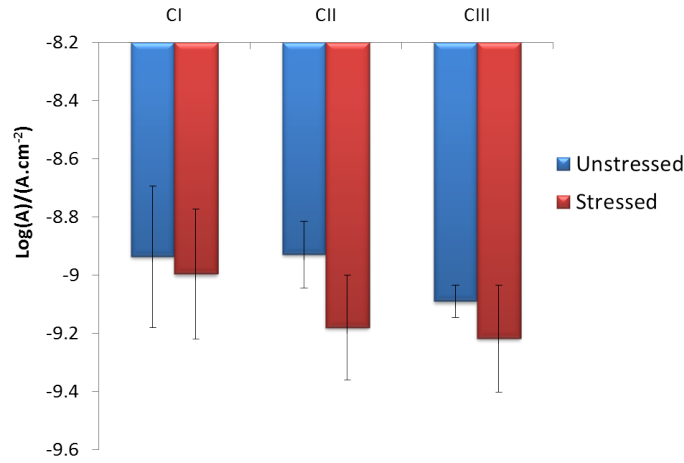


Figure 5.17: Illustration of  $\text{Log}(A)$  values calculated for the  $\log(j(t))$  vs  $1/q(t)$  curves over the low current transfer regime (ZoneII).

The values of the obtained  $\log(A)$  in the present work are of the same order of magnitude of those obtained by Burstein et al. for 304L stainless steel passivation in acidic mediums [27]. It's noticed that the  $A$  value has the tendency to decrease with the evolution of each new cycle. As  $A$  is related to the activation energy barrier for ion movement through the passive film, this indicates that the ion transfer becomes easier through the passive film at each new cycle. This confirms the conclusion made about the reduction of passivation rate as measured by the  $cBV$  with the evolution of experiments through CI to CIII.

Concerning the influence of stress on the  $A$  value, though the averages through the three cycles were higher for stressed samples which might imply easier ion migration and thus lower passivation rate, the effect is not very significant when compared to the experimental error domain as seen in Fig. 5.17.

## 5.7 Influence of Stress on Film Thickness and Protection Ability

### 5.7.1 Based on charge concept (conventional techniques)

So far, the repassivation kinetics was quantified and calculated for the different passivation experiments. An effect might possibly be detected due to the applied stress on the passivation rate, as measured by the  $cBV$  value which was clearly different for CII, indicating lower passivation rate for stressed samples which is not favorable in terms of corrosion protection.

In the present work, through the way to quantify properly the  $cBV$  value, it was necessary to quantify the charge portion due to metallic dissolution, and that responsible for passive film



formation processes as explained in section 5.4. It turns out quantifying this will enable us to calculate the corresponding passive film thickness using Faraday's law as was done previously. If this thickness is calculated at a given degree of passivation called the passivation current (was set earlier in Ch.4 to be  $j_p = 1 \text{ mA.cm}^{-2}$ ), the resulting thickness is called the passivation thickness. This doesn't represent the steady state thickness where the current reaches it's lowest values, but the thickness during the process of passive film formation which was enough to limit the current density to the predetermined value  $j_p$ . The higher this thickness means that the passive film conductivity is higher, thus the protectiveness of the film is lower, as it allows a faster ionic transfer. A thinner passivation thickness indicates good isolation properties, which reflects a compact and dense passive film properties, with low defects [33, 90].

If this passivation thickness defined above is combined with the value of  $cBV$ , they will both give a complete description of the passive film properties and quality as was done by [33, 90].

Thus, the passive film thickness required to reduce the anodic current to  $j(t)_p = 1 \text{ mA.cm}^{-2}$  was calculated for the stressed and unstressed samples, as indicated by Table: 5.10, and illustrated in Fig. 5.18.

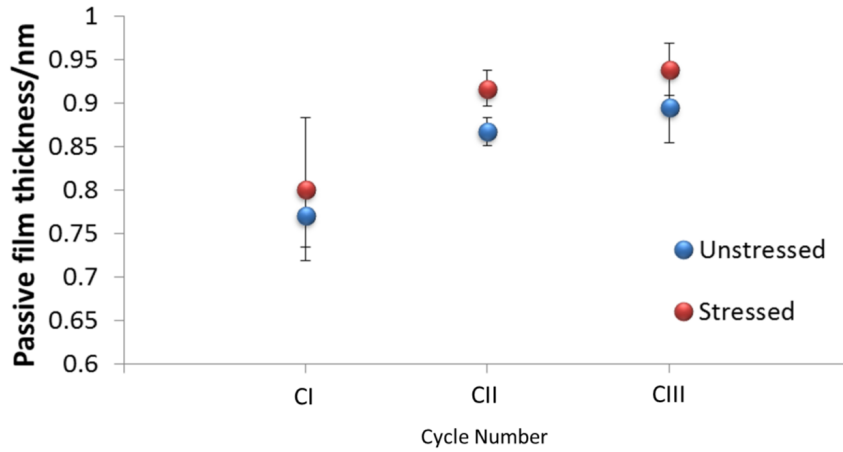


Figure 5.18: Passivation thickness (at  $j_p = 1 \text{ mA.cm}^{-2}$ ) of stressed and unstressed samples during the three passivation cycles in 2 M  $\text{H}_2\text{SO}_4$  electrolyte.

Clearly, as seen from Fig. 5.18 and regardless of the stress state, the passivation thickness tends to increase with the evolution of the experiment through the different cycles. This fits the passivation rate  $cBV$  that was found earlier for these experiments, where the  $cBV$  value had the tendency to increase with the cycle number.

Accordingly, the calculated passive film seems to fit the interpretation of  $cBV$  as a measure of the passivation rate. In other words, when the  $cBV$  goes higher, the activation energy for ionic transfer through the passive film, making it easier for charge exchange, rendering the passivation rate slower, which means more oxidation reaction required to construct a thicker passive film so that the determined passivation degree is reached.

As a conclusion, for a lower passive film protection ability indicated by the high  $cBV$  value, it is necessary to construct a thicker passive film to obtain the same degree of passivation of another film of a better quality, as illustrated by Fig. 5.19 for the two passive film constructed on the stressed sample (a), and that on the non-stressed sample (b).

This fits the conclusions drawn by [33, 90] when they compared the passive film quality and thickness of different material/environment combinations, where the passive film quality was related to the corresponding passivation rate and passive film thickness.

Practically, for the present work, the surface topography and chemical composition changes during the experiment as it passes from one cycle to another due to the successive activa-

tion/passivation processes. Thus, it would be interesting at this point to plot the passivation thickness vs the passivation rate as measured by the  $cBV$  value. The resulting plot is shown in Fig. 5.20.

What's interesting about this plot is that it shows both criteria we need to quantify the quality of the passive film: its ionic conduction rate expressed by  $cBV$  and the passive film thickness. Points at the lower left side of the plot have the lowest ionic conduction rate and the lowest thickness, which indicates a compact film with a high protection quality. On the other hand, the points at the upper right corner represent a passive film of a high ionic conduction permeability, and a high thickness, which reflects a defective passive film and poor protection ability.

Looking to the evolution of the passive film quality as indicated by this plot, the film seems to get thicker and less protective as the experiment evolves from a cycle to another. This could be due to the depletion of the surface from the Cr due to the successive dissolution/passivation steps during the cycles of the experiment. This argument clearly applies equally to the stressed and unstressed samples in an individual way.

Another interesting general remark can be made here is that regardless of cycle number or the stress state, the thickness was in all the time proportional to the  $cBV$  value in almost a linear way. This observation confirms what Cho et al. [33] have found for the passive film quality and thickness studied for stainless steel passivation tests. In their experiments, they used different Cr content in the alloy's matrix and using different passivation parameters such as  $\text{Cl}^-$  concentration, pH, or the temperature of the electrolyte. They found out that regardless of the material/electrolyte combination, the  $cBV$  value was all the time linear to the required passive film thickness required to each a pre-determined passive state [33].

For what concerns the influence of stress on the passive film quality as measured by this plot, the stressed samples tended to be shifted all the times towards the low-quality direction, as indicated by lower passivation rate (higher  $cBV$  value) and higher thickness. This means that regardless of the cycle number, the stressed samples seemed to develop a more defective passive film than the unstressed ones, with a higher thickness required to each the predetermined passivation criterion ( $j_p = 1 \text{ mA.cm}^{-2}$ ). This might be due to the passive film being of a porous nature, which makes it less resistant to local corrosion phenomena such as SCC.

This slight reduction of the passive film quality might justify the preferential attack at the crack tip in SCC, where the stress values might probably cause the construction of such defective films locally.

Though the influence of stress on the passive film properties was quantified here, however, this effect was not very considerable as compared to the effects found by Cho et al. [33] of the variation of Cr content of the alloy, or increasing the  $\text{Cl}^-$  concentration in the electrolyte for example. This might be due to the high acidic concentration which caused a severe dissolution of the metal that masked minor effect such as that related to the applied stress on the metallic dissolution. Using lower acidic concentrations might reveal a more pronounced effect of the applied stress on the passivation kinetics.

### 5.7.2 Based on concentration measurement (AESEC)

As was explained in the experimental part (section:2.4.4), the selective elemental dissolution can be quantified. The chromium enrichment,  $Q'_{\text{Cr}} / (\mu\text{g.cm}^{-2})$ , over the material's surface during passivation was quantified, according to Eq.2.10 [132]. By assuming that the passive film to be of  $\text{Cr}_2\text{O}_3$ , with a density of  $5.21 \text{ g.cm}^{-3}$ , the passive film thickness,  $\theta/10^{-6}.\text{cm}$ , resulting from the chromium enrichment can be consequently calculated using Eq.2.11. Table: 5.11 gives a summary of the chromium enrichment and the corresponding passive film thickness for the four passivation cycles conducted on stressed and unstressed samples.

So, the preferential dissolution favors the construction of a passive film by chromium enrichment during the dissolution. Results of the passive film thickness in Table :5.11 agree with the

Table 5.4: Summary of the average  $j_m/j_{Fe}$  values over the four passivation cycles.

	$j_{Cr}/j_{Fe}$	$j_{Mn}/j_{Fe}$	$j_{Cu}/j_{Fe}$
Average	0.218	0.011	0.006
Stdv	0.002	0.001	0.002

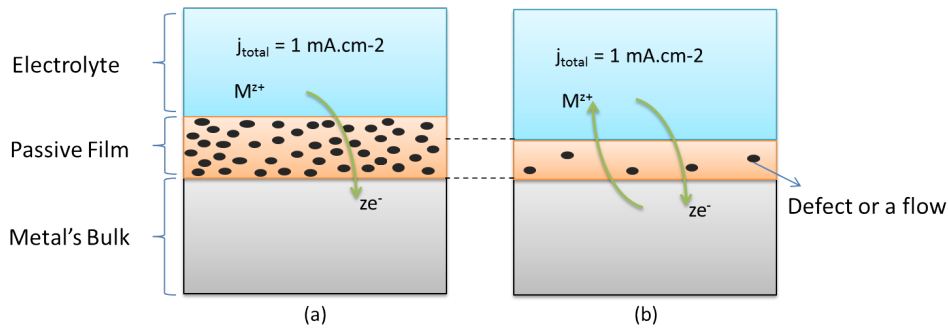
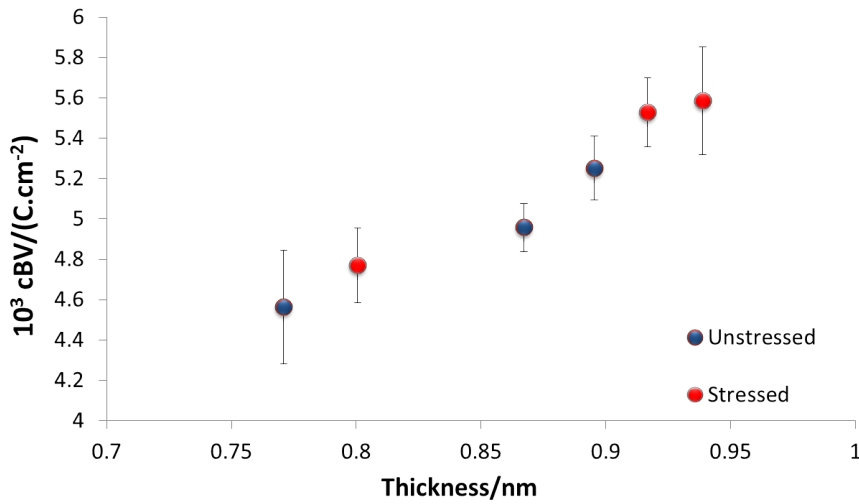
Figure 5.19: Passivation thickness (at  $j_p = 1 \text{ mA.cm}^{-2}$ ) of (a): a film with a low passivation rate (high  $cBV$ ) which is thought to be the case for stressed samples, (b): a film with a high passivation rate (low  $cBV$ ) which is thought to be the case for unstressed samples.Figure 5.20: Passivation thickness vs  $cBV$  of stressed and unstressed samples during the three passivation cycles in 2 M  $\text{H}_2\text{SO}_4$  electrolyte.

Table 5.5: A summary of the dissolution factor  $f_m$  for the four considered elements.

$f_{\text{Fe}}$	$f_{\text{Cr}}$	$f_{\text{Mn}}$	$f_{\text{Cu}}$	$\Sigma f_m$
0.740	0.163	0.007	0.005	0.916

range of values values obtained previously using the conventional techniques which are based on charge considerations.

## 5.8 Conclusions

The following general points can be given as a summary and of this chapter:

- The potetniiostatic pulse testing was used to simulate the surface activation and passivation which is described in SCC models such as the corrosion enhanced localized plasticity model.
- Passivation of 304L stainless steel in acidic solutions shows a fast metallic dissolution rate, and the passivation process was described by high field ion conduction model.
- The HFIC model was adapted for acidic solutions with the correction for the high metallic dissolution component. This was possible by experimentally measuring the metallic dissolution fraction out of the total anodic current. Conventional electrochemistry in addition to AESEC technique were used to perform the required measurements for this calculation.
- The fast metallic dissolution component during passivation causes the release of metallic composition from the surface, resulting in Cr-rich film growth.
- This dissolution is constructive; the Cr-rich layer isolates the bulk of the material, leading to passivity.
- The average thickness of the passive film built over stressed samples was slightly higher, with a lower passivation rate. This is believed to be due to the passive film being more defective on stressed samples than that built over the non-stressed samples as indicated by cBV factor and the corresponding thickness until a predefined passivation state.
- The higher dissolution and lower passive film quality for stressed samples compared to non-stressed ones might explain the particular chemistry causing selective attack at the crack tip in SCC, where the stress has very high values, and thus the passivation is slower and weaker.
- The passive film thickness calculated based on charge concept using conventional electrochemistry was in the range of the thickness calculated based on elemental concentration criteria using AESEC method.
- The effect of stress is expected to be more pronounced if a lower acidic concentration was used for the passivation experiments, as high acidic concentration is suspected to mask the influence of stress.

Table 5.6: Passive film thickness at  $t = 300$  s as calculated by Eq.1.4 with different  $q_{\text{film}}$ .

$q_{\text{film}} =$	$q_{\text{total}}$	$q_{\text{total}}(1 - f_{\text{Fe}})$	$q_{\text{total}}(1 - \Sigma f_m)$
Thickness/nm	16.19	4.20	1.36

Table 5.7: Dissolution ratios  $j_m/j_{\text{Fe}}$  as calculated by the polarization curve

Zone	$j_{\text{Cr}}/j_{\text{Fe}}$	$j_{\text{Mn}}/j_{\text{Fe}}$	$j_{\text{Cu}}/j_{\text{Fe}}$
A	0.0627	0.0095	0.0071
B	0.0610	0.0095	0.0099
C	0.2144	0.0101	-0.0001
D	0.2160	0.0101	-0.0001

Table 5.8:  $\Delta j(t)\%$  for selected instants of interest during the passivation.

t/s	1.6	2.4	2.9	5.4	7.4	9.3	13.2	20
$\Delta j(t)\%$	100	50	30	10	5	3	1	<0.01

Table 5.9:  $\log(A)$  values calculated for the  $\log j(t)$  vs  $1/q(t)$  curves over the low current transfer regime.

$\log(A)/$	CI		CII		CIII	
(A.cm <sup>-2</sup> )	avg	stdv	avg	stdv	avg	stdv
Unstressed	-8.94	0.24	-8.93	0.12	-9.09	0.06
Stressed ( $\sigma = 280$ MPa)	-9.00	0.22	-9.18	0.18	-9.22	0.18

Table 5.10: Passivation thickness (at  $j_p = 1$  mA.cm<sup>-2</sup>) of stressed and unstressed samples during the three passivation cycles in 2 M H<sub>2</sub>SO<sub>4</sub> electrolyte.

Thickness/	CI		CII		CIII	
(nm)	avg	stdv	avg	stdv	avg	stdv
Unstressed	0.771	0.036	0.867	0.016	0.895	0.041
Stressed	0.801	0.082	0.917	0.020	0.939	0.030

Table 5.11: Results of AESEC technique: the surface enrichment in chromium,  $Q'_{\text{Cr}}/(\mu\text{g.cm}^{-2})$ , and the corresponding passive film thickness,  $\theta$  /nm, during the four passivation cycles of unstressed samples.

	$Q [\mu\text{g.cm}^{-2}]$	$\theta [\text{nm}]$
CI	0.509	0.98
CII	0.476	0.91
CIII	0.532	1.02
CIV	0.526	1.01

### 6.1 Calculation of the Applied Stress

To apply certain value of tensile stress, the samples were elasto-plastically deformed using curved supports having different radii of curvature, as shown in Fig. 6.1.

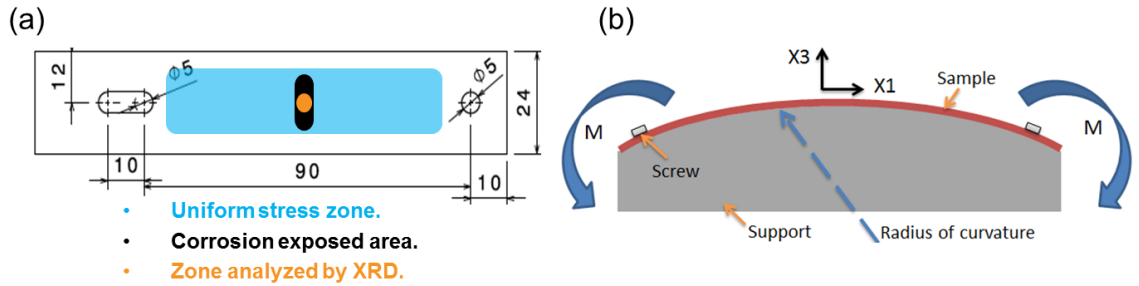


Figure 6.1: (a): Experimental dimensions of the sample and the experimentally involved zones. (b): The curved support to apply determined strain states.

By this assembly, the sample is deformed to predetermined levels around their transverse direction, which is normal to the rolling direction of the sample, as shown in Fig. 6.1 (b), Fig. 6.2 (a). The sample is thus subjected to a constant bending moment by the two screws fixing it to the curved support. This creates an applied uni-axial stress on the central part of the sample. For the elastic domain, if the volume is assumed constant, the sections of the sample remain flat after deformation, and the stress is uni-axial, the stress tensor is reduced to  $\sigma_1$ ; where  $\sigma_2$  and  $\sigma_3$  are negligible, and  $\sigma_{12}$  and  $\sigma_{23}$  are zero.

The stress and strain profiles under such assumptions are illustrated in Fig. 6.2 (b), where the upper surface undergoes tensile strain and tensile stress ( $\sigma_t$ ), while the lower surface has compressive strain and stress ( $\sigma_c$ ). The stress has its maximum tensile stress ( $\sigma_{\max}$  in Fig. 6.2 b) on the upper surface, where an area of uniform stress is assumed as shown in Fig. 6.1(a). The experiments are conducted over this uniform stress area, with an local corrosion exposed area which is controlled by the gasket area of the flow electrochemical cell used, as shown in Fig. 6.1 (a). Post-experimental XRD analysis are held on part of this corroded area, which is shown by the orange circle on the corroded surface in Fig. 6.1 (a).

The strain of the sample on the upper fibers,  $\varepsilon_{\text{tot}}$ , can be calculated using Eq. total-strain:

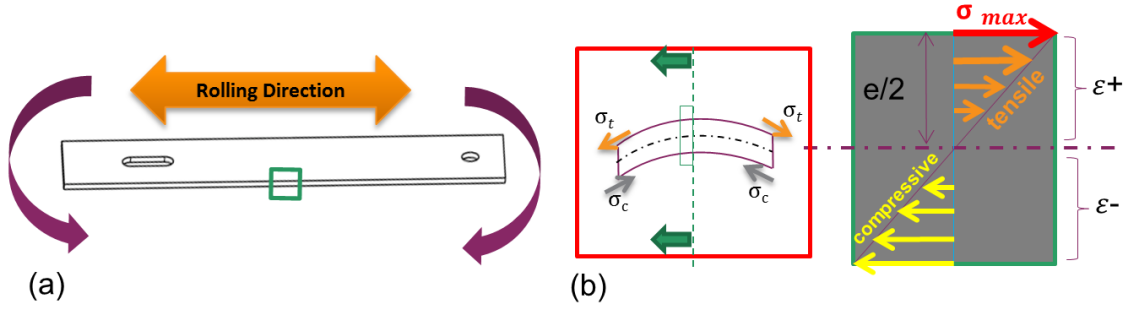


Figure 6.2: (a): The sample being curved around its transverse direction, and normal to the rolling direction. (b): The stress and strain profiles over the sample's cross-section.

$$\varepsilon_{\text{tot}} = \frac{e}{2R} \quad (6.1)$$

Where ( $e$ ) is the sample thickness (Fig. 6.2 b), and ( $R$ ) is the radius of curvature of the support as shown in Fig. 6.1 (b).

For samples strained by a radius of curvature  $R = (800, 500, 333)$  mm, the strains calculated by Eq.6.1 are  $\varepsilon_{\text{tot}} = (0.1, 0.16, 0.24)$  % respectively. By Hook's law, this strain can be related to the stress in the elastic domain by Eq.6.2:

$$\sigma_1 = \frac{Ee}{2R} \quad (6.2)$$

This relation is valid only if the stress remains below the elastic limit. For the 0.1 % $\varepsilon$ , using Eq.6.2, the corresponding applied stress is equal to 210 MPa. However, the supports exerting higher strain values; (0.16 and 0.24) %, Eq.6.2 gives (517 and 345) MPa respectively. This would count to the stress if the material was perfectly elastic. Due to plastification, the stress value would be lower than those calculated above. Thus, Eq.3.1 can be used to solve for the actual value of stress corresponding to these applied strains.

This is possible by defining a parameter  $\alpha = K(\frac{\sigma_o}{E})^{n-4}$ , which relates the material constant ( $K$ ) and the yeild strength of the material ( $\sigma_o$ ).

Rewriting the second term of Eq.3.1 using  $\alpha$ , this gives:

$$K(\frac{\sigma}{E})^n = \alpha \frac{\sigma}{E} (\frac{\sigma}{\sigma_o})^{n-1} \quad (6.3)$$

By making this replacement in Eq3.1, Ramberg-Osgood equation becomes:

$$\varepsilon = \frac{\sigma}{E} + \alpha \frac{\sigma}{E} (\frac{\sigma}{\sigma_o})^{n-1} \quad (6.4)$$

Having the values of the applied strains (0.24, and 0.16) % $\varepsilon$ , the corresponding stresses can be calculated for by iterations using Eq.6.4, which gives (280, and 250) MPa respectively.

Table 6.1 gives a summary of the supports used and the stress and strain values they provide. A reminder that the material's true elastic limit ( $\sigma_{0.2\%}$ ) was found to be 250 MPa in the rolling direction as was shown in section 2.2.3. This means that the sample remains in the elastic zone when R800 and R500 supports are used, while it undergoes plastificaion with R333 support.

The stress calculation made here was verified by finite element methods (Abaqus) in Appendix C, which confirmed these calculations.

Table 6.1: Stress and strain values provided by the curved supports.

$R[\text{mm}]$	800	500	333
$\varepsilon[\%]$	0.1	0.16	0.24
$\sigma [\text{MPa}]$	210	250	280

## 6.2 Experimental Procedure:

This part of work concerning SCC tests falls into two main categories: immersion tests and AESEC flow cell tests. The following sections explain the experimental conditions used for them.

### 6.2.1 Immersion tests

The first is a classical immersion test where severe conditions were used by the solution concentration and the applied stress and test duration. For this part, two samples with  $\sigma = (250, 280)$  MPa were left in immersion for 21 days in 2 M  $\text{H}_2\text{SO}_4$  and 2 M NaCl at room temperature. The choice of the composition of the solution was based on the necessity to have a chloride content, which accelerates SCC production. However, the selection of sulfuric acid is due to its anion ability to give a great stabilizing effect on the repassivation process [160]. The purpose of these experiments is to get a severe attack, where the basic post analysis might be made. Based on these results, the conditions were modified to be more controlled for the next experimental set.

### 6.2.2 Flow electrochemical cell tests

In the second experimental set, less chloride concentration, and less applied stress was used. Namely; 2 M  $\text{H}_2\text{SO}_4$  and 0.5 M NaCl at room temperature was, with stress value of  $\sigma = 210$  MPa. For this case, the chemical cell of AESEC system was used [131]. These experimental conditions allowed more control in terms of experimental time, and exposed surface area, in addition to the possibility to record/apply the electrochemical current and potential. Using this cell, stressed and unstressed samples were subjected to OCP corrosion tests. The purpose is to in-lab produce SCC within a reasonable period of time; in an order of a day. Several tests are made to study the kinetics of cracking and the crack propagation rate. Post analysis included SEM observation, EDS, EBSD, and XRD stress analysis. In-situ analysis of the surface OCP potential evolution and leaching solution concentration is possible.

## 6.3 Results and Discussion

### 6.3.1 Classical immersion tests

Both samples showed visible cracks after the 21 days of SCC immersion test. The following analysis was made to characterize the resulting samples.

#### Post-experimental SEM observation

The topography of the upper surface and the cracking profiles has been observed by SEM. Fig. 6.3 to 6.5 show the resulting images.

Since the produced cracks were very well developed in the depth of the sample, characterizing the crack fractography of the produced cracks was of interest. For this, the sample of  $\sigma = 250$  MPa was chosen. One of the cracks was opened such that SEM analysis can be made for its facet. Fig. 6.4 shows the crack facet on (ND,TD) plane below the dashed line, while the upper surface exposed to the electrolyte is (RD,TD) plane above this dashed line.



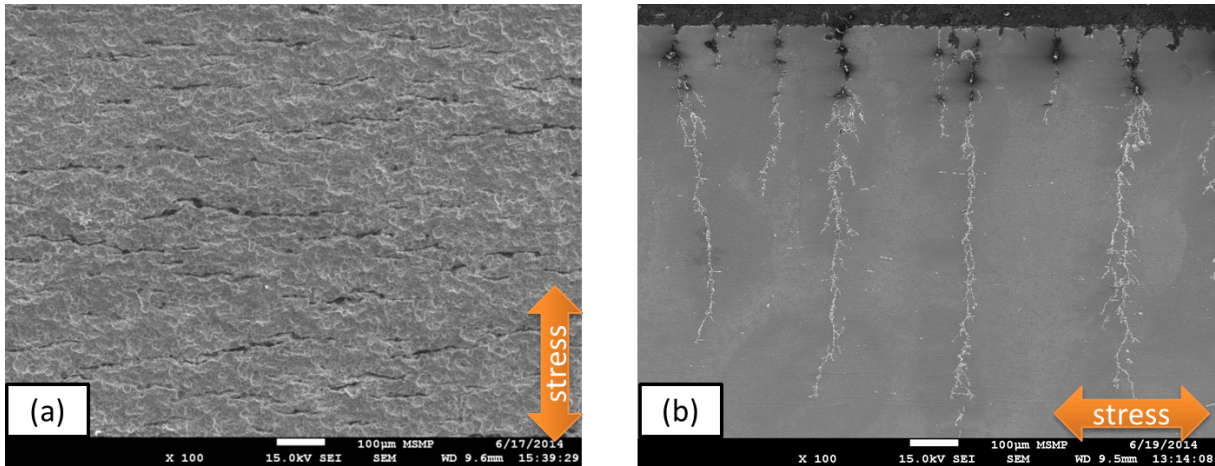


Figure 6.3: SEM observation of SCC of  $\sigma = 250$  MPa after 21 days in 2 M  $\text{H}_2\text{SO}_4$  and 0.5 M NaCl (a): The sample upper surface exposed to corrosion. (b): The cross-section showing the cracking profile.

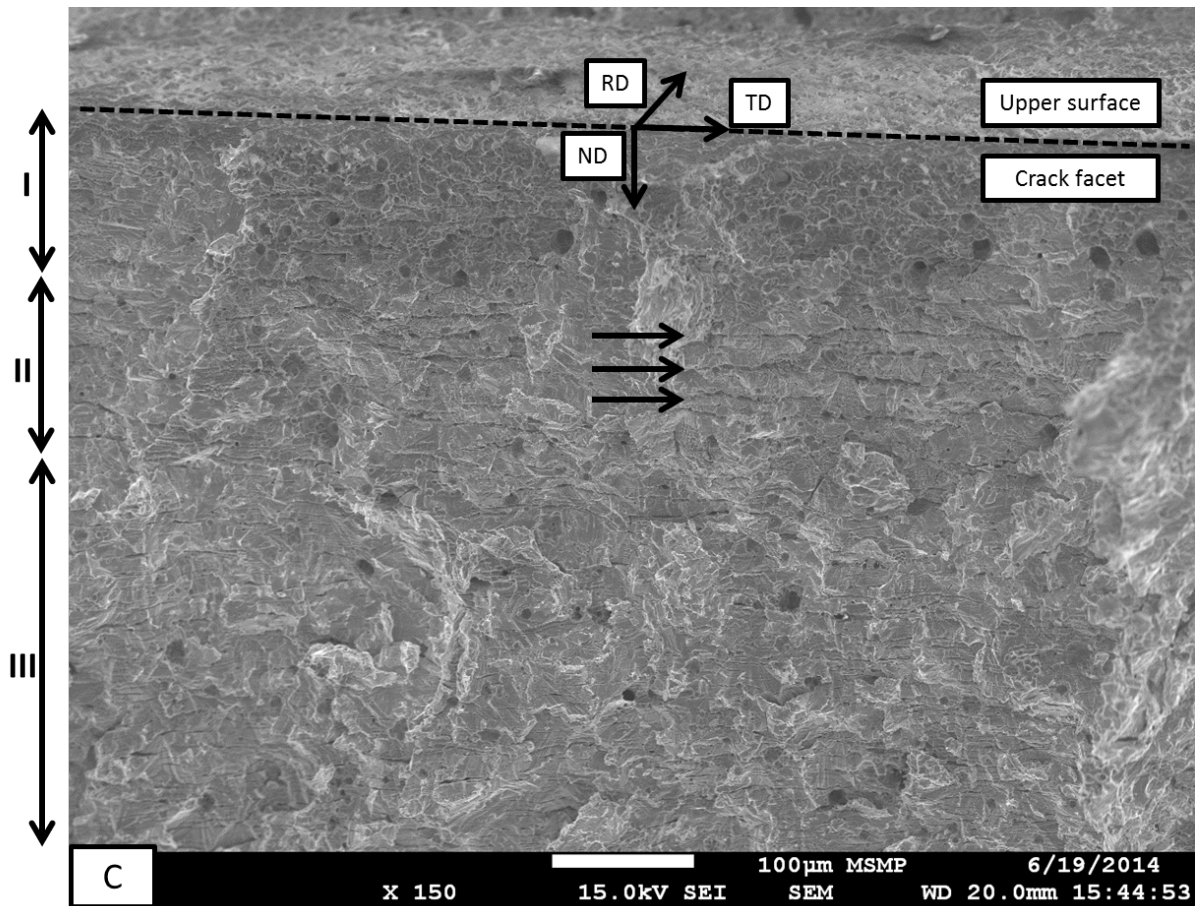


Figure 6.4: SEM observation of SCC crack facet of  $\sigma = 250$  MPa after 21 days in 2 M  $\text{H}_2\text{SO}_4$  and 0.5 M NaCl.

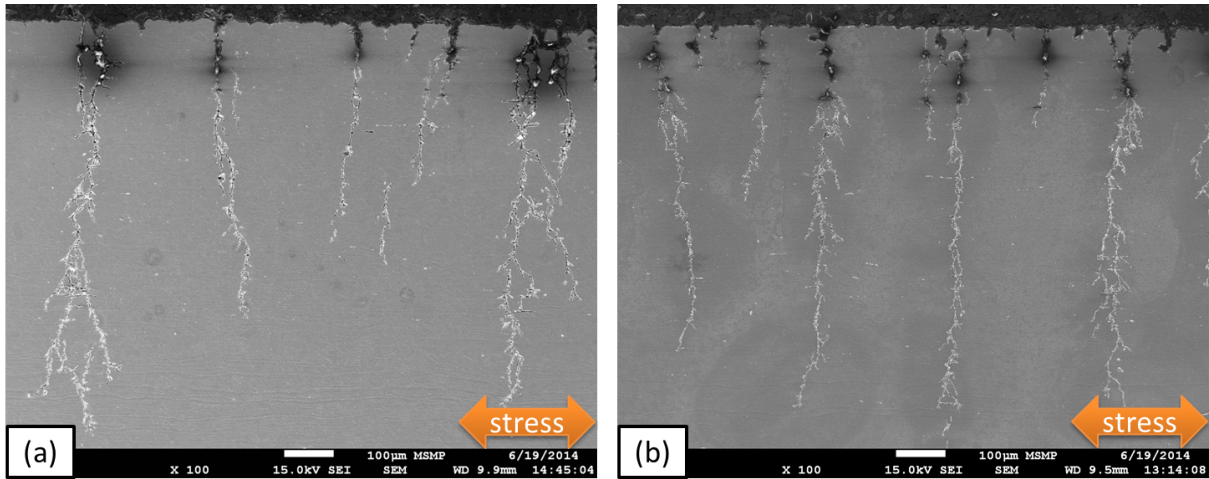


Figure 6.5: Cross-section showing SEM observation of SCC after 21 days in 2 M  $\text{H}_2\text{SO}_4$  and 0.5 M NaCl of (a):  $\sigma = 250$  MPa. (b):  $\sigma = 280$  MPa.

### Corrosion regimes and slipping traces

Fig. 6.4 shows three different corrosion regimes I, II, and III. Regime (I) corresponds to an aggressive corrosion after the crack propagation over the entire experiment. Following this is regime (II) where the three parallel lines indicated by the arrows in Fig. 6.4 are traces of the step wise mode of crack propagation. This might correspond to locations of slip system activation, followed by dissolution of freshly exposed surface. This stands as evidence in favor of the slip-dissolution based models. Such results were found by Parkins and others [141, 36]. The last regime is (III), which represents the rapid propagation of SCC, where the cracks have grown to make large decohesive crack coalesce with cleavage and fluting features. Such results were found by Russell [157], and Meyn [118]. These regimes can be seen even on the cross-sectional view, as given by Fig. 6.5. This cracking behavior is in agreement with cracking kinetics described earlier in section 1.9.4 which was proposed by Parkins [36, 143].

### Effect of stress on crack initiation sites

As seen from Fig. 6.5, the sample having higher stress value had more crack initiation sites. This result reinforces the role of stress on crack initiation.

This comes in agreement to the explanation given by Robertson and Tetelman [10], which was presented in section 1.10. Higher stress value will have a higher probability to produce Cottrell-Lomer sessile dislocations, which undergo preferential chemical dissolution, leading to crack site nucleation. Though conclusions concerning the effect of stress on crack length cannot be made here due to the very long experimental time in such aggressive environment, but cracks tended to be longer where higher stress was applied. On the other hand, for features of the upper surface topography after the test, no clear difference was detected between the two samples since their surfaces were totally altered by general corrosion after cracking, as seen in Fig. 6.3.

### Post-experimental EBSD characterization

Three cracks were selected to be analysed in this section. The orientation map shown in Fig. 6.6 is one of them. This is related to  $\sigma = 250$  MPa sample.

It's clear on this orientation map how in some cases, the cracking was of TGSCC type, while for the most cases the crack facet was severely attacked causing the loss of the fine details required for characterization.

For the other sample where higher stress of  $\sigma = 280$  MPa was used, EBSD map revealed no information about cracking mode. No ruptured grains by TGSCC were detected due to the



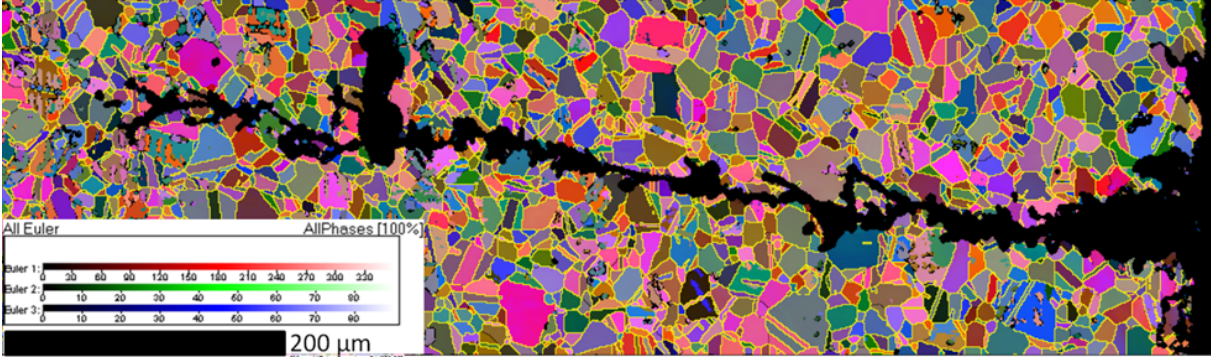


Figure 6.6: All Euler EBSD map after 21 days SCC,  $\sigma = 250$  MPa test in 2 M  $\text{H}_2\text{SO}_4$  and 0.5 M NaCl.

severe attack of the cracks facets. This might indicate that either cracking was intergranular or the cracked grains were totally dissolved during the corrosion test, and sample preparation for EBSD analysis. Same conclusion can be stated about the non-TGSCC path shown in Fig. 6.6.

### Orientation of the cracking planes

Having the EBSD map for the crystallographic orientation of the grains made it possible to analyze the cracking planes. The interest was to check if the cracking plane has any crystallographic common features. Thus, the ruptured grains were first isolated as shown by the dark half-grains in Fig. 6.7.

From the crack gross path within a grain, a straight line was assumed as the edge view of the cracking plane. An assumption is made here is that this plane is perpendicular to the sample's cross-sectional plane. To verify the validity of the perpendicularity assumption, four consequent polishing steps were made for a selected cracking zone on the sample's CS. Each step included the removal of 3 to 5  $\mu\text{m}$ , followed by EBSD mapping of the obtained surface. The results revealed that the perpendicularity assumption is applicable to most of the grains.

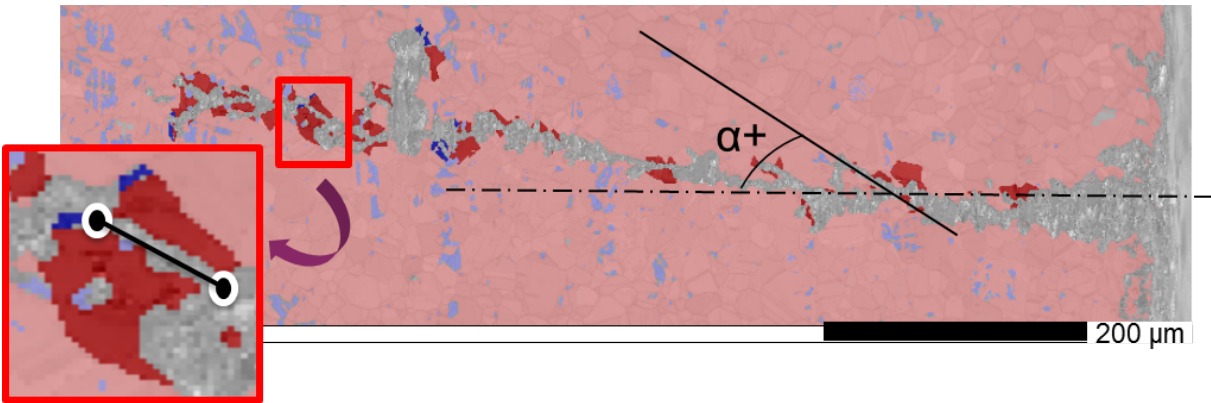


Figure 6.7: Isolation of TGSCC grains in EBSD map.

The EBSD map shown in Fig. 6.7 is one map among three that were used in this analysis. The required information to determine the orientation of the cracking plane can be stated as:

1. The three Euler angles defining the crystallographic orientation of the cracked grain,  $(\varphi_1, \phi, \varphi_2)$ , as shown in Fig. 6.8.
2. The crack orientation,  $\alpha$ , based on a straight line drawn in the path of the crack.
3. The rupture plane is assumed to be perpendicular to the surface.

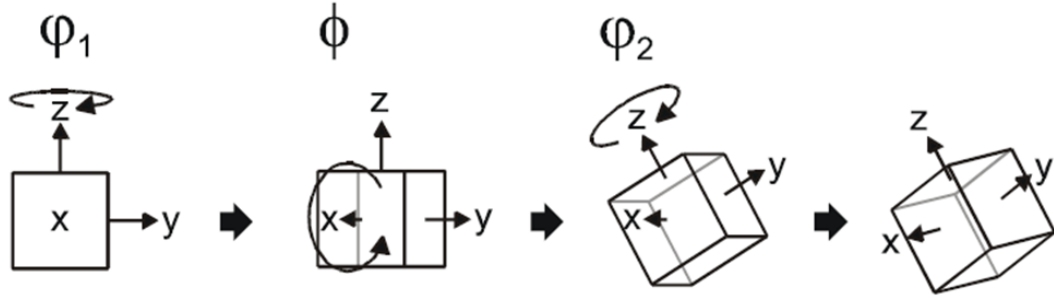


Figure 6.8: The three Euler angles defining the crystallographic orientation of the concerned grain,  $(\varphi_1, \phi, \varphi_2)$ . From [138].

**Example case:** for one of the analyzed grains, the Euler angles  $(\varphi_1, \phi, \varphi_2)$  were  $(347, 38, 51)^\circ$ , and the crack tilt angle from the horizontal was  $\alpha = +18^\circ$ . The resulting geometry is illustrated in Fig. 6.9. With the assumption that the rupture plane is perpendicular to the surface, the line shown in Fig. 6.9 will be the edge view of  $\{111\}$  planes. The crystalline orientation as presented in Fig. 6.9 was produced based on the given three Euler angles, using Twist software of CHANNEL 5 suite of programs [138].

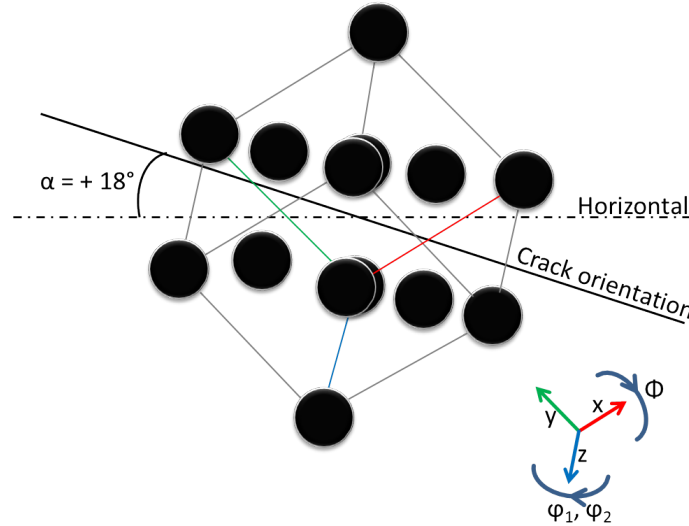


Figure 6.9: Cracking plane determination using Euler angles and the crack inclination.

From the three EBSD maps of the obtained cracks, 20 TGSCC grains were identified and analyzed as given in the example above. Four plane families were determined as the cracking plane, namely:  $\{110\}$ ,  $\{111\}$ ,  $\{211\}$ ,  $\{100\}$ , as given in Table: 6.2.

Table 6.2: Statistics of the cracking orientation for 21 SCC test of  $\sigma = 250$  MPa sample in 2 M  $\text{H}_2\text{SO}_4 + 2$  M NaCl.

Plane family	$\{111\}$	$\{110\}$	$\{211\}$ and $\{100\}$
Counts	7	9	4

The rupture plane showed to be preferential on  $\{110\}$  and  $\{111\}$  plane families, with percentages of 48% and 37% respectively. According to FRM, SCC takes place as repetition of cycles of passive film breakdown, dissolution, until it repassivates again. Slipping system in face centered cubic crystals is activated over  $\{111\}$  planes. This result confirms previous studies

performed by Scully et. al [70] and by Robertson [10]. On the other hand,  $\{110\}$  family of planes will be the cracking plane in FCC system if equal number of dislocations pile-up on the primary and conjugate  $\{111\}$  slip planes [143, 178]. These conclusions are in agreement with recent models explaining the cleavage-like cracking along the low-index planes in TGSCC such as AIDE (section: 1.8.2), and CELP (section: 1.8.4) models which were explained earlier.

### 6.3.2 Flow cell OCP SCC tests

#### Post-experimental SEM observation

For all the tests here, unless else stated, the initial surface state was as received, preceded by ultrasonic cleaning in ethanol for 15 min. Regardless of the initial surface state, upper surface observation was conducted to all tested samples before and after the SCC test. In post-experimental analysis, the cross section of each sample was subjected to SEM.

As Fig. 6.12 shows, corrosion features started to appear starting from 3 h in the form of flaking the upper surface. This flaking seems to be smoothed later at 8 h due to general surface dissolution. First cracking initiation were detected on the upper surface starting from 8 h of exposure to the corrosive flow, as seen in Fig. 6.10 to Fig. 6.13. As the solution was less aggressive than that used in the classical immersion tests (section 6.2.1), the surface observation reveal several interesting crystallographic features.

**Crack initiation:** Figure 6.10 illustrates the nucleation of possible cracking sites. An initial TGSCC site is nucleating in one grain as shown by the arrows holding number (1), while intergranular corrosion is spread in multiple locations as shown by arrows (2). Among those two kinds, several parallel crack initiation sites are accumulated in grain (A), which probably follow the direction of its crystallographic planes. Thus, nucleation can have any possible direction (normal or parallel to stress direction) and it could be either TGSCC or IGSCC.

More developed cracks were detected at 16 hours of exposure, as shown in Fig. 6.11 (a). What's interesting about this TGSCC is the crack tip inside the grain which is zoomed in Fig. 6.11 (b). Such fine near-tip features were detected in several other locations. Fig. 6.10 (b) shows another grain where parallel cracks have this sharp fine near tip feature, confirming that this is related to local crystallographic planes.

These are new evidences on crack nucleation and its relation to the direction of the applied stress, and the local crystallographic order.

#### Crack propagation kinetics

SCC tests with samples of  $\sigma = 210$  MPa in 2 M  $\text{H}_2\text{SO}_4 + 0.5$  M NaCl. Test durations were: 16, 21, 42, 88, and 125 h. SEM observation of selected upper surface and cross sections are shown in Fig. 6.12 and 6.13. For comparison, Fig. 6.13 (g) shows the developed cracks at no applied load conditions (only residual stress), which will be discussed later in section: 7.5.

Their cross sections were studied in order to measure the depth of the cracks found in each of them. Table 6.3 below makes a summary about the obtained results.

In this table, we have the average length of the cracks observed at the cross sections of each sample.

The fact that the crack has a semi-elliptical shape makes the interpretation of the measured lengths not straight forward. The location at which the cross section has been made might have passed through the mid of this semi-elliptical shape, or at the edge where it's almost seen as a pit, or somewhere in between which makes it appear shorter than its reality. Thus, to compare SCC tests of different periods, the criterion of average crack length might be taken with caution. Another effective way of comparison could be the maximum crack length. Estimation of the statistical validation of these measures are performed in section: 7.4.

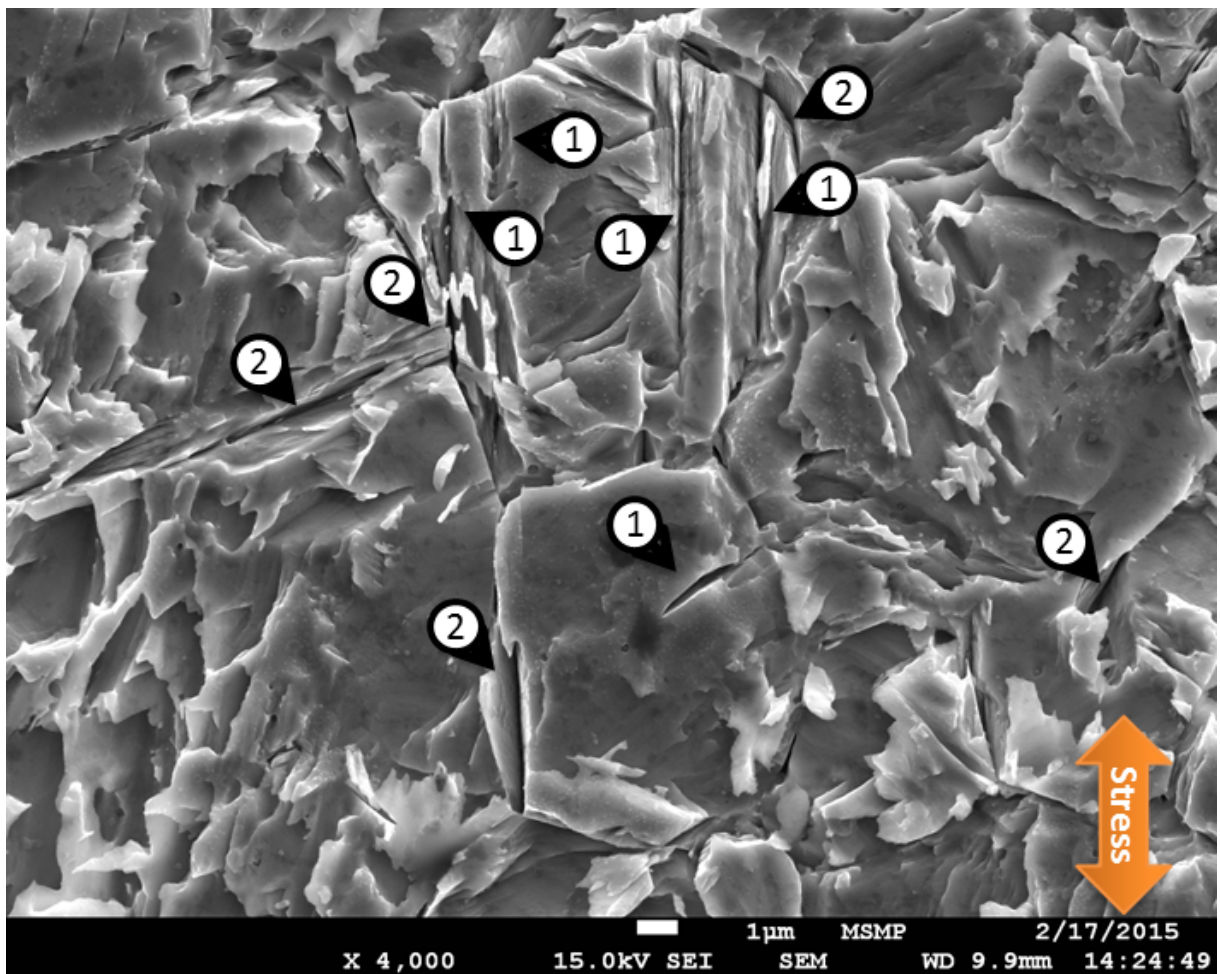


Figure 6.10: Post experimental SEM observation SCC 8 h OCP test, upper surface. Arrows (1): TGSCC. Arrows (2): IGSCC.

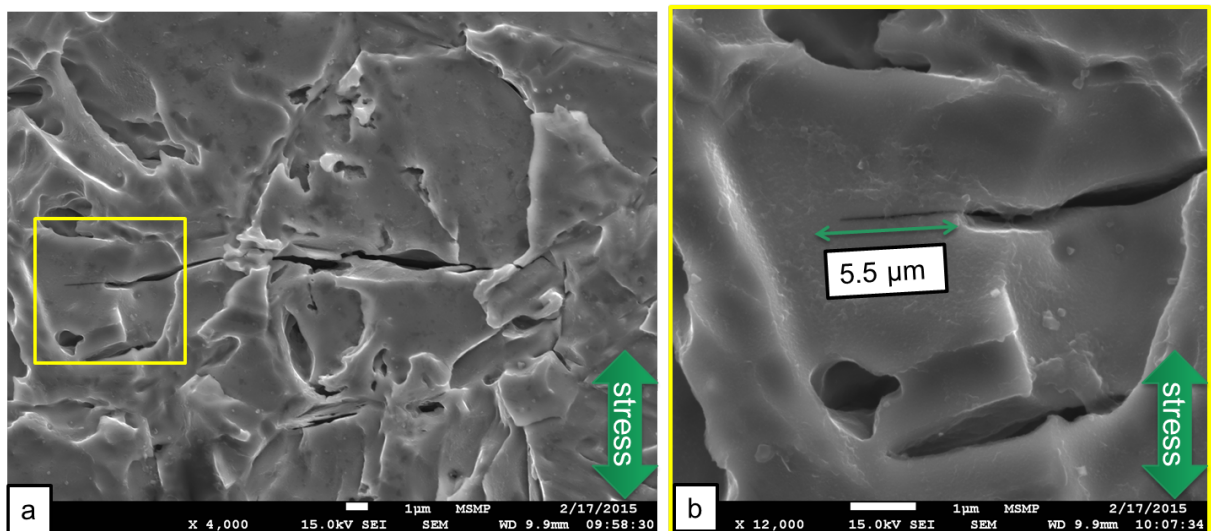


Figure 6.11: (a): SCC 16 h OCP test, showing TGSCC having very fine crack endings. (b): The selected zone of interest surrounded by the rectangle in (a) of this Figure.



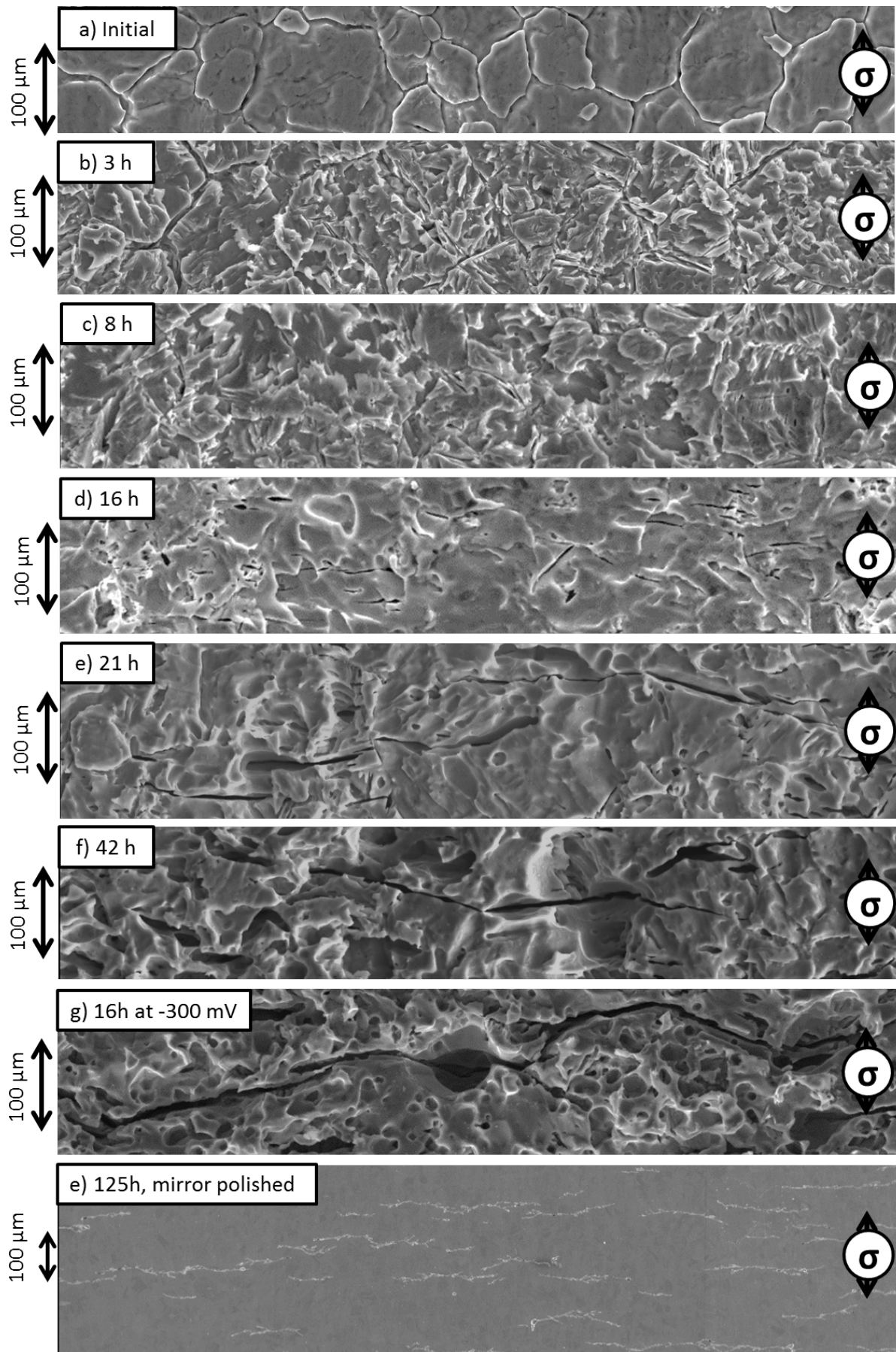


Figure 6.12: Kinetics of SCC by OCP test, upper surface. The direction of the applied stress is indicated by the ( $\sigma$ ) arrows.

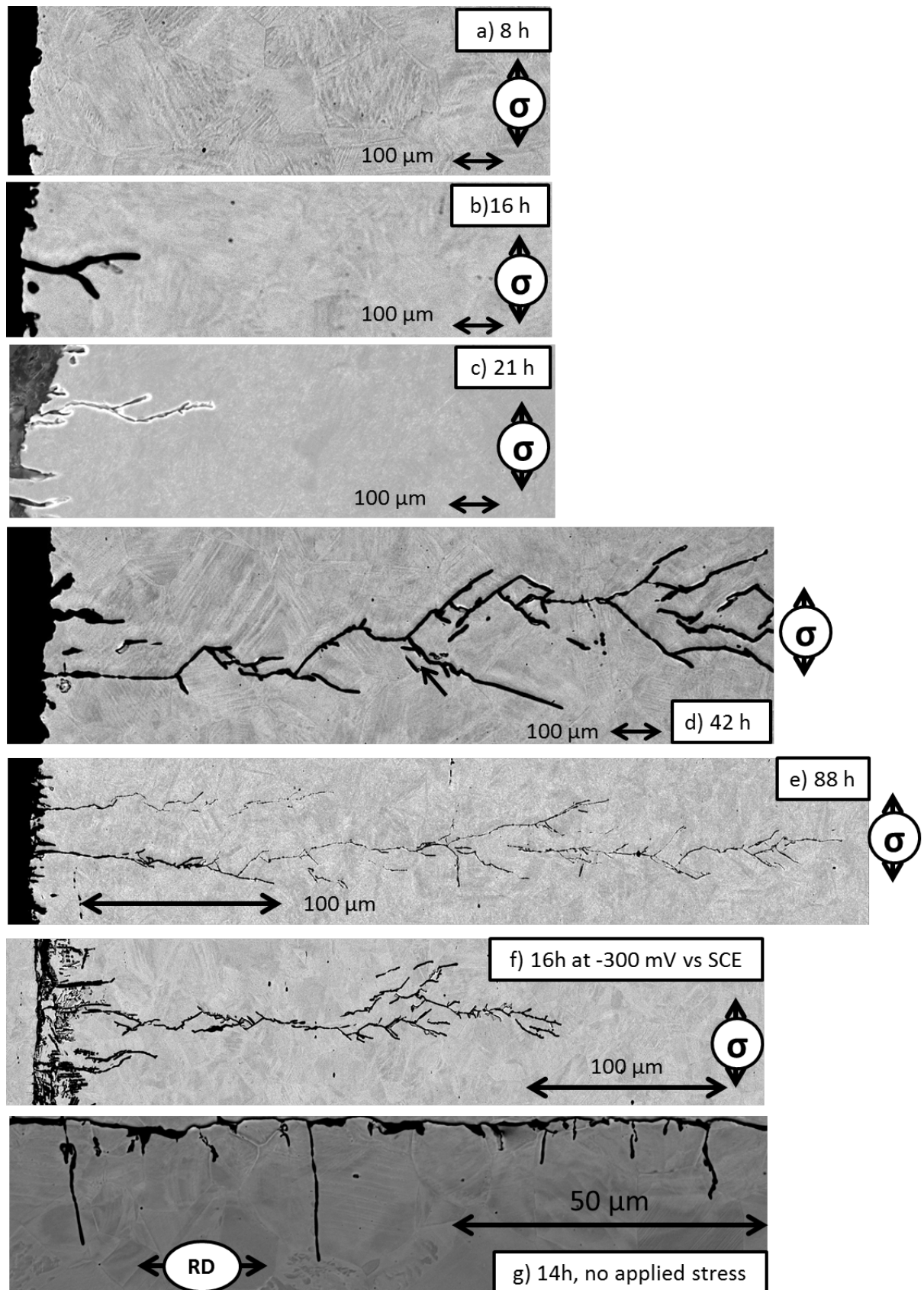


Figure 6.13: Kinetics of SCC by OCP test, cross-sectional view. RD: the rolling direction.



Table 6.3: Statistical analysis of crack depth ( $L$ ) over the different SCC test periods. ZOI: Length of the zone of interest.

Time /[h]	Number of cracks	ZOI [ $\mu\text{m}$ ]	Density [crack/mm]	avg ( $L$ ) [ $\mu\text{m}$ ]	stdv( $L$ ) [ $\mu\text{m}$ ]	Max. ( $L$ ) [ $\mu\text{m}$ ]	d $L$ /dt [ $\mu\text{m}/\text{h}$ ]
16	53	4049	13	21	12	83	1.3
21	70	3544	20	27	11	56	1.3
42	52	4407	12	93	52	174	3.1
88	51	4557	11	245	151	414	3.3
125	45	4510	10	360	218	697	3.1

**Two distinct propagation rates:** The crack propagation rate ( $dL/dt$ ) is calculated based on the average crack length evolution between a test and the previous interval. This revealed that the crack propagation rate has two distinguished values rather than being constant over the different experimental values. For the interval between 16 h to 21 h, it was  $1.3 \mu\text{m}/\text{h}$ . While for the three intervals (21 to 42) h, (42 to 88) h, and (88 to 125) h, the propagation rate was about three times the initial value.

**Cracking-site density:** Apart from 21 h SCC experiment, the number of cracks per length seems to be the same for all the experiments ( $11 \text{ crack}/\mu\text{m}$ ). This indicates that the number of crack initiation sites is not increasing with time. This result is reasonable; since crack initiation on the upper surface has a vital requirement, which is the existence of stress. Once the cracks are initiated almost simultaneously, they start to propagate, causing stress relaxation behind the crack front, and consequently limiting any new crack initiation on the upper surface.

**Cracking path and re-orientation:** Another important aspect to consider is cracking path, and the influence of microstructure on it. Figure 6.14 shows the cross section of a 42 h OCP SCC test in  $2 \text{ M H}_2\text{SO}_4 + 0.5 \text{ M NaCl}$  with  $\sigma = 210 \text{ MPa}$ . In this photo, the crack alters its direction in a regular way, which made it a suitable investigation site. This is the same location which was selected to verify the perpendicularity assumption, which is discussed in the next paragraph.

**Perpendicularity assumption:** to verify the perpendicularity assumption, SEM images and the corresponding EBSD maps (Fig. 6.15 to 6.18) are provided for a selected cracking zone. This SCC test was made in  $2 \text{ M H}_2\text{SO}_4 + 0.5 \text{ M NaCl}$ , for a sample of a non-polished initial surface. Four EBSD maps were done with surface removal steps by mechanical polishing of  $3\text{--}5 \mu\text{m}$ . For the preparation to EBSD test, the surface where mirror finished, with a slight electrochemical polishing in oxalic acid. By this, the perpendicularity assumption of TGSCC can be accepted over an estimated depth of  $16\text{--}20 \mu\text{m}$ , covering the average grain size of the material in hand.

According to the SEM images and EBSD maps (Fig. 6.15 to 6.18), the crack initiated by a TGSCC at location (1). The initial direction follows from an intergranular surface crack such as that shown in 6.11, propagating in a perpendicular direction to the tensile stress. This situation gets altered at the branching location (A), was revealed by the corresponding EBSD maps to be due to encountering a grain. The boundaries of this grain were oriented in a way that caused the re-orientation of the crack. A similar description can be made about the branching site (B). After the effect of grain boundary is over, the crack gets back to be of TGSCC type as shown at location (2,3,4,5, and 6).

Investigation of the grain boundary orientation which favors the crack re-orientation was conducted on site (A) and (B), as indicated by the blue angles. It turns out that grain boundaries were oriented by  $45^\circ$  and  $42^\circ$  from the horizon at location (A) and (B) respectively. For an element undergoing tensile stress in plane stress conditions, the maximum shear stress is on

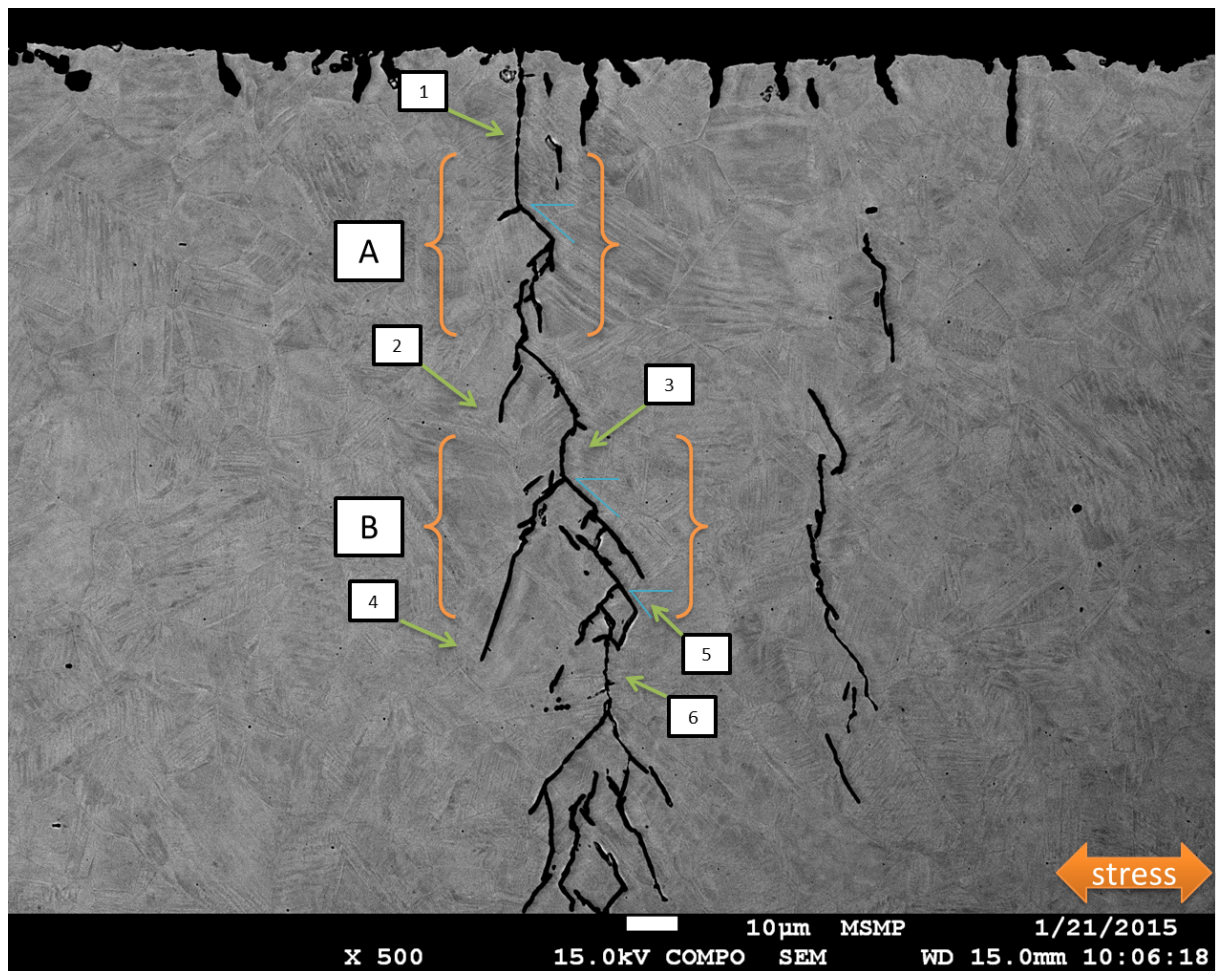


Figure 6.14: Re-orientation of cracking path by microscopic features. Cross-section of a 42 h OCP SCC test in 2 M  $\text{H}_2\text{SO}_4$  + 0.5 M NaCl with  $\sigma = 210$  MPa.

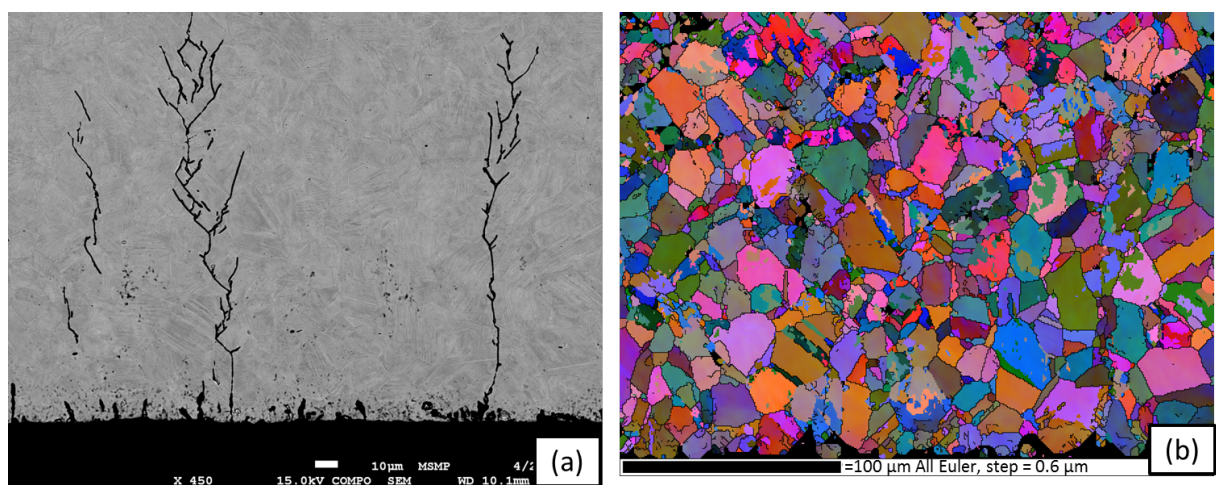


Figure 6.15: Initial surface for step-wise orientation maps.



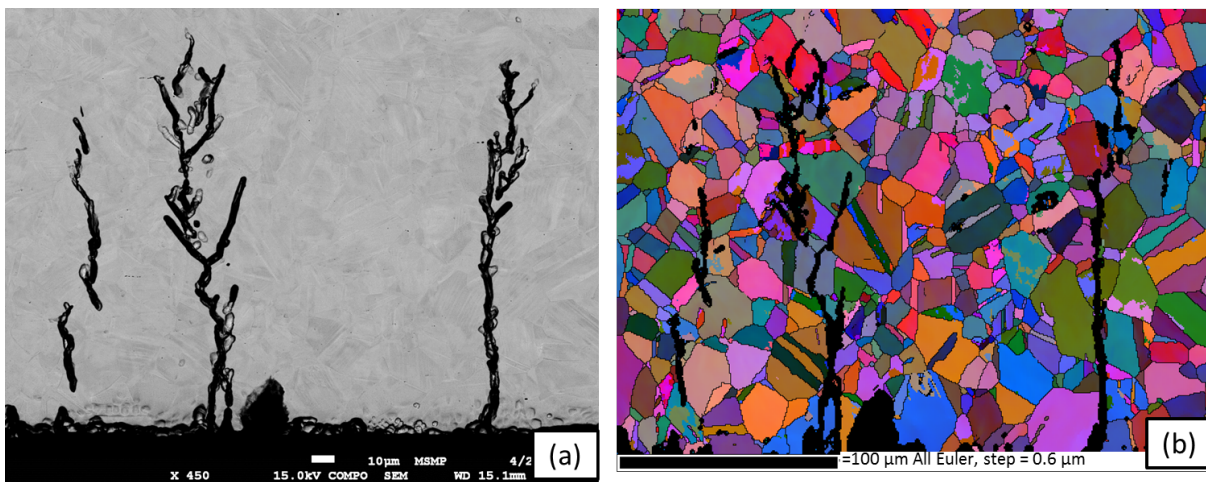


Figure 6.16: Second surface for step-wise orientation maps.

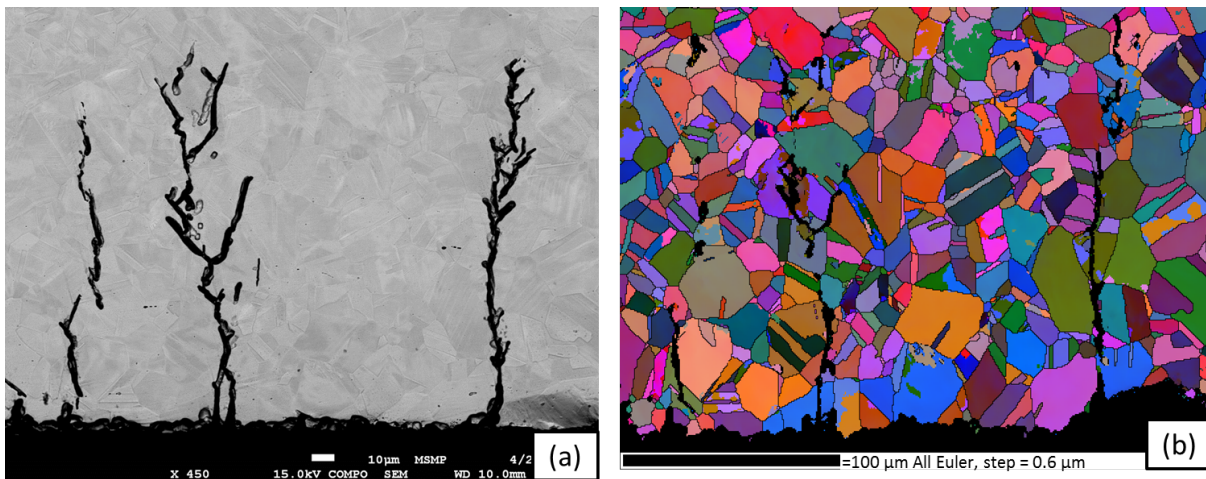


Figure 6.17: Third surface for step-wise orientation maps.

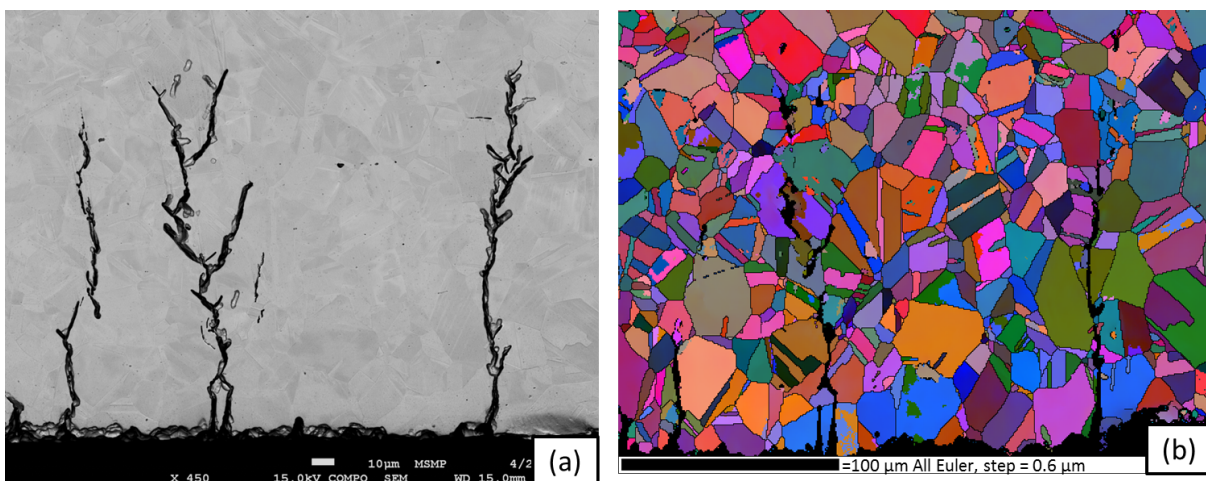


Figure 6.18: Fourth surface for step-wise orientation maps.

the plane  $45^\circ$  shifted from the applied normal stress direction, as illustrated in Fig. 6.19. This explains the re-orientation of the crack in to follow the grain boundary orientation.

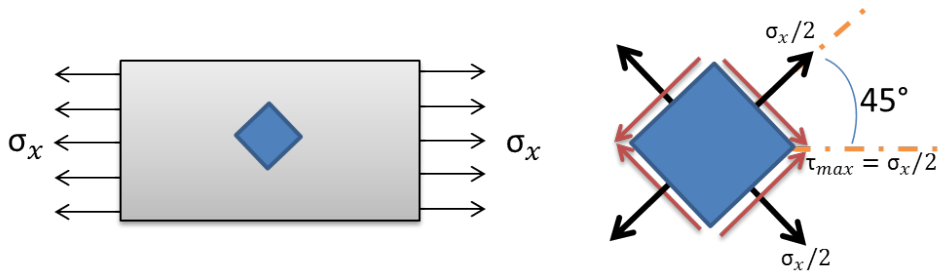


Figure 6.19: The object in blue represents a grain with boundary orientation corresponding to the plane of the resolved maximum shear at  $45^\circ$ .

On the other hand, the case was different for the 2 parallel cracks indicated by (5), which are crossing the same grain by a TGSCC, both the same orientation of  $55^\circ$ . This is believed to be due to the crystallographic planes of this grain, and this makes part of the preferential TGSCC orientations studied in section 6.3.6.

**The coincidence site lattice for IGSCC:** The characterization of the coincidence site lattice (CSL) of the grain boundaries was in most of the times not possible due to the dissolution of these boundaries either during the SCC test, or during sample preparation for post analysis. However, in rare cases, such as those shown in Fig. 6.20, the CSL was detected, and it was always of  $\Sigma 3$  type. This is the weakest interface between grains, where only one atom is shared between the two-grain lattice structure among each three atoms. Nevertheless, statistically, as seen from this map in Fig. 6.20,  $\Sigma 3$  CSL is the dominant type of granular interface (all red boundaries) in this material.

On the other hand, as shown by the yellow arrows, the TGSCC seems to cut grains, even when twin formation is included in those grains as shown by the yellow arrows. Thus, the path that the crack takes depends on the local condition, including the grain geometrical orientation of its boundaries, and the type of intergranular interface (CSL).

### OCP evolution durint SCC tests, and SCC acceleration

The OCP evolution during the SCC test shown in Fig. 6.21 was reproducible in all tests, as given in this figure for two different tests (42 hours and 88 hours). The initial surface state is passive, having an OCP value of 510 mV. Passivity break-up takes place in a steep gradient of potential at 15 min of surface exposure duration to the electrolyte. The cathodic peak at about 40 min and the OCP variations afterwards reflects the surface state evolution as was shown in Fig. 6.12 and explained in section 6.3.2. The OCP value gets to almost a stable value around -300 mV starting from 8-10 hours of exposure until the end of the test, which was 125 hours for the longest test performed.

To check if the OCP slight gradient is related to cracking or not, SCC tests were performed at 7 and 8 hours, as shown in Fig. 6.22 (a). Cross sections show no special cracking features related to the detected variation of OCP in the time domain 5-10 h. On the other hand, pit growth and crack propagation started to be distinguished at 16 h duration. Fig. 6.22(B) shows the evolution of crack growth between 16-21 h, while no OCP variation was detected due to this period (10-20) h. Thus, the OCP value didn't change as the cracks started to propagate out of the crack initiation sites.



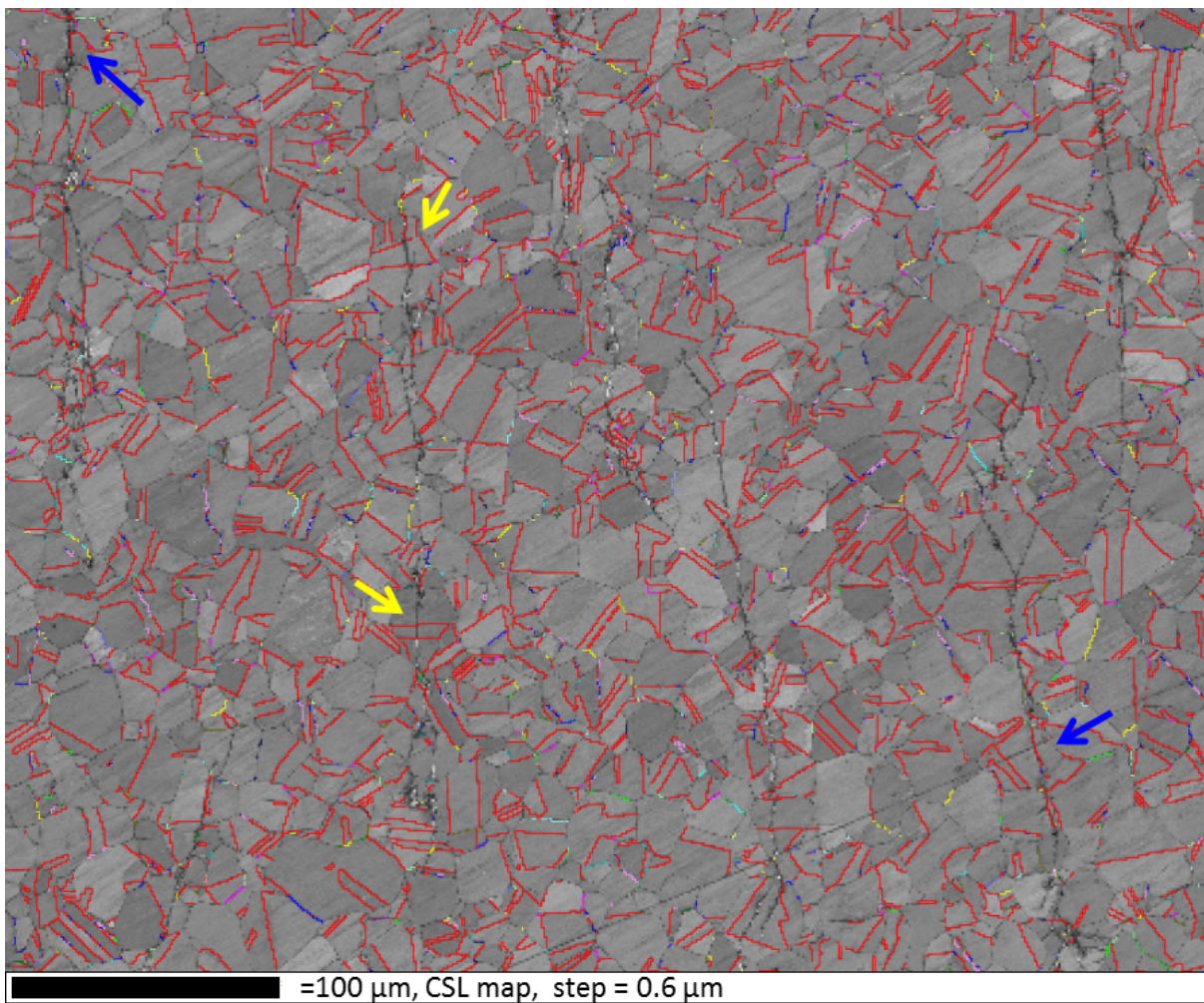


Figure 6.20: CSL interface for IGSCC (blue arrows). TGSCC is detected to traverse twins, regardless of their orientations (yellow arrows).

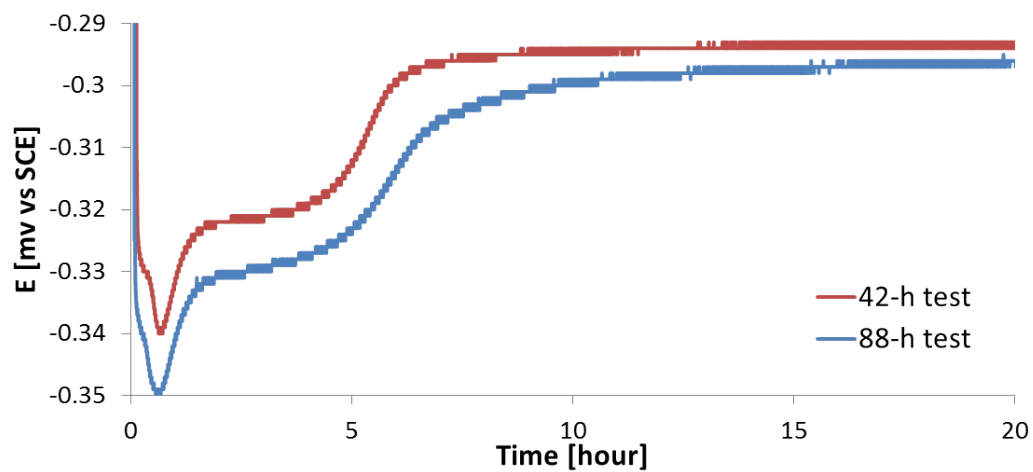


Figure 6.21: OCP evolution during SCC tests during the first 20 hours.

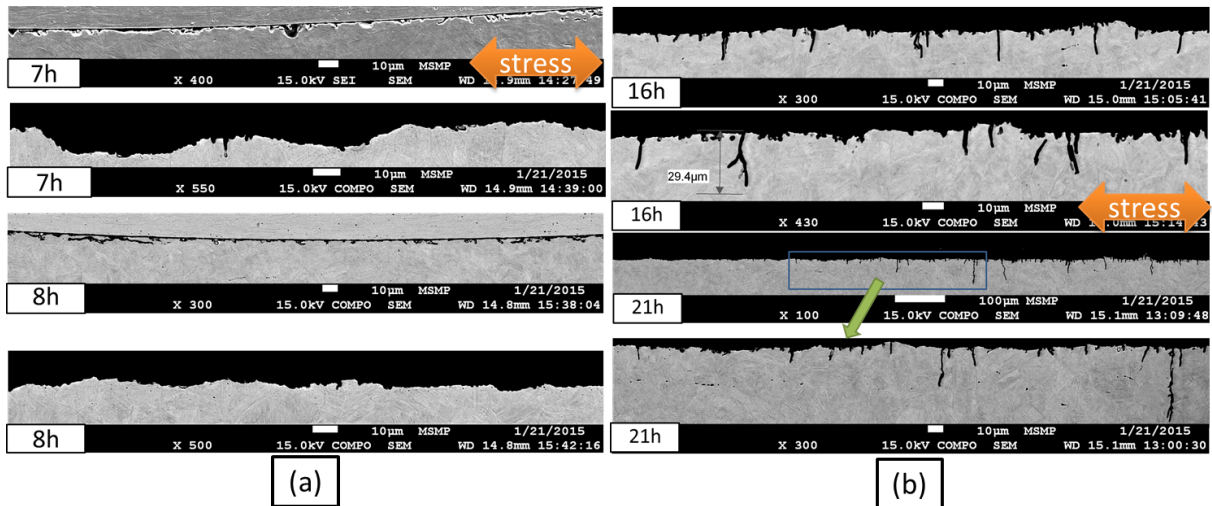


Figure 6.22: Checking if OCP evolution is related to cracking. (a): 7-8 h SCC test. (b): 16-21 h SCC test.

### SCC acceleration by an applied potential

For a given material/environment, susceptibility to SCC is the highest in three distinguished potential zones, as was shown in Fig. 2.5. The OCP evolution found in the previous section gave an idea about the potential on which SCC takes place. The steady OCP value after SCC was in the cathodic domain, which corresponds to the first SCC zone mentioned in Fig. 2.5. An applied cathodic potential pulse of -300 mV (vs SCE) over time duration of 2 hours was enough to generate cracks, while it took 16 hours when SCC tests were left to OCP values. Figure 6.23 and Fig. 6.24 show the upper surface and the cross-section of an accelerated SCC test vs OCP SCC test. For comparison with OCP kinetics, the upper surface and cross section of the accelerated test is given in Fig. 6.12 (g), and Fig. 6.13 (f) respectively.

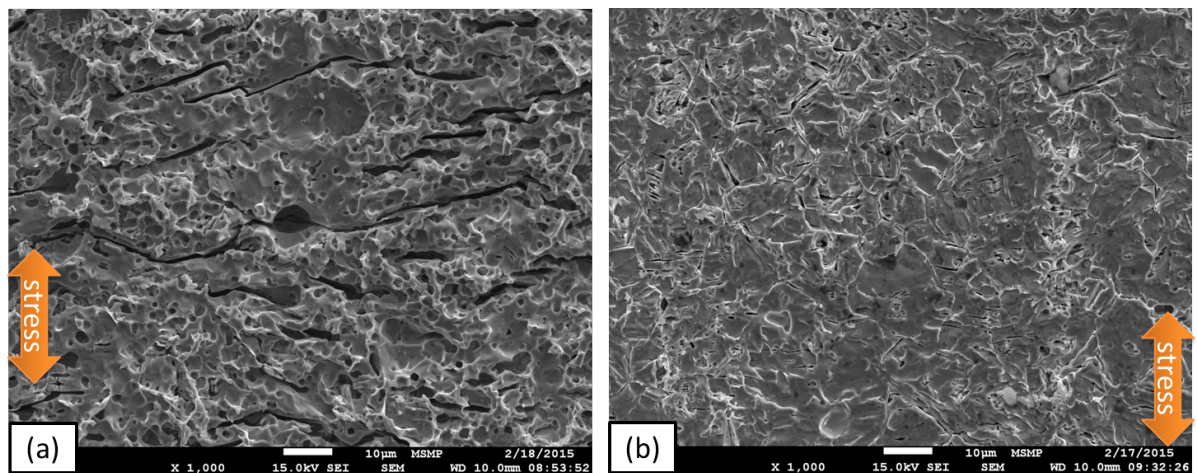


Figure 6.23: SCC accelerated tests, upper surface. (a): -300 mV (vs SCE) 16 h accelerated SCC test. (b): 16 h OCP SCC test.

It's noticed that the upper surface morphology has more roughness than that of the OCP test. The applied potential seems to enhance chances of pitting on the surface, which is much more observable in than in the OCP equivalent tests. In the contrary of the OCP test where crack initiation sites tend to have different orientations relative to the tensile stress direction, in the cathodic SCC test cracks tend to have clear perpendicular orientations.



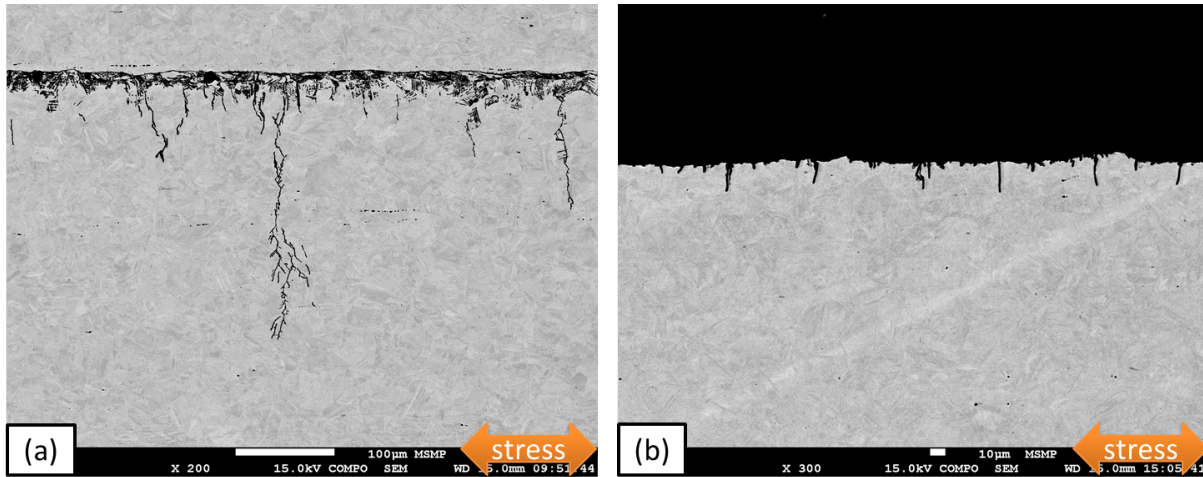


Figure 6.24: SCC accelerated tests, cross-section. (a): -300 mV (vs SCE) 16 h accelerated SCC test. (b): 16 h OCP SCC test.

### 6.3.3 Chemical composition analysis near the crack tip

Many models argue the special chemistry near crack tip. Preferential ionic/gas adsorption, or local depletion or enrichment of elements such as chromium might play a role in cracking mechanics. For this purpose, the SCC of 21 h was of special interest, as shown in Fig. 6.25. The cracks in this cross section had no excessive loss from their edges during sample preparation, and in the same time, the crack front is visible. One crack was selected from this sample for EDS analysis, where the area surrounded by the red rectangle in Fig. 6.25 (b) was analyzed. The results are given in Fig. 6.26. Though the sample seemed to have potential to reveal some information about specific crack chemistry, but the concentration maps showed no significant feature that could be related to preferential dissolution. The detection capacity of this technique might be not high enough for such analysis. Another possibility is that the interesting features has been removed during sample preparation after the SCC test.

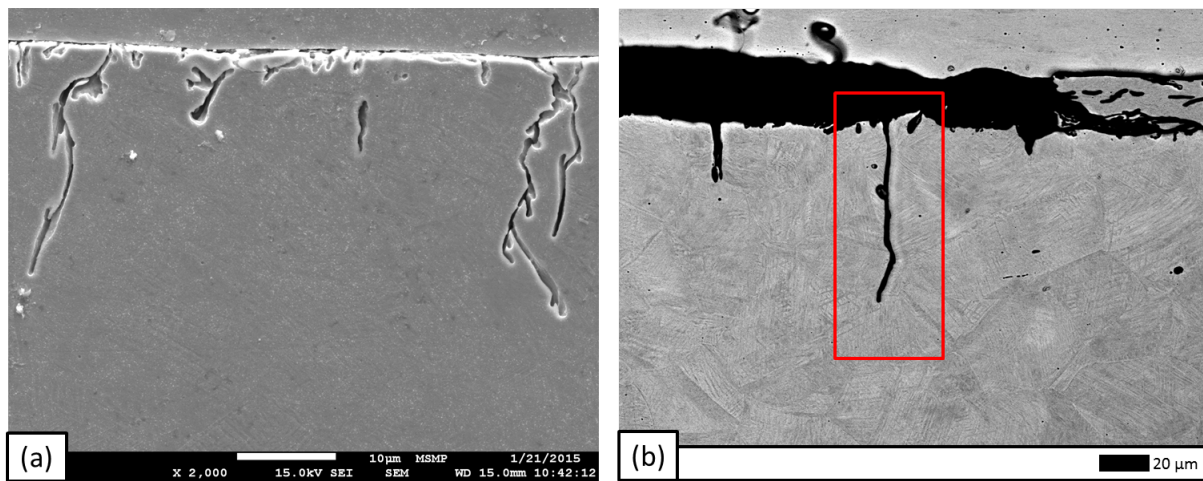


Figure 6.25: The sample selected to perform EDS analysis of the surrounding of a short crack. (a): SEM image show how the crack edges are conserved. (b): The selected crack and zone of EDS analysis (inside the red rectangle).

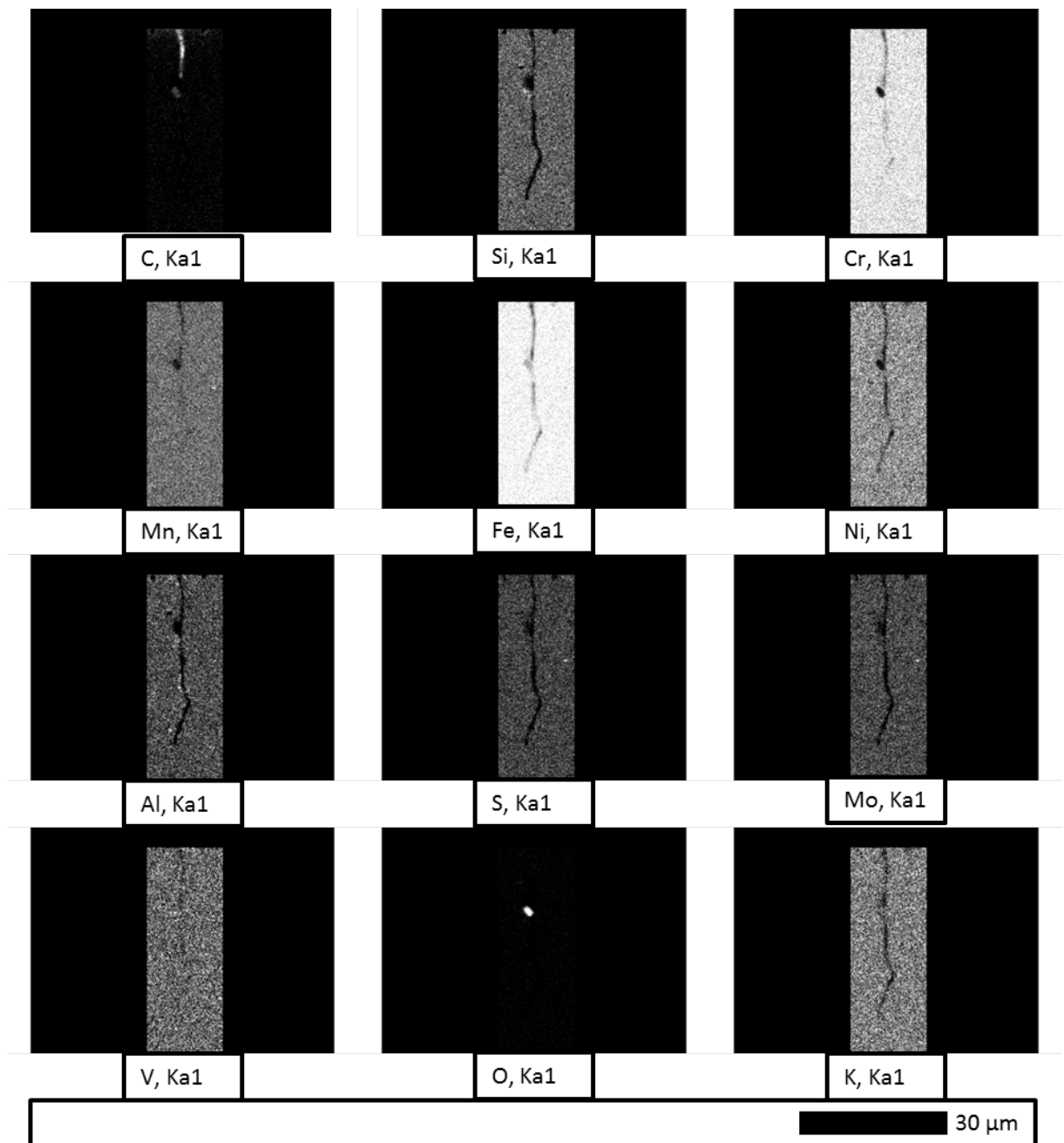


Figure 6.26: The elemental concentration maps resulting from EDS analysis of the surrounding of the short crack shown in Fig. 6.25.



### 6.3.4 Effect of surface state: polished/non-polished

To check the influence of initial surface preparation before the SCC tests on crack initiation and propagation, mirror polishing the samples was suggested. Fig. 6.27 shows the upper surface of a SCC test of 64 h, in 2 M  $\text{H}_2\text{SO}_4$  + 0.5 M NaCl with  $\sigma = 210$  MPa. An earlier stage of this test, at 14 h, is given in Appendix (J). In this figure, the crystalline slip lines  $\{111\}$  are clearly attacked preferentially. Nevertheless, this effect was much less observed on the slip lines which were parallel to the applied stress direction.

In all cases, as the red arrows indicate in Fig. 6.27 (b), the TGSCC were not along this preferential attack. As a matter of fact, the direction of the crack initiation is not related to the direction of the slip lines. However, this preferential attack brings up tiny tunnels at the conjunction of the Lomer-Cottrell sessil, where dislocations pile up. These tunnels generate high local stress, especially if they are sufficiently close to each other, leading to over passing the  $K_I$  value, and consequently the coalescence which generate a micro-crack. The process continues in a mechanism that is similar to what's described by CELP model (section: 1.8.4). These results are in agreement with [149].

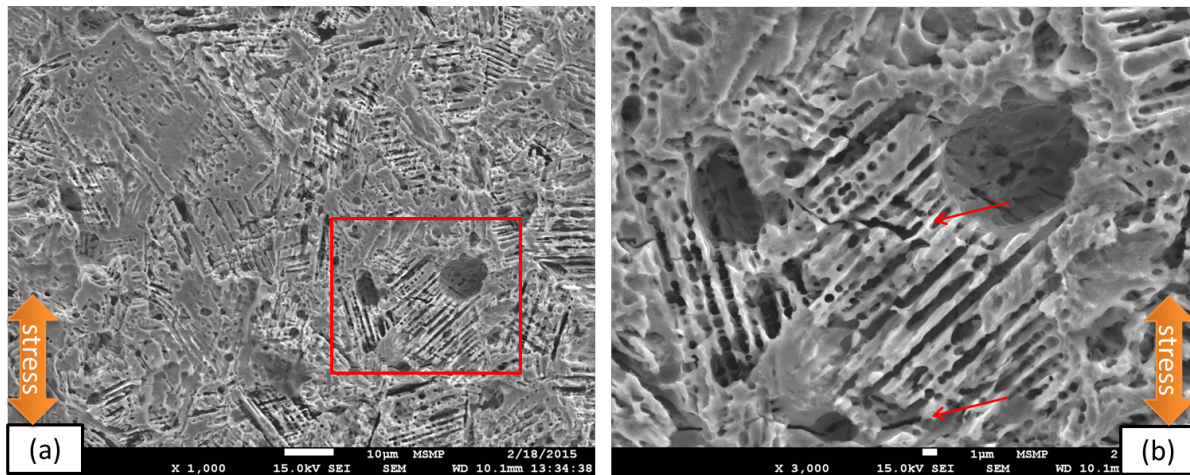


Figure 6.27: Upper surface post SCC test on a mirror-polished initial state. (a): The surface shows crystalline planes being preferentially attacked. (b): The preferentially attacked planes, with a TGSCC crossing them.

On the other hand, a cross-sectional view of the slip-lines attack is given in Fig. 6.28, which refers to a test of 21 h duration, in 2 M  $\text{H}_2\text{SO}_4$  + 0.5 M NaCl with  $\sigma = 210$  MPa. In this figure, the phenomenon of the preferential attack and how it might relate to the fore-coming cracks is better understood. It's noticed that the slipping planes that happen to be perpendicularly oriented to the direction of the applied stress undergo extra dissolution than the rest of other planes. Such feature is a very suitable location for a TGSCC propagation, who's orientation is along the  $\{111\}$  slipping planes. This preferential propagation is ascribed to the decohesion between the crystalline planes by the effect of the applied stress and the adsorption of hydrogen, as described by AIDE model (section: 1.8.2).

### 6.3.5 SCC under residual stress

To check the possibility of cracking for the initial state of the sample, without deformation, a SCC test was done in 2 M  $\text{H}_2\text{SO}_4$  + 0.5 M NaCl. This test is compared to that of another sample in the same environment, while  $\sigma = 210$  MPa was applied on it. The upper surface observation of these two tests is presented by Fig. 6.29. It's observed that for the non-stressed sample, cracks initiated on the surface anyway. However, the density of crack initiation sites is less for the non-stressed sample than that of  $\sigma = 210$  MPa.

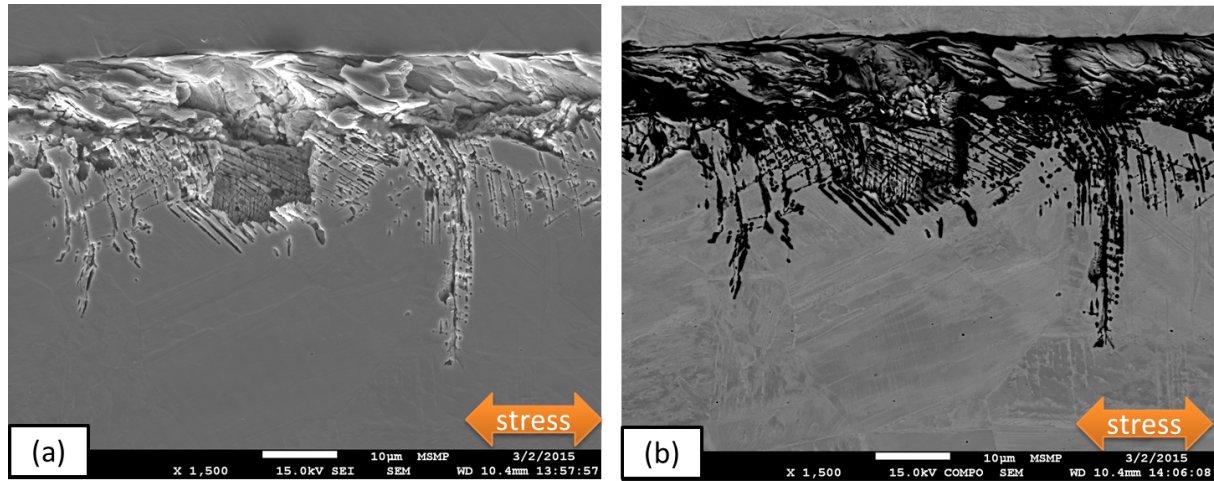


Figure 6.28: Cross-section post SCC test on a mirror-polished initial state. The slipping lines which are perpendicular to the stress direction are cites where crack propagated (a): secondary electron imaging mode. (b): Compo imaging mode.

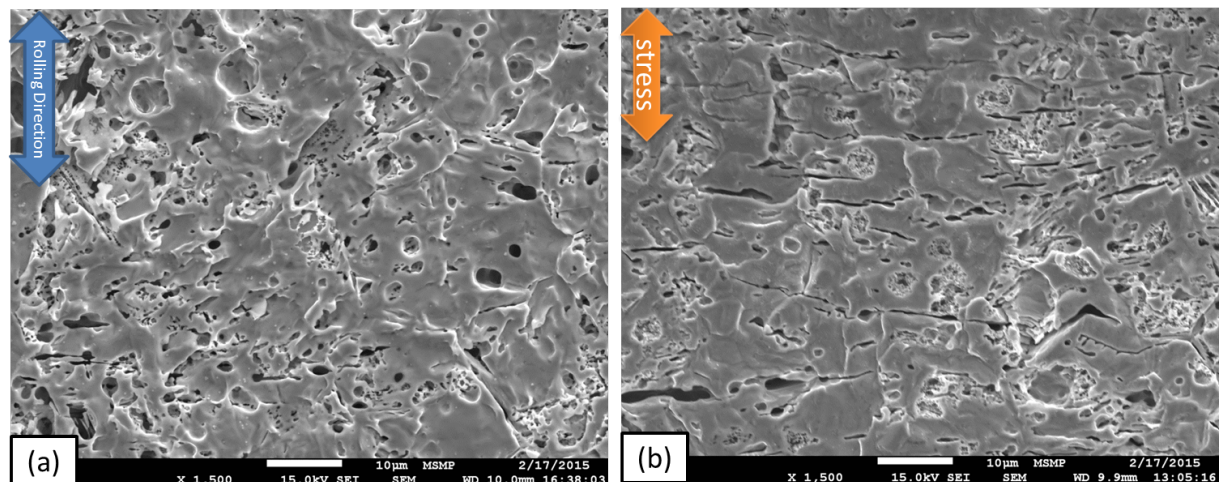


Figure 6.29: Upper surface of SCC under residual stress vs applied stress. (a): residual stress cracking after 60 h OCP test. (b):  $\sigma = 210$  MPa after 60 h OCP test.

On the other hand, Fig. 6.30 shows the difference between the cracking kinetics for these tests, at different test duration.

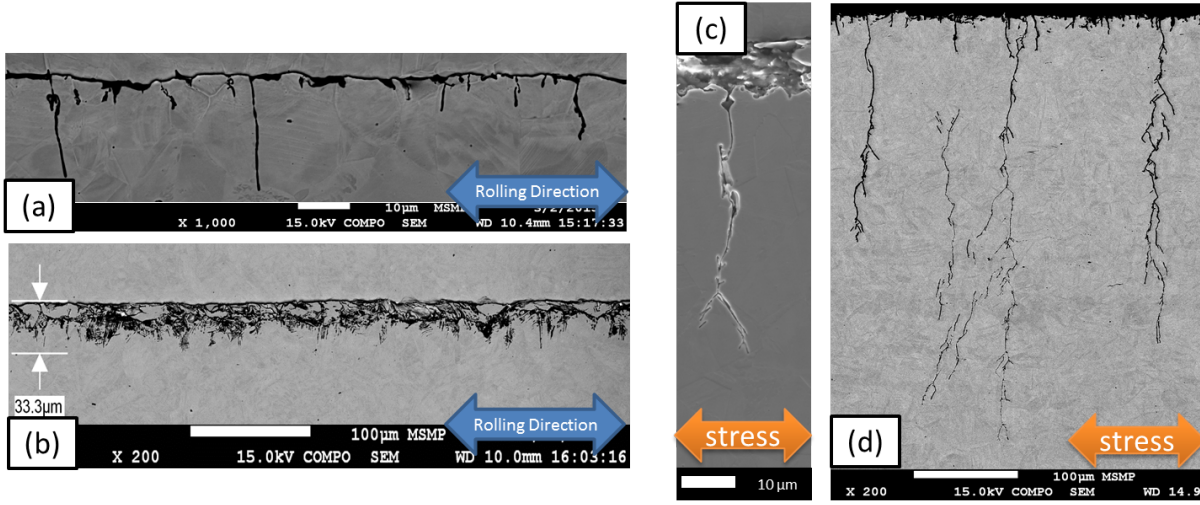


Figure 6.30: Cross-section of SCC under residual stress vs applied stress. (a) and (b): residual stress test at 14 and 60 h respectively. (c) and (d): SCC test with  $\sigma = 210$  MPa for 14 and 60 h respectively.

It's noticed that the sample with no applied stress cracked anyway, due to the effect of the residual tensile stress, which was in the order of  $(40 \pm 15)$  MPa, as was seen during initial material characterization. However, the kinetics of crack propagation is extremely slow, if not limited, when compared to the case with the applied stress, as seen from the cracks in Fig. 6.30(a)-(d).

The cross-section in Fig. 6.30 (b) shows more general attack of the slip planes taking place rather than crack propagation at long test duration when no stressed is applied.

### 6.3.6 EBSD maps for selected cracks

In this part, the sample having  $\sigma = 210$  MPa in 2 M  $\text{H}_2\text{SO}_4 + 0.5$  M NaCl was analyzed. The upper surface (Fig. 6.31) and the corss-section were characterized for the cracking planes orientations and families. Figure.6.32 refers to SCC test of 21 days,  $\sigma = 250$  MPa, in 2 M  $\text{H}_2\text{SO}_4 + 2$  M NaCl. On the othe hand, Fig. 6.33 is for the cross sectional view of 125 h SCC test of  $\sigma = 210$  MPa in 2 M  $\text{H}_2\text{SO}_4 + 0.5$  M NaCl.

The methodology of rupture plane identification described earlier in section 6.3.1 was used to analyze the obtained cracks. Table: 6.4 and Table: 6.5 give the summary of the results.

Table 6.4: Cross-section statistics about the preferential rupture planes, where  $\sigma = 210$  MPa in 2 M  $\text{H}_2\text{SO}_4 + 0.5$  M NaCl.

Plane family	{111}	{211}	{102}	{110}	{100}	{221}
Counts	11/43	7/43	12/43	8/43	3/43	2/43

Table 6.5: Upper surface statistics about the preferential rupture planes, where  $\sigma = 210$  MPa in 2 M  $\text{H}_2\text{SO}_4 + 0.5$  M NaCl.

Plane family	{111}	{211}	{102}	{110}	{100}	{221}
Counts	10/78	23/78	22/78	12/78	3/78	8/78



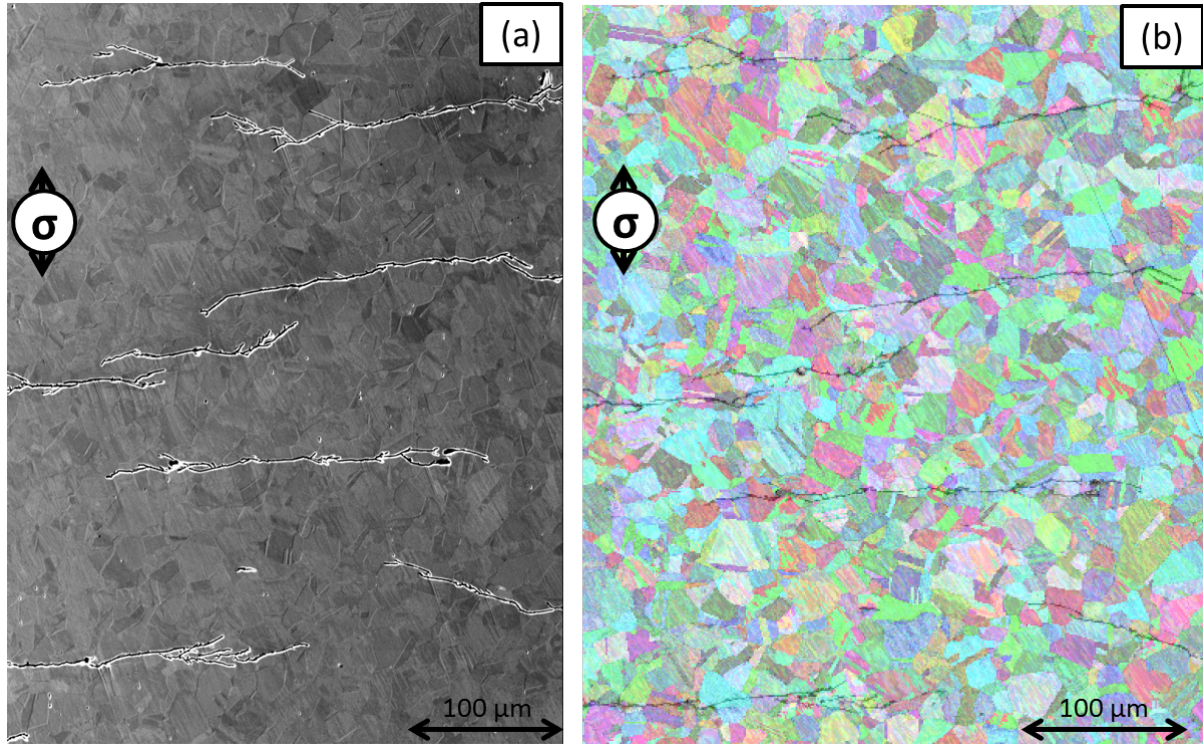


Figure 6.31: Upper surface of 125 h SCC of  $\sigma = 210$  MPa in 2 M  $\text{H}_2\text{SO}_4 + 0.5$  M NaCl. (a): SEM of the selected zone of interest (ZOI) (b): EBSD map of the ZOI.

The statistics obtained here are different from what was obtained previously in section: 6.2.1. This might be explained by the fact that less stress was applied here, (210 vs 250) MPa, which reduced the chance of slipping mechanics to operate in the current test.

On the other hand, the slight difference between results obtained on the upper surface (Table: 6.5) and those on the cross section (Table: 6.4) might be explained to the variation of the stress intensity factor at the upper crack tip ( $\phi = 0$ ) and the crack front ( $\phi = \pi/2$ ), where the value is higher at the minor axis of the elliptical crack.

Rather than the explanations given earlier in section 6.2.1), strict explanation of these cracking planes require micro-mechanical modeling and analysis at the crystalline level, taking into account the crack tip mechanics as a function of the local crystallographic orientation, and the corresponding stress distribution near the crack tip.

**Percentage of TGSCC in the cracks:** The zones of interest studied in Fig. 6.31 was suitable to make a statistical analysis about the percentage of TGSCC for the obtained cracks. To determine this, the equivalent grain diameters, and the total crack length were used. The percentage is given by the summation of the lengths of equivalent diameters of the TGSCC grains, over the entire crack length. For the rest of the crack length which was not of TGSCC type, it could be IGSCC, or it could be of a not determined type as well (due to loss of information by dissolution). This was conducted on 8 surface cracks, and the result is summarized in Table: 6.6. The percentage of TGSCC was thus different from a crack to another, with a range of 30-90% of the crack length.

## 6.4 Conclusions

- SEM observation of cracking facettes showed clear traces of slipping steps, and the consequent dissolution. In addition to this, clear crystallographic evidences were collected on the cracking behavior.

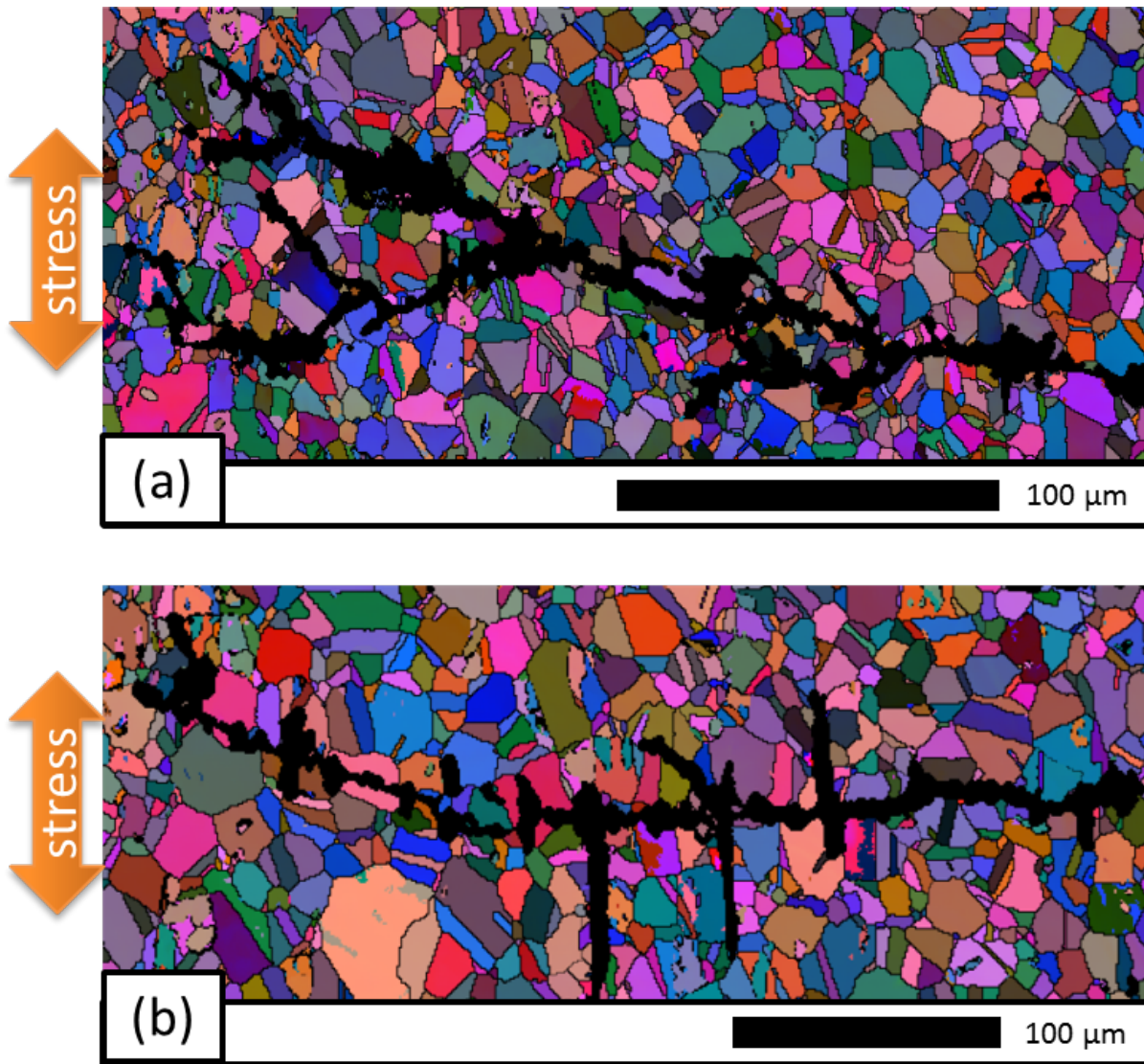


Figure 6.32: Cross-section EBSD maps of SCC test of  $\sigma = 250$  MPa, after 21 days in 2 M  $\text{H}_2\text{SO}_4$  + 2 M NaCl. (a) and (b) are two cracks selected for analysis.

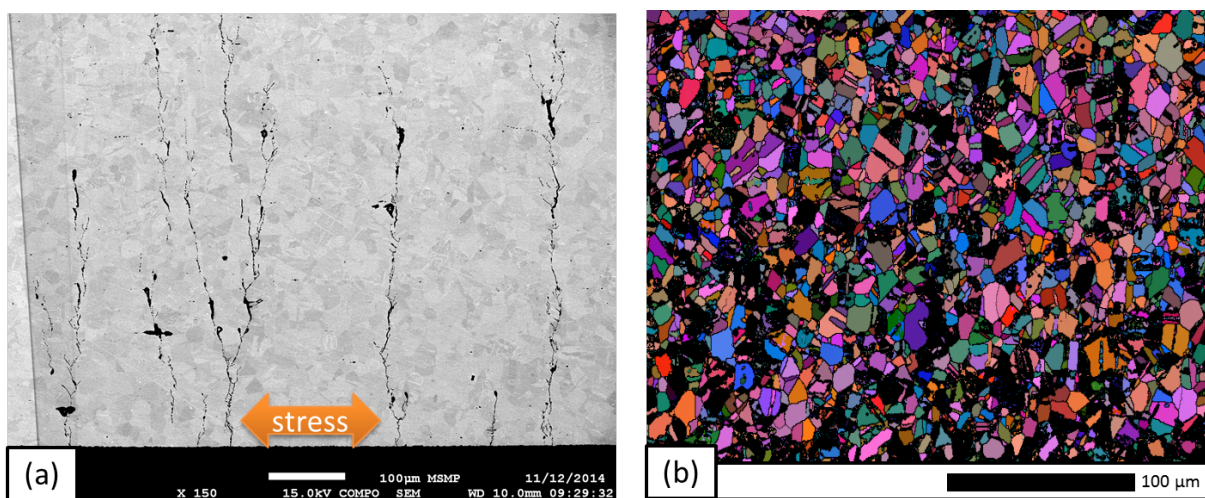


Figure 6.33: Cross-section of 125 h SCC test of  $\sigma = 210$  MPa in 2 M  $\text{H}_2\text{SO}_4$  + 0.5 M NaCl. (a): SEM image of ZOI. (b): EBSD map of ZOI.



Table 6.6: Percentage of TGSCC for eight selected surface SCC cracks in Fig. 6.31.

	Crack length [ $\mu\text{m}$ ]	TGSCC [ $\mu\text{m}$ ]	% TG/total
crack1	192	165	86
crack2	252	219	87
crack3	241	212	88
crack 4	141	78	55
crack5	113	103	91
crack 6	278	225	81
crack 7	117	36	31
crack 8	227	177	78

- The cracking density increases with increased applied stress. This is due to more active slipping systems leaving low chance of pit healing, which favors crack propagation. However, for a given stress state, the cracking density was constant for SCC of different duration.
- The OCP value of the surface during SCC test showed to get to a stable cathodic value ( $-350\text{ mV vs SCE}$ ). This corresponds to the time where the surface is generally attacked, giving a flak morphology.
- The acceleration of SCC kinetics was possible by the application of a cathodic constant pulse ( $-300\text{ mV vs SCE}$ ) in  $2\text{ M H}_2\text{SO}_4 + 2\text{ M NaCl}$ . This caused crack to develop in 2 hours in what's equivalent to that in 16-h SCC test.
- The polished surface showed the preferential attack of the  $\{111\}$  planes on the upper surface. Nevertheless, the TGSCC was not related to those planes, except if they were oriented perpendicularly to the direction of the applied stress. This is due to the decohesion between the attacked crystalline planes by the applied stress, where reduced mechanical properties resulted from the adsorption of hydrogen, as described by AIDE model.
- For samples subjected to  $\sigma = 250\text{ MPa}$  in  $2\text{ M H}_2\text{SO}_4 + 2\text{ M NaCl}$ , the crystallographic orientation analysis revealed two types of preferential rupture planes;  $\{110\}$ ,  $\{111\}$  with percentages around 48%, 37% respectively. For face centered cubic crystals,  $\{111\}$  planes are those over which slipping occurs. However, rupture planes could be of  $\{110\}$  family due to equal dislocation-pile-up on the primary and conjugate  $\{111\}$  planes. This result comes in agreement with recent SCC models, such as CELP and AIDE.
- However, other plane families were present such as  $\{211\}$  and  $\{102\}$  as a result of reducing the stress to an elastic stress ( $\sigma = 210\text{ MPa}$ ) in less severe SCC tests ( $2\text{ M H}_2\text{SO}_4 + 2\text{ M NaCl}$ ).
- The cracking orientation was influenced by the local microstructure, and the orientation of the grain boundaries ahead of the crack.
- SEM observation shows that crack propagation has a non-linear relation with exposure time, where it starts with low propagation kinetics within the period between 16-21 h, and goes to three times this speed between the period 21-125 h.
- The crack re-orientation and branching is affected by the local microstructure near the crack tip, and the orientation of the grain boundaries encountered by the crack front.
- SCC was produced by the effect of the residual tensile stress existing initially in the material. However, the cracking kinetics was very slow compared to stressed tests.



## 7.1 Introduction

The purpose of this chapter is to initiate a model for the cracking mechanics on a micro-scale. This might give an explanation of the obtained preferential cracking plane families which didn't relate to  $\{111\}$ , and  $\{110\}$ . On a future phase, this might be integrated with the oxidation kinetics at the crack tip, along with the passive film mechanical properties in order to approach further the real SCC for the given environment (2 M  $\text{H}_2\text{SO}_4$ ), material (304L SS), and stress state ( $\sigma = 210 \text{ MPa}$ ).

Cracking kinetics collected earlier for the different SCC tests in section (6.3.2) will be used for correlation purpose, and most importantly: to calculate the stress intensity factor ( $K$ ) of the considered cracks.

## 7.2 Do existing Models Cover the Considered Conditions?

As seen by the literature review of SCC, crack growth can take place at stress intensity factor values which are much lower than the conventional  $K_{\text{I}}$  value. Many reasons were suggested in the literature for this early cracking, focusing mainly on local near-crack-tip phenomena taking place due to special chemical conditions there. The situation gets more complicated when neighbor cracks are interacting with each other. In case they are close enough, crack coalescence takes place before the long-cracking regime gets established. Modeling in such conditions is very challenging. The modeling difficulty increases if the residual stress field near the crack tip has steep gradients[102]. Thus, any newly added feature in modeling, even for a specific material/environment system, counts later in building a more general and complete model.

In chapter 5, a methodology to precisely quantify the oxidation kinetics and passive film properties and construction kinetics was established for the material in hand in high acidic concentration. On the other hand, chapter 6 revealed preferential cracking planes related to low index planes when the material was stressed to its elastic limit. In addition to this, crystallographic features were observed for crack nucleation sites. Such advances, in addition to what will be discussed in this chapter, can be integrated together aiming to improve the SCC modeling and prediction in future.



### 7.3 Semi-Elliptical Cracking Aspects

To make an estimation of the crack propagation rate, information about the crack's dimensions and stress intensity factor should be present. In our case, the crack has a semi-elliptical shape with a minor non-equal to the major, as shown in Fig. 7.1.

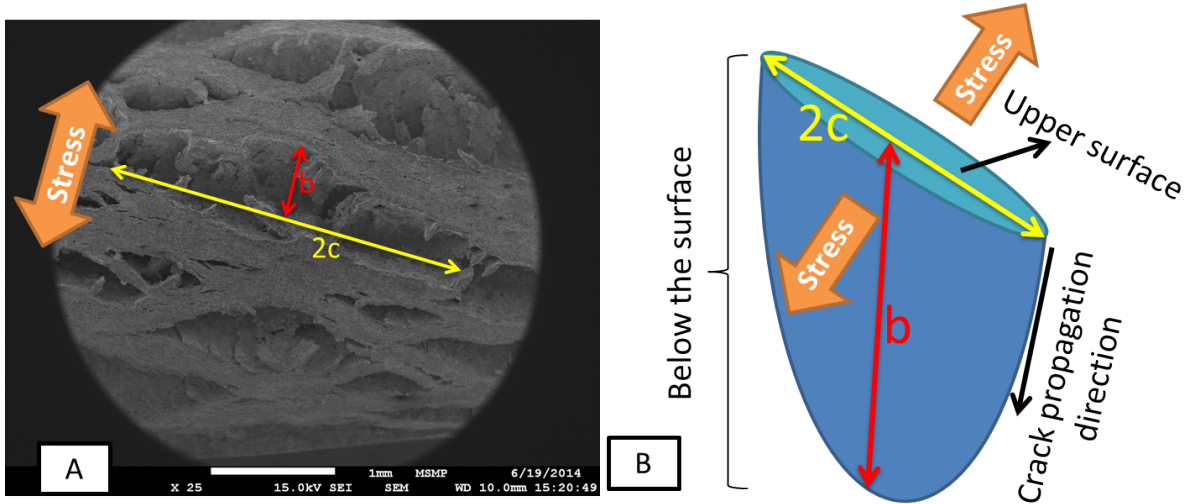


Figure 7.1: Illustration of the semi-elliptical shape of the crack. (A): An open SCC crack, showing its semi-elliptical shape. (B): An illustration of an approximate shape of the crack's dimensions.

Thus, to fully characterize a crack, the dimensions  $b$  and  $c$  should be known, in addition to the aspect ratio ( $b/c$ ). Previously in section (6.2.2), the analysis of the cracking kinetics was based on the cross-section observation, which is supposed to reveal the depth of the crack ( $b$ ) values. Measuring the other dimension was not doable due at that stage, due to the rough upper surface morphology as shown in Fig. 6.10 to Fig. 6.12.

Therefore, in order to complete crack characterization for its dimension ( $c$ ), the upper surface was slightly polished to remove the corrosion residual roughness, which gives a surface as the one shown in Fig. 7.2(A).

Having this SEM observation of the upper surface makes measuring the crack length ( $2c$ ) straight forward since the full crack length is directly accessed by the upper surface observation.

On the other hand, it's noticed from Fig. 7.2 (A) that the crack length varies greatly from a crack to another, resulting in a quite large variance. Table 7.1 gives a summary of the crack length statistics for the different examined tests.

Table 7.1: Experimental statistics about the crack dimensions rate on the upper surface ( $c$ ), and on the cross-section ( $b$ ). It's assumed here that  $b \approx L$ .

	Exp. $c$	$[\mu\text{m}]$	Exp. $b$	$[\mu\text{m}]$	Exp. ( $b/c$ )	$(dc/dt)$	$\mu\text{m.h}^{-1}$
Duration	avg	max	avg	max	avg	max	avg( $c$ )
16 h	3	17	15	83	4.7	4.9	0.2
42 h	12	40	80	174	6.7	4.4	0.3
88 h	24	60	245	415	10.2	6.9	0.3
125 h	71	242	360	697	5.1	2.9	1.3

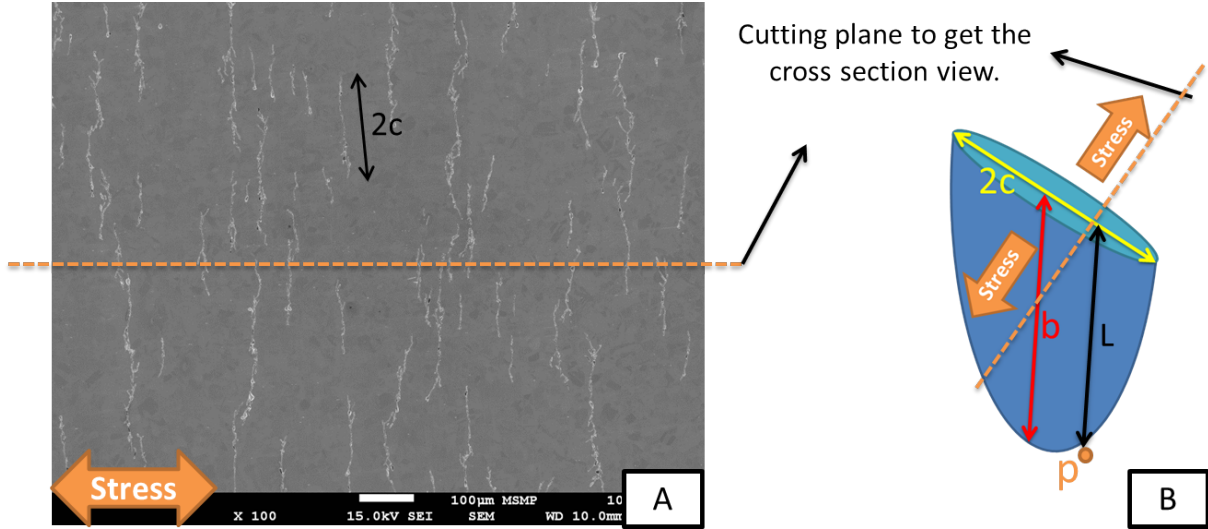


Figure 7.2: (A): Upper surface observation of SCC. (A)&(B): Showing the cutting plane to get the cross-sectional view.

### 7.3.1 Cracking kinetics along $(b)$ and $(c)$ direction

As illustrated in Fig. 7.3 (A), when first detected, the crack dimensions initiate by having almost similar lengths,  $(4.7, 3) \mu\text{m.h}^{-1}$  along  $(b)$  and  $(c)$  respectively. However, these two lengths show clear different trends, where the dimension  $(b)$  gets increasingly higher values than those of  $(c)$  as a function of time. It's noticed from Table: 7.1 that the aspect ratio,  $(a/b)$ , was higher than 2 in all cases. This is an odd behavior compared to pure mechanical elliptical cracks, which usually have an aspect ratio of less than unity. An attempt to explain this behavior will be conducted in the rest of this work.

### 7.3.2 Propagation rate along $(b)$ vs $(c)$ direction

The crack propagation rate along the  $(c)$  direction shows two distinct values. The first of those is very slow ( $\approx 0.3 \mu\text{m.h}^{-1}$ ), which remains almost constant, except for the last period, where it gets to  $(1.3 \mu\text{m.h}^{-1})$ . The trend of having two distinct temporal zones for the propagation rate along  $(c)$  is similar to that previously found along  $(b)$  direction (section: 6.3.2). These observations are in agreement of what was found in the literature (section: 1.9.4).

From a mechanical point of view, comparing the propagation rates along  $(b)$  and  $(c)$  directions vs time, as was done in Fig. 7.3 (B), might not be misleading. The crack propagation rate depends on the local intensity factor at the crack tip,  $K$ , and whether this intensity factor has exceeded the critical stress intensity factor which results in crack propagation,  $K_c$ .

According to Eq.1.19, the critical stress intensity factor depends on the applied stress ( $\sigma_\infty$ ), the crack length  $(c)$ , and the sample's geometry (depth ahead of the crack tip). Among these parameters, the most remarkable difference between our present cracks is the length difference between the lengths  $(b)$  and  $(c)$  at a given time. Thus, comparison of the propagation rates along these directions should be based on length rather than time.

For this purpose, a new parameter is defined to be the representative length. For a given time interval,  $(t_1, t_2)$ , the propagation rate is calculated as the slope of the straight line connecting these two states. This propagation rate represents the rate at the intermediate crack length over the considered interval, and thus called the representative length. This representative length was found for the different intervals of the cracking kinetics along both directions;  $(b)$  and  $(c)$ , as given by Table: 7.2.

Figure 7.4 shows the propagation rate as a function of the representative length for cracking along the  $(b)$  and  $(c)$  directions. Under this criterion, for all the considered points, the propaga-

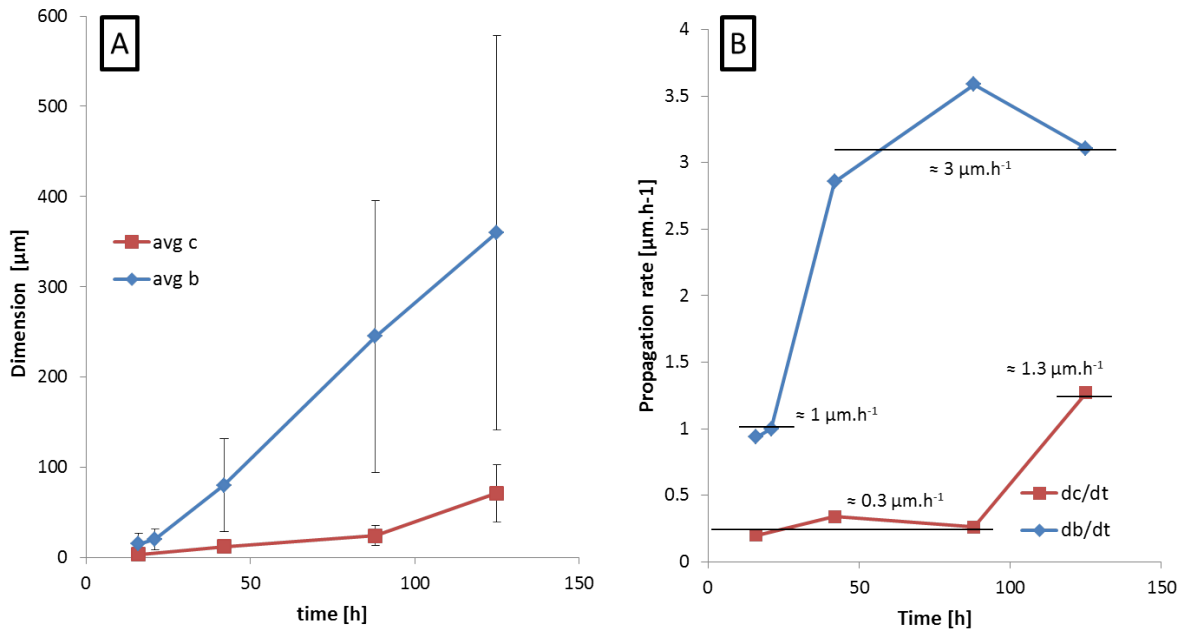


Figure 7.3: Illustrating the cracking statistics along ( $c$ ) and ( $b$ ) directions. (A): Experimentally measured crack aspects. (B): Crack propagation rate along ( $c$ ) and ( $b$ ) directions.

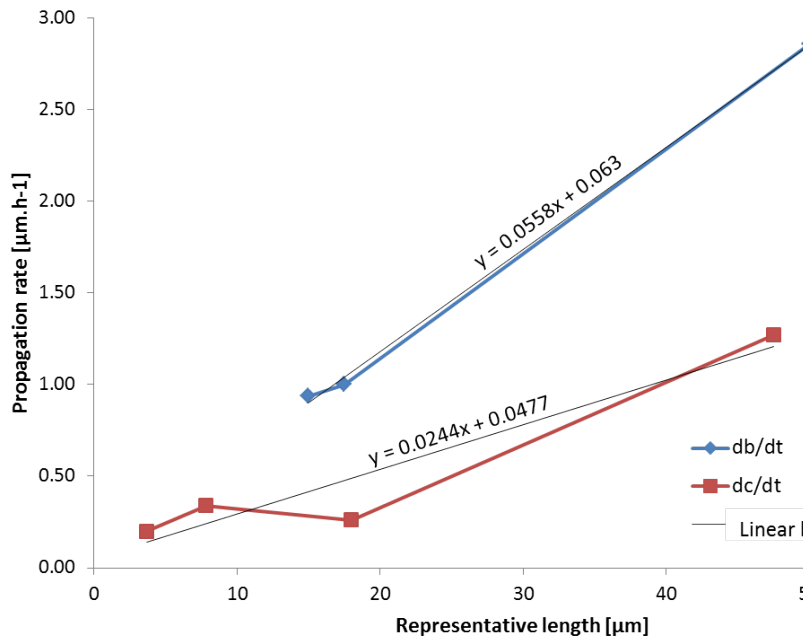


Figure 7.4: Illustrating the crack representative length along ( $b$ ) and ( $c$ ) direction vs the corresponding propagation rate.

Table 7.2: Representative length ( $b$ ) and ( $c$ ) vs their propagation rate.

Representative ( $c$ ) $c[\mu\text{m}]$	$dc/dt$ $[\mu\text{m.h}^{-1}]$	Representative ( $b$ ) $b[\mu\text{m}]$	$db/dt$ $[\mu\text{m.h}^{-1}]$
3.2	0.2	15	0.9
—	—	17.5	1.0
7.6	0.3	50	2.9
18	0.3	162.5	3.6
47.5	1.3	302.5	3.1

tion rate at a given length was lower in ( $c$ ) direction than that along ( $b$ ). Two points were close enough to make a quantitative comparison, at the representative length (18 and 50)  $\mu\text{m}$ . For these two points, the propagation rate was (0.3 and 1.0)  $\mu\text{m.h}^{-1}$  and (1.3 and 2.9)  $\mu\text{m.h}^{-1}$  for ( $c$ ) and ( $b$ ) respectively. This indicates in general, a propagation accelerated by a factor of  $\approx 3$  for ( $b$ ) direction than that along ( $c$ ).

This variation of propagation is due to the different local stress intensity factor at the crack tip on the upper surface ( $c$  direction), and the crack front inside the sample ( $b$  direction).

If the propagation rate is proportional to the local intensity factor at the crack tip, the crack tips at the upper surface ( $c$  direction) is higher than that of the crack front inside the sample ( $b$  direction). Equation 1.24 predicts the stress intensity factor along the profile of an elliptical crack function of the ellipse parametric angle  $\Phi$  (Fig. 1.31).

According to Eq.1.24, two remarks were reported [39]:

1.  $K_I$  takes the maximum at the minor axis of the ellipse ( $c$  in our case).
2. This maximum  $K_I$  value increases as the difference between ( $b$ ) and ( $c$ ) gets higher.

The first remark is totally contradictory to the current results, as the propagation rate is higher at the major axis of the present crack ( $b$  direction), as was presented in Fig. 7.3 (A). This aspect is thought to be due to having neighbor cracks resulting in stress relaxation, which alters the values of stress near the upper surface ( $c$  direction), leading to limit propagation along this direction. More on this will be revealed by the XRD analysis of the stress profile of the cracked sample (section: 7.5). However, regardless of the axis having the maximum  $K_I$ , our results seem to fit the second remark, where the propagation rate tends to increase as the difference between ( $b$ ) and ( $c$ ) increases as shown in Fig. 7.3 (B).

## 7.4 Estimation and simulation of cracking statistics

In the previous analysis, the aspect ratio used to characterize the cracks was based on statistical experimental measurements. Crack lengths were measured on the upper surface and the cross-section to obtain the dimensions ( $2c$ ) and ( $b$ ) respectively. These dimensions are the base to calculate the stress intensity factor, the stress field near the crack tip, and the estimation of the corresponding propagation rate. Thus, their validity should be verified, since in real life applications, crack propagation estimation is often directly related to safety issues.

In this part of the research, an estimation will be conducted about the validity of the statistics of ( $b$ ) and ( $c$ ), and the measures to improve them if required. The example case taken to explain and demonstrate the analysis will be the SCC test of 125 h with ( $\sigma = 210 \text{ MPa}$ ) in 2 M  $\text{H}_2\text{SO}_4$  + 0.5 M NaCl. Figure 7.5 shows samples of the analyzed area from the upper and cross section view, where the green lines indicate the measured lengths.

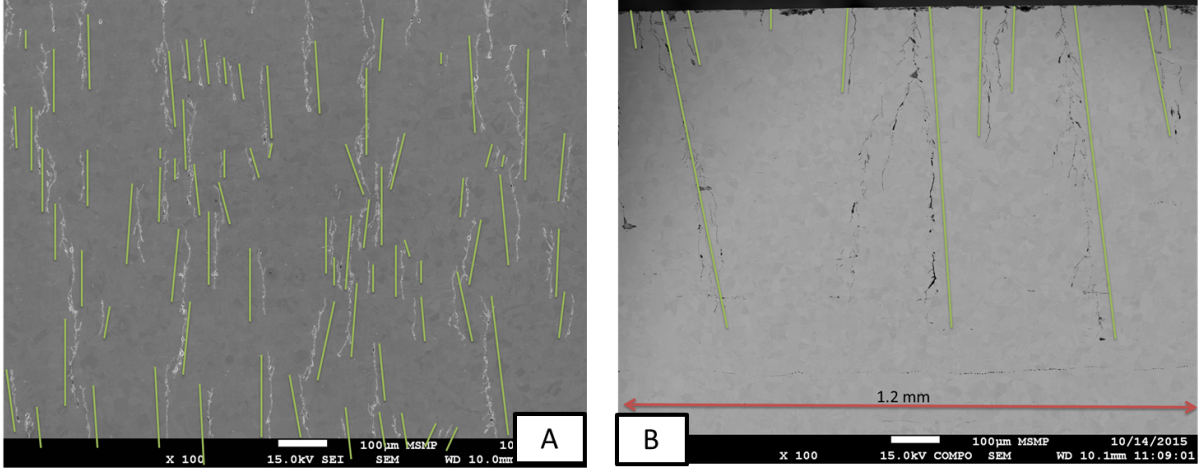


Figure 7.5: Sample of measured cracks for the statistical analysis.(A): The upper surface where  $(2c)$  is measured. (B): The cross-section view showing the measured crack depth  $(L)$ .

#### 7.4.1 The upper crack length $(2c)$

As seen earlier in Fig. 7.2 (A), the dimension  $(2c)$  can be directly accessed by the upper surface observation. The set of cracks taken for the statistical analysis was all cracks included in a rectangle of  $(2.4 \times 1.7)$  mm, which counts to 237 cracks. Figure 7.5(A) shows part of the investigated area. The histogram shown in Fig. 7.6 (A) represents the statistical distribution of the experimentally measured lengths, which are scattered around a central value  $\approx 70 \mu\text{m}$ .

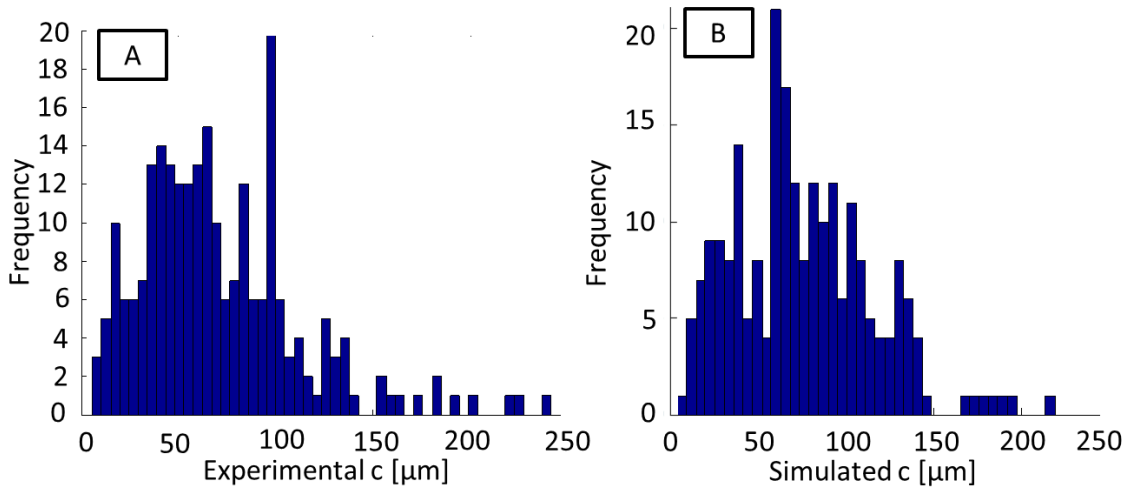


Figure 7.6: Histogram of the statistical distribution of the crack length  $(c)$ , (A): Experimental data. (B): Simulated data.

#### Estimation statistics validity of $(c)$

A Matlab program was used to generate random lengths having a gaussian distribution. These generated lengths had the same number of the measured cracks, and the experimental average and standard deviation of the measured lengths.

After omitting the negative generated lengths, the result of this simulation is given by the histogram shown in Fig. 7.6(B). By comparing the experimental data to the generated ones, the two histograms seem to be representing each other, indicated that the experimental data are

statistically representative. By this conclusion, no correction is required to the experimentally measured ( $c$ ) lengths.

#### 7.4.2 The crack depth ( $b$ )

The access to the crack depth is only possible by cutting the sample by a perpendicular plane to the ( $2c$ ) direction, enabling the observation of the cross-sectional view. This random plane is illustrated on the upper surface by the orange dashed line in Fig. 7.2 (A). The way a random elliptical crack is cut by this plane is illustrated in Fig. 7.2 (B), where the cutting plane is the plane passing by the orange dashed line and the point ( $p$ ) on the crack front.

To make the problem statement clearer, the three views of this crack are presented in Fig. 7.7 (A), with the dashed line representing the cutting plane. Measuring the actual crack depth ( $b$ ) on the resulting cross section is thus not possible. Instead, the only accessible measure is the crack length ( $L$ ) as shown in Fig. 7.7 (A) and (B). This length ( $L$ ) could have any random cut of the elliptical crack profile, having a range of  $(0, b]$ .

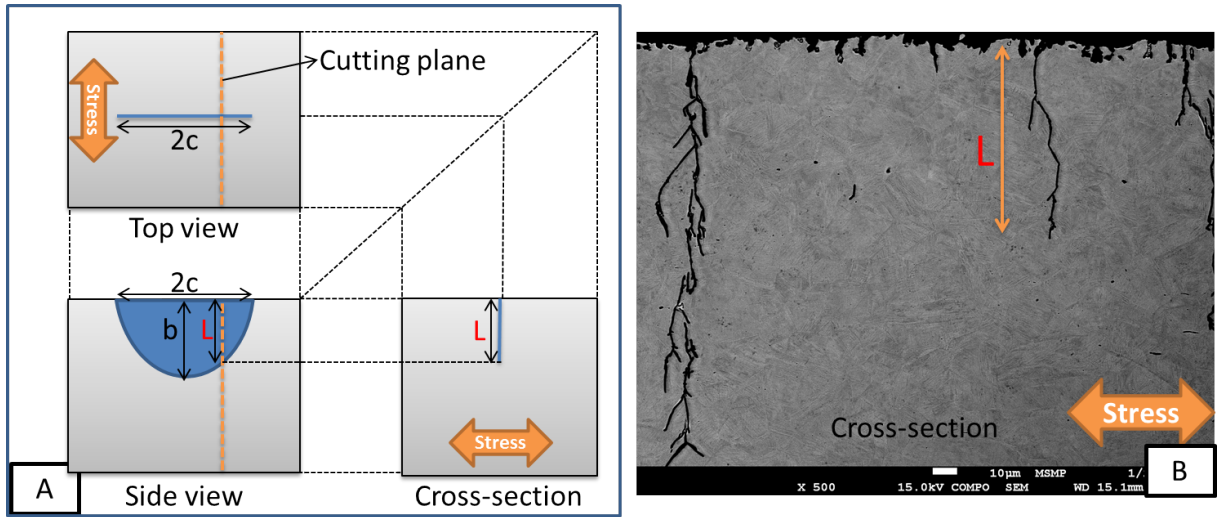


Figure 7.7: Illustration of the problem of the crack depth ( $L$ ). (A): The three views of the considered crack showing the cutting plane and the ( $L$ ) obtained length on the cross-section view. (B): The cross-section view showing the measured crack depth ( $L$ ).

#### Estimation of statistics validity of ( $b$ )

Regardless of the measures made experimentally, the distribution of the length ( $L$ ) obtained by a randomly-cut semi-elliptical crack of a given length should be estimated. This distribution is due to the geometry of the crack front and can be obtained by performing a simulation of this process.

**Simulating random cuts for a given crack:** The purpose of this simulation is to produce a high enough number of random cuts on the crack so that the geometrical statistical distribution is obtained. This simulation process is explained in Fig. 7.8, where the generated cuts are performed at random  $X_n$  points along ( $2c$ ) direction, which will result in random  $L_n$ . The range of the random variable  $X_n$  is thus  $X_n \in [-c, c]$ .

For any point on the ellipse profile, ( $X_n, L_n$ ), is given by Eq.7.1, which is the ellipse equation.

$$\frac{X_n^2}{c^2} + \frac{L_n^2}{b^2} = 1 \quad (7.1)$$



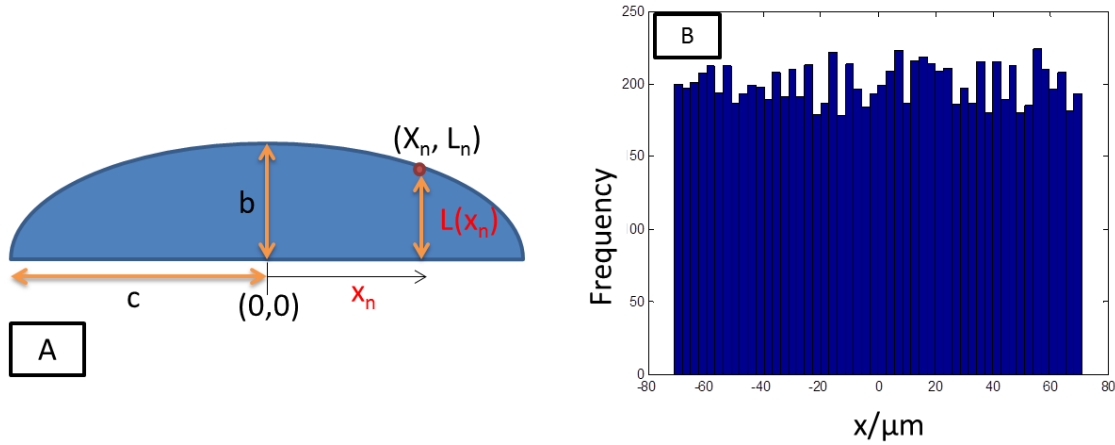


Figure 7.8: Simulation of the random cutting plane. (A): The generated cutting plane at any random point over the  $(2c)$  edge. (B): The distribution of randomly generated  $X_n$  values.

The number of generated cuts was taken to 10000 cut, with the random  $(X_n)$  values having a uniform distribution, as shown in Fig. 7.8(B).

The simulation inputs are thus:

1. The length of the semi-axis ( $c$ ) of the crack in consideration.
2. The characteristic aspect ratio ( $b/c$ ) of the considered crack.

Concerning the input ( $c$ ), it was set to the average of experimentally measured values for the considered simulated SCC test. However, as seen from the experimental statistics, Table: 7.1, the aspect ratio is calculated based on the experimental average as  $(b_{avg}/L_{avg})$ , ranged between 4.7, and 10.2. A range which is relatively large, especially that it didn't show a strict evolution tendency with time.

Therefore, two propositions were made about the input  $(b/c)$  ratio, based on which two simulations were made:

- To set  $(b/c)$  to the experimental averages of the measured  $(b)$  and  $(L)$  of the test in consideration. This was the input for the first simulation.
- To set  $(b/c)$  to a unique fixed value for all the simulated tests based on the experimental range of the  $(b_{avg}/L_{avg})$  ratio. This was set to 6, by which the second simulation was performed.

**Simulation results:** The distributions of  $(L)$  obtained by the two previously explained simulations are illustrated in Fig. 7.9.

Now, these results should be compared to the experimentally obtained distribution of the measured  $(L)$  lengths, which is shown in Fig. 7.10.

It's noticed that the distribution obtained by the two simulations (Fig. 7.9) have the same form of distribution, which is a function of the dimensions and geometry of the crack profile. Comparing these two distributions to the experimentally obtained distribution (Fig. 7.10), it's obvious that statistically, the number of measured  $(L)$  lengths is not high enough to be representative of the real distribution that was approached by the two simulations. Thus, it's not acceptable to assume the experimentally measured  $(L)$  to be equal to  $(b)$ . As a result, the simulated values of  $(L)$  will be taken instead for the calculation of  $(b/c)$  ratio.

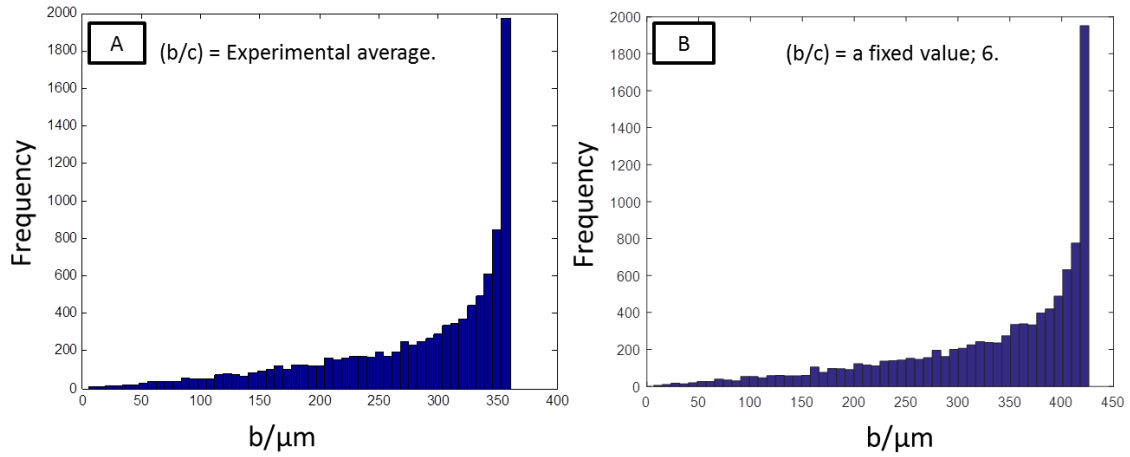


Figure 7.9: Results of  $(L)$  simulations. (A): Using  $(b/c) = (L_{\text{avg}}/c_{\text{avg}})$  of the considered test. (B): Using  $(b/c) = (6)$  as a fixed value.

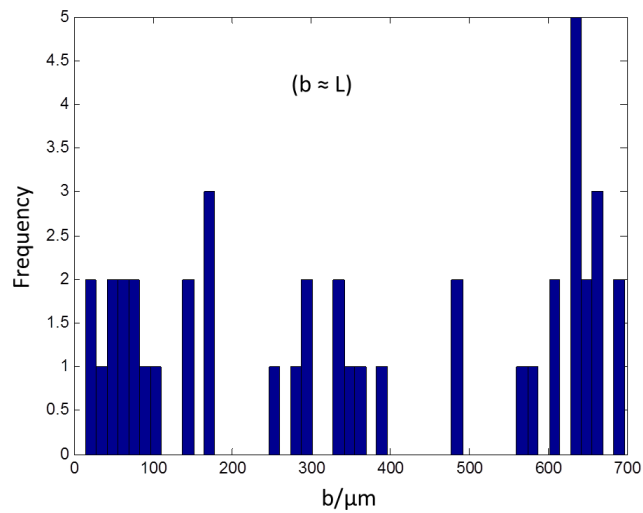


Figure 7.10: Distribution of the experimentally measured  $(L)$ .



On the other hand, as was explained earlier, the experimentally measured  $2c$  values were statistically representative of the real case. Consequently, the experimental values are kept for the following analysis. The given propagation rate ( $db/dt$ ) are based on the average of the simulated ( $b$ ) values.

As a conclusion, the experimental ( $c$ ) values will be combined with the simulated ( $b$ ) for any further analysis. Table: 7.3 and 7.4 make a summary of the resulting enhanced data for all the conducted tests.

Table 7.3: Enhanced statistics by the first simulation results, based on  $(b/c) = (L_{\text{avg}}/c_{\text{avg}})$  of the test in considerations.

	(Exp. $c$ / $\mu\text{m}$ )		(Sim. $b$ / $\mu\text{m}$ )		( $db/dt$ )	Resulting ( $b/c$ )	
Duration	avg	max	avg	max	/ $\mu\text{m.h}^{-1}$	avg	max
16 h	3	17	12	15	0.7	3.6	0.9
42 h	12	40	68	86	2.2	5.6	2.2
88 h	24	60	194	245	2.7	8.1	4.1
125 h	71	242	282	360	2.4	4.0	1.5

Table 7.4: Enhanced statistics by the second simulation results, based on  $(b/c) = 6$ .

	(Exp. $c$ / $\mu\text{m}$ )		(Sim. $b$ / $\mu\text{m}$ )		( $db/dt$ )	Resulting ( $b/c$ )	
Duration	avg	max	avg	max	/ $\mu\text{m.h}^{-1}$	avg	max
16 h	3	17	18	22	1.1	5.5	1.3
42 h	12	40	57	73	1.5	4.8	1.8
88 h	24	60	112	143	1.2	4.7	2.4
125 h	71	242	334	426	6.0	4.7	1.8

**Remarks and conclusions:** By comparing Table: 7.4 and Table:7.3 to the experimental values in Table: 7.1, the enhancement introduced by the two simulation cases is very remarkable. Example of this is the experimental  $L_{\text{max}}$  value of 125 h test was  $\approx 700 \mu\text{m}$ , which is very far from the experimental average value  $L_{\text{avg}}$  which was  $360 \mu\text{m}$ . This odd behavior was not obtained in the two simulation results.

Same about the range of the propagation rate, which got less variance in both simulation cases than the initial experimental values. To be more specific, the values obtained by the first case of simulation (Table: 7.3) seems to be more tight and coherent than the second case (Table: 7.4).

However, the propagation along ( $c$ ) direction is necessarily reflected on the propagation kinetics along the ( $b$ ) direction by having a fixed input ( $b/c$ ) value in the second simulation. This is why the propagation rate of ( $b$ ) had 2 distinct temporal zones as was the case along the ( $c$ ) direction. For this reason, the results obtained by the first simulation may be favored, where the propagation along ( $b$ ) is set based on experimental measurement rather than a prediction constant.

The aspect ratio ( $b/c$ ) in both simulations have less variance than the experimental ones. However, for all examined tests, this ratio was  $\approx 5$  in the second simulation, which is a little bit less than the simulation input ( $b/c$ ) ratio which was set to 6. On the other hand, from the first simulation results, concerning the last test of 125 h, a threshold occurs favoring the propagation along the ( $c$ ) over that of ( $b$ ), which is not the case for the other tests having a lower duration.

Deciding which simulation is better eventually requires further investigation, in addition to these discussed conclusions.

## 7.5 XRD Analysis of Experimental Strain Fields

### 7.5.1 Effect of SCC on applied and residual stress

Determining the stress (residual/applied) in the sample is an important element to understand and model SCC appropriately. For this purpose, XRD analysis was conducted on the base material to characterize the residual stress in the initial sample before being deformed. In a later step, XRD analysis of this sample while applied to the curved support of  $\sigma = 210$  MPa, in order to check the effect of this deformation on the stress profile.

Then a selected SCC test duration is conducted, which was taken to be 42 h in this case. A post-experimental XRD analysis is performed on the zone affected by the SCC, while still held on the support, in order to check the stress relaxation profile after cracking.

This XRD analysis over the sample depth profile gave the curves indicated in Fig. 7.11. The crude metal sheet shows to have residual stresses resulting from manufacturing processes such as rolling. This tensile residual stress explains the crack propagation under no applied stress conditions in  $2\text{M H}_2\text{SO}_4 + 0.5\text{ M NaCl}$ , as was shown in Fig. 6.13 (g). However, it's noticed from this figure that the crack propagation kinetics remains very slow under no applied load compared to the tests performed with  $\sigma = 210$  MPa.

The effect of the applied stress is very pronounced on the stress profile, representing the applied stress on the sample after deformation on the curved support. The average of the measured stress on the surface was  $(33 \pm 15)$  MPa. The sample was deformed using the support of  $\sigma = 210$  MPa. For the deformed sample, the same measurements were made on the upper surface giving a stress value equals to  $(217 \pm 17)$  MPa. This value of stress confirms the theoretical stress calculation made earlier in section (6.1) corresponding to this amount of deformation ( $\varepsilon = 0.1\%$ ).

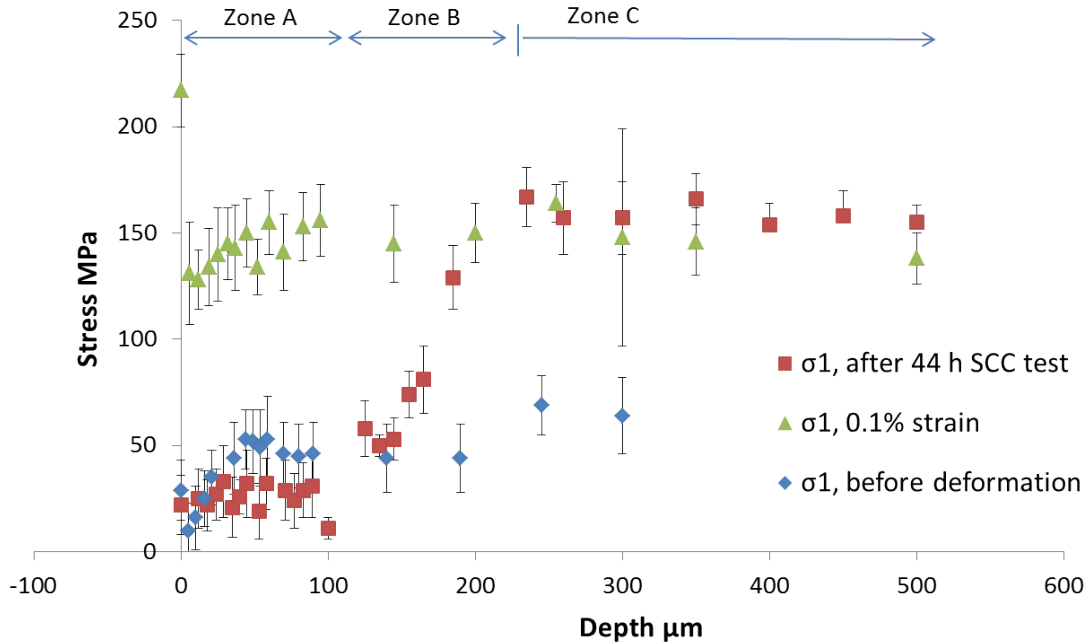


Figure 7.11: Stress field calculated by XRD measurement of: (a) The residual stress of the initial sample before straining. (b) The applied stress after deformation on the curved support. (c) The stress field after SCC 125-h test.

The main interest here is to obtain the stress field after the SCC test, while the sample is still on the curved support. This stress profile shows the operating stress at the crack tips, and how it varies through the sample's profile. The average crack length for this period of SCC test is about  $95\text{ }\mu\text{m}$ , and the maximum crack length is about  $175\text{ }\mu\text{m}$  as was indicated in Table: 6.3,

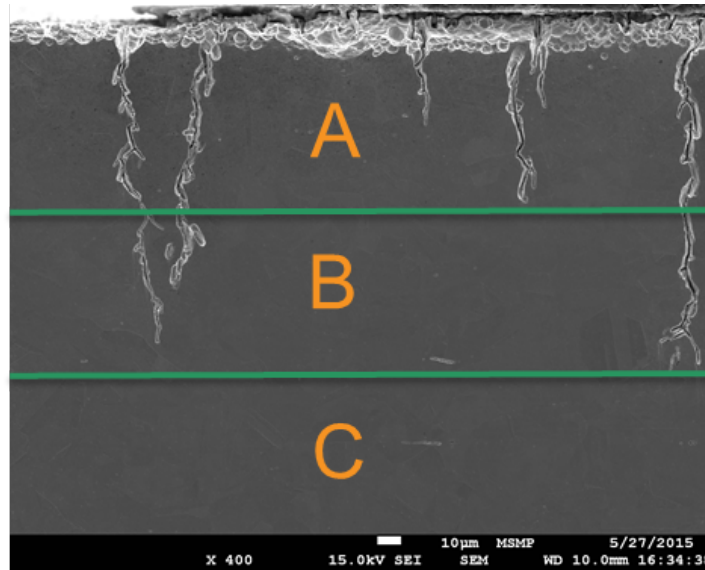


Figure 7.12: Cracking cross-sectional view of 42 h SCC test in 2 M  $\text{H}_2\text{SO}_4$  + 0.5 M NaCl, using  $\sigma = 210$  MPa support. (A): Total stress relaxation. (B): Gradual increase of the stress. (C): The stress due to sample deformation over the curved support.

and shown in Fig. 7.12. This is directly reflected on the measured stress profile over the sample's depth. From the upper surface (depth = 0) to the point at  $100 \mu\text{m}$ , the stress falls to a close value to the initial residual stress in the bulk of the material. And starting from this point, the measured stress starts to increase gradually with depth. This gradual increase stops at depth equals to  $175 \mu\text{m}$ , after which the stress profile shows a platform until  $500 \mu\text{m}$  depth representing the applied stress value. A summary of the results is made in Table: 7.5.

Table 7.5: A summary of the XRD stress profile analysis.

Zone	Surface (0)	A: (5-100)	B:(100-175)	C:(175-500)
		$\mu\text{m}$	$\mu\text{m}$	$\mu\text{m}$
Initial $0.0\%\epsilon$	29 MPa	40 MPa	45 MPa	65 MPa
$1\%\epsilon$	213 MPa	143 MPa	150 MPa	150 MPa
$1\%\epsilon$ after SCC	29 MPa	25 MPa	(25-160) MPa	160 MPa

### 7.5.2 Effect of stress relaxation on cracking

**High aspect ratio ( $b/c$ ):** In the light of this result about stress relaxation, the high aspect ratio ( $b/c$ ) found for the cracks can be explained by stress relaxation in Zone A, and B, which makes the effective dimensions, ( $b_{\text{eff}}$ ) and ( $c_{\text{eff}}$ ), be less than the measured dimensions ( $b$ ) and ( $c$ ) respectively, as illustrated in Fig. 7.13.

**Crack branching and arrests:** Another effect of stress relaxation is observed in long duration SCC tests. Figure 7.14 shows a cross section of an 88 hour OCP SCC test in 2 M  $\text{H}_2\text{SO}_4$  + 0.5 M NaCl with  $\sigma = 210$  MPa. The cracks can be divided into two classes; the long, and the short cracks. It's noticed that at the average location where the cracks branch, neighbor cracks tend to arrest. Explaining this by the effect of stress relaxation and redistribution after branching at this given depth indicated by the hatched orange line in Fig. 7.14. An interesting feature in this image as well is the crack interaction as the case is for the two cracks at the

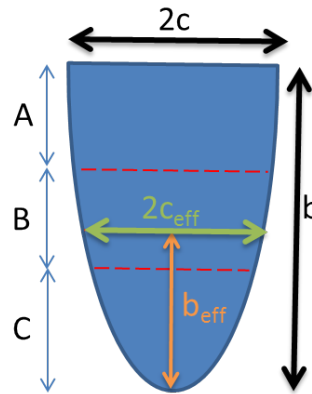


Figure 7.13: Explaining the high measured aspect ratio ( $b/c$ ). Zones A, B, and C are the three stress zones explained in Fig. 7.12.

most right of the given section, where their branches met together forming one cracking path afterward.

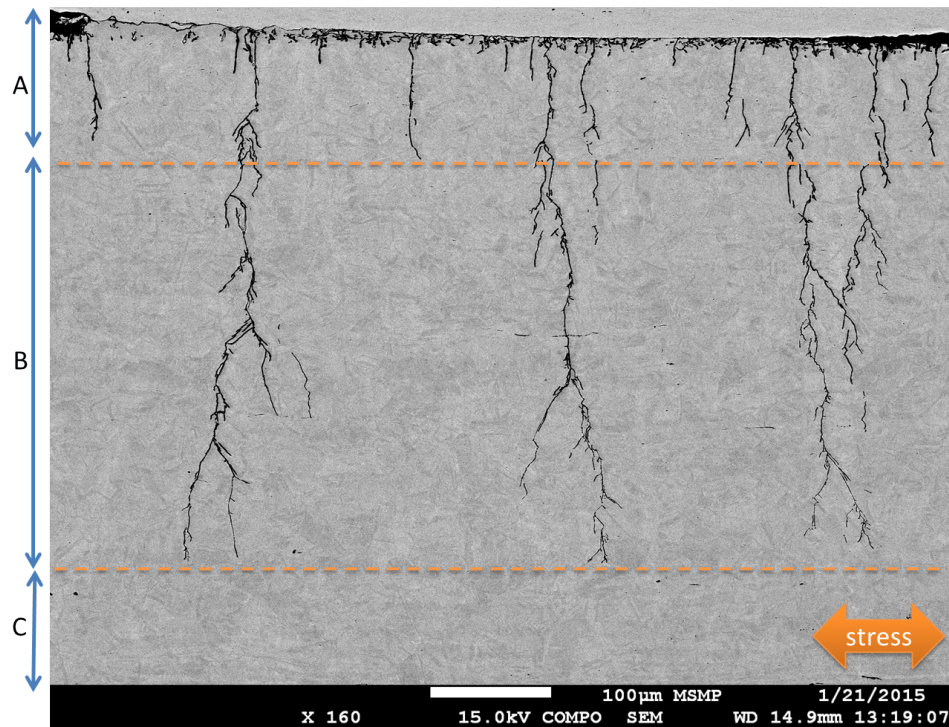


Figure 7.14: Effect of stress relaxation on crack arrests. This corresponds to an 88 hour OCP SCC test in 2 M  $\text{H}_2\text{SO}_4$  + 0.5 M NaCl with  $\sigma = 210$  MPa. Zone A, B, and C correspond to the relaxation zones described in section 7.5.1.

**Cracking macroscopic path** It should be evident now that the macroscopic cracking direction follows a direction which is perpendicular to the operating stress (applied/residual). This was the case in all cracking profiles shown earlier in the present work, such as that in Fig. 7.14. However, the special way the SCC tests are made in this work revealed how a crack would propagate if the tensile stresses on the sides of its facets are non-equal. This was the case in our experiments due to stress relaxation effect at the center of the confined cracked zone, which was subjected to the corrosive environments, while the rest of the sample is under bending mo-

ment. Figures 7.15 (a) and (b) show the left most and the right most edges of the SCC confined zone respectively. The effect of the reduced amount of stress at one side of the crack due to the neighbor cracks drifted the path of the crack towards the non-cracked direction, where the tensile stress is still operating.

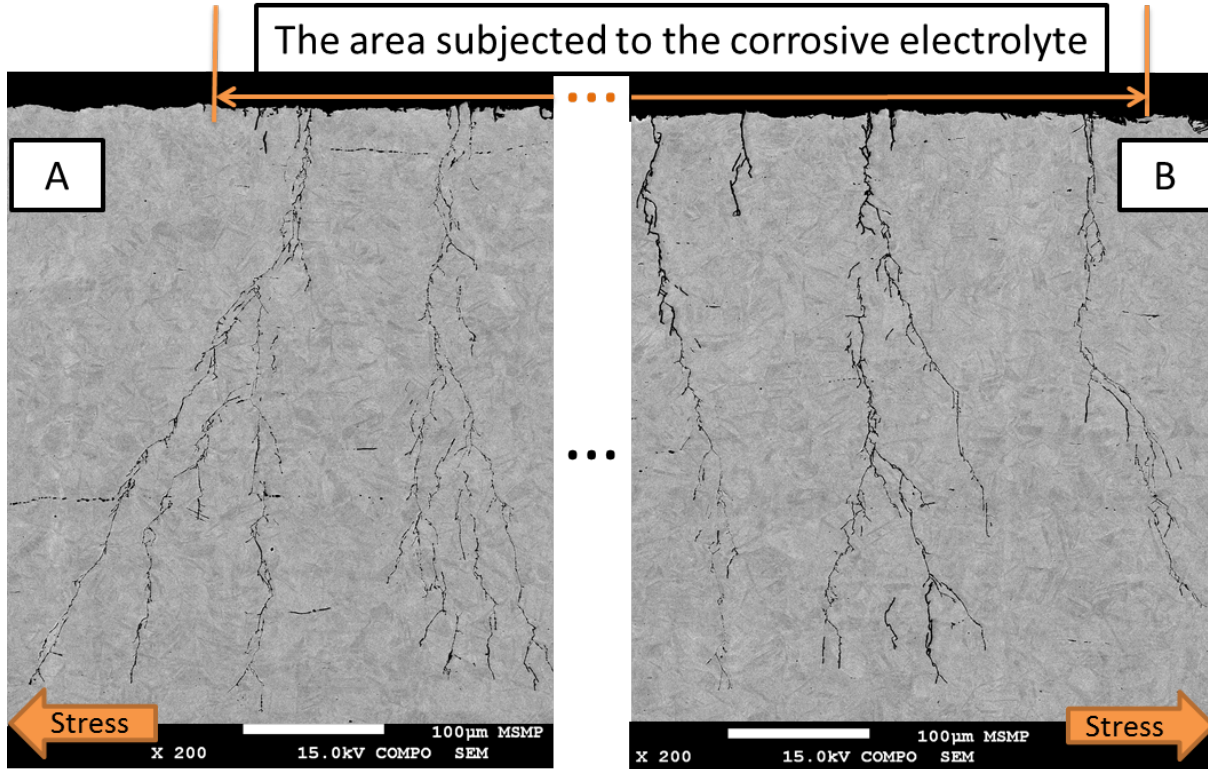


Figure 7.15: Cross-section of 88-hour SCC test in 2 M  $\text{H}_2\text{SO}_4$  + 0.5 M  $\text{NaCl}$  with  $\sigma = 210$  MPa. (A) and (B) show the left most and right most sides of the area which was subjected to the corrosive electrolyte.

The effect of stress relaxation was observed even by the upper surface observation. Figure 7.16 shows two cracks propagating towards each other. When the crack tips get close, the local stress principal direction changes from the macroscopically applied tensile stress (orange arrow) due to stress relaxation. The stress fields thus get re-oriented as shown by the red arrows, pulling the propagation of both cracks towards the center of the stress field, forming eventually what looks like an island between the two of them.

## 7.6 Conclusions

- An introductory to cracking modeling is presented with a review of the requirement of such modeling, along with the advances made in towards this in the present research.
- Experimental statistics of the semi-elliptical crack dimensions revealed ( $b/c$ ) ratio to be in the range of [4.7, 10.2], which is higher than that found in conventional fracture mechanics.
- The calculations based on the experimental measures show the propagation rate to be higher along ( $b$ ) than that along ( $c$ ), which is contradictory to predictions by fracture mechanics.
- A methodology of statistical estimation of the measured dimensions was proposed, in order to check their validity.



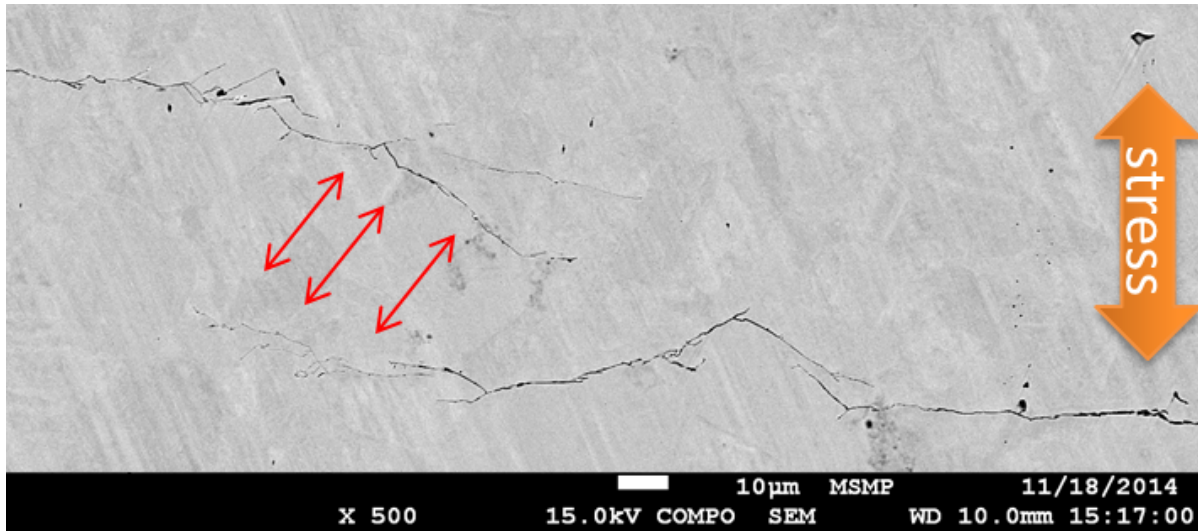


Figure 7.16: Effect of stress relaxation on crack macroscopic path on the upper surface. This corresponds to an 44 hour OCP SCC test in 2 M  $\text{H}_2\text{SO}_4$  + 0.5 M NaCl with  $\sigma = 210$  MPa.

- The measures made for  $(b)$  dimensions was found to be not representative of the estimated distribution obtained by random sectioning of the corresponding ellipse having the dimensions  $b_{\text{avg}}$  and  $c_{\text{avg}}$ .
- A methodology was suggested to enhance the statistics of  $(b)$  measurements by a random simulation. After this improvement was applied, it was found that:
  - The domain of  $(b/c)$  ratio for the different SCC tests was reduced to  $[3.6,8]$  compared to the initial range:  $[4.7,10.2]$ .
  - The calculated propagation rate based on the simulation results of  $(b)$  was less scattered for the SCC of different duration.
- The enhanced results by simulation is closer to the classical fracture mechanics than the original experimental values.
- XRD analysis revealed that the initial metal sheet has around 30 MPa of tensile residual stress attributed to the manufacturing processes.
- The measured strain on the upper surface corresponds to a stress of 213 MPa on the upper surface. This is the theoretically expected value resulting from the strain applied by the curved support ( $\varepsilon = 0.1\%$ ).
- After SCC tests, cracking causes stress relaxation to the basic residual stress value existing in the bulk material. This was the case between the surfaces, until 95  $\mu\text{m}$  depth which represents the average crack length obtained.
- A gradual stress increase was observed between the depth of 95  $\mu\text{m}$  to the depth of 175  $\mu\text{m}$ , which represents the maximum crack length obtained at this period. After this depth, the material gets back to 160 MPa, which corresponds to the applied stress value.
- Stress relaxation explained the obtained high  $(b/c)$  ratio. The propagation along  $(b)$  is less than the one expected to the crack geometry due to the stress relaxation by the neighbor cracks.
- Cracking arrests were observed to have a common depth, which corresponds to the zones defined by the stress relaxation profile after cracking.

- XRD analysis showed that the orientation of the crack propagation is directly influenced by the local stress field around the crack.

## 8.1 Conclusions

This work presented a multidisciplinary approach to study the stress corrosion cracking (SCC) of stainless steel in acidic medium. The main purpose was to verify the influence of the applied stress on the mechanical and chemical parameters related to SCC.

The approach starts by the characterization of the base material for its bulk and surface elemental composition, surface defects and their composition, the mechanical constants of the material, the residual stress, and the granular and phase analysis along the three directions.

The technique of atomic emission spectroelectrochemistry (AESEC) was adapted to perform corrosion tests of samples with controlled stress state. This technique allowed the access to current and potential transients during the controlled potentiodynamic corrosion tests. In addition to this, the metallic concentration was in-situ measured by coupling the downstream of the flow cell to the inductively coupled plasma optical emission spectroscope (ICP-OES). The technique was validated by comparing to previously produced experiments for classical unstressed samples.

### 8.1.1 Electrochemical statistics

The first set of experiments was dedicated to checking the direct effect of stress on the surface activation and passivation during linear and potentiostatic pulse tests. Mirror polishing the surface was considered as well to check the effect of surface preparation, and the corresponding effect on surface microstructure gradient on the corrosion parameters. Among five suggested solutions with different  $\text{H}_2\text{SO}_4$  and  $\text{NaCl}$  concentrations, 5 M  $\text{H}_2\text{SO}_4$  showed to be the solution giving the most reproducible polarization curves. A stagnant cell was used for part of the linear polarization experiments, for its relative ease in the experimental procedure. Different criteria on the current density transients and the OCP curves were selected for the purpose of comparing different experimental conditions.

The experimental technique managed successfully to detect a difference due to mirror polishing the surface; which showed to be more resistant to corrosion, as an effect of strain-hardening the surface during the polishing process. The influence of increasing the electrolyte acidity and/or chloride content was detected by this technique. However, for most of the selected criteria, the effect of applied stress was negligible compared to the effect of surface polishing, or increase in chloride concentration for example. This tells that the measuring technique is sensitive enough to detect reaction intensity variation resulting from changing surface state, but not to the applied stress. The effect of stress might have been masked by the high acidic concentration of the used electrolyte which is reflected on the high current density obtained at relaxed



conditions, making it difficult to detect small variations such as those due to the applied stress.

### 8.1.2 Statistics of potentiostatic pulse testing

For the passivation experiments, an electrolyte of 2 M  $\text{H}_2\text{SO}_4$  was used to perform potentiodynamic experiments on stressed and unstressed samples. Samples were subjected to an optimized potentiodynamic program where the material's surface passes through active to passive states in three repetitive cycles. The recorded electrochemical registered transients were analyzed to check for any possible influence of the applied tensile stress can be detected over the corrosion behavior as compared to samples in their relaxed state.

Surface active/passive transition and the other way around was successfully made by these experiments. During the activation step, the dissolution of the passive film was successfully achieved, reaching an intensive cathodic dissolution of 25 mA within less than 10 s. Four significant charge transfer zones were detected during the activation step: during the existence of the passive film, during the passive film dissolution, and as it thickens and gets to repeated passive film breakup-repair processes. The difference between the initial industrial passive film and the one experimentally build was successfully detected, indicating that the method holds for such analysis. However, no such difference was detected due to the influence of the applied mechanical stress over the surface.

On the other hand, the passivation charge showed to be higher for stressed samples, indicating more oxidation history during the passivation process. This can hold important interpretation concerning the passive film quality, properties, and its formation kinetics. Apart from the passivation charge, the other studied electrochemical parameters concerning this experimental set gave statistically equivalent results for stressed and unstressed samples. This could be due to the high acidic concentration which masks the effect of stress on surface activity, due to the severe corrosion reactions.

### 8.1.3 Passivation kinetics

The passivation analysis of 304L stainless steel in acidic solutions shows a fast metallic dissolution rate. The HFIC model was adapted to describe this passivation process. A challenge was using the HFIC for acidic solutions, where a correction for the high metallic dissolution component was necessary. This was possible by calculating the metallic dissolution fraction out of the total anodic current. Conventional electrochemistry in addition to AESEC technique were used to perform the required measurements for this calculation.

Analysis revealed that the fast metallic dissolution component during passivation causes the release of metallic composition from the surface, resulting in Cr-rich film growth. This dissolution is constructive, where the generated chromium rich layer isolates the bulk of the material, leading to passivity.

The calculated dissolution fraction of the total current was calculated, taking into account the dissolution of iron, chromium, manganese, and copper. After the separation of the passive film construction charge, the the instantaneous equivalent passive film thickness was calculated using Faraday's law. To check the validity of calculations, this thickness was used to recalculate the passivation current as seen by the HFIC model. By comparing the calculated current to the experimental total current, the domain of application of HFIC was quantified. This zone was used to calculate the passivation rate as measured by the  $cBV$  value in the HFIC equation. This analysis showed stressed samples to have lower passivation kinetic as compared to non-stressed samples.

Moreover, The average thickness of the passive film built over stressed samples was slightly higher, which is a logical result of the accompanied lower passivation rate. This is believed to be due to the passive film being more defective on stressed samples than that built over the non-stressed samples as indicated by  $cBV$  factor and the corresponding thickness until a predefined passivation state. The higher dissolution and lower passive film quality for stressed

samples compared to non-stressed ones might explain the particular chemistry causing selective attack at the crack tip in SCC, where the stress has very high values, and thus the passivation is slower and weaker.

The passive film thickness calculated based on charge concept using conventional electrochemistry was in the range of the thickness calculated based on elemental concentration criteria using AESEC method.

#### 8.1.4 SCC fractography and crystallography

Stress corrosion cracking of stainless steel was produced for  $\sigma = 250$  MPa in 2 M  $\text{H}_2\text{SO}_4 + 2$  M NaCl, and for  $\sigma = 210$  MPa in 2 M  $\text{H}_2\text{SO}_4 + 2$  M NaCl. Observation of cracking morphology revealed clear traces of slipping/dissolution systems on the crack facet. Other crystallographic evidences were collected by post experimental observation of the upper surface, and the cross section.

The cracking density was constant for a given stress state/environment system, while it increased as the applied stress increased.

The polished surface showed the preferential attack of the  $\{111\}$  planes on the upper surface. Nevertheless, the TGSCC was not related to those planes, except if they were oriented perpendicularly to the direction of the applied stress. This is due to the decohesion between the attacked crystalline planes by the applied stress, where reduced mechanical properties resulted from the adsorption of hydrogen, as described by AIDE model.

For samples subjected to  $\sigma = 250$  MPa in 2 M  $\text{H}_2\text{SO}_4 + 2$  M NaCl, the crystallographic orientation analysis revealed two types of preferential rupture planes;  $\{110\}$ ,  $\{111\}$  with percentages around 48%, 37% respectively. For face-centered cubic crystals,  $\{111\}$  planes are those over which slipping occurs. However, rupture planes could be of  $\{110\}$  family due to equal dislocation-pile-up on the primary and conjugate  $\{111\}$  planes. This result comes in agreement with recent SCC models, such as CELP and AIDE. However, other plane families were present such as  $\{211\}$  and  $\{102\}$  as a result of reducing the stress to an elastic stress ( $\sigma = 210$  MPa) in less severe SCC tests (2 M  $\text{H}_2\text{SO}_4 + 2$  M NaCl).

The cracking orientation was influenced by the local microstructure and the orientation of the grain boundaries ahead of the crack. SEM observation shows that crack propagation has a non-linear relation with exposure time, where it starts with low propagation kinetics within the period between 16-21 h, and goes to three times this speed between the period 21-125 h.

The OCP value of the surface during SCC test showed to get to a stable cathodic value (-350 mV vs SCE). This corresponds to the time where the surface is generally attacked, giving a flaked morphology. The acceleration of SCC kinetics was possible by the application of a cathodic constant pulse (-300 mV vs SCE) in 2 M  $\text{H}_2\text{SO}_4 + 2$  M NaCl. This caused the crack to develop in 2 hours in what's equivalent to that in 16-hour SCC test.

SCC was produced by the effect of the residual tensile stress existing initially in the material. However, the cracking kinetics was very slow compared to stressed tests.

#### 8.1.5 SCC modeling

An introductory to cracking modeling is presented with a review of the requirement of such modeling, along with the advances made in towards this in the present research. Experimental statistics of the semi-elliptical crack dimensions revealed ( $b/c$ ) ratio to be in the range of [4.7, 10.2], which is higher than that found in conventional fracture mechanics. The calculations based on the experimental measures show the propagation rate to be higher along ( $b$ ) than that along ( $c$ ), which is contradictory to predictions by fracture mechanics.

Statistical estimation of the measured dimensions was proposed, in order to check their validity. The measures made for ( $b$ ) dimensions was found to be not representative of the estimated distribution obtained by random sectioning of the corresponding ellipse having the dimensions

$b_{\text{avg}}$  and  $c_{\text{avg}}$ . A methodology was suggested to enhance the statistics of ( $b$ ) measurements by a random simulation. After this improvement was applied, it was found that:

- The domain of ( $b/c$ ) ratio for the different SCC tests was reduced to [3.6,8] compared to the initial range: [4.7,10.2].
- The calculated propagation rate based on the simulation results of ( $b$ ) was less scattered for the SCC of different duration.

The enhanced results by simulation are closer to the classical fracture mechanics than the original experimental values.

XRD analysis revealed that the initial metal sheet has tensile residual stress around 30 MPa attributed to the manufacturing processes. The measured strain on the upper surface corresponds to a stress of 213 MPa on the upper surface. This is the theoretically expected value resulting from the stain applied by the curved support ( $\varepsilon = 0.1\%$ ). After SCC tests, the cracking causes stress relaxation to the basic residual stress value existing in the bulk material. This was the case between the surfaces, until 95  $\mu\text{m}$  depth which represents the average crack length obtained. A gradual stress increase was observed between the depth of 95  $\mu\text{m}$  to the depth of 175  $\mu\text{m}$ , which represents the maximum crack length obtained at this period. After this depth, the material gets back to 160 MPa, which corresponds to the applied stress value.

Stress relaxation explained the obtained high ( $b/c$ ) ratio. The propagation along ( $b$ ) is less than the one expected to the crack geometry due to the stress relaxation by the neighbor cracks. Furthermore, cracking arrests was observed to have a common depth, which corresponds to the zones defined by the stress relaxation profile after cracking. XRD analysis showed that the orientation of the crack propagation is directly influenced by the local stress field around the crack.

## 8.2 Perspectives

### 8.2.1 Electrochemistry

- The high acidic acidity of the used electrolytes might have caused a masking effect of the influence of stress on electrochemical transients. Thus, using less concentrated acidic solution might be more favorable, due to less accompanied reaction intensity. This will improve the detected of minor effects such as the increase of corrosion reaction intensity due to the applied stress.

### 8.2.2 Passivation kinetics

- The effect of stress is expected to be more pronounced if a lower acidic concentration.
- The calculated charge ( $q_{\text{film}}$ ) was assumed to be spent to build  $\text{Cr}_2\text{O}_3$  film. Based on this, the calculation was made to find the thickness of this passive film and its corresponding properties.
- The charge exchange during conventional potentiodynamic pulse tests showed to be higher for stressed samples. To confirm this by another test, ICP cycling statistical experiments can reveal if there are variation in certain metal dissolution/deposition on the surface as an effect of the applied stress. Based on these same assumptions, the reduction of activity during the passivation pulse was explained to be due to the classical passive film construction. However, this apparent passivation could be equally due to mass limited corrosion reaction, where the less noble elements are depleted from the surface with an increased concentration profile along the depth of the sample.

- To have an estimation of the thickness of such concentration gradient layer, if it's actually the case, XPS should be made to find the elemental concentration profiles before and after both, the activation, and passivation pulses.
- The  $cBV$  value should be correlated with mechanical properties of this layer, such as yield strength, ductility, and hardness, or any other property of interest. This determines partially the SCC resistance of the material, where a film of high quality means less SCC susceptibility. Such a parameter, in addition to the passivation rate, can be added to existing SCC prediction models.
- The following step is to build a quantified database. In this process, each  $cBV$  value is correlated to the corresponding estimated time to crack initiation, propagation, and failure for a given material/environment combination in conditions where the passivation pulse are not applied (like that in real-life service conditions).

### 8.2.3 SCC kinetics and fracture mechanics

- It was shown that the technique to determine the SCC fracture planes is efficient and reproducible in the lab. However, the results were highly affected by the local microstructure, neighbor crack interaction, and the near to crack-tip grain boundary orientation.
- In most of the cases, especially for IGSCC, the features of interest were dissolved during the SCC test/sample preparation. To overcome the previous difficulties, a better characterization the SCC crystallographic and fractographic fundamental features can be obtained if single crystal samples of known orientations are used.
- Reducing the corrosion surface area by an adhesive (chloride free) mask can limit the number of produced cracks, and thus will give better results.
- Micro-mechanical analysis of the crack interaction can probably explain the preferential cracking planes of SCC tests samples of  $\sigma = 210$  MPa in (2 M  $\text{H}_2\text{SO}_4$  + 2 M NaCl).
- Since SCC includes IGSCC and TGSCC, modeling each of them should be done to simulate the real life cases. The first stage of this is to model each of them separately, then integrate both of them in one final model. This final model should be statically built such that it takes into account the grain boundary energy, in addition to the granular shape aspect and slope, size, and orientation.
- Modeling should integrate the applied stress field and the gradient of residual stress as was shown by the XRD analysis.



---

## Chemical Composition of the Base Material

---

The following figures give the spatial analysis of the chemical composition, as was described in section:2.2.1.

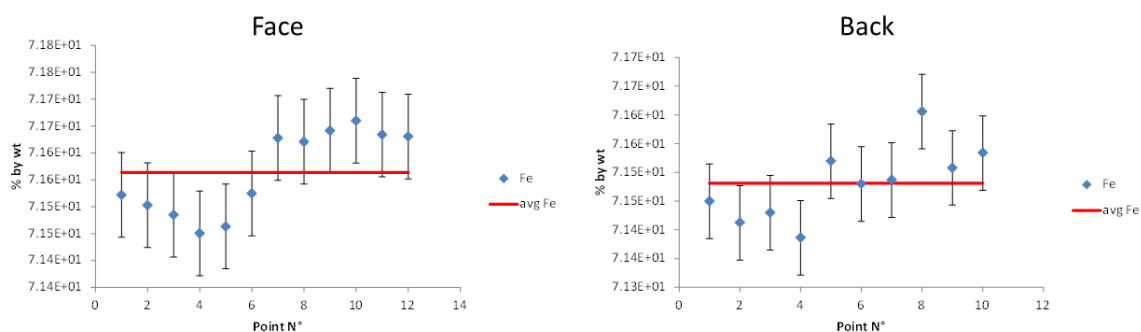


Figure A.1: Surface spatial statistical analysis of Fe concentration.

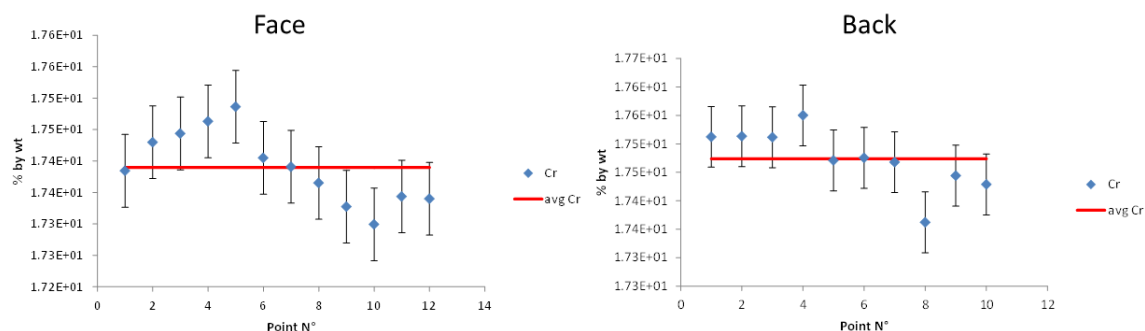


Figure A.2: Surface spatial statistical analysis of Cr concentration.

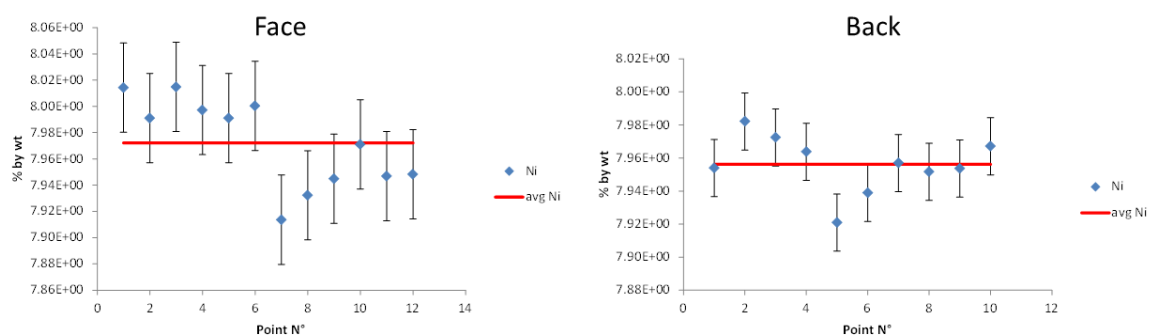


Figure A.3: Surface spatial statistical analysis of Ni concentration.

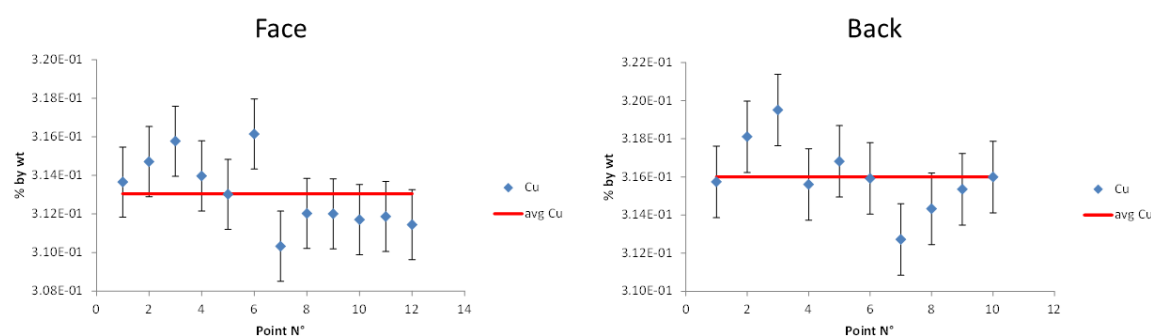


Figure A.4: Surface spatial statistical analysis of Cu concentration.

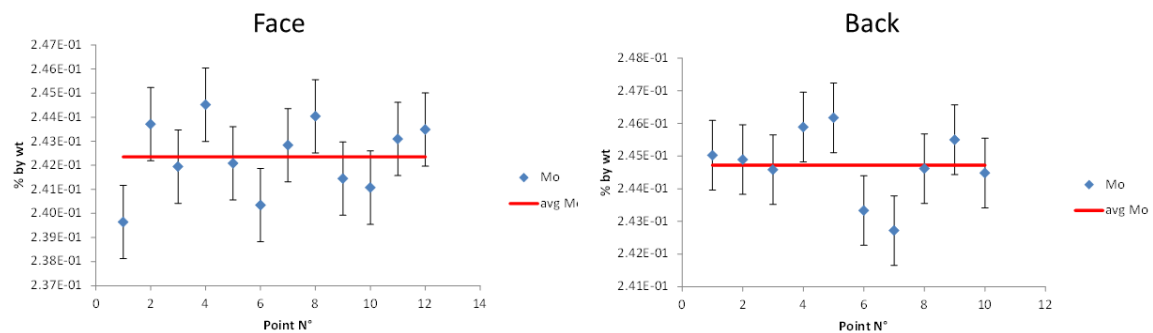


Figure A.5: Surface spatial statistical analysis of Mo concentration.

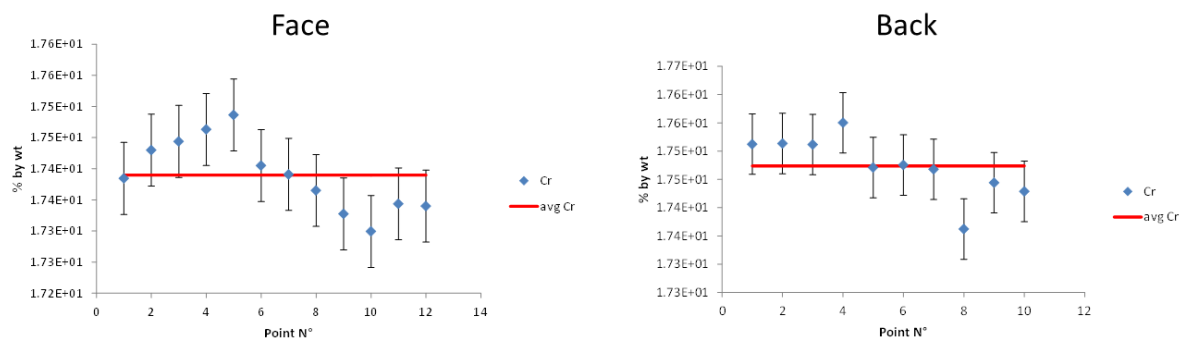


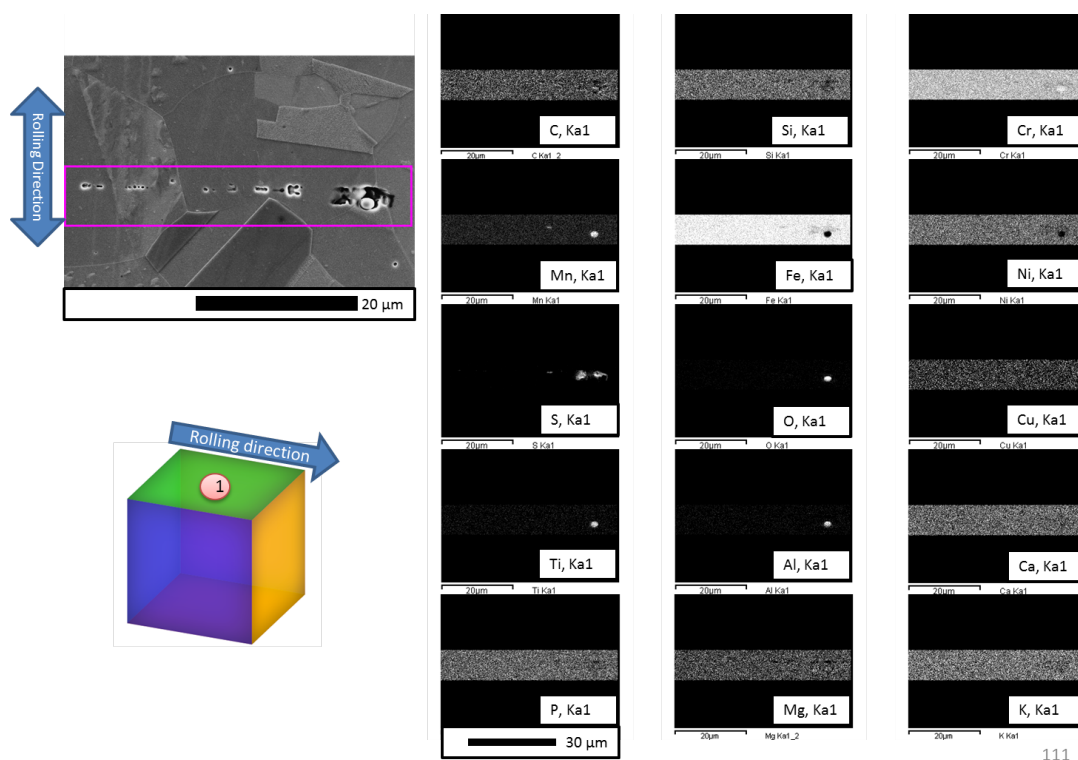
Figure A.6: Surface spatial statistical analysis of Cr concentration.

---

Chemical Composition of a Selected Surface Defect

---

The following EDS analysis reveals high Mn concentration, as an example among other defects which had similar composition (in the three directions). This defect shown in Fig.B.1 was one of the upper surface defects.



111

Figure B.1: EDS analysis of a selected upper surface defect with high Mn composition.





---

Simulation of the Experimental Applied Strain

---

The assembly of the curved support and sample were simulated using Abaqus. Figure C.1 shows the assembly with the load required to deform it, such that it takes the radius of the support. The case shown here is for R800 mm support. The sample geometry and loading corresponds to the real-life sample, as shown in Fig.C.2.

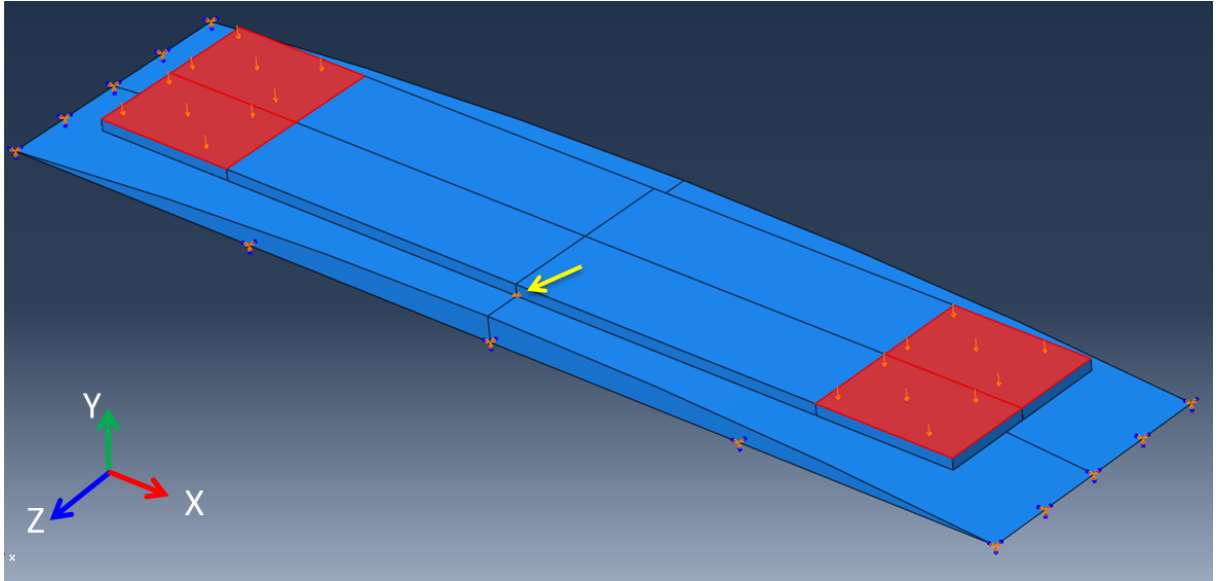


Figure C.1: Sample-support assembly in Abaqus.

**Material properties:** The parameters of the crystalline constitutive law identified to 304L steel are:  $(C_{11}, C_{12}, C_{44}) = (197.5, 125, 122)$  GPa respectively. The rest of the properties were the classical mechanical parameters obtained in section: 3.6.

**Boundary conditions:** The boundary conditions applied to the support was total limitation to all the degrees of freedom. While for the sample, the point shown in Fig.C.1 by the yellow arrow was limited for its displacement in the (x) direction.

**Loading:** The load in this case was a pressure of 1 MPa, applied to the boarder of the sample. This simulates the effect of the screws for the real life sample.

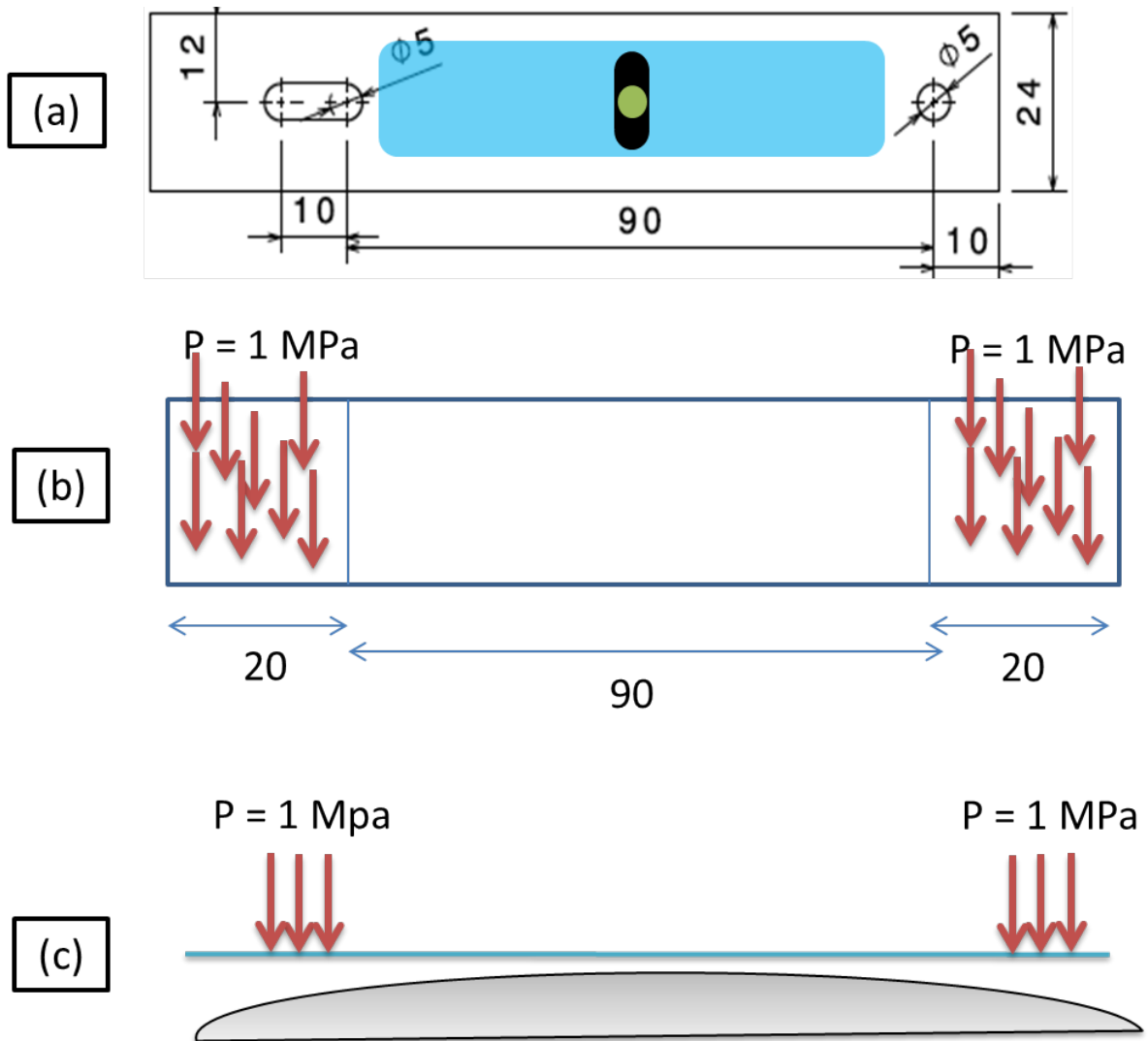


Figure C.2: Illustration of the simulated sample and loading. (a): the actual sample. (b): the simulated case. (c): the support sample assembly shown in Fig.C.1.

**Results:** The simulation result for  $\sigma_{11}$  is given in Fig.C.3.

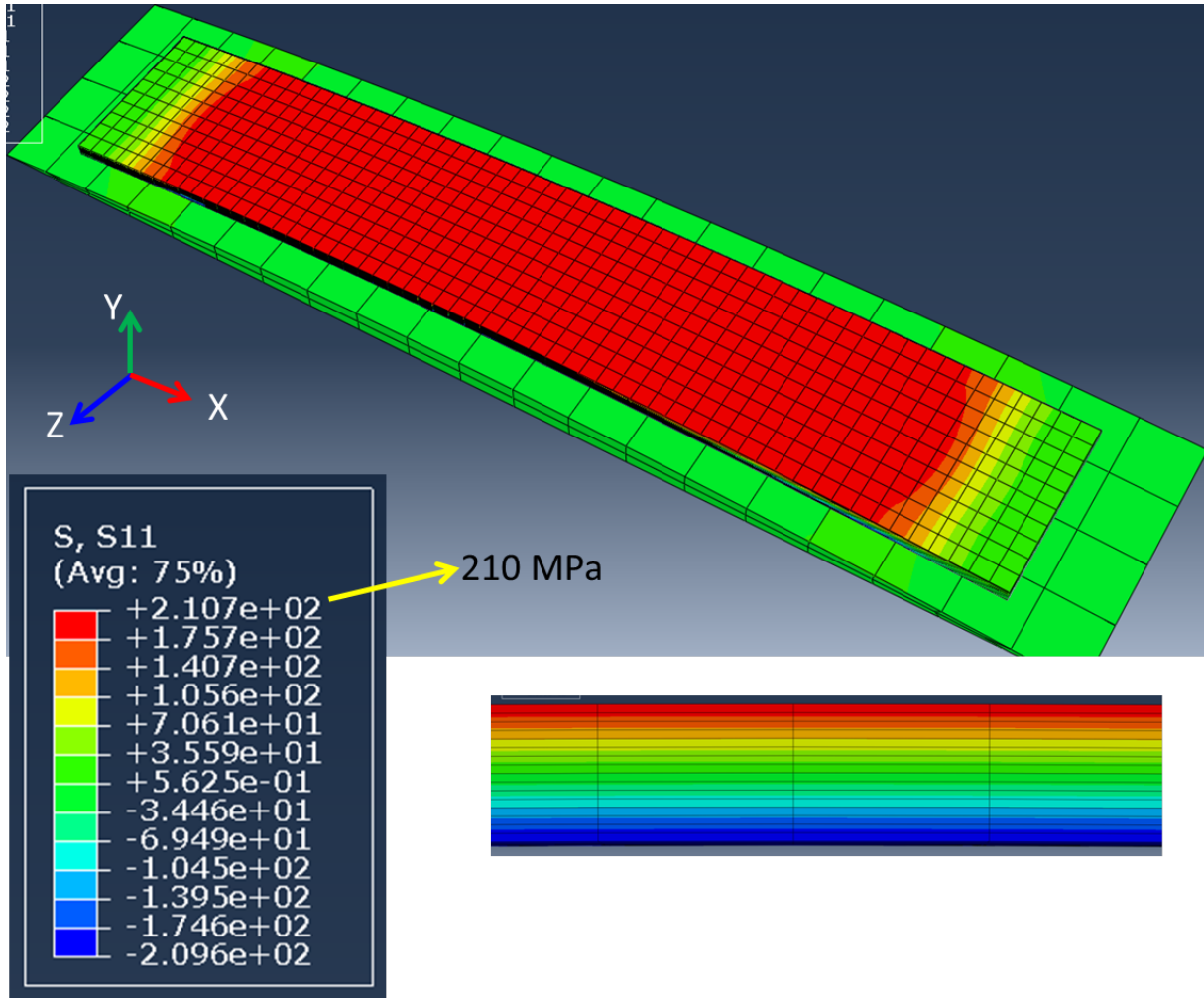


Figure C.3: Simulation results of  $\sigma_{11}$  stress using Abaqus.

It's noticed that the stress  $\sigma_{11}$  varies from being tensile in the upper surface with 210 MPa, to being compressive on the lower surface having -210 MPa. The stress gradient is illustrated in Fig.C.3 over the sample's cross-section along with the corresponding stress values. This result confirms the theoretical calculations performed earlier in section: 6.1.

This can be used to perform simulation at the micro-level of the material, if the appropriate representative volume element of the micro-structure. Such analysis has the potential to answer questions about the maximum stress/shear plans near a crack tip, by which the experimental results, such as those found in section: 6.3.6 could be better understood.



---

Granular Statistics by EBSD Analysis

---

The following curves (Fig.D.1 to D.5) represent the distribution of the grains (indicated by their number) according to the aspect in consideration. The grain numbers were ordered according to their area. The data are for the EBSD map presented in section: 3.4.

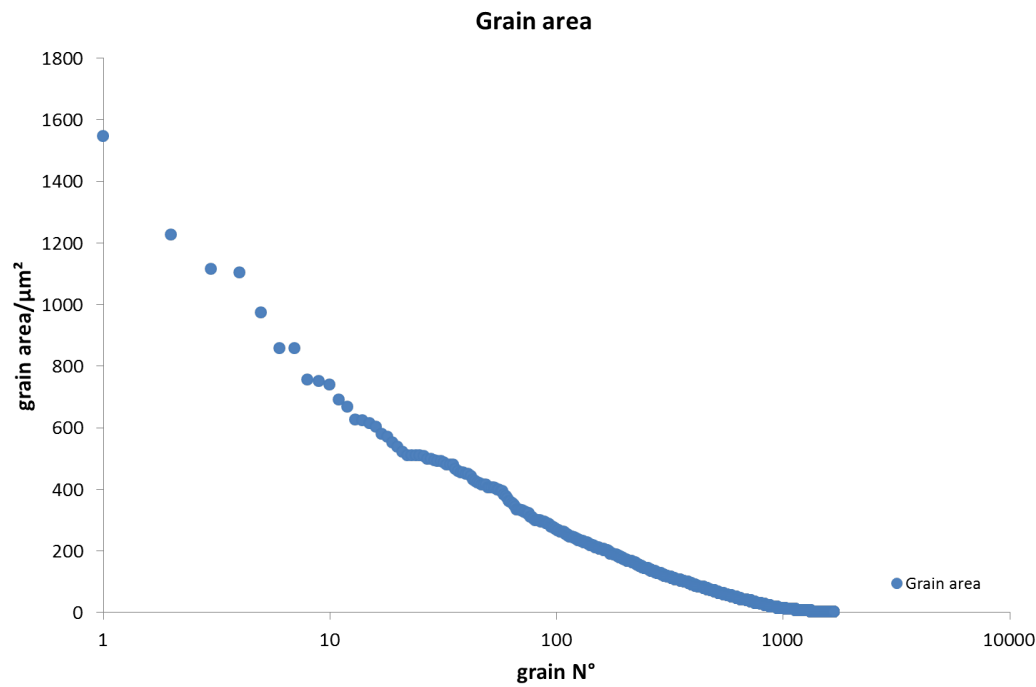


Figure D.1: Statistical distribution of the grain area in the base material.

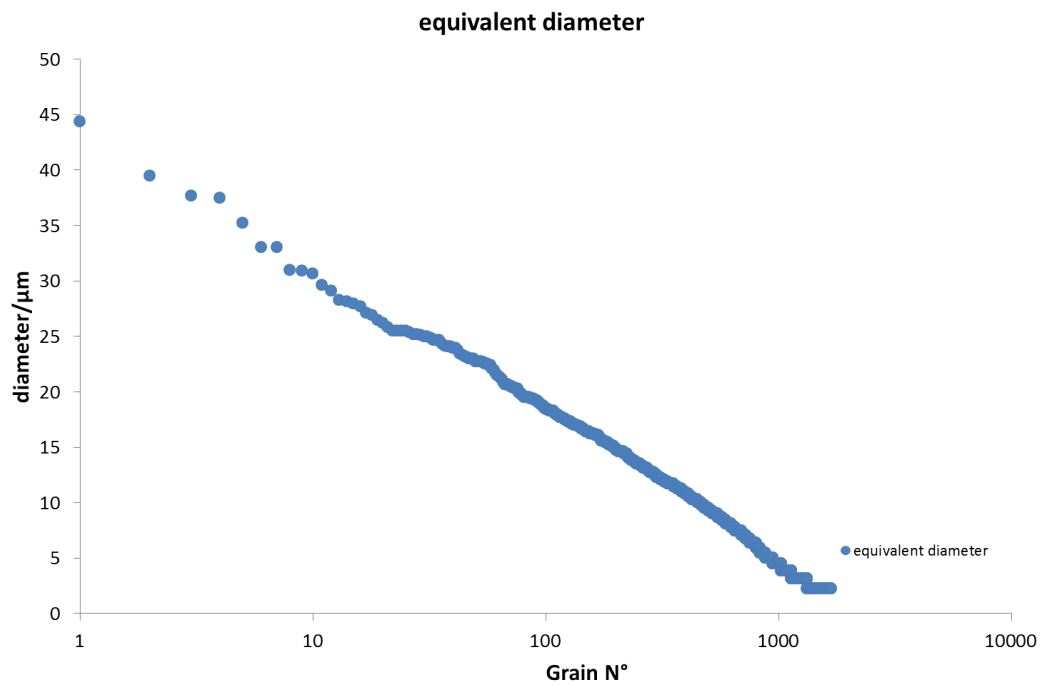


Figure D.2: Statistical distribution of the equivalent grain diameter in the base material.

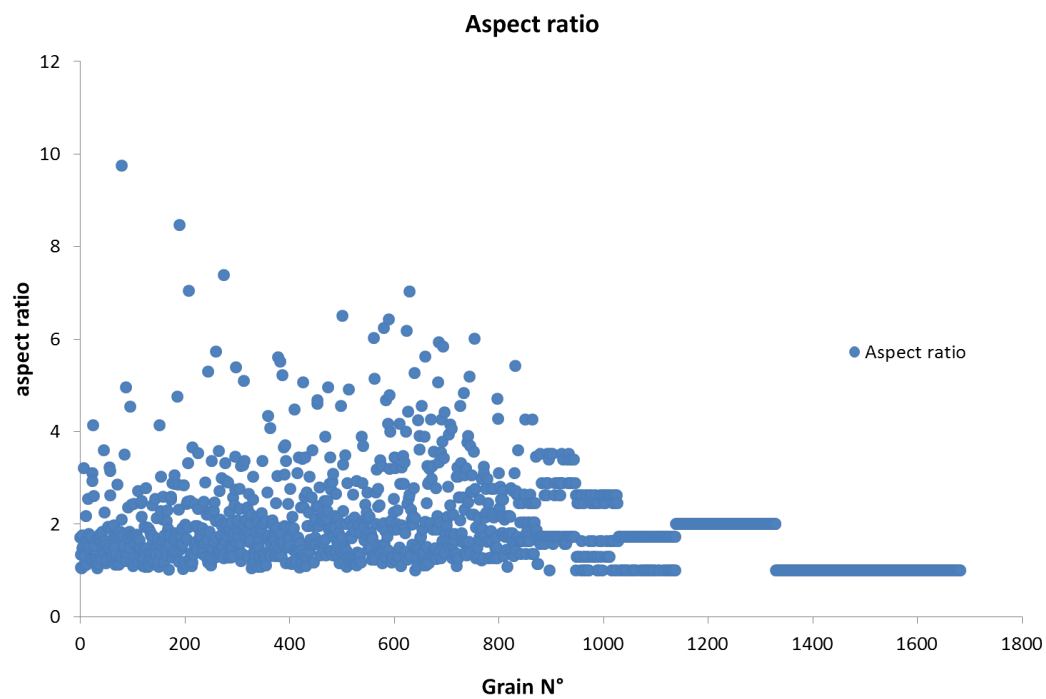


Figure D.3: Statistical distribution of the equivalent grain aspect ratio in the base material.

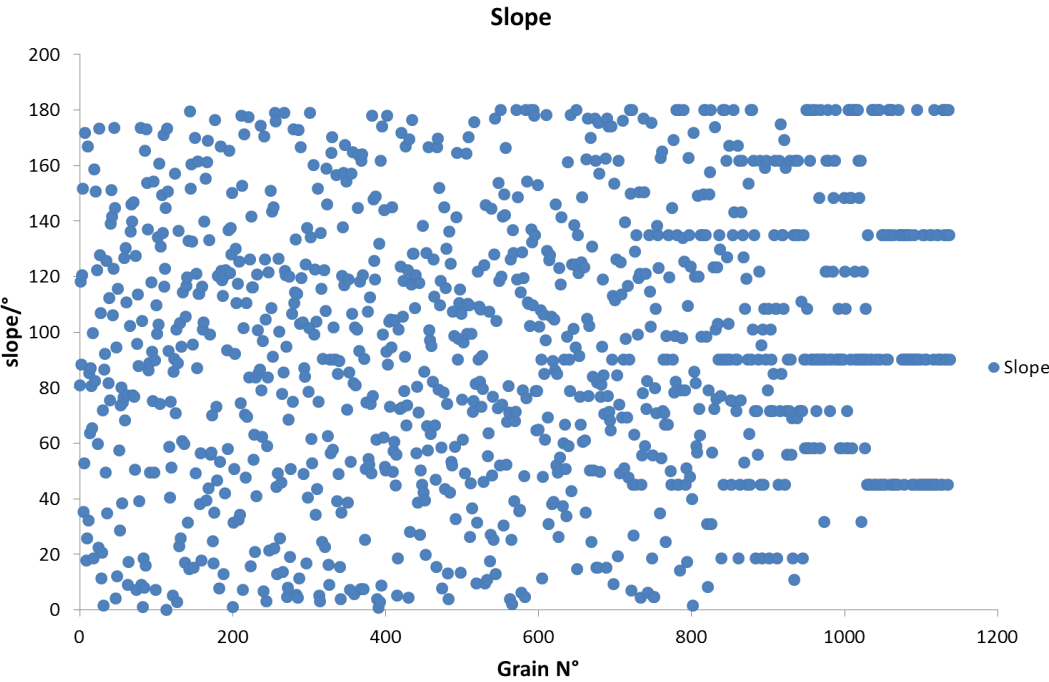


Figure D.4: Statistical distribution of the slope of the major axis of the equivalent elliptical grain in the base material.

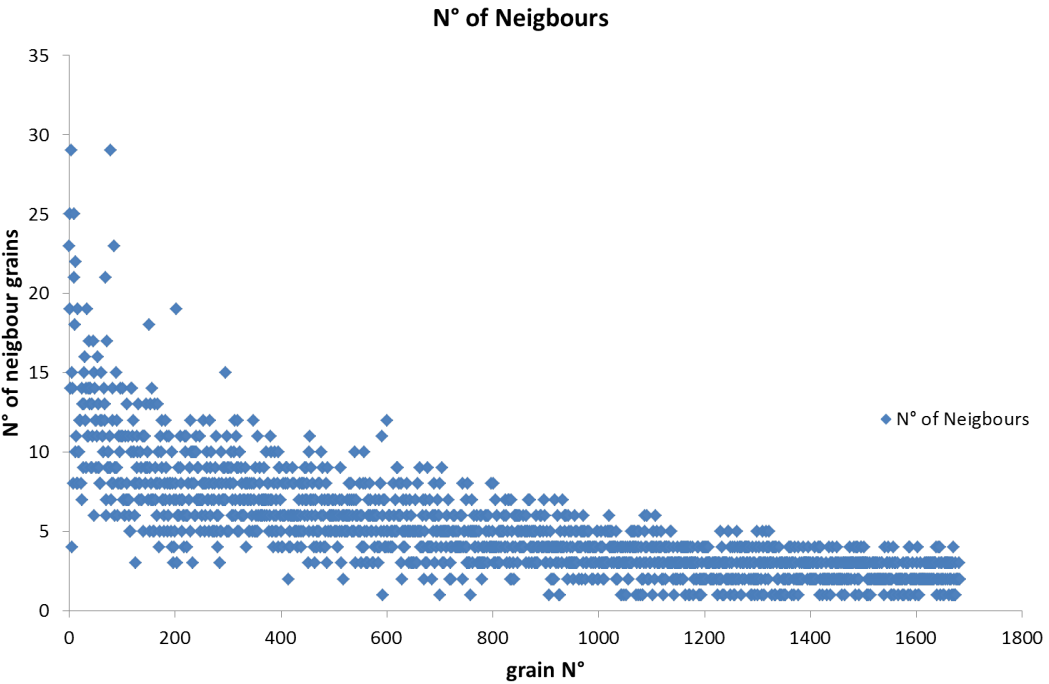


Figure D.5: Statistical distribution of the number of neighbor grains in the base material.





---

Electrolyte Preparation

---

To prepare the 1 l solution of 2 M  $H_2SO_4$ , using a concentrated acid having 95%  $H_2SO_4$  concentration by weight, we need to proceed as follows:

**The required mass of the concentrated solution:** Having the molar mass of the sulfuric acid,  $M_{H_2SO_4} = 98 g.mol^{-1}$ , then for 2 M  $H_2SO_4$  the mass will be 196 g of  $H_2SO_4$ . This is the required mass of pure  $H_2SO_4$  to prepare the required solution (1 l of 2 M  $H_2SO_4$ ).

Since the concentrated sulfuric acid concentration is 95% by wt., the required mass of this solution to give 196 g of  $H_2SO_4$  will be  $m_{H_2SO_4} = 196/0.95$ , which gives  $m_{H_2SO_4} = 206.32 g$ .

**The required volume of the concentrated acid** Since what we measure by the micro-pipette is the volume, we need to calculate this volume as:

$$\forall_{H_2SO_4} = \frac{m_{H_2SO_4}}{\rho_{H_2SO_4}} \quad (E.1)$$

Substituting the values will give  $\forall_{H_2SO_4} = 112.13 ml$  required volume of the concentrated acid to prepare the solution. This volume should be added to a flask already containing water (300 ml), since the opposite can produce a lot of vapor and can be seriously risky concerning the vapor inhalation, or due to the possible splash that can be caused.

**Chloride addition to the solution:** For the NaCl, the calculation is much easier. We only need to know the molar mass of this component which is  $M_{NaCl} = 58.44 g.mol^{-1}$ . So, for example, to prepare 0.5 M NaCl solution, we need to add  $58.44/2 g$  in one liter of solution.

**Filling the flask with water:** After the solution acid and the chloride additives are mixed with the water in the flask, the solution should be left to cool down so that it gets to the room temperature. This is necessary for the precision in volume which is affected by heating. Once the solution is cold enough, water is added to the flask until the volume of 1 l is obtained.



---

## Derivation of the Dissolution Current Formula

---

The aim here is to calculate the ratio of the current density due to the dissolution of a given metallic element. This can be done using Faraday's second law. Faraday's second law is given by Eq. F.1:

$$m = \frac{Q}{F} \cdot \frac{M}{z} \quad (\text{F.1})$$

Where:

- $m/(g)$ : the mass of the substance liberated (dissolved) at an electrode during the reaction.
- $Q/(C)$ : the total electric charge passed through the substance during the reaction duration.
- $z$ : the oxidation number of the considered metal in the given electrolyte.
- $F/(C.mol^{-1})$ : Faraday's constant equals to  $9.64853399(24) 10^4 C.mol^{-1}$ .
- $M/(g.mol^{-1})$ : the molecular weight of the considered element.

If the resulting current due to the oxidation of certain element is  $i/(A)$ , the charge  $Q$  can be given by  $Q = i.t$ , where  $t/s$  is the time duration of the current exchange. If this is introduced to Eq.F.1, the resulting equation is given by Eq.F.2:

$$m = \frac{i.t}{F} \cdot \frac{M}{z} \quad (\text{F.2})$$

Rearranging Eq.F.2, we get:

$$i = \frac{m.F.zt}{t.M} \quad (\text{F.3})$$

Multiplying Eq.F.3 by  $\frac{\forall}{t}$ , where  $\forall$  is the a unit volume of the electrolyte, we get:

$$i = \frac{m}{\forall} \cdot \frac{\forall}{t} \cdot \frac{F.z}{M} \quad (\text{F.4})$$

The concentration,  $C/(g.ml^{-1})$ , of a solution is defined as  $C = \frac{m}{\forall}$ . On the other hand, the ratio  $\frac{\forall}{t}$  represents the flow rate of the solution  $f_o$ . Substituting these in Eq.F.4, we get:

$$i = \frac{C.f_o.F.z}{M} \quad (\text{F.5})$$

If  $v(\mu g.cm^{-2}.s^{-1})$  is defined as the elementary dissolution rate,  $m$  can be obtained by:

$$m = v.t.S \quad (\text{F.6})$$

Where  $S$  is the area of the exposed surface to corrosion. If this is substituted in Eq.F.1, we get:

$$v.t.S = \frac{i.t}{F} \cdot \frac{M}{z} \quad (\text{F.7})$$

Where  $i.t = Q$  as was explained earlier. Rearranging Eq.F.7, we get:

$$\frac{i}{S} = \frac{v.F.z}{M} \quad (\text{F.8})$$

Where  $i/S$  is the current density defined by  $j$ . Thus, for a given instant of time,  $t$ , the dissolution current density of certain element  $j_m/(A.cm^{-2})$  can be given as:

$$j_m(t) = \frac{v_m(t).F.z_m}{M_m} \quad (\text{F.9})$$

Where the subscript  $m$  refers to a considered metallic element such as Fe, Cr, etc. Since  $C_m.f_o/S$  defines the metallic dissolution rate,  $v_m/(\mu g.cm^{-2}.s^{-1})$ , Eq.F.9 can be alternatively written as:

$$j_m(t) = \frac{C_m(t).f_o.F.z_m}{M_m} \quad (\text{F.10})$$

---

Multi-Element Corrosion System

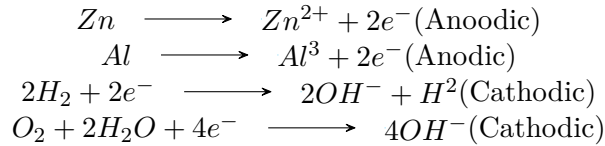
---

As presented in the previous section, the total measured current during polarization corresponds to the summation of the anodic and cathodic currents taking place at the recording instant.

This section aims to clarify the principle of polarization curves for a system consisting of multi-element such as the case in alloys.

Practically, each alloying element shows its own polarization curve, and all those elementary polarization curves sum up to provide the eventual polarization curve for the entire alloy. The principle is that balance should include all elements making any anodic or cathodic reactions, and the net of their summation will result in the external current detected by the measuring equipment.

A simple example can be given to make this clear is a Zn-Al alloy subjected to oxygen-containing water. Two elementary anodic reactions and two other elementary cathodic reactions will take place in this system as shown in the following equations:



If a polarization curve is produced for this alloy, the polarization current will be the sum of all electrochemical currents on the reacting surface.

$$\begin{aligned}
 i_e &= i_c + i_a \\
 i_e &= (i_{\text{Zn}} + i_{\text{Al}}) + (i_{\text{H}_2\text{O}} + i_{\text{O}_2})
 \end{aligned}$$

Again for this multi-element system, when there is no external polarization, the external current is equal to zero as a result of equality of both summation of anodic elementary currents and cathodic elementary currents [130]:

$$\begin{aligned}
 i_e &= 0.0 \\
 \Sigma i_a &= -\Sigma i_c
 \end{aligned}$$

Corrosion rate cannot be measured directly, but it can be determined at a certain instant from the measured current in the polarization test. It's known in literature how methods like linear polarization resistance or Tafel extrapolation can determine the corrosion current [121].



---

## Selection of Potential Zones on the Polarization Curve

---

In this section, the active, passive, and transpassive zones will be determined for polarization tests of 304L stainless steel. The curves are produced in  $2\text{ M H}_2\text{SO}_4$  by the flow electrochemical cell described in section (2.4.2). Fig.H.1 gives the obtained polarization curves for three tests. The potential domains for the active and passive and transpassive zones are chosen according to the current curves in the blue block shown in the sub figure in Fig.H.1.

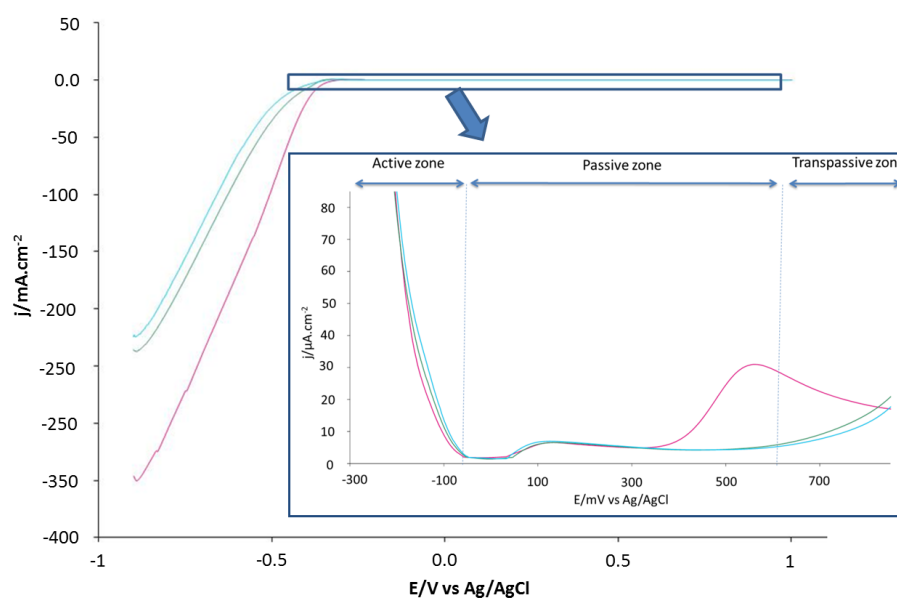


Figure H.1: Polarization curves of unpolished 304L SS samples in  $2\text{ M H}_2\text{SO}_4$ . Sub-figure shows the domain after the passivation peak.

As seen in the curve, the domain over which the sample was polarized is  $[-900, 1000]$  mV vs Ag/AgCl. Thus, within this domain, the passive region where the current gets to its lowest values was considered as a separation between the active and the transpassive zones. According to this, and as shown in the sub-Fig.H.1, the range of each zone was approximated as given in Table:H.1



Table H.1: Active, passive, and Transpassive potential domains of 304L stainless steel in 2 M H<sub>2</sub>SO<sub>4</sub>.

	Active	Passive	Transpassive
E/mV vs Ag/AgCl	[-900, -85]	[ -85, 685]	[ 685, 1000]

## Graphs Related to Passivation Analysis

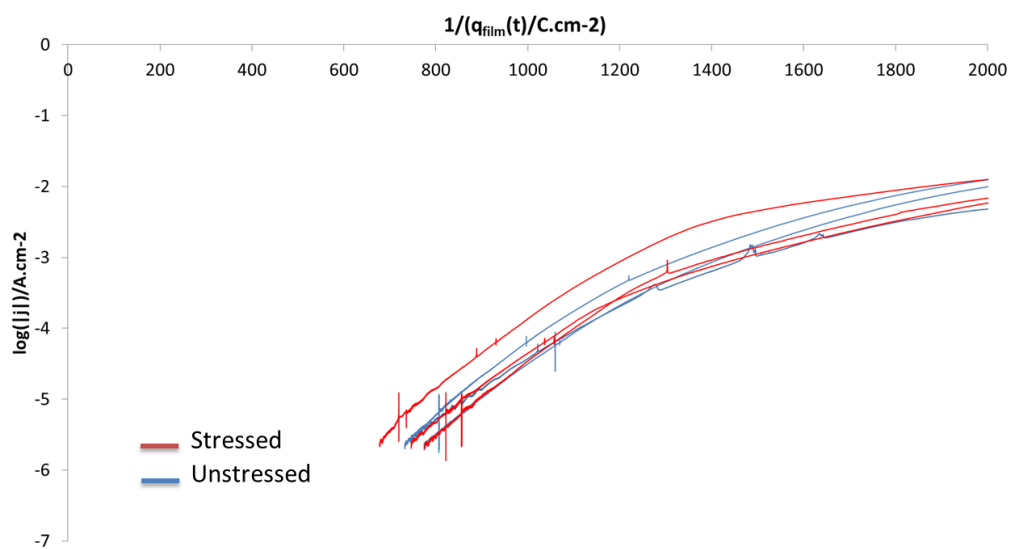


Figure I.1: The first cycle passivation anodic curves for stressed and unstressed tests in 2 M  $\text{H}_2\text{SO}_4$  plotted on  $\log j(t)$  vs  $1/q(t)$  axis.

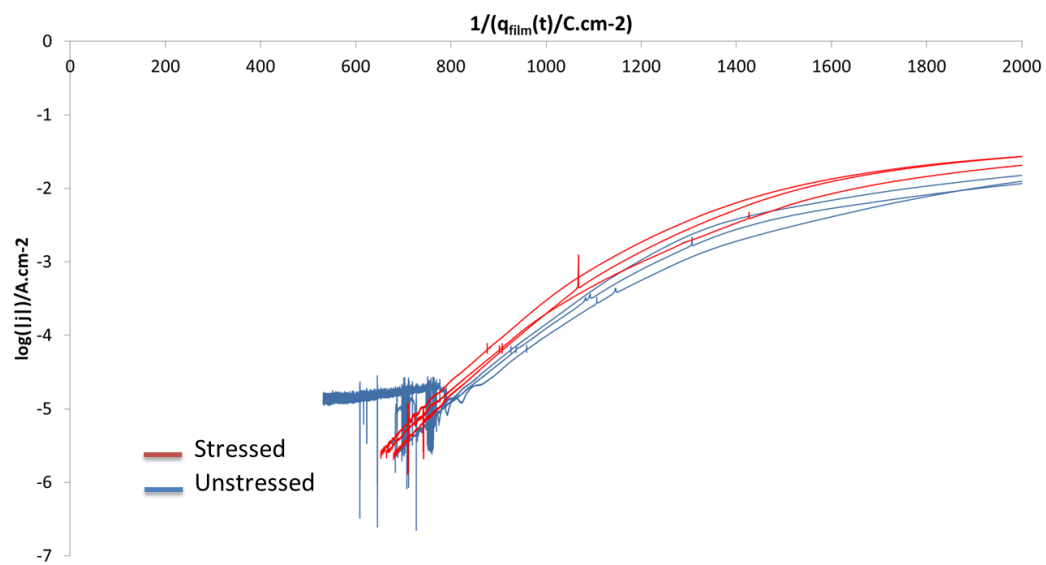


Figure I.2: The third cycle passivation anodic curves for stressed and unstressed tests in 2 M  $\text{H}_2\text{SO}_4$  plotted on  $\log j(t)$  vs  $1/q(t)$  axis.

---

## Early Surface State During SCC of a Mirror-polished Sample

---

Figure J.1 refers to a SCC test of  $\sigma = 210$  MPa in 2 M  $\text{H}_2\text{SO}_4 + 0.5$  M NaCl. the upper surface early stage preferential attack of the slipping lines. There is no relation between these slip lines and the initial dissolution with the crack orientation. The crack could be in their direction only if they were perpendicular to the direction of the normal applied stress.

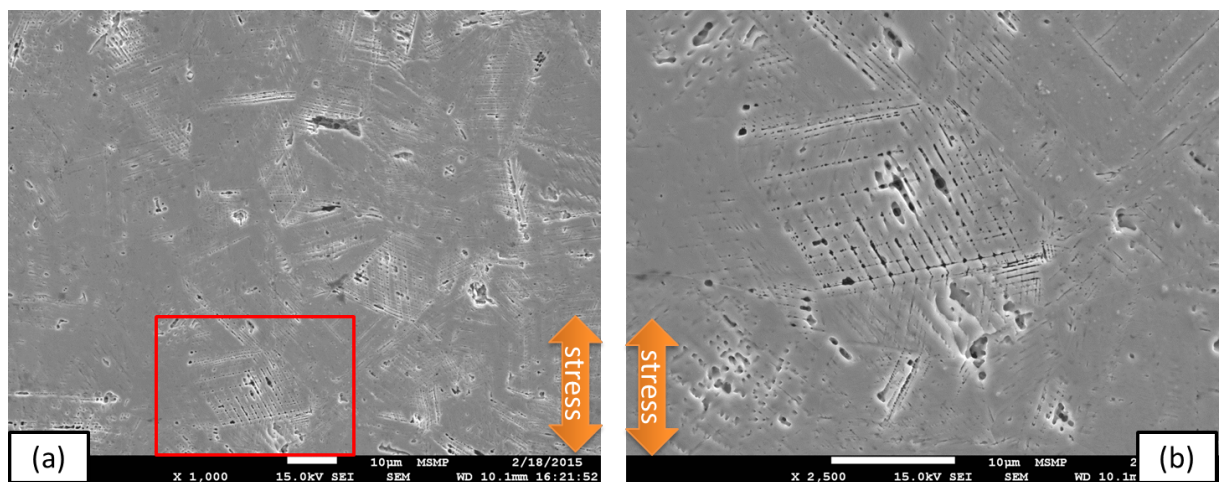


Figure J.1: Early surface state during SCC of a mirror-polished sample.



---

## List of Figures

---

1	Le critère de passivation défini à $i = i_p$ . Le test A nécessite plus de temps pour atteindre l'état passif ( $i_p$ ) que le test B [90] . . . . .	8
2	Illustration de la charge moyenne de passivation pour les trois cycles de passivation des échantillons sous contrainte et non-soumis à la contrainte. . . . .	9
3	Courbes du deuxième cycle de passivation anodique pour les tests (sous contrainte et non soumis à la contrainte) dans 2 M H <sub>2</sub> SO <sub>4</sub> . . . . .	10
4	Densité de courant de passivation, $j$ , calculé à partir de l'épaisseur de la couche passive, par rapport aux données expérimentales pour le cycle de passivation CII, pour l'acier inoxydable 304L, dans 2 M H <sub>2</sub> SO <sub>4</sub> . . . . .	10
5	Epaisseur de la couche passive (à $j = 1 \text{ mA.cm}^{-2}$ ) (des échantillons sous contraintes et non soumis aux contraintes) dans 2 M H <sub>2</sub> SO <sub>4</sub> . . . . .	12
6	Isolation des grains subis TGSCC de la carte de l'EBSD. . . . .	12
7	Résultats de simulation de la longueur de la fissure( $L$ ). . . . .	13
8	Analyse des contraintes (résiduelles/appliquées) en fonction de la profondeur. . .	14
9	The passivation criterion defined at $i = i_p$ . . . . .	17
10	Illustration of the average passivation charge for the three passivation cycles of stressed and unstressed samples. . . . .	18
11	The second cycle anodic passivation curves for stressed and unstressed tests in 2 M H <sub>2</sub> SO <sub>4</sub> plotted on $\log j(t)$ vs $1/q(t)$ axis. . . . .	20
12	The passivation current density, $j$ , as calculated based on the passive film thickness, compared to that recorded experimentally for CII passivation cycle on an unstressed 304L stainless steel in 2 M H <sub>2</sub> SO <sub>4</sub> . . . . .	20
13	Passivation thickness vs $cBV$ of stressed and unstressed samples during the three passivation cycles in 2 M H <sub>2</sub> SO <sub>4</sub> electrolyte. . . . .	21
14	Isolation of TGSCC grains in EBSD map. . . . .	21
15	Results of (L) simulations. . . . .	21
16	XRD residual/applied stress analysis over the profile of the sample . . . . .	22
1.1	Environmentally induced corrosion leading to component failure. . . . .	24
1.2	Metallic aqueous corrosion in an electrolyte containing oxygen. . . . .	26
1.3	Polarization curves of 304 stainless steel produced at different concentrations of H <sub>2</sub> SO <sub>4</sub> , and different sweep rates. . . . .	27
1.4	Scanning electron micrographs showing the effect of passivation of 302 stainless steel. . . . .	31
1.5	A: LEIS mapping on the area around the crack tip specimen under tensile stress. B: SVM map showing the local current densities. Ref. [181] . . . . .	32
1.6	Bare 304L stainless steel polarization curve in 1.0 M KOH . . . . .	34

1.7	Steady state 304L stainless steel polarization curve in 1.0 M KOH . . . . .	34
1.8	Passivatoin Current done by Kwon et al. . . . .	35
1.9	Passivatoin as described by HFIC, Experiments of by Kwon et al. . . . .	36
1.10	Passivatoin as described by HFIC, Experiments done [109] in acidic media . . . .	37
1.11	Current decay during passivation of stainless steel in acidic medium under passive applied potential. . . . .	38
1.12	Passivation experiments under active applied potential . . . . .	39
1.13	Effect of the applied potential during passivation . . . . .	40
1.14	Summary of the effect of different variables on the passivation kinetics . . . . .	40
1.15	Repassivation criterion redefined using the repassivation time. From [90] . . . .	42
1.16	(a), (b), and (c): the repassivation of Fe-Cr stainless steel with different Cr content [33], (d): The ( $cBV$ ) vs passive film thickness for the different passivation tests done by [33]. . . . .	44
1.17	SCC initiation sites. . . . .	47
1.18	A diagramme representing Crack propagation Models. . . . .	48
1.19	Representation of SCC as film rupture model describes it. . . . .	49
1.20	Polarization curve showing a passivation, activation cycle. . . . .	50
1.21	Adsorption effect on inter-atomic bonds . . . . .	50
1.22	AIDE model describing SCC. Voids nucleated in the plastic zone merge along the low index crystallographic planes causing the crack propagation in that direction. . . . .	51
1.23	Locations of hydrogen embrittlement in material matrix. . . . .	52
1.24	Schematic diagram of the tunnel mechanism of SCC and flat slot formation. . . .	53
1.25	An illustration of TGSCC. (a-c): sections at the crack tip. (d-f): plan view of a semicircular crack $\Delta x^*$ represents crack propagation length per event. . . . .	54
1.26	Corrosion Enhanced Localized Plasticity . . . . .	54
1.27	Griffth criterion for crack propagation . . . . .	55
1.28	The three decomposed fracture modes. . . . .	56
1.29	The cracking behavior as a function of the crack length and the stress intensity factor. . . . .	57
1.30	SCC propagation rate as a function of stress intensity factor. . . . .	58
1.31	An elliptical crack having b and c semi-axis, and loaded by a homogeneous load $\sigma_\infty$ . . . . .	60
2.1	Sample after the chemical analysis performed by SpectromaXx. . . . .	68
2.2	Tensile test sample's dimensions . . . . .	69
2.3	Sample's dimensions . . . . .	70
2.4	Polarization curve showing the cathodic and anodic current density curves, and the total (measured) current density. . . . .	71
2.5	Polarization curve showing features of interest. Zone A, B, and C are the critical potential zones for SCC. . . . .	73
2.6	Three-electrode electrochemical cell. RE: Reference Electrode. CE: Counter Electrode. WE: Working Electrode. . . . .	74
2.7	AESEC technique . . . . .	75
2.8	The flow cell . . . . .	76
2.9	Main steps in AESEC technique . . . . .	77
3.1	Initial surface state. . . . .	83
3.2	Optical microscopy of polished surface. . . . .	84
3.3	The three sample surfaces. . . . .	84
3.4	SEM characterization of the base material, upper surface and cross-section. . . .	85
3.5	Examples of upper surface defects. . . . .	85
3.6	EDS analysis of a selected upper surface defect. . . . .	86
3.7	SEM characterization of the base material, transverse direction. . . . .	87

3.8	EDS analysis of a selected upper surface defect. . . . .	88
3.9	EBSD analysis of the cross section. . . . .	89
3.10	Pole figures of FCC and BCC grains in the base material. . . . .	89
3.11	Initial residual stress in the sample. . . . .	90
3.12	Initial residual stress in the sample. . . . .	90
3.13	The true curve of the tensile test along the rolling direction. . . . .	91
4.1	Polarization curve in 0.05 M NaCl . . . . .	95
4.2	Polarization curve in 5 M H <sub>2</sub> SO <sub>4</sub> . . . . .	95
4.3	Polarization curve in 5 M H <sub>2</sub> SO <sub>4</sub> + 0.5 M NaCl. . . . .	96
4.4	Polarization curve in 2 M H <sub>2</sub> SO <sub>4</sub> . . . . .	96
4.5	Polarization curve in 2 M H <sub>2</sub> SO <sub>4</sub> + 0.05 M NaCl. . . . .	97
4.6	Post experimental surface observation of unstressed 304L stainless steel after the polarization experiments in the proposed electrolytes. . . . .	97
4.7	Selected points for statistical analysis : $j_{critical}$ and $j_{minimum}$ . . . . .	98
4.8	Relative standard deviation for $j_{critical}$ and $j_{minimum}$ of the proposed experimental electrolytes. . . . .	98
4.9	Effect of stress on post-experimental surface of 304L after polarization experiments in 2 M H <sub>2</sub> SO <sub>4</sub> . . . . .	99
4.10	Polarization curves of stressed and unstressed 304L SS unpolished samples in 5 M H <sub>2</sub> SO <sub>4</sub> (stagnant cell). . . . .	100
4.11	Illustration of (a): $j_{critical}$ (or equally $j_{max}$ ) and (b): $j_{minimum}$ values for stressed and non-stressed samples during polarization in 5 M H <sub>2</sub> SO <sub>4</sub> (stagnant cell). . . . .	100
4.12	OCP curves for stressed and non-stressed samples in 5 M H <sub>2</sub> SO <sub>4</sub> (stagnant cell). (a): before the polarization test. (b): after the polarization test. . . . .	102
4.13	Illustration of OCP <sub>i</sub> , OCP <sub>pre</sub> , and OCP <sub>f</sub> values for stressed and non-stressed samples in 5 M H <sub>2</sub> SO <sub>4</sub> (stagnant cell). . . . .	102
4.14	Effect of polishing on polarization curves of stressed and unstressed 304L SS samples in 5 M H <sub>2</sub> SO <sub>4</sub> (stagnant cell). . . . .	104
4.15	Illustration of (a): $j_{critical}$ (or equally $j_{max}$ ) and (b): $j_{minimum}$ values for polished and non-polished samples during polarization in 5 M H <sub>2</sub> SO <sub>4</sub> (stagnant cell). . . . .	104
4.16	OCP curves for polished and non-polished unstressed samples in 5 M H <sub>2</sub> SO <sub>4</sub> (stagnant cell). (a): before the polarization test. (b): after the polarization test. . . . .	105
4.17	Illustration of OCP <sub>i</sub> , OCP <sub>pre</sub> , and OCP <sub>f</sub> values for polished and non-polished unstressed samples in 5 M H <sub>2</sub> SO <sub>4</sub> (stagnant cell). . . . .	105
4.18	Effect of applied stress on polarization curves of polished 304L SS samples in 5 M H <sub>2</sub> SO <sub>4</sub> (stagnant cell). . . . .	107
4.19	Illustration of (a): $j_{critical}$ (or equally $j_{max}$ ) and (b): $j_{minimum}$ values for polished stressed and unstressed samples during polarization in 5 M H <sub>2</sub> SO <sub>4</sub> (stagnant cell). . . . .	107
4.20	OCP curves for polished stressed and unstressed samples in 5 M H <sub>2</sub> SO <sub>4</sub> (stagnant cell). (a): before the polarization test. (b): after the polarization test. . . . .	108
4.21	Illustration of OCP <sub>i</sub> , OCP <sub>pre</sub> , and OCP <sub>f</sub> values for polished and non-polished unstressed samples in 5 M H <sub>2</sub> SO <sub>4</sub> (stagnant cell). . . . .	108
4.22	All polarization curves of 304L stainless steel in 5 M H <sub>2</sub> SO <sub>4</sub> (stagnant cell) for 304L stainless steel. . . . .	110
4.23	Flow vs stagnant cell on polarization curves produced in 5 M H <sub>2</sub> SO <sub>4</sub> (unstressed samples). . . . .	110
4.24	Illustration of (a): $j_{critical}$ (or equally $j_{max}$ ) and (b): $j_{minimum}$ values for 304L polished samples during polarization in 5 M H <sub>2</sub> SO <sub>4</sub> stagnant vs flow cell. . . . .	112
4.25	OCP curves for polished samples in 5 M H <sub>2</sub> SO <sub>4</sub> stagnant vs flow cell. (a): before the polarization test. (b): after the polarization test. . . . .	112



4.26	Illustration of $OCP_i$ , $OCP_{pre}$ , and $OCP_f$ values for polished samples in 5 M $H_2SO_4$ stagnant vs flow cell. . . . .	113
4.27	Stress effect on polarization curves of 304L polished samples produced in 5 M $H_2SO_4$ + 0.05 M NaCl (Flow cell). . . . .	113
4.28	Illustration of (a): $j_{critical}$ (or equally $j_{max}$ ) and (b): $j_{minimum}$ values for polished stressed and unstressed samples during polarization in 5 M $H_2SO_4$ + 0.05 M NaCl (flow cell). . . . .	114
4.29	OCP curves for polished stressed and unstressed samples in 5 M $H_2SO_4$ + 0.05 M NaCl (flow cell). (a): before the polarization test. (b): after the polarization test. . . . .	114
4.30	Illustration of $OCP_i$ , $OCP_{pre}$ , and $OCP_f$ values for polished stressed and unstressed samples in 5 M $H_2SO_4$ + 0.05 M NaCl (flow cell). . . . .	126
4.31	Effect of stress on post-experimental surface of 304L after polarization experiments in 5 M $H_2SO_4$ + 0.05 M NaCl (flow cell). . . . .	126
4.32	(a): Initial OCP evolution, before the cycling program is applied, showing the water/ 2 M $H_2SO_4$ electrolyte switch. (b): the $OCP_{pre}$ values for stressed/ unstressed samples. . . . .	127
4.33	The first cycle 70-s activation step @ -700 mV (vs Ag/AgCl) performed on stressed and unstressed 304L SS samples in 2 M $H_2SO_4$ (flow cell). . . . .	127
4.34	The second cycle 70-s activation step @ -700 mV (vs Ag/AgCl) performed on stressed and unstressed 304L SS samples in 2 M $H_2SO_4$ (flow cell). . . . .	128
4.35	The 3rd cycle 70-s activation step @ -700 mV (vs Ag/AgCl) performed on stressed and unstressed 304L SS samples in 2 M $H_2SO_4$ (flow cell). . . . .	128
4.36	The different regimes of surface charge exchange during the three 70-s activation step @ -700 mV (vs Ag/AgCl) performed on unstressed 304L SS samples in 2 M $H_2SO_4$ (flow cell). . . . .	129
4.37	Stressed vs non-stressed activation during the first cycle in 2 M $H_2SO_4$ (flow cell). . . . .	129
4.38	Stressed vs non-stressed activation during the second cycle in 2 M $H_2SO_4$ (flow cell), showing the point of interest A, B, and C. . . . .	130
4.39	Stressed vs non-stressed activation during the second cycle in 2 M $H_2SO_4$ (flow cell). . . . .	130
4.40	Illustration of the cathodic current values during the activation steps. (a): Point A, (b): Point B as shown in Fig. 4.38 . . . . .	131
4.41	Illustration of the statistics of cathodic activation steps. (a): the cathodic current value for point C (defined as shown in Fig. 4.38), (b): the slope of the curve in zone II. . . . .	131
4.42	OCP evolution after activation step. (a): First cycle. (b): Second cycle. . . . .	131
4.43	(a):OCP evolution after activation step in third cycle. (b): $OCP_{pre}$ value statistics for the three cycles. . . . .	132
4.44	Current transients during the first passivation cycle for the stressed and unstressed samples. . . . .	132
4.45	Current transients during the second passivation cycle for the stressed and unstressed samples. . . . .	133
4.46	Current transients during the third passivation cycle for the stressed and unstressed samples. . . . .	133
4.47	Illustration of the average passivation current values during the three passivation cycles. (a): Point A. (b): Point B. . . . .	134
4.48	Illustration of the average passivation charge for the three passivation cycles of stressed and unstressed samples. . . . .	134
4.49	OCP evolution after passivation step. (a): First cycle. (b): Second cycle. . . . .	135
4.50	(a):OCP evolution after activation step in third cycle. (b): $OCP_{pre}$ value statistics for the three cycles. . . . .	135

5.1	The slopes ( $\alpha$ ) of $\log(j)$ vs $\log(t)$ curves of the three passivation cycles in 2 M $\text{H}_2\text{SO}_4$ (flow cell). . . . .	138
5.2	The second cycle passivation curves given as an example to check the validity of the linearity described by Eq.1.6. . . . .	139
5.3	The evolution of the passive film thickness in 2 M $\text{H}_2\text{SO}_4$ during the application of the anodic pulse as calculated by $j_{\text{total}}$ . . . . .	140
5.4	The polarization curve of 304L stainless steel showing the selected zones to calculate $j_m/j_{\text{Fe}}$ ratio. A, B, C, and D indicate zones of interest used in calculation. . . . .	141
5.5	The evolution of the passive film thickness during the passivation period after the introduced correction of $f_{\text{Fe}}$ . . . . .	144
5.6	Elemental dissolution currents as measured by AESEC technique from the corrosion leaching solution concentrations during the second potentiostatic pulse tests. (A): Cathodic activation pulse(70 s at -700 mV vs Ag/AgCl). (B): OCP (300 s). (C): Passivation (300 s). (D): OCP (600 s). . . . .	145
5.7	The evolution of the passive film thickness during the passivation period after the introduced correction of $\Sigma f_m$ . . . . .	146
5.8	The passivation current density, $j$ , as calculated by Eq.1.2 compared to that recorded experimentally for CII passivation cycle on an unstressed 304L stainless steel in 2 M $\text{H}_2\text{SO}_4$ . . . . .	147
5.9	The passive film thickness where the HFIC applies. (a): The actual non-uniform topography and thickness of the passive film. (b): The equivalent thickness $h(t)$ calculated by Faraday's law using $q_{\text{film}}$ . . . . .	148
5.10	The passive film formation during zone I of the passivation period. (a): The initial discrete nucleation of the passive film over the bare surface. (b): The equivalent thickness $h(t)$ calculated by Faraday's law using $q_{\text{film}}$ . . . . .	148
5.11	The relative difference between the current density $j_{\text{calc}}$ and $j_{\text{exp}}$ , as calculated by Eq.5.16 for CII passivation cycle on an unstressed 304L stainless steel in 2 M $\text{H}_2\text{SO}_4$ . . . . .	149
5.12	The passive film in zone III, where $j(t)$ deviates from the HFIC. (a): The dissolution of film leading to local passivity break-up/repair processes. (b): The equivalent thickness $h(t)$ calculated by Faraday's law using $q_{\text{film}}$ . . . . .	150
5.13	The second cycle passivation curve corrected to $q_{\text{film}}$ as described by the high field ion conduction in Eq.1.6. . . . .	151
5.14	The indication of the slope $cBV$ and how it varies according to the different passivation parameters. . . . .	152
5.15	The second cycle anodic passivation curves for stressed and unstressed tests in 2 M $\text{H}_2\text{SO}_4$ plotted on $\log j(t)$ vs $1/q(t)$ axis. . . . .	153
5.16	The passivation rate as measured by the slope $cBV$ of zone II of the $\log j(t)$ vs $1/q(t)$ anodic passivation transients. . . . .	154
5.17	Illustration of $\text{Log}(A)$ values calculated for the $\log(j(t))$ vs $1/q(t)$ curves over the low current transfer regime (ZoneII). . . . .	155
5.18	Passivation thickness (at $j_p = 1 \text{ mA.cm}^{-2}$ ) of stressed and unstressed samples during the three passivation cycles in 2 M $\text{H}_2\text{SO}_4$ electrolyte. . . . .	156
5.19	Passivation thickness (at $j_p = 1 \text{ mA.cm}^{-2}$ ) of (a): a film with a low passivation rate (high $cBV$ ) which is thought to be the case for stressed samples, (b): a film with a high passivation rate (low $cBV$ ) which is thought to be the case for unstressed samples. . . . .	158
5.20	Passivation thickness vs $cBV$ of stressed and unstressed samples during the three passivation cycles in 2 M $\text{H}_2\text{SO}_4$ electrolyte. . . . .	158
6.1	Experimental dimensions of the sample and curved supports . . . . .	161
6.2	Stress and strain profile over the sample's cross-section. . . . .	162

6.3	SCC SEM observation after 21 days . . . . .	164
6.4	SEM observation of crack facet after 21 days of SCC test. . . . .	164
6.5	Effect of increasing the stress on SCC. . . . .	165
6.6	All Euler EBSD map after 21 days SCC, $\sigma = 250$ MPa test in 2 M $\text{H}_2\text{SO}_4$ and 0.5 M NaCl. . . . .	166
6.7	Isolation of TGSCC grains in EBSD map. . . . .	166
6.8	Euler angles defining the crystallographic orientation of the concerned grain, ( $\varphi_1, \phi, \varphi_2$ ). . . . .	167
6.9	Cracking plane determination using Euler angles and the crack inclination. . . . .	167
6.10	Post experimental SEM observation SCC 8 h OCP test, upper surface. . . . .	169
6.11	TGSCC 16 h OCP test, very fine crack ending. . . . .	169
6.12	Kinetics of SCC by OCP test, upper surface. . . . .	170
6.13	Kinetics of SCC by OCP test, cross-sectional view. . . . .	171
6.14	Re-orientation of cracking path by microscopic features. . . . .	173
6.15	Initial surface for step-wise EBSD maps. . . . .	173
6.16	Second surface for step-wise EBSD maps. . . . .	174
6.17	Third surface for step-wise EBSD maps. . . . .	174
6.18	Fourth surface for step-wise EBSD maps. . . . .	174
6.19	Resolved maximum shear on grain-boundaries. . . . .	175
6.20	CSL interface for IGSCC. . . . .	176
6.21	OCP evolution during SCC tests. . . . .	176
6.22	Checking if OCP evolution is related to cracking. . . . .	177
6.23	SCC accelerated tests, upper surface. . . . .	177
6.24	SCC accelerated tests, cross-section. . . . .	178
6.25	EDS analysis of the surrounding of a short crack, the sample. . . . .	178
6.26	EDS analysis of the surrounding of a short crack, the concentration maps. . . . .	179
6.27	Upper surface post SCC test on a mirror-polished initial state. . . . .	180
6.28	Cross-section post SCC test on a mirror-polished initial state. . . . .	181
6.29	SCC under residual stress vs applied stress, upper surface view. . . . .	181
6.30	SCC under residual stress vs applied stress, cross-section view. . . . .	182
6.31	Upper surface SEM + EBSD of ZOI for 125 h SCC test of $\sigma = 210$ MPa in 2 M $\text{H}_2\text{SO}_4 + 0.5$ M NaCl. . . . .	183
6.32	Cross-section EBSD maps of SCC test of $\sigma = 250$ MPa, after 21 days in 2 M $\text{H}_2\text{SO}_4 + 2$ M NaCl. . . . .	184
6.33	Cross-section SEM + EBSD maps of 125 h SCC test of $\sigma = 210$ MPa in 2 M $\text{H}_2\text{SO}_4 + 0.5$ M NaCl. . . . .	184
7.1	Illustration of the semi-elliptical shape of the crack. . . . .	188
7.2	Upper surface observation of SCC, showing the cutting plane to get the cross- sectional view. . . . .	189
7.3	Illustrating the cracking statistics along ( $c$ ) and ( $b$ ) directions. . . . .	190
7.4	The representative crack length vs the corresponding propagation rate. . . . .	190
7.5	Sample of measured cracks for the statistical analysis. . . . .	192
7.6	Histogram of the statistical distribution of the crack length ( $c$ ), (A): Experimental data. (B): Simulated data. . . . .	192
7.7	Illustration of the problem of the crack depth ( $L$ ). . . . .	193
7.8	Simulation of the cutting plane. . . . .	194
7.9	Results of ( $L$ ) simulations. . . . .	195
7.10	Distribution of the experimentally measured ( $L$ ). . . . .	195
7.11	XRD residual/applied stress analysis over the profile of the sample . . . . .	197
7.12	Cracking cross-sectional view of 42 h SCC test in 2 M $\text{H}_2\text{SO}_4 + 0.5$ M NaCl, using $\sigma = 210$ MPa support. . . . .	198

7.13	Explaining the high measured aspect ratio ( $b/c$ ).	199
7.14	Effect of stress relaxation on crack arrests.	199
7.15	Effect of stress relaxation on crack macroscopic path.	200
7.16	Effect of stress relaxation on crack macroscopic path, upper surface.	201
A.1	Surface spatial statistical analysis of Fe concentration.	209
A.2	Surface spatial statistical analysis of Cr concentration.	209
A.3	Surface spatial statistical analysis of Ni concentration.	210
A.4	Surface spatial statistical analysis of Cu concentration.	210
A.5	Surface spatial statistical analysis of Mo concentration.	210
A.6	Surface spatial statistical analysis of C concentration.	210
B.1	EDS analysis of a selected upper surface defect with high Mn composition.	211
C.1	Sample-support assembly in Abaqus.	213
C.2	Illustration of the simulated sample and loading.	214
C.3	Simulation results using Abaqus.	215
D.1	Statistical distribution of the grain area in the base material.	217
D.2	Statistical distribution of the equivalent grain diameter in the base material.	218
D.3	Statistical distribution of the equivalent grain aspect ratio in the base material.	218
D.4	Statistical distribution of the slope of the major axis of the equivalent elliptical grain in the base material.	219
D.5	Statistical distribution of the number of neighbor grains in the base material.	219
H.1	Polarization curves of unpolished 304L SS samples in 2 M $\text{H}_2\text{SO}_4$ (flow cell).	227
I.1	The first cycle passivation anodic curves for stressed and unstressed tests in 2 M $\text{H}_2\text{SO}_4$ plotted on $\log j(t)$ vs $1/q(t)$ axis.	229
I.2	The third cycle passivation anodic curves for stressed and unstressed tests in 2 M $\text{H}_2\text{SO}_4$ plotted on $\log j(t)$ vs $1/q(t)$ axis.	230
J.1	Early surface state during SCC of a mirror-polished sample.	231



---

## List of Tables

---

1	Statistiques de la coupe transversale sur les plans de rupture préférentiels, avec $\sigma = 210$ MPa, dans 2 M $\text{H}_2\text{SO}_4$ + 0.5 M NaCl. . . . .	11
2	Statistiques de la surface supérieure sur les plans de rupture préférentiels, avec $\sigma = 210$ MPa, dans 2 M $\text{H}_2\text{SO}_4$ + 0.5 M NaCl. . . . .	11
3	Cross-section statistics about the preferential rupture planes, where $\sigma = 210$ MPa in 2 M $\text{H}_2\text{SO}_4$ + 0.5 M NaCl. . . . .	18
4	Upper surface statistics about the preferential rupture planes, where $\sigma = 210$ MPa in 2 M $\text{H}_2\text{SO}_4$ + 0.5 M NaCl. . . . .	19
1.1	Elemental composition of 304L stainless steel according to AISI standards . . . . .	26
2.1	The experimental tools used throughout the present research and their main purpose. . . . .	67
2.2	Concentration of the standards used for signal calibration. . . . .	69
2.3	The technical description of the monochromator and polychromator. . . . .	76
2.4	The program used for the production of the polarization curves. . . . .	77
2.5	Optimized potentio-dynamic program used for cycling experiments: . . . . .	78
3.1	Face elemental concentrations measured by SpectroMaXx. . . . .	81
3.2	Analysis results for carbon and sulfur content in the alloy in hand. . . . .	82
3.3	Analysis of the chemical composition of the base material 304L SS, based on Leco CS-300 and Spectromax analysis. . . . .	82
3.4	AISI standards for 304 and 304L ss composition vs our material. . . . .	82
3.5	Mechanical properties by true tensile test. . . . .	91
4.1	Concentrations of the proposed electrolytes. . . . .	94
4.2	The solutions used for polarization curves along with their concentrations. The figures in brackets (*) represent the electrolyte composition and concentration in units of Mol as: $([\text{NaCl}]/[\text{H}_2\text{SO}_4])$ . . . . .	94
4.3	$j_{\text{critical}}$ and $j_{\text{minimum}}$ values for stressed and non-stressed samples during polarization in 5 M $\text{H}_2\text{SO}_4$ (stagnant cell). . . . .	100
4.4	OCP <sub>i</sub> , OCP <sub>pre</sub> , and OCP <sub>f</sub> values for stressed and non-stressed samples in 5 M $\text{H}_2\text{SO}_4$ (stagnant cell). * avg: Average, stdv: Standard Deviation. . . . .	101
4.5	$j_{\text{critical}}$ and $j_{\text{minimum}}$ values for polished and non-polished samples during polarization in 5 M $\text{H}_2\text{SO}_4$ (stagnant cell). . . . .	103
4.6	OCP statistics before the polarization tests. . . . .	103
4.7	$j_{\text{critical}}$ and $j_{\text{minimum}}$ values for polished stressed and unstressed samples during polarization in 5 M $\text{H}_2\text{SO}_4$ (stagnant cell). . . . .	106

4.8	OCP <sub>i</sub> , OCP <sub>pre</sub> , and OCP <sub>f</sub> values related to polished stressed and unstressed polarization tests. . . . .	107
4.9	Electrolyte exposure before the polarization program is applied. . . . .	109
4.10	$j_{\text{minimum}}$ and $j_{\text{critical}}$ values for the experiments of flow vs stagnant cell. . . . .	110
4.11	OCP <sub>i</sub> , OCP <sub>pre</sub> , and OCP <sub>f</sub> values related to polished polarization tests performed in stagnant vs flow cell. . . . .	111
4.12	$j_{\text{critical}}$ and $j_{\text{minimum}}$ values for polished stressed and unstressed samples during polarization in 5 M H <sub>2</sub> SO <sub>4</sub> + 0.05 M NaCl (flow cell). . . . .	111
4.13	OCP <sub>i</sub> , OCP <sub>pre</sub> , and OCP <sub>f</sub> values related to polished stressed and unstressed polarization tests in 5 M H <sub>2</sub> SO <sub>4</sub> + 0.05 M NaCl (flow cell). . . . .	115
4.14	Cathodic current values for the selected points: A, B, and C during the three activation cycles for unstressed samples. . . . .	119
4.15	Cathodic current values for the selected points: A, B, and C during the three activation cycles for stressed samples. . . . .	119
4.16	Slopes of Zone II of the activation cycles for stressed and unstressed samples. . .	120
4.17	OCP <sub>pre</sub> values of the OCP periods in the three cycles after the activation pulse. .	121
4.18	Passive current value at point A for the three passivation cycles for stressed and unstressed samples. . . . .	122
4.19	Passive current value at point B for the three passivation cycles for stressed and unstressed samples. . . . .	122
4.20	Average passivation time for the three cycles of stressed and unstressed samples. .	123
4.21	The passivation charge calculated for the three cycles in stressed and unstressed experiments . . . . .	123
4.22	OCP <sub>pre</sub> values for the three cycles after passivation step. . . . .	124
5.1	Metallic oxidation numbers and their mass fraction in the alloy's matrix. . . . .	142
5.2	$f_{\text{Fe}}$ factor calculated with oxidation number (II) and (III) with variable elements considered to share in $j_{\text{dissolution}}$ . . . . .	143
5.3	Evolution of $j_{\text{Cr}}/j_{\text{Fe}}$ over the four cycles of the experiment . . . . .	145
5.4	Summary of the average $j_m/j_{\text{Fe}}$ values over the four passivation cycles. . . . .	158
5.5	A summary of the dissolution factor $f_m$ for the four considered elements. . . . .	159
5.6	Passive film thickness at $t = 300$ s as calculated by Eq.1.4 with different $q_{\text{film}}$ . . .	160
5.7	Dissolution ratios $j_m/j_{\text{Fe}}$ as calculated by the polarization curve . . . . .	160
5.8	$\Delta j(t)\%$ for selected instants of interest during the passivation. . . . .	160
5.9	$\log(A)$ values calculated for the $\log j(t)$ vs $1/q(t)$ curves over the low current transfer regime. . . . .	160
5.10	Passivation thickness (at $j_p = 1 \text{ mA.cm}^{-2}$ ) of stressed and unstressed samples during the three passivation cycles in 2 M H <sub>2</sub> SO <sub>4</sub> electrolyte. . . . .	160
5.11	Results of AESEC technique: the surface enrichment in chromium, $Q'_{\text{Cr}}/(\mu\text{g.cm}^{-2})$ , and the corresponding passive film thickness, $\theta$ /nm, during the four passivation cycles of unstressed samples. . . . .	160
6.1	Stress and strain values provided by the curved supports. . . . .	163
6.2	Statistics of the cracking orientation for 21 SCC test of $\sigma = 250$ MPa sample in 2 M H <sub>2</sub> SO <sub>4</sub> + 2 M NaCl. . . . .	167
6.3	Statistical analysis of crack depth ( $L$ ) over the different SCC test periods. ZOI: Length of the zone of interest. . . . .	172
6.4	Cross-section statistics about the preferential rupture planes, where $\sigma = 210$ MPa in 2 M H <sub>2</sub> SO <sub>4</sub> + 0.5 M NaCl. . . . .	182
6.5	Upper surface statistics about the preferential rupture planes, where $\sigma = 210$ MPa in 2 M H <sub>2</sub> SO <sub>4</sub> + 0.5 M NaCl. . . . .	182
6.6	Percentage of TGSCC for eight selected surface SCC cracks in Fig. 6.31. . . . .	185

7.1	Experimental statistics about the crack dimensions rate on the upper surface ( $c$ ), and on the cross-section ( $b$ ). It's assumed here that $b \approx L$ . . . . .	188
7.2	Representative length ( $b$ ) and ( $c$ ) vs their propagation rate. . . . .	191
7.3	Enhanced statistics by the first simulation results, based on $(b/c) = (L_{\text{avg}}/c_{\text{avg}})$ of the test in considerations. . . . .	196
7.4	Enhanced statistics by the second simulation results, based on $(b/c) = 6$ . . . . .	196
7.5	A summary of the XRD stress profile analysis. . . . .	198
H.1	Active, passive, and Transpassive potential domains of 304L stainless steel in $2\text{ M H}_2\text{SO}_4$ . . . . .	228





- [1] New Hampshire Materials Laboratory, INC website, 2013.
- [2] Corrosion Doctors website, 2016.
- [3] Stanford school of earth, energy, and environmental sciences., 2016.
- [4] M. Abdallah. Corrosion behaviour of 304 stainless steel in sulphuric acid solutions and its inhibition by some substituted pyrazolones. *Materials Chemistry and Physics*, 82(3):786–792, 2003.
- [5] Manfred Ahlers and Ernst Riecke. Stress corrosion cracking in single crystals of Fe-25Cr-20Ni. *Corrosion Science*, 18(1):21–38, 1978.
- [6] J. Amri, T. Souier, B. Malki, and B. Baroux. Effect of the final annealing of cold rolled stainless steels sheets on the electronic properties and pit nucleation resistance of passive films. *Corrosion Science*, 50(2):431–435, 2008.
- [7] P.L. Anderson. Fracture Mechanics Data and Modeling of Environmental Cracking of Nickel-Base Alloys in High-Temperature Water. In P.L. Anderson, editor, *CORROSION*, pages 9–17. GE Corporate Research and Development Center, NY, 12 edition, 1991.
- [8] P.L. Anderson and F. P. Ford. Life Prediction by Mechanistic Modeling and System Monitoring of Environmental Cracking of Iron and Nickel Alloys in Aqueous Systems. *Materials Science and Engineering*, 103(A):167–184, 1988.
- [9] T. Aoki, S. Shimizu, K. Miyazaki, M. Hayashi, and H. Kobayashi. Evaluation on crack growth analysis model based on the knowledge obtained from stress corrosion cracking in Ni-based alloy used for a long time in a BWR. *Maintenance*, 46–53(5):46–53, 2006.
- [10] A.S. Argon. *Strengthening mechanisms in crystal plasticity*. Oxford University Press, London.
- [11] ASM. *ASM Handbook Vol 13 - Corrosion*. 1992.
- [12] ASM. *ASM Handbook, Fatigue and fracture*, volume 19. 1996.
- [13] ASTM. ASTM G15: Standard Terminology Relating to Corrosion and Corrosion Testing. *ASTM standards*, (STD-55382):5, 2006.
- [14] D.R. Baer and M.T. Thomas. Influence of stress on H<sub>2</sub>S adsorption on iron. *Metallurgical Transactions A*, 15(A):853–860, 1984.

- [15] V. Bague, S. Chachoua, Q. T. Tran, and P. Fauvet. Determination of the long-term intergranular corrosion rate of stainless steel in concentrated nitric acid. *Journal of Nuclear Materials*, 392(3):396–404, 2009.
- [16] M.A. Baker and J.E. Castle. The initiation of pitting corrosion of stainless steels at oxide inclusions. *Corrosion Science*, 33:1295–1303, 1992.
- [17] Fanny Balbaud, Gérard Sanchez, Pierre Fauvet, Gérard Sanchez, and Gérard Picard. Mechanism of corrosion of AISI 304L stainless steel in the presence of nitric acid condensates. *Corrosion Science*, 42(10):1685–1707, 2000.
- [18] Bardal and Einar. *Corrosion and Protection*. Springer, Norway, 2004.
- [19] J.A. Bardwell, G.I. Sproule, D. F. Mitchell, B. MacDougall, and M.J. Graham. Nature of the passive film on Fe–Cr alloys as studied by  $^{18}\text{O}$  secondary ion mass spectrometry: reduction of the prior film and stability to ex situ surface analysis. *Journal of Chemical Society*, 87:1011–1019, 1991.
- [20] B. Baroux. The kinetics of pit generation on stainless steels. *Corrosion Science*, 28(10):969–986, 1988.
- [21] A. Ben Rhouma, H. Sidhom, C. Braham, J. Lédion, and M.E. Fitzpatrick. Effects of surface preparation on pitting resistance, residual stress, and stress corrosion cracking in austenitic stainless steels. *Journal of Materials Engineering and Performance*, 10(5):507–514, 2001.
- [22] Frederic Bernard, V. Shankar Rao, and Hyuk-Sang Kwon. A Study on the Repassivation Kinetics and SCC Behavior of Duplex Stainless Steel in Chloride Solution. *Journal of The Electrochemical Society*, 152(10):B415, 2005.
- [23] C. L. Briant. Hydrogen Assisted Cracking of Type 304 Stainless Steel. *Metallurgical Transactions A*, 10A(February):181–189, 1979.
- [24] S.M. Bruemmer, B.W. Arey, and L.A. Charlot. Influence of chromium depletion on intergranular stress corrosion cracking of 304 stainless steel. *Corrosion*, 48(1):42–49, 1992.
- [25] G.T. Burstein and G.W. Ashley. Kinetics of repassivation of scratch scars generated on iron in aqueous solutions. *National Association of Corrosion Engineers*, 40(3):110–115, 1984.
- [26] G.T. Burstein and P.I. Marshall. Growth of passivating films on scratched 304L stainless steel in alkaline solution. *Corrosion Science*, 23(4):125–137, 1983.
- [27] G.T. Burstein and P.I. Marshall. The coupled kinetics of film growth and dissolution of stainless steel repassivating in acid solutions. *Corrosion Science*, 24(5):449–462, 1984.
- [28] N. Cabrera and N.F. Mott. Theory of the oxidation of metals. Technical report, London, 1949.
- [29] M. J. Carmezim, A. M. Simoes, M. O. Figueiredo, and M. da Cunha Belo. Electrochemical behaviour of thermally treated Cr-oxide films deposited on stainless steel. *Corrosion Science*, 44(3):451–465, 2002.
- [30] M. J. Carmezim, A. M. Simoes, M. F. Montemor, and M. Da Cunha Belo. Capacitance behaviour of passive films on ferritic and austenitic stainless steel. *Corrosion Science*, 47(3 SPEC. ISS.):581–591, 2005.

- [31] T.B. Cassagne. Corrosion Sous Contrainte. Les Editions de physique, Les Ulis, France, 1992.
- [32] L. Castex, J.L. Lebrun, G. Maeder, and J.M. Sprauel. Détermination des contraintes résiduelles par diffraction des rayons x. Technical report, ENSAM, Paris, 1981.
- [33] Eun-Ae Cho, Chin-Kwan Kim, Joon-Shick Kim, and Hyuk-Sang Kwon. Quantitative analysis of repassivation kinetics of ferritic stainless steels based on the high field ion conduction model. *Electrochimica Acta*, 45(12):1933–1942, 2000.
- [34] S.S. Chouthai. Texture dependence of corrosion of mild steel after cold rolling. *Elayaperumal, K.*, 11(1):40–43, 1976.
- [35] A. Cigada, B. Mazza, P. Pedferri, G. Salvago, D. Sinigaglia, and G. Zanini. Stress corrosion cracking of cold-worked austenitic stainless steels. *Corrosion Science*, 22(6):559–578, 1982.
- [36] J Congleton, H.C Shih, T Shoji, and R.N Parkins. The stress corrosion cracking of type 316 stainless steel in oxygenated and chlorinated high temperature water. *Corrosion Science*, 25(8-9):769–788, 1985.
- [37] M .J. Couper and J.R. Griffiths. Casting Defects and the Fatigue Behaviour of an Aluminium Casting Alloy. *Fatigue & Fracture of Engineering Materials & Structures*, 13(3):213–227, 1990.
- [38] W. Dietzel and T. Turnbull. Stress corrosion cracking. In K.-H. Schwalbe, editor, *omprehensive Structural Integrity, Addendum 2007: Mechanical Characterization of Materials*. Elsevier,, Oxford, 2007.
- [39] François Dominique, Pineau André, and Zaoui André. *Mechanical Behaviour of Materials, Vomlume II: Viscoplasticity, Damage, Fracture and Contact Mechanics*. 1998.
- [40] Donghai Du, Kai Chen, Hui Lu, Lefu Zhang, Xiuqiang Shi, Xuelian Xu, and Peter L. Andresen. Effects of chloride and oxygen on stress corrosion cracking of cold worked 316/316L austenitic stainless steel in high temperature water. *Corrosion Science*, 110:134–142, 2016.
- [41] Donghai Du, Kai Chen, Lun Yu, Hui Lu, Lefu Zhang, Xiuqiang Shi, and Xuelian Xu. SCC crack growth rate of cold worked 316L stainless steel in PWR environment. *Journal of Nuclear Materials*, 456:228–234, 2015.
- [42] D. Dumont, A. Deschamps, and Y. Brechet. On the relationship between microstructure, strength and toughness in AA7050 aluminum alloy. *Materials Science and Engineering A*, 356(1-2):326–336, 2003.
- [43] K. Elayaperumal, P. K. De, and J Balachandra. Stress Corrosion Cracking of zircaloy-2 In Methanol-Iodine Solutions. *Journal of Nuclear Materials*, 45(1972/73):323–330, 1972.
- [44] George Engelhardt and Digby D. Macdonald. Unification of the deterministic and statistical approaches for predicting localized corrosion damage. I. Theoretical foundation. *Corrosion Science*, 46(11):2755–2780, 2004.
- [45] H.J. Engle. *The Theory of Stress Corrosion Cracking in Alloys*. North Atlantic Treaty Organization, 1971.
- [46] I. Epelboin, M. Keddam, O. R. Mattos, and H. Takenouti. The dissolution and passivation of Fe and Fe{single bond}Cr alloys in acidified sulphate medium: Influences of pH and Cr content. *Corrosion Science*, 19(7):1105–1112, 1979.

- [47] J.D. Eshelby, F.C. Frank, and F.R.N. Nabarro. The equilibrium of linear arrays of dislocations. *he London, Edinburgh, and Dublin Philosophical Magazine and Journal of Science*, 42(327):351–364, 1951.
- [48] J.A. Feeney and M.J. Blackburn. The status of stress corrosion cracking of titanium alloys in aqueous solutions. In J.C. Scully, editor, *The Theory of Stress Corrosion Cracking*, pages 355–398. NATO, Brussels, 1971.
- [49] T. Fett. A simple procedure for the estimation of local stress intensity factors for semi-elliptical surface cracks, 1999.
- [50] T. Fett. Estimation of stress intensity factors for semi-elliptical surface cracks. *Engineering Fracture Mechanics*, 66(4):349–356, 2000.
- [51] Theo Fett. Stress intensity factors and weight functions for special crack problems. Technical report, 1998.
- [52] Theo Fett and Gabriele Rizzi. Weight functions for stress intensity factors and T-stress for oblique cracks in a half-space. *International Journal of Fracture*, 132(1):9–16, 2005.
- [53] W. F. Flanagan, P. Bastias, and B. D. Lichter. Theory of transgranular stress-corrosion cracking. *Acta metallurgica et materialia*, 39(4):695–705, 1991.
- [54] Mars Fontana and Nobert Greene. *Corrosion Engineering*. New York, third edition, 1986.
- [55] F. P. Ford. *Corrosion Processes*. Applied Science Publishers, London, 1982.
- [56] F. P. Ford. *Environmental-induced Cracking of Metals*. NACE, houston, TX, 1990.
- [57] F. P. Ford. Slip dissolution model. In *Corrosion Sous Contrainte*, pages 307–344. 1990.
- [58] F. P. Ford. Quantitative Prediction of Environmentally Assisted Cracking. *Corrosion*, 52(5):375–395, 1996.
- [59] A.J. Forty. *Physical Metallurgy of Stress Corrosion Fracture*. Interscience, 1959.
- [60] J. Genescá, J Mendoza, R Duran, and E Garcia. Conventional Dc Electrochemical Techniques in Corrosion Testing. *XV International Corrosion Congress*, 2002.
- [61] Swati Ghosh, Vishav Preet Singh Rana, Vivekanand Kain, Vivek Mittal, and S.K. Baveja. Role of residual stresses induced by industrial fabrication on stress corrosion cracking susceptibility of austenitic stainless steel. *Materials & Design*, 32(7):3823–3831, 2011.
- [62] F.J. Graham, H.C Brookes, and J.W. Bayles. Nucleation and growth of anodic films on stainless steel alloys. *Journal of applied electrochemistry*, 20:45–53, 1990.
- [63] Taylor Group and Francis. *Analytical Methods in Corrosion Science and Engineering*. Taylor and Francis, New York, 2006.
- [64] H. Hadraba, O. Nemec, and I. Dlouhy. Conversion of transgranular to intergranular fracture in NiCr steels. *Engineering Fracture Mechanics*, 75(12):3677–3691, 2008.
- [65] N. B. Hakiki, S. Boudin, B. Rondot, and M. Da Cunha Belo. The electronic structure of passive films formed on stainless steels. *Corrosion Science*, 37(11):1809–1822, 1995.
- [66] N.E. Hakiki, A.M.P Da Cunha Belo, M, Simoes, and M.G.S. Ferreira. Hakiki, N.E. Da Cunha Belo, M, Simoes, A.M.P. *Journal of The Electrochemical Society*, 145(11):3821–3829, 1998.

- [67] M. M. Hall. An alternative to the Shoji crack tip strain rate equation. *Corrosion Science*, 50(10):2902–2905, 2008.
- [68] D. Hamm, K. Ogle, C.-O. A. Olsson, S. Weber, and D. Landolt. Passivation of Fe-Cr alloys studied with ICP-AES and EQCM. *Corrosion Science*, 44(7):1443–1456, 2002.
- [69] J.D. HARSTON and J.C. Scully. Stress Corrosion of Type 304 Steel in H<sub>2</sub>SO<sub>4</sub>/NaCl Environments at Room Temperature. *CORROSION*, 25(12):493–501, 1969.
- [70] J.D. HARSTON and J.C. Scully. Fractographic observations on the stress corrosion cracking of some austenitic stainless steels in MgCl<sub>2</sub> solutions at 154 C. *Corrosion-NACE*, 26(9):387–395, 1970.
- [71] E.W. Hart. *Surfaces and Interfaces II*. Syracuse University Press, 1968.
- [72] J.J. Harwood. *Stress Corrosion Cracking and Embrittlement*. John Wiley and Sons, 1956.
- [73] K. Hashimoto and K. Asami. An X-ray photo-electron spectroscopic study of the passivity of ferritic 19Cr stainless steels in 1 NHCl. *Corrosion Science*, 19:251, 1979.
- [74] K. Hashimoto, K. Asami, and K. Teramoto. An X-ray photo-electron spectroscopic study on the role of molybdenum in increasing the corrosion resistance of ferritic stainless steels in HCl. *Corrosion Science*, 19(1):3–14, 1979.
- [75] S. Haupt and H. H. Strehblow. A combined surface analytical and electrochemical study of the formation of passive layers on Fe Cr alloys in 0.5 M H<sub>2</sub>SO<sub>4</sub>. *Corrosion Science*, 37(1):43–54, 1995.
- [76] N.J.H Holroyd. *Environmental-Induced Cracking of Metals*. NACE, TX, 1990.
- [77] H.-W. Hoppe, S. Haupt, and H.-H Strehblow. Combined surface analytical and electrochemical study of the formation of passive layers on Fe/Cr alloys in 1 M NaOH. *surface Interface Analysis*, 21:514, 1994.
- [78] J.W. Hutchinson. Singular behaviour at the end of a tensile crack in a hardening material. *Journal of the Mechanics and Physics of Solids*, 16(1):13–31, 1968.
- [79] IAEA. *Stress Corrosion Cracking in Light Water Reactors : Good Practices and Lessons Learned*, volume No. NP-T-3. 2011.
- [80] D.A. Jones. A unified mechanism of stress corrosion and corrosion fatigue cracking. *Metallurgical Transactions A*, 16(A):1133–1141, 1985.
- [81] R. Jones. *Corrosion Mechanisms in Theory and Practice*. page 357. 3rd edition, 2012.
- [82] M.H. Kamdar. Liquid Metal Embrittlement. In ASM, editor, *Failure Analysis and Prevention*, pages 225–238. American Society for Metals,, Metals Park, OH, 1986.
- [83] F. H. Keating. No Title. In *Symposium on Internal Stress in Metals and Alloys.*, page 329, 1948.
- [84] M Keddarn, O. R. Mattos, and H Takenouti. MECHANISM OF ANODIC DISSOLUTION OF IRON-CHROMIUM ALLOYS INVESTIGATED BY ELECTRODE IMPEDANCES-I. EXPERIMENTAL RESULTS AND REACTION MODEL. *Electrochimica Acta*, 31(9):1147–1158, 1986.
- [85] M Keddarn, O. R. Mattos, and H Takenouti. MECHANISM OF ANODIC DISSOLUTION OF IRON-CHROMIUM ALLOYS INVESTIGATED BY ELECTRODE IMPEDANCES-II. ELABORATION OF REACTION MODEL. *Electrochimica Acta*, 31(9):1159–1165, 1986.

- [86] Jeong Kil Kim, Yeong Ho Kim, Jong Sub Lee, and Kyoo Young Kim. Effect of chromium content on intergranular corrosion and precipitation of Ti-stabilized ferritic stainless steels. *Corrosion Science*, 52(5):1847–1852, 2010.
- [87] R. Kirchheim, B. Heine, H. Fischmeister, S. Hofmann, H. Knote, and U. Stolz. The passivity of iron-chromium alloys. *Corrosion Science*, 29(7):899–917, 1989.
- [88] R. Kirchheim, B. Heine, S. Hofmann, and H. Hofmann. Compositional changes of passive films due to different transport rates and preferential dissolution. *Corrosion Science*, 31(C):573–578, 1990.
- [89] B. Ravi Kumar, Raghuvir Singh, Bhupeshwar Mahato, P. K. De, N. R. Bandyopadhyay, and D. K. Bhattacharya. Effect of texture on corrosion behavior of AISI 304L stainless steel. *Materials Characterization*, 54(2):141–147, 2005.
- [90] Kwon, H.S., E.A. Cho, and K.A. Yeom. Prediction of stress corrosion cracking susceptibility of stainless ... *National Association of Corrosion Engineers*, (January):32–40, 2000.
- [91] J. C. Langevoort, T. Fransen, and P. J. Gellings. On the influence of cold work on the oxidation of some stainless steels. *Materials and Corrosion*, 34(10):500–504, 1983.
- [92] R.M. Latanision and H. Opperhauser. The intergranular embrittlement of nickel by hydrogen: The effect of grain boundary segregation. *Metallurgical Transactions A*, 5:483, 1974.
- [93] Jae Bong Lee. Effects of alloying elements, Cr, Mo and N on repassivation characteristics of stainless steels using the abrading electrode technique. *Materials Chemistry and Physics*, 99(2-3):224–234, 2006.
- [94] Shiquiong Li, J.I. Dickson, J.P. Bailon, and D. Tromans. The influence of the stress intensity factor on the fractography of stress corrosion cracking of 316 stainless steel. *Materials Science and Engineering: A*, 119(A119):59–72, 1989.
- [95] H.L. Logan. Film-rupture mechanism of stress corrosion. *Journal of Research of the National Bureau of Standards*, 48(2):99, 1952.
- [96] M.R. Louathan. Initial stages of stress corrosion cracking in austenitic stainless steels. *Corrosion*, 21:289–295, 1965.
- [97] M.R. Louthan. The effect of hydrogen on metals. In F. Mansfeld, editor, *Corrosion Mechanics*, pages 329–365. Marcel Dekker, New York, 1987.
- [98] B. T. Lu, L. P. Tian, R. K. Zhu, J. L. Luo, and Y. C. Lu. Effects of dissolved calcium and magnesium ions on lead-induced stress corrosion cracking susceptibility of nuclear steam generator tubing alloy in high temperature crevice solutions. *Electrochimica Acta*, 56(4):1848–1855, 2011.
- [99] S.P. Lynch. Environmentally assisted cracking: Overview of evidence for an adsorption-induced localised-slip process. *Acta Metallurgica*, 36(10):2639–2661, 1988.
- [100] S.P. Lynch. Metallographic contributions to understanding mechanisms of environmentally assisted cracking. *Metallography*, 23(2):147–171, 1989.
- [101] S.P. Lynch. Comments on "A unified model of environment-assisted cracking". *Scripta Materialia*, 61(3):331–334, 2009.
- [102] S.P. Lynch. Mechanistic and fractographic aspects of stress-corrosion cracking (SCC). In V.S. Raja and T. Shoji, editors, *Stress Corrosion Cracking*, chapter 1, pages 3–89. Woodhead Publishing, 2011.

- [103] D.D. Macdonald. The point defect model for the passive state. *Journal of The Electrochemical Society*, 139:3434, 1992.
- [104] Digby D. Macdonald. *Transient Techniques in Electrochemistry*, volume 126. 1979.
- [105] T. Magnin, A. Chambreuil, and B. Bayle. The corrosion-enhanced plasticity model for stress corrosion cracking in ductile fcc alloys. *Acta Materialia*, 44(4):1457–1470, 1996.
- [106] T. Magnin, a. Chambreuil, and J. P. Chateau. Stress corrosion cracking mechanisms in ductile FCC materials. *International Journal of Fracture*, 79(2):147–163, 1996.
- [107] T. Magnin, R. Chieragatti, and R. Oltra. Mechanism of brittle fracture in a ductile 316 alloy during stress corrosion. *Acta Metallurgica et Materialia*, 38(7):1313–1319, 1990.
- [108] Miroslav Marek. *Stress Corrosion Cracking of Austenitic Stainless Steels*. PhD thesis, 1970.
- [109] P.I Marshall and G.T. Burstein. Effects of alloyed molybdenum on the kinetics of repassivation on austenitic stainless steels. *Corrosion Science*, 24(5):463–478, 1984.
- [110] F Mart, P.De De Tiedra, J.A A Heredero, M.L L Aparicio, C Garcia, F Martin, P.De De Tiedra, J.A A Heredero, and M.L L Aparicio. Effects of prior cold work and sensitization heat treatment on chloride stress corrosion cracking in type 304 stainless steels. *Corrosion Science*, 43(8):1519–1539, 2001.
- [111] F. A. Martin, C. Bataillon, and J. Cousty. In situ AFM detection of pit onset location on a 304L stainless steel. *Corrosion Science*, 50(1):84–92, 2008.
- [112] F.A. Martin, C. Bataillon, and J. Cousty. In situ AFM detection of pit onset location on a 304L stainless steel. *Corrosion Science*, 50:84–92, 2008.
- [113] V. Maurice, WP. Yang, and P. Marcus. XPS and STM Study of Passive Films Formed on Fe<sub>22</sub>Cr<sub>100</sub> Single Crystal Surfaces. *Journal of The Electrochemical Society*, 143(4):1182–1200, 1996.
- [114] V. Maurice, WP. Yang, and P. Marcus. X-Ray Photoelectron Spectroscopy and Scanning Tunneling Microscopy Study of Passive Films Formed on (100) Fe-18Cr-13Ni Single-Crystal Surface. *Journal of Electrochemical Society*, 145(3):909–920, 1998.
- [115] P. McIntyre. The relationships between stress corrosion cracking and sub-critical fl aw growth in hydrogen and hydrogen sulphide gases. In R.W. Staehle, editor, *Stress Corrosion Cracking and Hydrogen Embrittlement of Iron Base Alloys*, pages 788–815. NACE, Houston, TX, 1977.
- [116] E. I. Meletis and R. F. Hochman. The crystallography of stress corrosion cracking in face centered cubic single crystals. *Corrosion Science*, 24(10):843–862, 1984.
- [117] E. I. Meletis and R. F. Hochman. A review of the crystallography of stress corrosion cracking. *Corrosion Science*, 26(1):63–90, 1986.
- [118] D.A. Meyn and E.J. Brooks. Microstructural origin of flutes and their use in distinguishing striationless fatigue cleavage from stress corrosion cracking in titanium alloys. In L.N Gilbertson and R.D. Zipp, editors, *Fractography and Materials Science*, pages 5–29. 1979.
- [119] Nace. *CORROSION ENGINEER ' S REFERENCE Third Edition*. 2002.
- [120] M. Nagai, N. Miura, and M. Shiratori. Stress intensity factor solution for a surface crack with high aspect ratio subjected to an arbitrary stress distribution using the influence function method. *International Journal of Pressure Vessels and Piping*, 131:2–9, 2015.



- [121] K. A. Natarajan. Advances in Corrosion Engineering.
- [122] F. Navai. Effects of tensile and compressive stresses on the passive layers formed on a type 302 stainless steel in a normal sulphuric acid bath. *Journal of Materials Science*, 30(5):1166–1172, 1995.
- [123] F. Navai and O. Debbouz. AES study of passive films formed on a type 316 austenitic stainless-steels in a stress field. *Journal of Materials Science*, 34(5):1073–1079, 1999.
- [124] J C Newman. An empirical stress-intensity factor equation for the surface crack. 15(1), 1981.
- [125] R. C. Newman. Chemistry and Physics of Fracture. page 597. The Netherlands, Dordrecht, 1987.
- [126] R.C. Newman. Developments in the slip-dissolution model of stress corrosion cracking. *Corrosion*, 50(9):682–686, 1994.
- [127] R.C. Newman. Corrosion Mechanisms in Theory and Practice. page 502. CRC Press, 3rd edition, 2012.
- [128] C.J. Novak. *Handbook of Stainless Steels*. New York, 1977.
- [129] K. Ogle. Atomic emission spectroelectrochemistry: A new look at the corrosion, dissolution and passivation of complex materials. *Corrosion and Materials*, 37(3):58–65, 2012.
- [130] K. Ogle. The Electrochemical Stability of Materials, 2nd Edition. Technical report, Chimie ParisTech, Paris, 2013.
- [131] K. Ogle, J. Baeyens, J. Swiatowska, and P. Volovitch. Atomic emission spectroelectrochemistry applied to dealloying phenomena: I. The formation and dissolution of residual copper films on stainless steel. *Electrochimica Acta*, 54(22):5163–5170, 2009.
- [132] K. Ogle, M. Mokaddem, and P. Volovitch. Atomic emission spectroelectrochemistry applied to dealloying phenomena II. Selective dissolution of iron and chromium during active-passive cycles of an austenitic stainless steel. *Electrochimica Acta*, 55(3):913–921, 2010.
- [133] K. Ogle and S. Weber. Anodic Dissolution of 304 Stainless Steel Using Atomic Emission Spectroelectrochemistry. *Journal of The Electrochemical Society*, 147(5):1770, 2000.
- [134] I. Olefjord, B. Brox, and U. Jelvestam. Surface Composition of Stainless Steels during Anodic Dissolution and Passivation Studied by ESCA. *Journal of The Electrochemical Society*, 132(12):2854, 1985.
- [135] R. Olivier. International Committee on Electrochemistry, 6th meeting. page 314, Poitiers, Butterworths, London, 1955.
- [136] C.-O. A. Olsson. Electrochemical Quartz Crystal Microbalance Studies of the Passive Behavior of Cr in a Sulfuric Acid Solution. *Journal of Electrochemical Society*, 147(7):2563–2571, 2000.
- [137] C.-O. A. Olsson and D. Landolt. Passive films on stainless steels - Chemistry, structure and growth. *Electrochimica Acta*, 48(9 SPEC.):1093–1104, 2003.
- [138] Oxford Instruments HKL. *Hkl*. 2007.
- [139] Sarvesh Pal, R. N. Ibrahim, and R. K. Singh Raman. Studying the effect of sensitization on the threshold stress intensity and crack growth for chloride stress corrosion cracking of austenitic stainless steel using circumferential notch tensile technique. *Engineering Fracture Mechanics*, 82:158–171, 2012.

- [140] R.N. Parkins. Predictive approaches to stress corrosion cracking failure. *Corrosion Science*, 20:147–166, 1980.
- [141] R.N. Parkins. Stress corrosion cracking of  $\alpha$ -brass in waters with and without additions. *Metall. Trans.*, 16(A):1671, 1985.
- [142] R.N. Parkins. Factors influencing stress corrosion crack growth kinetics. *Corrosion*, 43(3):130–139, 1987.
- [143] R.N. Parkins. *Environmental-Induced Cracking of Metals*. NACE, Huston, TX, 1990.
- [144] J.H. Payer, D.G. Dippold, and W.H. Fisher. *Material Performance*. 1980.
- [145] S. Pednekar and S. Smialowska. The Effect of Prior Cold Work on the Degree of Sensitization in Type 304 Stainless Steel. *Corrosion*, 36(10), 1980.
- [146] Q. J. Peng, J. Kwon, and T. Shoji. Development of a fundamental crack tip strain rate equation and its application to quantitative prediction of stress corrosion cracking of stainless steels in high temperature oxygenated water. *Journal of Nuclear Materials*, 324(1):52–61, 2004.
- [147] E.N. Pugh. Progress Toward Understanding The Stress Corrosion Problem. *Corrosion*, 41(9):517, 1985.
- [148] Su Il Pyun, Chan Lim, and R. A. Oriani. The role of hydrogen in the pitting of passivating films on pure iron. *Corrosion Science*, 33(3):437–444, 1992.
- [149] L. J. Qiao, K. W. Gao, Alex A. Volinsky, and X. Y. Li. Discontinuous surface cracks during stress corrosion cracking of stainless steel single crystal. *Corrosion Science*, 53(11):3509–3514, 2011.
- [150] W. Ramberg and W.R. Osgood. Description of stress-strain curves by three parameters, Technical Note No 902. Technical report, National Advisory committee For Aeronautics, Washington DC, 1943.
- [151] L. Ratke and W. Gruhi. Modellversuch zum Mechanismus der Spannungsrißkorrosion von AlZnMg-Legierungen. *Materials and Corrosion*, 31(10):768–773, 1980.
- [152] P.A. Rehbinder and E.D. Shchukin. Surface Phenomena in Solids During Deformation and Fracture Processes. In *Progress in Surface Science* 3, pages 97–180, 1972.
- [153] J.R. Rice and G.F. Rosengren. Plane strain deformation near a crack tip in a power-law hardening material. *Journal of the Mechanics and Physics of Solids*, 16(1):1–12, 1968.
- [154] Pierre R Roberge and R Pierre. *Handbook of Corrosion Engineering Library of Congress Cataloging-in-Publication Data*. 1999.
- [155] David Roylance. *Introduction to Fracture Mechanics*. Cambridge, 2001.
- [156] J.L. Rudd and T.D. Gary. Quantification of fastener-hole quality. *Journal of Aircraft*, 15(3):143–147, 1978.
- [157] A.J. Russell and D. Tromans. Stress corrosion cracking of austenitic steels—Region II behavior. *Metallurgical Transactions A*, 12(4):613–621, 1981.
- [158] M.P. Ryan, D.E. Williams, R.J. Chater, B.M. Hutton, and D.D. MCPheil. Why stainless steel corrodes. *Nature*, 415(6873):770–774, 2002.

- [159] Lee Sang-Kwon, K. Daniel, and M. Digby D. On the shape of stress corrosion cracks in sensitized Type 304 SS in Boiling Water Reactor primary coolant piping at 288 °C. *Journal of Nuclear Materials*, 454(1-3):359–372, 2014.
- [160] W Schwenk and A Rahmel. Experimentelle Befunde und Diskussion über den Mechanismus der Passivschichtbildung auf Chrom-Nickel-Stählen. *Electrochemical Acta*, 5:180–201, 1961.
- [161] J. C. Scully. Stress corrosion crack propagation: A constant charge criterion. *Corrosion Science*, 15(4):207–224, 1975.
- [162] J.C Scully. Mechanism of dissolution-controlled cracking. *Metal Science*, 12(6):290–300, 1978.
- [163] K. Shiobara, Y. Sawada, and S Morioka. Potentiostatic Study on the Anodic Behaviour of Iron-Chromium Alloys. *Journal of the institute of metals*, 6:58, 1965.
- [164] T. Shoji, Z. Lu, and H. Murakami. Formulating stress corrosion cracking growth rates by combination of crack tip mechanics and crack tip oxidation kinetics. *Corrosion Science*, 52(3):769–779, 2010.
- [165] K. Sieradzki and R. C. Newman. Brittle behavior of ductile metals during stress-corrosion cracking. *Philosophical Magazine A*, 51(1):95–132, 1985.
- [166] Elzbieta Sikora and D.D Macdonald. The Passivity of Iron in the Presence of Ethylenediaminetetraacetic Acid I. General Electrochemical Behavior. *Journal of Electrochemical Society*, 147(11):4087–4092, 2000.
- [167] J.M. Silcock and P.R. Swann. *Environment Sensitive Fracture of Engineering Materials*. The Metallurgical Society, 1979.
- [168] H. Silman. *Corrosion and Corrosion Control: An introduction to corrosion science and engineering*, volume 7. 2008.
- [169] Spectro. *SPECTROMAXx mode emploi.pdf*. 2009.
- [170] D. T. Spencer, M. R. Edwards, M. R. Wenman, C. Tsitsios, G. G. Scatigno, and P. R. Chard-Tuckey. The initiation and propagation of chloride-induced transgranular stress-corrosion cracking (TGSCC) of 304L austenitic stainless steel under atmospheric conditions. *Corrosion Science*, 88:76–88, 2014.
- [171] Roger W. Staehle. Transient stability of passive films in aqueous solutions. *Corrosion Science*, 49(1):7–19, 2007.
- [172] R.W. Staehle. Theory of Stress Corrosion Cracking in Alloys. page 233. North Atlantic Treaty Organization, 1971.
- [173] R.W. Staehle. Stress Corrosion Cracking and Hydrogen Embrittlement of Iron Based Alloys. page 180. National Association of Corrosion Engineers, 1977.
- [174] R.W. Staehle. Historical views on stress corrosion cracking of nickel-based alloys: The Coriou effect. In *Stress Corrosion Cracking of Nickel Based Alloys in Water-cooled Nuclear Reactors*, pages 3–131. 2016.
- [175] Milton Stern. Evidence for a Logarithmic Oxidation Process for Stainless Steel in Aqueous Systems. *Journal of Electrochemical Society*, 106(5):376–381, 1959.
- [176] A.N. Stroh. The formation of cracks in Plastic flow. II. *Proceedings of the Royal Society of London*, 232(1191):548–560, 1955.

- [177] A.N. Stroh. The strength of Lomer-Cottrell Sessile Dislocations. *Philosophical Magazine*, 6:489–502, 1957.
- [178] A.M. Stroth. A theory on the fracture of metals. *Advances in Physics*, 6:418, 1957.
- [179] T.L. Sudesh, L. Wijesinghe, and Daniel John Blackwood. Real time pit initiation studies on stainless steels: The effect of sulphide inclusions. *Corrosion Science*, 49(4):1755–1764, 2007.
- [180] P.R. Swann and J.D. Embury. *High Strength Materials*. John Wiley and Sons, 1965.
- [181] X. Tang and Y. F. Cheng. Micro-electrochemical characterization of the effect of applied stress on local anodic dissolution behavior of pipeline steel under near-neutral pH condition. *Electrochimica Acta*, 54(5):1499–1505, 2009.
- [182] D. Tromans and J. Nutting. Stress corrosion cracking of Face-centered-cubic alloys. *Corrosion*, 21(5):143–159, 1965.
- [183] A. Turnbull. Stress Corrosion Cracking: Mechanisms. In *Encyclopedia of Materials: Science and Technology*, chapter Stress Cor, pages 8886–8891. Elsevier Inc, Teddington, 2001.
- [184] A. Turnbull, L. N. McCartney, and S. Zhou. A model to predict the evolution of pitting corrosion and the pit-to-crack transition incorporating statistically distributed input parameters. *Corrosion Science*, 48:2048–2105, 2006.
- [185] A. Turnbull, L. Wright, and L. Crocker. New insight into the pit-to-crack transition from finite element analysis of the stress and strain distribution around a corrosion pit. *Corrosion Science*, 52(4):1492–1498, 2010.
- [186] A. Turnbull and S. Zhou. Pit to crack transition in stress corrosion cracking of a steam turbine disc steel. *Corrosion Science*, 46(5):1239–1264, 2004.
- [187] D.A. Vermilyea. *Stress Corrosion Cracking and Hydrogen Embrittlement of Iron Based Alloys*. National Association of Corrosion Engineers, 1977.
- [188] V. Vignal, R. Oltra, M. Verneau, and L. Coudreuse. Influence of an elastic stress on the conductivity of passive films. *Materials Science and Engineering A*, 303(1-2):173–178, 2001.
- [189] S. Virtanen, P. Schmuki, H. Bohni, P. Vuoristo, and T. Mantylat. ARTIFICIAL CR-OXIDE AND FE-OXIDE PASSIVE LAYERS PREPARED BY SPUTTER-DEPOSITION. *Journal of The Electrochemical Society*, 142(9):3067–3072, 1995.
- [190] B. Vuillemin, X. Philippe, R. Oltra, V. Vignal, L. Coudreuse, L. C. Dufour, and E. Finot. SVET, AFM and AES study of pitting corrosion initiated on MnS inclusions by microinjection. *Corrosion Science*, 45(6):1143–1159, 2003.
- [191] R.J.H. Wanhill, R.T. Byrnes, and C.L. Smith. *Stress Corrosion Cracking*. Woodhead Publishing, Philadelphia, PA 19102-3406, USA, 1st edition, 2011.
- [192] David E. Williams, Matt R. Kilburn, John Cliff, and Geoffrey I N Waterhouse. Composition changes around sulphide inclusions in stainless steels, and implications for the initiation of pitting corrosion. *Corrosion Science*, 52(11):3702–3716, 2010.
- [193] R. E. Williford, C. F. Windisch, and R. H. Jones. In situ observations of the early stages of localized corrosion in Type 304 SS using the electrochemical atomic force microscope. *Materials Science and Engineering A*, 288(1):54–60, 2000.

- [194] Q. Wu and M. A. Zikry. Microstructural modeling of transgranular and intergranular fracture in crystalline materials with coincident site lattice grain-boundaries:  $\sigma_3$  and  $\sigma_{17b}$  bicrystals. *Materials Science and Engineering A*, 661:32–39, 2016.
- [195] T.N. Yama and M. TAKano. Direct observation of stress corrosion crack tips of 304 stainless steel in a boiling 42 % MgCl<sub>2</sub> solution. *Corrosion-NACE*, 37(4):226–231, 1981.
- [196] W.P. Yang, D. Costa, and P. Marcus. Chemical Composotion, Chemical States, and REsistance to Localized Corrosion of Passive Films on an Fe17Cr Alloy. *Journal of The Electrochemical Society*, 141(1):111–116, 1994.
- [197] A. Zareei and S.M. Nabavi. Calculation of stress intensity factors for circumferential semi-elliptical cracks with high aspect ratio in pipes. *International Journal of Pressure Vessels and Piping*, 146:32–38, 2016.
- [198] Longkui Zhu, Yu Yan, Jinxu Li, Lijie Qiao, Zhengcao Li, and Alex A. Volinsky. Stress corrosion cracking at low loads: Surface slip and crystallographic analysis. *Corrosion Science*, 100:619–626, 2015.

## Dégradation de l'acier inoxydable 304L en milieux acides : Influence des contraintes sur la cinétique de passivation et les mécanismes de fissuration à l'échelle cristalline

**RESUME :** Une approche expérimentale mettant en œuvre des techniques électrochimiques et mécaniques a été utilisée pour étudier la corrosion sous contrainte (CSC) de l'acier inoxydable 304L dans des électrolytes acides (0,5-5 M  $\text{H}_2\text{SO}_4$ ) avec et sans chlorure. La CSC a été réalisée dans le but d'étudier les aspects cristallographique et cinétique de la rupture. La microscopie électronique à balayage a dévoilé, d'une part, des traces successives au niveau des plans de glissement sur les facettes de la fissure, et d'autre part une vitesse non-linéaire de la fissuration. Une méthode a été proposée pour accéder à la cristallographie de fissuration en utilisant la diffraction d'électrons rétrodiffusés (EBSD). Il a été démontré que les ruptures préférentielles s'effectuent au niveau des plans {110} pour 48% du temps et 37% pour des plans {111}. Ces résultats soutiennent les modèles récents de la CSC, tels que la plasticité localisée rehaussée par la corrosion. Les profils d'évolution de la contrainte appliquée/résiduelles ont été déterminés par diffraction des rayons X avant et après CSC. Ces analyses serviront à développer un modèle de rupture micro-mécanique. Lors des essais potentiodynamiques optimisés de corrosion, les taux de dissolution élémentaires et le courant total ont été mesurés en combinant une cellule d'écoulement électrochimique et l'analyse des produits de corrosion par spectroscopie d'émission atomique à plasma à couplage inductif. Ces résultats ont été utilisés, pour séparer la partie de courant consacré à la formation de la couche passive du courant total. Le modèle de conduction ionique sous tension élevée a été mis à jour pour calculer le taux de passivation et l'épaisseur de la couche passive. Les contraintes dans le matériau expliquent une différence mesurable de la cinétique de croissance du film passif et de son épaisseur.

**Mots clés :** corrosion sous contrainte, cristallographie, passivation, milieu acide, acier inoxydable, 304L, plans de rupture, fissure elliptique, DRX, microscopie électronique à balayage, la diffraction d'électrons rétrodiffusés, spectroscopie d'émission atomique.

### Degradation of 304L stainless steel in acidic solutions: Influence of stress on passivation kinetics, and cracking mechanisms at crystallographic scale.

**ABSTRACT :** A multidisciplinary experimental approach of electrochemical and mechanical techniques was employed to study the corrosion of different stress states of 304L stainless steel in acidic electrolytes (0.5-5 M  $\text{H}_2\text{SO}_4$ ) with and without chloride additives. Stress corrosion cracking (SCC) conditions were applied to evidence cracking crystallographical and propagation aspects. Scanning electron microscopy of SCC revealed clear traces of successive slipping planes and consequent dissolutions on the crack facets and nonlinear crack propagation kinetics. A method was proposed to access cracking crystallography using electron backscatter diffraction. It demonstrated {110} and {111} preferential cracking planes in proportion of about 48% and 37% respectively, which supports recent SCC models such as corrosion enhanced localized plasticity. The profiles of (applied/residual) stress evolution measured by X-ray diffraction before and after SCC were used as an introduction to establish a micro-mechanical cracking model. During optimized potentiodynamic corrosion tests, elemental dissolution rates and total current transients were measured by combining electrochemical flow cell and downstream solution analysis by inductively coupled plasma atomic emission spectroscopy. The results were used to separate the current portion spent on passive film formation from the total current. The high field ion conduction model was upgraded to calculate the constructed passive film thickness and passivation rate. The applied stress caused a measurable difference in passive film growth kinetics and its thickness.

**Keywords :** stress corrosion cracking, crystallography, passivation, acidic solution, stainless steel, 304L, fracture, cracking planes, elliptical cracks, electrochemistry, X-ray diffraction, scanning electron microscopy, electron backscatter diffraction, atomic emission spectroscopy.